FIBER BRAGG GRATINGS

RAMAN KASHYAP

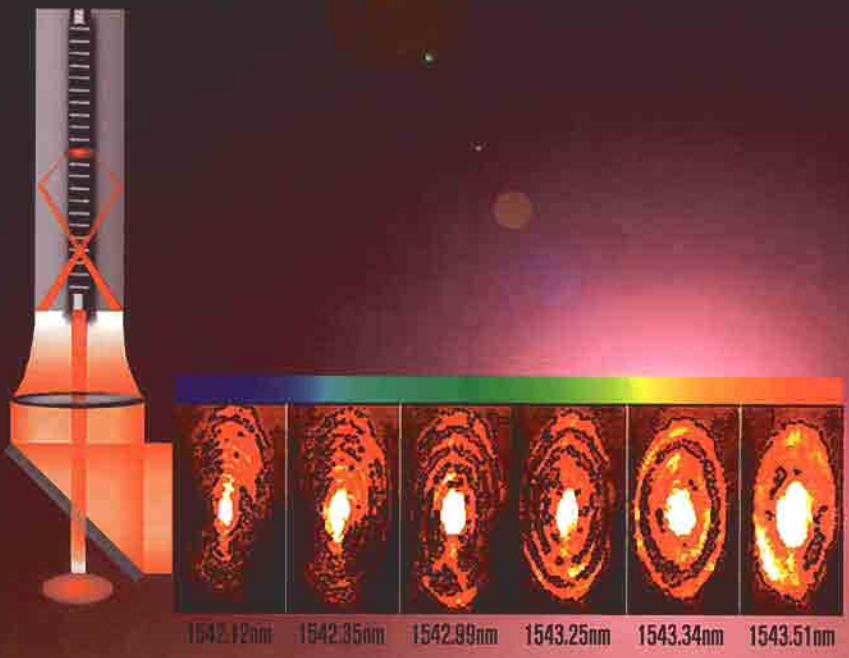

OPTICS AND PHOTONICS

Fiber Bragg Gratings

OPTICS AND PHOTONICS

(formerly Quantum Electronics)

EDITED BY

PAUL L. KELLY

Tufts University
Medford, Massachusetts

IVAN KAMINOW

Lucent Technologies
Holmdel, New Jersey

GOVIND AGRAWAL

University of Rochester
Rochester, New York

A complete list of titles in this series appears at the end of this volume.

Fiber Bragg Gratings

Raman Kashyap
BT Laboratories, Martlesham Heath
Ipswich, United Kingdom

ACADEMIC PRESS

San Diego London Boston
New York Sydney Tokyo Toronto

The cover picture shows the near-field photographs of radiation mode patterns of several low-order counterpropagating modes (LP_{0n}). These are excited by the forward propagating core mode in a 6-mm-long, side-tap grating with a 2° blaze angle, written into the core of a single mode fiber. *Artwork by Arjun Kashyap.*

This book is printed on acid-free paper. ♾

ACADEMIC PRESS
a division of Harcourt Brace & Company
525 B Street, Suite 1900, San Diego, CA 92101-4495, USA
http://www.apnet.com

ACADEMIC PRESS
24-28 Oval Road, London, NW1 7DX, UK
http://www.hbuk.co.uk/ao/

Library of Congress Catalog Card Number: 99-60954

International Standard Book Number: 0-12-400560-8

Printed in the United States of America
99 00 01 02 03 IP 9 8 7 6 5 4 3 2 1

For Monika, Hannah, and in memory of
Prof. Kedar Nath Kashyap

This page intentionally left blank

Contents

This page intentionally left blank

Preface

The field of fiber Bragg gratings is almost exactly twenty years old, dating back to its discovery by Ken Hill and co-workers in Canada. It grew slowly at first, but an important technological advance by Gerry Meltz and co-workers 10 years later, renewed worldwide interest in the subject. I was instrumental in setting up the first International Symposium on photosensitivity of optical fibers, jointly with Francois Ouellette in 1991, a meeting with 22 presentations and attended by approximately 50 researchers. Since, we have seen three further international conferences solely devoted to fiber Bragg gratings, the last of which was attended by approximately 300 researchers. As the applications of Bragg gratings are numerous, publications appear in widely differing conferences and journals. Surprisingly, apart from several review articles covering the most elementary aspects, no monograph is available on the subject and the quantity of available literature is spread across a number of specialist journals and proceedings of conferences. Thus, progress and the current state of the art are difficult to track, despite the approaching maturity of the field. More recently, poling of glass optical fibers has resulted in an electro-optic coefficient almost rivaling that of lithium niobate.

Germanium, the core dopant of low loss, fused silica optical fiber, is a rich defect former; ultraviolet radiation can strongly modify the nature of the defects causing large changes in the local refractive index. The mechanisms contributing to photosensitivity are complicated and still being debated. They depend on the types of defects present, dopants, and the presence of hydrogen whether in the molecular or in the ionic state. The lack of a thorough understanding has not, however, prevented the exploitation of the effect in a large number of applications. The very large index changes reported to date (~0.03) allow, for the first time, the fabrication of ultra-short (~100 μm long) broadband, high-reflectivity Bragg gratings in optical fibers. The maximum index change may be an

order of magnitude larger still, leading to many more exciting possibilities. There are a number of methods of the holographic inscription of Bragg gratings, with the phase-mask technique holding a prominent position.

This book was born as a result of growing demands for yet more review articles on the subject. It aims to fill the gap by bringing together the fundamentals of fiber gratings, their specific characteristics, and many of the applications. The book covers much of the fundamental material on gratings and should be of interest to beginners, advanced researchers, as well as those interested in the fabrication of many types of gratings.

It is impossible to cover the massive advances made in this field in a book of this size, a field that continues to grow at an enormous rate despite recent commercialization. A large reference list is provided, to allow the interested reader to seek out specific topics in more detail. The purpose of this book is therefore to introduce the reader to the extremely rich area of the technology of fiber Bragg, with a view to providing insight into some of the exciting prospects. It begins with the principles of fiber Bragg gratings, photosensitization of optical fibers, Bragg grating fabrication, theory, properties of gratings, and specific applications, and concludes with measurement techniques.

BT Laboratories,
Ipswich IP5 3RE,
United Kingdom
July 1998

Raman Kashyap

Acknowledgments

I am grateful to many individuals who have either directly contributed to the book or so generously provided material for it. I thank the members of the European ACTS Program, PHOTOS, whose efforts have greatly contributed to the growing knowledge in this area. In particular, I am indebted to Marc Douay, Bertrand Poumellec, René Salathe, Pierre Sansonetti, Isabelle Riant, Fatima Bhakti, Hans Limberger, and Christian Bungarzaneau, for providing several original exemplary figures and simulations. I thank Ken Hill, Jacques Albert, Stanislav Chernikov, Turan Erdogan, Phillip Russell, Feodor Timofeev, Malin Permanante, Raoul Stubbe, Vince Handerek, Sotiris Kanellopoulos, Tom Strasser, Peter Krug, Takashi Mizuochi, Nadeem Rizvi, Doug Williams, Alistair Poustie, Steve Kershaw, and Mike Brierley for their assistance with figures, Arjun Kashyap for the arrangement on the front cover, and others who have also provided data for inclusion in the book.

Melanie Holmes's vast contribution on radiation mode coupling is humbly acknowledged. I especially thank her for the many philosophical discussions, fun arguments and Mars bars exchanged on the subject! Jenny Massicott has generously contributed and provided significant help with the section on gain controlled amplifiers. 'Thanks' must go to Richard Wyatt for reading the manuscript so quickly and Marcello Segatto for his many constructive comments.

A special thank you to Domenico Giannone for his painstaking and careful reading of parts of the manuscript, and to Hans Georg Fröhlich and Simon Wolting for undertaking fun experiments during their summer student-ships. Monica de Lacerda-Rocha provided numerous measurements on chirped gratings. Walter Margulis and Isabel Cristina Carvalho are acknowledged for the amusing times in the lab in Rio, proving that writing in-fiber gratings on a piece of Amazonian hardwood "optical bench" is easy, even late at night! Bernhard Lesche and Isabel Cristina Carvalho

contributed to interesting discussions during the writing of the book. Martin Burley kept me amused with his music and sense of humor during the lulls in writing.

The IEEE, IEE, OSA and Elsevier Science are acknowledged for provision of copyright permission on several figures. I also gratefully acknowledge D. W. Smith of BT Laboratories for his generous support and provision of computer facilities for the production of the manuscript.

Finally, I am deeply appreciative of Monika and Hannah, whose unquestioning patience, support and provision of earthly comforts formed essential ingredients in the birth of this book.

Fiber Bragg Gratings

This page intentionally left blank

Chapter 1

Introduction

Optical fibers have revolutionized telecommunication. Much of the success of optical fiber lies in its near-ideal properties: low transmission loss, high optical damage threshold, and low optical nonlinearity. The combination of these properties has enabled long-distance communication to become a reality. At the same time, the long lengths enabled the optical power to interact with the small nonlinearity to give rise to the phenomenon of optical solitons, overcoming the limit imposed by linear dispersion. The market for optical fiber continues to grow, despite the fact that major trunk routes and metropolitan areas have already seen a large deployment of fiber. The next stage in the field of communication is the mass delivery of integrated services, such as home banking, shopping, Internet services, and entertainment using video-on-demand. Although the bandwidth available on single mode fiber should meet the ever-increasing demand for information capacity, architectures for future networks need to exploit technologies which have the potential of driving down cost to make services economically viable. Optical fiber will have to compete with other transport media such as radio, copper cable, and satellite. Short-term economics and long-term evolutionary potential will determine the type of technology likely to succeed in the provision of these services. But it is clear that optical fibers will play a crucial role in communication systems of the future. The technological advances made in the field of photosensitive optical fibers are relatively recent; however, an increasing number of fiber devices based on this technology are getting nearer to the market place. It is believed that they will provide options to the network designer that should influence, for example, the deployment of wavelength-divi-

sion-multiplexed (WDM) systems, channel selection, and deployment of transmitters in the upstream path in a network, and should make routing viable. The fascinating technology of photosensitive fiber is based on the principle of a simple in-line all-fiber optical filter, with a vast number of applications to its credit.

1.1 Historical perspective

Photosensitivity of optical fiber was discovered at the Canadian Communication Research Center in 1978 by Ken Hill *et al.* [1] during experiments using germania-doped silica fiber and visible argon ion laser radiation. It was noted that as a function of time, light launched into the fiber was increasingly reflected. This was recognized to be due to a refractive index grating written into the core of the optical fiber as a result of a standing wave intensity pattern formed by the 4% back reflection from the far end of the fiber and forward-propagating light. The refractive index grating grew in concert with the increase in reflection, which in turn increased the intensity of the standing wave pattern. The periodic refractive index variation in a meter or so of fiber was a Bragg grating with a bandwidth of around 200 MHz. But the importance of the discovery in future applications was recognized even at that time. This curious phenomenon remained the preserve of a few researchers for nearly a decade [2,3]. The primary reason for this is believed to be the difficulty in setting up the original experiments, and also because it was thought that the observations were confined to the one "magic" fiber at CRC. Further, the writing wavelength determined the spectral region of the reflection grating, limited to the visible part of the spectrum.

Researchers were already experimenting and studying the even more bizarre phenomenon of second-harmonic generation in optical fibers made of germania-doped silica, a material that has a zero second-order nonlinear coefficient responsible for second-harmonic generation. The observation was quite distinct from another nonlinear phenomenon of sum-frequency generation reported earlier by Ohmori and Sasaki [4] and Hill *et al.* [5], which were also curious. Ulf Österberg and Walter Margulis [6] found that ML-QS infrared radiation could "condition" a germania doped-silica fiber after long exposure such that second-harmonic radiation grew (as did Ken Hill's reflection grating) to nearly 5% efficiency and was soon identified to be a grating formed by a nonlinear process [7,8]. Julian

Stone's [9] observation that virtually any germania-doped silica fiber demonstrated a sensitivity to argon laser radiation reopened activity in the field of fiber gratings [10,11] and for determining possible links between the two photosensitive effects. Bures *et al.* [12] had pointed out the two-photon absorption nature of the phenomenon from the fundamental radiation at 488 nm.

The major breakthrough came with the report on holographic writing of gratings using single-photon absorption at 244 nm by Gerry Meltz *et al.* [13]. They demonstrated reflection gratings in the visible part of the spectrum (571–600 nm) using two interfering beams external to the fiber. The scheme provided the much-needed degree of freedom to shift the Bragg condition to longer and more useful wavelengths, predominantly dependent on the angle between the interfering beams. This principle was extended to fabricate reflection gratings at 1530 nm, a wavelength of interest in telecommunications, also allowing the demonstration of the first fiber laser operating from the reflection of the photosensitive fiber grating [14]. The UV-induced index change in untreated optical fibers was $\sim 10^{-4}$. Since then, several developments have taken place that have pushed the index change in optical fibers up a hundredfold, making it possible to create efficient reflectors only a hundred wavelengths long. Lemaire and coworkers [15] showed that the loading of optical fiber with molecular hydrogen photosensitized even standard telecommunication fiber to the extent that gratings with very large refractive index modulation could be written.

Pure fused silica has shown yet another facet of its curious properties. It was reported by Brueck *et al.* [16] that at 350°C, a voltage of about 5 kV applied across a sheet of silica, a millimeter thick, for 30 minutes resulted in a permanently induced second-order nonlinearity of ~1 pm/V. Although poling of optical fibers had been reported earlier using electric fields and blue-light and UV radiation [17–19], Wong *et al.* [20] demonstrated that poling a fiber while writing a grating with UV light resulted in an enhanced electro-optic coefficient. The strength of the UV-written grating could be subsequently modulated by the application of an electric field. More recently, Fujiwara *et al.* reported a similar photoassisted poling of bulk germanium-doped silica glass [21]. The silica–germanium system will no doubt produce further surprises.

All these photosensitive processes are linked in some ways but can also differ dramatically in their microscopic detail. The physics of the effect continues to be debated, although the presence of defects plays a

central role in more than one way. The field remains an active area for research.

1.2 Materials for glass fibers

Optical fiber for communications has evolved from early predictions of lowest loss in the region of a few decibels per kilometer to a final achieved value of only 0.2 dB km^{-1}. The reason for the low optical loss is several fortuitous material properties. The bandgap of fused silica lies at around 9 eV [22], while the infrared vibrational resonances produce an edge at a wavelength of around 2 microns. Rayleigh scatter is the dominant loss mechanism with its characteristic λ^{-4} dependence in glass fibers indicating a near perfect homogeneity of the material [23]. The refractive index profile of an optical fiber is shown in Fig. 1.1. The core region has a higher refractive index than the surrounding cladding material, which is usually made of silica. Light is therefore trapped in the core by total internal reflection at the core–cladding boundaries and is able to travel tens of kilometers with little attenuation in the 1550-nm wavelength region. One

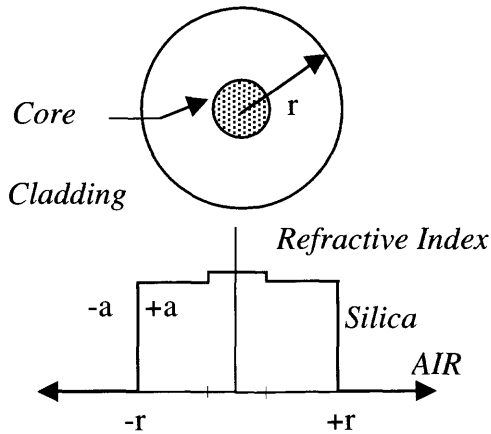

Figure 1.1: Cross-section of an optical fiber with the corresponding refractive index profile. Typically, the core-to-cladding refractive index difference for single-mode telecommunications fiber at a wavelength of 1.5 μm is $\sim 4.5 \times 10^{-3}$ with a core radius of 4 μm.

of the commonly used core dopants, germanium, belongs to Group IVA, as does silicon and replaces the silicon atom within the tetrahedron, coordinated with four oxygen atoms. Pure germania has a band edge at around 185 nm [24]. Apart from these pure material contributions, which constitute a fundamental limit to the attenuation characteristics of the waveguide, there may be significant absorption loss from the presence of impurities. The OH^- ion has IR absorptions at wavelengths of 1.37, 0.95, and 0.725 μm [25], overtones of a stretching-mode vibration at a fundamental wavelength of 2.27 μm. Defect states within the ultraviolet and visible wavelength band of 190–600 nm [26] also contribute to increased absorption. The properties of some of these defects will be discussed in Chapter 2.

The presence of phosphorus as P_2O_5 in silica, even in small quantities ($\sim$0.1%), reduces the glass melting point considerably, allowing easier fabrication of the fiber. Phosphorus is also used in fibers doped with rare earth compounds such as Yb and Er for fiber amplifiers and lasers. In high concentration rare earth ions tend to cluster in germanium-doped silicate glasses. Clustering causes ion–ion interaction, which reduces the excited state lifetimes [27]. Along with aluminum (Al_2O_3 as a codopant in silica) in the core, clustering is greatly reduced, enabling efficient amplifiers to be built. Phosphorus is also commonly used in planar silica on silicon waveguide fabrication, since the reduced processing temperature reduces the deformation of the substrate [28].

Fluorine and trivalent boron (as B_2O_3) are other dopants commonly used in germania-doped silica fiber. A major difference between germanium and fluorine/boron is that while the refractive index increases with increasing concentration of germanium, it decreases with boron/fluorine. With fluorine, only modest reductions in the refractive index are possible ($\sim$0.1%), whereas with boron large index reductions ($>$0.02) are possible. Boron also changes the topology of the glass, being trivalent. Boron and germanium together allow a low refractive index difference between the core and cladding to be maintained with large concentrations of both elements [29]. On the other hand, a depressed cladding fiber can be fabricated by incorporating boron in the cladding to substantially reduce the refractive index.

The density of the boron-doped glass may be altered considerably by annealing, by thermally cycling the glass, or by changing the fiber drawing temperature [30]. Boron-doped preforms exhibit high stress and shatter easily unless handled with care. The thermal history changes the density

and stress in the glass, thereby altering the refractive index. The thermal expansion of boron–silica glass is $\sim 4 \times 10^{-6\circ}C^{-1}$, several times that of silica ($7 \times 10^{-7\circ}C^{-1}$) [31]. Boron-doped silica glass is generally free of defects, with a much reduced melting temperature. Boron being a lighter atom, the vibrational contribution to the absorption loss extends deeper into the short wavelength region and increases the absorption loss in the 1500-nm window. Boron with germanium doping has been shown to be excellent for photosensitivity [29].

1.3 Origins of the refractive index of glass

The refractive index n of a dielectric may be expressed as the summation of the contribution of i oscillators of strength f_i each, as [32]

$$\frac{n^2 - 1}{n^2 + 2} = \frac{4\pi}{3} \frac{e^2}{m\varepsilon_0} \sum_i \frac{f_i}{\omega_i^2 - \omega^2 + i\Gamma_i\omega}, \tag{1.1.1}$$

where e and m are the charge and mass of the electron, respectively, ω_i is the resonance frequency, and Γ_i is a damping constant of the ith oscillator. Therefore, refractive index is a complex quantity, in which the real part contributes to the phase velocity of light (the propagation constant), while the sign of the imaginary part gives rise to either loss or gain. In silica optical fibers, far away from the resonances of the deep UV wavelength region, which contribute to the background refractive index, the loss is negligible at telecommunications wavelengths. However, the presence of defects or rare-earth ions can increase the absorption, even within in the transmission windows of 1.3 to 1.6 microns in silica optical fiber.

Γ_i can be neglected in low-loss optical fibers in the telecommunications transmission band, so that the real part, the refractive index, is [32]

$$n^2 = 1 + \sum_i \frac{A_i\lambda^2}{\lambda^2 - \lambda_i^2}. \tag{1.1.2}$$

With $i = 3$, we arrive at the well-known Sellmeier expression for the refractive index, and for silica (and pure germania), the λ_i ($i = 1 \rightarrow 3$) are the electronic resonances at 0.0684043 (0.0690) and 0.1162414 (0.1540) μm, and lattice vibration at 9.896161 (11.8419) μm. Their strengths A_i have been experimentally found to be 0.6961663 (0.8069),

0.4079426 (0.7182), and 0.8974794 (0.8542) [33,34], where the data in parentheses refers to GeO_2. The group index N is defined as

$$N = n - \lambda \frac{dn}{d\lambda}, \tag{1.1.3}$$

which determines the velocity at which a pulse travels in a fiber. These quantities are plotted in Fig. 1.2, calculated from Eqs. (1.1.2) and (1.1.3). We note that the refractive index of pure silica at 244 nm at 20°C is 1.51086. The data for germania-doped silica may be found by interpolation of the data for the molar concentration of both materials. Although this applies to the equilibrium state in bulk samples, they may be modified by the fiber fabrication process.

The change in the refractive index of the fiber at a wavelength λ may be calculated from the observed changes in the absorption spectrum in the ultraviolet using the Kramers–Kronig relationship [32,35],

$$\Delta n(\lambda) = \frac{1}{(2\pi)^2} \sum_i \int_{\lambda_2}^{\lambda_1} \frac{(\Delta\alpha_i(\lambda') \cdot \lambda^2)}{(\lambda^2 - \lambda'^2)} d\lambda', \tag{1.1.4}$$

where the summation is over discrete wavelength intervals around each of the i changes in measured absorption, α_i. Therefore, a source of photoinduced change in the absorption at $\lambda_1 \leq \lambda' \leq \lambda_2$ will change the refractive index at wavelength λ.

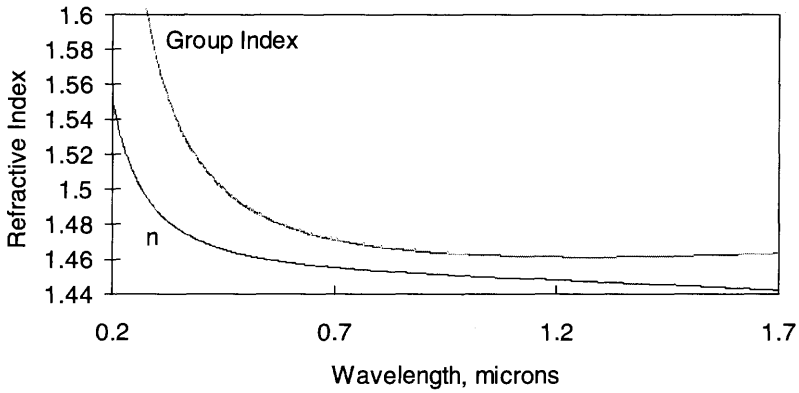

Figure 1.2: Refractive index n and the group index, N of pure silica at 20°C.

The refractive index of glass depends on the density of the material, so that a change in the volume through thermally induced relaxation of the glass will lead to a change Δn in the refractive index n as

$$\frac{\Delta n}{n} \approx \frac{\Delta V}{V} \approx \frac{3n}{2}\varepsilon, \tag{1.1.5}$$

where the volumetric change ΔV as a fraction of the original volume V is proportional to the fractional change ε in linear dimension of the glass.

We now have the fundamental components that may be used to relate changes in the glass to the refractive index after exposure to UV radiation.

Other interesting data on fused silica is its softening point at 2273°C, and the fact that it probably has the largest elastic limit of any material, ~17%, at liquid nitrogen temperatures [36].

1.4 Overview of chapters

The book begins with a simple introduction to the photorefractive effect as a comparison with photosensitive optical fibers in Chapter 2. The interest in electro-optic poled glasses is fueled from two directions: an interest in the physics of the phenomenon and its connection with photosensitive Bragg gratings, and as the practical need for devices that overcome many of the fabrication problems associated with crystalline electro-optic materials, of cutting, polishing, and in–out coupling. A fiber-compatible device is an ideal, which is unlikely to be abandoned. The fiber Bragg grating goes a long way in that direction. However interesting the subject of poled glasses and second-harmonic generation in glass optical fibers and nonlinear behavior of gratings, they are left for another time. With this connection left for the moment, we simply point to the defects, which are found to be in common with the process of harmonic generation, poling of glass, and Bragg gratings. The subject of defects alone is a vast spectroscopic minefield. Some of the prominent defects generally found in germania-doped fused silica that have a bearing on Bragg grating formation are touched upon. The nature and detection of the defects are introduced. This is followed by the process of photosensitizing optical fibers, including reduced germania, boron–germanium codoped fibers, Sn doping, and hydrogen loading. The different techniques and routes used to enhance the sensitivity of optical fibers,

including that of rare-earth doped fibers are compared in a summary at the end of Chapter 2.

Chapter 3 is on fabrication of Bragg gratings. It deals with the principles of holographic, point-by-point replication and the technologies involved in the process: various arrangements of the Lloyd and mirror interferometers, phase-mask, along with the fabrication of different type of Bragg and long-period gratings, chirped gratings, and ultralong gratings. The attributes of some of the laser sources commonly used for fabrication are introduced in the concluding section of the chapter.

Chapter 4 begins with wave propagation in optical fibers, from the polarization response of a dielectric to coupled mode theory, and formulates the basic equations for calculating the response of uniform gratings. A section follows on the side-tap gratings, which have special applications as lossy filters. Antenna theory is used to arrive at a good approximation to the filter response for the design of optical filters. Long-period gratings and their design follow, as well as the physics of rocking filters. The last section deals with grating simulation. Here two methods for the simulation of gratings of arbitrary profile and chirp based on the transfer-matrix approach and Rouard's method of thin films are described.

Chapter 5 looks in detail at the different methods available for apodization of Bragg gratings and its effect on the transfer characteristics. These include the use of the phase mask, double exposure, stretching methods, moiré gratings, and novel schemes that use the coherence properties of lasers to self-apodize gratings.

Chapter 6 introduces the very large area of band-pass filtering to correct for the "errant" property of the Bragg grating: as the band-stop filter! We begin with the distributed-feedback (DFB) structure as the simplest transmission Bragg grating, followed by the multisection grating design for the multiple band-pass function, chirped grating DFB band-pass filters widening the gap to address the Fabry–Perot structure, and moving on to the superstructure grating. Other schemes include the Michelson-interferometer-based filter, Mach–Zehnder interferometer, properties, tolerances requirements for fabrication, and a new device based on the highly detuned interferometer, which allows multiple band-pass filters to be formed, using chirped and unchirped gratings. An important area in applications is the optical add–drop multiplexer (OADM), and different configurations of these are considered, along with their advantages and disadvantages. The special filter based on the in-coupler Bragg grating as a family of filters is presented. Simple equations are suggested

for simulating the response of the Bragg reflection coupler. Rocking and mode-converting filters are also presented, along with the side-tap radiation mode and long period grating filter, as band-pass elements.

Chirped gratings have found a niche as dispersion compensators. Therefore, Chapter 7 is devoted to the application of chirped gratings, with a detailed look at the dispersive properties related to apodization and imperfect fabrication conditions on the group delay and reflectivity of gratings. Further, the effect of stitching is considered for the fabrication of long gratings, and the effect of cascading gratings is considered for systems applications. Systems simulations are used to predict the bit-error-rate performance of both apodized and unapodized gratings. Transmission results are also briefly reviewed.

The applications of gratings in semiconductor and fiber lasers can be found in Chapter 8. Here configurations of the external cavity fiber Bragg grating laser and applications in fiber lasers as single and multiple frequency and -wavelength sources are shown. Gain flattening and clamping of erbium amplifiers is another important area for long-haul high-bit-rate and analog transmission systems. Finally, the interesting and unique application of the fiber Bragg grating as a Raman oscillator is shown.

The ninth and final chapter deals with measurements and testing of Bragg gratings. This includes basic measurements, properties of different types of gratings, and measurement parameters. Life testing and reliability aspects of Bragg gratings conclude the book.

References

1 Hill K. O., Fujii Y., Johnson D. C., and Kawasaki B. S. "Photosensitivity in optical waveguides: Application to reflection filter fabrication," *Appl. Phys. Lett.* **32**(10), 647 (1978).

2 Bures J., Lapiere J., and Pascale D., "Photosensitivity effect in optical fibres: A model for the growth of an interference filter," *Appl. Phys. Let.* **37**(10), 860 (1980).

3 Lam D. W. K. and Garside B. K., "Characterisation of single-mode optical fibre filters," *Appl. Opt.* **20**(3), 440 (1981).

4 Ohmori Y. and Sasaki Y., "Phase matched sum frequency generation in optical fibers," *Appl. Phys. Lett.* **39**, 466–468 (1981).

5 Fujii Y., Kawasaki B. S., Hill K. O., and Johnson D. C., "Sum frequency generation in optical fibers," *Opt. Lett.* **5**, 48–50 (1980).

6 Österberg U. and Margulis W., "Efficient second harmonic in an optical fiber," in Technical Digest of *XIV Internat. Quantum Electron. Conf.,* paper WBB1 (1986).

7 Stolen R. H. and Tom H. W. K., "Self-organized phase-matched harmonic generation in optical fibers," *Opt. Lett.* **12**, 585–587 (1987).

8 Farries M. C., Russell P. St. J., Fermann M. E., and Payne D. N., "Second harmonic generation in an optical fiber by self-written $\chi^{(2)}$ grating," *Electron. Lett.* **23**, 322–323 (1987).

9 Stone J., "Photorefractivity in GeO_2-doped silica fibres," *J. Appl. Phys.* **62**(11), 4371 (1987).

10 Kashyap R., "Photo induced enhancement of second harmonic generation in optical fibers," *Topical Meeting on Nonlinear Guided Wave Phenomenon: Physics and Applications,* 1989, Technical Digest Series, Vol. 2, held on February 2–4, 1989, Houston (Optical Society of America, Washington, D.C. 1989), pp. 255–258.

11 Hand D. P. and Russell P. St. J., "Single mode fibre gratings written into a Sagnac loop using photosensitive fibre: transmission filters," *IOOC, Technical Digest,* pp. 21C3–4, Japan (1989).

12 Bures J., Lacroix S., and Lapiere J., "Bragg reflector induced by photosensitivity in an optical fibre: model of growth and frequency response," *Appl. Opt.* **21**(19) 3052 (1982).

13 Meltz G., Morey W. W., and Glenn W. H., "Formation of Bragg gratings in optical fibres by transverse holographic method," *Opt. Lett.* **14**(15), 823 (1989).

14 Kashyap R., Armitage J. R., Wyatt R., Davey S. T., and Williams D. L., "All-fibre narrowband reflection gratings at 1500 nm," *Electron. Lett.* **26**(11), 730 (1990).

15 Lemaire P., Atkins R. M., Mizrahi V., and Reed W. A., "High pressure H_2 loading as a technique for achieving ultrahigh UV photosensitivity and thermal sensitivity in GeO_2 doped optical fibres," *Electron. Lett.* **29**(13), 1191 (1993).

16 Myers R. A., Mukherjee N., and Brueck S. R. J., "Large second order nonlinearity in poled fused silica," *Opt. Lett.* **16**, 1732–1734 (1991).

17 Bergot M. V., Farries M. C., Fermann M. E., Li L., Poyntz-Wright L. J., Russell P. St. J., and Smithson A., *Opt. Lett.* **13**, 592–594 (1988).

18 Kashyap R., "Phase-matched second-harmonic generation in periodically poled optical fibers," *Appl. Phys. Lett.* **58**(12), 1233, 25 March 1991.

19 Kashyap R., Borgonjen E., and Campbell R. J., "Continuous wave seeded second-harmonic generation optical fibres: The enigma of second harmonic generation," *Proc. SPIE* **2044**, pp. 202–212 (1993).

20 Fujiwara T., Wong D., and Fleming S., "Large electro-optic modulation in a thermally poled germanosilicate fiber," *IEEE Photon. Technol. Lett.* **7**(10), 1177–1179 (1995).

21 Fujiwara T., Takahashi M., and Ikushima A. J., "Second harmonic generation in germanosilicate glass poled with ArF laser irradiation," *Appl. Phys. Lett.* **71**(8), 1032–1034 (1997).

22 Philipp H. R., "Silicon dioxide (SiO_2) glass," in *Handbook of Optical Constants of Solids* (E. D. Palik, Ed.), p. 749. Academic Press, London. 1985.

23 Lines M. E., "Ultra low loss glasses," *AT&T Bell Labs. Tech. Memo. TM 11535-850916-33TM* (1985).

24 Yeun M. J., "Ultraviolet absorption studies in germanium silicate glasses," *Appl Opt.* **21**(1), 136–140 (1982).

25 Keck D. B., Maurer R. D., and Shultz P. C., "On the ultimate lower limit of attenuation in glass optical waveguides," *Appl. Phys. Lett.* **22**, 307 (1973).

26 See, for example, *SPIE 1516,* and articles therein.

27 Georges T., Delevaque E., Monerie M., Lamouler P., and Bayon J. F., "Pair induced quenching in erbium doped silicate fibers," *IEEE Optical Amplifiers and Their Applications,* Technical Digest, **17**, 71 (1992).

28 Ladoucer F. and Love J. D., in *Silica-Based Channel Waveguides and Devices.* Chapman & Hall, London (1996).

29 Williams D. L., Ainslie B. J., Armitage J. R., Kashyap R., and Campbell R. J., "Enhanced UV photosensitivity in boron codoped germanosilicate fibres," *Electron Lett.* **29**, 1191 (1993).

30 Camlibel I., Pinnow D. A., and Dabby F. W., "Optical ageing characteristics of borosilicate clad fused silica core fiber optical waveguides." *Appl. Phys. Lett.* **26**(4), 1183–1185 (1992).

31 Bansal N. P. and Doremus R. H., "Handbook of glass properties," Academic Press, New York, (1978).

32 Smith D. Y., "Dispersion theory, sum rules and their application to the analysis of optical data," in *The Handbook of Optical Constants,* (E. P. Palik, Ed.), Chapter 3. Academic Press, New York (1985).

33 Malitson I. H., "Interspecimen comparison of the refractive index of fused silica," *J. Opt. Soc. Am.* **15**(10), 1205–1209 (1965).

34 Fleming J., "Dispersion in GeO_2–SiO_2 glasses," *Appl. Opt.* **23**(4), 4486 (1984).

35 Hand D. P. and Russel P. St. J., "Photoinduced refractive index changes in germanosilicate optical fibers," *Opt. Lett.* **15**(2), 102–104 (1990).

36 Data on fused quartz, Hareaus-Amersil Inc.

Chapter 2

Photosensitivity and Photosensitization of Optical Fibers

We have seen in the last chapter that optical fibers have very good optical properties for light transmission. Electronic absorptions that lead to attenuation are in the deep UV wavelength regime, and the molecular vibrations are far removed from the optical fiber transmission windows of interest to telecommunications. We have briefly considered the possible link between the change in absorption and the effect on the refractive index. Another possibility for the refractive index change is via an electro-optic nonlinearity. However, the symmetry properties of glass prohibit the electro-optic effect [1]. If there is an electro-optic contribution to the changes in the refractive index as a result of exposure to UV radiation, then an internal order would have to be created. This chapter considers aspects of defects connected with photosensitivity and techniques for photosensitization of optical fibers. We briefly compare in Section 2.1 the electro-optic effect [2] and how this may be invoked in glass. This aspect has recently received considerable interest worldwide but, as already stated, will not be studied in this book in any detail. Section 2.2 introduces some of the defects that are linked to the UV-induced change in refractive index of glass. The hot debate on defects has continued for a number of years and there are a vast number of "subtleties" with regards to the same nominal defect state, as well as pathways to achieving transformations from one state to the other. Some of the defects cannot be detected

by optical means and require sophisticated methods. The task is not made easy by the various nomenclature used in labeling, so that unraveling defects is made inaccessible to the layman. A simple *overview* of the important defects is given and we point to the literature for a detailed discussion [3,4]. Section 2.3 looks at the evidence of photoexcitation of electrons and, in conjunction with Section 2.2, the methods for the detection of defects. The routes used to photosensitize and fabricate fibers are presented in the last section.

2.1 Photorefractivity and photosensitivity

It is useful to distinguish the term *photorefractivity* from photosensitivity and photochromic effect. Photorefractivity refers to a phenomenon usually ascribed to crystalline materials that exhibit a second-order nonlinearity by which light radiation can change the refractive index by creating an internal electric field [5]. Photosensitivity invariably refers to a permanent change in refractive index or opacity induced by exposure to light radiation with the internal field playing an insignificant role. The term traditionally applies to the color change in certain glasses with exposure to ultraviolet radiation and heat. Photochromic glass does not depend on the application of heat to change opacity, and the action is reversible. However, a combination of these properties is possible in glasses and is a novel phenomenon, which is currently being studied, not least because it is poorly understood. Considering the normal polarization response of materials to applied electric fields may provide a physical insight into the phenomenon of photorefractivity and poling of glass.

The induced polarization, P, in a medium can be described by the relationship

$$D = \varepsilon_0 E + P, \tag{2.1.1}$$

where D is the displacement, E is the applied field, ε_0 is the free space permittivity, and P is the induced polarization. In a material in which the polarization is nonlinear, the polarization may be expanded in powers of the applied field as

$$\begin{aligned} P &= \varepsilon_0 \chi^{(1)} E + \varepsilon_0 \chi^{(2)} E^2 + \varepsilon_0 \chi^{(3)} E^3 + \ldots \\ &= \varepsilon_0 \{\chi^{(1)} E + \chi^{(2)} E^2 + \chi^{(3)} E^3 + \ldots\} \end{aligned} \tag{2.1.2}$$

and

$$\varepsilon_r = \frac{D}{\varepsilon_0 E} = 1 + \chi^{(1)}, \tag{2.1.3}$$

where $\varepsilon_r = 1 + \chi^{(1)}$ is the linear permittivity, $\chi^{(2)}$ is the first term of the nonlinear susceptibility (which can be nonzero in crystalline media), and $\chi^{(3)}$ is the third-order nonlinearity (nonzero in all materials).

Using Equations (2.1.2) and (2.1.3), the perturbed permittivity under the influence of an applied electric field is

$$\frac{D}{\varepsilon_0 E} = \varepsilon_r + \chi^{(2)}E + \chi^{(3)}E^2 \ldots \tag{2.1.4}$$

$$= \varepsilon_r + \Delta\varepsilon = \varepsilon, \tag{2.1.5}$$

and since the refractive index n is related to the permittivity as

$$\begin{aligned} \varepsilon &= n^2 \\ &= (n_0 + \Delta n)^2, \\ &\approx n_0^2 + 2n_0\Delta n \end{aligned} \tag{2.1.6}$$

from which immediately follows

$$\Delta n = \frac{1}{2n_0}[\chi^{(2)}E + \chi^{(3)}E^2 \ldots]. \tag{2.1.7}$$

In photorefractive materials with an active $\chi^{(2)}$, an internal charge can build up due to trapped carriers released from defects. These give rise to an internal field, which modulates the refractive index locally via the first term in Eq. (2.1.7). The induced index changes result directly from the linear electro-optic effect ($\chi^{(2)}$) and are in general quite large, $\sim 10^{-4}$. However, with $\chi^{(2)}$ being zero in glass, the induced refractive index with an applied field can only result from the nonzero third-order susceptibility, $\chi^{(3)}$. Even if an internal field could develop, the refractive index change is small, $\sim 10^{-7}$; however, as will be seen, if an internal field is possible in glass, it results in a modest nonlinearity [2]. We now assume the existence of an internal field E_{dc} and apply an external field $E_{applied}$. The induced index change is as follows:

$$\Delta n = \frac{1}{2n_0}\chi^{(3)}(E_{dc} + E_{applied})^2 \tag{2.1.8}$$

$$= n_2'(E_{dc}^2 + 2E_{dc} \times E_{applied} + E_{applied}^2). \tag{2.1.9}$$

The first term in Eq. (2.1.9) indicates a permanent index change, whereas the third term is the usual quadratic nonlinear effect known as the dc-Kerr effect. We have used a prime on the n_2', to distinguish it from the optical Kerr constant n_2. The interesting relationship is described by the remaining term,

$$\Delta n = 2n_2' E_{dc} \times E_{applied}. \tag{2.1.10}$$

This relationship is analogous to the linear electro-optic effect, in which the applied field operates on an enhanced nonlinearity, $2n_2' E_{dc}$, due to the frozen internal field. If the internal field is large, then a useful nonlinearity is possible. This effect is believed to be partly the basis of poled glass [2].

In crystalline media with a large photorefractive response, the nonlinearity $\chi^{(2)}$ is several orders of magnitude larger than the next higher order coefficient, $\chi^{(3)}$ (and hence n_2') in glass. From the first term in Eq. (2.1.9) we can calculate the required field for a change in the refractive index of 10^{-3}. With a measured value of $\chi^{(3)} \sim 10^{-22}\,\mathrm{m}^{-2}\mathrm{V}^{-2}$ for silica, a large internal field of $\sim 10^9$ V/m would be necessary, equivalent to n_2' of ~ 1 pm V^{-1}. These values have been exceeded in UV photoelectrically *poled* fiber, with the highest reported result of ~6 pm/V [6]! Combined with the low dielectric constant of silica, it has a potentially large bandwidth for electro-optic modulation. Just how such a large field may develop has been debated. However, it has been suggested by Myers *et al.* [7,8] that the poling voltage is dropped across a thin layer (~ 5 μm) within the glass, causing huge fields to appear.

The electro-optic nature of UV photoinduced refractive index in Bragg gratings has not been reported, although the presence charges related to defects could indeed develop an internal field, as in the case of second-harmonic generation in glass [9]. In the next section, we consider some of the important defects, which are of interest in unraveling the mystery of photosensitivity of glass.

2.2 Defects in glass

The nature of fabrication of glass is ideally suited to promoting defects. The chemical reactions that take place in a modified chemical vapor deposition (MCVD) [10] process are based on hot gases reacting to form a soot deposit on the inside of a silica support tube or on the outside in outside vapor phase deposition (OVD). The process allows the ratio of reactive gases such as silicon/germanium tetrachloride and oxygen to be

easily changed to arrive at a nearly complete chemical reaction, depositing a mixture of germanium and silicon dioxides. It is not possible to have a 100% reaction, so the deposited chemicals have a proportion of suboxides and defects within the glass matrix. With sintering and preform collapse, these reaction components remain, although further alterations may take place while the fiber is being drawn, when bonds can break [11–13]. The end result is a material that is highly inhomogeneous on a microscopic scale with little or no order beyond the range of a few molecular distances. The fabrication process also allows other higher-order ring structures [14] to form, complicating the picture yet further. There is a possibility of incorporating not only a strained structure, but also one which has randomly distributed broken bonds and trapped defects.

This is especially true of a fiber with the core dopant germanium, which readily forms suboxides as GeO_x (x = 1 to 4), creating a range of defects in the tetrahedral matrix of the silica host glass. Given this rich environment of imperfection, it is surprising that state-of-the-art germania-doped silica fiber has extremely good properties—low loss and high optical damage threshold—and is a result of better understanding of defects, which lead to increased attenuation in the transmission windows of interest.

Among the well-known defects formed in the germania-doped silica core are the paramagnetic Ge(n) defects, where n refers to the number of next-nearest-neighbor Ge/Si atoms surrounding a germanium ion with an associated unsatisfied single electron, first pointed out by Friebele *et al.* [17]. These defects are shown schematically in Fig. 2.1. The Ge(1) and Ge(2) have been identified as trapped-electron centers [18]. The GeE′, previously known as the Ge(0) and the Ge(3) centers, which is common in oxygen-deficient germania, is a hole trapped next to a germanium at an oxygen vacancy [19] and has been shown to be independent of the number of next-neighbor Ge sites. Here an oxygen atom is missing from the tetrahedron, while the germania atom has an extra electron as a dangling bond. The extra electron distorts the molecule of germania as shown in Fig. 2.2.

The GeO defect, shown in Fig. 2.2 (LHS), has a germanium atom coordinated with another Si or Ge atom. This bond has the characteristic 240-nm absorption peak that is observed in many germanium-doped photosensitive optical fibers [21]. On UV illumination, the bond readily breaks, creating the GeE′ center. It is thought that the electron from the GeE′ center is liberated and is free to move within the glass matrix via hopping or tunneling, or by two-photon excitation into the conduction

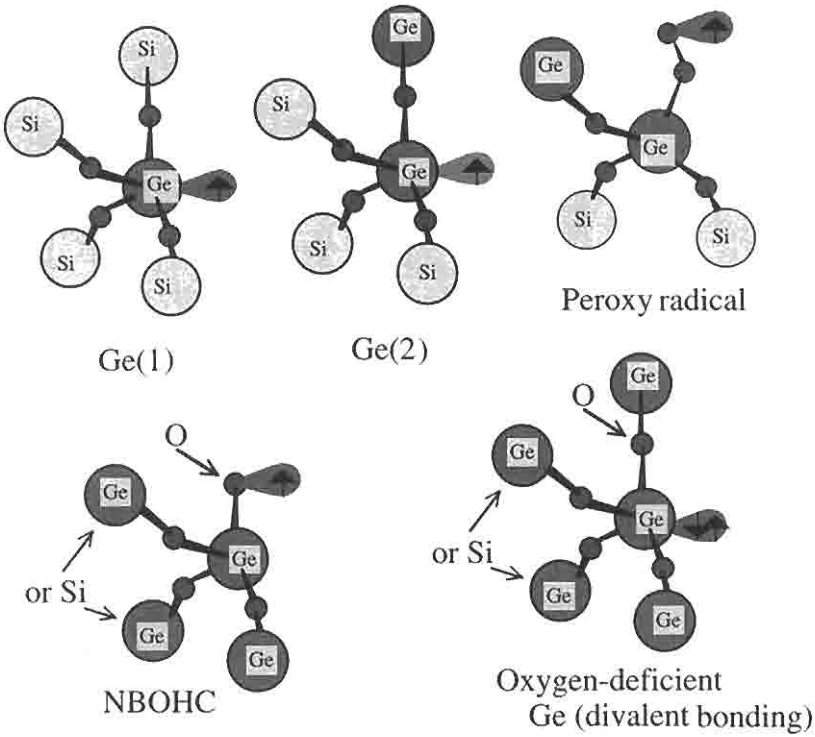

Figure 2.1: A schematic of proposed Ge (or Si) defects of germania-doped silica. The characteristic absorption of the Ge(1) is ~280 nm (4.4 eV) [18] and is a trapped electron at a Ge (or Si) site; Ge(2) has an absorption at 213 nm (5.8 eV) and is a hole center. The peroxy radical has an absorption at 7.6 eV (163 nm) and at 325 nm (3.8 eV) [15,16].

band [22–24]. This electron can be retrapped at the original site or at some other defect site. The removal of this electron, it is believed, causes a reconfiguration of the shape of the molecule (see Fig. 2.2), possibly also changing the density of the material, as well as the absorption. It appears that the Ge(1) center is the equivalent of the germanium defects observed in α-quartz, known as the Ge(I) and Ge(II), but less well defined [23].

Phosphorus forms a series of defects similar to those of germanium. However, the photosensitivity is limited at 240 nm and requires shorter wavelengths, such as 193-nm radiation [24].

Other defects include the nonbridging oxygen hole center (NBOHC), which is claimed to have absorptions at 260 and 600 nm, and the peroxy

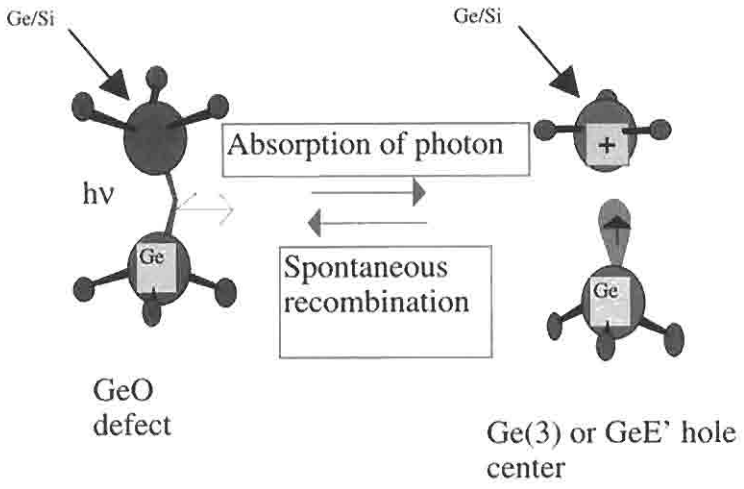

Figure 2.2: The GeO defect of germania-doped silica, in which the atom adjacent to germanium is either a silicon or another germanium. It can absorb a photon to form a GeE′ defect. The Ge(0) or Ge(3) are a GeE′ center [20]. The GeE′ defect shows the extra electron (associated with the Ge atom), which may be free to move within the glass matrix until it is retrapped at the original defect site, at another GeE′ hole site, or at any one of the Ge(n) defect centers.

radical (P-OHC) [25], believed to absorb at 260 nm. Both are shown in Fig. 2.1.

2.3 Detection of defects

A considerable amount of work has been done in understanding defects in glass. Detection of defects may be broadly categorized into four groups: optically active defects can be observed because of their excitation spectrum or excitation and luminescence/fluorescence spectrum while optically inactive defects are detectable by their electron spin resonance signature, or ESR spectrum, together with optical emission spectrum.

The model of the defects as shown in Fig. 2.2 suggests the liberation of electrons on absorption of UV radiation. It should therefore be possible to detect liberated charges experimentally; since silica has a high volume resistivity, it is necessary to choose a geometry that can directly enable the measurement of electric currents. Photosensitivity has been explored

both indirectly, e.g., by etching glass exposed to radiation or using second-harmonic generation [9,26,27] as a probe, and directly, e.g., by measurement of photocurrent in germania-doped planar waveguides [28] and across thin films of bulk glass [29].

It has been concluded that the photocurrent is influenced by the fluence of the exciting UV radiation; the photocurrent (probably by tunneling [29]) is a linear function of the power density for CW excitation [28], while for pulsed, high-intensity radiation, it takes on a two-photon excitation characteristic [29].

The paramagnetic defects of the Ge(n) type including the E′ center are detected by ESR. The GeE′ has an associated optical absorption at 4.6 eV [30].

2.4 Photosensitization techniques

A question often asked is: Which is the best fiber to use for the fabrication of most gratings? Undoubtedly, the preferred answer to this question should be standard telecommunications fiber. Although techniques have been found to write strong gratings in this type of fiber, there are several reasons why standard fiber is not the best choice for a number of applications. Ideally, a compatibility with standard fiber is desirable, but the design of different devices requires a variety of fibers. This does open the possibility of exploiting various techniques for fabrication and sensitization. Here we look in some detail at the behavior of commonly used species in optical fiber and present their properties, which may influence the type of application. For example, the time or intensity of UV exposure required for the writing of gratings affects the transmission and reliability properties. This results in either damage (Type II gratings) [31] or the formation of Type I, at low fluence, and Type IIA gratings [32], each of which have different characteristics (see Section 2.4.1).

The use of boron and tin as a codopant in germanosilicate fibers, hot hydrogenation and cold, high-pressure hydrogenation, and flame-assisted low-pressure hydrogenation ("flame-brushing") are well-established photosensitization methods. The type of the fiber often dictates what type of grating may be fabricated, since the outcome depends on the dopants.

The literature available on the subjects of photosensitivity, the complex nature of defects, and the dynamics of growth of gratings is vast

[34]. The sheer numbers of different fibers available worldwide, further complicates the picture and by the very nature of the limited fiber set available within the framework of a given study and the complex nature of glass, comparisons have been extremely difficult to interpret. This is not a criticism of the research in this field, merely a statement reiterating the dilemma facing researchers: how to deal with far too many variables! In order to draw conclusions from the available data, one can simply suggest a trend for the user to follow. A choice may be made from the set of commonly available fibers. For a certain set of these fibers (e.g., standard telecommunications fiber) the method for photosensitization may be simply hydrogenation, or 193-nm exposure. It is often the availability of the laser source that dictates the approach.

2.4.1 Germanium-doped silica fibers

Photosensitivity of optical fibers has been correlated with the concentration of GeO defects in the core [33,34]. The presence of the defect is indicated by the absorption at 240 nm, first observed by Cohen and Smith [35] and attributed to the reduced germania state, Ge(II). The number of these defects generally increases as a function of Ge concentration. Figure 2.3 shows the absorption at 242 nm in a perform with the germa-

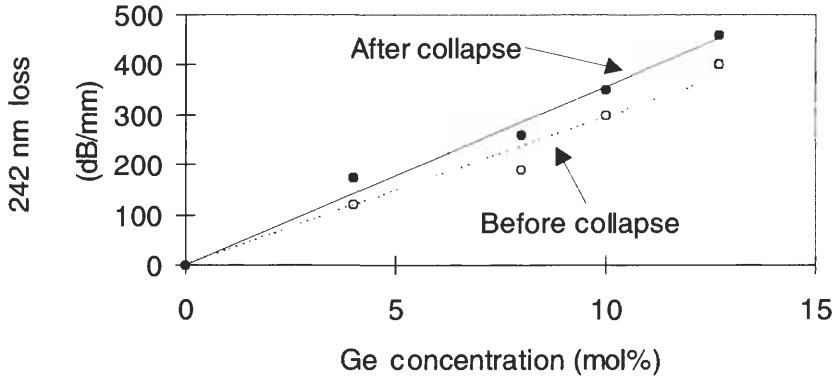

Figure 2.3: Absorption at 242 nm in preform samples before and after collapse as a function of Ge concentration (after Ref. [36]).

nium concentration [36]. The slope in this graph is ~28 dB/(mm-mol%) of Ge before the preform sample is collapsed (dashed line). After collapse, the number of defects increases, and the corresponding absorption changes to ~36 dB/(mm-mol%) (Fig. 2.3 continuous line).

Increasing the concentration of defects increases the photosensitivity of the fiber. This can be done by collapsing the fiber in a reducing atmosphere, for example, by replacing oxygen with nitrogen or helium [36] or with hydrogen [37,49].

The 240-nm absorption peak is due to the oxygen-deficient hole center defect, (Ge-ODHC) [38] and indicates the intrinsic photosensitivity. It can be quantified as [39]

$$k = \alpha_{242\ \mathrm{nm}}/C, \tag{2.4.1}$$

where $\alpha_{242\ \mathrm{nm}}$ is the absorption at 242 nm and C is the molar concentration of GeO_2. Normally C lies between 10 and 40 dB/(mm-mol% GeO_2). Hot hydrogenation is performed on fibers or preforms at a temperature of ~650°C for 200 hours is 1 atm hydrogen [40]. The absorption at 240 nm closely follows the profile of the Ge concentration in the fiber [33], and k has been estimated to be large, ~120 dB/(mm-mol% GeO_2).

The saturated UV-induced index change increases approximately linearly with Ge concentration after exposure to UV radiation, from $\sim 3 \times 10^{-5}$ (3 mol% $GeO\%_2$) for standard fiber to $\sim 2.5 \times 10^{-4}$ (~20 mol% GeO_2) concentration, using a CW laser source operating at 244 nm [49]. However, the picture is more complex than the observations based simply on the use of CW lasers. With pulsed laser sources, high-germania-doped fiber (8%) shows an the initial growth rate of the UV-induced refractive index change, which is proportional to the energy density of the pulse. For low germania content, as in standard telecommunications fiber, it is proportional to the square of the energy density. Thus, two-photon absorption from 193 nm plays a crucial role in inducing maximum refractive index changes as high as ~0.001 in standard optical fibers [41]. Another, more complex phenomenon occurs in untreated germania fibers with long exposure time, in conjunction with both CW and pulsed radiation, readily observable in high germania content fibers [47]. In high-germania fiber, long exposure erases the initial first-order grating completely, while a second-order grating forms. This erasure of the first-order and the onset of second-order gratings forms a demarcation between Type I and Type IIA gratings.

Increasing the energy density damages the fiber core, forming Type II gratings [31]. The thermal history of the fiber is also of great importance, as is the mechanical strain during the time of grating inscription. Significantly, even strains as low as 0.2% can increase the peak refractive index modulation of the Type IIA grating in high germanium content fiber [42,43]. High-germania-doped (30%Ge) fibers drawn under high pulling tension show the opposite behavior [44], indicating the influence of elastic stress during drawing rather than the effect of drawing-induced defects [45]. Annealing the fiber at 1100°C for 1 hour and then cooling over 2 days reduces the time for the erasure of the Type I grating, as well as increasing the maximum refractive index modulation achievable in the Type IIA regime. With tin as a codopant in high-germanium fiber, the general overall picture changes slightly, but the dynamics are similar, except for reduced index change under strained inscription [46]. Thus, absolute comparison is difficult, and one may use the germania content as an indicator, bearing in mind the complex nature of the dynamics of grating formation in germania-doped silica fiber. Typical results for a high-germania fiber are shown in Fig. 2.4. The growth of the refractive index modulation as a function of time stops in the case of all three fibers shown, dropping to zero before increasing once again to form Type IIA gratings.

Photosensitivity of fiber fabricated under reduced conditions as a function Ge concentration also increases, but it is not sufficient to interpret the data by the maximum index change. The reason for this is the induction of Type IIA gratings [47] in relatively low concentration of Ge. Measurements performed under pulsed conditions reveal that the onset of the Type IIA grating is almost certainly always possible in any concentration of Ge; only the time of observation increases with low concentrations, although for practical purposes this time may be too long to be of concern. Figure 2.5 shows data from the growth of the average index on UV exposure as a function of Ge concentration in fibers, which have been reduced. The maximum index should change monotonically; however, above a certain concentration, the onset of Type IIA forces the observed maximum index change for point B (20 mol% Ge), since the grating being written slowly disappears before growing again. While the maximum reflectivity should increase to higher levels, within the time frame of the measurements this fiber appears to be less sensitive. A better indicator is the initial growth rate of the index change, since Type IIA grating is not observed for some time into the measurements. Figure 2.5 shows an

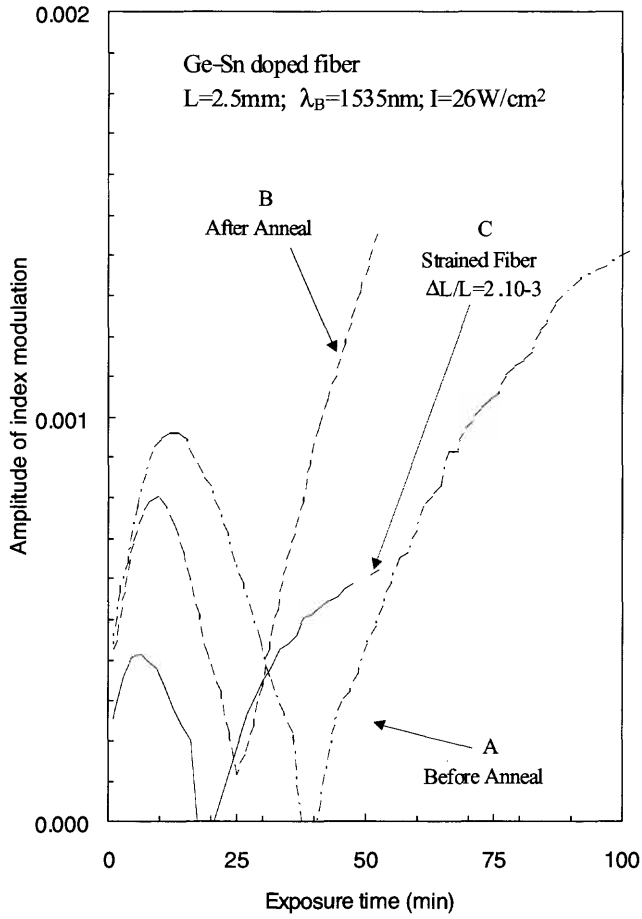

Figure 2.4: The growth dynamics of the refractive index change in 20 mol% Ge: 1 mol% Sn. The three data are for A: pristine fiber, B: after annealing, and C: under strain of 0.2%. The Type IIA grating begins after the initial erasure. (from: Douay M., Xie W. X., Taunay T., Bernage P., Niay P., Cordier P., Poumellec B., Dong L., Bayon J. F., Poignant H., and Delevaque E., "Densification involved in the UV based photosensitivity of silica glasses and optical fibers," *J. Lightwave Technol.* **15**(8), 1329–1342, 1997. © IEEE 1997.)

approximately linear increase in the rate of growth of the UV-induced average refractive index. The data has been interpreted from Ref. [48], bearing in mind that the for the initial growth rate in *low* germanium fibers, there is a time delay before the grating begins to grow.

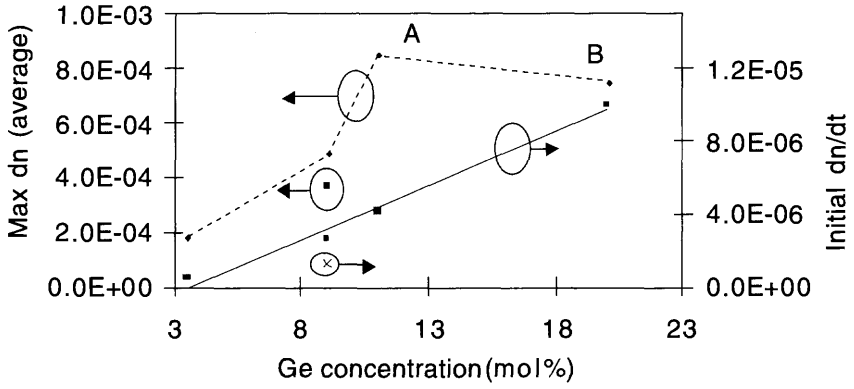

Figure 2.5: Concentration dependence of the maximum-index and its initial growth rate as a function of germania concentration in oxygen-deficient fibers. The two isolated points refer to unreduced samples (interpreted from Ref. [48]).

Figure 2.6 shows the actual growth of the transmission dip (equivalent to the increase in reflection) for several reduced germania fibers [48]. Note in particular the change in the transmission due to the onset of Type IIA grating. At this point, the Bragg wavelength shift is reduced [47], making the maximum average index measurement difficult.

Measurement of the shift in the Bragg wavelength is a reasonable indicator for the UV induced index change for a fiber well below the start of saturation effects. With saturation, care needs to be taken, since the bandwidth of the grating increases, making it more difficult to accurately measure the wavelength shift. The ac index change should be calculated from the bandwidth and the reflectivity data along with the Bragg wavelength shift to accurately gauge the overall ac and dc components of the index change (see Chapters 4 and 9).

The growth rate and the maximum index change are of interest if strong gratings are to be fabricated in a short time frame. This suggests that reduced germania is better than normal fiber on both counts. However, the maximum index change is still lower than required for a number of applications and the time of fabrication excessive. The use of hot hydrogen to reduce germania has the additional effect of increasing loss near 1390 nm due to the formation of OH^- hydroxyl ions [49,50]. The absorption loss at 1390 nm is estimated to be ~0.66, 0.5, and 0.25 dB/(m-mol%) at

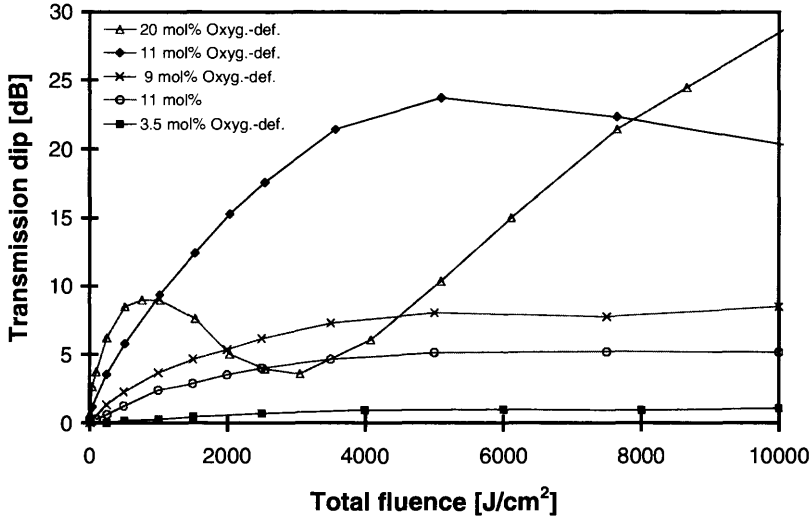

Figure 2.6: Growth of the transmission dip with fluence for different types of reduced germania fibers. For the 20 mol% germania fiber, a reduction in the reflectivity is probably due to Type IIA grating formation. (from: Grüner-Nielsen L. and Hübner J., "Photosensitive fiber for highly reflective Bragg gratings," in *Tech. Digest of Conf. on Opt. Fiber Commun. OFC'97,* paper WL16, p. 178, 1997.)

1390, 1500, and 1550 nm, respectively [40]. One major advantage of fibers that have been reduced is that they are rendered permanently photosensitive and require the minimum of processing, compared with hydrogenated fibers (see following sections).

The incorporation of 0.1% nitrogen in germanium-doped silica fiber by the surface plasma assisted chemical vapor deposition (SPCVD) process [51] has been shown to have a high photosensitivity [52]. The effect on the 240-nm absorption is dramatic, raising it to 100 dB/mm/mol% GeO_2, doubling it compared to the equivalent for germanium doping alone. The induced refractive index changes are reported to be large (2.8×10^{-3}) and much larger (0.01) with cold hydrogen soaking of 7 mol%Ge;0 mol%N fiber. The Type IIA threshold is reported to increase by a factor of ~6 over that in nitrogen-free, 20 mol% Ge fibers. However, there is evidence of increase in the absorption loss in the 1500-nm window with the addition of nitrogen. The next most photosensitive fibers are the germania–boron or tin-doped fibers.

2.4.2 Germanium–boron codoped silicate fibers

The use of boron in soda lime and silicate glass has been known for a long time [53]. It has also been established that boron, when added to germania-doped silicate glass, *reduces* the refractive index. The transformational changes that occur depend on the thermal history and processing of the glass. As such, it is generally used in the cladding of optical fibers, since the core region must remain at a higher refractive index. Compared to fluorine, the other commonly used element in the cladding (in conjunction with phosphorus), the refractive index modification is generally at least an order of magnitude larger, since more of the element can be incorporated in the glass. Thus, while the maximum index difference from fluorine can be approximately -10^{-3} with boron, the index change can be $>|-0.01|$. This opens up many possibilities for the fabrication of novel structures, not least as a component to allow the incorporation of even more germania into glass while keeping a low refractive index difference between the cladding and core when both are incorporated into the core. One advantage of such a composition is the fabrication of a fiber that is outwardly identical in terms of refractive index profile and core-to-cladding refractive index difference with standard single-mode optical fibers, and yet contains many times the quantity of germania in the core. The obvious advantage is the increased photosensitivity of such a fiber with the increased germania. Indeed, this is the case with boron–germanium (B-Ge) codoped fused silica fiber [54]. The typical profile of a B-Ge preform is shown Fig. 2.7. The raised refractive index dashed line shows the

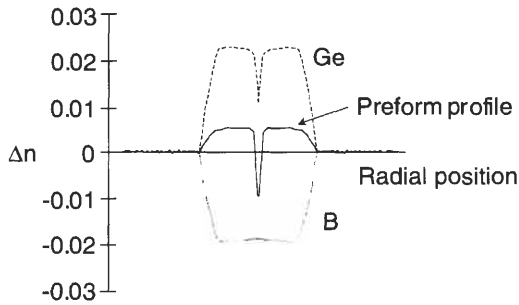

Figure 2.7: The refractive index components due to germanium and boron (dashed and dotted lines) contributing to the resultant preform profile (continuous line) [54].

contribution due to the germanium concentration, while the negative refractive contribution is due to the boron, resulting in the continuous line positive refractive index profile.

It should be noted that with boron and germanium, it is possible to selectively place a photosensitive region anywhere in the fiber, without altering the wave guiding properties. Other types of profiles possible are boron with highly doped germanium in a cladding matched to silica for liquid cored fibers [55], in-cladding gratings for lasers [56], and special fiber for side-tap filters and long-period gratings [57,58].

B-Ge codoped fiber is fabricated using MCVD techniques and a standard phosphorus–fluorine cladding matched silica tube with normal oxidizing conditions. The reactive precursor vapors are $SiCl_4$, BCl_3, and $GeCl_4$, with oxygen as a carrier for the core deposition. For a composition equivalent to ~16 mol% germanium, the photosensitivity in comparison with 20 mol% unreduced germanium fiber shows an improvement >3-fold in the UV-induced refractive index modulation as well as an order of magnitude reduction in the writing time. With respect to 10 mol% reduced germanium fiber, the improvement in the maximum refractive index modulation is ~40% with a ×6 reduction in the writing time. The maximum refractive index change is close to 10^{-3} for this fiber induced with a CW laser operating at 244 nm [54].

A point worth noting with B-Ge fibers is the increased stress, and consequently, increased induced birefringence [59]. The preforms are difficult to handle because of the high stress. However, the real advantages with B-Ge fibers are the shortened writing time, the larger UV-induced refractive index change, and, potentially, fibers that are compatible with any required profile, for small-core large NA fiber amplifiers, to standard fibers.

B-Ge fibers form Type IIA gratings [60] with a CW 244-nm laser, as is the case with the data shown in Fig. 2.4. This suggests that there is probably little difference due to the presence of boron; only the high germanium content is responsible for this type of grating. There is a possibility that stress is a contributing factor to the formation of Type IIA [61]; recent work does partially indicate this but for germanium-doped fibers [44].

Typically, gratings written with CW lasers in B-Ge fiber decay more rapidly than low germanium doped (5 mol%) fibers when exposed to heat. Gratings lose half their index modulation when annealed at ~400°C (B-Ge: 22:6.3 mol%) and ~650°C (Ge 5 mol%) [46] for 30 minutes. A detailed

study of the decay of gratings written in B-Ge may be found in Ref. [62]. The thermal annealing of gratings is discussed in Chapter 9.

Boron causes additional loss in the 1550-nm window, of the order of ~0.1 dB/m, which may not be desirable. For short gratings, this need not be of concern.

2.4.3 Tin–germanium codoped fibers

Fabrication of Sn codoped Ge is by the MCVD process used for silica fiber by incorporating $SnCl_4$ vapor. SnO_2 increases the refractive index of optical fibers and, used in conjunction with GeO_2, cannot be used as B_2O_3 to match the cladding refractive index, or to enhance the quantity of germanium in the core affecting the waveguide properties. However, it has three advantages over B-Ge fiber: The gratings survive a higher temperature, do not cause additional loss in the 1500-nm window, have a slightly increased UV-induced refractive index change, reported to be 3 times larger than that of B-Ge fibers. Compared with B-Ge, Sn-Ge fibers lose half the UV-induced refractive index change at ~600°C, similarly to standard fibers [63].

2.4.4 Cold, high-pressure hydrogenation

The presence of molecular hydrogen has been shown to increase the absorption loss in optical fibers over a period of time [64]. The field was studied extensively [65], and it is known that the hydrogen reacts with oxygen to form hydroxyl ions. The increase in the absorption at the first overtone of the OH vibration at a wavelength of 1.27 μm was clearly manifest by the broadband increase in loss in both the 1300-nm and, to a lesser extent, in the 1500-nm windows. Another effect of hydrogen is the reaction with the Ge ion to form GeH, considerably changing the band structure in the UV region. These changes, in turn, influence the local refractive index as per the Kramers–Kronig model. The reaction rates have been shown to be strongly temperature dependent [65]. It has been suggested that the chemical reactions are different on heat treatment and cause the formation of a different species compared to illumination with UV radiation. However, no noticeable increase in the 240-nm band is observed with the presence of interstitial molecular hydrogen in Ge-doped silica. The highest refractive index change induced by UV radiation is undoubtedly in cold hydrogen soaked germania fibers. As has been

seen, an atmosphere of hot hydrogen during the collapse process or hot hydrogen soaking of fibers enhances the GeO defect concentration [37]. The presence of molecular hydrogen has been known to induce increases in the absorption loss of optical fibers, since the early day of optical fibers [50]. Apart from being a nuisance in submarine systems, in which hydrogen seeps into the fiber, causing a loss that increases with time of exposure, cold high pressure hydrogen soaking has led to germanium-doped fibers with the highest observed photosensitivity [66]. Any germania-doped fiber may be made photosensitive by soaking it under high pressure (800 bar) and/or high temperature (<150°C). Molecular hydrogen in-diffuses to an equilibrium state. The process requires a suitable high-pressure chamber into which fibers may be left for hydrogen loading. Once the fiber is loaded, exposure to UV radiation is thought to lead to a dissociation of the molecule, leading to the formation of Si–OH and/or Ge–OH bonds. Along with this, there is formation of the Ge oxygen-deficient centers, leading to a refractive index change. Soaking the fiber at 200 bar at room temperature for ~2 weeks is sufficient to load the 125-micron diameter fiber at 21°C [66].

UV exposure of standard hydrogen fibers easily yields refractive index changes in excess of 0.011 [67] in standard telecommunications fiber, with a highest value of 0.03 inferred [68]. Almost all Ge atoms are involved in the reactions giving rise to the index changes. Figure 2.8 shows the changes in the refractive index profile of a standard fiber before and after exposure to pulsed UV radiation at 248 nm (~600 mJ/cm^2, 20 Hz, 60-minute exposure) [68]. The growth of gratings is long with CW lasers (duration of 20 minutes for strong gratings with refractive index changes of ~$1–2 \times 10^{-3}$). The picture is quite different with the growth kinetics when compared with non-hydrogen-loaded germania fibers. To date, Type IIA gratings have not been observed in hydrogen-loaded fibers. There is also no clear evidence of the stress dependence of grating growth [44]. Whereas in Type IIA the average UV-induced refractive index change is negative, in hydrogen-loaded fibers the average refractive index grows unbounded to large values (>0.01).

Heating a hydrogen-loaded fiber increases the refractive index rapidly, even in P_2O_5 and P_2O_5:Al_2O_3-doped multimode fibers [68], although pure silica is not sensitized.

The dynamic changes that occur in the process of fiber grating fabrication are complex. Even with hydrogen-loaded fibers, there are indications that as the grating grows, the absorption in the core increases in the UV,

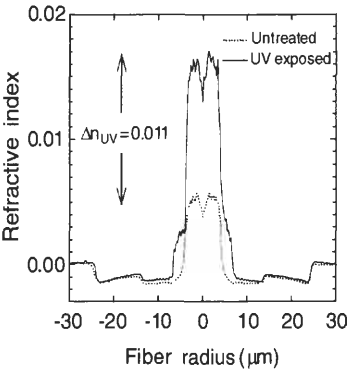

Figure 2.8: The refractive index profile of a 2.8% hydrogen-soaked standard fiber, before and after UV exposure with pulsed radiation at 248 nm (Courtesy P. Lemaire from: Lemaire P. J., Vengsarkar A. M., Reed W. A., and Mizarhi V., "Refractive index changes in optical fibers sensitized with molecular hydrogen," in *Technical Digest of Conf. on Opt. Fiber Commun., OFC'94,* pp. 47–48, 1994.)

as does the 400-nm luminescence [69]. Martin *et al.* [69] have found a direct correlation between refractive index change increase and luminescence. Figure 2.9 shows the transmission spectra of two gratings in hydrogenated standard fiber at different stages of growth, with the UV radiation at 244 nm CW switched on and off. With the UV switched on, the Bragg

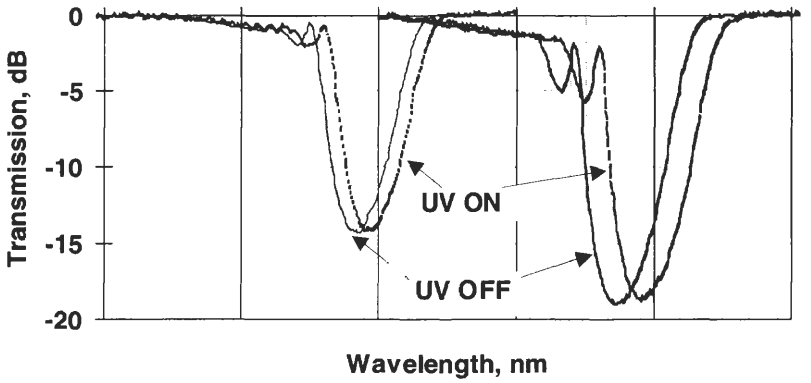

Figure 2.9: Shift in the Bragg wavelength as the UV radiation is switched on and off for two different strength gratings (after Ref. [70]).

wavelength shifts 0.05 nm to longer wavelengths at a grating reflectivity of ~1.4 dB. When the grating has grown to ~27 dB (different grating but same fiber), the shift is 0.1 nm, equivalent to an equilibrium temperature increase of the fiber of ~80°C. At the start of grating growth (<1 dB), the shift is not noticeable.

The formation of OH^- ions with UV exposure increases the loss in the 1500-nm window. There are two peaks associated with the formation of Si–OH (1.39 μm) and Ge–OH (1.42 μm) on UV exposure [71]. A concentration of 1 mol% of OH^- increases the loss at 1.4 μm by 5 dB. This is avoided by soaking the fiber in deuterium, which shifts the first overtone OD of the water peak to ~1.9 μm [74].

Another feature of hydrogen loading is the increased loss at wavelengths less than 1 μm after UV exposure of hydrogen-loaded fibers. The loss has a wavelength dependence at <0.95 μm of $e^{-4.6/\lambda}$, where λ is in microns [74].

Hydrogen loading of optical fibers

The loading of optical fibers with hydrogen is both temperature and pressure dependent. The diffusion coefficient of hydrogen is [50]

$$D = 2.83 \times 10^{-4} e^{(-40.19\ \text{kJ/mol})/RT},\ \text{cm}^2/\text{s}, \tag{2.4.2}$$

where $R = 8.311$ J/(K-mol) and T is the temperature in degrees Kelvin. The concentration of hydrogen in the fiber is calculated by solving the diffusion equation [72] as a function of radial position ρ and time t:

$$C(\rho,t) = \frac{2}{C_0} \sum_{n=1}^{\infty} \frac{J_0(\mu_n \rho)}{J_1^2(\mu_n \rho)} \, e^{-D(\mu_n/R)^2 t} \int_0^1 \varphi(\rho) J_0(\mu_n \rho) d\rho, \tag{2.4.3}$$

where μ_n are the nth zeroes of the J_0 Bessel function, D is the diffusion coefficient, and R is the radius of the fiber. C_0 is the initial concentration, and $\varphi(\rho) = 1$ if hydrogen is diffusing into the fiber and -1 for out-diffusion. The dynamics of the concentration have been modeled by Bhakti *et al.* [73] to study the effect on the drift of the resonance wavelength of a long-period grating. Under an ambient pressure of 200 bar, the in-diffusion of hydrogen is shown in Fig. 2.10 as a function of the radius of the radial position for different times. The out-diffusion of hydrogen is shown for different times as the fiber is removed from the high-pressure chamber [74] in Fig. 2.11. The first overtone OH^- peak at 1.245 μm can be used

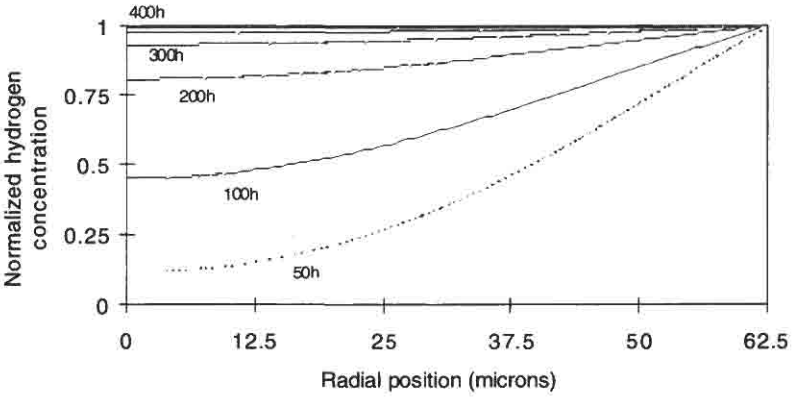

Figure 2.10: In-diffusion profile of hydrogen at 200 bar pressure in a 125-μm diameter fiber as a function of time at 23°C (courtesy F. Bhakti, Ref. [73]).

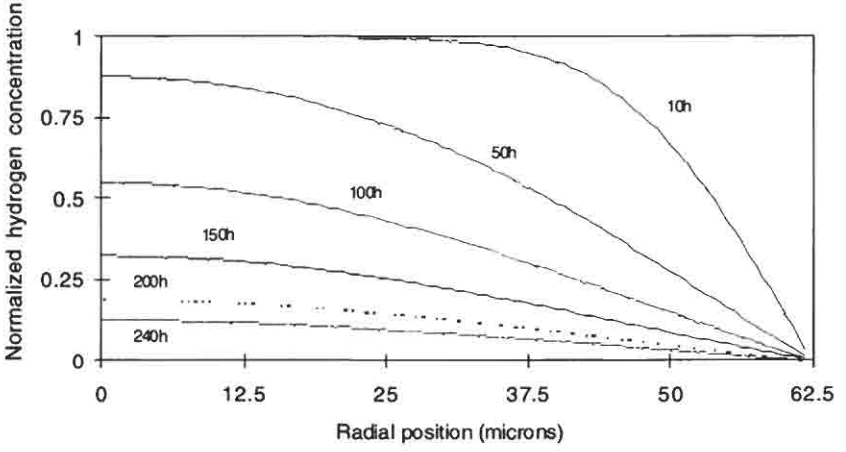

Figure 2.11: Out-diffusion profile of hydrogen in a 125-μm diameter fiber at 23°C (courtesy F. Bhakti, Ref. [73]).

to verify the concentration of hydrogen in the core [74,75]; the absorption at 1.245 μm is ~3 dB/(mol% H_2) (equivalent to 10^4 *ppm* in a mole of silica).

The wavelength shifts of long-period gratings (LPGs, see Chapter 4) resonances can be in excess of 150 nm to the long wavelength as the

hydrogen diffuses out of the core after fabrication of the grating, before returning to the original wavelength. Note that the resonance of the LPG is *only* dependent on the *difference* in the core and cladding refractive indexes, since it is the relative difference that is important (see Chapter 4). The effect on the refractive index of the fiber as the hydrogen out-diffuses is a complicated process, as shown by Malo *et al.* [76] using Bragg gratings. Once the fibers are removed from the chamber, the hydrogen begins to diffuse out but is fixed in the core by UV irradiation during grating fabrication. Depleted in the core, hydrogen in the cladding diffuses in before diffusing out. The stress changes the molecular polarizability of hydrogen [77], as well as the Bragg wavelength, first toward long, and then toward short wavelengths. The drift in the wavelength is found to be 0.72 nm for an initial pressure of 100 bar. The Bragg wavelength is sensitive to the net refractive index of the core, not to the difference between the core and the cladding as for the LPG. The dynamics of the coupling between the modes in LPGs has also been reported [78].

To prevent the fiber from out-gassing prematurely, it should be stored at low temperatures (−70°C) until it is used.

The diffusion time taken to reduce the hydrogen initial concentration, C_0/e, in the core is shown in Fig. 2.12a as a function of fiber diameter, at room temperature (20°C). Also shown is the diffusion time for standard fiber as a function of temperature (Fig. 2.12b).

2.4.5 Rare-earth-doped fibers

For a vast number of applications, such as fiber lasers and amplifiers, it is necessary to fabricate gratings in rare-earth-doped fibers. It is more difficult to write Bragg gratings in these fibers than in standard fibers. Worse, germanium is replaced by aluminum (Al_2O_3) to reduce the effect of quenching and lifetime shortening [79]. The lack of germanium reduces the photosensitivity of optical fibers, even with hydrogen sensitization, although gratings have been reported [46]. Gratings can be formed in most fibers, but the index changes remain weak ($<10^{-4}$) in all cases with 240-nm irradiation except in hydrogen-loaded Al/Ce or Al/Tb. With 193-nm irradiation, Al/Yb/Er fiber has shown index changes of 10^{-4} while hydrogen loading increases this figure to $\sim 10^{-3}$. The conclusion is that hydrogen loading improves the photosensitivity of germanium-free rare-earth-doped fibers. However, only a small subset of Er, Nd, and Ce and Tb-doped silicate fibers show reasonable photosensitivity ($>10^{-4}$) [46].

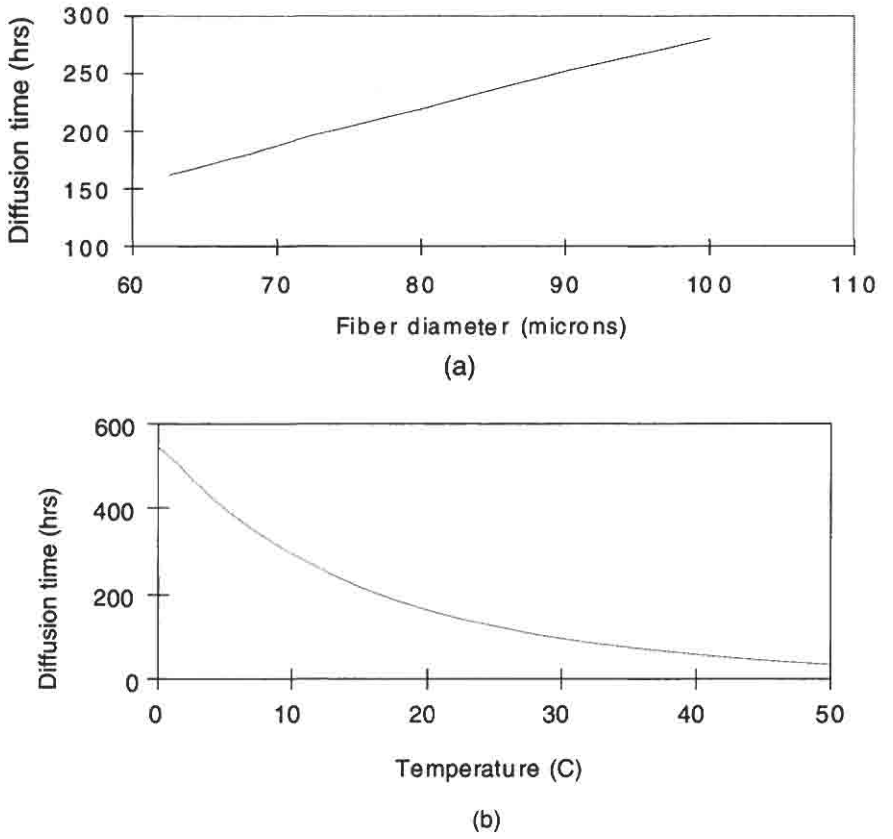

Figure 2.12: Out-diffusion time (1/*e* of initial concentration, C_0 of hydrogen as a function of fiber diameter at 20°C (a), and the diffusion time for a standard fiber as a function of temperature (b) (courtesy F. Bhakti).

The direct writing of gratings in RE fibers is limited to longish lengths, which suits the fabrication of narrow-band DFB fiber lasers. All gratings are of Type I or Type II; Type IIA has not been reported. A summary of the results on the most photosensitive fibers is listed in Table 2.1.

2.5 Densification and stress in fibers

There is increasing evidence that densification and stress increase in optical fibers contributes to the change in the refractive index [84–87]. Surface

TABLE 2.1: League table of rare-earth-doped silica photosensitive fiber.

Core dopant with Al, Ge-free	UV source: pulsed (nm)	$\sim\Delta n$ (pk–pk)	Reference
Undoped reference sample	193	5×10^{-5}	46
Eu^{2+}	248	2.5×10^{-5}	80
Ce^{3+}	265	3.7×10^{-4}	43, 81
Yb^{3+} and Er^{3+}	193	10^{-4}	46
P and Ce^{3+}	266	1.4×10^{-4}	82
Ce^{3+} and H_2	240	1.5×10^{-3}	43
Tb^{3+} and H_2	240	6×10^{-4}	83
Er^{3+} and H_2	235	5×10^{-5}	43
Tm^{3+} and H_2	235	8×10^{-5}	43
Yb^{3+}: Er^{3+} and H_2	193	5×10^{-4}	43

AFM scans of unetched samples show that the surface densifies in the UV illuminated regions [100]. In Fig. 2.13 is shown an atomic force microscope (AFM) scan of the surface of an Andrew Corp. D-fiber. After a grating has been written, the fiber is etched in buffered solution (3 vol% NH_4F 40%, 1 vol of HF 49% diluted with 50% saturated citric acid) with HF 25% for 110 minutes. The revealed pattern is indicative of structural modification in the glass, which influences the etch rate [88]. Stress measurement made optically show that the tensile stress increases in the core, *reducing* the induced refractive index change by as much as 30% [101] (see Chapter 9).

2.6 Summary of photosensitive mechanisms in germanosilicate fibers

There appear to be three routes by which a photo-induced refractive index change occurs in germanosilicate optical fibers:

1. Through the formation of color centers (GeE′)
2. Densification and increase in tension
3. Formation of GeH

Broadly speaking, all three mechanisms prevail in optical fibers. The relative importance of each contribution depends on the type of optical fiber and the photosensitization process used. Most fibers, if not all, show an increase in the population of GeE′ centers (trapped hole with an oxygen

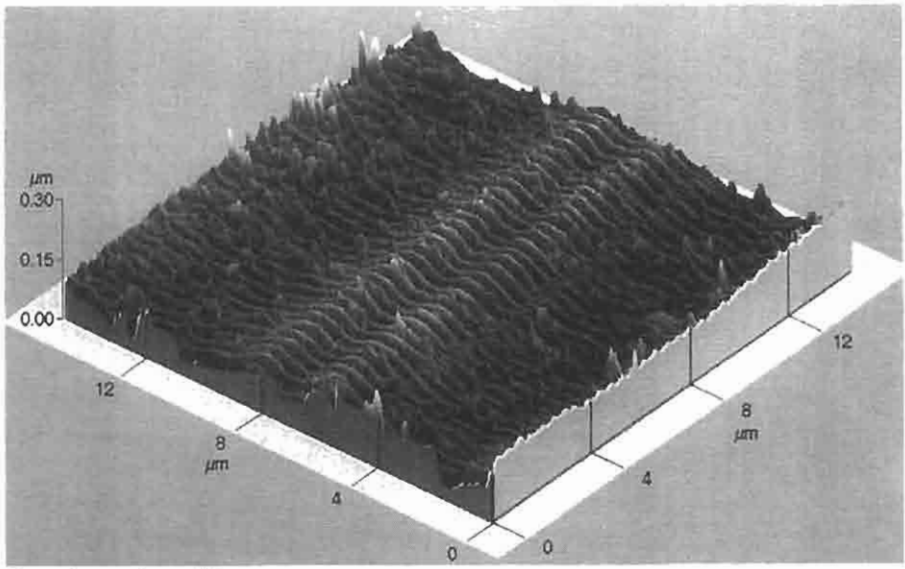

Experimental conditions :

• grating inscription : 8000 pulses at a fluence per pulse of 185 mJ/cm^2, grating pitch = 0.453 µm, R = R_{max}.

•• A.F.M. was performed after etching the fibre for 110 mn using buffered solution BOE mixed with 25% of HF.
BOE is (3 vol. of [NH_4F] 40%, 1 vol. of [HF] 49% diluted by 50% with saturated citric acid).

Figure 2.13: AFM scan of a D-fiber surface. Surface etched after grating inscription to reveal the chemically modified structure (courtesy Marc Douay, Ref. [88]).

vacancy) after UV exposure [89]. This is formed by the conversion of the electron-trapped Ge(I) center, which absorbs at ~5 eV. The change in the population of the GeE′ centers cause changes in the UV absorption spectra, which lead to a change in the refractive index directly through the Kramers–Kronig relationship [90] [Eq. (1.1.4)]. This process is common to all fibers. The color center model, originally proposed by Hand and Russell [91], only explains part of the observed refractive index changes of $\sim 2 \times 10^{-4}$ in nonhydrogenated optical fibers [92,93].

The second mechanism is a structural alteration in the mechanical nature of the glass and was pointed out several years ago by Bernardin and Lawandy [94]. In the model, a collapse of a higher-order ring structure was proposed as a possible effect of irradiation, leading to densification. The densification of silica under UV irradiation is well documented [95].

However, the picture is not as simple, since another mechanism opposes it: the relief of the internal stress frozen in during fiber fabrication, on UV exposure [96,97]. Stress relief can only remove the effect of the frozen-in stress and is therefore strongly dependent on the initial thermoelastic stress at fabrication. There is correlation between fiber drawing tension and the maximum induced index change for Type I gratings but reduced maximum index change for Type IIA [98]. The process of densification has been shown to occur in fibers as evidenced by scans using an atomic force microscope of the surface of D-shaped fibers and in etched fibers [99], and in preform samples that were drawn into a D-shaped fiber [100]. These observations are on the surface of the sample and are unable to replicate the stress profiles within the core of the fiber directly. Direct optical measurement of in-fiber stress has indicated that rather than the relief of the stress, tensile stress actually *increases* with an associated reduction in the average refractive index by ~30% of the observed UV induced refractive index change in non-hydrogen loaded, high-germania-content fibers [101]. The changes in the stress profile of the fiber are consistent with the shift in the Bragg wavelength of a grating during inscription [102].

The third mechanism for the UV induction of the refractive index change is via the formation of Ge–H and the generation of GeE′ centers; it was proposed by Tsai and Friebele [89]. The concentration of the GeE′ have been previously correlated with the presence of the precursor states of the Ge(I) and Ge(II) centers. However, the concentration of GeE′ centers continues to grow despite the saturation of both Ge(I) and Ge(II), indicating that the formation of the E′ centers has another route. The color center model for the changes in the refractive index is supported by the measurements made by Atkins *et al.* [103].

2.7 Summary of routes to photosentization

A method for photosensitizing silica optical fiber is based on the observation that increasing the 240-nm absorption enhances the effect [104]. Thus, reduced germania present as GeO has been shown to have a good photosensitive response. Other defect formers, such as europium [80], cerium [81], and thulium [43], also fall in this category, albeit with a smaller effect. Phosphorus, which is used extensively in the fabrication of germania-doped silica planar waveguides, shows a weak response with

radiation around 240 nm. However, the situation changes with radiation at 193 nm, as has been demonstrated [46].

Silica optical fibers with cores doped with germania, phosphorus, or alumina all exhibit increased photosensitivity when fabricated in a reducing atmosphere of hot hydrogen [105,106]. The negative effect of this type of treatment is the increase in the absorption due to the presence of OH^- ions and also an increase in the refractive index of the core. Flame-brushing, i.e., heating optical fiber or planar silica waveguides using a flame in a hydrogen-rich atmosphere, has also been used for photosensitization [107]. Hydrogen is able to diffuse into the fiber rapidly at elevated temperatures.

Germanosilicate optical fiber codoped with boron has been shown to be highly photosensitive [40]. Another advantage of the presence of boron is the large reduction in the background refractive index, allowing more germania to be added in the core for a given core–cladding index difference. It is believed that with boron physiochemical changes are responsible for the UV-induced index changes (approximately a few thousandths). Boron-codoped fiber gratings decay with temperature more rapidly than pure-germania doped fibers, although there are way to enhance their stability by using burn-in (see Chapter 9). The presence of boron also increases the absorption loss in the 1500-nm window by $\sim 0.1\ \mathrm{dB\ m^{-1}}$. An alternative scheme to circumvent the problems associated with boron is to use Sn codoping with germania [63]. This combination is more difficult to fabricate, but has virtually no additional absorption in the 1500-nm window, has a similar photosensitivity to the B–Ge system, and exhibits better temperature stability. There is no reduction in the refractive index with Sn doping.

Finally, the system that has demonstrated the largest photosensitive response in germanosilicate optical fibers is high-pressure cold hydrogen soaking [66]. It has been demonstrated that nearly every germanium ion is a potential candidate for conversion from the Ge–O to the Ge–H state [108], causing index changes as large as 0.01, although the ultimate magnitude of the index change is not known. Once hydrogenated, these fibers need to be stored at low temperatures to maintain their photosensitivity, since molecular hydrogen diffuses out just as readily as it can be introduced. A major disadvantage of writing gratings into cold-hydrogen-sensitized fiber gratings is the high loss of several decibels per meter at 1320 nm (OH^- absorption). Deuteration eliminates the absorption at 1320 nm, while maintaining the photosensitivity [68]. A summary of the all currently known techniques of photosensitizing fibers is listed in Table 2.2.

TABLE 2.2: Routes to photosensitization of optical fibers.

Fiber type	Fabrication process	Photosensitivity	Advantages	Disadvantages
Standard telecommunications germania-doped fiber ~3 mol%	Standard CVD/ PECVD	Very low: Photosensitive index change, $\delta n \sim 1 \times 10^{-6}$ (except one report of 1×10^{-3} [109])	Easy production, useful for low reflectivity gratings	Very low photosensitivity, low birefringence, good quality fiber
High germania 10–30 mol%	Standard CVD/ PECVD	Low photosensitive index change, slow growth of gratings, $\delta n \sim 1 \times 10^{-4}$	Good quality fiber, easy production	Birefringent, photosensitivity not enough to be useful in untreated fiber
Reduced germania (~10 mol%)	Production depleted oxygen atmosphere	Good photosensitivity, faster growth in index change, $\delta n \sim 5 \times 10^{-4}$	Low OH^- loss, circular cored fiber	Needs high germania (~10 mol%)
Boron–germania codoped	Needs additional calibration since boron reduces core index	Very good, faster increase in index, $\delta n \sim 8 \times 10^{-4}$	Low OH^- loss, can be compatible with standard telecommunication fiber	Difficult preform fabrication, highly stressed, increase in boron induced loss, elliptical core
Hot hydrogenated germania-doped fiber	Preform cooked at 750°C in hydrogen atmosphere	Good photosensitivity, $\delta n \sim$ 8c-4	Needs higher germania than standard tele-communications fiber; easy to store.	Slight increase in OH^- loss

Hot hydrogenated B–Ge codoped fiber	Same as above	Very good, $\delta n \sim 1 \times 10^{-3}$	Can be made compatible with standard telecommunication fiber	High stress, difficult to fabricate as B–Ge fiber. Loss at 1500 nm
High pressure cold hydrogen soaked germania-doped fiber	Easy fabrication since all types of above fiber may be used, including standard telecommunication fiber. But requires high pressure (up to 800Bar) facility	Excellent photosensitivity, $\delta n \sim 1 \times 10^{-2}$ in standard telecommunications fiber	Extremely versatile	OH loss with increase in index change. The loss can be ~0.1 dB per grating. Limited shelf life unless stored at low temperatures to prevent out-diffusion of H_2
High pressure cold deuterium soaked germania-doped fiber	Same as above	Same as above	No increase in loss at 1300/1500 nm since OD(OH) overtones are not in second or third telecommunications window	Extremely expensive option. Also limited shelf life unless stored at low temperatures to prevent out-diffusion of D_2
High-pressure hydrogen soaking of phosphorus rare-earth-doped fiber (Ge free)	Same as above	Can photosensitize many types of doped silica fibers	Intracore cavity fiber gratings possible for fiber lasers—no splice loss.	Requires 193-nm radiation for useful index changes and ease of writing

2.7.1 Summary of optically induced effects

The chemical reactions that take place in photosensitive optical fiber exposed to UV radiation are probably never going to be understood completely. However, several known factors influence the index change.

1. Bleaching of the 240-nm GeO band in reduced germania fibers. This has been measured and alludes to the following picture of chemical modification. The Ge–Si bonds break, liberating an electron, which may be retrapped at another defect site. What remains is the type of picture seen in Fig. 2.2 (GeE′). It is not known whether a volumetric change occurs as well. It is likely that, owing to the confinement of the photosensitive species within a massive cladding, any physical relaxation or contraction of molecular bonds will result in a stressed state. Recently, the stress change in fiber cores has been theoretically modeled and also measured using optical methods [110], with good agreement between the two. Douay *et al.* [99] have etched fibers and preforms previously exposed to interfering UV beams and found that a relief grating is revealed. Although this is not direct evidence that physical changes occur on UV exposure, it does show that the chemistry has indeed been altered. Riant *et al.* [100] performed atomic force microscopy (AFM) on the surface of D-shaped fibers in which gratings have been written. The surface of the fiber, a few microns above the photosensitive core of germanin-doped silica, showed a surface relief directly indicating stress changes. Therefore, not only does the absorption in the UV change, but so does the density of oscillators with UV exposure, both of which alter the refractive index based on the Kramers–Kronig rules. However, it must be remembered that the molecules within the core are not free to change their shape, but are elastically coupled to the mass in the cladding via bonds that remain predominantly unchanged. This is the basis for the induced stress and for part of the index modification by the stress-optic coefficient. Russell *et al.* [111] have estimated that a strain of only 10^{-4} is necessary to induce an index change in the effective index of the mode by the *same* order of magnitude. It is well known that fiber drawing conditions and stress annealing can alter the refractive index of boron-doped glasses [112].

2. There is a change in the position of the band edge of germania-doped silica in the deep-UV spectrum, which alters the refractive index after UV exposure. This effect is difficult to quantify owing to the problems associated with measurements in the vacuum ultraviolet and the low transparency of silica below a wavelength of ~190 nm, although some measurements have been made [113], suggesting that there is no shift in the edge, just an increase in the absorption in the deep UV.
3. High-temperature hydrogen treatment reduces germania, producing an enhanced concentration of GeO molecules [114]. Again bleaching of the absorption at 240 nm partly contributes to the index change. Other effects as in points 1 and 2 above prevail. Chemically, the reduction process may occurs as follows:

4. Molecular hydrogen. The suggested reaction is the formation of GeH and OH ions from a Ge(2) defect. The GeH is responsible for the change in the refractive index via the Kramers–Kronig rule. The possible route may be as follows:

It is not clear what the reactions with a pure alumina doped silica core may be, but it is possible that a similar set of observations may occur; the addition of phosphorus in germania-doped fibers reduces the concentration of GeE' centers, increasing with increased fabrication temperatures or reducing conditions [115].

Figure 2.14 compares a set of different fibers exposed to the same intensity of radiation at 262 nm for different times. The comparison shows the refractive index growth rate for fiber with different photosensitization treatments when exposed to UV radiation, per mol% Ge in the fiber,

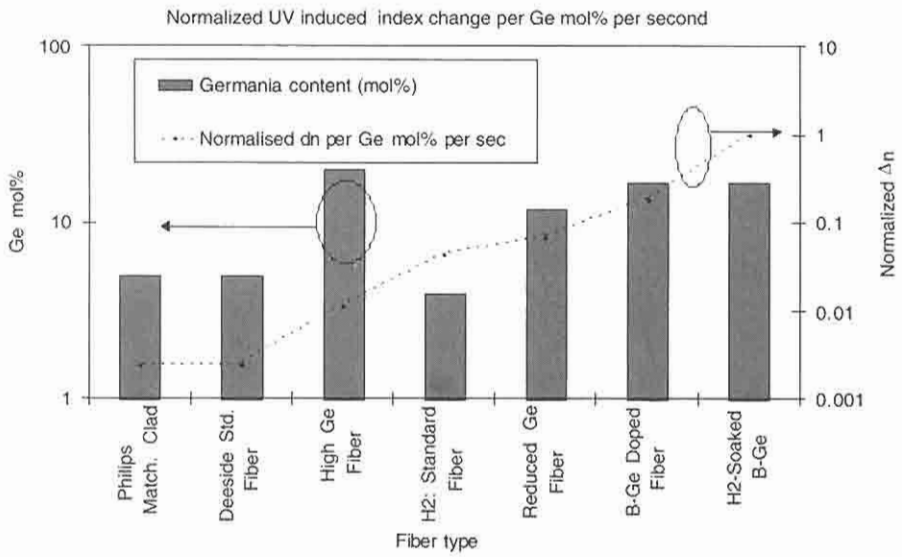

Figure 2.14: Comparison of time-averaged growth rate of the UV-induced refractive index change for different fibers compared to cold H_2-soaked:B-Ge fiber on the right column. Maximum index change recorded for the H–BGe codoped fiber was 6.76×10^{-3}. The UV source was a quadrupled diode pumped QS Nd:YLF laser operating at 262 nm with 60-mW writing power and used with a phase mask. This is a direct comparison of the induced index change in Type I gratings showing the sensitivity to UV radiation (adapted from Ref. [40]).

normalized to the fastest fiber: the H_2: BGe, which writes an 87% reflective, 1.5-mm long grating in 10 seconds.

References

1 Kleinmann D. A., "Nonlinear dielectric polarization in optical media," *Phys. Rev.* **126**(6), 1977–1979 (1962).

2 Kazansky P. G., Russell P. St. J., and Takebe H.,"Glass fiber poling and applications," *Lightwave Technol.* **15**(8), 1484–1493 (1997).

3 Griscom D. L., "Optical properties and structure of defects and structure of defects in silica glass," *Ceramic Soc. Jap.* **99**(10), 923–942 (1991).

4 Neustruev V. B., "Colour centres in germanosilicate glass and optical fibers," *J. Phys. Condens. Matter* **6**, 6901–6936 (1994).

5 Glass A. M., "The photorefractive effect," *Opt. Engg.* **17**, 470–479 (1978).

6 Fleming S. C., Fujiwara T., and Wong D., "UV excited poling of germanosilicate fibre," in *Photosensitivity and Quadratic Nonlinearity in Glass Waveguides: Fundamentals and Applications,* Vol. 22, 1995 OSA Technical Series (Optical Society of America, Washington DC, 1995), paper SUD1, pp. 180–183 (1995).

7 Myers R. A., Mukherjee N., and Brueck S. R. J., "Large second order nonlinearity in poled fused silica," *Opt. Lett.* **16**, 1732–1734 (1991).

8 Mukerjee N., Myers R. A., and Brueck S. R. J., "Dynamics of second order nonlinearities in poled silicate fibers," *J. Opt. Soc. Am. B* **11**, 665–669 (1994).

9 Dianov E. M., Kazansky P. G., Prokohorov A. M., and Stephanov D. Yu, "Photoinduced second-harmonic generation in glasses and glass optical fibers: Recent experiments," *Mol. Cryst. Liq. Cryst. Sci. Technol. Sec. B, Nonlinear Optics* **3**, 329–340 (1992).

10 Nagel S., MacChesney J. B., and Walker K. L., "An overview of the modified chemical vapor deposition (MCVD) process and performance," *IEEE J. Quantum Electron.* **QE-18**(4) 459–476, (1982).

11 Hibino Y. and Hanafusa H., "Defect structure and formation mechanism of drawing induced absorption at 630 nm in silica optical fibers," *J. Appl. Phys.* **60**, 1797 (1986).

12 Hibino Y. and Hanafusu H., "ESR study on E' centres induced by optical drawing process," *Jap. Journ. Appl. Phys.* **22**(12), 766–768 (1983).

13 Kaiser P., "Drawing induced coloration in vitreous silica fibers," *J. Opt. Soc. Am.* **64**, 475 (1974).

14 Lawandy N. M., "Light induced transport and delocalization in transparent and amorphous systems," *Opt. Commun.* **74**, 180–184 (1989).

15 Stapelbroek M., Griscom D. L., Friebele E. J., and Siegel G. H., "Oxygen-associated trapped-hole centers in high purity fused silica," *J. Non-Cryst. Solids* **32**, 313 (1979).

16 Nishikawa H., Tohmon R., Okhi Y., Hama Y., and Nagasawa K., "325nm absorption band by peroxy linkage in pure silica core fibre," in *Tech. Digest of Conf. on Optical Fiber Commun.,* OFC'89, p. 158 (1989).

17 Fribele E. J., Griscom D. L., and Siegel, G. H., Jr., "Defect centers in germania doped silica core optical fiber," *J. Appl. Phys.* **45**, 3424–3428 (1974).

18 Kawazoe H., "Effects of modes of glass formation on the structure of intrinsic or photoinduced defects centered on III, IV, or V cations in oxide glasses," *J. Non-Cryst. Solids* **71**, 213–234 (1985).

19 Tsai T. E., Griscom D. L., Fribele E. J., and Fleming J. W., "Radiation induced defect centers in high purity GeO_2 glass," *J. Appl. Phys.* **62**, 2262–2268 (1987).

20 Tsai T. E., Griscom D. L., and Fribele E. J., "On the structure of Ge-associated defect centers defect in irradiated high purity GeO_2 and Ge-doped SiO_2 glass," *Diffusion and Defect Data* **53–54**, 469–476 (1987).

21 Honso H., Abe Y., Kinser D. L., Weeks R. A., Muta K., and Kawazoe H., "Nature and origin of the 5 eV band in SiO_2:GeO_2 glasses," *Phys. Rev. B* **46**, II-445–II-451 (1995).

22 Hughes R. C., "Charge carrier transport phenomenon in amorphous SiO_2, direct measurement of the drift and mobility and lifetime," *Phys. Rev. Lett.* **30**, 1333–1336 (1973).

23 Isoya J., Weil J. A., and Claridge R. F. C., "The dynamical interchange and relationship between germanium centers in a-quartz," *J. Chem. Phys.* **62**, 4876–4884 (1978).

24 Malo B., Albert J., Bilodeau F., Kitagawa T., Johnson D. C., Hill K. O., Hattori K., Hibino Y., and Gujrathi S., "Photosensitivity in phosphorus doped silica glass and optical waveguides," *Appl. Phys. Lett.* **65**, 394–396 (1994).

25 Griscom D. L. and Mizuguchi M., "Determination of the visible range optical absorption spectrum of peroxy radicals in gamma irradiated fused silica," in *Bragg Gratings, Photosensitivity and Poling in Glass Fibers and Waveguides: Fundamentals and Applications,* Vol. 17, 1997 OSA Technical Series (Optical Society of America, Washington DC, 1997), paper JMD2, pp. 139–141 (1997).

26 MacDonald R. L. and Lawandy N. M., "Efficient second harmonic generation into the UV using optically encoded silicate glasses. *Opt. Lett.,* **18**(8), 595–597 (1993).

27 Dominic V. and Feinberg J., "Spatial shape of the dc-electric field produced by intense light in glass," *Opt. Lett.* **18**, 784–786 (1993).

28 Kashyap R., Maxwell G. D., and Williams D. L., "Photoconduction in Ge-P doped silica waveguides," *Appl. Phys. Lett.* **62**(3), 214–216 (1993).

29 Bagratshivilii V., Tsypina S. I., Chernov P. V., Rybaltovskii A. A. O., Zavorotny Y. S., Alimpiev S. S., Simanovskii Y. O., Dong L., and Russell P. St., "UV laser induced photocurrent in oxygen deficient silica and germanosilicate glasses," in *Photosensitivity and Quadratic Nonlinearity in Glass Waveguides: Fundamentals and Applications,* Vol. 22, 1995 OSA Technical Series (Optical Society of America, Washington DC, 1995), paper SUA1, pp. 66–69 (1995).

30 Purcell T. and Weeks R. A., "Electron spin resonance and optical absorption in GeO_2," *J Chem. Phys.* **78**, 1638–1651, (1987).

31 Archambault J-L., Reekie L., and Russell P. St. J., "100% reflectivity Bragg reflectors produced in optical fibres by single excimer pulses," *Electron. Lett.* **29**(5), 453 (1993).

32 Xie W. X., Douay M., Bernage P., Niay P., Bayon J. F., and Georges T., "Second order diffraction efficiency of Bragg gratings written within germanosilicate fibres," *Opt. Commun.* **101**, 85 (1993).

33 Williams D. L., Davey S. T., Kashyap R, Armitage J. R., and Ainslie B. J., *SPIE* **1513** 158, *Glasses for Optoelectronics* II, ECO4, The Hague (1991).

34 Poumellec B., Niay P., Douay M., and Bayon J. F., "The UV induced refractive index grating in Ge:SiO_2 preforms: additional CW experiments and the macroscopic origin of the index change in index," *J. Phys. D, Appl. Phys.* **29**, 1842–1856 (1996).

35 Cohen A. J. and Smith H. L., "Ultraviolet and infrared absorption of fused germania," *J. Phys. Chem.* **7**, 301–306 (1958).

36 Dong L., Pinkstone J., Russell P. St. J., and Payne D. N., "Study of UV absorption in germanosilicate fiber performs," in *Tech. Digest of Conf. on Lasers and Opto-Electronics, CLEO'94,* pp. 243–245 (1994).

37 Kohketsu M., Awazu K., Kawazoe H., and Yamane M., "Photoluminescence in VAD SiO_2:GeO_2 glasses sintered under reducing or oxidizing conditions," *Jap. J. Appl. Phys.* **28**(4), 622–631, 1989.

38 Skuja L. N., Truhkin A. N., and Plaudis A. E., "Luminescence in germanium doped glassy SiO_2," *Phys. Stat. Sol. A* **84**, K153–157 (1984).

39 Dong L., Pinkstone J., Russell P. St. J., and Payne D. N., "Ultraviolet absorption in modified chemical vapour deposition performs," *J. Opt. Soc. Am. B.* **11**, 2106–2111 (1994).

40 Williams D. L., Ainslie B. J., Kashyap R., Maxwell G. D., Armitage J. R., Campbell R. J., and Wyatt R., "Photosensitive index changes in germania doped silica fibers and waveguides," in *Photosensitivity and Self Organization in Optical Fibers and Waveguides, SPIE 2044,* pp. 55–68 (1993).

41 Albert J., Malo B., Hill K. O., Bilodeau F., Johnson D. C., and Theriault S., "Comparison of one-photon and two photon effects in photosensitivity of germanium doped silica optical fibers exposed to intense ArF excimer laser pulses," *Appl. Phys. Lett.* **67**, 3519–3521 (1995).

42 Niay P., Bernage P., Douay M., Taunay T., Xie W. X., Martinelli G., Bayon J. F., Poignant H., and Delevaque E., "Bragg grating photoinscription within various types of fibers and glasses," in *Photosensitivity and Quadratic Nonlinearity in Glass Waveguides: Fundamentals and Applications,* Vol. 22, 1995 OSA Technical Series (Optical Society of America, Washington DC, 1995), paper SUA1, pp. 66–69 (1995).

43 Tanuay T., Niay P., Bernage P., Douay M., Xie W. X., Puerer D., Cordier P., Bayon J. F., Poignant H., Delevaque E., and Poumellec B., "Bragg gratings

inscription within strained monomode high NA germania doped fibers: Part I—Experimentation," *J. Phys D: Appl. Phys.* **30**(1), 40–52, (1996).

44 Riant I. and Sansonetti P., "Influence of fiber drawing tension on photosensitivity in hydrogenated and unhydrogenated fibers," in *Tech. Digest of Conf. On Opt. Fiber Commun., OFC'98,* pp. 1–2 (1998).

45 Fribele E. J., Siegel G. H., and Griscom D. L., "Drawing induced defect centers in fused silica core fiber," *Appl. Phys. Lett.* **28**, 516–518 (1976).

46 Douay M., Xie W. X., Taunay T., Bernage P., Niay P., Cordier P., Poumellec B., Dong L., Bayon J. F., Poignant H., and Delevaque E., "Densification involved in the UV based photosensitivity of silica glasses and optical fibers," *J. Lightwave Technol.* **15**(8), 1329–1342 (1997).

47 Xie W. X., Niay P., Bernage P., Douay M., Bayon J. F., Georges T., Monerie M., and Poumellec B., "Experimental evidence of two types of photorefractive effects occurring during photoinscription of Bragg gratings within germanosilicate fibers," *Opt. Commun.* **104**, 185–195 (1993).

48 Grüner-Nielsen L. and Hübner J., Photosensitive fiber for highly reflective Bragg gratings," in *Tech. Digest of Conf. on Opt. Fiber Commun., OFC'97,* paper WL16, p. 178, (1997).

49 Williams D. L., Ainslie B. J., Armitage J. R., Kashyap R., and Campbell R. J., "Enhanced photosensitivity in germanium doped silica fibers for future optical networks," in *Proc. of the 18th European Conf. on Optical Commun., ECOC'92,* paper We B9-5, 425–428 (1992).

50 See, for example, Lemaire P. J., "Reliability of optical fibers exposed to hydrogen: prediction of long-term loss increases," *Opt. Eng.* **30**(6), 780–789 (1991).

51 Pavy D., Mosian M., Saada S., Cholet P., Leprince P., and Marrec J., in *Proc. ECOC'86,* pp. 132–141 (1986).

52 Dianov E. M., Golant K. M., Mashinsky V. M., Mededkov O. I., Nikolin I. V., Sazhin O. D., and Vasiliev S. A., "Highly photosensitive germanosilicate fiber codoped with nitrogen," in *Bragg Gratings, Photosensitivity and Poling in Glass Fibers and Waveguides: Fundamentals and Applications,* Vol. 17, 1997 OSA Technical Series (Optical Society of America, Washington DC, 1997), paper BME2, pp. 153–155 (1997).

53 Camlibel I, Pinnow D. A., and Dabby F. W., "Optical aging characteristics of borosilicate clad fused silica core fiber waveguides," *Appl. Phys. Lett.* **26**(4), 185–187 (1975).

54 Williams D. L., Ainslie B. J., Armitage J. R., Kashyap R., and Campbell R. J., "Enhanced UV photosensitivity in boron codoped germanosilicate optical fibres," *Electron. Lett.* **29**, 45–47 (1993).

55 Kashyap R., Williams D. L., and Smith R. P., "Novel liquid and liquid crystal cored fibre Bragg gratings," in *Bragg Gratings, Photosensitivity and Poling in Glass Fibers and Waveguides: Fundamentals and Applications,* Vol. 17, 1997 OSA Technical Series (Optical Society of America, Washington DC, 1997), paper BSuB5, pp. 25–27 (1997).

56 Dong L., Loh W. H., Caplen J. E., Hsu K., and Minelly J. D., "Photosensitive Er/Yb optical fibers for efficient single frequency fiber lasers," in *Tech. Digest. of Conf. on Opt. Fiber Commun., OFC'97,* pp. 29–30 (1997).

57 Kashyap R., Holmes M. H., Williams D. L., and Smith R. P., "Ultra-narrow band radiation mode filters," IOP, London, 1 May 1997.

58 Holmes M. J., Kashyap R., Wyatt R., and Smith R. P., "Development of radiation mode filters for WDM," *IEE Colloquia on multi-wavelength Networks: Devices Systems and Network Implementations, Ref. 1998/296,* June 1998.

59 Bonino S., Norgia M., Riccardi E., and Schiano M., "Measurement of polarisation properties of chirped fibre gratings," in *Technical Digest of OFMC'97,* pp. 10–13, (1997).

60 Kashyap R., Unpublished. Type IIA gratings have been regularly observed in B–Ge fibers with (15 mol% Ge) during writing with a CW 244-nm laser between 20 and 40 minutes of exposure. Presently, there is no other public domain data on this.

61 Douay M., private communication.

62 Baker S. R., Rourke H. N., Baker V., and Goodchild D., "Thermal decay of fiber Bragg gratings written in borongermania codoped silica fiber," *J. Lightwave Technol.* **15**(8), 1470–1477 (1997).

63 Dong L., Cruz J. L., Reekie L., Xu M. G., and Payne D. N., "Large photoinduced changes in Sn-codoped germanosilicate fibers," in *Photosensitivity and Quadratic Nonlinearity in Glass Waveguides: Fundamentals and Applications,* Vol. 22, 1995 OSA Technical Series (Optical Society of America, Washington DC, 1995), paper SUA2, pp. 70–73 (1995).

64 See, for example, Lemaire P. J., Watson H. A., DiGiovanni D. J., and Walker K. L., "Prediction of long term hydrogen induced loss increases in Er-doped amplifiers," *IEEE. Photonic Technol. Lett.* **5**(2), 214–217 (1993), and references therein.

65 Lemaire P. J., "Reliability of optical fibers exposed to hydrogen: prediction of long-term loss increases," *Opt. Eng.* **30**(6), 780–789 (1991).

66 Lemaire P., Atkins R. M., Mizrahi V., and Reed W. A., "High pressure H_2 loading as a technique for achieving ultrahigh UV photosensitivity and thermal sensitivity in GeO_2 doped optical fibres," *Electron. Lett.* **29**(13), 1191 (1993).

67 Atkins R. M., Lemaire P. J., Erdogan T., and Mizrahi V., "Mechanisms of enhanced UV photosensitivity via hydrogen loading in germanosilicate glasses," *Electron. Lett.* **29**, 1234–1235 (1993).

68 Lemaire P. J., Vengsarkar A. M., Reed W. A., and Mizrahi V., "Refractive index changes in optical fibers sensitized with molecular hydrogen," in *Technical Digest of Conf. on Opt. Fiber Commun., OFC'94,* pp. 47–48, (1994).

69 Martin J., Atkins G., Ouellette F., Tetu M., Deslauriers J., and Dugay M., "Direct correlation between luminescence and refractive index change in photosensitive Ge-doped and hydrogenated optical fibre," in *Photosensitivity and Quadratic Nonlinearity in Glass Waveguides: Fundamentals and Applications,* Vol. 22, 1995 OSA Technical Series (Optical Society of America, Washington DC, 1995), paper PMA2, pp. 200–203 (1995).

70 Kashyap R., unpublished (1997).

71 Atkins R. M. and Lemaire P. J., "Effects of elevated temperature on hydrogen exposure on short wavelength optical loss and defect concentration in germanosilicate optical fibers," *J. Appl. Phys.* **72**(2), 344–348 (1992).

72 Carslaw H. S. and Jaeger J. C., *Conduction of Heat in Solids,* Clarendon Press, Oxford (1978).

73 Bhakti F., Larrey J., Sansonetti P., and Poumellec B., "Impact of in-fiber and out-fiber diffusion on central wavelength of UV-written long period gratings," in *Bragg Gratings, Photosensitivity and Poling in Glass Fibers and Waveguides: Fundamentals and Applications,* Vol. 17, 1997 OSA Technical Series (Optical Society of America, Washington DC, 1997), paper BSuD2, pp. 55–57 (1997).

74 Stone J., "Interactions of hydrogen and deuterium with silica optical fibers: a review," *J. Lightwave Technol.* **5**(5), 712–733 (1987).

75 Shackelford J. F., Studt P. L., and Fulrath R. M., "Solubility of gases in glass: II: He, Ne, H_2 in fused silica," *J Appl. Phys.* **43**(4), 1619–1629 (1972).

76 Malo B., Albert J., Kill K. O., Bilodeau F., and Johnson D. C., "Effective index drift from molecular hydrogen loaded optical fibres and its effect on Bragg grating fabrication," *Electron. Lett.* **30**(5), 442–444 (1994).

77 Miller T. M., "Atomic and molecular polarizabilities," in *CRC Handbook of Chemistry and Physics,* pp. E68–E72, CRC Press, Boca Raton, FL (1989).

78 Jang J. N. and Kwack K. H., "Dynamics of coupling by H_2 diffusion in long period grating filters," in *Bragg gratings, Photosensitivity and Poling in Glass Fibers and Waveguides: Fundamentals and Applications,* Vol. 17, 1997 OSA Technical Series (Optical Society of America, Washington DC, 1997), paper BMG10, pp. 213–215 (1997).

79 Desurvire E., in *Erbium-Doped Fiber Amplifiers: Principles and Applications*. Wiley, New York (1994).

80 Hill K. O., Malo B., Bilodeau F., Johnson D. C., Morse T. F., Kilian A., Reinhart L., and Kyunghwan Oh., "Photosensitivity in Eu^{2+}:Al_2O_3-doped-core fibre: preliminary results and application to mode converters," *Proc. Conference on Optical Fiber Communications, OFC'91, paper PD3-1,* pp. 14–17 (1991).

81 Broer M. M., Cone R. L., and Simpson J. R., "Ultraviolet-induced distributed-feedback gratings in Ce^{3+} doped silica optical fibres," *Opt. Lett.* **16**(18), 1391–1393 (1991).

82 Dong L., Wells P. J., Hand D. P., and Payne D. N.,"Photosensitivity in Ce^{3+} doped optical fibers," *J. Opt. Soc. Am. B* **10**, 89–93 (1993).

83 Taunay T., Bernage P., Martenelli G., Douay M., Niay P., Bayon J. F., and Poignant H., "Photosensitization of terbium doped aluminosilicate fibers through high pressure H_2 loading," *Opt. Commun.* **133**, 454–462 (1997).

84 Douay M., Ramecourt D., Taunay T., Niay P., Bernage P., Dacosta A., Mathieu C., Bayon J. F., and Poumellec B., "Microscopic investigations of Bragg grating photowritten in germanosilicate fibers," in *Photosensitivity and Quadratic Nonlinearity in Glass Waveguides: Fundamentals and Applications,* Vol. 22, 1995 OSA Technical Series (Optical Society of America, Washington DC, 1995), paper SAD2, pp. 48–51.

85 Riant I., Borne S., Sansonetti P., and Poumellec B., "Evidence of densification in UV-written Bragg gratings in fibers," in *Photosensitivity and Quadratic Nonlinearity in Waveguides: Fundamentals and Applications,* Vol. 22, 1995, OSA Technical Digest Series (Optical Society of America, Washington DC, 1995), pp. 51–55.

86 Douay M., Xie W. X., Taunay T., Bernage P., Niay P., Cordier P., Poumellec B., Dong L., Bayon J. F., Poignant H., and Delevaque E., "Densification involved in the UV based photosensitivity of silica glasses and optical fibers," *J. Lightwave Technol.* **15**(8), 1329–1342, (1997).

87 Fonjallaz P. Y., Limberger H. G., Salathé R. P., Cochet F., and Leuenberger B., "Tension increase correlated to refractive index change in fibers containing UV written Bragg gratings," *Opt. Lett.* **20**(11), 1346–1348 (1995).

88 Courtesy Marc Douay, Bertrand Poumellec and Pierre Sansonetti. The AFM scan was performed after a grating with a 0.453-μm pitch had been inscribed with 8000 pulses at 185 mJ/cm^2 at 244 nm, doubled dye pumped by a XeCl laser, before etching. Details may be found in Ref. [86].

89 Tsai T. E., Williams G. M., and Friebele E. J., "Index structure of fiber Bragg gratings in Ge-SiO_2 fibers," *Opt. Lett.* **22**(4), 224–226 (1997).

90 Tsai T. E. and Friebele E. J., "Kinetics of defect centers formation in Ge–SiO_2 fibers of various compositions," in *Bragg Gratings, Photosensitivity and Poling in Glass Fibers and Waveguides: Applications and Fundamentals,* Vol. 17, 1997 OSA Technical Digest Series (Optical Society of America, Washington DC, 1997), pp. 101–103.

91 Hand D. P. and Russell P. St. J., "Photoinduced refractive index changes in germanosilicate optical fibers," *Opt. Lett.* **15**(2), 102–104 (1990).

92 Williams D. L., Davey S. T., Kashyap R., Armitage J. R., and Ainslie B. J., "Direct observation of UV induced bleaching of 240 nm absorption band in photosensitive germanosilicate glass fibres," *Electron. Lett.* **28**(4), 369 (1992).

93 Dong L., Archambault J. L., Russell P. St. J., and Payne D. N., *Proc. ECOC'94,* 997 (1994).

94 Bernardin J. P. and Lawandy N. M., "Dynamics of the formation of Bragg gratings in germanosilicate optical fibers," *Opt. Commun.* **79**, 194 (1990).

95 Rothschild M., Erlich D. J., and Shaver D. C., "Effects of excimer irradiation on the transmission, index of refraction, and density of ultraviolet grade fused silica," *Appl. Phys. Lett.* **55**(13), 1276 (1989).

96 Sceats M. G. and Krug P. A., "Photoviscous annealing—dynamics and stability of photorefractivity in optical fibers," *SPIE 2044,* 113–120 (1993).

97 Wong D., Poole S. B., and Skeats M. G., "Stress birefringence reduction in elliptical-core fibers under ultraviolet irradiation," *Opt. Lett.* **24**(17), 1773 (1992).

98 Riant I. and Poumellec B., "Influence of fiber drawing tension on photosensitivity in hydrogenated and nonhydrogenated fibers," in *Tech. Digest of Conf. on Opt. Fib. Commun, OFC'98,* paper TuA1, pp. 1–2 (1998).

99 Douay M., Ramecourt D., Tanuay T., Bernage P., Niay P., Dacosta D., Mathiue C., Bayon J. F., and Poumellec B., "Microscopic investigations of Bragg gratings photowritten in germanosilicate fibers," in *Photosensitivity and Quadratic Nonlinearity in Waveguides: Fundamentals and Applications,* Vol. 22, 1995 OSA Technical Digest Series (Optical Society of America, Washington, DC, 1995), pp. 48–51.

100 Riant I., Borne S., Sansonetti P., and Poumellec B., "Evidence of densification in UV-written Bragg gratings in fibers," in *Photosensitivity and Quadratic Nonlinearity in Waveguides: Fundamentals and Applications,* Vol. 22, 1995 OSA Technical Digest Series (Optical Society of America, Washington, DC, 1995), pp. 51–55.

101 Limberger H. G., Fonjallaz P. Y., and Salathé R. P., "UV induced stress changes in optical fibers," in *Photosensitivity and Quadratic Nonlinearity in*

Waveguides: Fundamentals and Applications, Vol. 22, 1995 OSA Technical Digest Series (Optical Society of America, Washington, DC, 1995), pp. 56–60.

102 Douay M., Xie W. X., Taunay T., Bernage P., Niay P., Cordier P., Poumellec B., Dong L., Bayon J. F., Poignant H., and Delevaque E., "Densification involved in the UV based photosensitivity of silica glasses and optical fibers," *J Lightwave Technol.* **15**(8), 1329–1342 (1997).

103 Atkins R. M., Mizrahi V., and Erdogan T., "248 nm induced vacuum UV spectral changes in optical fibre preform cores: support for a colour centre model of photosensitivity," *Electron. Lett.* **29**(4), 385 (1993).

104 Williams D. L., Anslie B. J., Kashyap R., Maxwell G. D., Armitage J. R., Campbell R. J., and Wyatt R., "Photosensitive index changes in germania doped silica glass fibers and waveguides" *SPIE* **2044**, 55–68, (1993).

105 Maxwell G. D., Kashyap R., Ainslie B. J., Williams D. L., and Armitage J. R., "UV written 1550 nm reflection filters in singlemode planar silica waveguides," *Electron. Lett.* **28**(22), 2106–2107, (1992).

106 Meltz G. and Morey W. W., "Bragg grating formation and germanosilicate fiber photosensitivity," *SPIE* **1516**, 185–199 (1991).

107 Bilodeau F., Malo B., Albert J., Johnson D. C., Hill K. O., Hibino Y., Abe M., and Kawachi M., "Photosensitization in optical fiber and silica on silicon/silica waveguides," *Opt. Lett.* **18**, 953–955 (1993).

108 Krol D. M., Atkins R. M., and Lemaire P. J., "Photoinduced second-harmonic generation and luminescence of defects in Ge-doped silica fibers," *SPIE* **1516**, 38–46 (1991).

109 Limberger H. G., Fonjallaz P. Y., and Salathé R., "Spectral characterization of photoinduced high efficient Bragg gratings in standard telecommunication fibers," *Electron. Lett.* **29**(1), 47–49 (1993).

110 Fonjallaz P. Y., Limberger H. G., Salathé R., Cochet F., and Leuenberger B., "Tension increase correlated to refractive index change in fibers containing UV written Bragg gratings," *Opt. Lett.* **20**(11), 1346–1348 (1995).

111 Russell P. St. J., Hand D. P., Chow Y. T., and Poyntz-Wright L. J., "Optically-induced creation, transformation and organisation of defects and colour centres in optical fibres," *SPIE* **1516**, 47–54 (1991).

112 Camlibel I., Pinnow D. A., and Dabby F. W., "Optical ageing characteristics of borosilicate clad fused silicacore fibre optical waveguides," *Appl. Phys. Lett.* **26**(4), 185–187 (1975).

113 Atkins R. M., Mizrahi V., and Erdogan T., "248 nm induced vacuum UV spectral changes in optical fibre preform cores: Support for the colour centre model of photosensitivity," *Electron. Lett.* **29**(4), 385 (1993).

114 Iino A., Kuwabara M., and Kokura K., "Mechanisms of hydrogen induced losses in silica based optical fibers," *J. Lightwave Technol.* **8**(11), 1675–1675, 42 (1990).

115 Atkins G. R., Poole S. B., Sceats M. G., Simmons H. W., and Nockolds C. E., "The influence of codopants and fabrication conditions on germanium defects in optical fiber preforms," *IEEE Photon. Technol. Lett.* **4**(1), 43–46 (1992).

Chapter 3

Fabrication of Bragg Gratings

3.1 Methods for fiber Bragg grating fabrication

This chapter reviews many of the schemes proposed for both holographic and nonholographic grating inscription and considers some of the salient features of the methods. This introduction excludes methods used for internal grating writing, traditionally known as "Hill" gratings, for which the reader is directed to other sources [1–12].

Fiber Bragg gratings, which operate at wavelengths other than near the writing wavelength (non-Hill gratings), are fabricated by techniques that broadly fall into two categories: those that are holographic [13] and those that are noninterferometric, based on simple exposure to UV radiation periodically along a piece of fiber [14]. The former techniques use a beam splitter to divide a single input UV beam into two, interfering them at the fiber; the latter depend on periodic exposure of a fiber to pulsed sources or through a spatially periodic amplitude mask. There are several laser sources that can be used, depending on the type of fiber used for the grating, the type of grating, or the intended application. The sources used for grating production are also discussed in this chapter.

3.1.1 The bulk interferometer

The method for the side writing of fiber gratings demonstrated by Meltz *et al.* [15] is shown in Fig. 3.1. The interferometer is one encountered in

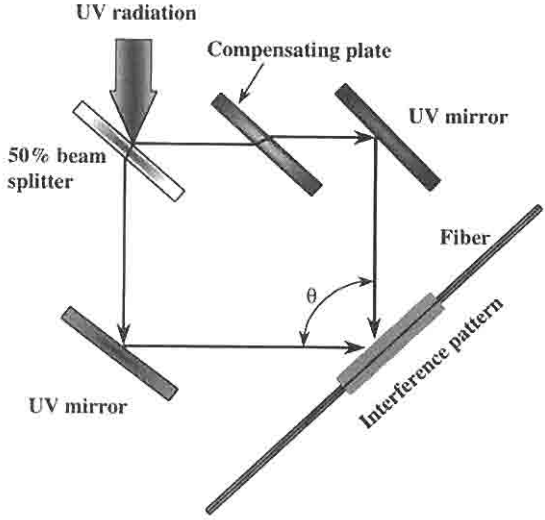

Figure 3.1: UV interferometer for writing Bragg gratings in optical fibers. Note the use of an additional phase plate (mirror blank) in one arm to compensate for the path length difference.

standard holography [16], with the UV beam divided into two at a beam splitter and then brought together at a mutual angle of θ, by reflections from two UV mirrors. This method allows the Bragg wavelength to be chosen independently of the UV wavelength as

$$\lambda_{Bragg} = \frac{n_{eff}\,\lambda_{uv}}{n_{uv}\,\sin\left(\dfrac{\theta}{2}\right)}, \tag{3.1.1}$$

where λ_{Bragg} is the Bragg reflection wavelength, n_{eff} is the effective mode index in the fiber, n_{uv} is the refractive index of silica in the UV, λ_{uv} is the wavelength of the writing radiation, and θ is the mutual angle of the UV beams. The essential difference between a "Hill" grating and one produced by external interference of two UV beams is that with the holographic technique the Bragg reflection wavelength depends on UV radiation wavelength and geometric factors. Since λ_{uv} is around 240 nm, θ lies between 0° and 180°, and assuming that the refractive index in the UV is approximately equal to the effective index, the Bragg wavelength is adjustable from one nearly equal to the UV source wavelength to infinity [see Eq. (3.1.1) with $\theta = 0$].

The fiber is held at the intersection of the beams. This method was originally successfully used to write gratings at visible wavelengths. The interferometer is ideal for single-pulse writing of short gratings, and great care has to be taken in the design of the optical mounts. Mechanical vibrations and the inherently long path lengths in air can cause the quality of the interferogram to change over a period of time, limiting its application to short exposures. For low-coherence sources, the path difference between the two interfering beams must be equalized; a simple method is to introduce a mirror blank in one arm to compensate for the path imbalance imposed by the beam splitter, as shown in Fig. 3.1. Note that the in arriving at the fiber, the beam that is transmitted through the beam splitter undergoes a 180° rotation so that they have *different* spatial profiles. This is an important factor for spatially incoherent beams.

The interferometer shown in Fig. 3.1 has several beams paths in open air. It is important that these are shielded from turbulence, since the interference fringes formed at the fiber can drift if the paths of the two beams change during the inscription time. As is common with all holographic arrangements, it is not sensible to mount mirrors, beam splitters, or the fiber on flimsy platforms prone to disturbance, such as tall 10-mm diameter mounting posts. The interferometer needs to be built on a sturdy base, with stable optical mounts. This is especially true in cases that require long (minutes to hours) exposures. It is common practice to enclose the entire interferometer within a Perspex housing, which allows visual and physical access to the setup, at the same time protecting the interferometer from constant path-length variations and the operator from accidental exposure to UV radiation. Extreme care needs to be taken to minimize exposure of personnel to high-energy UV radiation or long-term exposure to low-power radiation. Adhering to safe operating practices is essential when using UV radiation.

In principle, a diffraction grating used in reflection can replace the 50% beam splitter shown in Fig. 3.1. In this interferometer, two coherent beams are required, so that reflection from a diffraction grating to divide the input UV beam into two is equally feasible. However, a simpler component, the transmission phase-grating, otherwise known as the *phase mask,* is better suited to this application.

3.1.2 The phase mask

A major step toward easier inscription of fiber gratings was made possible by the application of the phase mask as a component of the interferometer.

Used in transmission, a phase mask is a relief grating etched in a silica plate. The significant features of the phase mask are the grooves etched into a UV-transmitting silica mask plate, with a carefully controlled mark–space ratio as well as etch depth. The principle of operation is based on the diffraction of an incident UV beam into several orders, $m = 0, \pm 1, \pm 2 \ldots$. This is shown schematically in Fig. 3.2. The incident and diffracted orders satisfy the general diffraction equation, with the period Λ_{pm} of the phase-mask,

$$\Lambda_{pm} = \frac{m\lambda_{uv}}{\left(\sin\frac{\theta_m}{2} - \sin\theta_i\right)}, \tag{3.1.2}$$

where $\theta_m/2$ is the angle of the diffracted order, λ_{uv} the wavelength, and θ_i the angle of the incident UV beam. In instances when the period of the grating lies between λ_{uv} and $\lambda_{uv}/2$, the incident wave is diffracted into only a single order ($m = -1$) with the rest of the power remaining in the transmitted wave ($m = 0$).

With the UV radiation at normal incidence, $\theta_i = 0$, the diffracted radiation is split into $m = 0$ and ± 1 orders, as shown in Fig. 3.3. The interference pattern at the fiber of two such beams of orders ± 1 brought together by parallel mirrors (as in Fig. 3.1) has a period Λ_g related to the diffraction angle $\theta_m/2$ by

$$\Lambda_g = \frac{\lambda_{uv}}{2\sin(\theta_m/2)} = \frac{\Lambda_{pm}}{2}. \tag{3.1.3}$$

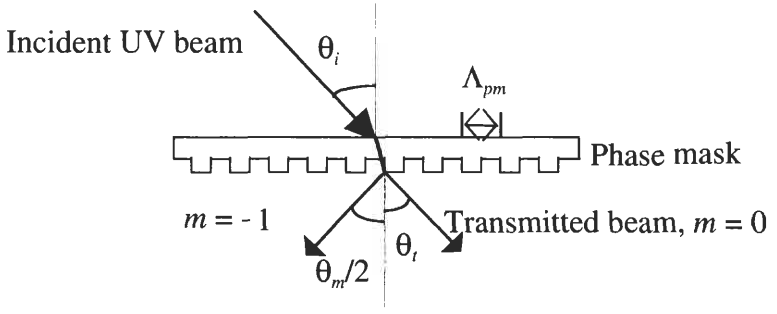

Figure 3.2: A schematic of the diffraction of an incident beam from a phase mask.

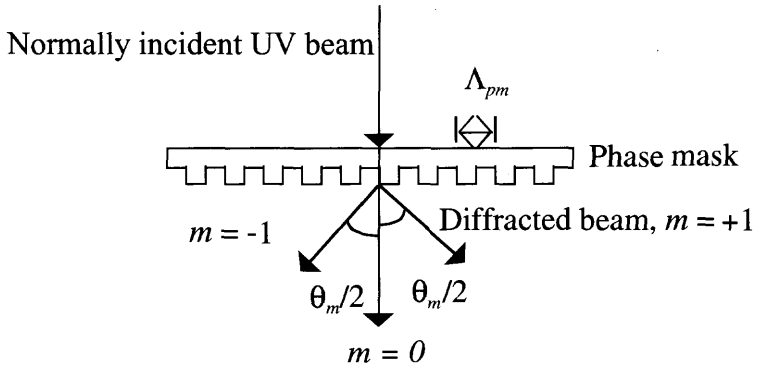

Figure 3.3: Normally incident UV beam diffracted into two ±1 orders. The remnant radiation exits the phase-mask in the zero order ($m = 0$).

The period Λ_{pm} of the grating etched in the mask is determined by the Bragg wavelength λ_{Bragg} required for the grating in the fiber (see Chapter 4) and using Eq. (3.1.3) to arrive at

$$\Lambda_g = \frac{N\lambda_{Bragg}}{2n_{eff}} = \frac{\Lambda_{pm}}{2}, \tag{3.1.4}$$

where $N \geq 1$ is an integer indicating the order of the grating period.

For *nonnormal* incidence of the UV radiation on the phase mask, intensities in the $m = 0$ and -1 orders are not necessarily equal. However, for the visibility of the interference pattern to be a maximum, the intensities must be equalized. This is important if gratings are to be inscribed efficiently. For a first-order ($N = 1$) grating at a Bragg wavelength of 1.55 μm and a mode effective index $n_{eff} \approx 1.46$, $\Lambda_{pm} = 1.06$ μm, which is greater than the wavelength of the UV radiation used for grating inscription (0.193 to 0.360 μm). Therefore, more than a single diffracted order ($m = 0, \pm 1, \pm 2 \ldots$) exists. To suppress the positive orders and control the diffraction efficiency, and to equalize the power between the -1 order and the transmitted beam ($m = 0$), one face of the etched grating walls may be coated with a metal film to form reflecting mirrors. This may be done by evaporating the metal on to the phase-mask plate at an angle so that only the walls facing the evaporation source are coated [17]. Another method uses a deeper etched grating in the phase mask [18] to suppress higher orders and control the relative intensities. However, it is easier

and more cost-effective simply to use a phase mask at normal incidence. If necessary, an antireflection coating may be applied to the back facet of the phase-mask plate to reduce reflections, which can cause the quality of the interference fringes to be degraded [25].

The depth d of the etched sections of the grating is a function of the UV wavelength, but the period is dependent only on the Bragg wavelength and the effective index of the mode. However, in the case of UV writing of gratings, it is necessary to ensure that the intensity of the transmitted zero-order beam is minimized and, ideally, blocked from arriving at the fiber.

To minimize the zeroth order from a UV beam normally incident on a phase mask, the smallest etch depth d of the relief grating in silica is,

$$d(n_{uv} - 1) = \lambda_{uv}/2. \tag{3.1.5}$$

Equation (3.1.5) assumes monochromatic radiation with no divergence; however, for a practical nonmonochromatic source, the $m = 0$ order cannot be eliminated. In practice, the zeroth order can be reduced to a level of a percent or so. At a wavelength of 244 nm, $d \approx 262$ nm. The phase-mask zero order can be nulled only at a single wavelength. Changing the laser source wavelength will require a different phase mask, unless the zero order is physically blocked. For efficient diffraction onto the first orders, it is necessary for the relief grating to have a mark–space ratio of 1:1, or for the corrugations in the phase mask to be purely sinusoidal.

Fabrication of the phase mask

The phase mask is normally fabricated by one of two methods: by exposure of a photoresist overcoated, silica maskplate to an electron beam to form the pattern [19,20], or by holographic exposure [21]. With the e-beam facility, a silica wafer, which has a bilevel resist comprising a 450-nm layer of AZI400-27 is hard baked at 190°C for 30 minutes, followed by a 200-nm layer of silicon-containing negative resist (SNR) baked at 85°C, also for 30 minutes. Charge dispersal during the e-beam exposure is effected by a evaporating a thin layer of aluminum. After exposure to delineate the pattern, the A1 coating is removed in an alkaline solution and the SNR spray developed in MIBK for 35 sec, then rinsed in a 50:50 ratio of MIBK+IPA solution for 5 sec, followed by 15 sec in IPA. The developed pattern is transferred to the AZI400-27 layer by reactive ion etching (RIE) at 10 m torr in oxygen and 50 W RIE. The resist is then

used as a mask for etching into the silica plate using CHF_3:Ar RIE. The final depth of 262 nm, for use at a UV wavelength of 244 nm, is achieved by a two-stage etch. A scanning electron microscope photograph of a phase-mask plate is shown in Fig. 3.4. Generally, the phase mask is fabricated in small fields, which are then stitched together to form a long grating. Common problems with phase masks processed by e-beams have to do with inaccurate stitching of the fields. The positioning accuracy of the e-beam and variation of the silica mask plate height cause phase steps to occur between fields, and the resolution of the photoresist causes random variations in the individual periods of the grating. Techniques have been developed to minimize these errors [46,20]; however, the random variation in the absolute positioning of the e-beam is a fundamental limitation. Typically, the writing of long phase-masks by e-beam needs constant referencing and correcting owing to small temperature variations during the exposure period, which may last several hours. These problems are of greater importance as the length of the grating increases. Phase masks as long as 120 mm have been reported [22], although the quality of the fabricated Bragg grating has not been reported in detail. Stitching is not an issue when the alternative technique of holographic phase-mask fabrication is used. This technique is, in principle a superior method for phase-mask production. However, long phase masks have been difficult

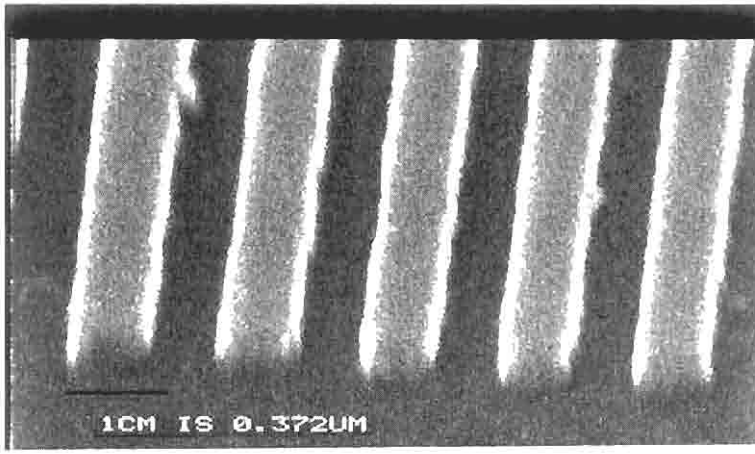

Figure 3.4: SEM photograph of a high-quality phase mask used for grating inscription of ~1060-nm Bragg gratings. (Courtesy Ian Lealman, BT Labs)

to produce holographically, owing to problems with uniformity of illumination and the requirement for large mirrors. Lenses can be used to alter the phase front of one of the interfering beams to allow the fabrication of *continuously* chirped gratings, as opposed to step-chirped gratings by e-beam fabrication [23]. Since the fabrication of the holographic phase mask depends on geometrical alignment of interfering beams, the mass production of identical phase masks may remain a problem.

3.1.3 The phase mask interferometer

UV lithographic replication has been used extensively to fabricate phase masks directly in silica plates using e-beam writing and plasma etching [24], to function as lenses and complex spatial elements. This technique has also been applied successfully to fiber Bragg grating inscription and reported in the literature by several laboratories at around the same time [25–28]. There are several methods of using the phase mask: as has been stated, it may perform the function of simple beam splitting in the interferometer in Fig. 3.1. So why is it such a useful element, when a far cheaper dielectric beam-splitter can be used instead? Its primary aim is to be used simply as a wavelength-*defining* element in an interferometer (as shown in Fig. 3.5); used as a beam splitter with the beam-combining mirrors (Fig. 3.5) to adjust the wavelength of the fiber grating.

The change in the Bragg wavelength as a function of the change in the mutual angle between the two interfering beams as shown in Fig. 3.5 is found by substituting Eqs. (3.1.3) and (3.1.4) into Eq. (3.1.1) and differentiating with respect to θ:

$$\frac{\Delta\lambda}{\lambda_{Bragg}} = -\frac{\Delta\theta}{2}\cot\frac{\theta}{2}. \tag{3.1.5a}$$

Figure 3.6 shows the Bragg wavelength in the fiber as a function of the half-writing angle. With the diffraction angle fixed at ~10° (phase mask for ~1550 nm), a change of 5° alters the Bragg wavelength by ~800 nm [29]. The enormous tunability of this interferometer, as well the ability to find a reference position for the phase-mask Bragg wavelength, makes it highly flexible. It requires a single-phase mask, which is used as both a beam splitter *and* a Bragg wavelength reference. It can also be used to replicate chirped phase masks, and a tunability of the Bragg wavelength of ~250 nm has been demonstrated [29].

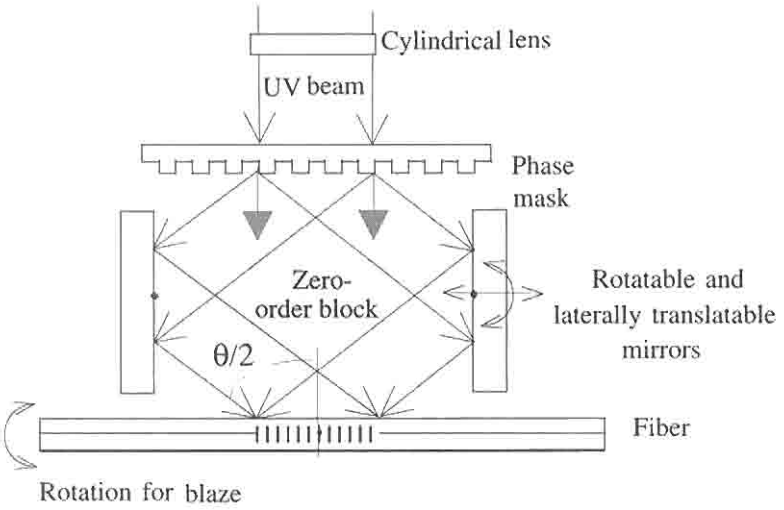

Figure 3.5: The phase mask used as a beam splitter in an interferometer for inscription of fiber gratings. The phase mask predefines the wavelength of the reflection grating, when the mirrors are at right angles to the axis of the fiber and the phase-mask plate (Talbot interferometer) [see Eq. 3.1.3 and 3.1.4]. In this scheme, the paths of the two interfering beams are identical, making the interferometer suitable for use with low-spatial-coherence sources.

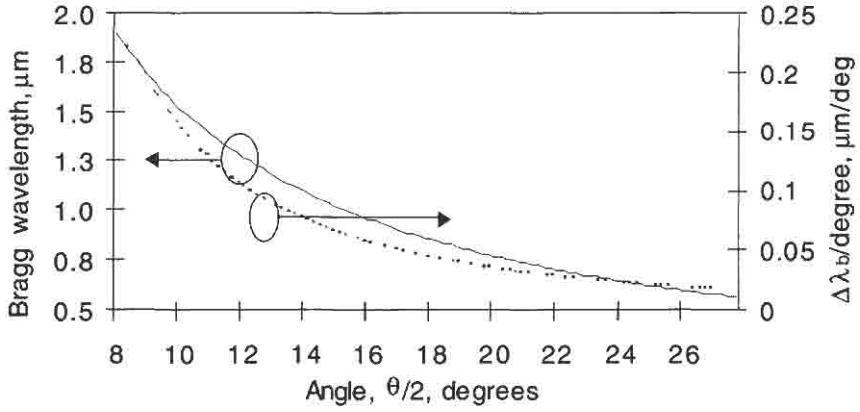

Figure 3.6: The Bragg wavelength (dashed curve) and the rate of change of the Bragg wavelength (continuous curve) as a function of the phase-mask diffraction angle. A change of ~1.6° around a mean diffraction angle of 10° is equivalent to a change in the Bragg wavelength of ~250 nm.

Alternatively, the fiber may be placed directly behind the phase mask for photo imprinting of the grating. In this scheme, there are two important issues. First, since the diffracted beams interfere in the region of overlap immediately behind the phase mask, the fiber core needs to be at the phase-mask surface for maximum overlap. The closest the phase mask can be placed to a fiber core is a distance equal to the fiber radius (unless a "D-fiber" is used), which means that there is no overlap of the two beams in a short region at either end of the grating. Second, the interference pattern generated at the fiber core is the sum of the interference of *all* the diffracted orders. For a pure sinusoidal pattern at the fiber core, it is important to allow only the two ± 1 orders to interfere with the zero-order suppressed. As has been observed with the phase mask in contact with the fiber, even with a zero-order nulled phase mask, the period of the imprinted grating depends strongly on the intensity of the writing UV beam. At low intensities, the period is half the phase-mask period [see Eq. (3.1.3)], but at high intensities, even a low zero-order intensity can interfere with the ± 1 orders to create a grating of the same period as the phase mask itself [120]. Tilting the fiber at an angle α behind the phase mask so that one end is further away shifts the Bragg reflection to longer wavelengths as the inverse of cosine α, since the fringe planes are no longer orthogonal to the propagation axis. This method for tuning the Bragg wavelength has been demonstrated [30]; it should, however, be remembered that the grating length shortens with tilt, and not only does the reflectivity drop (due to limited coherence of the UV source), but radiation loss can increase [41] (see Section 3.1.4).

The zero-order beam may be avoided by repositioning the mirrors. This is shown in Fig. 3.7a, where the grating is written at a point well removed from the incident zero order. The path length of the two interfering beams remains identical. A similar result may be achieved by tilting the beam-folding mirrors by an angle α from the perpendicular to the horizontal plane. On reflection from the surfaces, the beams are directed at angles of 2α to the horizontal plane, out of the plane of the zero-order beam, as shown in Fig. 3.7b.

It is usual to place a cylindrical focusing lens before the phase mask in the path of the UV beam so as to allow two stripes (within the plane of the paper in Fig. 3.7a) to overlap at the fiber. This has the advantage of focusing in one plane and increasing the power density, while leaving the length of the grating unaltered. Care need to be taken in adjusting

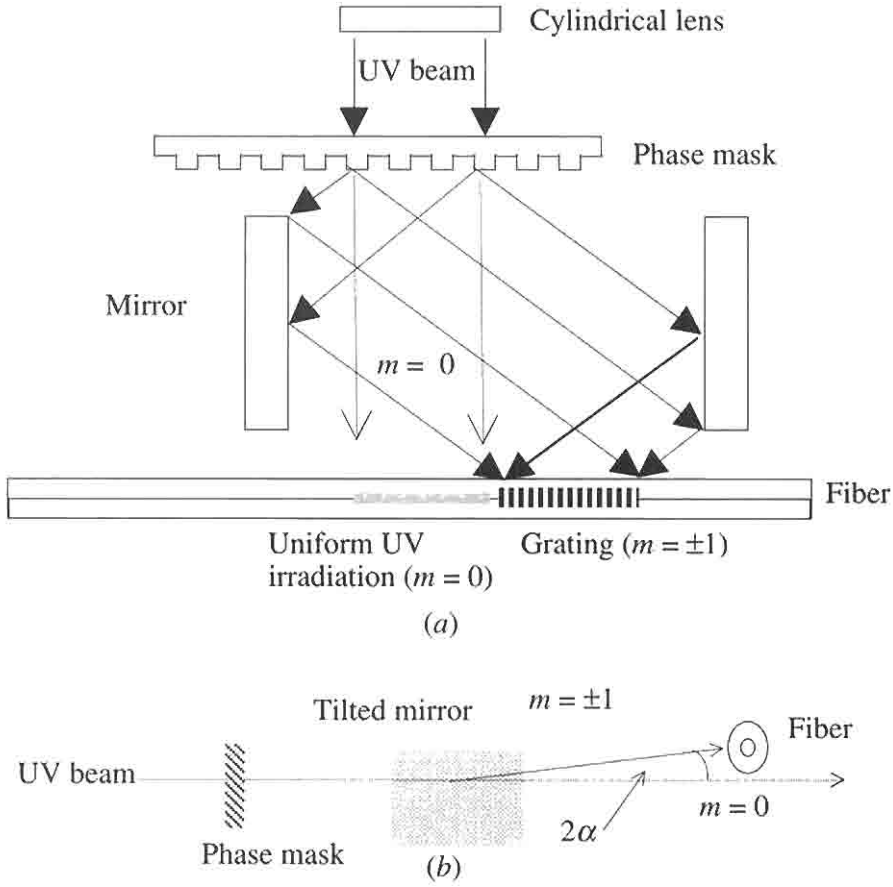

Figure 3.7: (a) Avoiding the zero order from the region of the grating by repositioning the interferometer mirrors. Alternatively, tilting the mirrors outward from their normally vertical positions, means that the beams no longer interfere in the plane of the zero order (b).

this interferometer, since the orientation of the phase mask determines whether the two beams will overlap at the fiber, while the cylindrical lens determines whether or not the overlapping stripes align along the fiber core. It is important to ensure that the path lengths from the phase mask to the fiber are identical so that the mutual coherence of the beams is

maximized [31]. The fiber should be placed in the region of the fringes such that the propagation axis is normal to the fringe planes, since any angular misalignment increases radiation loss from the light propagating in the fiber (see Chapter 4) and shifts the Bragg wavelength.

If mutual counterrotation of the mirrors is incorporated in the phase-mask interferometer, grating inscription becomes infinitely flexible with a *single* phase mask. Two modifications are required if Bragg wavelength tunability is required: the mirrors need to be rotated, and the distance of the fiber from the phase mask must be changed. Using a translation stage to hold the fiber *in situ* easily incorporates the latter. The alignment of the interferometer is simply and quickly carried out by using a borosilicate glass microscope coverslip to view the fluorescence of the individual UV beams. The coverslip is moved toward or away from the interferometer until the fluorescence from the two beams overlaps. The fiber simply replaces the glass slide for grating inscription. Figure 3.8 shows a photograph of the fully flexible interferometer in use at BT Laboratories.

The polarization of the UV laser beam affects the inscription of the grating in the fiber [32–39]. To ensure that the inscribed grating has low polarization sensitivity, the polarization of the UV laser beam should be oriented parallel to the propagation axis of the fiber [40]. (Gratings inscribed with UV laser radiation polarized orthogonal to the propagation direction show significant birefringence due to effects of induced birefringence.) This may be achieved by placing an appropriately oriented half-wave plate before the phase mask.

Replacement of the two mirrors in Fig. 3.5 by a rectilinear UV transmitting silica block [23] results in an extremely compact and stable interferometer. The diffracted UV beams enter a face of the silica block and are totally internally reflected by adjacent sides to emerge through the opposite face, interfering at the fiber. The beam paths are shown in Fig. 3.9.

The silica block is placed halfway between the phase mask and the fiber. The maximum grating length, which can be written in a fiber is related to the dimensions of the block. The length L_g of the grating is a function of the length of the side of the silica block (mirror) as

$$L_g = L_s \tan\left[\sin^{-1}\left(\frac{\sin(\theta_m/2)}{n_s}\right)\right], \tag{3.1.6}$$

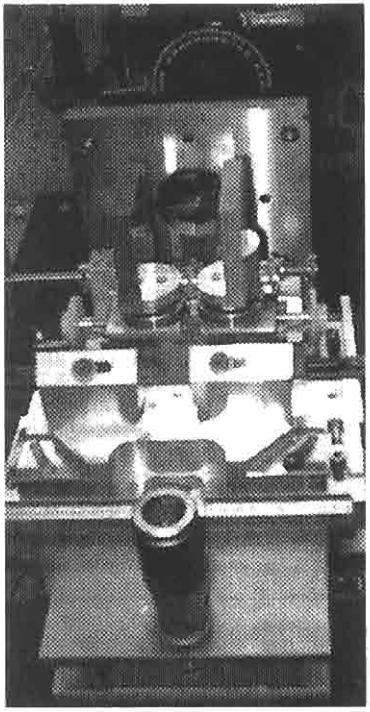

Figure 3.8: The photograph shows the tunable phase-mask interferometer. The distance between the mirrors can also be altered without misaligning the interferometer. The fiber can also be rotated around the vertical axis to allow the inscription of slanted gratings (see Section 3.1.4).

where n_s is the refractive index of the silica block at the writing UV wavelength. Assuming that $\sin \theta_m/2 \approx \theta_m/2$ for small angles, the maximum length of the grating, which may be written with a side of L_g is

$$L_g \approx \frac{L_s \theta_m}{2n_s} \approx \frac{L_s \theta_m}{3} . \tag{3.1.7}$$

For fiber Bragg gratings at a wavelength of 1500 nm, the angle $\theta_m/2 \sim 10°$; the length of the silica block side is then approximately 17 times the grating length. The minimum width of the silica block W_s is equal to the grating length L_g without in-line zero-order suppression. However, if the zero order is to be physically blocked by an opaque element,

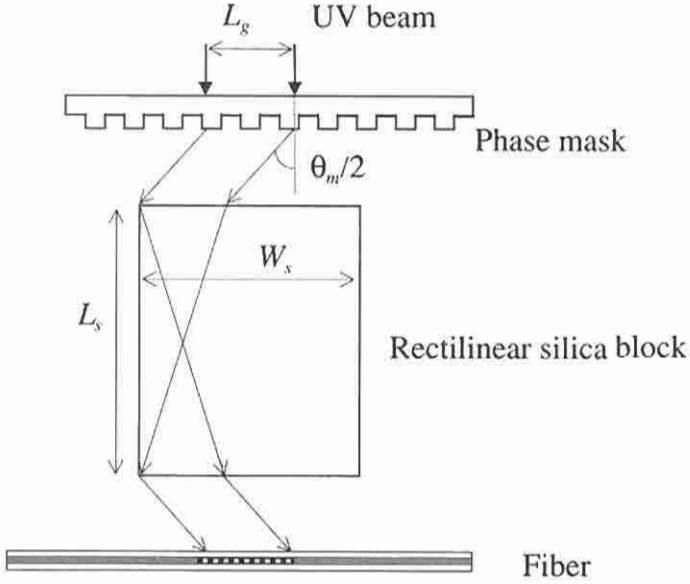

Figure 3.9: Replacement of the two mirrors in Fig. 3.5 by a UV-transmitting silica block. Only one set of diffracted UV beams is shown for simplicity.

then the width $W_s \geq 3L_g$. This width is reduced to $2L_g$ if the interferometer in Fig 3.5 is used with the zero-order beam block halfway in between the mirrors. For long gratings the dispersion of the silica block is a limitation if the interferometer is used with a low-coherence source. However, simplification of grating inscription makes this setup highly attractive.

There are many advantages of using a phase mask. It allows the wavelength of the fiber grating to be defined precisely for replication. Matching fiber grating reflection wavelengths is made easier, since the phase mask is the interferometer itself. Mass production of identical fiber gratings is thus possible. Another advantage of the phase mask is that a predetermined function may be inscribed in it for replication into the fiber [23] (see Section 3.1.13). The phase mask forms a very stable interferometer since there are no adjustable parts, allowing long inscription times. It is also insensitive to the translation of the inscribing UV beam and tolerant to beam-pointing instability of the laser beam. The advantage of translation insensitivity allows long fiber gratings to be written by the scanning technique, discussed in Section 3.1.5. Disadvantages of using

the phase mask nearly in contact with the fiber are the dangers of contamination and permanent damage of the phase mask. A different phase mask is required for each specific Bragg wavelength. This need not a problem, since several gratings can be written on a single phase-mask plate, each at the required wavelength [41]. Alternatively, a tunable interferometer can be used with a single phase mask; however, it does require careful calibration and alignment.

3.1.4 Slanted grating

If the fiber is tilted out of the plane of Fig. 3.5, the grating inscribed in the fiber will be slanted in the direction of propagation of the mode. This, however, requires the interfering beams to have a large cross-sectional area so that the beams may overlap, as shown in Fig. 3.10a. This is inconvenient for most interferometers, since the cylindrical lens focuses the beams *in the plane* of the figure, unless the unfocused beam intensity is already high. An alternative and simple method for inscribing slanted gratings is to tilt the fiber in the plane of the figure, as shown in Fig. 3.10b [41]. In this case, the coherence properties of the laser will determine the visibility of the fringes at the fiber. Since the fiber is at an angle to the incoming beams, the inscription of the grating depends on the overlap of the two beams and is slightly shortened; the depth D of the fringes for the interferometer shown in Fig. 3.10b is

$$D \leq \frac{W}{\tan(\theta_m/2)}, \tag{3.1.8}$$

where W is the width of the normally incident UV beam and $\theta_m/2$ is the diffraction angle shown in Fig. 3.3. Figure 3.11 shows the depth of the fringes and the overlap of the beams. For small tilt angles α, the period Λ_s of the slanted grating in the direction of propagation varies as

$$\Lambda_s \approx \frac{\Lambda_g}{\cos\,\alpha}. \tag{3.1.9}$$

The fringe pattern shown in Fig. 3.3 is unchanged; however, since the fiber core is at an angle to the fringes, a grating, which is blazed with respect to the propagation direction of the mode, is formed. These gratings have special applications as lossy filters and are discussed in Chapters 4 and 8. In Fig. 3.14, the extent of the fringes formed in the overlap region

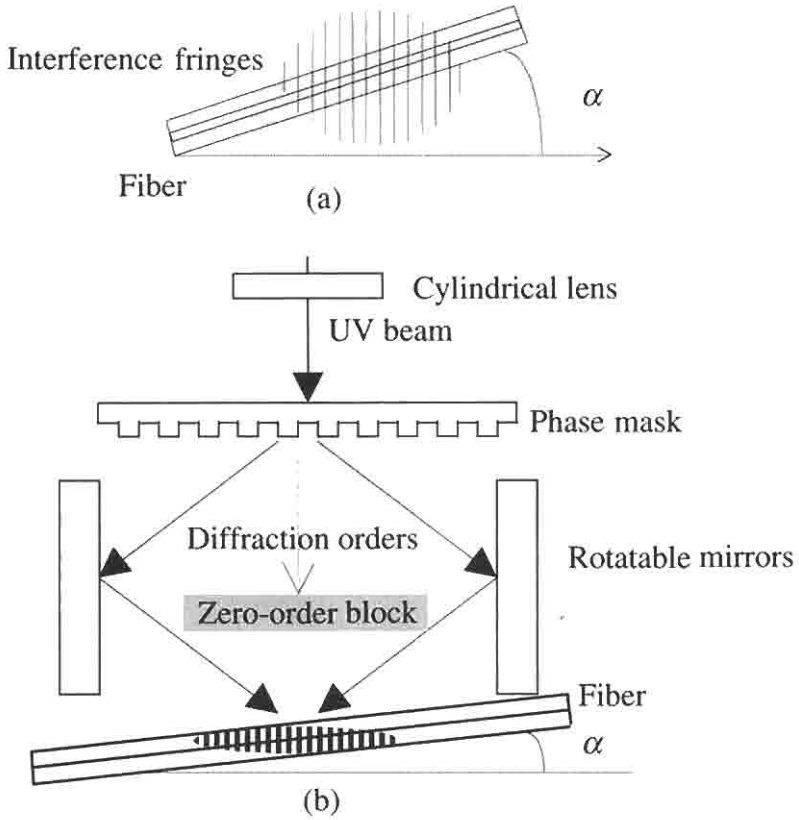

Figure 3.10: (a) The fringes formed at the point of intersection need a large cross-sectional area for a slanted grating to be written in the fiber. Shown in (a) is view of the fringes in a plane normal to the zero-order, and α is the rotation angle in that plane. (b) shows another method for writing slanted gratings, in the plane of the incoming beams [41]. The fiber is rotated by an angle α within the plane of the beams such that it overlaps with the interference fringes; the coherence properties of the UV source as well as the depth of fringes determine this.

is shown. The maximum possible fringe depth D is indicated in Fig. 3.11. Coherence, both temporal and spatial, limits D to less than this value, as described in Eq. (3.1.8). For a phase mask used in near contact with the fiber, the depth of the fringes is less than $D/2$.

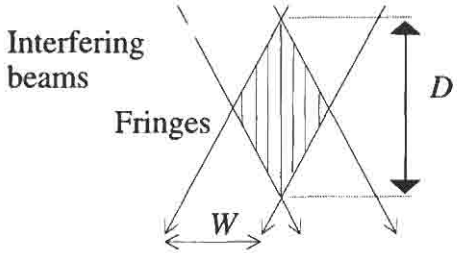

Figure 3.11: The overlap of the two interfering beams forms a diamond figure, with a depth of the fringes D. The grating length varies depending on the placement of the fiber within the fringes.

3.1.5 The scanned phase mask interferometer

Figure 3.12 shows how the phase mask may be scanned for inscribing long gratings into fibers. This technique was first demonstrated by Ouellette *et al.* [42]. It was shown that 19-mm long gratings may be faithfully reproduced in fibers; a slight nonuniformity in the phase mask was also removed by applying a temperature gradient across the fiber length after writing the grating. Byron *et al.* [43] reported a 50-mm long grating in which the quality of the interferogram was varied by adjusting the intensity of the writing beam along the length of the grating. This method allows the tailoring of the transfer characteristics of the fiber grating and

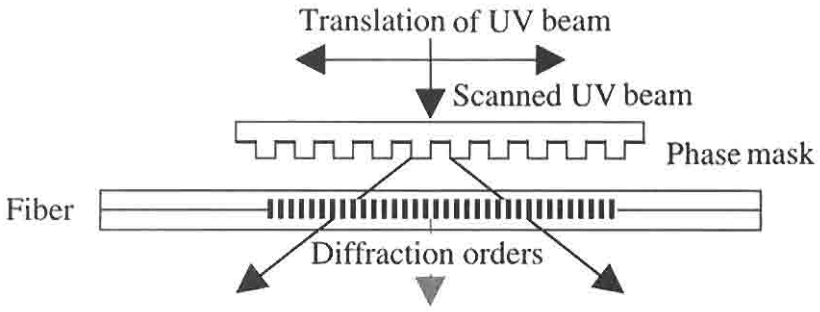

Figure 3.12: The phase mask used as a scanned interferometer is a powerful method of fabricating long-fiber gratings. The quality of the grating is dependent on the uniformity of the phase mask.

will be discussed in Chapter 5. The length and the quality of the phase mask limit the scanning technique. With the best e-beam facility, the absolute positional accuracy is around 5 nm. This positional error sets the limit on the stitching of the fields. Although the error is random and the effects are averaged out over the length of the mask [44], the stitching errors are manifest in the transfer characteristics of the grating [45]. This causes multiple reflections and structure within the reflection envelope determined by the field size, while the reflection bandwidth is inversely dependent on the overall length of the grating. Techniques have be applied to reduce the effects of stitching errors in phase masks by altering the field size of each subgrating processed by the e-beam. By overlaying N e-beam exposures with different field sizes, each with $1/N$ of the dose, the total dose required to imprint the grating pattern in the photoresist on the phase mask is maintained while averaging out the periodic nature of the stitching errors. Developing the resist dramatically reduces the effects of the stitch errors, which appear as multiple out-of-band reflections. This has been successfully demonstrated [46], and the effects on the reflection spectrum are shown in Fig. 3.13.

Another technique, albeit used less successfully, monotonically increased the field sizes for a 14-mm long grating, from 100 μm to 200 μm in steps of 1.055 μm. Although many of the features were eliminated, field sizes around 200 μm produced a cluster in the reflection spectrum [46], since the fractional change in the field-size remains small.

Stitching errors or undesirable chirp in a phase mask are replicated in a fiber grating. It is possible to use the technique of "UV trimming" [47] to adjust the local refractive index in the fiber to correct the transmission spectrum. Scanning a UV beam across a phase mask while also moving the fiber, enables the chirp in the phase mask to be compensated for [48,49]. By adjusting the velocity of the fiber relative to the scanning UV beam at different positions along the phase mask, the induced refractive index change can be changed, altering the local Bragg wavelength. If the phase mask has an unintended chirp, the fiber grating can be "trimmed." This technique has been applied to reduce the chirp of a grating written by using a 100-mm long phase mask that had undesired chirp situated close to the middle of the mask. This was found by monitoring the growth of the reflection of a grating. The velocity is adjusted in steps (5 sec to 22 nm/sec) with the help of a piezoelectric stage, while the UV beam is scanned at a velocity of 250 μm/sec during fabrication of a second grating. The induced wavelength shift is directly related to the velocity of the

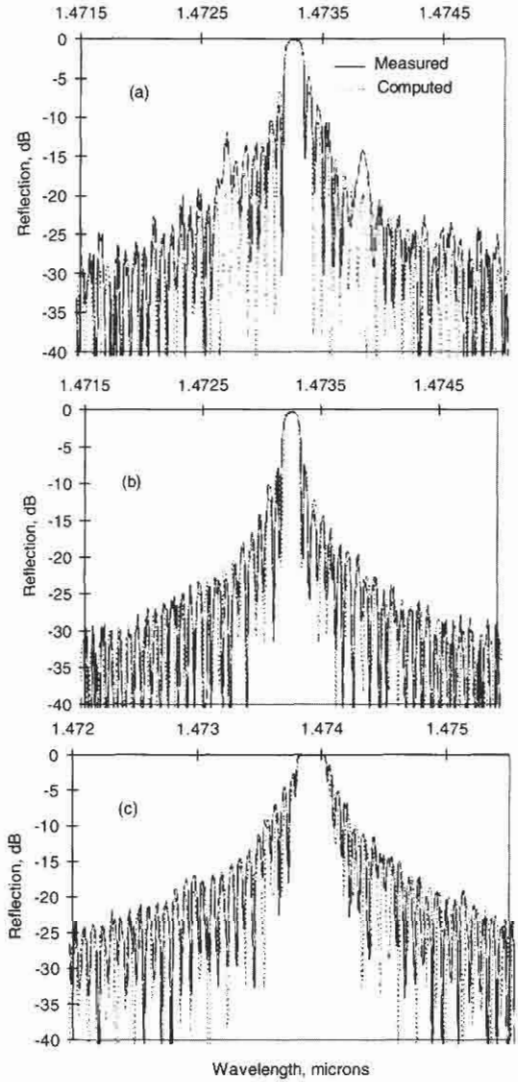

Figure 3.13: Reflection spectra from imprinting with different phase masks as a function of the number of overlaid e-beams exposures of the phase mask. This grating is discussed in Section 3.1.13. (a) Single-pass field size of 65 μm; (b) three passes with 65.4, 55.3, and 59.26 μm; (c) as for (b) with additional 66.04 μm pass (from: Albert J, Theriault S, Bilodeau F, Johnson D C, Hill K O, Sixt P, and Rooks M J, "Minimisation of phase errors in long fiber Bragg grating phase masks made using electron beam lithography," *IEEE Photon. Technol. Lett.* **8**(10), 1334–1336, 1996. © 1996 IEEE [46]).

scanning beam v_{uv} and that of the fiber v_f as $\Delta\lambda = \lambda v_f / v_{uv}$. Removal of the chirp reduced the bandwidth of the grating from 0.23 nm to 0.1 nm [48].

The elimination of out-of-band ghosts is important for telecommunications, while the postfabrication repair of expensive phase masks is very useful for fabrication.

3.1.6 The Lloyd mirror and prism interferometer

In the double mirror arrangement of the interferometer shown in Fig. 3.1 the incident beam is split into two, and fringes form from interference between identical copies of the incident radiation. Any phase distortion across the input beam is automatically compensated for at the fringe plane, or can be compensated for by the introduction phase plates, so that local visibility of the fringes remains close to unity and chirp in the period of the fringes reduced to zero.

Figure 3.14 shows an arrangement for an interferometer based on a single mirror known commonly as the Lloyd mirror. A parallel beam

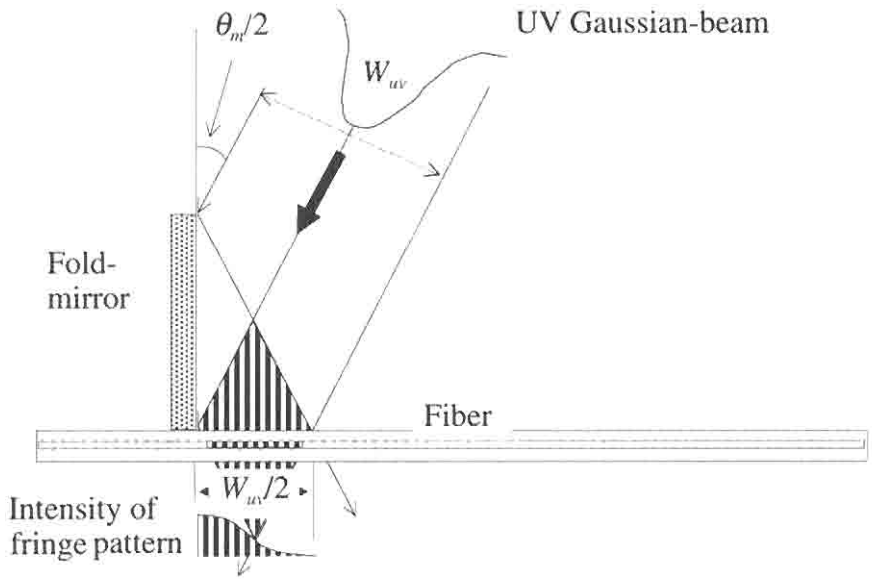

Figure 3.14: The Lloyd mirror interferometer, showing the intensity of the fringes formed at the fiber with a folded Gaussian beam [50].

incident at the surface of the mirror at a shallow angle is reflected across the path of the beam. Interference occurs in the region of overlap of the reflected and unreflected parts of the incident beams. The interferometer is therefore extremely simple and easy to use. However, since half of the incident beam is reflected, interference fringes appear in a region of length equal to half the width of the beam. Secondly, since half the beam is folded onto the other half, interference occurs, but the fringes may not be of high quality. In the Lloyd arrangement, the folding action of the mirror limits what is possible. It requires a source with a coherence length equal to at least the path difference introduced by the fold in the beam. Although a phase plate may be used over half the beam to compensate, experimentally this is not straightforward. Ideally, the intensity profile and coherence properties should be constant across the beam; otherwise, the fringe visibility will be impaired and the imprinted grating will be nonuniform. Since most sources tend to have a Gaussian beam profile, it is difficult to produce fringes which have a uniform transverse profile. The grating profile remains half-Gaussian, unless the beam is expanded to provide a more uniform profile. The Gaussian intensity profile of the fringes introduces a chirp in the imprinted grating. Diffractive effects at the edge of the mirror may also cause a deterioration of the fringes closest to it.

The Lloyd arrangement with the single mirror is easy to tune. However, the fiber axis should be placed orthogonal to the plane of the mirror so that the grating is not slanted.

Replacement of the mirror by a prism in the Lloyd arrangement results in a more stable interferometer. This is shown in Figure 3.15. The UV writing beam is now directed at the apex of a UV-transmitting silica right-angled prism such that the beam is bisected, as in the Lloyd mirror. Both halves of the UV beam are therefore refracted and no longer travel in air paths, which can change with time.

The interferometer thus becomes intrinsically stable and was used to produce the first photoinduced fiber Bragg gratings in the 1500-nm wavelength window [51]. The interferometer has been used to demonstrate a distributed-feedback dye laser. Interfering the pump beams in the dye at the appropriate angle to create a Bragg reflector (absorption grating) caused the dye to emit laser radiation [52].

The advantages and disadvantages of this interferometer are similar to those of the Lloyd mirror. However, there are two further points of interest. Owing to the shallow angle subtended by the UV beam on the hypotenuse, the prism face has to be much larger than the beam width,

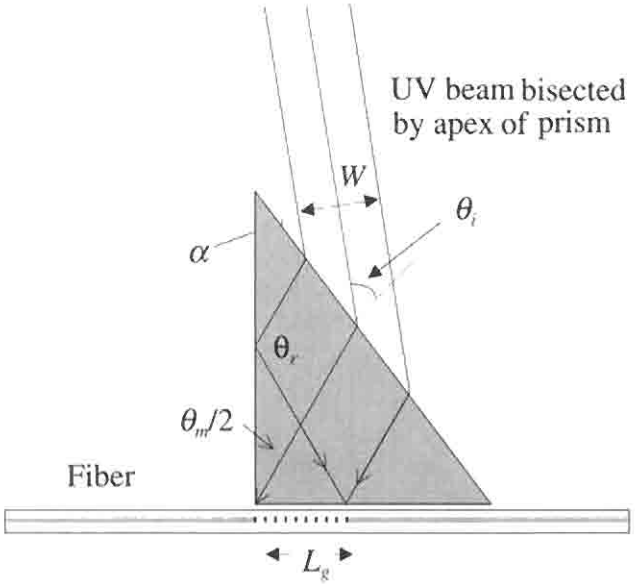

Figure 3.15: The Lloyd prism interferometer. The interfering beam paths are within the bulk of the prism; however, there is a path difference introduced between them due to the refractive index of the prism. The UV beam must be spatially and temporally coherent with a uniform intensity for the production of high-quality gratings.

but because of refraction, the side of the prism at which total internal refraction occurs is smaller than the length of the Lloyd mirror [see Section 3.1.3, similar to Eq. (3.1.6)]. For a given beam width, the prism interferometer expands the length of the grating, and this is shown in Fig. 3.16. Using simple geometry, the length of the grating L_g may be shown to be

$$L_g = \frac{W}{2 \cos \theta_i} \left[\sin \alpha + \cos \alpha \tan\left(\frac{\theta_m}{2}\right) \right], \qquad (3.1.9a)$$

the parameters for which are defined in Fig. 3.15.

At large angles of incidence (small apex angles), the grating length increases rapidly but reflection losses increase at the same time. The polarization useful for writing a grating with low birefringence (p-polarized) is reflected more than the unwanted polarization (s-polarized) [40] [see Section 3.1.8]. Antireflection coating of the surface will naturally

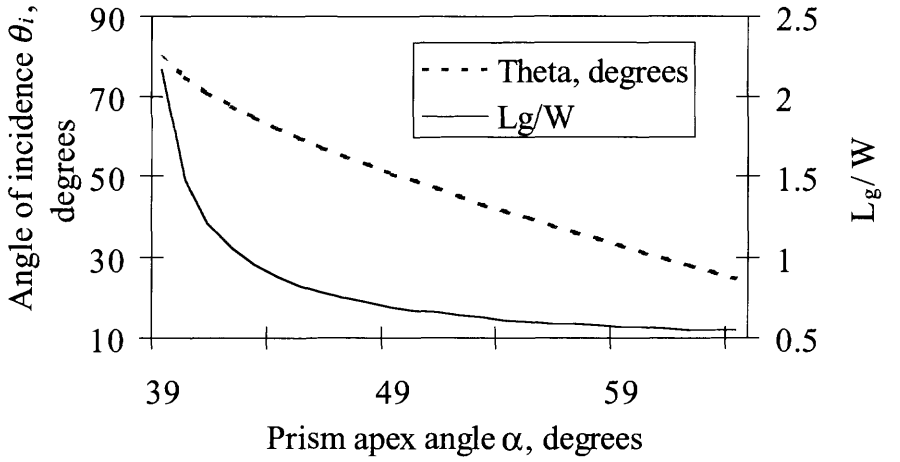

Figure 3.16: Length of a grating normalized to the width of the UV beam as a function of prism apex angle α. The writing angle $\theta_m/2$ is fixed at 10° for a Bragg wavelength of ~1500 nm. Also shown is the external writing angle of incidence on the surface of the prism, θ_i. Note that since the beam is folded about the center, the grating length is approximately half the width for the Lloyd mirror, whereas with the prism, the grating can be longer.

reduce this loss. Dispersion in the silica prism may also be an issue when writing gratings longer than a few millimeters.

Other techniques for the production of gratings with a single prism in a slightly modified version of that shown in Fig. 3.15 have also been reported [53,54]. These methods require precision-fabricated prisms and are restricted in tunability of the Bragg wavelength but may prove to be useful in cases where a rudimentary inscription procedure is necessary.

3.1.7 Higher spatial order masks

According to Equation (3.1.4) the period of the mask may be integer multiples of the Bragg wavelength. It is therefore possible to use a coarser grating period than the fundamental period required for the reflection wavelength. As the period gets larger, it is not practical to use the phase mask as a diffraction element, and it is necessary to use an amplitude mask for direct replication of the grating. The larger periods also allow the photoreduction of the mask using imaging to imprint the correct period

grating in a fiber [55,56]. The latter scheme requires the higher-order mask to be $M \times$ the length of the photo-reduced grating, where M is the demagnification factor, posing a problem for the production of fiber gratings that are longer than a few millimeters. The projection scheme enables the production of gratings with a single 20 ns pulse from a KrF excimer laser at a wavelength of 248 nm.

One- to six-micron period gratings have been produced by projection of an amplitude mask with multilayer stacked high-reflectivity dielectric stripes as the pattern (5 to 120 μm wide stripes). An image demagnification of 1:10 was used with 0.3NA optics to produce 4-mm from long gratings of 6th, 11th, and 12th order. Reflectivities as high as ~70% were noted for the lower-order gratings with correspondingly lower reflectivities of 8 and 2% for the 11th and 12th orders, respectively. An advantage of the projection system is that the fluence at the fiber is increased by the demagnification, reducing the power density at the mask plate [56]. Also noted was the imprinting of a physical grating on the surface of the fiber cladding, penetrating some 2 μm into the cladding. A threshold for the production of the grating in the core at ~0.8 J/cm^2 was observed, while 1.4 J/cm^2 was required for optimal production of the grating. It appears that the physical damage grating in the cladding produces a phase grating in the core due to heavy surface modification, causing light to be scattered out of the core. Gratings formed by physical damage, known as Type II, will be discussed in Section 3.2.

A similar technique of photoreduction can also be applied for the projection of a phase mask and is shown schematically in Fig. 3.17. Projection of the phase mask rather than the amplitude mask overcomes the problem of the Rayleigh-limited resolution for the 0.3NA UV transmitting lens used in a photoreducer. The limit with the amplitude mask is 0.6 μm. It therefore cannot be used for the production of first-order gratings [55] with periods of ~0.5 μm. Disadvantages of the projection scheme for use with both the amplitude and phase mask are the requirement of large-scale high-quality UV-grade spherical optics, and the use of large-area amplitude and phase masks. The additional cost and complexity of the projection system may well offset the cost advantage of using coarser features.

A 10.66-μm period phase mask has been photoreduced by $\times$10 to generate first-order gratings in a Ge-doped fiber at a Bragg wavelength of 1530 nm. It was reported that the production of damage type II gratings was more reproducible using the phase-mask projection scheme [55].

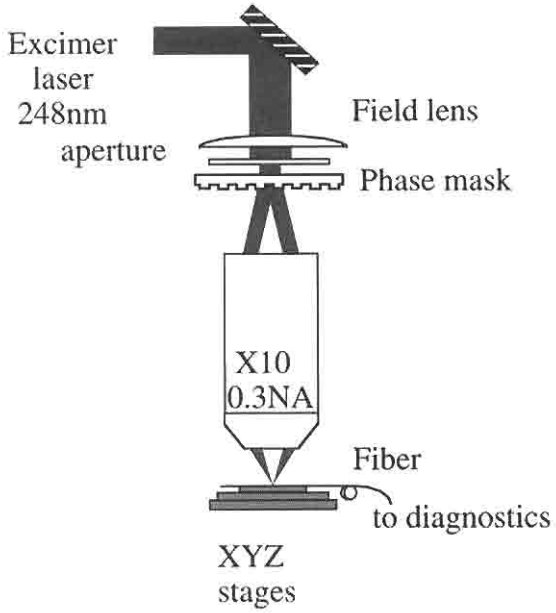

Figure 3.17: The projection system used to photoinscribe gratings by the photoreduction of the phase-mask (from Rizvi N H, Gower M C, Godall F C, Arthur G, and Herman P, "Excimer laser writing of submicrometre period fiber Bragg gratings using a phase-shifting mask projection," *Electron Lett.* **31**(11), 901–902, 1995, © IEE [55]).

Observation of higher-order interactions is possible with a first-order phase mask. This is simply governed by Eq. (3.1.4). A grating written for a Bragg wavelength λ_{Bragg} in first order will also operate at wavelengths $\lambda = \lambda_{Bragg}/N$. Additionally, if the grating imprinted in the fiber has a nonsinusoidal amplitude profile, for example, by effects of saturation of the refractive index modulation or physical damage (e.g., square wave modulation amplitude), then the grating will have Fourier frequency components at multiples of the first order, as $\Lambda = \Lambda_g/m$ (m = 1,2,3 . . .). These will in turn affect the efficiency of the reflections at shorter wavelengths, but function as *first*-order gratings for the Bragg wavelengths matching each of the spatial harmonic frequencies.

High-intensity UV printing through a phase mask results in multiple-order reflections, not least by the interference of the zero-order beam

through the phase mask with the ± 1 orders, but also due to the formation of a damage grating which is no longer sinusoidal in amplitude [120].

3.1.8 Point-by-point writing

The period of a reflection grating operating at 1.5 μm is $\sim$0.5 μm, as per Eq. (3.1.3). Since a diffraction-limited spot size of radiation at 244 nm is $\sim$0.25 μm, it is possible in principle to form a periodic refractive index grating by illuminating a single spot at a time using a point-by-point writing scheme. Technically, using positioning sensors linked to an interferometer, a grating of such periods can be written. This is only suitable for short gratings, since it is difficult to control translation stage movement accurately enough to make point-by-point writing of a first-order grating routinely practical. Other methods, including the use of a phase mask or the multiple-printing in-fiber-grating scheme, are better suited to writing long first-order gratings. However, high-quality high-order gratings have been demonstrated for $N = 3$ and 5 [57]. While excellent reflection gratings can be written using other schemes, point-by-point writing is extremely useful for fabricating gratings of long periods ($>$10 μm). These gratings couple light from one propagating polarization mode to another in the backward [58] or forward direction as in a rocking filter [59–61] (discussed in Chapters 4 and 6), to forward-propagating radiation modes (also see Chapter 4), or from one guided mode to another [62–64]. Figure 3.18 shows the technique used for point-by-point writing of reflection gratings and polarization couplers. For the simple reflection grating, the fiber is illuminated by a tightly focused spot through a mask for the required duration before being translated by a motorized micropositioner for the next illumination. In this way, a reflection grating of any order may be written. Naturally, the method benefits from the use of a pulsed laser, since the motion of the fiber can be stepped without the need to control the operation of the laser as well. However, the method is most useful for long-period gratings, which do not require such a demanding positional accuracy.

3.1.9 Gratings for mode and polarization conversion

Polarization mode converters may be fabricated in birefringent fibers using this scheme. In this case, it is necessary to orient the birefringent axes of the fiber at 45° to the illuminating beam. Two methods have been

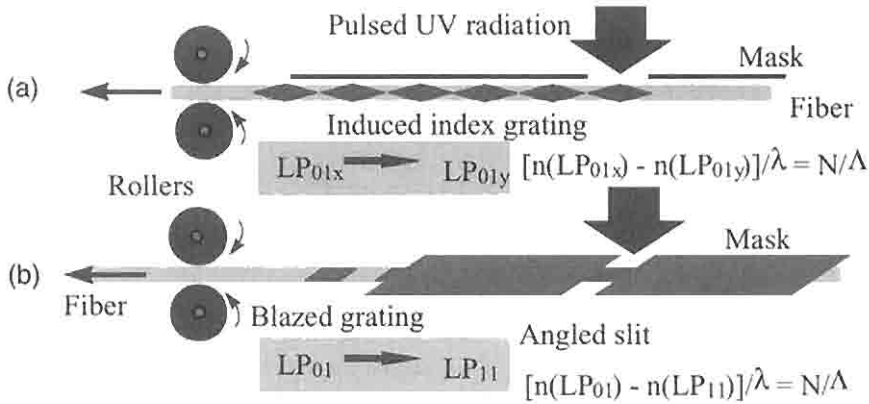

Figure 3.18: Point-by-point writing of fiber gratings. (a) shows a uniform grating being written as the fiber is pulled forward. A focused beam from a pulsed laser illuminates the fiber through a slit. The fiber pulling speed and the laser pulse-rate determines the period of the grating. (b) Blazed gratings are written with a slanted mask. Coupling between dissimilar modes is therefore possible (after Ref. [57]).

demonstrated to form such polarization converters. In order to use a *non*birefringent standard telecommunication fiber for a polarization mode converter, it must be made birefringent. The fiber can be wrapped on a cylinder of an appropriate diameter to induce a specific birefringence [65]. The beat length of the modes in the fiber is a function of the bend-induced birefringence and may be changed by altering the diameter of the cylinder. The induced birefringent axes are along the radius and parallel to the surface of the cylinder, with the fast axis in the radial direction. The induced birefringence B is [66]

$$B = n_{fast} - n_{slow} = -\alpha\left(\frac{d_{fiber}}{D_{cylinder}}\right)^2, \tag{3.1.10}$$

where d_{fiber} and $D_{cylinder}$ are the diameters of the fiber and cylinder, respectively, and the fast and slow axis refractive indices n are indicated by the subscripts. α is a constant that is dependent on the photoelastic properties of the fiber material, ~0.133 for fused silica.

Typically, the induced birefringence in fibers wrapped around the smallest practicable diameter cylinders ($D_{cylinder} \sim 25$ mm), based on consideration of mechanical strength, is of the order of -2×10^{-6}. While

this value is large compared to the intrinsic birefringence of standard telecommunications fiber, it is well below that of birefringent optical fibers (maximum birefringence $B_{max} \sim 0.4 \times \Delta n^2$, where Δn is the core cladding index difference [67]; for $\Delta n = 0.04$, $B_{max} \sim 6.4 \times 10^{-4}$). If a grating with a period, $\Lambda_g = \lambda/B$ is written in the fiber, then coupling between the two polarizations will occur. However, the grating has to be written oriented at 45° to the fast and slow axes. This may be done simply by arranging the UV illumination in a direction of the axis of the cylinder but rotated at an angle of 45° to the surface of the cylinder. As the fiber moves across the slit, the laser is switched on so that half the period of the grating is exposed to UV radiation before it is switched off for the second half. The process is repeated until the required number of periods is written [59]. Parameters that may be varied are the angle of inclination Ψ (known as the *rocking angle*), as shown in Fig. 3.19, and the mark–space ratio A_g of the grating given by the ratio of the length of fiber exposed to UV radiation and the grating period, in any one grating period.

A transversely uniform grating will promote coupling between modes of the same order whereas coupling of different-order modes requires a blazed grating [68] or, equivalently, a grating that is transversely nonuniform. A blaze may be imparted by rotating the mask slit so that the exposed region makes an angle to the propagation axis in the fiber, as shown in Fig. 3.18b. The blaze angle and the mark-space ratio $A_g = L_{exposed}/\Lambda_g$, are again parameters that may be adjusted to alter the performance of the filter. Blaze also enhances coupling to radiation modes of the fiber, inducing transmission loss, as has been mentioned in Section 3.1.4. However, the period of the grating Λ_g required to couple between modes is generally much longer than that required to couple to the radia-

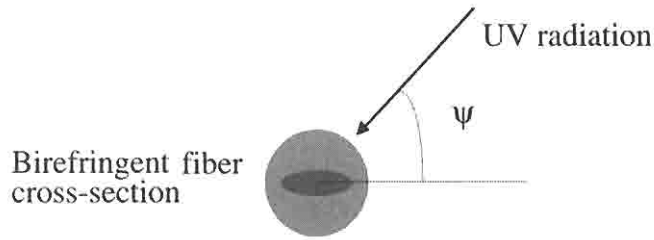

Figure 3.19: The rocking angle Ψ may be varied to alter the coupling coefficient for the filter.

tion modes in the counterpropagating direction. This is no longer true for coupling to copropagating radiation modes, and care needs to be taken to ensure that the periods of the gratings are not identical, by choosing an appropriate fiber. Intermodal coupling has been demonstrated using internally [62,69], as well as externally written gratings for different order mode coupling [61], as well as similar order modes [64]. The functioning of these devices is discussed in Chapter 6.

3.1.10 Single-shot writing of gratings

Single-shot writing of fiber gratings has been demonstrated using pulses from an excimer laser [118–121]. Higher reflectivity gratings have also demonstrated in boron–germanium codoped optical fiber [123]. Although the quality of these gratings has not been comparable with those written with other methods, the principle has led to a novel scheme of writing grating in the fiber while it is being drawn from a preform.

The process of writing a grating in an optical fiber generally requires the stripping of the protective polymer coating, which is opaque to short-wavelength UV radiation. Stripped fiber is weakened owing to mechanical processing (see Chapter 9) during grating inscription and should ideally be recoated. However, grating inscription on a fiber-drawing tower enables the fiber grating to be coated immediately after fabrication. Further, an array of gratings may be fabricated sequentially in a length of fiber by stepping the Bragg wavelength after each inscription. Figure 3.20 shows a schematic of grating fabrication during fiber drawing that was originally proposed by Askins *et al.* [122] and subsequently demonstrated [123]. Stepped-wavelength gratings were demonstrated using an interferometer that was tuned to a different Bragg wavelength between pulses from the excimer laser [122]. Although the gratings can be written during fiber drawing, the quality and repeatability remains poor, owing to problems of beam uniformity, mechanical alignment, and stability. For some applications in which a simple reflection is required, the quality of the grating may not be a critical parameter.

Advances in polymer coating materials have resulted in perfluorinated polymers that are essentially transparent in the longer UV wavelength regions of 266–350 nm [70,71]. Grating inscription at these wavelengths has been demonstrated as well, indicating that high-quality *and* high-reflectivity gratings may be possible without stripping the coating off the fiber. The fabrication of gratings in fiber with the primary

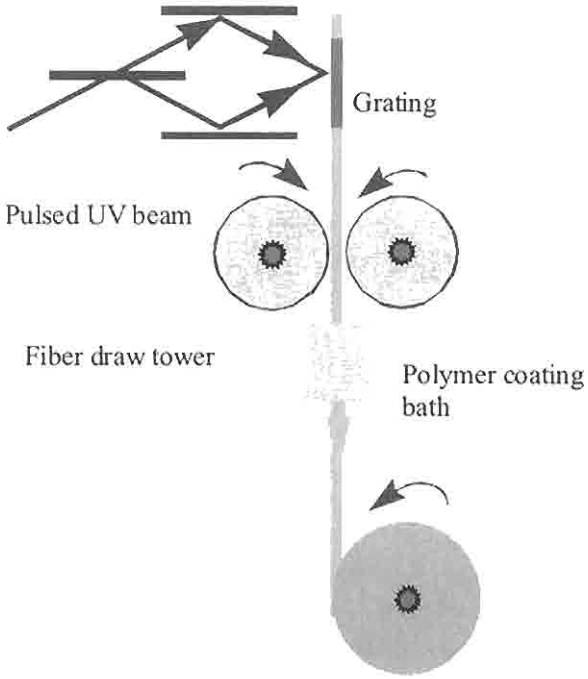

Figure 3.20: The scheme of writing gratings in a fiber while it is being drawn from a preform: 20-ns pulses at a wavelength of 248 nm were used to inscribe a sequential array of 50 gratings stepped at 0.1 nm. Also demonstrated were 120 gratings written at the same wavelength. The wavelength stability was good, but the peak reflectivity was ~3%. Gratings with a wavelength spacing of 5 nm were also reported [122].

coating may well be restricted to the use of CW UV sources, since high-power pulsed sources are likely to damage the polymer coating unless tight focusing is used to reduce the intensity at the surface [119].

3.1.11 Long-period grating fabrication

Long-period gratings have found applications as lossy filters. These gratings couple the guided and the radiation modes in the copropagating direction, and typically require periods in the region of 100 to 500 μm. LPGs are therefore most conveniently fabricated by UV exposure through a shadow mask [72]. These gratings tend to be longer than reflective Bragg gratings (tens of millimeters) since the periods are a few hundred

times longer. However, shadow masks are easily available, and the inscription requires simple contact printing as with the phase mask, but without the complexity of interferometry. Point-by-point writing is also possible.

Long-period amplitude masks have been patterned on dielectric mirrors to reduce the problem of optical damage with excimer lasers. In this application, a dielectric mirror coated with photoresist was first exposed to an amplitude pattern using a UV laser. The photoresist was developed to expose the dielectric mirror, which was then etched in 5% HF solution in deionized water. The resultant mirror had stripes at the required period for the LPG. Exposure through this mirror only allows the UV radiation to be transmitted through the regions where the mirror has been etched away. These mirrors were shown to withstand 200 mJ/cm^2 per pulse over several pulses, thus making them better suited for use than chrome-coated silica masks with an average damage threshold of ~50–100 mJ/cm^2 [131].

3.1.12 Ultralong-fiber gratings

To circumvent the limitations of the finite length of the phase mask, several techniques have been proposed to fabricate gratings of arbitrary length >200 mm [49, 73–75]. The simplest method is to sequentially inscribe gratings in a fiber from a phase mask of length L, to result in a grating with a length equal to the number of sequential inscriptions $\times L$ [74]. This is a powerful technique, which has special applications in the fabrication of long chirped gratings and is discussed in Section 3.1.15.

A technique based on the principle of inscribing small, more elementary gratings to create a longer one has also been reported [73]. The principle of inscription may be understood as follows: A short (4 mm) interference pattern is printed periodically in a continuously but slowly moving fiber. Using a pulsed laser (20-ns pulses), a 4-mm long section is imprinted in the fiber at any one time. The velocity of the fiber is such that within the pulse width, it may be regarded as being stationary. When the fiber has moved a few integral numbers of grating periods, a second pulse arrives, imprinting yet another grating partially overlapped with the previous grating but adding a few extra periods to the length. A mini–Michelson interferometer operating at 633 nm is attached to the moving fiber platform to track its position relative to the interference fringes. The latter is undertaken by the use of serrodyne control [73]. The resulting gratings have the narrowest reported bandwidths of 0.0075 nm,

although the quality of the grating was not perfect. It is important to eliminate stitching errors between the imprinted fields, as in the case of the phase mask, requiring a positional accuracy of better than 0.1Λ over the length of the grating. As an example, this implies maintaining an overall positional accuracy of less than 50 nm over the entire length of the 200-mm long grating, a demanding task.

Figure 3.21 shows the apparatus used for writing long gratings by the multiple printing in fiber (MPF) technique [73]. The fiber is held in a glass V-groove along its entire length and translated along the pulsed interference fringes in sychronym with the pulses. By moving the fiber at a constant velocity with a *linear* motor, the vibrations common in stepper-motor-driven systems are eliminated. Mounting the fiber carriage on an air bearing further helps this. The critical features of the technique are the requirement of a long precision glass V-groove to hold the fiber in position with submicron accuracy, high beam quality of the pulsed laser, an accurate control system for fiber translation, and above all, stability of the pulsed source for imprinting gratings of a well-determined index of modulation. Since the fabrication process imprints overlapping gratings, it is possible to change the period or the modulation index locally or continuously along the length of the grating. A detail of the printing process is shown in Fig. 3.22. This system is flexible and is able to cater for any type of grating, including those with phase steps, chirp, apodization (see Section 3.1.9 and Chapter 5).

A slight modification of the MPF scheme is shown in Fig. 3.23. Here not only the fiber is allowed to move, but also the interferometer [49]. In this case, the interferometer is the phase mask that moves at a velocity

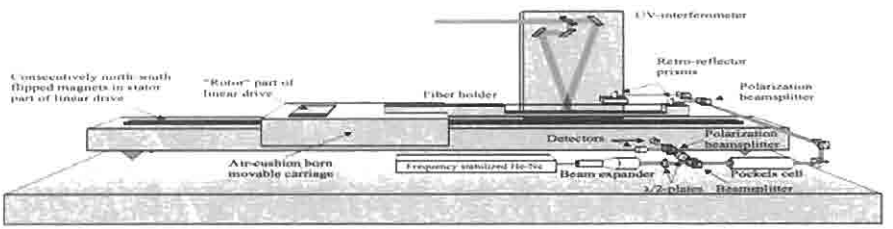

Figure 3.21: The multiple printing in fiber (MPF) grating technique. The substantial carriage is potentially capable of movements of up to 1 meter (courtesy R. Stubbe).

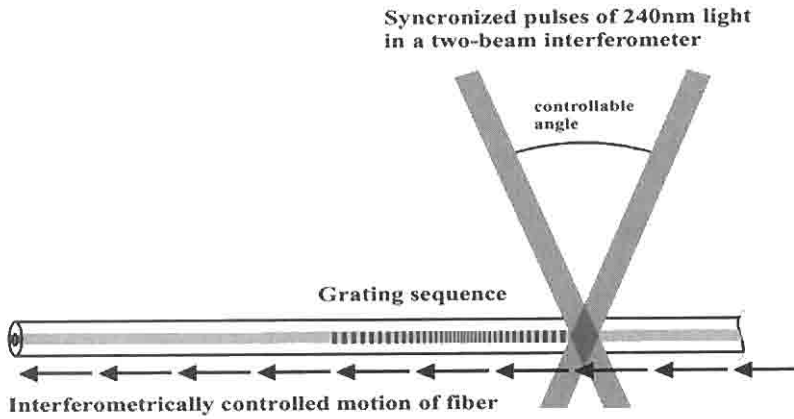

Figure 3.22: A detail of the MPF technique showing the imprinting of a mini overlapping grating to produce the required profile or chirp; the movement of the fiber is interferometrically controlled, and the imprinting is synchronized with the arrival of the UV pulses (courtesy R. Stubbe).

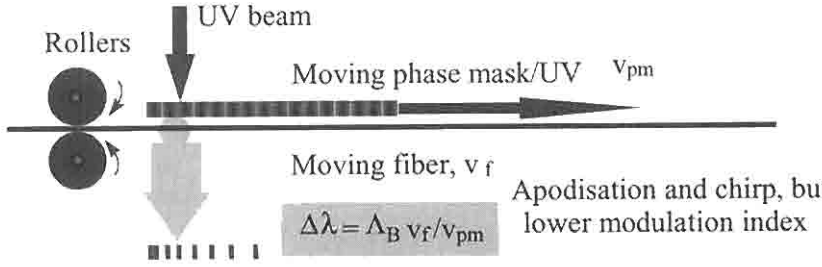

Figure 3.23: A technique based on the moving phase mask and fiber. If the phase mask is not moved, it is identical to the MPF method, but can only be used to write unchirped gratings using a pulsed source.

of v_{pm}, while the fiber moves with a velocity v_f. The change $\Delta\lambda$ in the period Λ_g of the grating is a function of the relative velocities, as

$$\Delta\lambda = \Lambda_{Bragg} \frac{v_f}{v_{pm}}. \tag{3.1.11}$$

Thus, a chirp may be programmed in the control computer by altering the relative velocities locally. A limitation is the need for a small spot size if a large chirp is being imparted in the grating in a long fiber, since the

maximum change in the period is a single period over the length of the UV writing spot, as

$$\Delta\lambda = \frac{\Lambda_{Bragg}}{2w}, \tag{3.1.12}$$

where w is the radius of the spot used for writing the short section of grating. Combining Eqs. (3.1.11) and (3.1.12) gives the following interesting relationship:

$$2w = \frac{v_{pm}}{v_f}. \tag{3.1.13}$$

Equation (3.1.13) suggests the use of a minimum spot size related to the relative velocities. Further, it should be noted that at any one time, an entire grating of spot size $2w$ is written with a constant amplitude and period. In the limit, this method trades in some of the refractive index modulation for chirp, but can at best imprint a quasi-stepped function instead of a continuous one, especially when the grating is being apodized.

3.1.13 Tuning of the Bragg wavelength, moiré, Fabry–Perot, and superstructure gratings

The effective index of a propagating mode in a fiber is both temperature and strain sensitive. The functional dependence of the mode index is given by the relationship

$$\partial n_{eff} = \frac{\partial n_{neff}}{\partial T}\Delta T + \frac{\partial n_{neff}}{\partial \sigma}\Delta\sigma, \tag{3.1.14}$$

where $\partial n/\partial T$ is the temperature coefficient of refractive index, ΔT is the change in temperature, $\partial n/\partial\sigma$ is the longitudinal stress optic coefficient, and $\Delta\sigma$ is the applied longitudinal stress. Since the Bragg wavelength is a function of n_{eff} [see Eq. (3.1.4)], the simplest method of altering the transfer characteristics of a fiber grating is to impose a temperature or strain profile along the length of the grating. However, prestraining a fiber during grating fabrication alters the Bragg grating wavelength in the relaxed state [7]. It is also possible to multiplex several gratings at the same location to form moiré type gratings [7,77]. It should be noted that the Bragg wavelengths of all multiplexed gratings written at the same location shift to longer wavelengths as each grating is superimposed.

The shift in the wavelength of the gratings is dependent on the *overall* change in the index of modulation, resulting in a change in the period averaged n_{eff} of the mode in the fiber. The *shift* $\Delta\lambda_{Bragg}$ in the Bragg wavelength, λ_{Bragg} as the UV induce index change δn increases can be shown to be

$$\Delta\lambda_{Bragg} = \lambda_{Bragg} \frac{\eta \delta n}{n_{eff}}, \tag{3.1.15}$$

where $\eta < 1$, is the overlap of the guided mode and the distribution of the refractive index modulation (see Chapter 4). Thus, when a grating is superimposed on an already-written grating, both gratings move to longer Bragg wavelengths.

By altering the angle of the interfering beams, several gratings may be written at a single location using the prism interferometer or the Lloyd mirror arrangement discussed in Section 3.1.6. These gratings show interesting narrow band-pass features with uniform period [77] or chirped gratings [78], and are discussed in Chapter 6.

If the temperature distribution along the length of a uniform grating is a linear function of length, then the Bragg wavelength, too, will vary linearly with length. The grating will demonstrate a linear chirp. This means that the different wavelengths within the bandwidth of the grating will not be reflected from the same physical location and the grating will behave as a dispersive component. The temperature profile (or the strain profile) may be altered to change the functional property of the grating [79]. On the other hand, prestraining or imposing a temperature profile along a fiber prior to writing a fiber grating will also result in a chirped fiber grating once it is written and the stress/temperature profile is removed [80,81]. However, the chirp in a grating fabricated in such a way will have the opposite sign of a grating chirped by the application of a temperature or strain profile after it has been manufactured.

During fabrication of the grating at an elevated temperature T_w, the Bragg wavelength will be defined by the period, Λ_g of the grating. After fabrication, when the temperature is returned to a final temperature T_f, the Bragg wavelength will be

$$\lambda_{Bragg} = 2\Lambda_g(1 + \alpha[T_f - T_w])\left(n_{eff} + \frac{dn_{eff}}{dT}\left[T_f - T_w\right]\right), \tag{3.1.16}$$

where α is the thermal expansion coefficient of the fiber and dn_{eff}/dT is the temperature coefficient of the mode index; to the first approximation,

this is merely the change in the refractive index of the fiber core as a function of temperature. Equation (3.1.16) may be simplified by expanding and rearranging to

$$\lambda_{Bragg} = 2\Lambda_g\left\{n_{eff}[1 + \alpha(T_f - T_w)] + \frac{dn_{eff}}{dT}(T_f - T_w)\right\}. \quad (3.1.17)$$

The thermal expansion coefficient of silica α is approximately $+5.2 \times 10^{-7}$, whereas $dn/dT \approx +1.1 \times 10^{-5}$ °C^{-1}; the contribution of the thermal expansion coefficient term is approximately 10% in comparison. Equation (3.1.17) is further simplified to

$$\lambda_{Bragg} \approx 2\Lambda_g\left\{n_{eff} + \frac{dn'}{dT}(T_f - T_w)\right\}, \quad (3.1.18)$$

where the combined effect of the thermal expansion and the refractive index change is included in n', so that the change shift in the Bragg wavelength is simply

$$\Lambda\lambda_{Bragg} \approx 2\Lambda_g \frac{dn'}{dT}(T_f - T_w). \quad (3.1.19)$$

Typically, $dn'/dT \approx 0.5$ to 1.0×10^{-2} °C^{-1}. At a wavelength of 1500 nm the change in the Bragg wavelength with temperature is ~1 to 2×10^{-2} nm °C^{-1} [82,7].

With long uniform gratings, a thin heating wire suitably placed below a point in the grating can result in a distributed feedback (DFB) structure, with a double-peaked reflection spectrum. The transfer characteristics of each half of the grating are identical; however, a $\lambda/4$ phase difference induced by the heating wire causes a hole to appear within the band stop [83]. Such a grating in rare-earth-doped fiber can be used in DFB lasers, which require the suppression of one of the two lasing modes to force the laser into single-frequency operation, and in narrow band-pass filters. A number of methods have been reported for fabricating DFB structures in fibers, including postprocessing a uniform grating to locally induce a "gap" in the center of the grating [84]. Alternatively, two gratings may be written on top of each other, each with a slightly shifted wavelength to form a Moiré phase-shifted grating, opening a bandgap once again [77].

Radic and Agrawal [85] reported that using an additional quarter-wave phase shift within a grating opens up yet another gap. An extension of this principle directly leads to the superstructure grating, which has been extensively used in tunable semiconductor-laser design [86]. A schematic of the superstructure grating is shown in Fig. 3.24. The composite grating consists of a number of subgratings of length ΔL (but not necessarily of identical lengths), which are separated by "dead" zones of length δl (these lengths may be different). The superstructure grating was first demonstrated in an optical fiber by Eggleton *et al.* [87], produced by a phase mask. A more general problem of stitching errors in phase masks has been addressed by Ouellette *et al.* [88]. Multiple reflections occur within the bandwidth of a single subgrating; each reflection has a bandwidth defined by the length of the grating without the gaps, i.e., $N\Delta L = L_g - (N-1)\delta l$.

The Fourier components of the grating shown in Fig. 3.24 basically have a fundamental component with a uniform period Λ_g and a fundamental modulation envelope of period $\Lambda_e = \delta l + \Delta L$. Thus, the reflection spectrum will have components at the sum and difference frequencies. The new reflection wavelengths, λ^{-}_{Bragg} and λ^{+}_{Bragg}, are calculated from Eq. (3.1.4):

$$\frac{1}{\lambda^{-}_{Bragg}} = \frac{1}{2n_{av}\Lambda_g} + \frac{1}{2n_{av}\Lambda_e} \tag{3.1.20}$$

and

$$\frac{1}{\lambda^{+}_{Bragg}} = \frac{1}{2n_{av}\Lambda_g} - \frac{1}{2n_{av}\Lambda_e}, \tag{3.1.21}$$

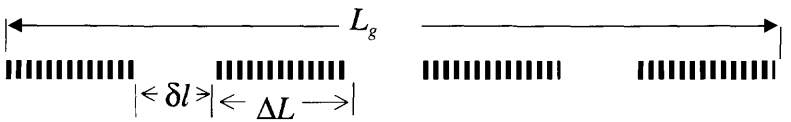

Figure 3.24: A schematic of a superstructure grating. This is constructed by blanking $(N-1)$ sections of length δl in a long continuous grating of length L_g. The superstructure grating is a collection of cascaded Fabry–Perot interferometers.

where n_{av} is the average index of the mode. It follows, therefore, from Eqs. (3.1.20) and (3.1.21) that the new grating periods Λ_g^- and Λ_g^+ corresponding to the superscripted Bragg wavelengths are

$$\Lambda_g^- \approx \Lambda_g\left(1 - \frac{\Lambda_g}{\Lambda_e}\right)$$
$$\Lambda_g^+ \approx \Lambda_g\left(1 + \frac{\Lambda_g}{\Lambda_e}\right). \tag{3.1.22}$$

From Eqs. (3.1.4) and (3.1.22), it follows that the spacing $\Delta\lambda$ between the reflected wavelengths in any such superstructure is

$$\Lambda\lambda = 2n_{av}\frac{\Lambda_g^2}{\Lambda_e}. \tag{3.1.23}$$

Depending on the shape of the composite structure (and thus the magnitudes of the individual Fourier components), higher order components can appear [87].

Superstructure gratings represent a number of types of gratings: the DFB with a single phase step $\phi < 2\pi$ [85,86]; the grating Fabry–Perot with $\phi \gg 2\pi$ resulting in multiple high-finesse transmission peaks [89]; cascaded grating Fabry–Perots in which the phase steps $\phi \gg 2\pi$ [87], leading to replicated multi-band-pass transmission spectra; gratings with multiple-flat-top reflection spectra, fabricated with unequal grating lengths as well as phase steps [90]; and truly flat-top reflection gratings fabricated by introducing regular $\pi/2$ phase shifts ($\lambda/4$) at equal intervals, while altering the strength of the grating amplitude in each section to mimic a *sinc* function [91].

There are several methods of making these gratings. In order to introduce a specific phase step, the simplest and most reliable is via the replication of a phase mask with the appropriately prerecorded phase steps [92]. Another method successfully used for introducing a $\pi/2$ phase step in a grating is by UV postprocessing [84]. After the grating has been written, the small central section is illuminated with UV radiation to introduce a phase shift. As the refractive index of the exposed region of length δl increases by δn, the transmission spectrum of the grating is monitored to stop the exposure when $\delta n\,\delta l = \lambda/4$. A disadvantage of post-UV exposure is that it not only changes the phase between the two halves of the grating, but also alters the local n_{eff} of the fiber. This in turn shifts the Bragg wavelength of the already-written grating exposed to UV

radiation to a longer wavelength. The effect of the shift is a slightly broader overall reflection spectrum.

The use of an amplitude mask in conjunction with a phase mask allows the precise printing of a superstructure grating [93]. Of course, mini-gratings may be printed by precise translation of the fiber between imprints [91,73]. This method has been used to write a *sinc* function grating with remarkably good results. However, it is difficult to write a continuous *sinc* function. Approximating the *sinc* function in a limited number of steps creates additional side bands, which limits the out-of-band rejection in the reflection spectrum. Combing the *sinc* function grating with apodization results in an improved transfer function, increasing the depth of the out-of-band rejection [91].

Chirped gratings are useful for many applications. There are a number of ways of chirping gratings, including writing a uniform period grating in a tapered fiber [94], by application of varying strain after fabrication [43,79,95], by straining a taper-etched fiber, by fabrication by a step-chirped [96] or continuously chirped phase mask, or by using one of the several schemes of writing a cascade of short, varying-period gratings to build a composite, long grating. These methods for writing chirped gratings are discussed in Section 3.1.14.

The properties of many of these gratings along with their applications may be found in Chapter 6.

3.1.14 Fabrication of continuously chirped gratings

Short, continuously chirped gratings are relatively straightforward to fabricate; longer (>50 mm) ones become more difficult. One of the simplest methods is to bend a fiber such that a continuously changing period is projected on it. This is shown in Figure 3.25 in which the fiber is bent either in the fringe plane or orthogonal to it. Altering the lay of the fiber may change the functional dependence of the period on position, so that either linear or quadratic chirp may be imparted.

Figure 3.26 shows a curved fiber with a radius of curvature R in a fringe plane. At any point of arc a distance S from the origin O where the fiber axis is normal to the fringe planes, the local period of the grating can be shown to be

$$\Lambda_s = \frac{\Lambda_g}{\cos(S/R)}, \tag{3.1.24}$$

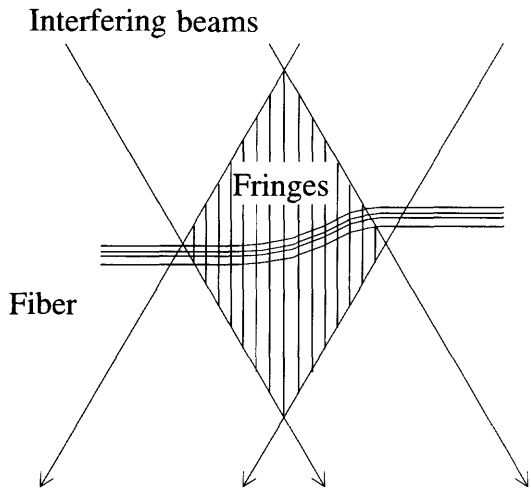

Figure 3.25: Writing of a continuously chirped grating by bending the fiber in the fringe plane. Note that the bending also causes the grating to be blazed with respect to the fiber axis.

so that even with a large radius of curvature, the grating may be substantially chirped. Gratings with bandwidths of 7.5 nm and peak reflectivity of 99%, as well as 15-nm bandwidth with a peak reflectivity of 5%, have been reported with this technique [98].

As in the case of fiber tilted with respect to the fringe planes, bending has a similar effect of imparting a blaze and consequently radiation loss. The loss, which manifests itself on the short-wavelength side of the Bragg wavelength even in unblazed gratings, is increased by blazing and may not be desirable; for a chirped grating, this can be a serious problem, if the radiation loss spectrum lies within the chirped bandwidth of the grating. Loss due to coupling to cladding modes in chirped gratings can be reduced by using fibers that are strongly guiding, but cannot be entirely eliminated. It may be substantially reduced, however by the use of special fibers with a photosensitive cladding [97] (see Chapter 4).

A constant strain along the length of a fiber while a grating is imprinted merely shifts the Bragg wavelength on strain release. In order to impart a chirp, a nonuniform strain profile has to be used, and there are several practical methods for implementing this. If an optical fiber is tapered (e.g., by etching) such that the outer diameter varies smoothly in the region of grating, the application of a longitudinal force leads directly to strain that

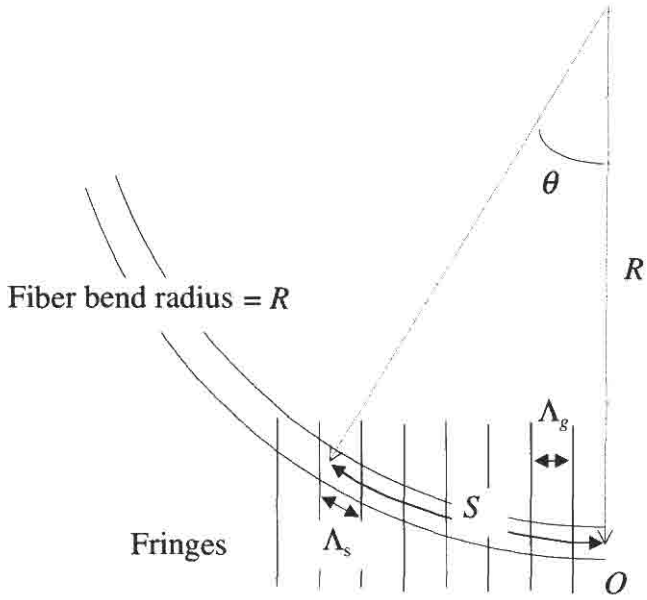

Figure 3.26: A fiber curved with a radius R in the fringe plane. The period of the grating seen by the fiber varies continuously along its length S.

is nonuniformly distributed along its length. The local strain ε_l may be computed from the local cross-sectional area A_i as [80]

$$\varepsilon_i = \varepsilon_{i-1} \frac{A_{i-1}}{A_i}, \tag{3.1.25}$$

where the subscript $(i - 1)$ refers to the previous section of the grating. Thus, a linear change in the cross-sectional area leads to a linear chirp. Applying positive strain to a uniform-period grating in a tapered fiber has three effects: the mean Bragg wavelength of the entire grating shifts to *longer* wavelengths, and the grating reflection spectrum broadens, while being reduced in reflectivity. Alternatively, the tapered fiber may be strained before writing of the grating. On strain release, the grating becomes chirped, but now shifts to a *shorter* wavelength. If a chirped grating is written in a strained tapered fiber such that the longer wavelength is inscribed in the narrower diameter, releasing the strain has the

effect of *unchirping* the grating. If the relieved strain is too large, the grating becomes chirped once again but with an *opposite* sign of chirp: i.e., the narrower diameter end has a shorter wavelength than the larger diameter end. The method is capable of high reproducibility, is simple to implement, and allows nonlinear chirps to be programmed into the grating [80]. There are two factors that affect the Bragg wavelength in strained etched fibers: the change in the physical length of the fiber, and the effective index of the mode through the stress-optic effect,

$$\Lambda\lambda|_{\sigma=0} = 2\Lambda_g \partial n_{eff} + 2n_{eff}\Lambda_g \varepsilon_i, \tag{3.1.26}$$

where the change in the Bragg wavelength is $\Delta\lambda$ under zero stress, *after* the grating has been written under local strain of ε_i, and δn_{eff} is the change in the effective index of the mode due to the strain-optic coefficient. The two quantities on the RHS in Eq. (3.1.26) have opposite signs, with the strain term being much larger than the stress-optic coefficient. Nevertheless, when a grating is written in a tapered fiber under strain, it appears chirped, although the period of the grating is uniform. Because of the stress-optic effect, the local effective index of the mode is not uniform along the length of the grating. On removal of the strain after the grating has been inscribed, the effective index of the mode becomes uniform, but the period is altered because of the change in local strain, and the grating becomes uniform at some lower strain value and chirped with the opposite sign when fully relaxed.

Etched linear tapers produce nonlinear chirp, since the chirp is inversely proportional to the square of the radius of the section according to Eq. (3.1.25). Since the Bragg wavelength is directly proportional to the applied strain [see Eq. (3.1.14)], the induced chirp becomes nonlinear. To compensate for this disparity, a nonlinear etching profile [99] can be used, resulting in a linear chirp. In order to fabricate a predetermined etch profile, the time of immersion of the fiber in the etching solution (usually buffered hydrofluoric acid) must be controlled, since the etch rate at constant temperature is highly reproducible. A three-section vessel with a layer A of a mixture of decahydronaphthalene and dichlorotoluene (10%) floating above layer B of 32% HF and with a third layer C of trichloroethylene below it may be used. This allows the acid to come into contact only with a small section of the fiber when it is immersed vertically into it. With the fiber remaining in position, the vessel is lowered at a programmed rate to expose another part of the fiber in section B, while the top layer A immediately stops the fiber from etching any further. Using this method, highly repeatable tapers have been produced and linear chirps of 4.8 nm

demonstrated [100]. Using the same method, different structures have been fabricated, such as a grating with a $\pi/2$ phase shift in the middle. A fiber in which the taper in one half has been etched more than the other was stretched before a grating was written. Relaxing the fiber introduced a phase shift and therefore a band pass in the center of the transmission spectrum of the otherwise unchirped grating [99].

A somewhat less flexible method relies on the tapering of the fiber core [94]. Tapering the core affects the local effective index n_{eff} of the mode. To the first approximation, the effective index varies linearly with decreasing diameter for an initial fiber V-value of approximately 2.4, but varies more slowly, asymptotically approaching the cladding index, as the core diameter goes to zero. Thus, a uniform-period grating written in tapered section will be chirped. The *maximum* chirp $\Delta\lambda$ achievable in a fiber may be calculated from

$$\Delta\lambda \approx \lambda_{Bragg} \frac{\Delta n}{n_{eff}}, \tag{3.1.27}$$

where Δn is the difference between the mode index and the cladding refractive index, Equation (3.1.27) translates to a maximum chirp on the order of 30 nm ($\Delta n = 0.03$); however, it would be difficult for practical reasons to achieve more than ~10 nm of chirp.

A chirp of 2.7 nm for a 10-mm long grating was reported for a fiber tapered by 50 μm over that length [94]. Local heating and stretching may fabricate a tapered fiber. Note, however, that a fiber with a large taper will have a lower reflectivity for the shorter wavelengths (with a uniform period grating), since the mode power spreads to the nonphotosensitive cladding, reducing the efficiency of the grating.

Another technique, that overcomes the problem associated with the core-taper method described above is based on expanding the core by thermal out-diffusion of the photosensitive core dopant [101]. The important difference between the two methods is that while the tapering of the core *reduces* the V-value of the fiber, the out-diffusion of the photosensitive core leaves the V-value *unchanged* [102]. This may be understood by remembering that the reduction in the core index as the dopant out-diffuses is compensated for by the increase in the core radius. The fractional power in the core remains unchanged (due to the fixed V-value), but since the core index is reduced, so is the mode index.

Heating the fiber locally by an oxyhydrogen flame for 2 minutes resulted in the mode field diameter expanding from 7.8 to 16.8 μm. Subsequent writing of a 10-mm long grating in the tapered core region of a

hydrogenated sample resulted in a chirped grating with a bandwidth of 6.0 nm [101].

Stretching a fiber prior to writing a grating shifts the Bragg wavelength in the relaxed state [7]. Byron and Rourke [103] applied the stretch–write technique to form a chirped grating with a scanned phase mask. As the UV beam (2 mm long) was stepped across the phase mask (and the fiber), the prestrained (0.6%) fiber was also relieved of strain in 15 steps of 0.04%. A chirped grating with a bandwidth of 10 nm for a grating length of 30 mm was demonstrated. Care has to be taken with this method, since the fiber can easily slip when under tension.

As will be appreciated with the above methods, the bandwidth of the chirp is generally small; in order to increase the chirp, it is necessary to write a chirped grating in the first place. Continuously chirped gratings with larger chirp values can be fabricated with two beams with dissimilar phase fronts. If one parallel beam is interfered with a second diverging beam, the resulting interference pattern will have a period that varies with spatial position in the fringe plane. Figure 3.27 shows the scheme for writing chirped gratings with two diverging, two converging, or a

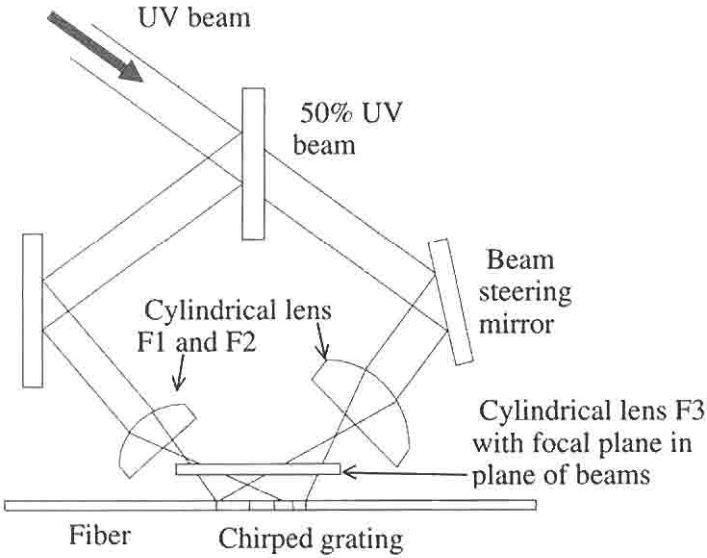

Figure 3.27: Nonuniform wave fronts used in the interferometer to produce chirped gratings [104]. Two cylindrical lenses with focal lengths F1 and F2 create a chirped interference pattern at the fiber. The third cylindrical lens with focal length F3 focuses the interfering beams into a stripe at the fiber.

combination of interfering beams. The advantage of using lenses as chirp-adjusting elements is that any chirp bandwidth is possible, limited only by the photosensitive response of the fiber. Using such an interferometer, chirp bandwidths of 44 nm have been demonstrated with a reflectivity of ~80%, covering the entire erbium amplifier gain band. The mechanical and geometrical positioning of the lenses makes the interferometer easy to use, although the repeatability may be not be so good. A disadvantage of this method is the strong curvature of the fringe pattern inscribed in the fiber, which results in coupling of light to the radiation modes on the blue side of the grating transmission spectrum [104].

3.1.15 Fabrication of step-chirped gratings

Gratings that are chirped in discrete steps are known as step-chirped. The concept was introduced by the fabrication of phase masks, which were not continuously chirped [23]. Figure 3.28 shows the principle of this type of grating. The grating of length L_g is split into N sections, each of length δl and uniform period Λ_n ($1 < n < N$), differing from the previous one by $\delta\Lambda$, with

$$\delta\Lambda = \frac{\Delta\Lambda_g \delta l}{L}, \tag{3.1.28}$$

where $\Delta\Lambda_g$ is the total chirp of the grating and $L_g = \delta l \times N$. If the change in the period and the sections are sufficiently small, then the grating becomes continuously chirped. The important choice is the number of sections required to build in the chirp. This has been analyzed [105], and it was shown that the length δl of the uniform period section should be

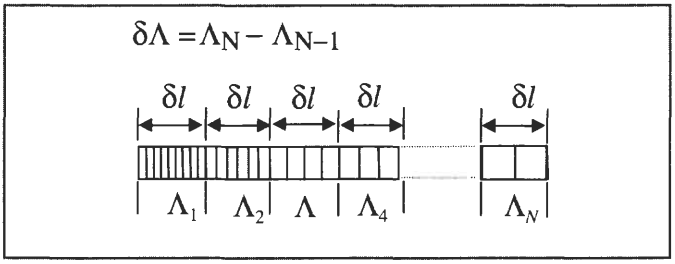

Figure 3.28: The step-chirped phase mask. It is important to ensure that each section of the grating has an integral number of grating periods, so that the section lengths δl are only nominally identical [23].

such that its bandwidth is ~50% greater than the chirp $\Delta\Lambda_g$ of the grating, irrespective of length of the grating. Making this choice results in a deviation of the characteristics of the grating that differ <1% from those of a continuously chirped grating. There must be an integer number of periods in each subsection to ensure that phase mismatch does not occur. A result of this requirement is that the lengths of the subsections are only approximately equal.

The step-chirped grating is ideally implemented in the phase mask using e-beam lithography [23]. Splitting a grating into small fields is exactly how the e-beam process works [20], so that it is naturally suited to the fabrication of step-chirped phase masks. Wide and narrow bandwidth (1–50 nm) phase masks have been fabricated with linear and quadratic step chirps [23] and used for pulse recompression of femtosecond pulses transmitted over optical fiber [106]. Step-chirped phase masks 100 mm long, useful for dispersion compensation in telecommunications transmission links [107], have also been demonstrated [108,74].

There are other techniques that mimic the step-chirped gratings, for example, with a limited chirp capability, using stretch and write [103] discussed in Section 3.1.14. Riant and Sansonetti have also shown that by the use of a focusing lens and a phase mask, small sections with different wavelengths can be built up to create a step-chirped grating [109]. Focusing or defocusing a beam at a phase mask changes the wavelength of the inscribed period in the fiber immediately behind the phase mask. Thus, stepping the spot along the mask while adjusting the focus allows the inscribed wavelength to be altered at each step. Using this method, 50-mm long gratings have been demonstrated with chirp values of ~1 nm [109].

There is great advantage in the use of the step-chirped phase-mask, since it allows not only the definition of the grating wavelength, but also any value of chirp rate. The minimum chirp bandwidth possible is, of course, limited by the natural bandwidth of a grating of length L_g.

An extension of the step-chirped principle is the concept of super-step-chirped gratings [75]. This technique allows even longer gratings to be assembled using a set of short step-chirped phase masks. This overcomes a major limitation of e-beam fabrication: the writing of masks longer than 100 mm is difficult and expensive. An alternative is to fabricate several gratings on a single-phase mask plate, each with a fixed chirp. Each phase mask is designed to begin at a wavelength $\delta\lambda$ longer than the wavelength at which the last phase mask finished. The gratings on the phase mask are aligned one above the other with exactly the

correct lengths. After a single grating is scanned into the fiber, the fiber is translated along accurately, and the next phase mask grating moved vertically into position for writing the succeeding grating. Any small inaccuracy in the placement (stitching) of the phase mask grating can be "trimmed" [110], using a single UV beam exposure to adjust the phase between adjacent sections [112].

Using this method, gratings 2 *meters* long have been written in a single contiguous piece of fiber, with a chirp bandwidth of ~15 nm [111], and a 1.3-*meter* long grating with a bandwidth of 10 nm has been used for multichannel dispersion compensation [75,112].

The detailed characteristics of step-chirped and super-step-chirped gratings are discussed in Chapter 4.

3.2 Type II gratings

Fiber gratings formed at low intensities are generally referred to as Type I. Another type of grating is a damage grating formed when the energy of the writing beam is increased above approximately 30 mJ [119]. Physical damage is caused in the fiber core on the side of the writing beams. The definite threshold is accompanied by a large change in the refractive index modulation. It is therefore possible to write high-reflectivity gratings with a single laser pulse. Above 40–60 mJ, the refractive index modulation saturates at around 3×10^{-3}. Energy of the order of 50–60 mJ can destroy the optical fiber. The sudden growth of the refractive index is accompanied by a large short-wavelength loss due to the coupling of the guided mode to the radiation field. The gratings generally tend to have an irregular reflection spectrum due to "hot spots" in the laser beam profile. By spatially filtering the beams, gratings with better reflection profiles have been generated but with a much reduced reflectivity [113]. These gratings decay at much higher temperatures than Type I, being stable up to ~700°C. Some of the properties of these gratings are outlined in Chapter 9.

3.3 Type IIA gratings

Yet another type of grating is formed in *non*-hydrogen-loaded fibers. These may form at low power densities or with pulsed lasers after long exposure [114]. The characteristics of a Type IIA grating are the growth of a zero-order ($N = 1$) grating, and its erasure during which a second-order grating

grows at approximately half the initial Bragg wavelength, followed by the growth of the $N = 1$ grating. The final grating is stronger than the original and is able to withstand a higher temperature. These gratings form in most fibers, although they have yet to be observed in hydrogen-loaded fibers. The gratings are reviewed in Chapters 2 and 9.

3.4 Sources for holographic writing of gratings

There are several UV laser sources that may be used for inducing refractive index changes and for fabricating gratings in optical fibers. Methods for generating UV or deep UV radiation require the use of excimer lasers, nonlinear crystals for frequency mixing of coherent visible/infrared radiation, or line-narrowed dye laser radiation. UV laser sources may be categorized into two types — low spatial/temporal coherence or spatially coherent sources. Sources in the first category have been used extensively for grating fabrication but need to be used with care for high-quality grating production. The primary advantage is in the high average and peak power available in the UV region. On the other hand, some frequency mixing methods produce UV radiation of high temporal and spatial coherence and are ideally suited for grating formation. Typically, these lasers demonstrate high average power capability but have the disadvantage of lower peak power densities. Nevertheless, these have also been shown to be highly successful for inducing large index changes while maintaining excellent grating quality.

3.4.1 Low coherence sources

The first source reported for use in grating formation was the excimer-laser pumped frequency doubled oscillator–amplifier dye laser operating in the 240-nm window [13]. This source can produce approximately 0.1 W average tunable radiation between 240 and 260 nm using a β-barium borate (BBO) crystal by doubling the (CHRYSL 106) dye-laser output. The laser must be line-narrowed to increase the coherence length, and longitudinal pumped dye lasers are preferable since they produce a higher quality beam compared to side-pumped dyes which produce a triangular beam profile. An alternative pump laser for the dye is the frequency-mixed output at 355 nm from a YAG laser operating at a wavelength of 1064 nm. Similar output may be achieved with a maximum of around

120 mW average at 244 nm for a 20-Hz system with 12-ns pulses [115]. The frequency-doubled tunable dye-laser source can be line-narrowed to increase temporal coherence, helping maintain interference despite path-length differences. However, the UV beam may need to be spatially filtered if the beam-quality is not good so as to be able to write uniform reflection gratings. High-quality gratings have been reported using this method [116], however, by multiple pulse writing.

With low transverse coherence, it is still possible to write good gratings, provided the spatial nonuniformity averages out over the time period required to write the grating. However, the pulse-to-pulse transverse beam variation affects single-pulse writing of gratings [117–121] or, for example, during fiber drawings [122,123], as was originally suggested by Askins *et al.* [118]. The power density variation manifests itself in two ways: first, the reflectivity varies from grating to grating, and second, the peak reflection wavelength, which is a function of the induced index change, varies between gratings. Beam profile nonuniformity has a rather more serious deleterious effect on the grating reflection spectrum, causing multiple peaks and chirp. The spectral shape is discussed in more detail in Chapters 4 and 9. Multiple pulses can ensure that each section of the grating can be driven into saturation (for a given UV flux), although if the beam profile has a Gaussian average intensity profile, the grating will appear chirped. The regions with low flux will see a smaller index change and hence a smaller change in the effective index of the mode than the central region of the beam. Since the Bragg wavelength is proportional to the effective index of the mode, the beam profile imparts a Bragg wavelength profile proportional to the intensity profile, leading to chirp [124]. It is for this reason that there is a concern over the use of a laser with "hot-spots" in the beam. The grating may show *fine* structure in the reflection spectrum due to the nonuniform refractive index modulation of the inscribed grating. This has so far not been reported in the literature but may well be a problem for long gratings.

Another aspect of low coherence sources, which must be taken into account when designing an interferometer, is the effect of the coherence length. These laser sources are generally better suited to direct printing using a phase mask with the fiber immediately behind the phase plate. Alternatively, a one-to-one imaging system may be used to form the interferometer such that the path of the two beams are equalized and overlapped. If, however, the paths are not equal or the beams do not overlap, degradation in the visibility can result in poor grating reflectivity and/or spectral profile. The limiting factor for all lasers is the divergence of the

beam, which determines how far away the fiber may be placed from the phase mask as (see Fig. 3.1)

$$\delta\lambda \, \delta\phi \ll \lambda^2 \frac{\cos(\theta_m/2)}{2L}, \tag{3.4.1}$$

where $\delta\lambda$ is the source bandwidth, $\delta\phi$ the source angular divergence, λ the source wavelength, $\theta_m/2$ the half diffraction angle, and L the distance of the fiber from the phase mask. The physical significance of Eq. (3.4.1) is that as the diffracted beams are brought together, the divergence causes a dephasing of the interfering beams, reducing the visibility. The contact method is therefore ideally suited for use with low-coherence sources. However, it must be remembered that the phase mask is more likely to be damaged owing to contamination from the fiber, i.e., dust, etc., using high-intensity pulses.

High peak-power laser sources do allow the writing of Type II gratings, which depend on physical damage to the core region [125]. This aspect is discussed in Section 3.2.

3.4.2 High coherence sources

Lasers with good spatial and/or temporal coherence fall in this category. Examples include CW intracavity frequency doubled argon-ion lasers operating at 257 nm/244 nm [26,126], QS frequency quadrupled YLF [127], spatially filtered, line-narrowed frequency doubled dye lasers [13]. The first laser has excellent spatial and temporal coherence, being derived from the argon ion laser mode. Even with this laser, there can be fine structure in the transverse beam profile of the UV mode due to the low walk-off angle in the frequency doubling crystal, BBO. The beam is elliptical, but this is an advantage because the shape is suited to writing fiber gratings. The latter two lasers can be made to have good temporal coherence by line narrowing, but requires good spatial filtering to generate a satisfactory Gaussian mode profile. The pinholes used for filtering require careful alignment and have a tendency to burn after a short time owing to the high peak power; they require frequent replacement.

The quadrupled Nd:YLF and the intracavity frequency doubled argon ion lasers belong to the class of turnkey systems. These are reliable lasers and need little attention other than routine maintenance; for example, mirrors need occasional cleaning. The frequency doubling crystals tend to be KTP for the YLF followed by a BBO crystal enclosed in an airtight holder with silica windows. Although the transverse mode profile may

not be uniform shot-to-shot for this laser, it does allow the use of cylindrical lenses for focusing into the BBO crystal. This scheme overcomes the transverse walk-off problem in BBO associated with spherical lens focusing. However, it is not possible to use cylindrical focusing in the intracavity frequency doubling in BBO. A schematic of the Z-folded resonator is shown in Fig. 3.29. With careful adjustment of the fold and focusing mirrors, this laser can be operated at a stable CW output in excess of 300 mW at 244 nm. A cylindrical lens can be used at the output to circularize the beam. Typically, the beam diameter is approximately 2 mm.

The coherence length of the argon-ion laser operating in the single-frequency mode is more than adequate for use in a beam splitting interferometer even with path length differences approaching several centimeters, although the path length difference is usually not so large. This laser is also suited for use in the scanned phase-mask interferometer, or for writing blazed gratings, as discussed in Section 3.1.4.

Recent work on writing grating with near-UV wavelength radiation [128–130] means that other high-quality laser sources may be used for grating fabrication. An argon laser operating at 302 nm is one option, which allows the inscription of gratings directly through the silicone resin polymer jacket [71] or the use of a novel polymer at a wavelength of 257 nm [70]. The lifetime of the argon ion laser operating in the UV is probably an issue for the fabricator. However, other sources as yet not demonstrated, e.g., the intracavity krypton ion laser operating at 647 nm, frequency doubled to 323.5 nm, would be an attractive option, with plenty of power available at the UV wavelength.

3.1 lists a summary of the different types of lasers operating in the UV, used for grating fabrication.

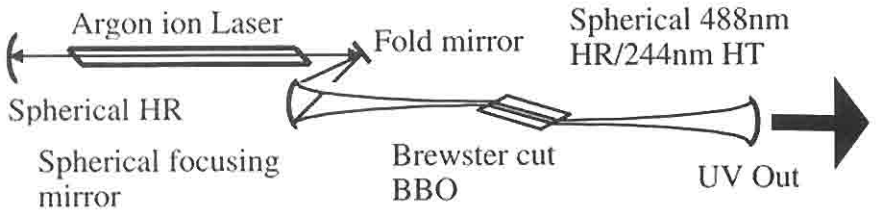

Figure 3.29: A schematic of the intracavity frequency-doubled, argon ion laser. 488-nm wavelength radiation is doubled to generate 244-nm UV emission. Angle tuning does phase matching of the BBO crystal. It is not necessary to temperature stabilize the BBO crystal [26].

Table 3.1: Common options of UV laser sources for grating formation.

Pump laser	UV wavelength (nm)	UV power/energy	Beam shape	Beam quality	Application
KrF	248	1 J/100Hz, QS	Few cm diameter	Low spatial/ temporal coherence: requires injection locking	Mass production, fiber drawing tower grating fabrication, TYPE II gratings
ArF	193	1 J(100Hz) QS	Few cm diameter	Low spatial/ temporal coherence	Planar devices, non-Ge fibers/planar, direct writing
Quadrupled Nd:YAG (1064 nm)	266, KDP/BBO frequency doublers	>100 mW 5 ns QS pulses at >1kHz	1 mm diameter	10 mm coherence length, low transverse beam coherence	Hydrogen loaded fibers, planar Ge/P doped silica, + RE-doped silica, Type II gratings
Nd:YAG (355 nm via frequency mixing)	220–260 tunable extra cavity BBO frequency doubled	>100 mW, 4 ns QS	2 mm diameter, not Gaussian, flat-topped or triangular	Low coherence, unless line-narrowed	UV-induced index change studies, grating writing, material studies, Type II grating formation, scanned phase mask

XeCl (308 nm) pumped dye laser	Same as above	Same as above	Same as above	Same as above	Same as above
Argon ion laser, 514/488 nm	257, 244, intracavity frequency-doubled in KDP/BBO	Up to ~2 W; up to ~1 W CW	1 mm, elliptical TEM00	High coherence, can be operated single-frequency but not necessary	Source with an excellent beam quality for grating fabrication; contact and noncontact phase mask/interferometer but not ideal for Type II gratings
Diode pumped quadrupled QS Nd:YLF (1048 nm)	262, frequency-doubled externally in KTP and BBO	~100 mW QS 100 ns pulses	~1 mm elliptical TEM00	Medium coherence, good beam quality	Good source for Type I and II grating writing in fibers and planar
Argon ion laser at 302 nm	Fundamental wavelength	~200 mW	1 mm TEM00	Excellent coherence: tube lifetime?	Writing through the jacket of D/H_2 loaded fibers
Krypton ion laser at 647 nm[a]	Frequency-doubled in BBO to 323.5 nm	>1 W	1 mm TEM00	Ideal near-UV source; long lifetime	Through the jacket inscription of D/H_2 loaded fibers

[a]Proposed by author; unused as yet.

References

1 Hill K. O., Fujii Y., Johnson D. C., and Kawasaki B. S., "Photosensitivity in optical waveguides: Application to reflection filter fabrication," *Appl. Phys. Lett.* **32**(10), 647 (1978).

2 Hill K. O., Malo B., Bilodeau F., and Johnson D. C., "Photosensitivity in optical fibers," *Ann. Rev. Mater. Sci.* **23**, 125–157 (1993).

3 Lam D. K. W. and Garside B. K., "Characterization of single-mode optical fiber filters," *Appl. Opts.* **20**(3), 440–445 (1981).

4 Lapiere J., Bures J., and Chevalier G., "Fiber-optic integrated interference filters," *Opt. Lett.* **7**(1), 37–39 (1982).

5 Kawasaki B. S., Hill K. O., Johnson D. C. and Fujii Y, "Narrow-band Bragg reflectors in optical fibers" *Opt. Lett.*, **3**(2), 66–68 (1978).

6 Bures J., Lapiere J., and Pascale D., "Photosensitivity effect in optical fibers: a model for the growth of an interference filter," *Appl. Phys. Lett.* **37**(10), 860 (1980).

7 Campbell R. J. and Kashyap R., "Spectral profile and multiplexing of Bragg gratings in photosensitive fiber," *Opt. Lett.* **16**(12), 898–900, (1991).

8 Stone J., "Photorefractivity in GeO_2-doped silica fibers," *J Appl Phys* **62**(11), 4371 (1987).

9 Hand D. P. and Russell P. St. J., "Single mode fibre gratings written into a Sagnac loop using photosensitive fibre: transmission filters," *IOOC, Technical Digest,* pp. 21C3–4, Japan (1989).

10 Bures J., Lacroix S., and Lapiere J., "Bragg reflector induced by photosensitivity in an optical fibre: model of growth and frequency response," *Appl. Opt.* **21**(19), 3052 (1982).

11 An Sungyuk and Sipe J. E., "The dynamics of phase grating formation in optical fibres," *SPIE* **1516**, International Workshop on Photoinduced Self-Organisation in Optical Fibre, Québec (1991).

12 Campbell R. J. and Kashyap R., "Properties and applications of photosensitive germanosilicate fibre," *International J. Optoelectron.* **9**(1), 33–57 (1994), and references therein.

13 Morey W. W., Meltz G., and Glenn W. H., "Holographically generated gratings in optical fibres," *Optics & Photonics News* **1**(7), 8 (1994).

14 Hill K. O., Malo B., Vineberg K. A., Bilodeau F., Johnson D. C., and Skinner I., "Efficient mode conversion in telecommunication fibre using externally written gratings," *Electron. Lett.* **26**(16), 1270 (1990).

15 Meltz G., Morey W. W., and Glenn W. H., "Formation of Bragg gratings in optical fibres by transverse holographic method," *Opt. Lett.* **14**(15), 823 (1989).

16 Lerner J. M., Flamand J., Laude J. P., Passereau G., and Thevenon A., "Diffraction gratings ruled and holographic — a review," in *Proc. of SPIE Symposium on Periodic Structures, Gratings, Moiré Patterns, and Diffraction Phenomenon,* vol. 240, pp. 82–88 (1980).

17 Okai M., Tsui S., Chinone N., and Harada, "Novel method to fabricate corrugations for a $\lambda/4$ shifted distributed feedback laser using a grating photomask," *Appl. Phys. Lett.* **55**, 415–416 (1989).

18 Enger R. C. and Case S. K., "Optical elements with ultrahigh spatial frequency surface corrugations," *Appl. Opt.* **22**, 3220 (1983), and references therein.

19 Dix C. and Mckee P. F., "High accuracy electron-beam grating lithography for optical and optoelectronic devices," *J. Vac. Sci. Technol.* **10**(6), 2667 (1992).

20 Swanton A., Armes D. J., Young-Smith K. J., Dix C., and Kashyap R., "Use of e-beam written, reactive ion etched, phase masks for the generation of novel photorefractive fibre gratings," *Special Issue, J. Micro. Electron. Eng.* **30**, 509–512 (1996).

21 Curran J. E., "Production of surface patterns by chemical plasma etching," *J. Phys. E.* **14**, 393–407 (1981).

22 Hill P. C. and Eggleton B. J., "Strain gradient chirp of fiber Bragg gratings," *Electron. Lett.* **30**, 1172–1174 (1994).

23 Kashyap R., McKee P. F., Campbell R. J., and Williams D. L., "A novel method of writing photo-induced chirped Bragg gratings in optical fibres," *Electron. Lett.* **12**, 996–997 (1994).

24 McKee P. F., Towers J. R., Wilkinson M. R., and Wood D., "New applications of optics from modern computer design methods," *BT Technol. J.* **11**(2), 161–169, (1993).

25 Pakulski G., Moore R., Maritan C., Shepard F., Fallahi M., Templeton I., and Champion G., "Fused silica masks for printing uniform and phase adjusted gratings for distributed feedback lasers," *Appl. Phys. Lett.* **62**(3), 222 (1993).

26 Kashyap R., Armitage J. R., Campbell R. J., Williams D. L., Maxwell G. D., Ainslie B. J., and Millar C. A., "Light-sensitive optical fibres and planar waveguides," *BT Technol. J.* **11**(2), 150–160 (1993).

27 Anderson D. Z., Mizrahi V., Erdogan T., and White A. E., "Phase-mask method for volume manufacturing of fiber phase gratings," Post-deadline paper PD16, *Technical Digest of Post-Deadline Papers Proc. Conf. on Optical Fiber Communications, OFC '93,* p. 68 (1993).

28 Hill K. O., Malo B., Bilodeau F., Johnson D. C., and Albert J., "Bragg grating fabricated in monomode photosensitive optical fiber by UV exposure through a phase mask," *Appl. Phys. Lett.* **62**(10), 1035 (1993).

29 Kashyap R., "Assessment of tuning the wave length of chirped and unchirped fibre Bragg grating with single phase masks," *Electron. Lett.,* **34**(21), 2025–2027 (1998).

30 Othonos A. and Lee X., "Novel and improved methods of writing Bragg gratings with phase masks," *IEEE Photon. Technol. Lett.* **7**(10), 1183–1185 (1995).

31 Dyer P. E., Farley R. J., Giedl R., Ragdale C., and Reid D., "Study and analysis of submicron-period grating formation on polymers ablated using a KrF irradiated phase mask," *Appl. Phys. Lett.* **64**(25), 3389–3391 (1995).

32 Parent M., Bures J., Lacroix S., and Lapierre J., "Propriétés de polarisation des réflecterus de Bragg induits par photosensibilité dans les fibres optiques monomode," *Appl. Opt.* **24**(3), 354 (1985).

33 Ouellette F., Gagnon D., and Porier M., "Permanent birefringence in Ge-doped fiber," *Appl. Phys. Lett.* **58**(17), 1813 (1991).

34 Bardal S., Kamal A., and Russell P. St. J., "Photoinduced birefringence in optical fibres: a comparative study of low-birefringence and high-birefringence fibers," *Opt. Lett.* **17**(6), 411 (1992).

35 An S. and Sipe J. E., "Polarisation aspects of two photon photosensitivity in birefringent optical fibres," *Opt. Lett.* **17**(7), 490 (1992).

36 Poirier M., Thibault S., Lauzon J., and Ouellette F., "Dynamic and orientational behaviour of UV induced luminescence bleaching in Ge-doped silica optical fiber," *Opt. Lett.* **18**(11), 870 (1993).

37 Wong D., Poole S. B., and Skeats M. G., "Stress-birefringence reduction in elliptical-core fibres under ultraviolet irradiation," *Opt. Lett.* **17**(24), 1773 (1992).

38 Vengsarkar A. M., Zhong Q., Inniss D., Reed W. A., Lemaire P. J., and Kosinski S. G., "Birefringence reduction in side written photoinduced fibre devices by a dual/circumferential exposure method," *Proc. Optical Fiber Conference, OFC'94,* post-deadline paper PD5, pp. 31–34 (1994).

39 Hill K. O., Bilodeau F., Malo B., and Johnson D. C., "Birefringent photosensitivity in monomode optical fibre: application to external writing of rocking filters," *Electron. Lett.* **27**(17), 1548 (1991).

40 Mizrahi V. and Sipe J. E., "Optical properties of photosensitive fiber phase gratings," *J. Lightwave Technol.* **1**, 1513–1517 (1993).

41 Kashyap R., Wyatt R., and McKee P. F., "Wavelength flattened saturated erbium amplifier using multiple side-tap Bragg gratings," *Electron. Lett.* **29**(11), 1025 (1993).

42 Martin J., Lauzon J., Thibault S., and Ouellette F., "Novel writing technique of long highly reflective in fiber gratings and investigation of the linearly chirped component," Post-deadline paper PD29-1, 138, *Proc. Conference on Optical Fiber Communications, OFC'94* (1994).

43 Byron K. C., Sugden K., Bircheno T., and Bennion I., "Fabrication of chirped Bragg gratings in photosensitive fibre," *Electron. Lett.* **29**(18), 1659 (1993).

44 Ouellette F., Eggleton B. J., Hill P. C., and Krug, P. A., "Chirp, self chirp and meta chirp in sampled Bragg gratings," in *Photosensitivity and Quadratic Nonlinearity in Glass Waveguides: Fundamentals and Applications,* Vol. 22, 1995 OSA Technical Series (Optical Society of America, Washington, DC, 1995), pp. PMC5, 247–250 (1995).

45 Ouellette F., Krug P., and Pasman R., "Characterization of long phase masks for writing fibre Bragg gratings," in *Photosensitivity and Quadratic Nonlinearity in Glass Waveguides: Fundamentals and Applications,* Vol. 22, 1995 OSA Technical Series (Optical Society of America, Washington, DC, 1995), pp. SuB7, 116–119 (1995).

46 Albert J., Theriault S., Bilodeau F., Johnson D. C., Hill K. O., Sixt P., and Rooks M. J., "Minimisation of phase errors in long fiber Bragg grating phase masks made using electron beam lithography," *IEEE Photon. Technol. Lett.* **8**(10), 1334–1336 (1996).

47 Kashyap R., Maxwell G. D., and Ainslie B. J., "Laser trimmed four-port bandpass filter fabricated in singlemode planar waveguides," *IEEE Photon. Technol. Lett.* **5**(2), 191 (1993).

48 Loh W. H., Cole M. J., Zervas M. N., and Laming R. I., "Compensation of imperfect mask with moving fibre-scanning beam technique for production of fibre gratings," *Electron. Lett.* **31**(17), 1483–1485 (1995).

49 Cole M. J., Loh W. H., Laming R. I., Zervas M. N., and Barcelos S., "Moving fibre/phase mask-scanning beam technique for enhanced flexibility in producing fibre gratings with a uniform phase mask," *Electron. Lett.* **31**(17), 92–94 (1995).

50 Eggleton B., Krug P. A., and Poladin L., "Dispersion compensation by using Bragg grating filters with self induced chirp," in *Tech. Digest Opt. Fib. Comm. Conf., OFC'94,* p. 227 (1994).

51 Kashyap R., Armitage J. R., Wyatt R. W., Davey S. T., and D. L., Williams, "All-fibre narrow-band reflection gratings at 150 nm," *Electron. Lett.* **26** (12), 730–731 (1990).

52 Chandra S., Takeuchi N., and Hartmann S. R., "Prism dye laser," *Appl. Phys. Lett.* **21**(4), 144–146 (1972).

53 Zhang Q., Brown D. A., Reinhart L., and Morse T. F., "Simple prism-based scheme for fabricating Bragg gratings in optical fibres," *Opt. Lett.* **19**(23), 2030–2032 (1994).

54 Rizvi N. H. and Gower M. C., "Production of submicron period Bragg gratings in optical fibers using wavefront division with a biprism and an excimer laser source," *Appl. Phys. Lett.* **67**(6), 739–741, (1995).

55 Rizvi N. H., Gower M. C., Godall F. C., Arthur G., and Herman P., "Excimer laser writing of submicrometre period fiber Bragg gratings using a phase-shifting mask projection," *Electron. Lett.* **31**(11), 901–902 (1995).

56 Mihailov S. J. and Gower M. C., "Recording of efficient high-order Bragg reflectors in optical fibres by mask image projection and single pulse exposure with an excimer laser," *Electron. Lett.* **30**(9), 707–709 (1994).

57 Malo B., Bilodeau F., Albert J., Johnson D. C., Hill K. O., Hibino Y., and Abe M., "Photosensitivity in optical fiber and silica on substrate waveguides," *SPIE* **2044**, 46–54 (1993).

58 Kanellopoulos S. E., Valente L. C. G., Handerek V. A., and Rogers A. J., "Comparison of photorefractive effects and photogenerated components in polarisation maintaining fibres," *SPIE* **1516**, "International Workshop of Photoinduced Self-Organisation effects in Optical Fibres," p. 200 (1991), and references therein.

59 Stolen R. H., Ashkin A., Pliebel W., and Dziedzic J. M., "In-line fiber-polarisation-rocking rotator and filter," *Opt. Lett.* **9**, 300–303 (1984).

60 Russell P. St. J. and Hand D. P., "Rocking filter formation in photosensitive high birefringence optical fibres," *Electron. Lett.* **26**, 1846–1848 (1990).

61 Johnson D. C., Bilodeau F., Malo B., Hill K. O., Wigley P. G. J., and Stegeman G. I., "Long length, long-period rocking filters fabricated from conventional monomode telecommunications optical fibers," *Opt. Lett.* **17**(22), 1635 (1992).

62 Park H. G. and Kim B. Y., "Intermodal coupler using permanently photoinduced grating in two mode optical fibre," *Electron. Lett.* **25**(12), 797 (1989).

63 Hill K. O., Malo B., Vineberg K. A., Bilodeau F., Johnson D. C., and Skinner I., "Efficient mode conversion in telecommunication fiber using externally written gratings," *Electron. Lett.* **26**, 1270–1272 (1990).

64 Bilodeau F., Hill K. O., Malo B., Johnson D. C., and Skinner I. M., "Efficient, narrowband $LP_{01} \leftrightarrow LP_{02}$ mode converters fabricated in photosensitive fiber: Spectral response," *Electron. Lett.* **27**, 682–682, (1991).

65 Ulrich R., Rashleigh S. C., and Eichoff W., "Bending induced birefringence in single mode fibres," *Opt. Lett.* **5**, 273–275 (1980).

66 Lefevre H. C., "Single-mode fibre fractional wave devices and polarisation controllers," *Electron. Lett.* **16**, 778–779 (1980).

67 Dyott R. B., Cozens J. R., and Morris D. G., "Preservation of polarisation in optical-fibres with elliptical cores," *Electron. Lett.* **19**, 380–382 (1979).

68 Morey W. W., Meltz G., Love J. D., and Hewlett S. J., "Mode-coupling characteristics of photo-induced Bragg gratings in depressed cladding fiber," *Electron. Lett.* **30**, 730–731 (1994).

69 Ouellette F., "Phase-matching of optical fibre photosensitive intermodal couplers in infra-red," *Electron. Lett.* **25**(23), 1590–1591 (1989).

70 Espinola R. P., Atkins R. M., Wang N. P., Simoff D. A., Paczkowski M. A., Windeler R. S., Brownlow D. L., Shenk D. S., Glodis P. A., Strasser T. A., DeMarco J. J., and Chandonnet P. J., "40 dB fiber Bragg grating written through the fiber coating at 257 nm," in *Bragg Gratings, Photosensitivity, and Poling in Glass Fibers and Waveguides: Applications and Fundamentals,* Vol. 17, OSA Technical Digest Series (Optical Society of America, Washington, DC, 1997), post-deadline paper PD2.

71 Starodubov D. S., Grubsky V., Feinberg J., Disnov D., Semjonov S. L., Guryanov A. N., and Vechkanov N. N., "Fiber Bragg gratings with reflectivity >97% fabricated through polymer jacket using near-UV radiation," in *Bragg Gratings, Photosensitivity, and Poling in Glass Fibers and Waveguides: Applications and Fundamentals,* Vol. 17, OSA Technical Digest Series (Optical Society of America, Washington, DC, 1997), post-deadline paper PD1.

72 Vengsarkar A. M., Lemaire P. J., Judkins J. B., Bhatia V., Erdogan T., and Sipe J. E., "Long period fiber gratings as band rejection filters," *IEEE J. Lightwave. Technol.* **14**, 58–64 (1996).

73 Stubbe R., Sahlgren B., Sandgren S., and Asseh A., "Novel technique for writing long superstructured fiber Bragg gratings," in *Photosensitivity and Quadratic Nonlinearity in Glass Waveguides: Fundamentals and Applications,* Vol. 22, 1995 OSA Technical Series (Optical Society of America, Washington, DC, 1995), pp. PD1-(1–3) (1995).

74 Kashyap R., Froehlich H-G., Swanton A., and Armes D. J., "Super-step-chirped fibre Bragg gratings," *Electron. Lett.* **32**(15), 1394–1396 (1996).

75 Kashyap R., Froehlich H-G., Swanton A., and Armes D. J., "1.3 m long super-step-chirped fibre Bragg grating with a continuous delay of 13.5 ns and bandwidth 10 nm for broadband dispersion compensation," *Electron. Lett.* **32**(19), 1807–1809 (1996).

76 Zhang Q., Brown D. A., Reinhart L., Morse T. F., Wang J. Q., and Xiao G., "Tuning Bragg wavelength by writing gratings on prestrained fibers," *IEEE Photon. Technol. Lett.* **6**(7), 839–841 (1994).

77 Legoubin S., Fertein E., Douay M., Bernage P., Niay P., Bayon F., and Georges T., "Formation of Moiré gratings in core of germanosilicate fibre by transverse holographic double exposure," *Electron. Lett.* **27**(21), 1945 (1991).

78 Sugden K., Zhang L., Williams J. A. R., Fallon L. A., Everall L. A., Chisholm K. E., and Bennion I., "Fabrication and characterization of bandpass filters based on concatenated chirped fiber gratings," *IEEE J. Lightwave Technol.* **15**(8), 1424–1432 (1997).

79 Byron K. C., Sugden K., Bircheno T., and Bennion I., "Fabrication of chirped Bragg gratings in photosensitive fibre," *Electron. Lett.* **29**(18), 1659 (1993).

80 Putnam M. A., Williams G. M., and Friebele E. J., "Fabrication of tapered, strain-gradient chirped fibre Bragg gratings," *Electron. Lett.* **31**(4), 309–310 (1995).

81 Martin J., Lauzon J., Thibault S., and Ouellette F., "Novel writing technique of long highly reflective in fiber gratings and investigation of the linearly chirped component," post-deadline paper PD29-1, 138, *Proc. Conference on Optical Fiber Communications, OFC'94* (1994).

82 Morey W. W., Meltz G., and Glenn W. H.,"Fiber optic Bragg grating sensors," *SPIE* **1169**, *Fibre Optics Sensors VII,* pp. 98–107 (1989).

83 Kringlebotn J. T., Morkel P. R., Reekie L., Archambault J. L., and Payne D. N., "Efficient diode-pumped single frequency erbium:ytterbium fibre laser," *IEEE Photon. Technol. Lett.* **5**(10), 1162 (1993).

84 Canning J. and Skeats M. G., "π-Phase shifted periodic distributed structures in optical fibers by UV post-processing," *Electron. Lett.* **30**(16), 1244–1245 (1994).

85 Agrawal G. P. and Radic S., "Phase-shifted fiber Bragg gratings and their applications for wavelength demultiplexing," *IEEE Photon. Technol. Lett.* **6**, 995–997 (1994).

86 Jayaraman V., Cohen D. A., and Coldren L. A., "Demonstration of broadband tunability of a semiconductor laser using sampled gratings," *Appl. Phys. Lett.* **60**(19), 2321–2323 (1992).

87 Eggleton B. J., Krug P. A., Poladin L., and Ouellette F., "Long periodic superstructure Bragg gratings in optical fibres," *Electron. Lett.* **30**(19), 1620–1621 (1994).

88 Ouellette F., Krug P. A., and Pasman R., "Characterisation of long phase masks for writing fibre Bragg gratings," in *Photosensitivity and Quadratic Nonlinearity in Glass Waveguides: Fundamentals and Applications,* Vol. 22, 1995 OSA Technical Series (Optical Society of America, Washington, DC, 1995), pp. 116–119.

89 Legoubin S., Douay M., Bernage P., Niay, Boj S., and Delevaque E., "Free spectral range variations of grating-based Fabry–Perot photowritten in optical fibers," *J. Opt. Soc. Am. A* **12**(8), 1687–1694 (1995).

90 Zengerle R. and Leminger O., "Phase-shifted Bragg-grating filters with improved transmission characteristics," *J. Lightwave Technol.* **13**, 2354–2358 (1995).

91 Storøy H., Engan H. E., Sahlgren B., and Stubbe R., "Position weighting of fibre Bragg gratings for bandpass filtering," *Opt. Lett.* **22**(11), 784–786 (1997).

92 Kashyap R, McKee P. F., and Armes D., "UV written reflection grating structures in photosensitive optical fibres using phase-shifted phase-masks," *Electron. Lett.* **30**(23), 1977–1979 (1994).

93 Ibsen M., Eggleton B. J., Sceats M. G., and Ouellette F., "Broadly tunable DBR fibre using sampled Bragg gratings," *Electron. Lett.* **31**(1), 37–38, (1995).

94 Byron K. C., Sugden K., Bircheno T., and Bennion I., "Fabrication of chirped Bragg gratings in a photo sensitive fibre," *Electron. Lett.* **29**(18), 1659–1660 (1993).

95 Krug P. A., Stephens T., Yoffe G., Ouellette F., Hill P., and Doshi G., "270 km transmission at 10Gb/s in nondispersion shifted fiber using an adjustably chirped 120 mm long fiber Bragg grating dispersion compensator," in *Tech. Digest Conf. on Opt. Fiber Commun., OFC'95,* post-deadline paper PDP27 (1995).

96 Kashyap R., McKee P. F., Campbell R. J., and Williams D. L., "A novel method of writing photo-induced chirped Bragg gratings in optical fibres," *Electron. Lett.* **12**, 996–998 (1994).

97 Delavaque E., Boj S., Bayon J-F., Poignant H., Le Mellot J., Monerie M., Niay P., and Bernage P., "Optical fiber design for strong grating photo imprinting with radiation mode suppression," in *Proc. Post-Deadline Papers of OFC'95,* paper PD5 (1995).

98 Sugden K., Bennion I., Moloney A., and Cooper N. J., "Chirped grating produced in photosensitive optical fibres by fibre deformation during exposure," *Electron. Lett.* **30**(5), 440–441 (1994).

99 Dong L., Cruz J. L., Reekie L., and Trucknott J. A., "Fabrication of chirped fibre gratings using etched tapers," *Electron. Lett.* **31**(11), 908–909 (1995).

100 Dong L., Cruz J. L., Reekie L., and Trucknott J. A., "Chirped fiber Bragg gratings fabricated using etched tapers," *Opt. Fiber Technol.* **1**, 363–368 (1995).

101 Okude S., Sakai T., Wada A., and Yamauchi R., "Novel chirped fiber grating utilizing a thermally diffused taper-core fiber," in *Proc. OFC'96,* paper TuO7, pp. 68–69 (1996).

102 Shiraishi K., Aizawa Y., and Kawakami S., *J. Lightwave Technol.* **8**, 1151 (1990).

103 Byron K. C. and Rourke H. N., "Fabrication of chirped fibre gratings by novel stretch and write technique," *Electron. Lett.* **31**(1), 60–61 (1995).

104 Farries M. C., Sugden K, Reid D. C. J., Bennion I., Molony A., and Goodwin M. J., "Very broad reflection bandwidth (44 nm) chirped fibre gratings and narrow-bandpass filters produced by the use of an amplitude mask," *Electron. Lett.* **30**(11), 891–892 (1994).

105 Kashyap R., "Design of step-chirped fibre Bragg gratings," *Opt. Comm.*, **136**(5–6), 461–469 (1997).

106 Kashyap R., Chernikov S. V., Mckee P. F., and Taylor J. R., "30 ps chromatic dispersion compensation of 400 fs pulses at 100 Gbits/s in optical fibres using an all fibre photoinduced chirped reflection grating," *Electron. Lett.* **30**(13), 1078–1079 (1994).

107 Kawase L. R., Carvalho M. C. R., Margulis W., and Kashyap R., "Transmission of chirped optical pulses in fibre-grating dispersion compensated system," *Electron. Lett.* **33**(2), pp. 52–54 (1997).

108 Kashyap R., Swanton A., and Armes D. J., "A simple technique for apodising chirped and unchirped fibre Bragg gratings," *Electron. Lett.* **32**(14), 1227–1228 (1996).

109 Riant I. and Sansonetti P., "New method to control chirp and wavelength of fibre Bragg gratings for multichannel chromatic dispersion compensation", in Colloquium on Optical Fibre Gratings, *IEE Ref.*, 1997/037, pp. 18/1-18/3, London (1997).

110 Kashyap R., Maxwell G. D., and Ainslie B. J., "Laser-trimmed four-port bandpass filter fabricated in single-mode photosensitive Ge-doped planar waveguide," *IEEE J. Photon. Technol.* **5**(2), 191–194 (1993).

111 Kashyap R., unpublished.

112 Kashyap R., Ellis A., Malyon D., Froehlich H-G., Swanton A., and Armes D. J., "Eight wavelength × 10Gb/s simultaneous dispersion compensation over 100km singlemode fibre using a single 10 nm bandwidth, 1.3 metre long, super-step-chirped fibre Bragg grating a continuous delay of 13.5 ns," in *Proc. Post-Deadline Papers of the 22nd ECOC'97,* Oslo, Norway, Sept. 15–19, 1996.

113 Archambault J-L., Ph.D. Thesis, Southampton University, United Kingdom (1994).

114 Xie W. X., Niay P., Bernage P., Douay M., Bayon J. F., Georges T., Monerie M., and Poumellec B., "Experimental evidence of two types of photorefractive

effects occurring during photoinscription of Bragg gratings within germanosilicate fibers," *Opt. Commun.* **104**, 185–195 (1993).

115 Duval Y., Kashyap R., Fleming S., and Ouellette F., "Correlation between ultraviolet-induced refractive index change and photoluminescence in Ge-doped fibre," *Appl. Phys. Lett.* **61**(25) 2955 (1992).

116 Limberger H. G., Limberger P. Y., and Salathé R., "Spectral characterization of photoinduced high efficient Bragg gratings in standard telecommunication fibers," *Electron. Lett.,* **29**(1), 47–49 (1993).

117 Kashyap R. and Maxwell G. D., unpublished (1991).

118 Askins C. G., Tsai T-E., Williams G. M., Puttnam M. A., Bashkansky M., and Friebele E. J., "Fibre Bragg reflectors prepared by a single excimer pulse," *Opt. Lett.* **17**(11), 833 (1992).

119 Archambault J-L., Reekie L., and Russell P. St. J., "High reflectivity and narrow bandwidth fibre gratings written by a single excimer pulse," *Electron. Lett.* **29**(1), 28 (1993).

120 Malo B., Johnson D. C., Bilodeau F., Albert J., and Hill K. O., "Single-excimer-pulse writing of fiber gratings by use of a zero-order nulled phase mask: grating spectral response and visualization of index perturbations," *Opt. Lett.* **18**(15), 1277 (1993).

121 Archambault J-L., Reekie L., and Russell P. St. J., "100% reflectivity Bragg reflectors produced in optical fibres by single excimer pulses," *Electron. Lett.* **29**(5), 453 (1993).

122 Askins C. G., Putnam M. A., Williams G. M., and Friebele E. J., "Stepped-wavelength optical-fiber Bragg grating arrays fabricated in line on a draw tower," *Opt. Lett.* **19**(2), 147–149 (1994).

123 Dong L., Archambault J. L., Reekie L., Russell P. St. J., and Payne D. N., "Single pulse Bragg gratings written during fibre drawing," *Electron. Lett.* **29**(17), 1577 (1993).

124 Mizrahi V. and Sipe J. E., "Optical properties of photosensitive fiber phase gratings," *Lightwave Technol.* **11**(10), 1513–1517 (1993).

125 Dong L., Archambault J. L., Reekie L., Russell P. St. J., and Payne D. N., "Single pulse Bragg gratings written during fibre drawing," *Electron. Lett.* **29**(17), 1577 (1993).

126 Patrick H., and Gilbert S. L., "Growth of Bragg gratings produced by continuous-wave ultra-violet light in optical fiber," *Opt. Lett.* **18**(18), 1484 (1993).

127 Armitage J. R., "Fibre Bragg reflectors written at 262 nm using frequency quadrupled Nd^{3+}:YLF," *Electron. Lett.* **29**(13), 1181–1183 (1993).

128 Dianov E. M., and Starodubov D. S., "Microscopic mechanisms of photosensitivity in germanium-doped silica glass," *SPIE Proc, 2777,* pp. 60–70 (1995).

129 Starodubov D. S., Dianov E. M., Vasiliev S. A., Frolov A. A., Medvedkov O. I., Rybaltovskii A. O., and Titova V. A., "Hydrogen enhancement of near-UV photosensitivity of germanosilicate glass," *SPIE Proc. 2998,* pp. 111–121 (1997).

130 Starodubov D. S., Grubsky V., Feinberg J., and Erdogan T., "Near-UV fabrication of ultrastrong Bragg gratings in hydrogen loaded germanosilicate fibers," *Proc. of CLEO'97,* post-deadline paper CDP24, 1997.

131 Patrick H. J., Askins C. G., McElhanon R. W. and Friebele E. J. *Electron. Lett., 33*(13), 1167–1168, 19 June 1997.

Chapter 4

Theory of Fiber Bragg Gratings

Wave propagation in optical fibers is analyzed by solving Maxwell's equations with appropriate boundary conditions. The problem of finding solutions to the wave-propagation equations is simplified by assuming weak guidance, which allows the decomposition of the modes into an orthogonal set of transversely polarized modes [1–3]. The solutions provide the basic field distributions of the bound and radiation modes of the waveguide. These modes propagate without coupling in the absence of any perturbation (e.g., bend). Coupling of specific propagating modes can occur if the waveguide has a phase and/or amplitude perturbation that is periodic with a perturbation "phase/amplitude-constant" close to the sum or difference between the propagation constants of the modes. The technique normally applied for solving this type of a problem is coupled-mode theory [4–9]. The method assumes that the mode fields of the unperturbed waveguide remain unchanged in the presence of weak perturbation. This approach provides a set of first-order differential equations for the change in the amplitude of the fields along the fiber, which have analytical solutions for uniform sinusoidal periodic perturbations.

A fiber Bragg grating of a constant refractive index modulation and period therefore has an analytical solution. A complex grating may be considered to be a concatenation of several small sections, each of constant period and unique refractive index modulation. Thus, the modeling of the transfer characteristics of fiber Bragg gratings becomes a relatively simple

matter, and the application of the transfer matrix method [10] provides a clear and fast technique for analyzing more complex structures.

Another technique for solving the transfer function of fiber Bragg gratings is by the application of a scheme proposed by Rouard [11] for a multilayer dielectric thin film and applied by Weller-Brophy and Hall [12,13]. The method relies on the calculation of the reflected and transmitted fields at an interface between two dielectric slabs of dissimilar refractive indexes. Its equivalent reflectivity and phase then replace the slab. Using a matrix method, the reflection and phase response of a single period may be evaluated. Alternatively, using the analytical solution of a grating with a uniform period and refractive index modulation as in the previous method, the field reflection and transmission coefficients of a *single period* may be used instead. However, the thin-film approach does allow a refractive index modulation of arbitrary shape (not necessarily sinusoidal, but triangular or other) to be modeled with ease and can handle effects of saturation of the refractive index modulation. The disadvantage of Rouard's technique is the long computation time and the limited dynamic range owing to rounding errors.

The Bloch theory [14,15] approach, which results in the exact eigenmode solutions of periodic structures, has been used to analyze complex gratings [16] as well. This approach can lead to a deeper physical insight into the dispersion characteristics of gratings. A more recent approach taken by Peral *et al.* [17] has been to develop the Gel'Fand–Levitan–Marchenko coupled integral equations [18] to exactly solve the inverse scattering problem for the design of a desired filter. Peral *et al.* have combined the attributes of the Fourier transform technique [19,20] (useful for low reflection coefficients, since it does not take account of resonance effects within the grating), the local reflection method [21], and optimization of the inverse scattering problem [22,23] to present a new method that allows the design of gratings with required features in both phase and reflection. The method has been recently applied to fabricate near "top-hat" reflectivity filters with low dispersion [24]. Other theoretical tools such as the effective index method [25], useful for planar waveguide applications, discrete-time [26], Hamiltonian [27], and variational [28], are recommended to the interested reader. For nonlinear gratings, the generalized matrix approach [29] has also been used. For ultrastrong gratings, the matrix method can be modified to avoid the problems of the slowly varying approximation [30].

The straightforward transfer matrix method provides high accuracy for modeling in the frequency domain. Many representative varieties of the types and physical forms of practically realizable gratings may be analyzed in this way.

4.1 Wave Propagation

The theory of fiber Bragg gratings may be developed by considering the propagation of modes in an optical fiber. Although guided wave optics is well established, the relationship between the mode and the refractive index perturbation in a Bragg grating plays an important role on the overall efficiency and type of scattering allowed by the symmetry of the problem. Here, wave-propagation in optical fiber is introduced, followed by the theory of mode coupling.

We begin with the constitutive relations

$$\overline{D} = \varepsilon_0 \overline{E} + \overline{P} \tag{4.1.1}$$

$$\overline{B} = \mu_0 \overline{H} \tag{4.1.2}$$

where ε_0 is the dielectric constant and μ_0 is the magnetic permeability, both scalar quantities; $\overline{D}$ is the electric displacement vector; $\overline{E}$ is the applied electric; $\overline{B}$ and $\overline{H}$ are the magnetic flux and field vectors, respectively; and $\overline{P}$ is the induced polarization,

$$\overline{P} = \varepsilon_0 \chi_{ij}^{(1)} \overline{E}. \tag{4.1.3}$$

The linear susceptibility $\chi_{ij}^{(1)}$ is in general a second-rank tensor with two laboratory frame polarization subscripts ij and is related to the permittivity tensor ε_{ij} with similar subscripts as

$$\varepsilon_{ij} = 1 + \chi_{ij}^{(1)}. \tag{4.1.4}$$

Assuming that the dielectric waveguide is source free, so that

$$\nabla \cdot \overline{D} = 0, \tag{4.1.5}$$

and in the absence of ferromagnetic materials,

$$\nabla \cdot \overline{B} = 0, \tag{4.1.6}$$

the electric field described in complex notation is

$$\overline{E} = \frac{1}{2}[Ee^{i(\omega t - \beta z)} + Ee^{-i(\omega t - \beta z)}], \tag{4.1.7}$$

and the induced polarization vector is also similarly defined.

Using Maxwell's equations,

$$\nabla \times \overline{E} = -\frac{\partial \overline{B}}{\partial t} \tag{4.1.8}$$

$$\nabla \times \overline{H} = \frac{\partial \overline{D}}{\partial t} + \overline{J}, \tag{4.1.9}$$

where J is the displacement current, and using Eq. (4.1.1) in Eq. (4.1.9) and with $J = 0$, we get

$$\nabla \times \overline{H} = \frac{\partial}{\partial t}[\varepsilon_0 \overline{E} + \overline{P}]. \tag{4.1.10}$$

Taking the curl of Eq. (4.1.8) and using Eqs. (4.1.2)–(4.1.5) and the time derivative of Eq. (4.1.10), the wave equation is easily shown to be

$$\nabla^2 \overline{E} = \mu_0 \varepsilon_0 \frac{\partial^2 \overline{E}}{\partial t^2} + \mu_0 \frac{\partial^2 \overline{P}}{\partial t^2}. \tag{4.1.11}$$

Using Eq. (4.1.3) and (4.1.4) in (4.1.11), we arrive at

$$\nabla^2 \overline{E} = \mu_0 \varepsilon_0 \frac{\partial^2}{\partial t^2}[1 + \chi_{ij}^{(1)}]\overline{E}, \tag{4.1.12}$$

or

$$\nabla^2 \overline{E} = \mu_0 \varepsilon_0 \varepsilon_{ij} \frac{\partial^2 \overline{E}}{\partial t^2}. \tag{4.1.13}$$

4.1.1 Waveguides

The next step in the analysis is to introduce guided modes of the optical fiber into the wave equation. The modes of an optical fiber can be described as a summation of l transverse guided mode amplitudes, $A_\mu(z)$, along with a continuum of radiation modes, $A_\rho(z)$ [2], with corresponding propagation constant, $\beta\mu$ and $\beta\rho$,

$$E_t = \frac{1}{2}\sum_{\mu=1}^{\mu=1}[A_\mu(z)\xi_{\mu t}e^{i(\omega t - \beta_\mu z)} + cc] + \sum \int_{\rho=0}^{\rho=\infty} A_\rho(z)\xi_{\rho t}e^{i(\omega t - \beta_\rho z)}\, d\rho, \tag{4.1.14}$$

where $\xi_{\mu t}$ and $\xi_{\rho t}$ are the radial transverse field distributions of the μth guided and ρth radiation modes, respectively. Here the polarization of the fields has been implicitly included in the transverse subscript, t. The summation before the integral in Eq. (4.1.14) is a reminder that all the different types of radiation modes must also be accounted for [e.g., transverse electric (TE) and transverse magnetic (TM), as well as the hybrid (EH and HE) modes]. The following orthogonality relationship ensures that the power carried in the μth mode in watts is $|A_{\mu t}|^2$:

$$1/2 \int_{-\infty}^{+\infty} \int_{-\infty}^{+\infty} \hat{e}_z \cdot [\xi_{\mu t} \times \xi_{vt}^*] \, dxdy = 1/2 \left[\frac{\beta\mu}{\omega\mu_0} \right] \int_{-\infty}^{+\infty} \int_{-\infty}^{+\infty} \xi_{\mu t} \cdot \xi_{vt}^* \, dxdy = \delta_{\mu v}. \tag{4.1.15}$$

Here, $\hat{e}_z$ is a unit vector along the propagation direction z. $\delta_{\mu v}$ is Kronecker's delta and is unity for $\mu = v$, but zero otherwise. Note that this result is identical to integrating Poynting's vector (power-flow density) for the mode field transversely across the waveguide. In the case of radiation modes, $\delta_{\mu v}$ is the Dirac delta function which is infinite for $\mu = v$ and zero for $\mu \neq v$. Equation (4.1.15) applies to the weakly guiding case for which the longitudinal component of the electric field is much smaller than the transverse component, rendering the modes predominantly linearly polarized in the transverse direction to the direction of propagation [1]. Hence, the transverse component of the magnetic field is

$$H_t = \sqrt{\frac{\varepsilon_0 \varepsilon_r}{\mu_0}} \left[\hat{e}_z \frac{\partial}{\partial z} \times \xi_t \right]. \tag{4.1.16}$$

The fields satisfy the wave equation (4.1.13) as well as being bounded by the waveguide. The mode fields in the core are J-Bessel functions and K-Bessel functions in the cladding of a cylindrical waveguide. In the general case, the solutions are two sets of orthogonally polarized modes. The transverse fields for the μth x-polarized mode that satisfy the wave equation (4.1.13) are then given by [2]

$$\xi_x = C_\mu J_\mu \left(u \frac{r}{a} \right) \begin{Bmatrix} \cos \mu\phi \\ \sin \mu\phi \end{Bmatrix} \tag{4.1.17}$$

$$H_y = n_{eff} \sqrt{\frac{\varepsilon_0}{\mu_0}} \, \xi_x, \tag{4.1.18}$$

and the corresponding fields in the cladding are

$$\xi_x = C_\mu \frac{J_\mu(u)}{K_\mu(w)} K_\mu\left(w \frac{r}{a}\right)\begin{Bmatrix}\cos \mu\phi \\ \sin \mu\phi\end{Bmatrix} \tag{4.1.19}$$

$$H_y = n_{eff}\sqrt{\frac{\varepsilon_0}{\mu_0}}\,\xi_x, \tag{4.1.20}$$

where the following normalized parameters have been used in Eqs. (4.1.17)–(4.1.20):

$$v = \frac{2\pi a}{\lambda}\sqrt{n_{core}^2 - n_{clad}^2} \tag{4.1.21}$$

$$u = \frac{2\pi a}{\lambda}\sqrt{n_{core}^2 - n_{eff}^2} \tag{4.1.22}$$

$$w^2 = v^2 - u^2, \tag{4.1.23}$$

and

$$n_{eff} = n_{clad}\left[b\left(\frac{n_{core} - n_{clad}}{n_{clad}}\right) + 1\right], \tag{4.1.24}$$

where n_{eff} is the effective index of the mode and

$$b = \frac{w^2}{u^2}. \tag{4.1.25}$$

Finally, assuming only a single polarization, the y-polarized mode,

$$\xi_y = H_x = 0. \tag{4.1.26}$$

The choice of the cosine or the sine term for the modes is somewhat arbitrary for perfectly circular nonbirefringent fibers. These sets of modes become degenerate. Since the power carried in the mode in watts is $|A_\mu|^2$, from the Poynting's vector relationship of Eq. (4.1.15), the normalization constant C_μ can be expressed as

$$C_\mu = \frac{2w}{av}\left[\frac{\sqrt{\mu_0/\varepsilon_0}}{n_{eff}\,\pi\varepsilon_\mu |J_{\mu-1}(u) J_{\mu+1}(u)|}\right]^{1/2}, \tag{4.1.27}$$

where $e_\mu = 2$ when $\mu = 0$ (fundamental mode) and 1 for $\mu \neq 0$. Matching the fields at the core–cladding boundary results in the waveguide characteristic eigenvalue equation, which may be solved to calculate the propagation constants of the modes:

$$u \frac{J_{\mu\pm1}(u)}{J_\mu(u)} = w \frac{K_{\mu\pm1}(w)}{K_\mu(w)}. \tag{4.1.28}$$

4.2 Coupled-mode theory

The waveguide modes satisfy the unperturbed wave equation (4.1.13) and have solutions described in Eqs. (4.1.17) through (4.1.20). In order to derive the coupled mode equations, effects of perturbation have to be included, assuming that the modes of the unperturbed waveguide remain unchanged. We begin with the wave equation (4.1.11)

$$\nabla^2 \overline{E} = \mu_0 \varepsilon_0 \frac{\partial^2 \overline{E}}{\partial t^2} + \mu_0 \frac{\partial^2 \overline{P}}{\partial t^2}. \tag{4.2.1}$$

Assuming that wave propagation takes place in a perturbed system with a dielectric grating, the total polarization response of the dielectric medium described in Eq. (4.2.1) can be separated into two terms, unperturbed and the perturbed polarization, as

$$\overline{P} = \overline{P}_{unpert} + \overline{P}_{grating}, \tag{4.2.2}$$

where

$$\overline{P}_{unpert} = \varepsilon_0 \chi^{(1)} \overline{E}_\mu. \tag{4.2.3}$$

Equation (4.2.1) thus becomes,

$$\nabla^2 E_{\mu t} = \mu_0 \varepsilon_0 \varepsilon_r \frac{\partial^2}{\partial t^2} E_{\mu t} + \mu_0 \frac{\partial^2}{\partial t^2} P_{grating,\mu}, \tag{4.2.4}$$

where the subscripts refer to the transverse mode number μ. For the present, the nature of the perturbed polarization, which is driven by the propagating electric field and is due to the presence of the grating, is a detail which will be included later.

Substituting the modes in Eq. (4.1.14) into (4.2.4) provides the following relationship:

$$\nabla^2\left[\frac{1}{2}\sum_{\mu=1}^{\mu=l}[A_\mu(z)\xi_{\mu t}e^{i(\omega t-\beta_\mu z)}+cc]+\sum\int_{\rho=0}^{\rho=\infty}A_\rho(z)\xi_{\rho t}e^{i(\omega t-\beta_\rho z)}\,d\rho\right]$$
$$-\mu_0\varepsilon_0\varepsilon_r\frac{\partial^2}{\partial t^2}\left[\frac{1}{2}\sum_{\mu=1}^{\mu=1}[A_\mu(z)\xi_{\mu t}e^{i(\omega t-\beta_\mu z)}+cc]+\sum\int_{\rho=0}^{\rho=\infty}A_\rho(z)\xi_{\rho t}e^{i(\omega t-\beta_\rho z)}\,d\rho\right]$$
$$=\mu_0\frac{\partial^2}{\partial t^2}P_{grating,\mu}. \tag{4.2.5}$$

Ignoring coupling to the radiation modes for the moment allows the left-hand side of Eq. (4.1.13) to be expanded. In weak coupling, further simplification is possible by applying the slowly varying envelope approximation (SVEA). This requires that the amplitude of the mode change slowly over a distance of the wavelength of the light as

$$\frac{\partial^2 A_\mu}{\partial z^2}\ll\beta_\mu\frac{\partial A_\mu}{\partial z}, \tag{4.2.6}$$

so that

$$\nabla^2E_t=\frac{1}{2}\sum_{\mu=1}^{\mu=1}\left[-2i\beta_\mu\frac{\partial A_\mu}{\partial z}\xi_{\mu t}e^{i(\omega t-\beta_\mu z)}-\beta_\mu^2A_\mu\xi_{\mu t}e^{i(\omega t-\beta_\mu z)}+cc\right]. \tag{4.2.7}$$

Expanding the second term in Eq. (4.2.5), noting that $\omega^2\mu_0\varepsilon_0\varepsilon_r=\beta_\mu^2$, and combining with Eq. (4.2.7), the wave equation simplifies to

$$\sum_{\mu=1}^{\mu=l}\left[-i\beta_\mu\frac{\partial A_\mu}{\partial z}\xi_{\mu t}e^{i(\omega t-\beta_\mu z)}+cc\right]=\mu_0\frac{\partial^2}{\partial t^2}P_{grating,t}. \tag{4.2.8}$$

Here, the subscript t on the polarization $P_{grating,t}$ reminds us that the grating has a transverse profile. Multiplying both sides of Eq. (4.2.8) by ξ_μ^* and integrating over the wave-guide cross-section leads to

$$\sum_{\mu=1}^{\mu=1}\int_{-\infty}^{+\infty}\int_{-\infty}^{+\infty}\left[-i\beta_\mu\frac{\partial A_\mu}{\partial z}\xi_{\mu t}\xi_{\mu t}^*e^{i(\omega t-\beta_\mu z)}+cc\right]dxdy$$
$$=\int_{-\infty}^{+\infty}\int_{-\infty}^{+\infty}\mu_0\frac{\partial^2}{\partial t^2}P_{grating,t}\xi_{\mu t}^*\,dxdy. \tag{4.2.9}$$

Applying the orthogonality relationship of Eq. (4.1.15) directly results in

$$\sum_{\mu=1}^{\mu=l}\left[-2i\omega\mu_0\frac{\partial A_\mu}{\partial z}e^{i(\omega t-\beta_\mu z)}+cc\right] = \int_{-\infty}^{+\infty}\int_{-\infty}^{+\infty}\mu_0\frac{\partial^2}{\partial t^2}P_{grating,t}\xi^*_{\mu t}\,dxdy. \tag{4.2.10}$$

Equation (4.2.10) is fundamentally the wave propagation equation, which can be used to describe a variety of phenomena in the coupling of modes. Equation (4.2.10) applies to a set of forward- and backward-propagating modes; it is now easy to see how mode coupling occurs by introducing forward- and backward-propagating modes. The total transverse field may be described as a sum of both fields, not necessarily composed of the same mode order:

$$E_t = \frac{1}{2}(A_v\xi_{vt}e^{i(\omega t-\beta_v z)}+cc+B_\mu\xi_{\mu t}e^{i(\omega t+\beta_\mu z)}+cc) \tag{4.2.11}$$

$$H_t = \frac{1}{2}(A_vH_{vt}e^{i(\omega t-\beta_v z)}+cc-B_\mu H_{\mu t}e^{i(\omega t+\beta_\mu z)}-cc). \tag{4.2.12}$$

Here the negative sign in the exponent signifies the forward- and the positive sign the backward-propagating mode, respectively. The modes of a waveguide form an orthogonal set, which in an ideal fiber will not couple unless there is a perturbation. Using Eqs. (4.2.11) and (4.2.12) in Eq. (4.2.10) leads to

$$\left[\frac{\partial A_v}{\partial z}e^{i(\omega t-\beta_v z)}+cc\right]-\left[\frac{\partial B_\mu}{\partial z}e^{i(\omega t+\beta_\mu z)}+cc\right] = +\frac{i}{2\omega}\int_{-\infty}^{+\infty}\int_{-\infty}^{+\infty}\frac{\partial^2}{\partial t^2}P_{grating,t}\xi^*_{\mu,vt}\,dxdy \tag{4.2.13}$$

4.2.1 Spatially periodic refractive index modulation

In a medium in which the dielectric constant varies periodically along the wave-propagation direction, the total polarization can be defined with the perturbed permittivity, $\Delta\varepsilon(z)$ and the applied field as

$$P = \varepsilon_0[\varepsilon_r - 1 + \Delta\varepsilon(z)]E_\mu. \tag{4.2.14}$$

The terms within the parentheses are equivalent to $\chi^{(1)}$, and ε_r is the relative permittivity of the unperturbed core. The constitutive relations between the permittivity of a material and the refractive index n result in the perturbation modulation index being derived from $n^2 = \varepsilon_r$ so that

$$[n + \delta n(z)]^2 = \varepsilon_r + \Delta\varepsilon(z). \tag{4.2.15}$$

Assuming the perturbation to be a small fraction of the refractive index, it follows that

$$\Delta\varepsilon(z) \approx 2n\,\delta n(z). \tag{4.2.16}$$

Defining the refractive index modulation of the grating as

$$\delta n(z) = \overline{\Delta n}\left\{1 + \frac{\nu}{2}\left(e^{i[(2\pi N/\Lambda)z + \phi(z)]} + cc\right)\right\}, \tag{4.2.17}$$

where $\overline{\Delta n}$ is the refractive index change averaged over a single period of the grating, v is the visibility of the fringes, and the exponent term along with the complex conjugate cc describe the real periodic modulation in complex notation. An arbitrary spatially varying phase change of $\phi(z)$ has been included. Λ is the period of the perturbation, while N is an integer ($-\infty < N < +\infty$) that signifies its harmonic order. The period-averaged change in the refractive index has to be taken into account since it alters the effective index n_{eff} of a mode.

Combining Eqs. (4.2.15) and (4.2.17), the total material polarization is

$$P = \varepsilon_0\left\{n^2 - 1 + 2n\overline{\Delta n}\left[1 + \frac{\nu}{2}\left(e^{i[(2\pi N/\Lambda)z + \phi(z)]} + cc\right)\right]\right\}E_\mu, \tag{4.2.18}$$

where the first term on the RHS is the permittivity, the second term is the *dc* refractive index change, and the third term is the *ac* refractive index modulation. Finally, defining a new modulation amplitude by incorporating the visibility,

$$\delta n(z) = 2n\left[\overline{\Delta n} + \frac{\Delta n}{2}\left(e^{i[(2\pi N/\Lambda)z + \phi(z)]} + cc\right)\right], \tag{4.2.19}$$

with $\Delta n = \nu\overline{\Delta n}$ as the amplitude of the ac refractive index modulation. Equation (4.2.19) describes the UV-induced refractive index change due to a grating written into the fiber core. Figure 4.1 shows the refractive index modulation for a uniform grating on a background index of the core

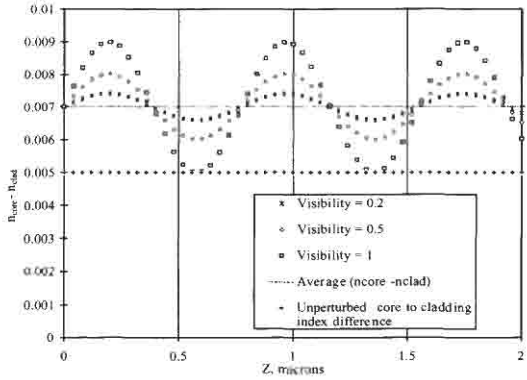

Figure 4.1: Refractive index modulation in the core of a fiber for different visibilities of the fringe pattern. Also shown is the average refractive index change in the core (dashed line). The unperturbed core-to-cladding refractive index difference is 5×10^{-3}, while the maximum refractive index modulation for unity visibility is $\pm 2 \times 10^{-3}$.

of the fiber for different visibilities. Also shown is the effect on the average core index. Note that the change in the average index in the core is constant, irrespective of the visibility of the fringes, although it remains a function of δn. In the example shown, however, both the average index and the refractive index modulation δn increase with UV exposure time.

The perturbed polarization can now be related to refractive index change shown in Eq. (4.2.19) to give

$$P_{pert} = 2n\varepsilon_0\left[\overline{\Delta n} + \frac{\Delta n}{2}\left(e^{i[(2\pi N/\Lambda)z+\phi(z)]} + cc\right)\right]E_\mu. \qquad (4.2.20)$$

Including Eq. (4.2.20) in Eq. (4.2.13) results in

$$\begin{aligned}
&\left[\frac{\partial A_\upsilon}{\partial z}e^{i(\omega t-\beta_\upsilon z)} + cc\right] - \left[\frac{\partial B_\mu}{\partial z}e^{i(\omega t+\beta_\mu z)} + cc\right] \\
&= +\frac{i\varepsilon_0}{2\omega}\int_{-\infty}^{+\infty}\int_{-\infty}^{+\infty}\frac{\partial^2}{\partial t^2}\delta n(z)\left[A_\upsilon e^{i(\omega t-\beta_\upsilon z)}\xi_{\upsilon t} + B_\mu e^{i(\omega t+\beta_\mu z)}\xi_{\mu t}\right]\xi^*_{\mu,\upsilon t}\,dxdy + cc \\
&= -in\omega\varepsilon_0 A_\upsilon\int_{-\infty}^{+\infty}\int_{-\infty}^{+\infty}\left[\overline{\Delta n} + \frac{\Delta n}{2}(e^{i[(2\pi N/\Lambda)z+\phi(z)]} + cc)\right]\xi_{\upsilon t}e^{i(\omega t-\beta_\upsilon z)}\xi^*_{\mu,\upsilon t}\,dxdy \\
&\quad -in\omega\varepsilon_0 B_\mu\int_{-\infty}^{+\infty}\int_{-\infty}^{+\infty}\left[\overline{\Delta n} + \frac{\Delta n}{2}(e^{i[(2\pi N/\Lambda)z+\phi(z)]} + cc)\right]\xi_{\mu t}e^{i(\omega t+\beta_\mu z)}\xi^*_{\mu,\upsilon t}\,dxdy + cc.
\end{aligned} \qquad (4.2.21)$$

On the LHS of Eq. (4.2.21), the rate of variation of either A_v or B_μ is determined by the mode order μ or v of the electric field $\xi^*_{\mu,vt}$ chosen as the multiplier according to the orthogonality relationship of Eq. (4.1.15). This was shown in Eq. (4.2.9) for the case of the single field. Once the term on the LHS has been chosen, the next question is the choice of the terms on the RHS. Before this is examined, we consider the terms on the RHS in general.

The RHS of Eq. (4.2.21) has two generic components for both A and B modes as

$$\begin{aligned} RHS = & -in\omega\varepsilon_0 B_\mu e^{i(\omega t+\beta_\mu z)} \times \int_{-\infty}^{+\infty}\int_{-\infty}^{+\infty} \overline{\Delta n}\,\xi_{\mu t}\xi^*_{\mu t}\,dxdy \\ & -in\omega\varepsilon_0 A_v e^{i(\omega t-\beta_p z+\phi(z))} \times \int_{-\infty}^{+\infty}\int_{-\infty}^{+\infty} \frac{\Delta n}{2}\,\xi_{vt}\xi^*_{\mu t}\,dxdy + cc, \end{aligned} \tag{4.2.22}$$

where the first exponent must agree with the exponent of the generated field on the LHS of Eq. (4.2.21) and has a dependence on the dc refractive index change, $\overline{\Delta n}$. The reason is that any other phase-velocity dependence (as for other coupled mode) will not remain in synchronism with the generated wave. The second term on the RHS has two parts. The first one is dependent on the phase-synchronous factor,

$$\beta_p = \frac{2\pi N}{\Lambda} \pm \beta_v. \tag{4.2.23}$$

The mode interactions that can take place are determined by the right-hand sides of Eqs. (4.2.21) and (4.2.22). Two aspects need to be taken into account: first, conservation of momentum requires that the phase constants on the LHS and the RHS of Eq. (4.2.22) be identical [Eq. (4.2.23)] and so influences the coupling between copropagating or counterpropagating modes. Secondly, the transverse integral on the RHS of Eq. (4.2.22), which is simply the overlap of the refractive-index modulation profile and the distributions of the mode fields, determines the strength of the mode interactions. Let us first consider the conservation of momentum, otherwise known as phase matching.

4.2.2 Phase matching

We begin with Eq. (4.2.23) in which the phase factor is the sum or difference between the magnitude of the driving electric-field mode propagation

constant β_v and the phase factor of the perturbation. The resultant β_p is the phase constant of the induced polarization wave. This is the propagation constant of a "boundwave" generated by the polarization response of the material due the presence of sources. For there to be any significant transfer of energy from the driving field amplitude A_v to the generated fields on the LHS of Eq. (4.2.22), the generated and the polarization waves must remain in phase over a significant distance, z. For continuous transfer of energy,

$$\beta_\mu = \beta_p. \tag{4.2.24}$$

Equation (4.2.24) then describes the phase-matching condition. A phase mismatch $\Delta\beta$ is referred to as a detuning,

$$\Delta\beta = \beta_\mu - \beta_p. \tag{4.2.25}$$

Including Eq. (4.2.23) in (4.2.25), we get,

$$\Delta\beta = \beta_\mu \pm \beta_v - \frac{2\pi N}{\Lambda}. \tag{4.2.26}$$

If both β_v and β_μ have identical (positive) signs, then the phase-matching condition is satisfied ($\Delta\beta = 0$) for counterpropagating modes; if they have opposite signs, then the interaction is between copropagating modes.

Identical relationships for co- and counterpropagation interactions apply to radiation mode phase matching. A schematic of the principle of phase matching is shown in Fig. 4.2.

Finally, energy conservation requires that the frequency ω of the generated wave remains unchanged.

4.2.3 Mode symmetry and the overlap integral

The orthogonality relationship of Eq. (4.1.15) suggests that only modes with the same order μ will have a nonzero overlap. However, the presence of a nonsymmetric refractive index modulation profile across the photosensitive region of the fiber can alter the result, allowing modes of different orders to have a nonzero overlap integral. The reason for this fundamental departure from the normalization of Eq. (4.1.15) is the nonuniform *transverse* distribution of sources, giving rise to a polarization wave that has an allowed odd symmetry. This is graphically displayed in Fig. 4.3: A driving fundamental mode (LP_{01}, $\mu = 0$) electric field, ξ_v, interacts with

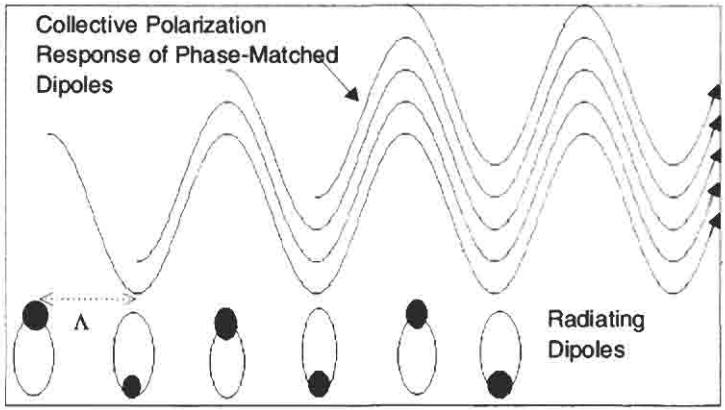

Figure 4.2: The principle of phase matching. The polarization wave grows in synchronism with the driving field. The radiating dipoles are shown to be spatially distributed with a period of Λ, allowing the radiated wave to remain in phase with the driving field. This schematic applies to guided or radiation-mode coupling.

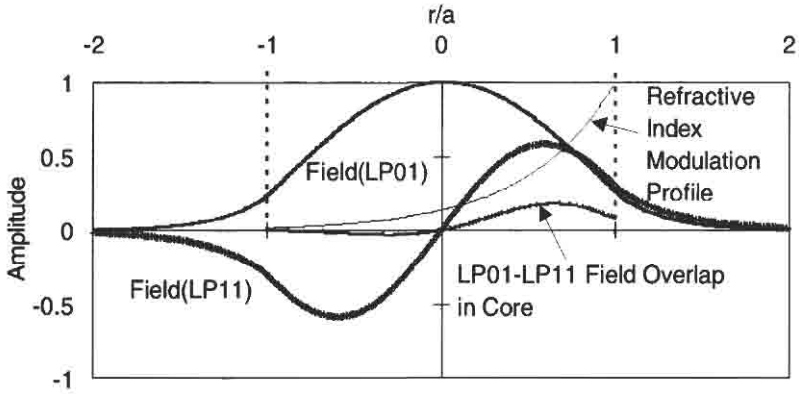

Figure 4.3: A cross-section of the fiber showing the fields of the LP_{01} and the LP_{11} modes, along with the transverse refractive index modulation profile. The overlap of the two fields with the profile of the index modulation [as per Eq. (4.2.22)] changes sign across the core but does not have with the same magnitude. The field overlap is therefore nonzero. The transverse profile of the refractive index thus influences the symmetry of the modes allowed to couple. The transverse profile of the perturbation is equivalent to a "blaze" across the core (tilted grating), which benefits coupling to odd-order radiation modes as well. The two dashed lines indicate the core boundary.

a modulated permittivity that has a uniform transverse profile. Also shown is a polarization field that is in the LP_{11} mode ($v = 1$). Examining the transverse overlap (which is proportional to the product of the field amplitudes and the refractive-index profile) on the left half of the core, we find that magnitude is the same as on the right half, but they have the opposite signs, resulting in a zero overlap. The orthogonality relationship holds and exchange of energy is not possible between the different order modes. If, however, the refractive index profile is not uniform across the core (Fig. 4.3), then although the signs of the overlap in the two halves (around a plane through the axis of the fiber) are different, the magnitudes are no longer identical.

Thus, the overlap is now not zero, allowing a polarization wave to exist with a symmetry (and therefore, mode-order) different from that of the driving mode. The selection rules for the modes involved in the exchange of energy are then determined by the details of the terms in the integral in Eq. (4.2.22) and apply equally to radiation mode orders.

The consequence of the asymmetric refractive index perturbation profile may now be appreciated in Eq. (4.2.21). On the RHS, the integrals with the electric fields of the driving field $\xi_{\mu t}$ and the polarization wave ξ_{vt} along with the asymmetric profile of the refractive index modulation are nonzero for dissimilar mode orders, i.e., $\mu \neq v$. The magnitude of the overlap for a particular mode combination will depend on the exact details of the perturbation profile.

4.2.4 Spatially periodic nonsinusoidal refractive index modulation

Note that in Eq. (4.2.21), the refractive-index perturbation can have a $\pm$ sign in the exponent. This is a direct result of the Fourier expansion of the permittivity perturbation. However, since it is equivalent to an additional momentum, which can be either added to or taken away from the momentum vector of a driving field, it may be viewed as a factor that can take place, as already discussed.

In the general case when the refractive index modulation is not simply sinusoidal but a periodic complex function of z, it is more convenient to expand δn in terms of Fourier components as

$$\delta n(z) = 2n\left[\overline{\Delta n} + \frac{\Delta n}{2}\sum_{N=-\infty}^{N=+\infty} \alpha_N (e^{i[(2\pi N/\Lambda)z + \phi(z)]} + cc)\right], \quad (4.2.27)$$

where α_N is the Fourier amplitude coefficient of the Nth harmonic of the perturbation. Differently shaped periodic functions have their corresponding α_N coefficients, which in turn influence the magnitude of the overlap integral, and hence the strength of the mode coupling.

4.2.5 Types of mode coupling

The phase-matching condition is defined by setting $\Delta\beta$ in Eq. (4.2.26) to zero. Therefore,

$$\beta_v = \pm\left(\frac{2\pi N}{\Lambda} - \beta_\mu\right). \tag{4.2.28}$$

Equation (4.2.28) states that a mode with a propagation constant of β_μ will be synchronously drive another mode A_v with a propagation constant of β_v, provided, of course, the latter is an allowed solution to the unperturbed wave equation (4.1.28) for guided modes and its equivalent for radiation modes.

The guided modes of the fiber have propagation constants that lie within the bounds of the core and the cladding values, although only solutions to the eigenvalue Eq. (4.1.28) are allowed. Consequently, for the two lowest order modes of the fiber, LP_{01} and LP_{11}, the propagation constants β_v and β_μ are the radii of the circles $2\pi n_v/\lambda$ and $2\pi n_\mu/\lambda$. A mode traveling in the forward direction has a mode propagation vector $\overline{K}_{LP01}$ that combines with the grating vector $\overline{K}_{grating}$ to generate $\overline{K}_{result}$. Since the grating vector is at an angle θ_g to the propagation direction, and the allowed mode solution, $\overline{K}_{LP11}$ is in the propagation direction, the phase-matching condition reduces to

$$\Delta\beta = |\beta_{LP01}| + |\beta_{LP11}| - \overline{K}_{grating} \cos\theta_g, \tag{4.2.29}$$

Under these circumstances, the process of phase matching reverses in sign after a distance (known as the coherence length l_c) when

$$\Delta\beta l_c = \pi. \tag{4.2.30}$$

Consequently, the radiated LP_{11} mode (traveling with a phase constant of β_μ) propagates over a distance of l_c before it slips exactly half a wavelength out of phase with the polarization wave (traveling with a phase constant β_v).

In order to understand the various phase-matching conditions, we shall begin with the dispersion diagram of modes. The propagation constants of modes and their dispersion is crucial to the understanding of phase matching. To facilitate an insight into the properties of modes, we use the approximate analogy between rays and modes, since the visual aspect of rays is easier to understand. In Fig. 4.4 we see a section of an optical fiber with a ray incident at the angle at which it is refracted out of the fiber core to exit in a direction parallel to the z-axis. The propagation direction is indicated as the z-axis while the transverse direction is the x-axis. The angle $\theta_{critical} = \sin^{-1}(n_{clad}/n_{core})$is marked as the critical angle for that ray. The ray propagation angle is θ_{cutoff}. Thus, all ray angles below θ_{cutoff} are allowed, but only those that form standing waves [2] exhibit mode properties, with a specific effective propagation index n_{eff}. We note an important relationship in the ray picture: Since the effective index of at mode at cut-off is the cladding refractive index, the effective index of a mode *is the cutoff index of a mode propagating in a waveguide with a cladding refractive index of* n_{eff}.

We now transfer this picture to the one shown in Fig. 4.5. Three circles with radii n_0, n_{clad}, and n_{core} form the boundaries for the waveguide.

Figure 4.5 shows the generalized dispersion diagram for an optical fiber. The outer circle has a radius of n_{core}, the middle circle has a radius of n_{clad}, and the shaded circle represents free space and has a radius of unity. It is based on the ray diagram shown in Fig. 4.4, so that the critical angle for the backward-propagating guided modes is marked as $\theta^m_{critical}$ between the dotted and the dashed lines at point G^m_b, with a similar angle at G^m_f for the forward-propagating modes. The two vertical dotted lines

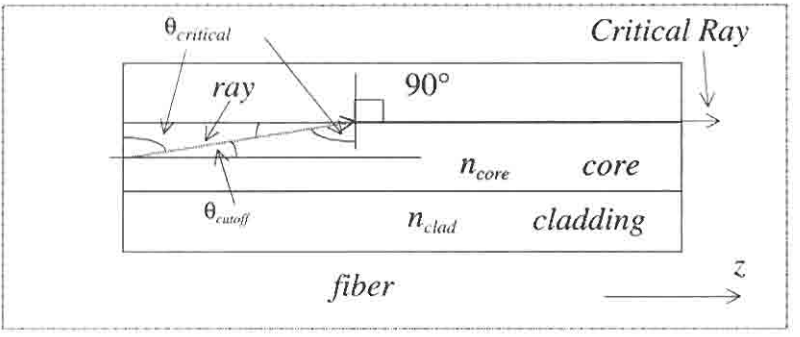

Figure 4.4: Ray propagation in a waveguide.

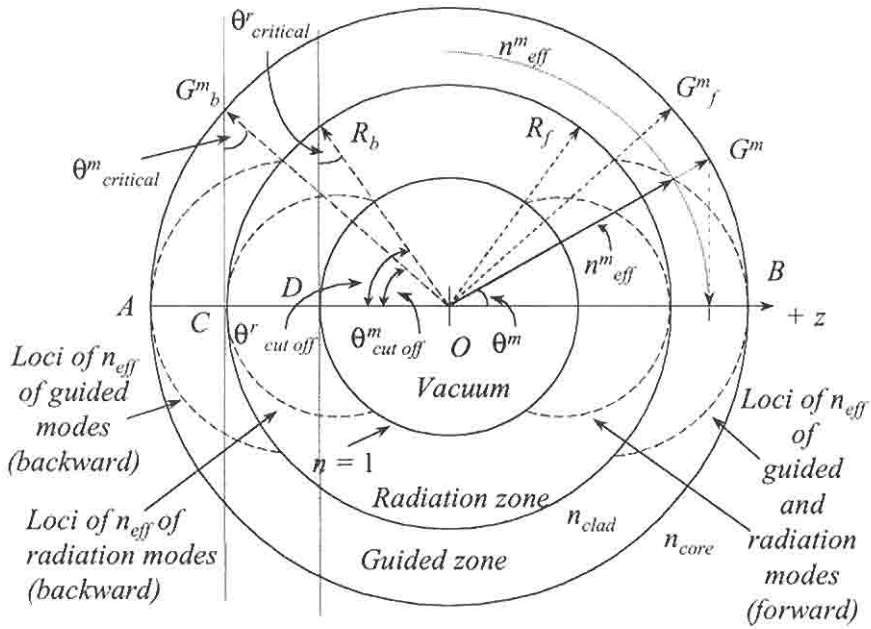

Figure 4.5: Generalized dispersion diagram for guided and radiation modes and radiation field for waveguides.

are tangential to the cladding and inner circles, respectively. All guided modes have their cutoff at $\theta^m_{critical}$. The equivalent cutoff angles in the propagation direction for all guided modes are also marked at the origin, as θ^m_{cutoff}.

For the radiation (cladding) modes the equivalent angles are $\theta_{critical}$ and θ_{cutoff}, subtended by the dashed lines to points R_b and R_f. The dashed lines in Fig. 4.5 mark these. We note that all guided modes have effective indexes lying within the region bounded by the outer two circles. A forward-propagating guided mode has an effective index of n^m_{eff}, which lies on a circle of radius n^m_{eff} (part of a dashed circle is shown) and on a vector OG^m, propagating at an angle θ^m to the z-axis. It is easy to show that the loci of all the effective indexes of the (forward- and backward-propagating) modes lie on circles (shown as the outer two dashed circles). The length of the vector from the origin to the intercept with the n^m_{eff} circle subtends the ray angle θ^m for that mode. The point at which these dashed circles meet the n_{clad} circle defines the cutoff of the guided modes. A

similar set of circles intersects the free space shaded inner circle to define the cutoff of *all* cladding modes. Beyond this point and into the inner shaded circle is the radiation field region. If the cladding were extended to infinity, the middle circle would become the locus of *all* cladding space modes (continuum). In the present situation, the inner circle remains the locus of the free space modes, which are the cladding modes beyond cutoff.

Having defined the phase space for all the modes, we can proceed to the phase-matching diagram, shown in Fig. 4.6. Here we see a forward-propagating mode, with an effective index of $n_{core}\cos\theta_f^n$, phase matched to a counterpropagating mode with an effective index of $n_{core}\cos\theta_b^n$ (point G_{pm}) with a grating that has an "effective index" of $n_g\cos\theta_g$. The grating period $\Lambda_g = \lambda/(n_g\cos\theta_g)$. When $\theta_g = 0$, we have the normal Bragg condition. We can now see the effect of detuning this interaction to shorter wavelengths. The point G^m moves down toward B, dragging the grating vector n_g with it. This action carves out a phase-matching curve on the LH side of the figure, marked by the dashed curve. Phase matching is lost since

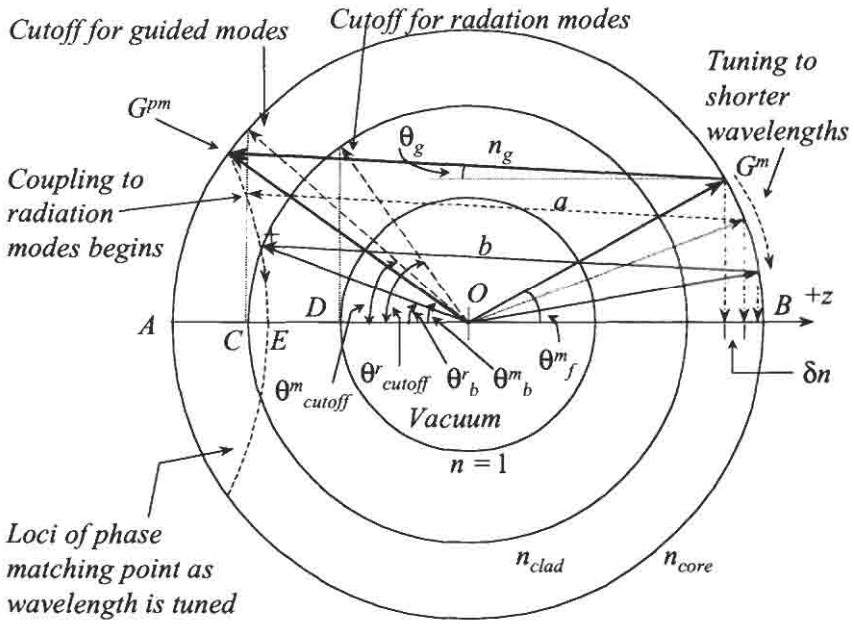

Figure 4.6: Guided mode and radiation mode/field phase-matching diagram for the slanted Bragg grating (counterradiating coupling).

there is no intersection with the outer or inner circles. There is a gap in the spectrum, in which no phase matching is possible. At some point the arrowhead meets the vertical dotted line for the radiation modes on line a, and phase matching to the radiation modes begins. This will couple to the lowest-order modes. With an infinite cladding, free-space radiation mode phase matching occurs. As the wavelength becomes even shorter, the angle of the radiation modes increases, and only when the vector b meets the n_{clad} circle is radiation mode coupling at an angle of θ_b. After this point, the angle of the radiation mode increases beyond θ_b. We now note that the change in the mode index is δn from the RH side of the figure, so that we can calculate the wavelength at which the radiation loss starts to occur.

Figure 4.6 shows the phase-matching diagram for coupling to the guided and radiation modes and fields with a tilted grating, known as *side-tap-grating* (STG, also see Chapter 6). This grating has a period similar to Bragg gratings but does not have its grating planes normal to the fiber axis, and it is tilted at an angle, θ_g. The diagram specifically deals with the case of coupling to counterpropagating fields.

In the first interaction with n_g, we have Bragg reflection at λ_{Bragg}. We assume that the grating angle $\theta_g = 0$, and that when the wavelength is tuned, the effective index of the mode is n_{eff}^{start} at the point indicated by a on Fig. 4 6, so that mathematically, this is simply phase matching to a mode with the cladding index as

$$\frac{2\pi n_{eff}^{start}}{\lambda_{start}} + \frac{2\pi n_{clad}^{start}}{\lambda_{start}} = \frac{2\pi N}{\Lambda_g} = \frac{4\pi n_{eff}^{Bragg}}{\lambda_{Bragg}}, \tag{4.2.31}$$

where *start* indicates the wavelength at which the radiation mode coupling begins.

Rearranging and using the approximation $n_{eff} \approx n_{eff}^{start} \approx n_{eff}^{Bragg}$, it follows that

$$\lambda_{start} = \frac{\lambda_{Bragg}}{2}\left(1 + \frac{n_{clad}}{n_{eff}}\right). \tag{4.2.32}$$

Therefore, radiation loss begins at a wavelength slightly shorter than the Bragg wavelength, governed by the ratio in the brackets in Eq. (4.2.32). For example, in a fiber with a large core–cladding index difference with a tightly confined Bragg wavelength (1550 nm) mode ($n_{eff} = 1.475$), the start wavelength will be at ~1537 nm, some 13 nm away.

We can estimate the maximum angle for the radiation by observing the point E on the phase-matching curve in Fig. 4.6. The tangent to this point on the phase matching at E intersects the cladding circle at the "+" point. This point subtends the largest radiation mode angle for this particular grating, at the origin. The maximum angle of the radiation for an untilted grating is at the shortest wavelength and is easily shown to be

$$\theta'_{\max} = \cos^{-1}\left(\frac{2n_{eff} - n_{core}}{n_{clad}}\right), \tag{4.2.33}$$

which is maximum if $n_{eff} = n_{clad}$. For a core-to-cladding refractive index difference of 0.01 in a silica fiber, $\theta'_{max} \approx 6.7°$. It should be remembered that phase matching to specific radiation *modes* will only occur if a cladding mode exists with the appropriate mode index. However, with an infinite cladding, coupling to a continuum of the radiation field occurs so that the spectrum is continuous.

There is another possibility for coupling to radiation modes. We begin with $\theta_g = 0$ and the condition for Bragg reflection from, for example, the forward to the counterpropagating LP_{01} mode. If the grating is tilted at an angle θ_g, it is shown simply as a rotation of n_g around the pivot at G^m. Following the mathematical approach taken for Eq. (4.2.33), we find that at some angle θ'_g the radiation mode is at the Bragg wavelength, i.e., the start wavelength moves toward the Bragg wavelength, until they coincide. At this point, there is strong coupling to the radiation modes. Referring to Fig. 4.6, the angle is easily found by changing the tilt of the grating. This directly leads to

$$K_g - K_g \cos\theta'_g = \frac{4\pi}{\lambda_{Bragg}}(n_{eff} - n_{clad}), \tag{4.2.34}$$

where n_{eff} is the effective index of the mode at the Bragg wavelength of the untilted grating (when $\theta_g = 0$), so that

$$\cos\theta'_g = \frac{n_{clad}}{n_{eff}}. \tag{4.2.35}$$

Again, the tilt angle of the grating for this condition to be met increases with n_{eff} and is a maximum when $n_{eff} = n_{core}$. We can calculate

that for a standard fiber, with an $n_{eff} \approx n_{clad} + b\Delta n$ ($\delta n = 4.5 \times 10^{-3}$) and $b = 0.4$ at 1550 nm [2], the angle at which the Bragg wavelength equals the radiation wavelength is $\theta_g' \approx 2.85°$. It is clear from Eq. (4.2.35) that the angle becomes larger with increasing core–cladding index difference.

Finally there is a set of unconfined radiation modes at a continuum of angles subtended at O, but with vector lengths within the space of the radiation zone. Making the grating "effective index" n_g small so that the arrowhead remains on the RH side of Fig. 4.6, one can see that phase matching will occur between copropagating modes, or to radiation modes in the forward direction. This is better shown in Fig. 4.7.

The following points should be noted regarding the phase-matching diagram. The guided mode propagation constants have discrete values and lie on the loci for the particular mode propagation constants. The grating vector can have any angle θ_g to the propagation direction, as can the radiated field, provided the cladding is assumed to be at infinity. If,

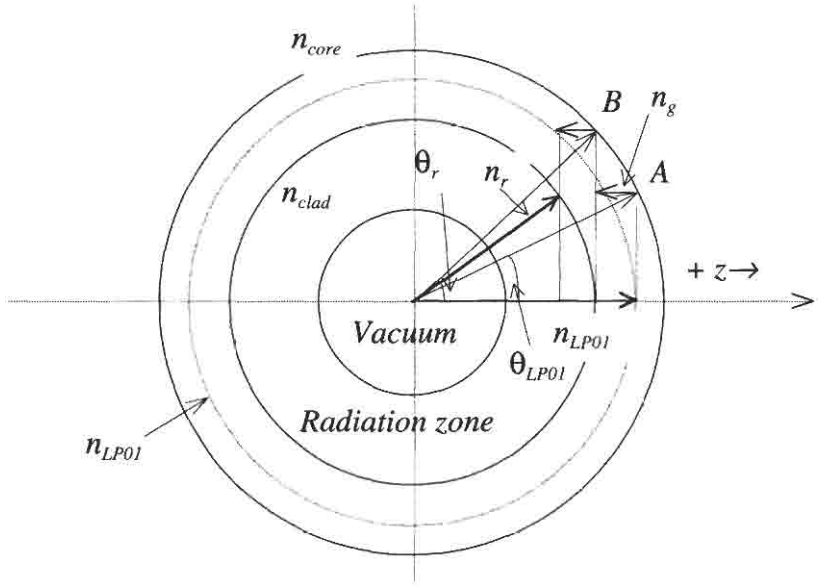

Figure 4.7: The phase-matching diagram for copropagating modes with radiation mode coupling with a long-period grating.

however, a cladding boundary is present as shown by the innermost dashed circle, then the radiated modes only have allowed β-values. This radiation may be viewed as the modes of a waveguide with a core of refractive index n_{clad} and a radius equal to the fiber-cladding radius surrounded by an infinite cladding of air/vacuum refractive index. The diagram then acquires a set of circles with radii $n_{vacuum} < n_\rho < n_{clad}$ representing discrete *cladding* modes, similar to those for guided modes, at the points of intersection with the dispersion curves. The radiation mode fields are slightly modified by the presence of the high-index fiber core.

Coupling is also possible to the forward-radiating modes and fields. This requires a different grating, known as a long-period grating, which has a much longer period than a Bragg grating, since the momentum of the mode does not change sign (as in forward-to-backward coupling). The phase matching for the generalized case of the tilted grating for copropagating coupling is shown in Fig. 4.7. The form of the diagram is similar to Figs. 4.5 and 4.6.

For phase matching, the movement of the n_g arrowhead for the LPG is opposite to that of the STG. We begin with an LP_{01} mode with the propagation index arrow $n_{LP_{01}}$ pointing in the $+z$ direction. The grating n_g starts at the tip of the guided mode arrow, inclined at $\theta_g = 0$ to the fiber axis. The wavelength at which radiation is first emitted is when the tip of the grating vector from point A intersects the tangent to the cladding mode circle (dashed vertical line). This point represents the longest-wavelength LP_{01} mode that has a propagation constant equal to the cladding index and has the lowest angle. Light is coupled to radiation modes within the radiation zone as n_g is moved to the left and *the LP_{01} mode is "cut off" at the radiation angle*, θ_r. Therefore, θ_r is the angular spread of the radiated fields. Mode coupling is only possible if there is phase matching to specific modes. Note that this wavelength approaches ∞, since the fundamental guided mode effective index approaches n_{clad}. The wavelength vs angle has the opposite dependence of the STG, i.e., long wavelengths exit at the largest angle in the LPG, while it is the shortest wavelengths in the STG. The first Bragg wavelength reflection (very weak) is at the *short* wavelength side of the LPG radiation loss spectrum, while it is on the *long* wavelength side of the STG radiation loss spectrum. The spectrum of the LPG is "reversed" around the Bragg wavelength.

Figure 4.8 shows various types of phase-matched interactions possible with different types of gratings.

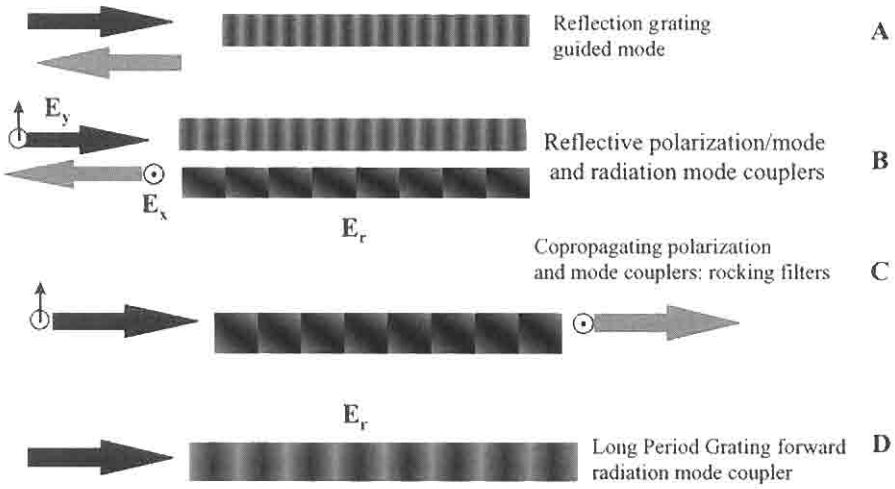

Figure 4.8: Types of Bragg gratings categorized by action of coupling. The schematics show various gratings in the core of an optical fiber. All gratings are shown to be transversely uniform. A nonuniform transverse refractive index modulation profile enhances coupling to either different mode orders of guided or to the radiation field. ***A*** shows a guided mode reflection grating. ***B*** shows a reflecting guided mode polarization coupler, mode converter, or radiation mode coupler ("side-tap" grating). ***C*** is a polarization coupler for copropagating modes, also knows as a "rocking filter" [31]. ***D*** is the copropagating guided-mode to radiation-mode coupler, also known as the "long-period grating."

4.3 Coupling of counterpropagating guided modes

The simplest form of interaction is between a forward-propagating and an identical backward-propagating mode. However, for a general approach, dissimilar modes are considered for the counterpropagating (reflected) mode phase matching with Eq. (4.2.21) rewritten as

$$\frac{\partial B_\mu}{\partial z} e^{i(\omega t+\beta_\mu z)} + cc = in\omega\varepsilon_0 B_\mu \int_{-\infty}^{+\infty}\int_{-\infty}^{+\infty} \overline{\Delta n}\,\xi_{\mu t}\xi_{\mu t}^{*} e^{i(\omega t+\beta_\mu z)}\,dxdy$$
$$+ in\omega\varepsilon_0 A_v \int_{-\infty}^{+\infty}\int_{-\infty}^{+\infty} \frac{\Delta n}{2} e^{i[(2\pi N/\Lambda)z+\phi(z)]}\xi_{vt}\xi_{\mu t}^{*} e^{i(\omega t-\beta_v z)}\,dxdy + cc. \tag{4.3.1}$$

By choosing the appropriate β value for identical modes ($\mu = v$) but with opposite propagation directions in Eq. (4.3.1) and dividing both sides by $\exp[i(\omega t + \beta_\mu z)]$,

$$\begin{aligned}\frac{\partial B_\mu}{\partial z} &= in\omega\varepsilon_0 B_\mu \int_{-\infty}^{+\infty}\int_{-\infty}^{+\infty} \overline{\Delta n}\,\xi_{\mu t}\xi_{\mu t}^{*}\,dxdy \\ &\quad + in\omega\varepsilon_0 A_v \int_{-\infty}^{+\infty}\int_{-\infty}^{+\infty} \frac{\Delta n}{2}\, e^{i([(2\pi N/\Lambda)-\beta_v-\beta_\mu]z+\phi(z))}\xi_{vt}\xi_{\mu t}^{*}\,dxdy,\end{aligned} \tag{4.3.2}$$

which leads to the following simple coupled-mode equations by choosing the appropriate synchronous terms,

$$\frac{\partial B_\mu}{\partial z} = i\kappa_{dc}B_\mu + i\kappa_{ac}A_v e^{-i(\Delta\beta z-\phi[z])}, \tag{4.3.3}$$

with

$$\Delta\beta = \beta_\mu + \beta_v - \frac{2\pi N}{\Lambda}, \tag{4.3.4}$$

and the dc coupling constant,

$$\kappa_{dc} = n\omega\varepsilon_0 \int_{-\infty}^{+\infty}\int_{-\infty}^{+\infty} \overline{\Delta n}\,\xi_{\mu t}\xi_{\mu t}^{*}\,dxdy, \tag{4.3.5}$$

while the *ac* coupling constant κ_{ac} includes the overlap integral,

$$\begin{aligned}\kappa_{ac} &= n\omega\varepsilon_0 \int_{-\infty}^{+\infty}\int_{-\infty}^{+\infty} \frac{\Delta n}{2}\,\xi_{vt}\xi_{\mu t}^{*}\,dxdy \\ &= \frac{v}{2}\,\kappa_{dc},\end{aligned} \tag{4.3.6}$$

if $\mu = v$. The change in the amplitude of the driving mode may also be derived from Eq. (4.2.21) as

$$\frac{\partial A_v}{\partial z} = -i\kappa_{dc}A_v - i\kappa_{ac}^{*}B_\mu e^{i(\Delta\beta z-\phi(z))}. \tag{4.3.7}$$

Eqs. (4.3.3) and (4.3.7) are the coupled-mode equations from which the transfer characteristics of the Bragg grating can be calculated.

To find a solution, the following substitutions are made for the forward (reference) and backward propagating (signal) modes [32]:

$$\begin{aligned} R &= A_v e^{-(i/2)[\Delta\beta z - \phi(z)]} \\ S &= B_\mu e^{(i/2)[\Delta\beta z - \phi(z)]}. \end{aligned} \tag{4.3.8}$$

Differentiating Eq. (4.3.8) and substituting into Eqs. (4.3.3) and (4.3.7) results in the following coupled-mode equations:

$$\frac{dR}{dz} + i\left[\kappa_{dc} + \frac{1}{2}\left(\Delta\beta - \frac{d\phi(z)}{dz}\right)\right]R = -i\kappa_{ac}^* S \tag{4.3.9}$$

$$\frac{dS}{dz} - i\left[\kappa_{dc} + \frac{1}{2}\left(\Delta\beta - \frac{d\phi(z)}{dz}\right)\right]S = i\kappa_{ac} R. \tag{4.3.10}$$

The physical significance of the terms in brackets is as follows: κ_{dc} influences propagation due to the change in the average refractive index of the mode, as has already been discussed. Any absorption, scatter loss, or *gain* can be incorporated in the magnitude and sign of the imaginary part of κ_{dc}. Gain in distributed feedback gratings will be discussed in Chapter 8. There are also two additional terms within the parentheses in Eqs. (4.3.9) and (4.3.10), the first one of which, $\Delta\beta/2$, is the detuning and indicates how rapidly the power is exchanged between the "radiated" (generated) field and the polarization ("bound") field. This weighting factor is proportional to the inverse of the distance the field travels in the generated mode. At phase matching, when $\Delta\beta = 0$, the field couples to the generated wave over an infinite distance Finally, the rate of change of ϕ signifies a chirp in the period of the grating and has an effect similar to that of the detuning. So, for uniform gratings, $d\phi/dz = 0$, and for a visibility of unity for the grating, $\kappa_{ac} = \kappa_{dc}/2$.

The coupled-mode Eqs. (4.3.9) and (4.3.10) are solved using standard techniques [33]. First the eigenvalues are determined by replacing the differential operator by λ and solving the characteristic equation by equating the characteristic determinant to zero. The resultant eigenvalue equation is in general a polynomial in the eigenvalues λ. Once the eigenvalues are found, the boundary values are applied for uniform gratings: We assume that the amplitude of the incident radiation from $-\infty$ at the input of a fiber grating (of length L) at $z = 0$ is $R(0) = 1$, and that the field $S(L) = 0$. The latter condition is satisfied by the fact that the reflected field at the output end of the grating cannot exist owing to the absence of the

perturbation beyond that region. These conditions result in the following analytical solution for the amplitude reflection coefficient:

$$\rho = \frac{S(0)}{R(0)} = \frac{-\kappa_{ac} \sinh(\alpha L)}{\delta \sinh(\alpha L) - i\alpha \cosh(\alpha L)}, \tag{4.3.11}$$

where

$$\delta = \kappa_{dc} + \frac{1}{2}\left(\Delta\beta - \frac{d\phi(z)}{dz}\right) \tag{4.3.12}$$

and

$$\alpha = \sqrt{|\kappa_{ac}|^2 - \delta^2}. \tag{4.3.13}$$

A few points regarding Eqs. (4.3.9)–(4.3.13) are worth mentioning. First, for reflection gratings that have a constant period Λ, the variation in the phase $d\phi(z)/dz = 0$. Second, at precise phase matching, $\Delta\beta = 0$, and the ac coupling constant κ_{ac} is a real quantity. Finally, the power reflection coefficient is $|\rho|^2$,

$$|\rho|^2 = \frac{|\kappa_{ac}|^2 \sinh^2(\alpha L)}{|\kappa_{ac}|^2 \cosh^2(\alpha L) - \delta^2}, \tag{4.3.14}$$

in which Eq. (4.3.13) has been used to simplify the result. Noting from Eq. (4.3.14) that α can be real or imaginary, the following regimes may be identified:

1. α is real when $|\kappa_{ac}| > \delta$ and Eqs. (4.3.11) and (4.3.14) apply.
2. α is zero when $|\kappa_{ac}| = \delta$.
3. α is imaginary when $|\kappa_{ac}| < \delta$ and Eqs. (4.3.11) and (4.3.14) transform to

$$\rho = \frac{-\kappa_{ac} \sin(\alpha L)}{i\alpha \cos(\alpha L) + \delta \sin(\alpha L)}, \qquad |\kappa_{ac}| < \delta, \tag{4.3.15}$$

and

$$|\rho|^2 = \frac{|\kappa_{ac}|^2 \sin^2(\alpha L)}{\delta^2 - |\kappa_{ac}|^2 \cos^2(\alpha L)}, \qquad |\kappa_{ac}| < \delta. \tag{4.3.16}$$

4.4 Codirectional coupling

In a multimode fiber, coupling can occur between orthogonally polarized modes of the same order, or to cladding modes (LPG) if the transverse

profile of the refractive index perturbation is uniform. However, as has been described by the general mode-coupling constants of Eqs. (4.2.5) and n(4.2.6) dissimilar mode orders that normally cannot couple owing to the orthogonality relationship [Eq. (4.1.15)] are allowed to couple when the transverse profile of the refractive index is nonuniform. This applies equally to copropagating modes. In this case, coupling may normally occur between

1. Copropagating orthogonal polarizations, e.g., $(HE_{11})_{x,y} \leftrightarrow (HE_{11})_{y,x}$ ($LP_{01,x}$ and the $LP_{01,y}$). A uniform grating profile is necessary for good efficiency. To allow coupling between these modes, the grating is written at 45° to the principle birefringent axes of the fiber (see Section 4.5 and Chapter 6).
2. $(LP_{01})_{x,y} \leftrightarrow (LP_{v\mu})_{x,y}$. Here, the transverse profile of the grating strongly influences the strength of the coupling. With a uniform profile, the coupling is zero for $v \neq 0$.
3. Coupling to the radiation field E_ρ (as with LPGs). Since the radiation field is evanescent in the core of the fiber and oscillatory in the cladding, coupling can be strongly influenced if a grating extends into the cladding as well. The latter diminishes the overlap integral between the guided lowest-order mode and the radiation modes, while an asymmetric transverse grating profile can enhance the interaction with odd modes.

Following the analysis developed in Section 4.2 and 4.3, the mode coupling equations for copropagating modes are

$$\frac{\partial B_\mu}{\partial z} = -i\kappa_{dc,\mu}B_\mu - i\kappa_{ac,v\mu}A_v e^{-i(\Delta\beta z - \phi[z])}, \tag{4.4.1}$$

but with the phase-mismatch factor

$$\Delta\beta = \beta_v - \beta_\mu - \frac{2\pi N}{\Lambda}, \tag{4.4.2}$$

and the dc self-coupling constant for each of the modes,

$$\kappa_{dc,\mu} = n\omega\varepsilon_0 \int_{-\infty}^{+\infty}\int_{-\infty}^{+\infty} \overline{\Delta n}\,\xi_{\mu t}\xi_{\mu t}^* \, dxdy \tag{4.4.3}$$

$$\kappa_{dc,v} = n\omega\varepsilon_0 \int_{-\infty}^{+\infty}\int_{-\infty}^{+\infty} \overline{\Delta n}\,\xi_{vt}\xi_{vt}^* \, dxdy. \tag{4.4.4}$$

The cross-coupling constant κ_{ac} remains the same as for contradirectional coupling as

$$\kappa_{ac,v\mu} = n\omega\varepsilon_0 \int_{-\infty}^{+\infty} \int_{-\infty}^{+\infty} \frac{\Delta n}{2} \xi_{vt} \xi_{\mu t}^* \, dxdy. \tag{4.4.5}$$

The amplitude of the input mode evolves as

$$\frac{\partial A_v}{\partial z} = -i\kappa_{dc,v} A_v - i\kappa_{ac,\mu v}^* B_\mu e^{i(\Delta\beta z - \phi(z))}. \tag{4.4.6}$$

Notice that the dc coupling constants may be different for the evolution of the input and coupled modes. To resolve this problem, we introduce new variables, R and S as before, but slightly modified, to result in a common coupling factor:

$$A_v = \mathrm{Re}^{-i((\kappa_{dc,\mu} + \kappa_{dc,v})/2)z} \times e^{(i/2)[\Delta\beta z - \phi(z)]} \tag{4.4.7}$$

$$B_\mu = Se^{-i((\kappa_{dc,\mu} + \kappa_{dc,v})/2)z} \times e^{(-i/2)[\Delta\beta z - \phi(z)]}. \tag{4.4.8}$$

The subscripts μ and v on the dc coupling constants κ_{dc} are specific to each mode and is defined by Eq. (4.2.5) for identical modes. Differentiating R and S, collecting terms, and substituting into Eqs. (4.4.1) and (4.4.6) leads to

$$\frac{dR}{dz} - \frac{i}{2}\left[\kappa_{dc,\mu} - \kappa_{dc,v} + \Delta\beta + \frac{d\phi(z)}{dz}\right]R = -i\kappa_{ac}^* S \tag{4.4.9}$$

$$\frac{dS}{dz} - \frac{i}{2}\left[\Delta\beta + \kappa_{dc,v} - \kappa_{dc,\mu} - \frac{d\phi(z)}{dz}\right]S = -i\kappa_{ac} R. \tag{4.4.10}$$

The phase-mismatch factor $\Delta\beta$ is now proportional to the *difference* in the propagation constants of the two modes as shown in Eq. (4.4.2).

The *cross*-coupling constant κ_{ac} is defined by Eqs. (4.2.6) and (4.4.5) as $\kappa_{ac,\mu v}$ for identical or nonidentical modes. Note that the coupling constant is real so that $\kappa_{ac,\mu v} = \kappa_{ac,v\mu}^* = \kappa_{ac}$.

The grating transmission function comprises two modes — in the simplest case, two orthogonal modes of the same order. However, the general case includes nonidentical modes (including a radiation mode) with the same or orthogonal polarization. The details of the coupling constants κ_{ac} and κ_{dc} need to be evaluated numerically. Radiation modes are considered in Section 4.7, while coupling between different polarizations is presented in Section 4.5.

The solutions to the coupled-mode Eqs. (4.4.9) and (4.4.10) are found by applying the boundary values as in the case of the reflection grating. However, for the transmission grating, the input fields, $R(-L/2) = 1$ and $S(-L/2) = 0$. The power couples from R to S so that the transmission in the uncoupled state is

$$\frac{|R(L/2)|^2}{|R(-L/2)|^2} = \frac{\delta^2}{\alpha^2}\sin^2(\alpha L) + \cos^2(\alpha L), \tag{4.4.11}$$

and the transmission in the coupled state (also known as the crossed state) is

$$\frac{|S(L/2)|^2}{|R(-L/2)|^2} = \frac{\kappa_{ac}^2}{\alpha^2}\sin^2(\alpha L). \tag{4.4.12}$$

In Eqs. (4.4.11) and (4.4.12), $\alpha = (|\kappa_{ac}|^2 + \delta^2)^{1/2}$, and

$$\delta = \frac{1}{2}\left[\kappa_{dc,v} - \kappa_{dc,\mu} + \Delta\beta - \frac{d\phi(z)}{dz}\right].$$

The difference between reflection as in contradirectional coupling and codirectional mode coupling is immediately apparent according to Eqs. (4.2.14) and (4.4.12). While the reflected signal continues to increase with increasing αL, the forward-coupled mode *recouples* to the input mode at $\alpha L > \pi/2$. Therefore, a codirectional coupler requires careful fabrication for maximum coupling.

Figure 4.9 demonstrates the optimum coupling to the crossed state with $\kappa_{ac}L = \pi/2$ (curve A) as the coupling length doubles, the transmission band becomes narrower (C), while B shows the situation of $\kappa_{ac}L = \pi$, when the light is coupled back to the input mode.

4.5 Polarization couplers: Rocking filters

Equations (4.4.9) and (4.4.10) also govern coupling of modes with orthogonal polarization. An additional subscript is used to distinguish between the laboratory frame polarizations. However, there are differences in the detail of the coupling mechanism. In order to couple two orthogonally polarized modes, the perturbation must break the symmetry of the waveguide. This requires a source term, which can excite the coupled mode. In perfectly circular fibers, any perturbation can change the state of the

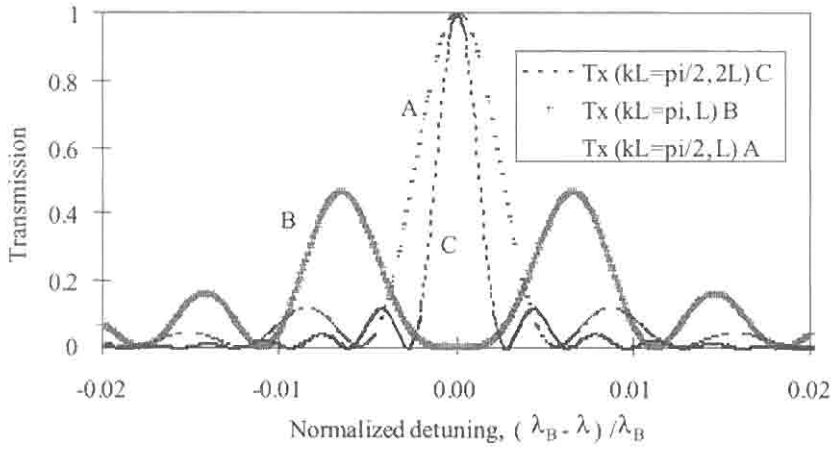

Figure 4.9: Cross-coupled transmission for codirectional coupling. The data shown is for coupling constants of $\pi/2$ with a grating length of L (curve A) and length $2L$ (curve C). The bandwidth is halved for the longer grating. Also shown is data for $\kappa L = \pi$ and grating length L (curve B). Note that the grating overcouples at zero detuning. The transmission spectra of LPGs are identical to that shown above for each of the cladding modes to which the guided mode couples.

output polarization. Nondegenerate orthogonally polarized modes can only exist in birefringent fibers and so require a periodic perturbation equal to the beat length.

Generically, the polarization coupler behaves in a similar way to the intermodal coupler, except that the coupling is between the two eigenpolarization states of the fiber rather than two different order modes. As a result, gratings that have a uniform refractive index modulation across the core are used rather than blazed (or tilted) gratings. Coupling between two dissimilar order modes occurs when symmetry is broken by slanting the grating in the direction of propagation; for coupling between the eigenpolarization states of the same order, symmetry is broken by orienting the grating at 45° to the polarization axes of the fiber. "Slanting" the grating azimuthally at an angle of 45° to the birefringent axes "rocks" the birefringence [34] of the fiber backward and forward, with a period equal to the beat length,

$$\frac{2\pi}{L_b} = \beta_x - \beta_y, \tag{4.5.1}$$

where L_b is the beat length, so that the rocking period Λ_r is

$$\Lambda_r = \frac{L_b}{N}. \tag{4.5.2}$$

N is the order of the grating, and the detuning parameter is

$$\Delta\beta = \beta_x - \beta_y - \frac{2N\pi}{\Lambda_r}. \tag{4.5.3}$$

We assume that the dielectric constants of the principal axes are ε_x and ε_y. A UV beam incident at an angle θ degrees to the x-axis and orthogonal to the propagation direction induces a new set of orthogonal birefringent axes with a change $\Delta\varepsilon_{x'}$ and $\Delta\varepsilon_{y'}$ in the dielectric constants. Figure 4.10 shows the incident UV beam on the cross-section of the fiber. The major and minor axes of the ellipse are the birefringent axes of the fiber. The beam is incident at an angle θ. As a result, the birefringence changes locally, inducing a rotation in the birefringent axes of the fiber. The rotation angle ϕ is related to the change in the birefringence as [35]

$$\tan 2\phi = \frac{\delta\Delta\varepsilon \sin 2\theta}{\Delta\varepsilon + \delta\Delta\varepsilon \cos 2\theta}, \tag{4.5.4}$$

where $\delta\Delta\varepsilon = \Delta\varepsilon_{x'} - \Delta\varepsilon_{y'}$ and $\Delta\varepsilon = \varepsilon_x - \varepsilon_y$. For the case when the induced birefringence is much less than the intrinsic birefringence, then the rotation angle ϕ is small, and it follows that

$$2\phi = \frac{\delta\Delta\varepsilon}{\Delta\varepsilon} \sin 2\theta. \tag{4.5.5}$$

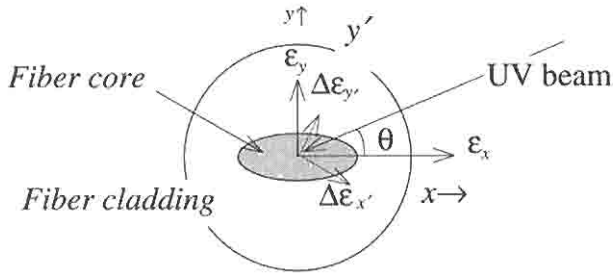

Figure 4.10: Birefringence induced by the incident UV beam in a birefringent fiber for the formation of a rocking filter.

Remembering that $\delta\Delta\varepsilon/\Delta\varepsilon = 2n_{av}(\delta\Delta n')/(2n_{av}\Delta n)$, with $\delta\Delta n' = \Delta n_{x'} - \Delta n_{y'}$,

$$\phi = \frac{1}{2}\frac{\Delta n'}{B}\sin 2\theta, \tag{4.5.6}$$

where B is the difference in the refractive index of the principle axes.

For the special case of $\theta = \pi/4$, Eq. (4.5.6) simplifies to $\phi = \delta\Delta n'/(2B)$. A rotation that changes sign over one beat length implies a change in the rotation of 2ϕ radians per beat length so that the coupling constant, κ_{ac},

$$\kappa_{ac}L_b = 2\phi = \frac{\delta\Delta n'}{B}, \tag{4.5.7}$$

and remembering that $B = \lambda/L_b$ leads to

$$\kappa_{ac} = \frac{\delta\Delta n'}{\lambda}, \tag{4.5.8}$$

where λ is the resonance wavelength. The coupler length L_r is given by the distance at which the input polarization is rotated by $\pi/2$, from which it follows that

$$\kappa_{ac}L_r = \frac{\pi}{2}. \tag{4.5.9}$$

Substituting Eq. (4.5.8) into Eq. (4.5.9), we get the rotation length for 100% polarization conversion as

$$L_r = \frac{\pi\lambda}{2\delta\Delta n'}. \tag{4.5.10}$$

In order to calculate the bandwidth between the first zeroes of the transmission spectrum, we note the argument of Eq. (4.4.12), $\alpha L_r = \pm\pi$, which leads to

$$2\frac{\Delta\lambda}{\lambda} = 2\frac{\pi L_b}{L_r}. \tag{4.5.11}$$

Using typical figures for the reported changes in the birefringence [36,37,35,31], at a wavelength of 1550 nm, we find that the rocking filter has a length of ~0.5 m. Note that the coupler length is only dependent on the wavelength of operation and the induced birefringence, but not

the *intrinsic* birefringence of the fiber. If however, the "duty cycle" of the UV-exposed region is varied so that less than half of a beat length is exposed per beat length, then the effective rocking angle per beat length will be reduced, as with the change in θ.

4.6 Properties of uniform Bragg gratings

Quantities of interest are the bandwidth, $\Delta\lambda$, reflectivity, transmissivity, the variation in the phase ϕ, and the grating dispersion D as a function of detuning.

For the purpose of illustration, Fig. 4.11 shows the reflection spectrum of two Bragg gratings with different coupling constants $\kappa_{ac}L$ of 2 and 8 calculated from Eq. (4.3.16). Note that the central peak is bounded on either side by a number of subpeaks. This feature is characteristic of a uniform-period grating of finite length, with a constant fringe visibility. The abrupt start and end to the grating is responsible for the side structure. In the weak grating limit ($R < 0.2$), the Fourier transform of the variation in the index modulation results in the reflection spectrum [5].

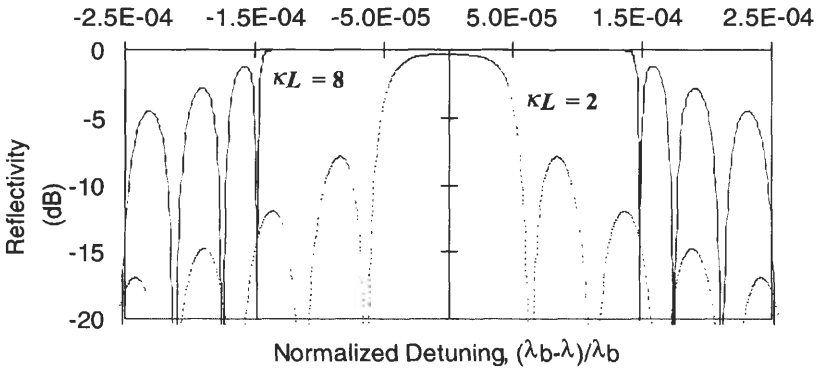

Figure 4.11: Reflectivity of two gratings with coupling constants $\kappa_{ac}L$ of 2 and 8, as a function of normalized detuning. Note that for the weaker reflection grating ($\kappa_{ac}L = 2$, dashed curve), the bandwidth to the first zeroes (between the main reflection peak and the next subpeaks) is much narrower than for the stronger grating ($\kappa_{ac}L = 8$, continuous curve). The side-mode structure increases rapidly for stronger gratings.

Thus, a uniform period and index-modulation grating ("top hat") will produce side lobes. However, for stronger gratings, a Fourier transform for the fundamental component of the refractive index modulation alone is no longer appropriate and gives rise to increasing errors.

For the uniform grating, $d\phi/dz = 0$, the peak reflectivity occurs at a wavelength at which $\delta = 0$ [and therefore, $\alpha = \kappa_{ac}$], and Eq. (4.3.16) leads to

$$\kappa_{dc} + \frac{\Delta\beta}{2} = 0. \tag{4.6.1}$$

At the phase matching wavelength, the reflectivity reduces to

$$|\rho|^2 = \tanh^2(\kappa_{ac}L). \tag{4.6.2}$$

For identical forward- and counterpropagating modes, it is simple to show by using the orthogonality relationship of Eq. (4.1.15) in Eqs. (4.3.5) and (4.3.6) that

$$\kappa_{dc} = \frac{4\pi\eta\overline{\Delta n}}{\lambda}, \tag{4.6.3}$$

where the overlap integral $\eta \approx 1$ for identical modes, and it therefore follows that the peak of the Bragg reflection is at

$$\lambda_{\max} = \lambda_B\left(1 + \frac{\eta\overline{\Delta n}}{n}\right). \tag{4.6.4}$$

The Bragg wavelength λ_B is defined at the phase-matching point $\Delta\beta = 0$ for the general case of dissimilar modes,

$$\frac{2\pi}{\Lambda} = \frac{2\pi n_{eff,v}}{\lambda} + \frac{2\pi n_{eff,\mu}}{\lambda}, \tag{4.6.5}$$

with the result

$$\Lambda = \frac{\lambda}{n_{eff,v} + n_{eff,\mu}}. \tag{4.6.6}$$

For identical forward- and counterpropagating modes or nearly identical mode indexes, Eq. (4.6.6) reduces to

$$\Lambda = \frac{\lambda_{Bragg}}{2n_{eff}}. \tag{4.6.7}$$

The reason why the reflection peak is at a longer wavelength than the Bragg wavelength is because the average refractive mode index $\overline{\Delta n}$ continuously increases with a positive refractive index modulation.

For nonidentical modes, the integral in Eq. (4.3.5) has to be integrated numerically. However, the integral is simply a weighting factor, $0 < \eta < 1$, dependent on the mode and refractive index profiles. It is for this reason that η has been introduced in Eq. (4.6.3), normalized to unity for identical modes.

There are several definitions of bandwidth. However, the most easily identifiable one is bandwidth between the first minima on either side of the main reflection peak (with reference to Fig. 4.11). This may be calculated by equating the argument αL in Eq. (4.3.11) to π,

$$\alpha L = \sqrt{\kappa_{ac}^2 - \delta^2} L = i\pi. \tag{4.6.8}$$

Therefore,

$$(\kappa_{ac}^2 - \delta^2)L = -\pi^2, \tag{4.6.9}$$

which, after rearranging, becomes

$$\delta = \frac{1}{L}\sqrt{\kappa_{ac}^2 L^2 + \pi^2}. \tag{4.6.10}$$

From Eq. (4.3.12), assuming $\kappa_{dc} = 0$ and $d\phi/dz = 0$ (no chirp in the grating), we get

$$\delta = \frac{\Delta\beta}{2}, \tag{4.6.11}$$

so that the detuning from the peak to the first zero is

$$\Delta\beta L = 2\sqrt{\kappa_{ac}^2 L^2 + \pi^2}. \tag{4.6.12}$$

For identical modes, $\mu = v$, using Eq. (4.3.4) we get,

$$\Delta\beta = \frac{4\pi n_{eff}(\lambda_B - \lambda)}{\lambda\lambda_B} \approx \frac{4\pi n_{eff}\Delta\lambda}{\lambda^2}, \tag{4.6.13}$$

where the bandwidth from the peak to the first zero is $\Delta\lambda$. Combining Eqs. (4.16.12) and (4.6.13), and noting that the bandwidth between the

first zeroes is twice the bandwidth between the peak and the first zero, leads to

$$2\Delta\lambda = \frac{\lambda^2}{\pi n_{eff} L}\sqrt{(\kappa_{ac}L)^2 + \pi^2}. \tag{4.6.14}$$

From Eq. (4.6.14) it follows that if $(\kappa_{ac}L)^2 \ll \pi^2$, then the bandwidth is an inverse function of the grating length as

$$2\Delta\lambda \approx \frac{\lambda^2}{n_{eff}L}, \tag{4.6.15}$$

while if the reverse is true, $(\kappa_{ac}L)^2 \gg \pi^2$, then the bandwidth is independent of the length of the grating and is proportional to the ac coupling constant,

$$2\Delta\lambda \approx \frac{\lambda^2\kappa_{ac}}{\pi n_{eff}}, \tag{4.6.16}$$

so that increasing κ_{ac} increases the bandwidth.

Zeroes in the reflection spectrum of the grating can be evaluated by using a similar analysis, to occur at

$$\alpha L = iM\pi, \qquad M = 1,2,3,\ldots \tag{4.6.17}$$

from which the corresponding detuning follows,

$$\Delta\lambda = \pm\frac{\lambda^2}{\pi n_{eff}}\sqrt{\kappa_{ac}\kappa_{ac}^* + \left(\frac{M\pi}{L}\right)^2}. \tag{4.6.18}$$

It is also useful to note the approximate position of the side-lobe peaks at

$$\alpha L = i\left(M + \frac{1}{2}\right)\pi, \qquad M = 1,2,3,\ldots, \tag{4.6.19}$$

which leads to

$$\delta\lambda_{sl} = \pm\frac{\lambda^2}{\pi n_{eff}}\sqrt{\kappa_{ac}\kappa_{ac}^* + \left[\frac{\left(M + \frac{1}{2}\right)\pi}{L}\right]^2}. \tag{4.6.20}$$

4.6.1 Phase and group delay of uniform period gratings

Figure 4.12 shows the phase response of the two gratings in Fig. 4.11, as a function of detuning, in units of radians per meter of grating. In the

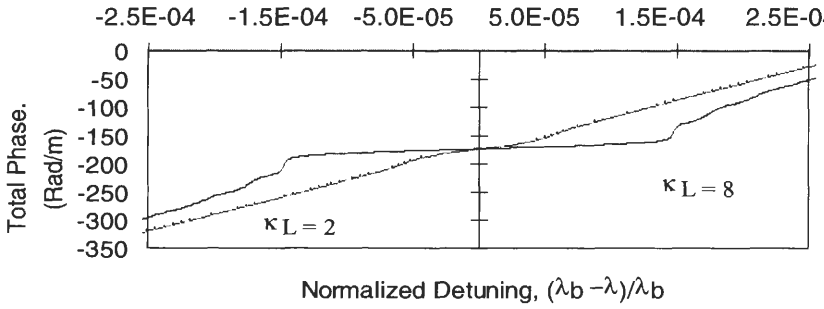

Figure 4.12: Total phase change in reflection from a uniform-period grating as a function of detuning for $\kappa_{ac}L = 2$ (dashed line) and $\kappa_{ac}L = 8$ (solid line). The stronger gratings behaves as a point reflector, since the phase change on reflection is large and almost constant for the same bandwidth when compared with the weaker grating.

region outside of the band stop of the grating, the phase of the light changes according to the unperturbed material refractive index. Into the band stop, the phase velocity slows down with increasing strength of the grating.

In Fig. 4.13 is the group delay of the same grating as in Fig. 4.12 in units of psec/m. This group delay per meter is

$$\frac{\tau}{L_g} = -\frac{1}{L_g}\frac{\lambda^2}{2\pi c}\frac{d\phi}{d\lambda}. \tag{4.6.21}$$

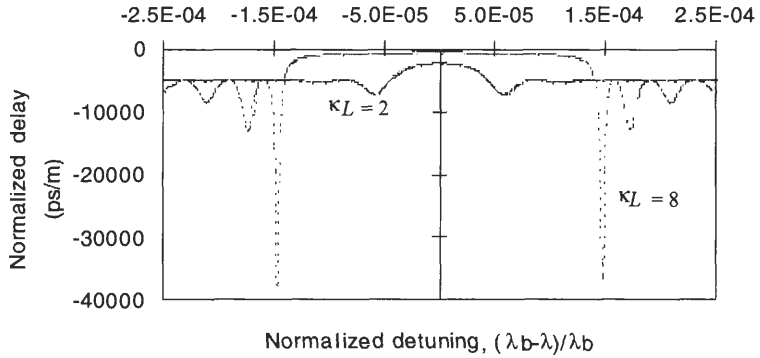

Figure 4.13: The normalized delay of a uniform period grating as a function of normalized de-tuning. For the larger coupling constant, the group delay in the center of the band is constant, while at the edges it increases rapidly, but is confined to a small spectrum.

Close to the edge of the band stop, strong dispersion can be seen with increasing strength of the grating. However, this dispersion is limited to a small bandwidth. At the center of the band, the group delay is a minimum and is approximately $1/(2\kappa_{ac}L_g)$ for gratings with a reflectivity close to 100%.

4.7 Radiation mode couplers

4.7.1 Counterpropagating radiation mode coupler: The side-tap grating

These gratings couple from a forward-propagating guided mode to a backward-propagating cladding mode, or a continuum of radiation modes. In this section, a new and simple theory is presented to gain a physical insight into the scattering of a guided mode into the counterpropagating radiation modes. The theory for radiation mode coupling has been presented elsewhere by various authors: Marcuse [2], Erdogan and Sipe [38], Mizrahi and Sipe [39], Erdogan [40], and Morey and Love [41]. These articles explain the phenomenon of radiation mode coupling using coupled mode theory and have successfully described the short-wavelength radiation loss from unblazed gratings [39], as well as the fine detailed spectrum observed under cladding mode resonance in tilted gratings [38,40]. Surprisingly little work has been reported on the application of these gratings. The term "side-tap" is appropriate for such gratings since the radiation is tapped from the side of the fiber, as happens when bending a fiber. A particular difference from bending is the reduced bandwidth and wavelength selectivity of the loss induced by such blazed gratings. Important properties of blazed gratings are their stability and low intrinsic temperature sensitivity, which may be reduced even further by appropriate design of fiber or coating [42,43]. Although the reflectivity into the counterpropagating guided mode is not generally zero, for acceptable performance in practical applications, it can be made very low by careful design of the filter.

The intention of this section is to provide a physical insight into the functioning of blazed gratings with the purpose of intentionally designing filters, which predominantly exhibit only radiation loss. The potential applications are numerous, e.g., in-fiber noninvasive taps, spectrum analyzers [44], and gain flattening of optical amplifiers using a single blazed grating [45] and multiple blazed gratings [46] and mode converters [47].

Figure 4.14 shows a schematic of the blazed "side-tap" grating written in the core of an optical fiber. The guided mode shown on the LHS of the figure can couple to the radiation field or to a "supermode" of a composite waveguide formed by the cladding and air interface. These are shown as a field distribution leaving the core at an angle and as a mode of the waveguide formed by the cladding, respectively. While the radiated fields form a continuum if unbounded [see Eq. (4.2.5)], they evolve into the bound supermodes of the composite waveguide in the presence of a cladding. The power in the radiated field and the radiated bound mode may grow provided the overlap of the interacting fields and the transverse distribution of the "source" (refractive index perturbation) is nonzero (see Section 4.2.3). The exchange of energy between the core mode and the radiated bound supermode is determined by the prevailing phase-matching conditions discussed in Section 4.2.5 and is solely a *coherent* interaction; the coupling to the unbound continuum of the radiation field is, however, only partly governed by this requirement. Physically, the radiated field exiting from the fiber core at a nonzero angle is spread away so that the distance over which it is coupled to the driving field is limited. This may be understood by the following: The driving mode field amplitude, which is assumed to be spatially constant, overlaps with a radiation field that is spreading

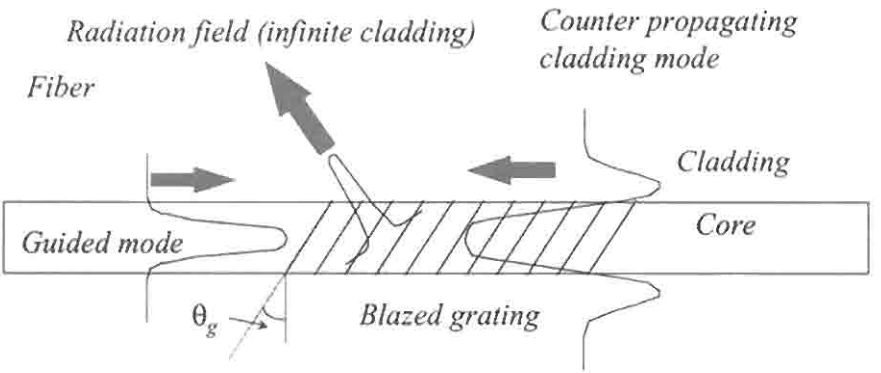

Bragg phase-matching condition:

$$2\pi n_{eff}/\lambda + 2\pi n_{cl}/\lambda = 2\pi N \cos\theta_g/\Lambda_g$$

Figure 4.14: Schematic of counter-propagating radiation field and bound cladding mode coupling from a forward propagating guided mode with a blazed grating.

rapidly away from the guided mode. For a coherent interaction, the fields must overlap over a distance with the correct phases. While the phases may remain synchronous, the radiated field spreads away, reducing the overlap as a function of propagation distance. With the cladding present, the field forms a mode, which propagates in the cladding and is then strongly coupled to the guided mode. This type of coupling is similar to simple Bragg reflection to discrete modes of the cladding. The transmission spectrum of a grating, which demonstrates this effect, is shown in Fig. 4.15. In this case, coupling is to modes of the HE_{1n} order (LP_{0n}), with a blaze angle close to zero. The cladding resonances are clearly visible.

Also shown in Fig. 4.14 is the equation describing the phase-matching condition for coupling to counterpropagating radiation at zero angles. This radiated field is at the *longest* wavelength at which coupling to the radiation field is possible, and only to zero-order modes, i.e., LP_{0m}. Note that the period of the grating, Λ_g, is dependent on the *sum* of the propagation constants of the guided driving mode and the radiated field (see also Fig. 4.5). As a consequence, any change in the cladding mode index only weakly affects the *radiated* field, but does change the coherent coupling to the supermodes. For a radiation mode tap, it is useful to consider the coupling to the unbounded radiation field. Another point to note is the angle of the *radiated* field, which is always slightly *more* than twice the tilt angle of the grating, apparent from Fig. 4.6. However, this angle is reduced when the overlap to the radiated field is taken into account.

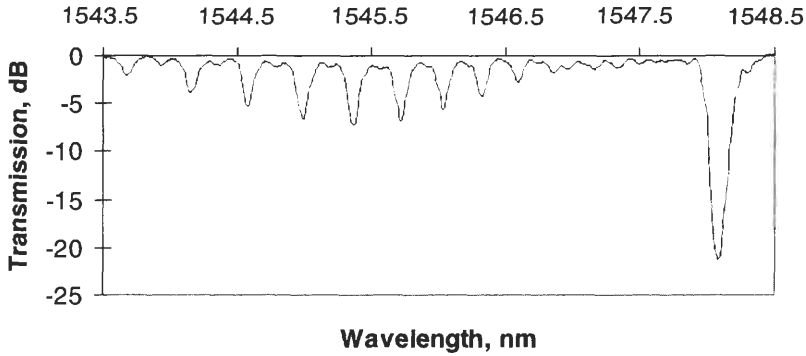

Figure 4.15: Cladding mode resonance in untilted gratings. On the right is the $LP_{01} \rightarrow LP_{01}$ guided mode reflection, while the others are to the LP_{0n} cladding modes (n = 2 to 10). See cover picture for example of cladding modes.

In Fig. 4.16 is shown the practical case of side illumination of optical fiber with UV irradiation. The absorption in the fiber causes the refractive index to be highly asymmetric [48]. This asymmetry is like a blaze, since one side of a propagating mode experiences more of a perturbation than the other. Consequently, such an asymmetric grating breaks the symmetry to allow coupling to odd, $l = 1$, order modes i.e., LP_{1m}. This is also true of blazed gratings, which are uniform across the core with the same effect on the guided mode.

A few points should be noted about scattering from a blazed grating. It is known that scattering of light from bulk blazed gratings [49] is directional and the phase-matching conditions easily derived for scattering, in thin and thick holograms [32]. The general approach taken in the next section is similar in so far as the scattering element is considered nonlocal and all the scattering events summed to arrive at the final unbounded coupling to the radiation field.

Theoretical model for coupling to the radiation field

The STG is a useful device for filter applications when used to couple the guided mode to the radiation field, rather than a mode. It forms a narrow band stop, whose spectral width is not dependent on the length of the grating in the same way as a Bragg grating. The wavelength and bandwidth is easily adjusted by choice of fiber, and the properties of the grating are as robust as those of the Bragg grating in terms of temperature

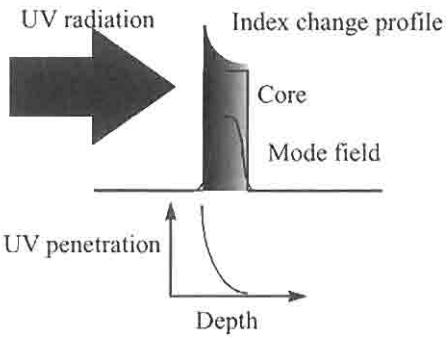

Figure 4.16: Effect of side illumination of a fiber core with UV radiation, giving rise to a tilted grating

sensitivity and strain. This allows the design of filters that depend only on the properties of the guidance of the core.

The side-tap grating is modeled as a periodic collection of uniform inclined planes of perturbed refractive index across the core. The mode fields are defined by the wave-guiding parameters, but it is assumed for the grating that the boundary of the cladding is absent; i.e., the grating is written in an infinite medium, although it is itself confined to the core. A consequence of this approximation is that refraction at the core–cladding boundary may be ignored, but can be accounted for later, to form modes. The assumption allows the design of *filters* in the same way in which the Bragg grating can be modified. The physical phenomenon of scattering is treated as Fraunhofer diffraction, with the amplitude of the scattering obeying the laws of conservation of energy. Figure 4.17 shows the schematic of the blazed grating. The mathematical description that follows shows that this type of a grating is equivalent to an infinite sum of small gratings written perpendicular to the axis of the fiber, but has an azimuthal dependence that makes it possible to couple to a particular set of radiation modes. In other words, the z-dependence of the grating due to the inclination of the planes is translated into a transverse variation in refractive index modulation, with the result that it immediately connects with the idea of the mode overlap integral, while separating the

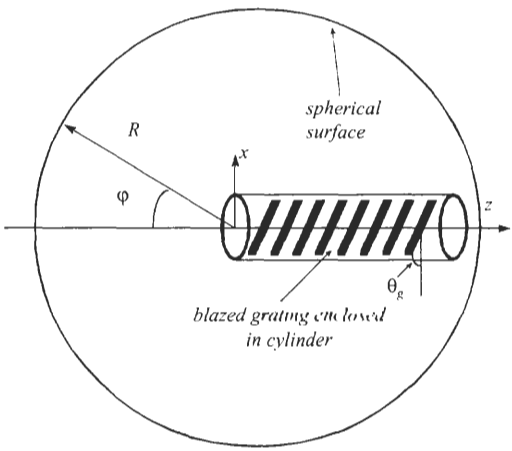

Figure 4.17: Scattering of power from a blazed grating entirely embedded in a cylinder.

issue of phase matching. The grating inclination angle is θ_g with respect to the transverse axis, x, in the x–z plane. The refractive index perturbation of the grating, $\delta n(x,y,x)$, simply described as a product of a grating of infinite extent and a "window" function W_{grating}, which takes account of the transverse variation in the amplitude of the grating, as

$$\delta n(x,y,z) = 2n\Delta n W_{grating}(r)\cos\left\{\left(\frac{2\pi N}{\Lambda_g}\right)(x\sin\theta_g - z\cos\theta_g)\right\}. \quad (4.7.1)$$

Converting Eq. (4.7.1) into cylindrical coordinates leads to the grating function

$$\delta n(r,\phi,z) = W_{grat}(r)2n\Delta n \times \left\{\begin{array}{l}\cos\left(\dfrac{2\pi Nz\cos\theta_g}{\Lambda_g}\right)\left(J_0(\gamma r) + 2\sum\limits_{m=1}^{\infty}(-1)^m J_{2m}(\gamma r)\cos(2m\phi)\right) \\ + \sin\left(\dfrac{2\pi Nz\cos\theta_g}{\Lambda_g}\right)2\sum\limits_{m=1}^{\infty}(-1)^m J_{2m+1}(\gamma r)\cos((2m+1)\phi)\end{array}\right\}, \quad (4.7.2)$$

where $\gamma = 2\pi N \sin\theta_g/\Lambda_g$. Equation (4.7.2) requires explanation, since it has real physical significance for the process of mode coupling. Each term on the RHS is responsible for coupling from the guided mode (here the fundamental) to a different set of radiation modes. Terms in the Bessel function J_m couple to modes with an azimuthal variation of $\cos(m\phi)$, i.e., to even-order radiation modes, while the J_0 terms leads to the guided mode back-reflection from the grating. Similarly, odd modes couple via the remaining set of terms within the curly brackets. Immediately obvious is the dependence of the back-reflection on γ, which periodically reduces the reflection to zero as a function of θ_g.

We refer to Fig. 4.17, in which a grating blazed at angle θ_g is shown entirely within a cylinder. The scattered total power at a wavelength λ impinging on a surface of radius R can be shown to be due to radiation from a current dipole situated at the grating [3] as

$$P_{scatter}(\lambda) = \int_{\phi=0}^{2\pi}\int_{\varphi=0}^{\pi} R^2 S_{scatter}(R,\phi,\varphi,\lambda)\sin\varphi\, d\varphi\, d\phi, \quad (4.7.3)$$

where ϕ is the angle between projection of the radius vector R and the x-axis. The Poynting vector is

$$S_{scatter}(R,\phi,\varphi,\lambda) = \frac{1}{2} n_{cl}\sqrt{\frac{\varepsilon_0}{\mu_0}}\,|E_{scatter}(R,\phi,\varphi,\lambda)|^2. \quad (4.7.4)$$

By integrating the scattered contributions from each part of the grating separated by δR, the scattered field, $E(R,\phi,\varphi,\lambda)$ may be derived by neglecting the angular dependence on φ and ϕ and follows as

$$E_{scatter}(R,\phi,\varphi,\lambda) = \frac{k^2 e^{i\beta_{clad}R}}{4\pi R} \iiint e^{i\beta_{clad}\delta R}\delta\varepsilon(x,y,z)E_{incident}(x,y,z)dxdydz. \tag{4.7.5}$$

The above result is consistent with Fraunhofer diffraction theory [3], and we note that it is in the same form as scattering due to the polarization response of a material. We note that far away from the grating,

$$\delta R \approx -x \cos\phi \sin\varphi - y \sin\phi \sin\varphi + z \cos\varphi. \tag{4.7.6}$$

The result in Eq. (4.7.5) neglects secondary scattering, so that it is implicitly assumed that the incident radiation is the primary cause for the radiation. This may be justified for STGs, since it is the aim of the exercise to consider radiation loss to the exclusion of reflection by proper choice of blaze angle, and because the radiation field is only weakly bound to the core.

We are now in a position to calculate the propagation loss of the incident radiation. The power scattered as a function of length of the grating described in Eq. (4.7.1) and into even azimuthal mode orders can be described as

$$P_{scatter}(z) = \alpha' P_{incident}(z)\cos^2(2\pi z \cos\theta_g/\Lambda_g)dz. \tag{4.7.7}$$

α' is a loss coefficient, which is dependent on the wavelength, the transverse profile of the grating, and the incident field and is equivalent to the overlap integral of Eq. (4.3.6). The incident field therefore decays as

$$P_{incident}(z) = P_{incident}(0) \times \exp\left[-\frac{\alpha' z}{2}\left\{1 + \frac{\Lambda_g}{4\pi z \cos\theta_g}\sin\left(\frac{4\pi z \cos\theta_g}{\Lambda_g}\right)\right\}\right]. \tag{4.7.8}$$

The contribution due to the oscillating term within the exponent becomes insignificant for large z, and the power decays as

$$P_{incident}(z) \approx P_{incident}(0)e^{-(\alpha' z/2)}. \tag{4.7.9}$$

From Eq. (4.7.9) follows the approximate decay of the incident electric field,

$$E_{incident}(x,y,z) \approx E_0(x,y)e^{(i\beta_f - \alpha)z}, \tag{4.7.10}$$

where $\alpha = \alpha'/4$ is a function of wavelength only, and β_f is the propagation constant for the incident fundamental mode. The longitudinal component of the guided mode field is small and has been neglected in Eq. (4.7.10).

The physical analogy of the STG as a distributed antenna is particularly useful, equivalent to an infinite sum of mirrors, each contributing to the light scattered from the fiber core. For small lengths, we have to include the oscillating term in quadrature in Eq. (4.7.8), but with $z \gg \Lambda_g$, the electric field for the fundamental mode decays approximately as it would for constant attenuation per unit length. The attenuation constant depends on wavelength and the transverse distribution of the grating and the incident field, but not on z. This approximate result suggests that the filter loss spectrum should be independent of the length of the grating, which is indeed the case.

To calculate the scattered power and the spectrum of the radiation, we use Eq. (4.7.6) in Eq. (4.7.5) and include the grating function $W_{grating}$ to arrive at

$$E_{scatter}(R,\phi,\varphi) = \frac{\Gamma}{R}\iint W_{grating}(x,y)E_0(x,y)e^{i\beta_{clad}(-x\cos\phi\sin\varphi - y\sin\phi\sin\varphi)} \times I_L(x,L_g)dxdy, \tag{4.7.11}$$

where L_g is the length of the fiber grating, the constant Γ is given

$$\Gamma = \frac{\beta_{clad}\Delta n e^{i\beta_{clad}R}}{\lambda}, \tag{4.7.12}$$

and $I_L(x, L_g)$ is obtained by integration with respect to z,

$$I_L(x,L_g) = \frac{e^{i\gamma x}}{2}\frac{e^{(i\Delta\beta_b-\alpha)L_g}-1}{i\Delta\beta_b-\alpha} + \frac{e^{-i\gamma x}}{2}\frac{e^{(i\gamma\beta_f-\alpha)L_g}-1}{i\Delta\beta_f-\alpha}, \tag{4.7.13}$$

where γ was defined in (4.7.2), and $\Delta\beta_f$ and $\Delta\beta_b$ are the forward and backward phase mismatch factors,

$$\begin{aligned}\Delta\beta_b &= \beta_f + \beta_{clad}\cos\varphi - \frac{2\pi\cos\theta_g}{\Lambda_g}\\ \Delta\beta_f &= \beta_f + \beta_{clad}\cos\varphi + \frac{2\pi\cos\theta_g}{\Lambda_g},\end{aligned} \tag{4.7.14}$$

where $\beta_{clad} = 2\pi n_{clad}/\lambda$, and the signs are consistent with the measurement of the angle, φ. The forward scattering process can easily be included

if necessary but is ignored for now. For the backward phase-matching condition, the radiation angle at resonance, φ_L, is given by the $\Delta\beta_f = 0$, as has been seen in Section 4.2.5, so that

$$\beta_f + \beta_{clad} \cos \varphi_L = 2\pi \cos \theta_g / \Lambda_g. \tag{4.7.15}$$

The last result is a longitudinal phase-matching condition, which is exactly the same as normal Bragg reflection. It requires that the path difference between light scattered from points that are both on a line parallel to the optical axis of the fiber, and on adjacent fringes of the grating, should be exactly λ (Fig. 4.18).

Ignoring the forward scatter, we find the scattered counterpropagating power from Eqs. (4.7.11), (4.7.3), and (4.7.4) as

$$P_{scatter}(\lambda) = \frac{1}{2} n_{clad} \sqrt{\frac{\varepsilon_0}{\mu_0}} \Gamma^* \Gamma e^{-\alpha L} \tag{4.7.16}$$

$$\times \int_{\phi=0}^{2\pi} \int_{\phi=0}^{\pi} |I_{core}(\gamma,\varphi,\phi)|^2 \frac{\sinh^2(\alpha L/2) + \sin^2(\Delta\beta_b L/2)}{\Delta\beta_b^2 + \alpha^2} \sin \varphi \, d\varphi \, d\phi,$$

where the overlap integral over the profile of the grating, which we refer to as the transverse phase-matching condition, is

$$I_{core}(\gamma,\varphi,\phi) \tag{4.7.17}$$

$$= \iint W_{grating}(x,y) E_0(x,y) e^{i[x(\gamma - \beta_{clad} \cos \phi \sin \varphi) - \beta_{clad} y \sin \phi \sin \varphi]} dx dy.$$

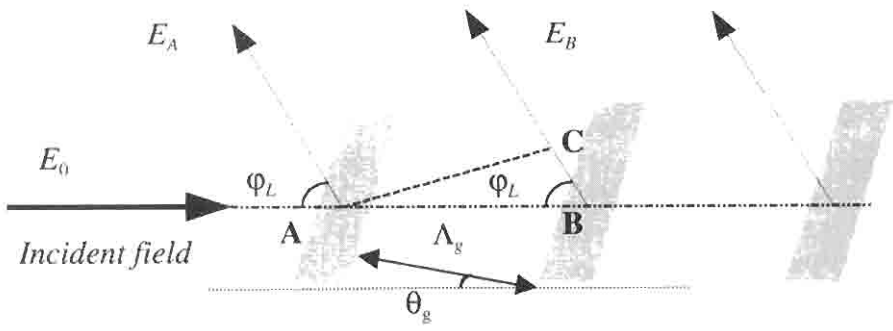

Figure 4.18: Scattered light from the fringe planes of the gratings adds up in phase when the resonance condition for longitudinal phase matching is met. AB + BC = $N\lambda$, at resonance.

In understanding the physics of the scattering, we consider separately the two components of the integral, the transverse phase-matching term (Eq. 4.7.17) and the longitudinal phase-matching (pm) term which depends on the detuning, $\Delta\beta_b$.

In the low-loss regime ($\alpha \ll \Delta\beta_b$), the longitudinal pm term is simply like the Bragg matched reflection condition, but now as a function of φ. For all practical purposes, this term is like a delta function that is only significant at very small angles of radiation ($\varphi \ll 1°$). The integral has a term dependent on $\cos\varphi$, which becomes broader and asymmetric in its angular bandwidth as $\varphi \to 0°$ and which is also inversely dependent on the length of the grating. For typical filter lengths of a few millimeters, we find the angular bandwidth to be ~1°. The asymmetry and broadening at small phase-matching angles have been observed in phase-matched second-harmonic generation with periodic structures [50].

In the high-loss regime, we find that the delta function broadens but has a width similar to that of the low-loss case. We can therefore choose to consider the dependence of the scattered power on the longitudinal phase matching as a very narrow filter at a given angle. Comparison of the longitudinal term with the transverse pm condition of Eq. (4.7.17) shows that the angular dependence of the radiation for the transverse case varies much more slowly and may be approximated to be a constant over the region of the longitudinal bandwidth. Figure 4.19 shows the dependence of the longitudinal and the transverse pm as a comparison for standard fiber and a uniform grating profile, $W_{grating} = 1$. The longitudinal response for a blaze angle of 5° and the transverse response for three blaze angles are shown.

The analytical result for the loss coefficient α has been shown to be [51],

$$\alpha \approx \frac{k^2 a^2 \beta_{clad} \Delta n^2}{32\pi^2} \frac{\int_{\phi=0}^{2\pi} |I_{core}(\gamma, \varphi, \phi)|^2 d\phi}{\int_{r=0}^{\infty} r E_0^2(r) dr}. \tag{4.7.18}$$

By normalizing the radius as $\rho = r/a$ (a is the core radius),

$$\alpha \approx \frac{\pi k^2 a^2 \beta_{clad} \Delta n^2}{4} \frac{I_0^2 + 2\sum_{m=1}^{\infty} I_m^2}{\int_{r=0}^{\infty} \rho E_0^2(\rho) d\rho}, \tag{4.7.19}$$

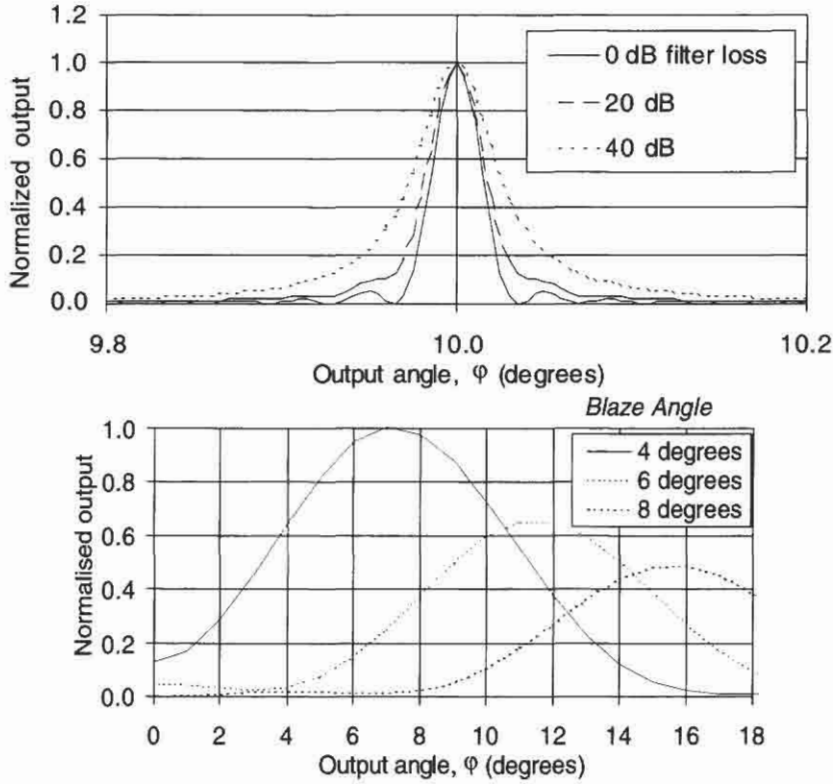

Figure 4.19: (a) shows the longitudinal integral and (b) is the transverse integral for different blaze angles.

and $E_0(\rho)$ is the field distribution of the fundamental mode. The integrals I_0 and I_m are defined as

$$I_0 = \int_{R=0}^{\infty} W_{grat}(\rho)E_0(\rho)J_0(\gamma\rho a)J_0(\xi_L\rho a)\rho d\rho$$
$$I_m = \int_{r=0}^{\infty} W_{grat}(\rho)E_0(\rho)J_m(\gamma\rho a)J_m(\xi_L\rho a)\rho d\rho. \tag{4.7.20}$$

In Eq. (4.7.20), we remind ourselves that γ is the transverse grating momentum that allows the mode to couple out of the core and is a function of the grating period as well as the blaze angle,

$$\gamma = \frac{2\pi \sin \theta_g}{\Lambda_g}. \tag{4.7.21}$$

ξ_L is the transverse momentum of the mode, depending on the output radiation angle of the scattered light, φ_L, at a given wavelength, and is

$$\xi_L = \beta_{clad} \sin \varphi_L. \tag{4.7.22}$$

In Fig. 4.20 is shown the calculated and measured loss spectrum of fibers with nominally the same v-value, but different core radii. The agreement between the measured loss and the calculated loss spectrum is quite good for two fibers. The blaze angle for the grating is 8°. The results also show that the loss spectrum due to scattering into the radiation modes is independent of the fiber length, and, indeed, this has been confirmed by experimental observations [51].

The reflection coupling constant for a tilted grating [38] with an arbitrary profile is

$$\kappa_{ac} \propto \frac{\int_{\rho=0}^{\infty} \rho W_{grating}(\rho) J_0(2\pi a \sin \theta_g \rho/\Lambda) E_0^2(\rho) d\rho}{\int_{\rho=0}^{\infty} \rho E_0^2(\rho) d\rho}. \tag{4.7.23}$$

This integral has been plotted in Fig. 4.21 and shows that zero Bragg reflection into the guided mode occurs at a lower blaze angle if the grating is moved outward from the core. For comparison, the back reflection from two fibers has been shown, one with a grating situated entirely in the cladding and the other with a standard telecommunications fiber core.

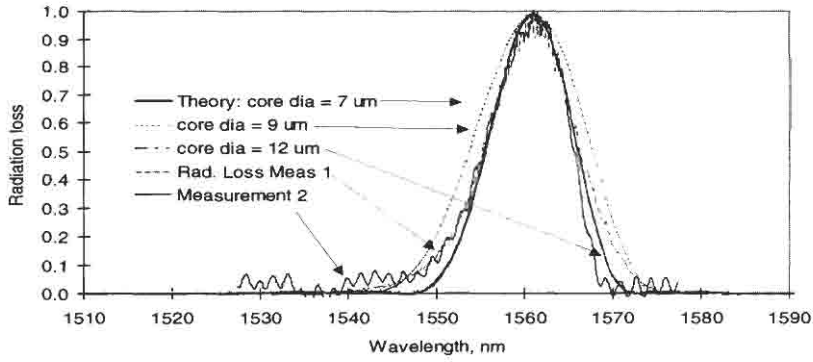

Figure 4.20: Measured radiation loss from large core weakly guiding fibers with radii of 7, 9, and 12 microns and a v-value of 1.9. Two measurements on 12-micron core-diameter fibers are also shown (after Ref. [52]).

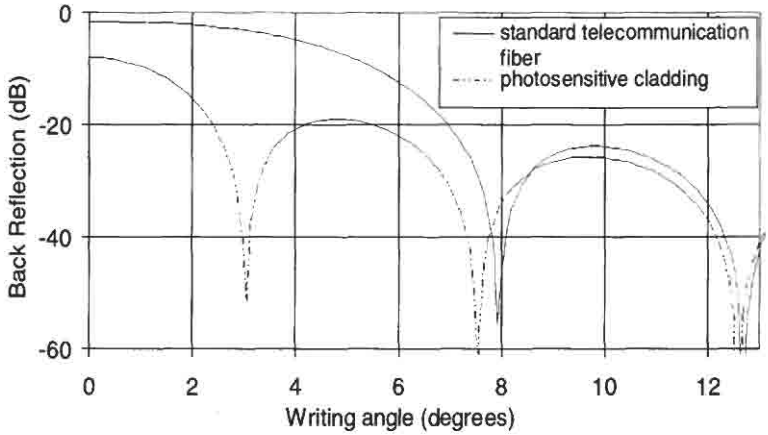

Figure 4.21: Comparison of back reflection from two fibers: both have nominally the same v-values, but one has a photosensitive cladding only (after Ref. [52]).

We note that the first back reflection minimum occurs at ~3° external writing angle for the photosensitive cladding fiber, compared with 8° for the standard fiber. This has an additional benefit of reducing the bandwidth over which radiation loss occurs, as seen from the phase-matching diagram in Section 4.2.5.

In Fig. 4.22 is shown the filter response for coupling to radiation modes for the photosensitive cladding fiber. The benefit of making the cladding photosensitive is clear, since it reduces the bandwidth at the zero reflection writing angle (measured at 3° and calculated for the fiber to be ~3.6°). The core radius of this fiber is 3.4 μm, and the photosensitive cladding extends from a to $4a$.

The agreement between the theoretical and experimentally observed properties of tilted fiber Bragg gratings is extremely good [38] using the complete theory presented by Erdogan [40,38]. In particular, the measured peak visible at 1545 nm in Fig. 4.22 is shown to be due to leaky mode coupling. The polarization dependence of tilted Bragg gratings in fibers with a core radius of ~2.6 μm and a core-to-cladding refractive index difference of 5.5×10^{-3} becomes obvious as the tilt angle exceeds 6.5° [38]. Above this angle, the p-polarization scatters less efficiently than the s-polarization. Below a tilt angle of 6.5°, the radiation loss is predominantly due to coupling to even-azimuthal order radiation modes, giving

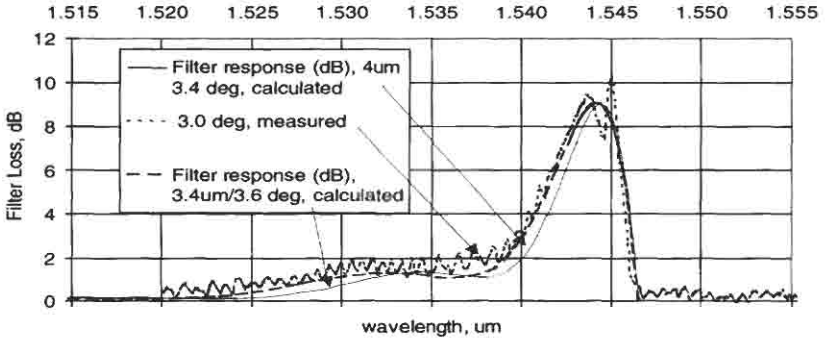

Figure 4.22: The loss spectrum (calculated and measured) for a photosensitive cladding fiber. The ripple in the loss spectra is a measurement artifact (after Ref. [52]).

rise to a sharp narrow-bandwidth peak. Above 6.5°, the coupling is to odd-azimuthal order modes and becomes much broader. By making angles for the back-reflection small (Fig. 4.21), one benefits from both low polarization sensitivity and a narrow-loss spectrum.

In Fig. 4.23 is shown the design diagram for STG filters as a function of the core-to-cladding refractive index difference, assuming an infinite

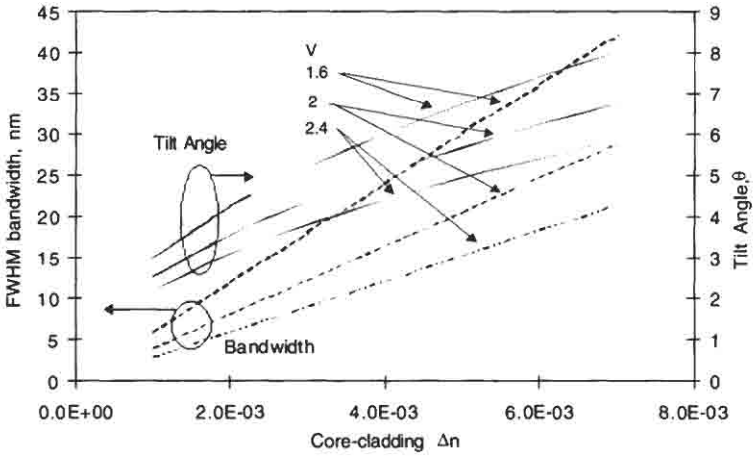

Figure 4.23: The design diagram for tilted STG filters with infinite cladding.

cladding. Two important parameters, the FWHM bandwidth and the tilt angle for zero back reflection into the fundamental mode for step index fibers for different v-values, are shown. The trend is as follows. Small core-cladding index difference and large v-value give the smallest radiation loss bandwidths, as well as the smallest tilt angles and accordingly the lowest polarization sensitivity. The penalty is the increased bend loss sensitivity.

4.7.2 Copropagating radiation mode coupling: Long-period gratings

These gratings couple light from forward-propagating guided modes to the forward-propagating cladding modes (as with an LPG) and the radiation field.

A schematic of the interaction and the phase-matching condition for coupling to forward-propagating radiation modes is shown in Fig. 4.24. The mode-coupling equations for forward coupling are given in Section 4.4 [Eqs. (4.4.11) and (4.4.12)]. The overlap integrals governing the interaction are shown in Eqs. (4.4.14)–(4.4.17) with the appropriate phase-matching terms. This type of coupling is similar to counterpropagating interactions, so far as the overlap of the modes is concerned. However, the power is exchanged between the radiated and guided modes periodically, as shown in Fig. 4.9, so that the filter length governs the bandwidth

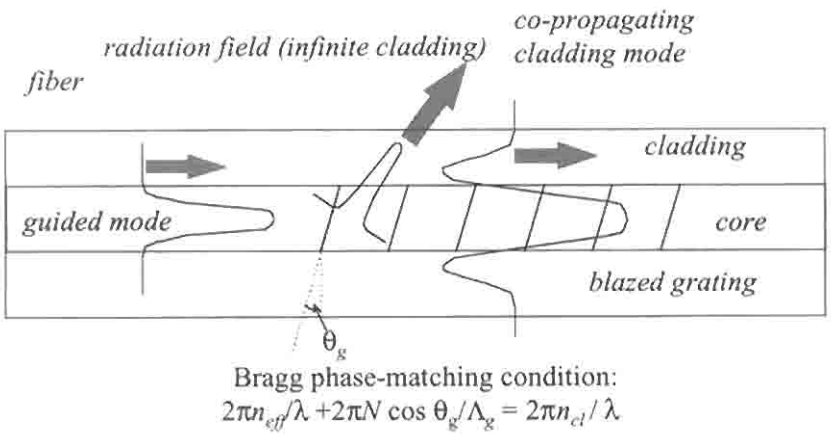

Figure 4.24: Schematic of co-propagating radiation field and bound cladding mode coupling from a forward propagating guided mode with a blazed grating.

of the coupling to the radiation mode (as it does to the individual cladding modes in the counterpropagating direction). The fundamental, LP_{01} guided mode can only couple to the even-order cladding modes of the same order, LP_{0n} [53]. Only if there is an asymmetry in the transverse profile will modes of different order couple. For example, in depressed cladding fibers that support a leaky LP_{11} mode, coupling to the LP_{16} mode is possible because of the very large overlap of the fields in the core [53], almost as large as the $LP_{01} \rightarrow LP_{01}$ modes. For fibers that support only the LP_{01} mode, a tilt in the grating allows coupling to copropagating (and counterpropagating) modes of different order. Erdogan has shown that the coupling constants to the radiation modes of the order v and the core mode (LP_{01}) follow the definitions of Eqs. (4.4.3) and (4.4.4). They are [40]

$$\kappa_{v\rightarrow 01}(z) = \frac{n\omega\varepsilon_0\Delta n(z)}{2}\int_0^{2\pi} d\phi \int_0^a (E_r^{clad}E_r^{core^*} + E_\phi^{clad}E_\phi^{core^*})rdr. \tag{4.7.24}$$

The eigenvalues and the field distributions for the cladding modes may be calculated by field matching at the boundaries as for the core for the low-order LP_{0n} modes, using a procedure similar to the guided core modes of the fiber [54]. Only coupling to the radiation modes with the azimuthal order $l = 1$ ($LP_{l-1,v}$ type) has a nonzero integral. The equations that describe the overlap integral, Eq. (4.7.24) of the modes for a transversely uniform grating are involved and cumbersome [40]. For the $v = 2, 4$ modes, the field in the core is very low, and therefore contributes little to the coupling. However, the field for the odd-numbered v modes has high intensity and these fields dominate the coupling for the lower-order modes. In Fig. 4.25 is shown the calculated coupling constants for a set of 168 cladding modes for a fiber at 1550 nm, normalized to the refractive index modulation, $\Delta n(z)$. The important point is that coupling to the low-even-order modes is weak compared to the odd modes. For $v > 40$, both even and odd order modes have almost identical coupling constants, but remain <20% of the maximum possible for the odd modes. Therefore, for many applications, it is necessary only to take account of a maximum of first 20–30 cladding modes, especially when computing the loss spectrum of an infinite cladding fiber (pure radiation loss).

A major difference between the STG and the LPG is shown in the phase-matching Eq. (4.7.14). We note that the detuning $\Delta\beta_f$ for a LPG is sensitive to the *difference* in the propagation constants of the guided and radiation modes. Any UV-induced change in the core index will result

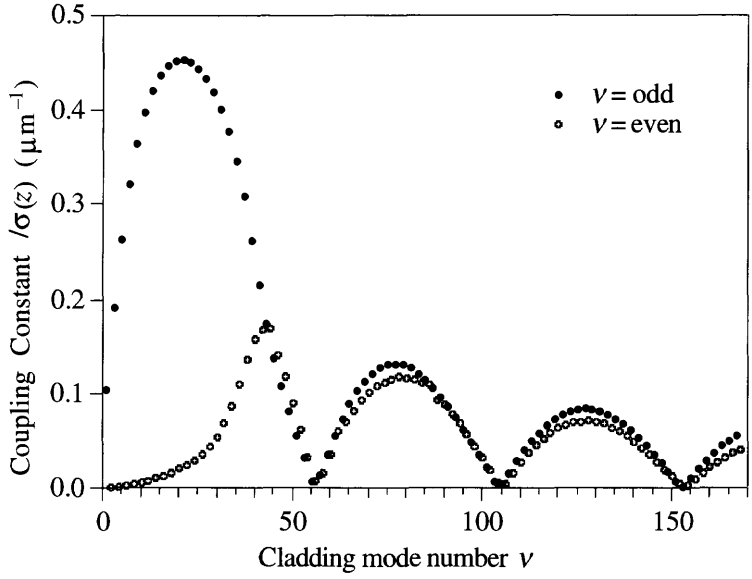

Figure 4.25: The coupling constants for the fundamental guided mode to 168 even- (l = 2) and odd-order cladding modes with azimuthal order 1 (type LP_{0n}) (from: Erdogan T, "Cladding mode resonances in short and long period fiber grating filters," *Opt. Soc. Am. A* ***14***(8), 1765, 1997.).

in a shift in the propagation constants, and thereby strongly affect the resonance wavelength. This aspect does not affect the counterpropagating resonance strongly, since the percentage change in the sum of the propagation constants is small. The change in the resonance condition for the STG in which only the core mode is affected can be calculated as [55]

$$\frac{\delta\lambda_{STG}}{\lambda_{STG}} = \frac{\eta\delta\beta_{UV}}{\beta_{core} + \beta_{clad}} \approx \frac{\eta\delta\beta_{UV}}{2\beta_0}, \tag{4.7.25}$$

whereas the resonance condition for the LPG changes as

$$\frac{\delta\lambda_{LPG}}{\lambda_{LPG}} = \frac{\eta\delta\beta_{UV}}{\beta_{core} - \beta_{clad}} \approx \frac{\eta\delta\beta_{UV}}{\Delta\beta}, \tag{4.7.26}$$

β_0 is the average propagation constant of the core and cladding modes, and $\eta\delta\beta_{UV}$ is the effect of the additional UV-induced detuning over and

above the initial mismatch, $\Delta\beta$ between the modes, and η is the overlap of the field within the core. A comparison between the two leads to

$$\delta\lambda_{LPG} \approx \frac{2n_{core}}{\delta n_{core \to clad}} \delta\lambda_{STG}. \tag{4.7.27}$$

In Eq. (4.7.27) the average effective index has been replaced by n_{core} and the difference in the mode propagation constants by the core-to-cladding index difference. Therefore, for a typical fiber, the LPG is between $\sim\times100$ and $\times1000$ more sensitive than the STG to the changes *between* the propagation constants of the core and the cladding modes.

The transmission spectra of a typical LPG is shown in Fig. 4.26. A number of resonances beginning with the coupling of the fundamental guided mode to the cladding n = 2, 3, 4, 5, and 6 modes can be seen. It should be noted that the transmission loss for each mode depends on the strength of the coupling constant κ_{ac} and κ_{dc}. The former indicates the length of the grating required for 100% coupling, while the latter causes the resonance wavelengths to shift [see Eq. (4.7.26)]. This requires a grating period to be adjusted according to the conversion efficiency *and*

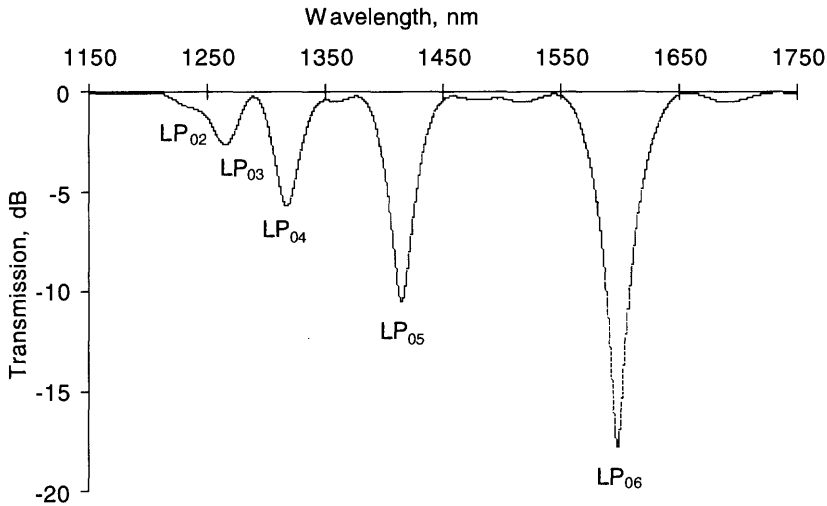

Figure 4.26: Transmission spectra of a ten mm long LPG in standard single mode type fiber (Corning SMF 28), with a period of 450 μm. Coupling is shown from the fundamental core mode to the odd (v = 1), n = 2 $\rightarrow$ 6 cladding modes (LP_{0n}).

the required resonance wavelength. The bandwidth of a single resonance of an LPG filter is approximately [56]

$$\Delta\lambda \approx \frac{\lambda^2_{resonance}}{\Delta n_{eff} L_g} \sqrt{\frac{4\kappa_{v\to 01}}{\pi} L_g}, \tag{4.7.28}$$

where coupling from the fundamental guided mode to the appropriate $1v$ cladding mode has the core-to-cladding mode effective index difference of Δn_{eff}. The resonance wavelength is determined by Eq. (4.6.4).

Long-period gratings for coupling a guided mode to the cladding may be designed for standard single-mode fibers by the data in Figs. 4.27 and 4.28. The period of a grating normalized to resonance wavelength $\lambda_{resonance}$ is shown as a function of the difference of guided mode effective index from the cladding index. For example, a resonance peak at 1550 nm requires a grating with a period $100 \times 1.55 = 155$ microns for a mode-effective index difference of 0.01.

We note that the change in the resonance wavelength of a long-period grating is influenced by the change in the core refractive index as a grating is being written [Eq. (4.7.30)]. As the coupling constant increases, the coupling loss increases until [Eq. (4.4.12)]

$$\alpha L_g = \frac{\pi}{2}, \tag{4.7.29}$$

and at the resonance wavelength, $\alpha = \kappa_{ac}$. To maintain the maximum loss, the length of the grating or the coupling constant has to be adjusted for a given bandwidth.

Figs. 4.27 and 4.28 may also be used to show how the period of the grating varies as a function of the *change* in the effective index of the mode. The desired resonance wavelength for an LPG may be calculated for the final mode effective index after the grating has been fabricated, using the data in Fig. 4.28 for the real modes of standard SMF fiber. For a required transmission loss, the refractive index modulation can be calculated to arrive at the final mode effective index. With this data, and from the required bandwidth of the grating, the appropriate choice for the grating period can be made.

Figure 4.29 shows the effect of immersing a long-period grating in oil. The resonance condition for coupling to the forward-propagating cladding mode is destroyed as the cladding is index matched. With further increases in the index of the oil, we note another resonance due to partial reflection

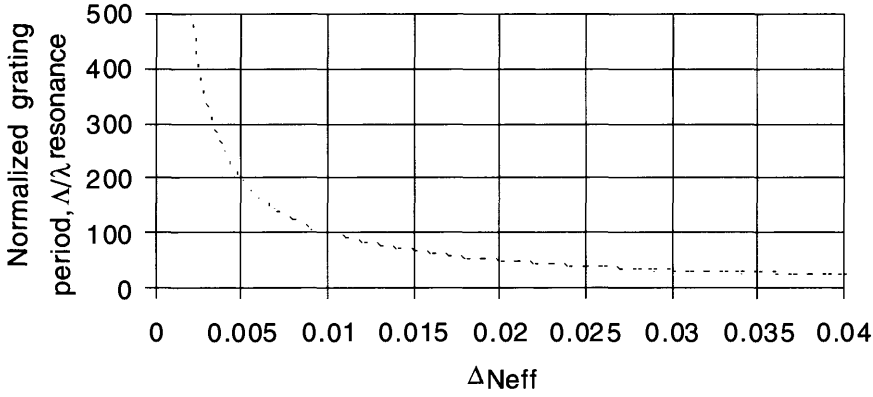

Figure 4.27: Normalized approximate resonance wavelength for phase-matched radiation mode coupling for LPG.

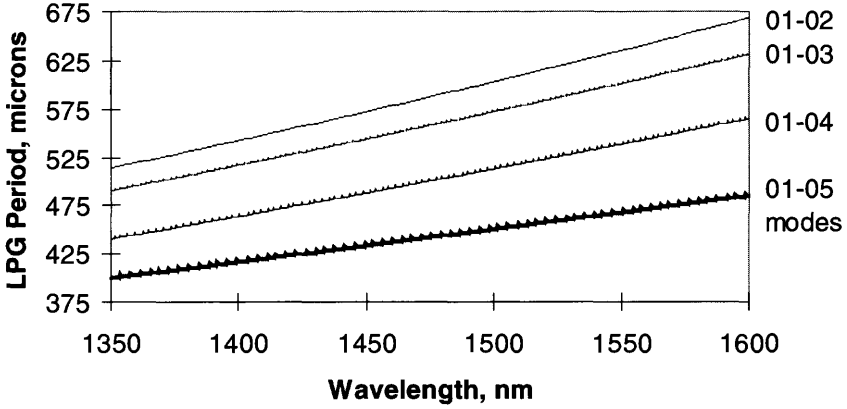

Figure 4.28: The computed grating periods for coupling of the LP_{01} core mode to the of the first four LP_{0n} cladding modes in standard (Corning SMF) fiber.

at the cladding surface to form leaky modes. The loss (to $1/e^2$ of the input) by leakage at the boundary of the cladding and the oil is [57]

$$L \approx -\left(1 + \frac{1}{\ln r}\right) L_b, \tag{4.7.30}$$

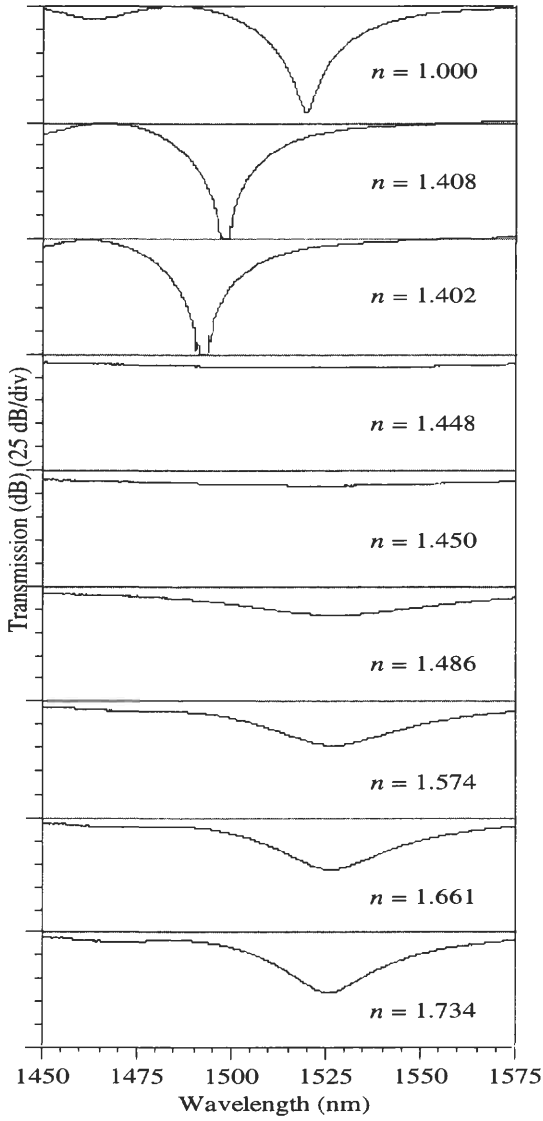

Figure 4.29: Radiation loss from a long-period grating as a function of the index of the oil that surrounds the fiber (from: Stegall D B and Erdogan T, "Long period fiber for grating devices based on leaky cladding modes," in *Bragg Gratings, Photosensitivity, and Poling in Glass Fibers and Waveguides: Applications and Fundamentals*, Vol. 17, OSA Technical Digest Series (Optical Society of America, Washington DC, 1997), paper BSuB2, pp. 16–18.).

where r is the Fresnel amplitude reflection coefficient at the cladding surface, and L_b is the distance between the successive reflections at the cladding surface.

4.8 Grating simulation

4.8.1 Methods for simulating gratings

Many of the techniques for simulating fiber Bragg gratings were introduced at the beginning of the chapter [10,58,9,19]. All the techniques have varying degrees of complexity. However, the simplest method is the straightforward numerical integration of the coupled-mode equations such as Eqs. (4.3.9) and (4.3.10). While this method is direct and capable of simulating the transfer function accurately, it is not the fastest. Another technique is based on the Gel'Fand–Levitan–Marchenko inverse scattering [58] method. This is again a powerful scheme based on integral coupled equations but has the primary disadvantage of obscuring the problem being solved. It has, however, the advantage of allowing a grating with particular characteristics to be designed. Perhaps the most attractive method is based on techniques developed for the analysis of metal waveguides by Rouard [11] and carries his name as a result. This technique, extended by Weller-Brophy and Hall [12], works on the principle that the waveguide may be segmented into subwavelength thin films. Standard thin-film techniques for calculating the amplitude and phase of the transmitted and reflected electric fields at each interface are propagated backward from the output end of the grating. The method is slow, but is one of the few that offers complete piecemeal control of the spatial variation in the refractive index modulation of the grating. For example, the transfer function of a grating with a sawtooth modulation is analyzed equally as well as a square or sinusoidal profile. The influence on the phase and amplitude response of the grating cannot be fully characterized if the Fourier coefficient of the phase-synchronous term for phase matching as shown in Eq. (4.2.27) alone is used. Thus, it is a laborious and time-intensive computation; however, the results accurately simulate the characteristics of complex-shaped grating periods with reasonable reflectivities, being limited by the rounding errors in the computation.

A fast and accurate technique is based on the T-matrix (transfer) for calculating the input and output fields for a short section δl of the grating

[10]. The outputs of the first matrix M^1 are used as the input fields to the second matrix, M^2, not necessarily identical to M^1. The process is continued until an entire complex profile grating is modeled. This method is capable of accurately simulating both strong and weak gratings, with or without chirp and apodization. It has the advantage of handling a *single* period of grating as the minimum unit length for the matrix in the case when the period or amplitude is a *slowly* varying function of length. In the following section, two methods, Rouard's and the T-matrix, will be presented for simulating gratings of arbitrary profile and chirp.

4.8.2 Transfer matrix method

An analytical solution for a grating of length L_g, with an arbitrary coupling constant $\kappa(z)$ and chirp $\Lambda(z)$, is desirable but no simple form exists. The variables cannot be separated since they collectively affect the transfer function. In the T-matrix method, the coupled mode equations [for example, Eq. (4.3.9)] are used to calculate the output fields of a short section δl_1 of grating for which the three parameters are assumed to be constant. Each may possess a unique and independent functional dependence on the spatial parameter z. For such a grating with an integral number of periods, the analytical solution results in the amplitude reflectivity, transmission, and phase. These quantities are then used as the input parameters for the adjacent section of grating of length δl_2 (not necessarily $= \delta l_1$). The input and output fields for a single grating section are shown in Fig. 4.30. The grating may be considered to be a four-port device with

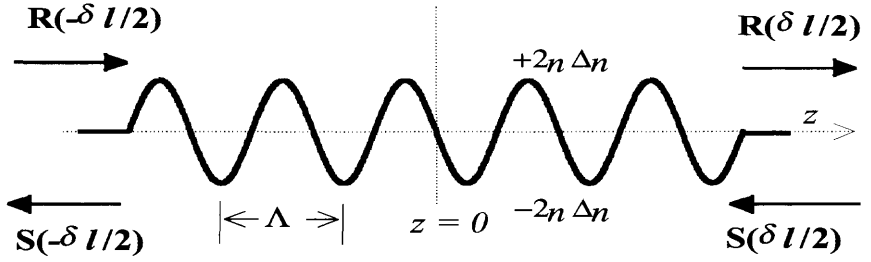

Figure 4.30: Refractive index modulation in the core of a fiber. Shown in this schematic are the fields at the start of the grating on the LHS and the fields at the output on the RHS. The modulated refractive index is $\pm$ $2n\Delta n$ about a mean index.

four fields: input fields $R(-\delta l_1/2)$ and $R(\delta l_1/2)$ and output fields $S(-\delta l_1/2)$ and $S(\delta l_1/2)$. A transfer matrix T^1 represents the grating amplitude and phase response. For a short uniform grating, the two fields on the RHS of the following equation are transformed by the matrix into the fields on the LHS as

$$\begin{bmatrix} R(-\delta l_1/2) \\ S(-\delta l_1/2) \end{bmatrix} = [T^1] \begin{bmatrix} R(\delta l_1/2) \\ S(\delta l_1/2) \end{bmatrix}. \tag{4.8.1}$$

The boundary conditions applied to Eq. (4.8.1) lead directly to the reflectivity and transmissivity of the grating. These conditions depend on whether the grating is a contradirectional or a codirectional coupler.

Reflection grating

For a reflection grating, the input field amplitude $R(-\delta l_1/2)$ is normalized to unity, and the reflected field amplitude at the output of the grating $S(\delta l_1/2)$ is zero, since there is no perturbation beyond the end of the grating.

Writing the matrix elements into Eq. (4.8.1) and applying the boundary conditions leads to

$$\begin{bmatrix} 1 \\ S(-\delta l_1/2) \end{bmatrix} = \begin{bmatrix} T_{11} & T_{12} \\ T_{21} & T_{22} \end{bmatrix} \begin{bmatrix} R(\delta l_1/2) \\ 0 \end{bmatrix}, \tag{4.8.2}$$

in which, the superscript for T^1 has been dropped for clarity. The transmitted amplitude is easily seen to be

$$R(\delta l_1/2) = \frac{1}{T_{11}}. \tag{4.8.3}$$

The reflected amplitude follows from Eqs. (4.8.2) and (4.8.3) as

$$S(-\delta l_1/2) = \frac{T_{21}}{T_{11}}. \tag{4.8.4}$$

Consequently, these are now the new fields on the RHS that can be transformed again by another matrix, T^2 and so on, so that for the entire grating after the Nth section, where $L = \sum_{j=1}^{N} \delta l_j$, is

$$\begin{bmatrix} R(-L/2) \\ S(-L/2) \end{bmatrix} = [T^N] \cdots [T^3][T^2][T^1] \begin{bmatrix} R(L/2) \\ S(L/2) \end{bmatrix}, \tag{4.8.5}$$

in which the field amplitudes on the RHS are the same as the those expressed in Eq. (4.8.1).

Replacing the N multiplied 2×2 matrices in Eq. (4.8.5) by a single 2×2 matrix, we get the transfer function of the whole grating,

$$\begin{bmatrix} R(-L/2) \\ S(-L/2) \end{bmatrix} = [\mathbf{T}] \begin{bmatrix} R(L/2) \\ S(L/2) \end{bmatrix}, \tag{4.8.6}$$

where the matrix $\mathbf{T}$ is

$$[\mathbf{T}] = \prod_{j=1}^{N} [T^j]. \tag{4.8.7}$$

Now the transmissivity τ of the whole grating follows from Eqs. (4.8.3) and (4.8.4),

$$\tau = (1 - \rho) = \frac{R(L/2)}{R(-L/2)} = \frac{1}{T_{11}}, \tag{4.8.8}$$

and reflectivity ρ,

$$\rho = \frac{S(-L/2)}{R(-L/2)} = \frac{T_{21}}{T_{11}}. \tag{4.8.9}$$

From the solution to the coupled-mode equations (4.3.9) and (4.3.10), the transfer matrix elements for the jth section are

$$T_{11} = \cosh(\alpha \delta l_j) - \frac{i\delta \sinh(\alpha \delta l_j)}{\alpha} \tag{4.8.10}$$

$$T_{22} = \cosh(\alpha \delta l_j) + \frac{i\delta \sinh(\alpha \delta l_j)}{\alpha} \tag{4.8.11}$$

$$T_{12} = -\frac{i\kappa_{ac} \sinh(\alpha \delta l_j)}{\alpha} \tag{4.8.12}$$

$$T_{21} = \frac{i\kappa_{ac} \sinh(\alpha \delta l_j)}{\alpha}. \tag{4.8.13}$$

A schematic of the sectioned gratings with the relevant parameters is shown in Fig. 4.31.

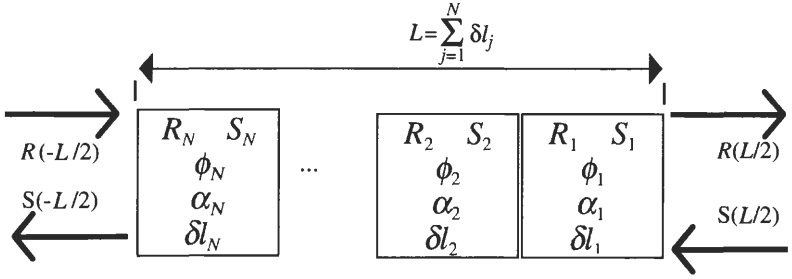

Figure 4.31: The concatenation of several short reflection gratings with constant parameters to form a composite grating. The phase ϕ_N is the phase of the grating in each section.

Codirectional coupling

For transmission gratings, different boundary conditions have to be used; $R(-L/2)$ is again normalized to unity. However, the field $S(L/2)$ on the LHS in Figure 4.30 is copropagating and has an amplitude of zero. At the output, $S(L/2)$ is also a copropagating mode. Codirectional coupling is shown in Figure 4.32. Applying boundary conditions, one arrives at

$$\begin{bmatrix}1\\0\end{bmatrix}=\begin{bmatrix}T_{11} & T_{12}\\ T_{21} & T_{22}\end{bmatrix}\begin{bmatrix}R(\delta l_1/2)\\ S(\delta l_1/2)\end{bmatrix}, \tag{4.8.14}$$

The uncoupled $[R(\delta l/2)]$ and cross-coupled $[S(\delta l/2)]$ amplitudes are then simply derived from Eq. (4.8.14) as

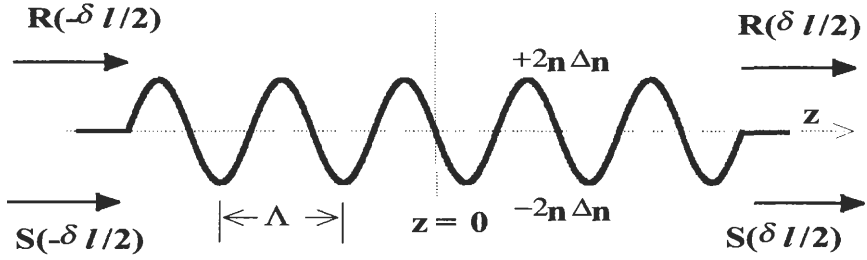

Figure 4.32: For codirectional coupling, the direction of propagation of the S-fields is reversed on both ends of the grating; compare with the reflection grating.

$$T_{11}R + T_{12}S = 1 \tag{4.8.15}$$
$$T_{21}R + T_{22}S = 0,$$

so that the crossed state amplitude is

$$S = \frac{1}{T_{12} - T_{11}(T_{22}/T_{21})}, \tag{4.8.16}$$

and the uncoupled amplitude,

$$R = \frac{T_{22}}{T_{21} - T_{11}T_{22}}. \tag{4.8.17}$$

Following the solutions for the codirectional coupled-mode Eqs. (4.4.9) and (4.4.10), the T-matrix elements for the jth section are

$$T_{11} = \cos(\alpha\delta l_j) + \frac{i\delta \sinh(\alpha\delta l_j)}{\alpha} \tag{4.8.18}$$

$$T_{22} = \cos(\alpha\delta l_j) - \frac{i\delta \sin(\alpha\delta l_j)}{\alpha} \tag{4.8.19}$$

$$T_{12} = \frac{i\kappa_{ac}\sin(\alpha\delta l_j)}{\alpha} \tag{4.8.20}$$

$$T_{21} = \frac{i\kappa_{ac}\sin(\alpha\delta l_j)}{\alpha}. \tag{4.8.21}$$

Equations (4.8.18–21) complete the analysis for guided-mode interactions.

Phase shifts within a grating

It is often useful and necessary to incorporate phase jumps within a distributed grating structure. The phase jump opens up a bandgap within the reflection bandwidth, creating a narrow transmission band. This procedure has been applied to distributed feedback (DFB) lasers to allow stable single-mode operation [59]. A phase shift is accomplished in the T-matrix by multiplying the reflectivity of the jth section by matrix elements containing only phase terms. On this basis, the transfer matrix takes on the form

$$\begin{bmatrix} R(-L/2) \\ S(-L/2) \end{bmatrix} = [T^N] \cdots [T^3][T_{ps}][T^1] \begin{bmatrix} R(L/2) \\ S(L/2) \end{bmatrix}, \tag{4.8.22}$$

where T_{ps} is the new phase-shift matrix for a reflection grating,

$$T_{ps} = \begin{bmatrix} e^{-i\phi/2} & 0 \\ 0 & e^{i\phi/2} \end{bmatrix}. \tag{4.8.23}$$

For codirectional coupling we replace the phase-shift matrix (4.8.23) by its conjugate. The phase factor, $\phi/2$, is any arbitrary phase and may be as a result of a change in the n_{eff} or a discontinuity within the grating. The phase change could have arisen from a region in which the grating was not present or from exposure to uniform UV radiation, thereby changing the local n_{eff}. In either case this phase

$$\phi = \frac{4\pi}{\lambda}(n_{eff} + \partial n)\Delta L, \tag{4.8.24}$$

where ∂n is the local phase change over a length ΔL. The calculation of the reflectivity and transmissivity proceeds in the same manner as without the phase step.

General conditions and restrictions for the T-matrix method

The transfer matrix method requires that certain conditions be met for accurate simulation of grating response [10]. First, when the grating parameters are a function of z, the minimum length of the section $\delta l_j \geq \Lambda_j \times K$, where K is a suitably large number. The actual factor K is a consequence of the slowly varying approximation. The magnitude of K depends on chirp rate $d\Delta\lambda/dL$ where $\Delta\lambda$ is the total chirp bandwidth in the grating. This value determines the upper limit to the number of sections allowed in any simulated grating. Figure 4.33 shows the effect on the reflectivity of reducing the number of sections from 37 periods to one period per section of a 2-mm-long grating with a chirp of 6 nm. The refractive index modulation is 2×10^{-3}.

Second, care must be taken to ensure that each section j has an integer number of grating periods in order to have a smooth transition between sections. An abrupt change in the grating modulation is equivalent to a phase jump and hence the formation of a Fabry–Perot cavity, as has been explained in Section 3.1.13. A consequence of not maintaining this condition over several sections is that it can lead to a deleterious effect outside of the bandwidth of the grating, by forming a superstructure of cascaded Fabry–Perot cavities.

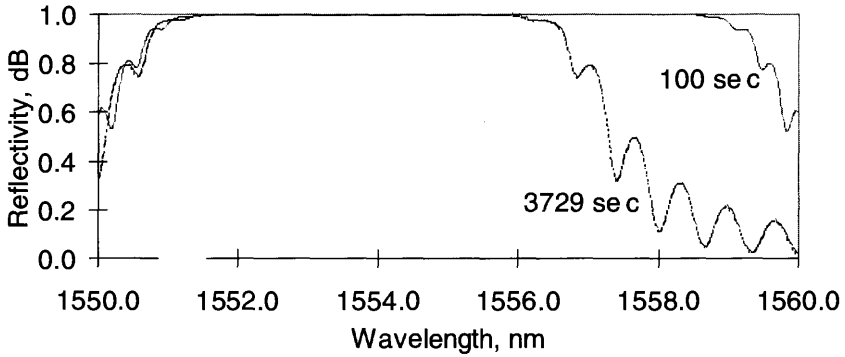

Figure 4.33: The effect of too many sections on the simulation of a 6-nm chirped 2-mm-long grating with 3729 (1 period/section) and 100 (37 periods/section) sections. The 100-section grating accurately models the grating, while the assumptions for the simulation are violated for too many sections.

Third, adequate care must also be taken to smooth any spatial variation in the refractive index modulation. Sections of constant κ_{ac} but different from adjacent ones inevitably form a superstructure [60, 61]. Superstructure can be responsible for replicas of the main Bragg reflection peak at far-removed wavelengths, causing spurious cross-channel interference in filters. The smaller the section, the wider the wavelength band over which the superstructure replicas may appear. Thus, there is a lower limit to the number of grating sections that must be used to reduce this detrimental effect. However, superstructure gratings, when carefully designed, can be used to perform useful functions [62] and are covered in Chapters 6 and 7.

Fourth, when simulating long chirped gratings, care must be taken to allow adequate spectral resolution in order to calculate the group delay accurately.

4.9 Multilayer analysis

4.9.1 Rouard's method

Simulation using this method relies on sectioning the grating into multilayers and replacing the layer by an interface with a complex reflectivity, which includes the phase change through the layer. To accurately

model the refractive index profile of the grating, the period may be subdivided into further sections. A recursive technique is then applied to calculate the reflectivity of the composite period of the grating. Thus, the problem is reduced to calculating the amplitude reflectivity ρ of each single period. The processes is repeated for N single-period sections, each with any local function for the refractive index modulation, period, or phase steps. It is easy to realize that any type of grating, microns or meters long, is then easily modeled. Alternatively, for certain types of pure sinusoidal refractive index modulation, the analytical solution for the constant period grating can be used [Eq. (4.3.11)] so long as the conditions described in Section 4.8.2 are adhered to. The power of this technique is, however, restricted by the computational errors when calculating the reflectivity and transmission of a large number of thin films. Despite this restriction, many types of gratings are adequately realized, provided the maximum reflectivity is limited to values ~99.99%. With care and appropriate computational algorithms, better results may be possible. The basic analysis is similar to the T-matrix approach; however, the reflectivity is simply calculated from the difference in the refractive index between two adjacent layers.

4.9.2 The multiple thin-film stack

Figure 4.34 shows a thin film on a substrate with light propagating at normal incidence and with transverse field components. The refractive index of each section is indicated. The reflectivities, r_1 and r_2, at each interface depends purely on the refractive indexes of the two dielectric materials on either side and are also shown.

The field in each region E_j is the sum of the forward R_j and backward, S_j, traveling fields:

$$E_j = R_j + S_j. \tag{4.9.1}$$

Applying continuity of the transverse field components (which are tangential to the interface) at the bottom layer, 1, and assuming propagation in a nonmagnetic medium, we get,

$$R_1 + S_1 = R_2 + S_2 \tag{4.9.2}$$

$$n_1(R_1 - S_1) = n_2(R_2 - S_2). \tag{4.9.3}$$

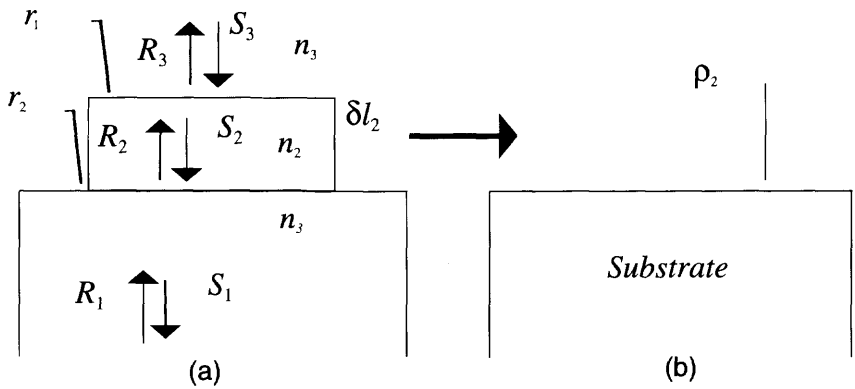

Figure 4.34: (*a*) Two layers on a substrate. The refractive index of each layer is also indicated. The left-hand figure is transformed into the problem shown in (*b*), with a complex reflectivity ρ_2 at the interface with the substrate, replacing the layer n_2.

Equations (4.9.2) and (4.9.3) can be expressed by algebraic manipulation in the following matrix form:

$$\begin{bmatrix} R_1 \\ S_1 \end{bmatrix} = \frac{1}{t_1} \begin{bmatrix} 1 & r_1 \\ r_1 & 1 \end{bmatrix} \begin{bmatrix} R_2 \\ S_2 \end{bmatrix}. \tag{4.9.4}$$

The reflectivity r_1 at the substrate interface is

$$r_1 = \frac{n_1 - n_2}{n_1 + n_2}, \tag{4.9.5}$$

and the transmission coefficient, t_1,

$$t_1 = \frac{2n_1}{n_1 + n_2}. \tag{4.9.6}$$

Once again applying continuity at the second interface from the bottom, the reflected and transmitted fields are described as

$$\begin{bmatrix} R_2 \\ S_2 \end{bmatrix} = \frac{1}{t_2} \begin{bmatrix} e^{i\varphi_2} & r_2 e^{i\varphi_2} \\ r_2 e^{-i\varphi_2} & e^{-i\varphi_2} \end{bmatrix} \begin{bmatrix} R_3 \\ S_3 \end{bmatrix}. \tag{4.9.7}$$

The phase $\varphi_j = \beta_j \delta l_j = 2\pi n_j \delta l_j / \lambda$.

As before for the matrix method, combining Eqs. (4.9.3)–(4.9.7) leads to

$$\begin{bmatrix} R_1 \\ S_1 \end{bmatrix} = \frac{1}{t_1 t_2} [T_1][T_2] \begin{bmatrix} R_3 \\ S_3 \end{bmatrix}. \tag{4.9.8}$$

Equation (4.9.8) may be simplified as for the T-matrix method as,

$$\begin{bmatrix} R_1 \\ S_1 \end{bmatrix} = [\mathbf{T}] \begin{bmatrix} R_3 \\ S_3 \end{bmatrix}, \tag{4.9.9}$$

from which the matrix elements follow as

$$\begin{aligned} T_{11} &= \frac{1}{t_1 t_2} (e^{i\varphi_2} + r_1 r_2 e^{-i\varphi_2}) \\ T_{12} &= \frac{1}{t_1 t_2} (r_2 e^{i\varphi_2} + r_1 e^{-i\varphi_2}) \\ T_{21} &= \frac{1}{t_1 t_2} (r_1 e^{i\varphi_2} + r_2 e^{-i\varphi_2}) \\ T_{22} &= \frac{1}{t_1 t_2} (r_1 r_2 e^{i\varphi_2} + e^{-i\varphi_2}). \end{aligned} \tag{4.9.10}$$

Applying the boundary condition in the region n_3, which is infinite, leads to $S_3 = 0$ as applied to Eq. (4.8.2). The simple complex reflectivity for the layer n_2 follows

$$\rho_2 = \frac{T_{21}}{T_{11}} = \frac{r_1 + r_2 e^{-i2\varphi_2}}{1 + r_1 r_2 e^{-i2\varphi_2}}, \tag{4.9.11}$$

and the transmission coefficient τ_2 is given by

$$\tau_2 = \frac{1}{T_{11}} = \frac{t_1 t_2}{e^{i\varphi_2} + r_1 r_2 e^{-i\varphi_2}}. \tag{4.9.12}$$

Replacing the second section by a single interface as shown in Fig. 4.34b and adding another layer with fields R_4 and S_4 above section 3, the composite reflectivity ρ follows from

$$\begin{bmatrix} R_1 \\ S_1 \end{bmatrix} = \frac{1}{\tau_2} \begin{bmatrix} e^{i\varphi_3} & \rho_2 e^{i\varphi_3} \\ \rho_2 e^{-i\varphi_3} & e^{-i\varphi_3} \end{bmatrix} \begin{bmatrix} R_4 \\ S_4 \end{bmatrix}, \tag{4.9.13}$$

so that in a similar manner to Eqs. (4.9.11) and (4.9.12),

$$\rho = \frac{T_{21}}{T_{11}} = \frac{r_4 + \rho_2 e^{-i2\varphi_3}}{1 + r_4\rho_2 e^{-i2\varphi_3}}. \tag{4.9.14}$$

It is now straightforward to appreciate that a single period of a grating may be divided into j sections and the composite reflectivity computed using this piecewise linear method for any complex shape for the grating.

References

1. Gloge D., "Weakly guiding fibres," *Appl. Opt.* **10**(10), 2252–2258 (1971).
2. Marcuse D., in *Theory of Dielectric Optical Waveguides*. Academic Press, New York, 1994.
3. Snyder A. W. and Love J. D., in *Optical Waveguide Theory*. Chapman-Hall, London, 1983.
4. Kogelnik H. and Shank C. W., "Coupled wave theory of distributed feedback lasers," *J. Appl. Phys.* **43**, 2327–2335 (1972).
5. Kogelnik H., "Filter response of nonuniform almost-periodic structures," *Bell. Syst. Tech. J.*, **55**(1), 109–126 (1976).
6. Yariv A., in *Optical Electronics*, 4th ed. Saunders College Publishing (1991).
7. Hung-Chia H., in *Coupled Mode Theory*. VNU Science Express, The Netherlands (1984).
8. Haus H. A., in *Waves and Fields in Optoelectronics*. Prentice Hall, Englewood Cliffs, NJ, (1984).
9. Matsuhara M., Hill K. O., and Watanabe, "Optical waveguide filters: Synthesis," *J. Opt. Soc. Am.* **65**(7), 804–809 (1975).
10. Yamada M. and Sakuda K., "Analysis of almost periodic distributed feedback slab waveguides via a fundamental matrix approach," *Appl. Opts.* **26**(16), 3474–3478 (1987).
11. Rouard M. P., "Etudes des proprietes optiques des lames metalliques tres minces," *Annal. Phys. II* **7**(20), 1937.
12. Weller-Brophy L. A. and Hall D. G., "Analysis of waveguide gratings: application of Rouard's method," *J. Opt. Soc. Am. B* **2**(6), 863–871 (1985).
13. Weller-Brophy L. A. and Hall D. G., "Analysis of waveguide gratings: a comparison of the results of Rouard's method and coupled-mode theory," *J. Opt. Soc. Am. A* **4**(1), 60–65 (1987).

14. Elachi C., "Waves in active and passive periodic structures: a review," *Proc. IEEE* **64**, 1666–1698 (1976).

15. Russell P. St. J., "Bloch wave analysis of dispersion and pulse propagation in pure distributed feedback structures," *J. Mod. Opts.* **38**, 1599–1619 (1994).

16. Peral E. and Capmany J., "Generalized Bloch wave analysis for fiber Bragg and waveguide gratings," *J. Lightwave Technol.* **15**(8), 1295–1302 (1997).

17. Peral E., Capmany I., and Marti J., "Iterative solution to the Gel'Fand-Levitan Marchenko coupled equations and application to the synthesis of fibre gratings," *IEEE J. Quant. Electron.* **32**(12), 2078–2084 (1996).

18. Song G. H. and Shin S. Y., "Design of corrugated waveguide filters by the Gel'Fand-Levitan-Marchenko inverse scattering method," *J. Opt. Soc. Am.* **2**(11), 1905–1915 (1995).

19. Verly P. G., Dobrowolski J. A., Wild W. J., and Buron R. L., "Synthesis of high rejection filters with the Fourier transform method," *Appl. Opt.* **28**(14), 2864–2875 (1989).

20. Roman J. E. and Winnick K. A., "Design of corrugated waveguide filters by Fourier transform techniques," *IEEE J. Quantum. Electron.* **26**, 1918–1929 (1990).

21. Xia J., Jordan A. K. and Kong J. A., "Electromagnetic inverse-scattering theory for inhomogeneous dielectrics: the local reflection model," *J. Opt. Soc. Am.* **11**(3), 1081–1086 (1994).

22. Tikhonravov A. V. and Dobrowolski J. A., "Quasioptimal synthesis for antireflection coatings: a new method," *Appl. Opt.* **32**(22), 4265–4275 (1993).

23. Little B. E., Wu C. and Huang W. P., "Synthesis of codirectional couplers with ultralow sidelobes and minimum bandwidth," *Opt. Lett.* **20**, 1259 (1995).

24. Storoy H., Engan H. E., Sahlgren B., and Stubbe R. "Position weighting of Fiber Bragg gratings for bandpass filtering," *Opt. Lett.*, **22**(11), 784–786 (1997).

25. Winick K. A., "Effective-index method and coupled-mode theory for almost periodic waveguide gratings," *Appl. Opts.* **31**, 757–764 (1992).

26. Frolik J. L. and Yagle A. E., "An asymmetric discrete-time approach for the design and analysis of period waveguide gratings," *J. Lightwave. Technol.* **13**, 175–185 (1995).

27. Russell P. St. J. and Birks T. A., "A Hamiltonian approach to propagation in chirped and nonuniform Bragg grating structures," in *Proc. of OSA Topical meeting in Photosensitivity and Quadratic Nonlinearity in Glass Waveguides: Fundamentals and Applications*, Portland, OR, 1995, p. PMD2/257–260.

28. Poladin L., "Variational technique for nonuniform gratings and distributed feedback lasers," *J. Opt. Soc. Am.* **A-11**, 1846–1853 (1974).

29. Radic S., George N. and Agrawal G. P., "Analysis of nonuniform nonlinear distributed feedback structures: generalised transfer matrix approach," *IEEE J. Quantum Electron.* **31**(7), 1326–1336 (1995).

30. Matuschek N., Kärtner F. X., and Keller U., "Exact coupled mode theories for multilayer interference coatings with arbitrary strong index modulation," *IEEE J. Quantum Electron.* **33**(3), 295–302 (1997).

31. Johnson D. C., Bilodeau F., Malo B., Hill K. O., Wigley P. G. J. & Stegeman G. I., "Long length, long-period rocking filters fabricated from conventional monomode telecommunications optical fibres," *Opt. Lett.* **17**(22), 1635 (1992).

32. Kogelnik H., "Coupled wave theory for thick holograms," *Bell Syst. Tech. J.* **48**(9), 2909–2947 (1969).

33. Kreyszig E., in *Advanced Engineering Mathematics*, 5th Ed., p. 345. Wiley, New York (1992).

34. Stolen R. H., Ashkin A., Pliebel W., and Dziedzic, "In-line fiber polarization rocking rotator and filter," *Opts. Lett.* **9**, 300–303 (1984).

35. Hill K. O., Bilodeau F., Malo B., and Johnson D. C., "Birefringent photosensitivity in monomode optical fibre: application to external writing of rocking filters," *Electron. Lett.* **27**(1), 1548 (1991).

36. Russell P. St. J. and Hand D. P., "Rocking filter formation in photosensitive high birefringence optical fibres," *Electron. Lett.* **26**, 1846–1848 (1990).

37. Ouellette F., Gagnon D., and Porier M., "Permanent birefringence in Ge-doped fiber," *Appl. Phys. Lett.* **58**(17), 1813 (1991).

38. Erdogan T. and Sipe J. E., "Tilted fiber phase gratings," *J. Opt. Soc. Am. A* **13**, 296–313 (1996).

39. Mizrahi V. and Sipe J. E., "Optical properties of photosensitive fiber phase gratings," *J. Lightwave. Technol.* **11**, 1513–1517 (1996).

40. Erdogan T., "Cladding mode resonances in short and long period fiber grating filters," *J. Opt. Soc. Am. A* **14**(8), 1760–1773 (1997).

41. Morey W. W., Meltz G., Love J. D., and Hewlett S. J., "Mode-coupling characteristics of photo-induced Bragg gratings in depressed cladding fiber," *Electron. Lett.* **30**, 730–731 (1994).

42. Kashyap R., Hornung S., Reeve M. H., and Cassidy S. A., "Temperature desensitisation of delay in optical fibres for sensor applications," *Electron. Lett.* **19**(24), 1039–1040 (1983).

43. Kashyap R., Reeve M. H., Cassidy S. A., and Hornung S., "Temperature desensitization of delay in optical fibers". UK Patent no. *8328204*, March 31, 1987. US Patent no. *4923278*, May 8, 1990.

44. Wagener J. L., Strasser T. A., Pedrazzani J. R., and DeMarco J., "Fiber grating optical spectrum analyser tap," in *Tech. Digest of ECOC'97, Publn. No. 448*, pp. 65–68.

45. Kashyap R., Wyatt R., and Campbell R. J., "Wideband gain flattened erbium fiber amplifier using a blazed grating," *Electron. Lett.* **24**(2), 154–156 (1993).

46. Kashyap R., Wyatt R., and McKee P. F., "Wavelength flattened saturated erbium amplifier using multiple side-tap Bragg gratings," *Electron. Lett.* **29**(11), 1025 (1993).

47. Johlen D., Klose P., Renner H., and Brinkmeyer E., "Strong LP_{11} mode splitting in UV side written tilted fiber gratings," in *Bragg Gratings, Photosensitivity, and Poling in Glass Fibers and Waveguides: Applications and Fundamentals*, Vol. 17, OSA Technical Digest Series (Optical Society of America, Washington DC, 1997), paper BMG12, 219–221.

48. Lemaire P. J., Vengsarkar A. M., Reed W. A., and DiGiovanni D. J., "Thermal enhancement of UV photosensitivity in H_2 loaded optical fibers," in *Tech. Digest of Conf. on Opt. Fib. Commun., OFC'95*, paper WN1, pp.158–159.

49. See, for example, Syms R. A. and Cozens, in *Optical Guided Waves and Devices*, McGraw-Hill, London (1992).

50. Kashyap R., Figure 15, Inset in "Phase-matched periodic-electric-field-induced second-harmonic generation in optical fibres," *J. Opt. Soc. Am. B* **6**(3), 313–328 (1989).

51. Holmes M. J., Kashyap R., Wyatt R., and Smith R. R., "Ultra narrow-band optical fiber sidetap filter," *ECOC'98*, pp. 137–138, 1998.

52. Holmes M. J., Kashyap R., Wyatt R., and Smith R. P., "Development of radiation mode filters for WDM," in *Proc. of IEE Symposium on WDM Technology, IEE*, 16–17 June 1998.

53. Hewlett S. J., Love J. D., Meltz G., Bailey T. J., and Morey W. W., "Cladding-mode resonances in Bragg fibre gratings depressed and matched-cladding index profiles," in *Photosensitivity and Quadratic Nonlinearity in Glass Waveguides: Fundamentals and Applications*, Vol. 22, 1995 OSA Technical Series (Optical Society of America, Washington DC, 1995), pp. PMC2(235–238) (1995).

54. Monerie M., "Propagation in doubly clad single mode fibers," *IEE Trans. Microwave Theory and Techniques* **MTT-30**(4), 381–388 (1982).

55. Dianov E. M., Kurkov A. S., Medvedkov O. I., and Vasil'ev, "A new method for measuring induced refractive index change in optical fiber core," in *Photosensitivity and Quadratic Nonlinearity in Glass Waveguides: Fundamentals and Applications*, Vol. 22, 1995 OSA Technical Series (Optical Society of America, Washington DC, 1995), pp. SuB4-(104–107) (1995).

56. Hall D. G., "Theory of waveguides and devices," in *Integrated Optical Circuits and Components* L. D. Hutchinson, Ed. Marcel Dekker, New York (1987).

57. Stegall D. B. and Erdogan T., "Long period fiber grating devices based on leaky cladding modes," in *Bragg Gratings, Photosensitivity, and Poling in Glass Fibers and Waveguides: Applications and Fundamentals*, Vol. 17, OSA Technical Digest Series (Optical Society of America, Washington DC, 1997), paper BSuB2, pp. 16–18.

58. Roman J. E. and Winnick K. A., "Waveguide grating filters for dispersion compensation and pulse compression," *IEEE J. Quantum Electron.* **29**(3), 975 (1993).

59. Haus H. A. and Lai Y., "Theory of cascaded quarter wave shifted distributed feedback resonators," *IEEE J. Quantum Electron.* **28**(1), 205–213 (1992).

60. Jayaraman V., Cohen D. A., and Coldren L. A., "Demonstration of broadband tunability of a semiconductor laser using sampled gratings," *Appl. Phys. Lett.*, **60**(19), 2321–2323 (1992).

61. Ibsen M., Eggleton B. J., Sceats M. G., and Ouellette F., "Broadly tunable DBR fibre using sampled Bragg gratings," *Electron. Lett.* **31**(1), 37–38 (1995).

62. Ouellette F., Krug P. A., Stephens T., Doshi G., and Eggleton B., "Broadband and WDM dispersion compensation using chirped sampled fibre Bragg gratings," *Electron. Lett.* **31**(11), 899–901 (1995).

This page intentionally left blank

Chapter 5

Apodization of Fiber Gratings

Light + Light does not always give more light,
but may in certain circumstances give darkness.
—Max Born

Interestingly enough, *apodization*[1] is a word often encountered in filter design; a word that flows easily off the tongue. Yet many readers are not aware of the exact meaning of the term. Etymologically, the word has its roots firmly in Greek, *a podos*, meaning "private-foot," in other words, hidden foot — footless. Curiously, any of the approximately 150 species of the amphibian order *Gymnophiona*, known as caecilian, were formerly known as *Apoda*. They are burrowing or swimming, secretive animals, without limbs but with an elongate body length between 100 and 1500 mm, occurring in the Western Hemisphere [1]. Not unlike fiber gratings. . .

So what does the word mean when applied to fiber grating filter design? Fiber gratings are not infinite in length, so they have a beginning and an end. Thus, they begin abruptly and end abruptly. The Fourier transform of such a "rectangular" function immediately yields the well-known *sinc* function, with its associated side-lobe structure apparent in the reflection spectrum. The transform of a Gaussian function, for example, is also a Gaussian, with no side lobes. A grating with a similar

[1]Etymology: Greek. *a*, private, *podos*, a foot. Source: *Chambers 20th Century Dictionary.*

refractive modulation amplitude profile diminishes the side lobes substantially. The suppression of the side lobes in the reflection spectrum by gradually increasing the coupling coefficient with penetration into, as well as gradually decreasing on exiting from, the grating is called apodization. Hill and Matsuhara [2,3] showed that apodization of a periodic waveguide structure suppresses the side lobes. However, simply changing the refractive index modulation amplitude changes local Bragg wavelength as well, forming a distributed Fabry–Perot interferometer [4], which causes structure to appear on the blue side of the reflection spectrum of the grating, although side-lobe amplitudes are reduced [5]. To avoid this complication, the key is to *maintain* an unchanging average refractive index throughout the length of the grating while gradually altering the refractive index modulation amplitude.

The alternative approach for generating a reflection spectrum that has a constant reflectivity over a certain band and zero outside of it is to write a sin x/x refractive index modulation envelope. From the Fourier transform analogy, it is apparent that the grating reflection spectrum will be a "top-hat" function. The problem, however, is to incorporate the grating in such a way that the fringes have the appropriate phase relationship on either side of the zeroes of the *sinc* function. Since the induced refractive index change is proportional to the square of the electric field amplitude (intensity), it is always positive. The phase change can be physically incorporated either by including a $\lambda/4$ dead zone in which no grating exists at each zero or by changing the phase of the grating abruptly, for example in a phase mask [6] or slowly over the length of the section [7]. Strictly speaking, the Fourier transform analogy is only applicable to weak gratings, as mentioned in Chapter 4. However, the principle of using the space–frequency transform does allow the techniques to be used for the design of gratings.

The beneficial effects of apodization are not manifest only in the smoothness of the reflection spectrum, but also in the dispersion characteristics. There are many techniques, as there are appropriate profile functions (*shading*) for the refractive index modulation amplitude to achieve the end result. However, they all rely on a single principle: keeping the *sum* of the dc index change and the amplitude of the refractive index modulation constant throughout the grating. In the following section, several of these techniques and types of "shading" functions used for apodization are reviewed.

5.1 Apodization shading functions

In filter and information theory, there are well-established functions for capturing a signal with a given bandwidth for the required signal to noise ratio [8]. Generally, these are known as Hamming and Hanning functions. The distinguishing feature between the two is whether or not the function forces the filter parameter to zero at infinite "detuning." For example, if the window function profiling the refractive index modulation amplitude reduces it to zero at either end of the grating, it is known as a Hanning, and otherwise a Hamming function. There are various types of functions, each of which results in a compromise between roll-off of the filter and the useable bandwidth. For the numerical analysis commonly used for the computation of the response and also to define the functions for apodization and chirp, it is convenient to define the grating function as

$$\Delta n(z) = \frac{\Delta n_{\max}}{2} f_A(z) f_g(z) + \varepsilon \frac{\Delta n_{\max}}{2}, \tag{5.1.1}$$

where the maximum ac index change is indicated by the subscripted variable n, $f_A(z)$ and $f_g(z)$ are the apodization envelope and periodic refractive index modulation functions, and $0 \leq \varepsilon \leq 2$ is a parameter that controls the level of the background, dc index change. In general the function, $f_g(z)$ includes chirp as

$$f_g(z) = \cos\left(\frac{2\pi z}{\Lambda_0 + \mathbf{F_g}\left(\left[TRUNC\left(\frac{N_g z}{L}\right)\delta\Lambda\right]^m\right)}\right), \tag{5.1.2}$$

where Λ_0 is the period at the start of the of the grating, and $\mathbf{F_g}$ is a function that describes the spatial variation of the grating period with a power dependence m and chirp step $\delta\Lambda = \Delta\Lambda/N_g$ (where $\Delta\Lambda$ is the total chirp of the grating). The grating is composed of N_g discrete sections. The apodisation factor $f_A(z)$ is described by a number of commonly used functions $\mathbf{F_g}(\theta)$ and has an argument of the form

$$\theta = 2\pi\left[\text{Trunc}\left(\frac{N_A z}{\Lambda_A}\right) + \phi_A\right] \tag{5.1.3}$$

where N_A is the number of sections in the entire grating, Λ_A is the apodisation envelope period, and ϕ_A is a starting phase.

Commonly used functions are as follows:

1. Raised cosine: $$f_A(z) = \cos^n(\theta) \tag{5.1.4}$$

2. Gaussian: $$f_A(z) = \exp\left[-G\left(\frac{\theta}{2\pi}\right)^2\right] \tag{5.1.5}$$

3. Tanh: $$f_A(z) = 1 + \tanh\left[T\left(1 - 2\left|\frac{\theta}{\pi}\right|^{\alpha}\right)\right], \tag{5.1.6}$$

where the phase offset has been set to zero.

4. Blackman: $$f_A(z) = \frac{1 + (1 + B)\cos(\theta) + B\cos(2\theta)}{2 + 2B} \tag{5.1.6}$$

5. Sinc: $$f_A(z) = \sin^A\left[0.5\left(\frac{\theta}{\pi}\right)^B\right] \tag{5.1.7}$$

6. Cauchy: $$f_A(z) = \frac{1 - (\theta/\pi)^2}{1 - (C\theta/\pi)^2}\cdot \tag{5.1.8}$$

Three of these apodisation functions, the Tanh, raised cosine, and cosine, are shown in Fig. 5.1 for a grating that has a full chirped bandwidth of 0.8nm and is 100 mm long. The reflectivity has been adjusted to be ~90%, with a peak-to-peak refractive index modulation of 8×10^{-5}.

The beneficial effect of apodization is in the removal of a strong ripple in the group delay. The corresponding effect on the relative group delay as

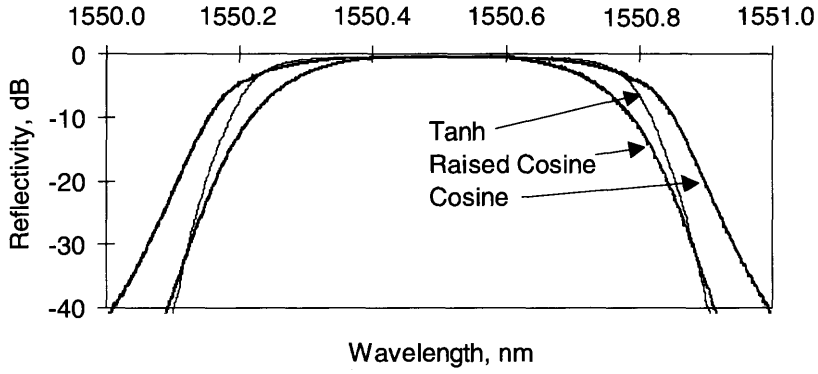

Figure 5.1: The reflectivity spectrum of a 100-mm-long, 0.8-nm bandwidth chirped grating, designed to compensate the dispersion of 80 km of standard fiber, with tanh, $\cos^2$, and cosine apodization envelopes.

a function of wavelength, of the apodization profiles shown in Fig 5.1 is demonstrated in Fig. 5.2. The role of the ripple is considered in Chapter 7.

5.2 Basic principles and methodology

In the discussion that follows, the aim of the exercise is to ensure that the effective index of the grating remains constant, even though the coupling constant becomes a slowly varying function of grating length. The approaches taken to solve this problem are either optical or mechanical, i.e., to program the variation in the coupling constant of the grating at a point, or a combination of both. Optical methods include the use of coherence properties of the UV source and the stamping of short overlapping gratings to build a composite. Mechanical techniques rely of physically blurring out the fringes in a controlled manner, by physically stretching the fiber or shaking it. Finally, a combination of the two may also be used to make complex gratings. Also discussed in the following sections is a specific example of the "top-hat" grating, one with the ideal filter characteristics: a reflectivity that is constant in-band and zero out-of-band, being another form of apodization. This type of a function is highly desirable for a vast number of applications in telecommunications but is restricted to unchirped gratings. Chirping apodizes a uniform refractive index modulation grating as well and may be used for broadband reflectors. Chirped

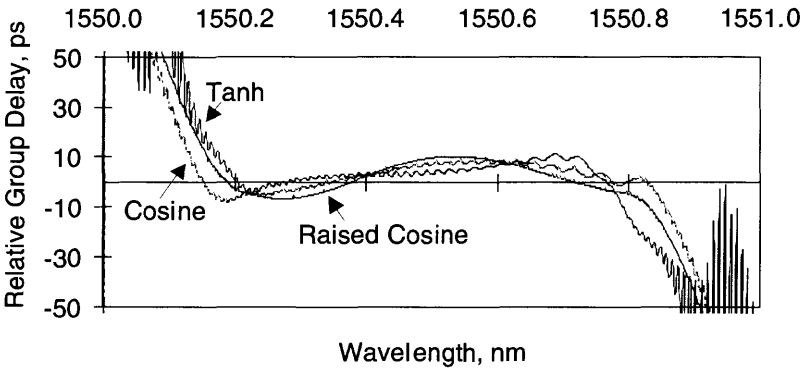

Figure 5.2: The effect on the relative group delay of the apodization profiles used for Fig. 5.1. Although the tanh profile has a flatter characteristic, it also has more residual ripple.

gratings have an associated dispersion that may not be desirable for high-speed applications, unless the grating length is much less than the length of the pulse in the fiber, in which case the grating becomes a point reflector.

5.2.1 Self-apodization

Figure 5.3 shows the region of overlap of two monochromatic UV beams with intensities I_1 and I_2 with a mutual angle θ_m. The intensity $I(z)$ at any point z along the z-axis varies according to the phase-difference between the two beams and can be shown to be

$$I(z) = I_1 + I_2 + 2\sqrt{I_1 I_2}\cos\left[\frac{2\pi}{\lambda_{UV}}\sin\left(\frac{\theta_m}{2}\right)(L_g - 2z)\right], \quad (5.2.1)$$

where the term in brackets is the mutual phase difference between the two beams, and L_g is the length of the overlap, where a fiber grating can form. The function is periodically modulated, and its visibility is

$$v = \frac{I_{\max} - I_{\min}}{I_{\max} + I_{\min}}, \quad (5.2.2)$$

determined by the maximum and minimum intensities in the fringes. The visibility is unity along the entire length L_g only if the radiation is monochromatic *and* the amplitudes of the two beams are identical.

If the UV radiation is composed of two monochromatic frequencies, then the interference pattern is the sum of Eq. (5.2.1) for the frequencies

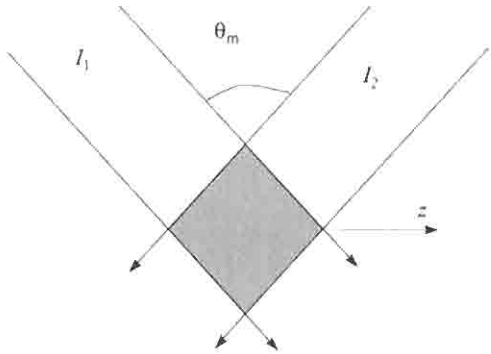

Figure 5.3: The overlap of two beams in the z direction.

present in the source. This leads to a situation in which the visibility of the fringes becomes a function of z. The two sets of fringes with different periods according to Eq. (5.2.1), one for each frequency. For this simple case, the form of the visibility function is simply the "beat" envelope, with the fringe visibility vanishing at positions $\pm z$ from the center of the overlap region at which the fringes from one frequency get out of phase with those from the other. The envelope is described by the function

$$I(z) \cong 2 + 2\cos\left(\frac{2\pi Z_g}{\lambda_{UV}}\right)\cos\left(\frac{2\pi Z_g}{\lambda_{UV}}\left(\frac{\Delta\lambda}{\lambda_{UV}}\right)\right), \tag{5.2.3}$$

where

$$Z_g = \sin\left(\frac{\theta_m}{2}\right)(L_g - 2z). \tag{5.2.4}$$

In Eq. (5.2.3), the interference term has been retained from Eq. (5.2.1), and equal, unity UV intensity of the interfering beams has been assumed. The first term on the RHS is identical to that of Eq. (5.2.1). However, notice that the fringes are now modulated by a slowly varying function with the argument dependent on $\Delta\lambda$, the difference in the wavelength between the two frequencies of the source.

For the general case of a source with a Gaussian spectral content, the visibility function becomes an integral over the bandwidth. The points at which the visibility vanishes are determined by the bandwidth of the source. For a particular length of the illuminated region, the fringes vanish at the edges, replaced by constant UV illumination. For a uniform intensity beam profile of the laser beam, the fringes are *self-apodizing* [9]. With the induced index change being proportional to the fringe amplitude, the interference pattern is written into a fiber core when exposed at this position. Figure 5.4 shows the fringes including the self-apodizing envelope for a 100-micron-long grating. The fringe period has been chosen for illustration purposes only. For real laser systems, it is possible to apodize grating lengths approaching ~50 mm [9].

The principle of apodisation described above is based on the moiré effect. Apodization occurs in the presence of two gratings of different periods, without affecting the total UV dose. The envelope of such a moiré grating is a cosine function, and to alter it, for example, to a Gaussian, a laser with the appropriate spectral shape may be used. This could be a broadband frequency-doubled dye laser source.

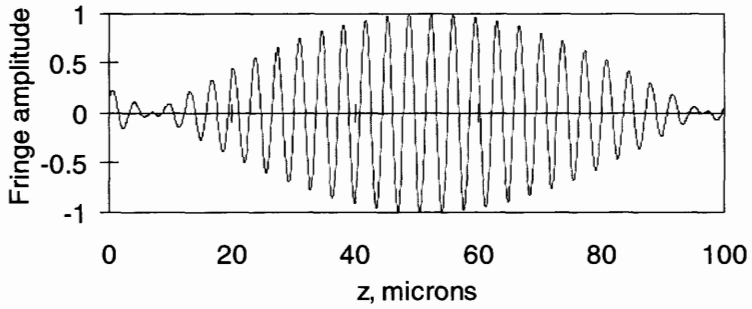

Figure 5.4: The self-apodized fringe profile of a two-wavelength source. The parameters have been chosen for illustration purposes only [9]. The grating length must be chosen to exactly match a single period of the envelope. Since this process has not modified the beam intensity profile, the change induced in the effective index of the mode by the UV dose is the same all along the fiber.

There are other methods of generating moiré[2] patterns for apodization. An optical wedge placed in the path of one of the beams of the UV interferometer will change the Bragg wavelength of the grating being written. Removal changes the Bragg wavelength; if the wedge angle is chosen such that the wavelength difference between the two Bragg periods is exactly *one* period more or less over the length of the grating, then apodization will occur. In this case, the difference in the Bragg grating period is given by

$$\Delta\lambda \approx \frac{\Lambda_{Bragg}^2}{L_g} . \tag{5.2.5}$$

The wedge required for this purpose must impart a π phase change from one end of the grating to the other. Thus, for ~10-mm-long gratings, a wedge angle of the order of 5′ to 10′ of arc is required at a Bragg wavelength of ~1550 nm [9].

Now that the principles have been set out whereby apodization can be performed without altering the intensity of illumination across the length of the grating, other practical implementations are discussed in the following sections.

[2]Etymology: *Fr.*, watered silk; referring to pattern formed on it.

5.2.2 The amplitude mask

Amplitude shading of the intensity profile of the interference pattern (for example, the natural Gaussian profile of a laser beam) helps reduce the side lobes in the reflection spectrum. However, a symmetric "chirp" is also incorporated in the grating such that the blue part of the reflection spectrum acquires an ugly structure (see Chapter 9). This is not good for systems in which many such filters may be required to isolate tightly packed channels. Clearly, simple amplitude shading is not in itself useful for apodization. However, amplitude masks may be used in conjunction with corrective measures to alter the waveguide parameters to result in a constant effective index of the mode. The method developed to apodize gratings relies on a double exposure: the first to precondition the fiber with an amplitude mask, followed by the inscription of the grating again with another amplitude mask in conjunction with a phase mask [10]. The dose in the preconditioning exposure is adjusted to allow for the inscription of the grating with a symmetric fringe intensity profile.

In Fig. 5.5 the preconditioning and grating illumination profiles are shown along with the period-averaged UV intensity. The envelopes of the precondition and the fringes are orthogonal functions. The result of apodization on the reflection spectrum due to the double exposure is

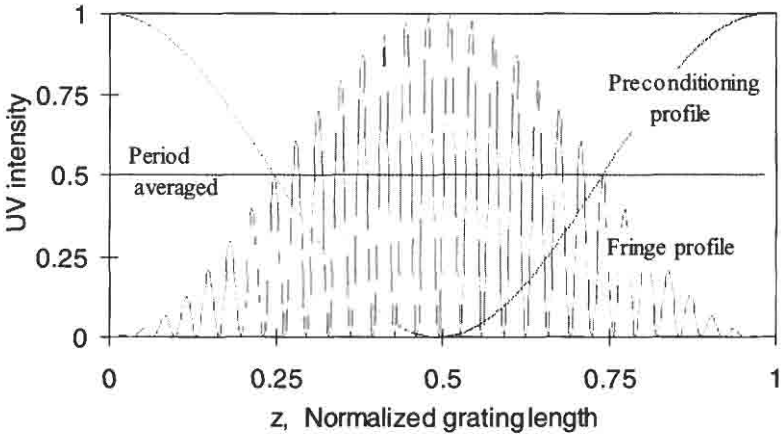

Figure 5.5: The preconditioning UV intensity shaped by the amplitude mask, the fringe profile, and the period-averaged UV intensity is shown. Since the average UV intensity is constant as a function of position, so is the effective index.

shown in Fig. 5.6. A clear reduction of ~20 dB in the side lobes is apparent over the unapodized grating of the same strength, with a reflectivity of 90% and a FWHM bandwidth of 0.24 nm. At ±0.4 nm away from the peak of the reflection, the reflection is less than −40 dB relative to the peak. The fiber used for fabricating the grating was standard Corning SMF-28, which was hydrogen loaded prior to processing. The refractive index modulation profile chosen for this grating was a $\cos^2$ function, which was closely reproduced in the resultant grating. This type of a filter is difficult to fabricate using any other technology and demonstrates the immense signal discrimination available with properly fabricated fiber gratings.

While the process of double exposure can produce excellent results as already demonstrated, it requires a careful study of each and every type of fiber to be used for the fabrication of apodized gratings. The final result depends not only on the photosensitivity and composition of the

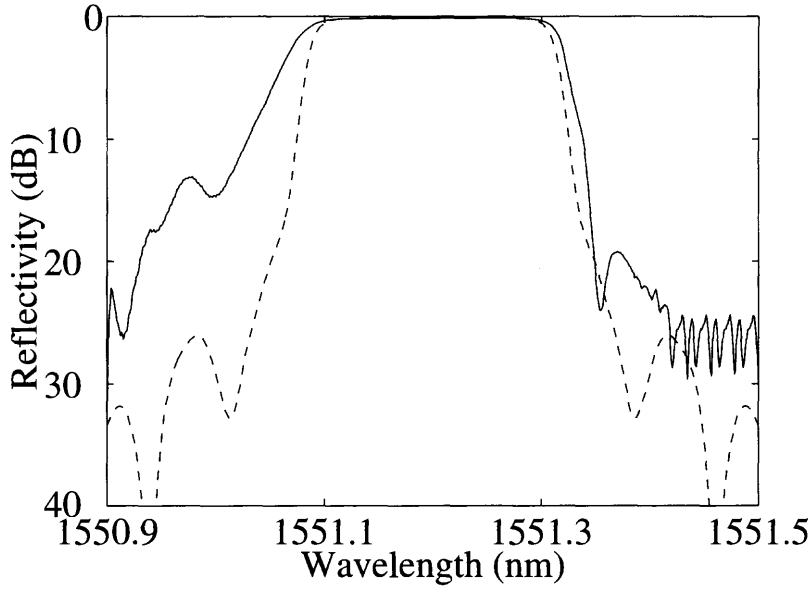

Figure 5.6: The reflection spectrum of an unapodized grating and a $\cos^2$ fringe envelope profile apodised grating written by the double exposure method. The grating length is 10 mm (from: Malo B., Thériault S., Johnson D. C., Bilodeau F., Albert J., and Hill K. O., "Apodised in-fibre Bragg grating reflectors photoimprinted using a phase mask," *Electron. Lett.* **31**(3), 223–225, 1995.) © *IEE* 1995.

fiber, but also on the type of exposure, whether hydrogen loaded or not, use of a pulsed or CW source, as well as the wavelength of the UV radiation. A further complication may occur due to the effects of "incubated" grating formation [11], in which nonlinear growth of a grating occurs. It is therefore expected that other methods may be easier to use routinely, requiring less processing.

5.2.3 The variable diffraction efficiency phase mask

A phase mask with a variable diffraction efficiency has been used for the fabrication of apodized gratings [12]. There are two methods of fabricating such a mask. The diffraction efficiency into the +1 and −1 orders is maximized for a 1:1 mark–space ratio of the grating and the zero order minimized for a specific groove depth (see Chapter 3). Therefore, there are two degrees of freedom to alter the diffraction efficiency. The mark–space ratio of the grating etched in the phase mask or the groove depth may be varied. In the technique reported, a variable diffraction efficiency phase mask, was fabricated by direct exposure of a silica plate to an ion beam of silicon. In this direct write method the ion beam was focused to a spot diameter of 100 nm and scanned across the plate to delineate the grooves. Wet etching in a 1-mol% solution of hydrofluoric acid in water was used to develop the mask. It was demonstrated that the etching rate is dose dependent. Groove widths between 100 and 550 nm and depths from 7.5 to 300nm could be achieved by varying the ion dose from 0.5 to 4×10^{14} ions/cm^2. The etch rate is faster for regions exposed to higher doses. The diffraction efficiency into the ± 1 and 0 orders was measured as a function of the dose; the diffracted orders were shown to be a linear function up to a dose of 2.25×10^{14} ions/cm^2. Thus, a variable diffraction efficiency phase mask was fabricated, using a Gaussian profile dose of $(2.25 \times 10^{14}$ ions/cm$^2)$ $\exp(-x^2/(0.420)^2)$, where x is measured in mm from the center of the 1-mm-long grating, with a period of 1.075 μm. One of the difficulties of fabricating such a grating is the stepped movement of the ion beam. As a result, the Gaussian phase mask profile can only be approximated, and altering the dose in 40 dose steps did this.

Subsequently, apodized gratings were imprinted in standard telecommunications hydrogen loaded fiber and shown to have reduced the first set of side lobes by approximately 14 dBs for a 10% reflectivity grating. These results are not as good as those from the double exposure method (see Section 5.2.2) in which a reduction in the side lobes of 20 dB was

achieved for a reflectivity 10× greater. It is anticipated that the fabrication of longer gratings is not only likely to be difficult owing to uniformity of the grating but also very expensive and time-consuming.

Phase masks fabricated with stepped sections have been demonstrated [13]. However, one of the problems with e-beam fabrication of phase masks is the step size, which can be programmed to allow a variable mark–space ratio of the grooves. An alternative to this approach is to write a moiré grating on the photoresist of the phase mask plate. Writing two gratings of different wavelengths so that at the edges, the two patterns are exactly half a period out of phase as shown in Section 5.2.1 easily does this. The dose delivered by the e-beam for each overlaid grating is half that required for the resist to be fixed. With two exposures, the correct dose is delivered [14] and on developing the mask, the moiré grating is revealed [15]. In this phase mask, the diffraction efficiency varies continuously along its length, and it is possible to fabricate phase masks for long gratings. While it is attractive and convenient to replicate apodized gratings directly using apodized phase masks, there are issues that need to be addressed, which are definite drawbacks in the fabrication and use of such a mask. The feature size of the mask near the edges of the grating becomes infinitesimal, and as a result, the features have no strength. Nor is there any guarantee that they will survive the phase mask fabrication process in a repeatable fashion. The fragility of such a phase mask makes it impossible to handle. It is likely to be damaged easily, either optically or mechanically, during the process of fiber grating replication. There is also the additional problem of the removal of contamination from such a fragile phase mask. The better option for an apodized phase mask is to alter the *etch depth* while keeping the mark–space ratio constant. This ensures the strength and eases handling and cleaning processes.

The next section explores two techniques based on the application of a combination of optical and mechanical methods. Both are highly flexible and capable of produce a variety of gratings, apart from simple apodization.

5.2.4 Multiple printing of in-fiber gratings applied to apodization

The multiple printing in fiber (MPF) method has been discussed in Chapter 3. In this section, the particular attributes and requirements for the fabrication of (a) apodised gratings and (b) top-hat reflection gratings is

discussed. The principle of this method is to write short (4-mm) gratings that are overlapped, so that at each printing only a few new periods are printed [16]. This is possible with a pulsed UV laser system but requires extreme precision in positioning the fiber. To overcome this problem, the fiber is supported over the entire length of the grating to be fabricated in a long glass vee-groove. The vee-groove is fabricated using two pieces of glass assembled together with a small gap at the apex of the vee. This allows a vacuum system to be used to hold the fiber precisely in position as it is translated. Figure 3.21 shows the overall fabrication equipment. Other important issues are the smoothness of the fiber translation system and the precise timing of the laser pulse. The former problem is overcome by translating the fiber *continuously* at a constant speed on an air bearing, during fabrication, using a linear motor capable of long translation (500 mm). The location of a point on the fiber carriage is measured continuously by an interferometer, which is modulated by a Pockels cell. This tracking interferometer has a resolution of ~0.3 nm over the translation distance. Part of the tracking signal is fed back to maintain a constant speed and to compensate for vibrations. The position of the interferometer is fixed, and the fiber is translated across the fringes, both backward and forward. The process is entirely controlled by a computer, which is programmed to generate a particular function in the firing sequence of the laser, movement direction, and speed of translation.

The schematic of the printing is shown in Figure 5.7. Overlapping fringes are shown in a sequence. The center shows the first printing of a grating; the bottom shows the position of the second printing relative to the first arranged to arrive just ahead of a fringe maximum already printed by a distance $+\delta$, and the top is the position of the third printing, which arrives immediately after the second pulse to write on top of the same fringe maximum but delayed by a distance $-\delta$. Also shown is the fringe in the fiber core at the third pulse, being a combination of the fringes due to the second and the third pulses only. As can be seen, the fringe spreads symmetrically around the original maximum. By altering the sequence of pulses, the fringes can be filled in so that the grating gradually disappears toward the edges.

Using this method, unapodized gratings with a FWHM bandwidth of 4.6 pm (L_g = 200 mm) and apodised gratings with a bandwidth of 27 pm (L_g = 50 mm) have been demonstrated [17], both close to theoretically predicted values for low-reflectivity gratings (2–3%). The method naturally allows any type of apodization to be programmed in.

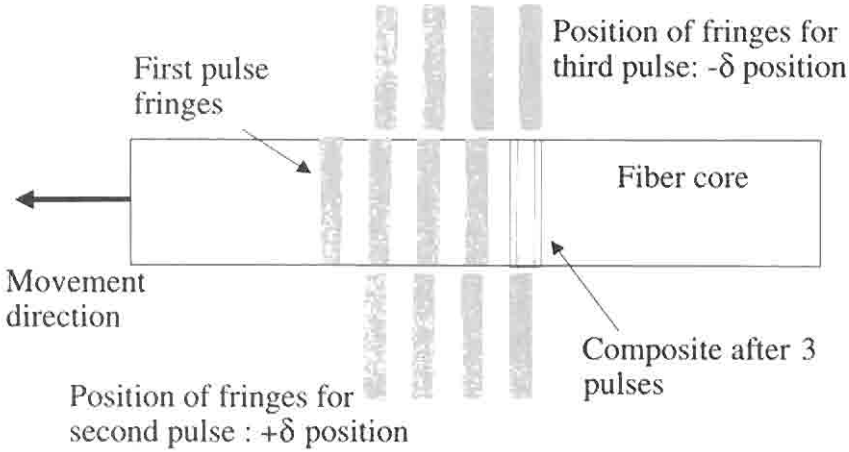

Figure 5.7: The sequence of pulses is staggered so that a fringe is spread symmetrically around the mean position of the fringe already printed in the first printing.

There are some points that need to be considered in the use of this method. The minimum step size determines how smoothly the grating can be apodized. The step size is of the order of 0.01 mm, so that typically in a grating length of 100 mm, full symmetric apodization can be achieved with a maximum of ~10,000 steps, which is more than adequate for a smooth profile. These parameters are discussed in Section 5.3.

This technique has been applied to the fabrication of apodized chirped gratings as well. In this case, not only does the mark–space ratio have to be changed but also the period.

5.2.5 Position-weighted fabrication of top-hat reflection gratings

The MPF method is suited to writing gratings with a "top-hat" (TH) reflection spectrum, shown in Fig. 5.8, along with the spatial profile of the refractive index modulation of the grating required for these characteristics (Fig. 5.9). For a perfect TH, an infinite number of cycles of a *rect* or *sinc* function are needed. This is not possible for practical gratings, since the continuous *sinc* function can only be approximated in a discrete number of steps. This task is demanding in any case, but a good approxi-

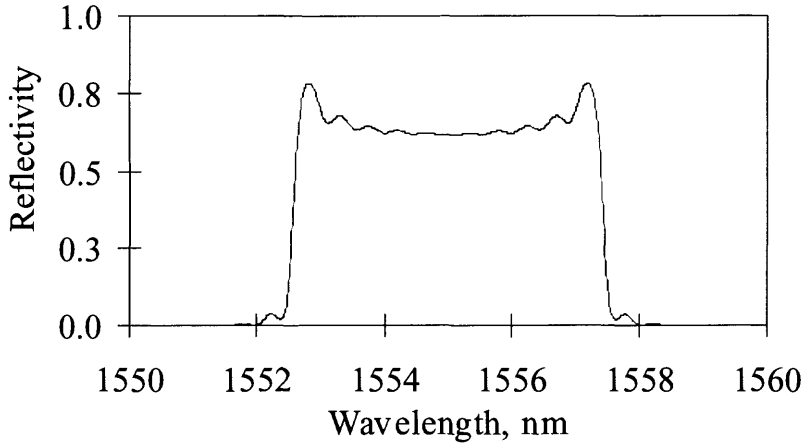

Figure 5.8: Simulated reflection spectrum of a *sinc* function approximated by including 22 zeroes for a grating 4 mm long. The peak-to-peak index difference is 6×10^{-3}, and the grating has 1000 sections. These gratings demand better step resolution than is possible with the MPF scheme.

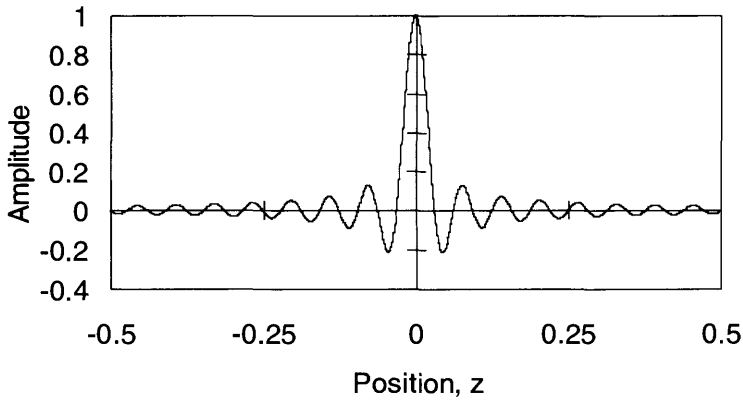

Figure 5.9: The refractive index modulation profile showing 31 zeroes along the length of the grating. Figure 5.8 shows a top-hat reflection spectrum for a grating with 22 zeroes. The modulation amplitude must have positive and negative components in order to faithfully reproduce a top-hat spectrum. Truncation leads to a limiting out-of band rejection of ~ -20 dB.

mation is possible with a few cycles. In order to invert the phase between the sections, additional UV exposure is given to induce a $\lambda/2$ phase shift.

The MPF scheme caters for both the changes in the amplitude of the refractive index modulation and the phase change. For the former, overlaid subgratings with the appropriate phase step between each printing reduce the fundamental component of the amplitude of the refractive index modulation. By the same technique, a phase change of π can also be introduced by shifting the fiber by the appropriate distance prior to the printing of the next subgrating. This method allows a very high degree of flexibility in the fabrication of gratings [17].

The positions for the phase steps are shown in the refractive index amplitude profile in Fig. 5.10. In trying to reproduce faithfully the TH function by an approximate method, two difficulties are encountered. The truncated *sinc* function throws up additional frequency components, which create out-of-band reflections, since exact cancellation of the phases is no longer possible. Secondly, the approximate envelope of each period of the *sinc* function introduces additional phase shifts, which has a deleterious effect in the out-of-band spectrum. Typically, the background reflection remains just below 20 dB over a wide out-of-band frequency spectrum. A measured response of a 100-mm-long truncated *sinc*, TH grating is

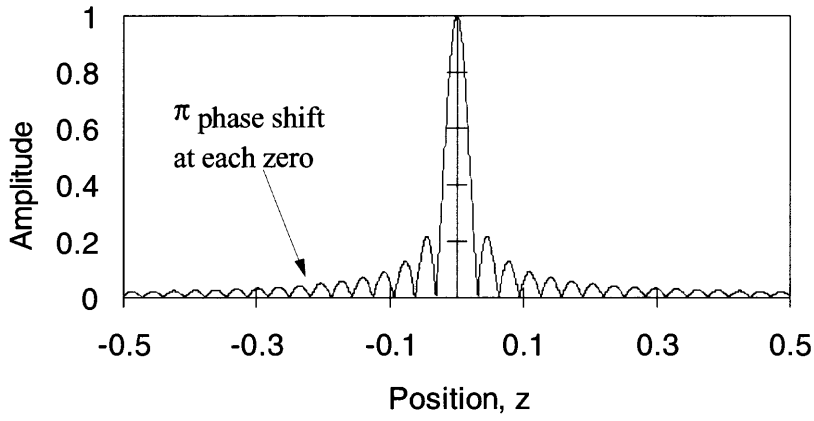

Figure 5.10: The actual refractive index modulation amplitude written in the fiber. In order to introduce the change in the sign of the modulation, a phase change can be placed at the zero.

shown in Fig. 5.11. The achieved results are close to those of the simulation. The bandwidth is ~20 GHz, with a roll-off of 4 dB/GHz at the band edges, and a peak in band reflectivity of ~55%. The out-of-band rejection was not ideal, being only 16 dB below the in-band reflection, but can be improved by making the grating longer.

Combining other shading functions with the *sinc* profile can reduce the out-of-band reflection to below 50 dB [19]. Although it is possible to fabricate such gratings with the MPF method, the steep edges of the TH spectrum are degraded, and it is not clear whether or not a strong grating apodized using another simple function may be a better option.

5.2.6 The moving fiber/phase mask technique

The MPF technique relies on the fiber being translated across an interference fringe pattern in synchronism with the arrival of the UV writing pulse. With the use of a CW beam, this is not possible since the grating would be washed out. This is exactly the principle of the moving fiber/phase mask (MPM) writing scheme: The fiber is moved along with the phase mask in front of a stationary UV beam, or with the UV beam scanned across a fixed phase mask, with the fiber moving slowly relative to phase mask. Figure 5.12 demonstrates the principle of scanning the UV beam across the phase mask. The fiber is mounted on a holder that can be moved in its entirety (as with the MPF method) but using a

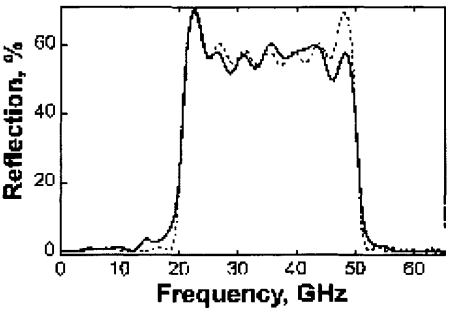

Figure 5.11: The reflection spectrum of a 100-mm-long TH grating. The grating is a result of a truncated *sinc* function made with the MPF method (from: Storøy H., Engan H. E., Sahlgren B., and Stubbe R., "Position weighting of fiber Bragg gratings for bandpass filtering," *Opt. Lett.* **22**(11), 784–786, June 1, 1997.)

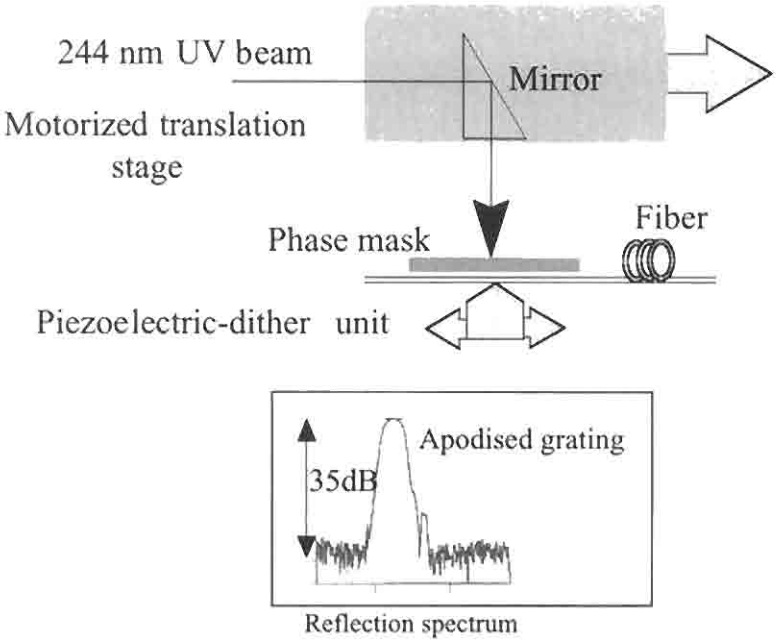

Figure 5.12: The moving phase mask/fiber method for apodizing gratings as well as inducing chirp. The lower inset shows the achieved reflection spectrum of an unchirped grating, with side lobes 35 dB below the peak (after Ref. [20]).

precision piezoelectric translator. Depending on the position of the UV beam, the fiber is dithered in the scanning direction backward and forward, to wash out the grating being inscribed by the required amount. Thus, if the dither amplitude is a linear function of position of the UV beam, with zero movement at the center of the phase mask, an apodized grating is written. Note that the smearing of the grating occurs over the entire length of the writing beam width, so it is essential that the spot size be kept small. The result of apodization is also shown in the inset in Fig. 5.12. The side lobes have been suppressed by approximately 13 dB below the side modes of a uniform period grating [20,21].

If the velocity of the fiber is v_f, the scanning UV beam moves at v_{sc} and the width of the beam is W, then the normalized amplitude of the refractive index modulation Δn varies as a sinc function:

$$\Delta n = \frac{\sin(\pi W v_f / \Lambda_g v_{sc})}{(\pi W v_f / \Lambda_g v_{sc})}. \tag{5.2.6}$$

From Eq. (5.2.6) it follows that the modulation index goes to zero for the |argument| = π radians, so that

$$v_f = \frac{\Lambda_g}{W} v_{sc}. \tag{5.2.7}$$

Equation (5.2.7) shows the obvious result that if the width of the beam is equal to the period, then $v_f = v_{sc}$ to wash out the refractive index modulation. In general, the beam width $W \gg 100 \times \Lambda_g$, so that the velocity of the fiber is $\ll 1\%$ of the scanning velocity.

The relative movement of the fiber with respect to the scanning beam changes the Bragg wavelength of the grating, which is easily calculated as

$$\frac{\Delta\Lambda}{\Lambda_g} = \frac{v_f}{v_{sc}}. \tag{5.2.8}$$

Combining Eqs. (5.2.7) and (5.2.8) directly leads to the chirp as a function of the width of the UV beam,

$$\frac{\Delta\Lambda}{\Lambda_g} = \frac{\Lambda_g}{W}. \tag{5.2.9}$$

Therefore, the maximum wavelength shift is inversely proportional to the width of the beam. This condition is similar to the one encountered in the MPF technique: The maximum is equivalent to the fiber moving one period during the time it takes the UV beam to move a distance equal to its width at the scanning velocity. Using Eq. (5.3.9) in Eq. (5.3.7), and recalling the relationship between the grating period and the Bragg wavelength, leads to

$$\Delta n = \frac{\sin(\Delta\beta W)}{(\Delta\beta W)}, \tag{5.2.10}$$

where

$$\Delta\beta = \frac{2\pi_{eff}}{\lambda_{Bragg}} \cdot \frac{\Delta\lambda}{\lambda_{Bragg}}$$

is the equivalent of "phase detuning" between the Bragg wavelength and the grating that is being written over the width of the beam. Note here that at constant fiber velocity (and scanning beam), the wavelength shifts; if the fiber velocity changes during the scan, the result is a chirped grating.

This is especially useful, since apodization and chirp can be programmed in at the same time. A parameter that needs to be attended to while fabricating a chirped grating is the loss in the amplitude of the refractive index modulation. This must be compensated for, since otherwise the grating will have a varying reflectivity as a function of wavelength. There are two possibilities. The first one is to slow down both v_f and v_{sc} while maintaining the ratio so that a stronger grating results as the grating is chirped. Alternatively, the intensity of the writing beam may be increased to take account of the reduction in the amplitude of the modulation index. There is no published data available on the choice of either approach [20].

It is useful to consider the application of this technique in the fabrication of longer, chirped apodized gratings. Very much in the spirit of the *sinc* profile TH reflection grating and the superstructure grating, another approach to the production of long chirped gratings uses a simple analogy in Fourier transforms. A grating with a uniform period, modulated by a low spatial frequency, pure sinusoidal envelope of period Λ_e, will produce two side bands only. This grating has the following refractive index amplitude modulation profile:

$$\Delta n(z) = 2n\Delta n_0 \cos\left(\frac{2\pi N}{\Lambda_g}\right) \cos\left(\frac{2\pi M}{\Lambda_e}\right), \tag{5.2.11}$$

where N and M are integers indicating the orders of the periods involved, and $2n\Delta n_0$ is the UV induced index change. Simplifying Eq. (5.2.11) directly leads to the resultant spatial frequencies,

$$\begin{aligned}\Delta n(z) = n\Delta n_0 \Bigg\{ &\cos\left(\frac{2\pi N}{\Lambda_g}\left[1 + \frac{M\Lambda_g}{N\Lambda_e}\right]z\right) \\ &+ \cos\left(\frac{2\pi N}{\Lambda_g}\left[1 - \frac{M\Lambda_g}{N\Lambda_e}\right]z\right)\Bigg\}.\end{aligned} \tag{5.2.12}$$

There are only two spatial frequencies present, at the sum and difference frequencies. Note that in Eq. (5.2.12) the amplitude of the index modulation for each spatial frequency has been halved and that two Bragg reflections will occur. Note also that there can be higher order terms according to the ratio of N and M. The next reflection will occur at roughly half the fundamental Bragg wavelength, for $N = M = 2$, and at shorter wavelengths for other orders, predicted here but not as yet reported in the literature. The new reflections occur at a wavelength separation of

$$\Delta\lambda = \frac{\lambda_{Bragg}^2}{2n_{eff}\Lambda_e} \approx \lambda_{Bragg}\frac{\lambda_{Bragg}}{\lambda_e}. \tag{5.2.13}$$

In Eq. (5.2.13), the denominator is approximately the Bragg wavelength λ_e "phase matched" to the period of the *envelope*, so that the fractional change in the fundamental Bragg wavelength is the same as the ratio of the two wavelengths.

As in the case of the TH grating, a phase shift of π radians has to be introduced at each zero crossing, shown in Fig. 5.13. With a chirped grating, the bandwidth and the envelope period may be chosen so that the side bands are adjacent to each other. Ibsen *et al.* [22] demonstrated such a grating by incorporating a continuous chirp of 2.7 nm over a grating length of 1 meter, as well as an envelope period of 291 μm. Approximately 3500 individual periods were printed with as many π-phase stitches. The grating was apodized using a raised cosine envelope over 10% of the length of the grating on each edge. The reflection and delay spectrum is shown in Fig. 5.14. The dispersion of each section was reported to be 3.630 nsec/nm (short wavelength) and 3.607 nsec/nm (long wavelength), respectively, with a total delay of 9.672 ns. These gratings are designed to compensate the dispersion of 200 km of standard fiber with a dispersion of 17 ps/nm/km.

Typically, to produce side bands at 2 nm away from the Bragg matched wavelength, the period of the envelope will be in the region of 300–400 microns. This is roughly the period required to couple a guided mode to a copropagating radiation mode (long-period gratings, see Chapter 4), so that at some wavelength (not necessarily within the chirped bandwidth), it is predicted that strong radiation loss will be observed. The radiation loss will be due to the *stitches* and not the envelope, since for the latter

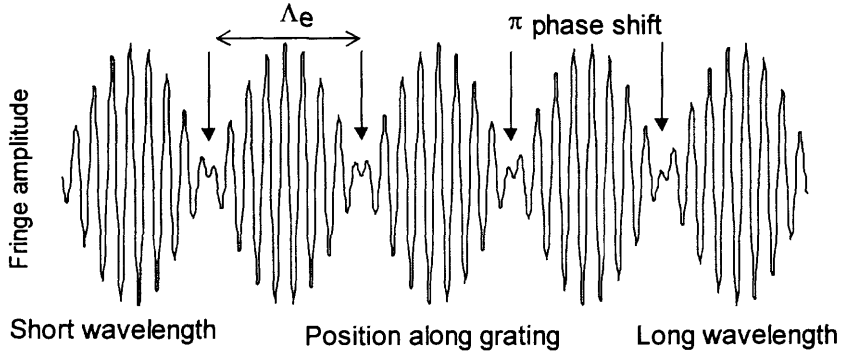

Figure 5.13: The modulated fringe profile of the moiré chirped grating with periodic π phase shifts.

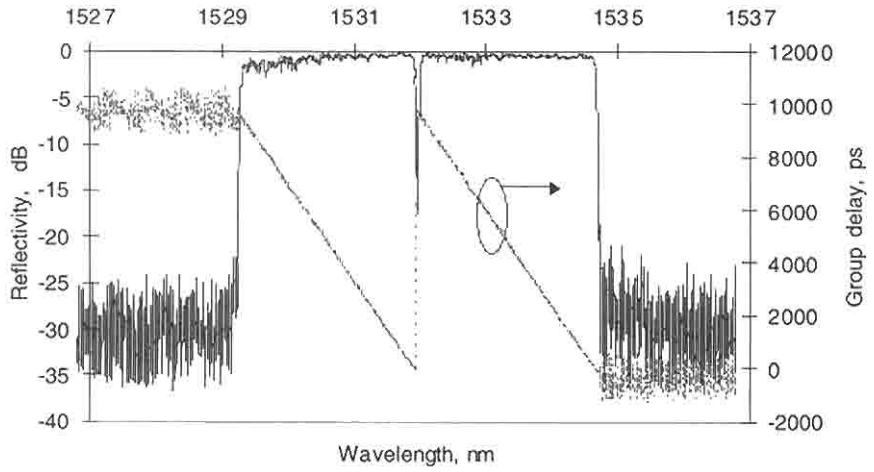

Figure 5.14: Reflectivity and delay characteristics of the chirped moiré grating (from: Ibsen M., Durkin Michael K., and Laming R. I., "Chirped Moiré gratings operating on two-wavelength channels for use as dual-channel dispersion compensators," *IEEE Photon. Technol. Lett.* **10**(1), 84–86, 1998.)

the average index remains unchanged. This prediction has not yet been confirmed. In order to avoid this problem, it is necessary to choose the bandwidth of the grating and the envelope period judiciously.

5.2.7 The symmetric stretch apodization method

The methods for apodization that are most flexible also require active management under the control of a computer. This inevitably means synchronization of the grating inscribing UV pulse and the position of the fiber (cf. MPF as well as the MPM methods). While the flexibility is desirable for a number of applications, simpler methods such as the apodized phase mask are intrinsically faster and probably better suited to mass production. However, as has been discussed, the apodized phase mask is fragile in its reported implementation and perhaps less predictable in fabrication. It also has the severe limitation of allowing an apodized grating that is only as long as the phase mask. This requires a selection of phase masks, unless a tunable interferometer is used; this, unfortunately, counters the argument for using the phase mask, since it defines the

wavelength for mass replication. Thus, a number of apodized phase masks may be required, each of a different wavelength and length.

Apodization requires that the refractive index modulation at the edges of the grating gradually disappear. As described in Section 5.2.1, a moiré grating is composed of two individual gratings, which leads to apodization. The Bragg wavelength of a grating can be changed by stretching the fiber prior to writing [23,24]. Therefore, two gratings written at the same location but differing in wavelength by exactly one period will be apodized. The problem is, how can the two gratings be overlaid such that they have the correct relative phase between them? One possibility is to use symmetric fiber stretching during the inscription of a grating [25]. This poor man's apodization technique — the symmetric stretch apodization method (SAM) — is not only simple to operate, but also applicable to *any* type of grating that needs to be apodized.

Figure 5.15 shows the schematic of the principle of inscription by symmetric stretching of the fiber. The technique can be understood as follows: A grating is first written into a fiber in its relaxed state (Fig 5.15b), for example, by scanning a phase mask, although the method of inscription is unimportant. The fiber is then stretched by straining it in opposite directions by exactly one period of the grating in the fiber, and another grating written on top of the first. Since the fiber is stretched, the inscribed grating is one period longer than the first (Fig. 5.15a) and also symmetrically overlaid (Fig. 5.15c).

The central part of the grating periods are overlaid in phase, while farther away from the center they become increasingly out of phase, until the edges, where they are π out of phase. The difficulty of ensuring that

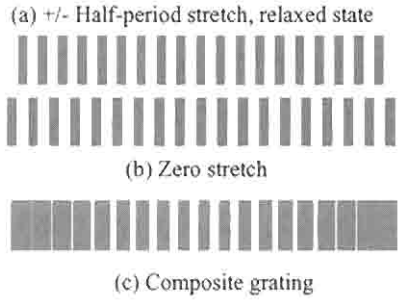

Figure 5.15: A schematic of the symmetric stretch scheme for apodizing gratings. See text for explanations.

both gratings receive the same UV dose is overcome by stretching the fiber back and forth continuously, e.g., by using two piezoelectric transducers, oscillating out of phase. If the fiber is periodically stretched at a high enough frequency, a perfectly apodized grating will result. The apodization function has a pure half-sinusoidal period as an envelope.

For a scanning phase mask interferometer, it is necessary to ensure that the scan speed is such that each point of the fiber is exposed to the UV beam for at least a single stretching cycle, for each scan. This is easily achieved by adjusting the scan speed to be slow enough, depending on the frequency of the stretcher. For a given UV beam width, W_{UV}, and scan speed, V_{UV} m/sec, the frequency f of the stretching oscillator is

$$f = \frac{V_{UV}}{W_{UV}}. \tag{5.2.14}$$

Apodization works for a variety of situations: If the UV beam is static, the stretching scheme frequency is really not that important, so long as the UV power is low enough to enable the grating to form in a time frame much greater than a single period of the oscillator frequency. This condition is generally met unless the grating is written in a single shot from a pulsed laser. A certain amount of care does need to be taken if the apodization is to be performed with a pulsed laser source. It is important that the grating be inscribed over many pulses so that pulse averaging takes place, as well as than every possible position of the stretch of the fiber be inscribed with a grating. One exception is if the grating is inscribed in two uniform pulses of identical intensity, one for each extreme position of the stretch.

Apodization of the grating is *continuous* and not stepped, since each part of the fiber is stretched exactly the correct amount for apodization. This is not true of the MPM technique, in which a whole subgrating length is "smeared" out by the same amount, so that only quasi-continuous apodization is possible. The same applies to the MPF technique. The reason both techniques work is because some of the index change is sacrificed over the finite length of the subgrating. In the case of the MPF scheme, each subgrating tries to print the new grating on what was printed before, but slightly altered. In the MPM, it continuously builds on the regions that have been "wrongly" printed, the result of a finite length of subgrating. There is normally enough refractive index change available for this limitation not to be a problem.

The apodization scheme is independent of the length of the grating, the only requirement being that the fiber be stretched by half-a-period in each direction, so that for a chirped grating, one end of the fiber is stretched slightly more than the other, by adjusting the stretch on that side. For uniform period gratings, no adjustment is necessary when changing the wavelength of the phase mask in the same spectral window (e.g., 1500 nm). Figure 5.16 shows the experimental setup of the equipment used in SAM.

The required stretch to form perfectly apodized gratings as a function of length is shown in Fig. 5.17. Even for relatively short gratings, the strain is easily applied. Another possibility with this method is to write two gratings under static strain to form moiré gratings.

By switching off one stretcher, the grating will be apodized only on the stretched side. As a result, left- and right-hand-end apodization may be performed independently. For super-step-chirped gratings [26], this feature allows apodization of each end of the grating. For the first, shortest-wavelength grating, the short-wavelength end is apodized; other intermediate gratings are printed sequentially without apodization, except for the last, longest-wavelength grating, in which the right-hand, long-wavelength end is apodized by switching on the RH piezoelectric stretcher.

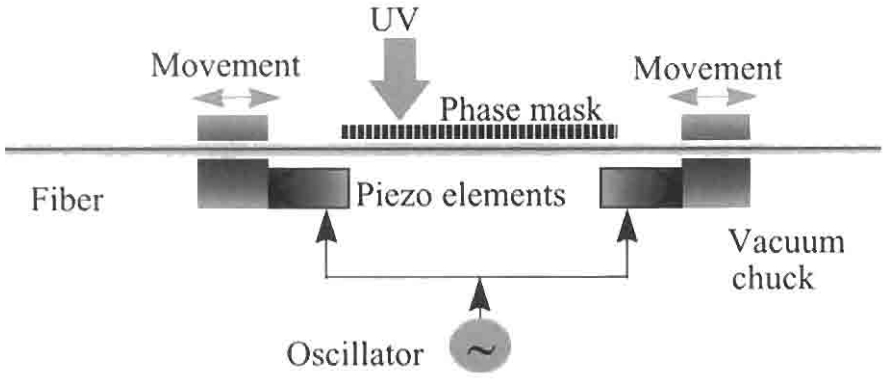

Figure 5.16: The symmetric stretching apodization method (SAM). The phase mask may be replaced by any interferometer. The displacement of the piezoelectric stretchers is monitored by position sensors to set the required stretch [25].

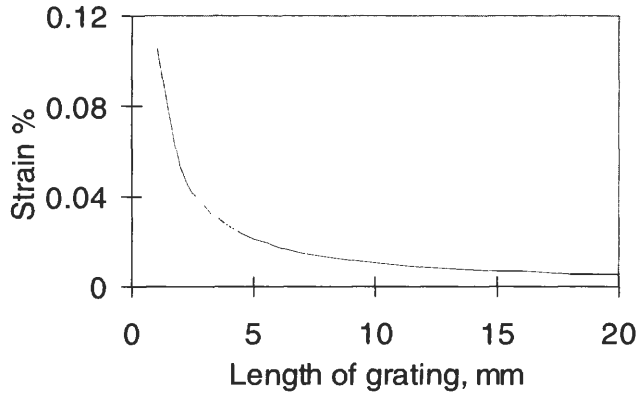

Figure 5.17: The strain applied to a fiber for perfect apodization as a function of grating length for the SAM technique.

A schematic of this principle of making ultralong gratings is shown in Fig. 5.18.

With greater stretch of the fiber, a larger number of cycles of the apodization profile may be written, for example, a *bowtie* profile. Turning off both stretchers may alter the apodization profile after a single pass. The next over laid grating is left unapodized, thereby building a modified cosine refractive index modulation profile.

Increasing the stretch further forms a single cosine envelope, shown in Fig. 5.19. The stretch method has the same effect as the dual frequency moiré grating apodization. At the zero crossing of the envelope, a π phase

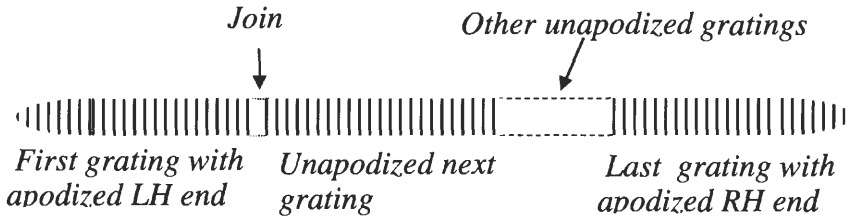

Figure 5.18: The super-step chirped grating, apodized on each end. With a uniform period phase mask, the chirp is zero so that a long, unchirped apodized grating can be written. Careful alignment can eliminate the stitch error at the join, or it may be UV "trimmed" [26].

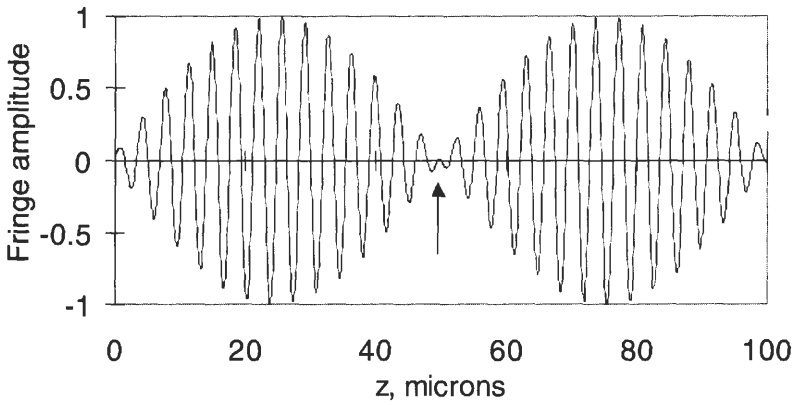

Figure 5.19: A single-period cosine envelope moiré grating formed by stretching the fiber by twice the required amount for perfect apodization (as in Fig. 5.15). The arrow indicates the position of the *automatically* introduced π phase shift in the fringes, equivalent to a $\pi/2$ phase shift at the Bragg wavelength. The length of the grating has been chosen to be deliberately short to show the occurrence of the phase shift.

change occurs between the two sections of the fringes, as can be seen in Fig. 5.19. This effect can be used to automatically introduce multiple, regularly spaced $\pi/2$ phase shifts at the Bragg wavelength for the fabrication of a top-hat reflection spectrum and multiple band-pass filters (also see Section 5.2.6). The difference between stretching or the dual-frequency multiple-period moiré gratings and the MPF technique for writing a similar grating is that in the latter, a deliberate phase shift has to be written in, whereas in the former, the phase shift is *automatically* introduced.

5.3 Fabrication requirements for apodization and chirp

As has been demonstrated in Section 5.2.6, the maximum chirp that can be written using the two mini-grating replication methods (MPF and MPM) is dependent on the length of the subgrating; in the case of the 1-mm-long subgrating for the MPF method, it is only possible to write a grating with a chirp of ~1 nm, since it is equivalent to a change of one period in 1 mm. In order to write larger chirps and apodize the grating

at the same time, a smaller subgrating must be written. The maximum chirp that can be produced from a subgrating length of δL_g is

$$\Delta\lambda = 2n_{eff}\frac{\Lambda_g}{\delta L_g}. \tag{5.3.1}$$

A grating with a bandwidth of 10 nm near the Bragg wavelength of ~1.55 μm requires a subgrating length of ~300 μm. The second point to remember is that the refractive index modulation remains almost unchanged with the chirp induced using the MPF scheme, which can only be used with a pulsed laser. A reduction in the refractive index modulation occurs when a chirp is induced with the MPM method. It can be compensated for to some extent by adjusting the irradiation intensity or by changing the movement velocities of the fiber or phase mask and UV beam, but it requires a CW writing beam. Both methods allow the inscription of long gratings but do require a movement stage with a translation capability at least as long as the grating to be written.

The complication of saturation effects [27,28] has not been addressed in the case of strong gratings written using either of these methods, although certain fibers show a linear response to the time of exposure to UV radiation at a longer wavelength of 334 nm and a much increased writing time [29]. Undoubtedly these will play an important role as the requirements for the types of gratings become more demanding. The effect of linearity of the photosensitive response of the fiber to, for example, the change in the local intensity is as yet unknown. The further, more serious issue of the out-diffusion of hydrogen/deuterium from long gratings has also not been discussed. Out-diffusion causes a reduction in the refractive index of both the UV-exposed and the unexposed regions [30,31]. A differential change in the refractive index between the two regions will lead to a degradation in the transfer characteristics of long gratings, since the phase change accumulates over its entire length.

Both the MPF and MPM methods are flexible and capable of apodizing gratings with arbitrary refractive index modulation profiles and are capable of the production of identical grating characteristics.

The issues related to the other schemes, such as the apodized phase mask, although convenient, are limited flexibility allowing only the replication of the type of apodization programmed in the phase mask. There is a restriction on the maximum size of the phase mask as well as on the reproducibility of the apodized phase mask. Although, as with the step-chirped phase mask [6], it is possible to combine apodization and chirp

in a phase mask. However, the symmetric stretch apodization method combines the two and is flexibly applied to any length of grating. SAM is excellent for long gratings, since the stretch is fixed by the period of the grating, and therefore the strain changes inversely with length. This is shown in Fig. 5.17. For a 1-mm grating, the fiber has to be strained by ~0.1%, which is acceptable, but drops to an insignificant 0.01% for a 10-mm grating. It is, however, very important to ensure that the stretch *is* symmetric; otherwise, the apodization will not be satisfactory. Once the interferometer is aligned, then any length of grating may be apodized. If the grating is not symmetrically placed between the stretchers, then the piezoelectric movement can be adjusted to stretch one end of the fiber more than the other, easily compensating for the misalignment. Finally, certain types of fiber show a photosensitivity that is a function of applied strain [27]. However, the strain used for the apodization of fibers is only a small fraction of that reported in Ref. [27] and should not pose a problem for gratings longer than a millimeter. For long moiré grating formation, the applied strain will also remain low enough to not to cause nonlinearity in the photosensitivity.

References

1 "Caecilla," *Encyclopedia Britannica, Micropaedia*, Vol. 2, p. 715.

2 Hill K. O., "Aperiodic distributed-parameter waveguides for integrated optics," *Appl. Opt.* **13**, 1853–1856 (1974).

3 Matsuhara M. and Hill K. O., "Optical-waveguide band-rejection filters: design," *Appl. Opt.* **13**, 2886–2888 (1974).

4 Mizrahi V. and Sipe J. E., "Optical properties of photosensitive fiber phase gratings," *J Lightwave Technol.* **11**(10), 1513–1517 (1993).

5 Meltz G., Morey W. W., and Glenn W. H., "Formation of Bragg gratings in optical fibres by transverse holographic method," *Opt. Lett.* **14**(15), 823 (1989).

6 Kashyap R., McKee P. F., and Armes D., "UV written reflection grating structures in photosensitive optical fibres using phase-shifted phase-masks," *Electron. Lett.* **30**(23), 1977–1978 (1994).

7 Pakulski G., Moore R., Maritan C., Shepard F., Fallahi M., Templeton I., and Champion G., "Fused silica masks for printing uniform and phase adjusted gratings for distributed feedback lasers," *Appl. Phys. Lett.* **62**(3), 222 (1993).

8 See, for example, Morgan D. P., "Surface-Wave Devices for Signal Processing." Elsevier, Oxford (1985).

9 Froehlich H.-G. and Kashyap R., "Two methods of apodisation of fibre Bragg gratings," *Opt. Commun., 157*(6), 273–281 (1998).

10 Malo B., Thériault S., Johnson D. C., Bilodeau F., Albert J., and Hill K. O., "Apodised in-fibre Bragg grating reflectors photoimprinted using a phase mask," *Electron. Lett.* **31**(3), 223–225 (1995).

11 Dyer P. E., Farley R. J., Giedl R., Byron K. C., and Reid D., "High reflectivity fibre gratings produced by incubated damage using a 193 nm ArF laser," *Electron. Lett.* **30**(11), 860–862 (1994).

12 Albert J., Hill K. O., Malo B., Théirault S., Bilodeau B., Johnson D. C., and Erikson L. E., "Apodisation of spectral response of fibre Bragg gratings using a phase mask with a variable diffraction efficiency," *Electron. Lett.* **31**(3), 222–223 (1995).

13 Kashyap R., McKee P. F., Campbell R. J., and Williams D. L., "A novel method of producing photo-induced chirped Bragg gratings in optical fibres," *Electron. Lett.* **30**(12), 996–997 (1994).

14 Albert J., Thériault S., Bilodeau F., Johnson D. C., Hill K. O., Sixt P., and Rooks M. J., "Minimisation of phase errors in long fiber Bragg grating phase masks made using electron beam lithography," *IEEE Photon. Technol. Lett.* **8**(10), 1334–1336 (1996).

15 Albert J., Hill K. O., Johnson D. C., Bilodeau F., and Rooks M. J., "Moiré phase masks for automatic pure apodisation of fibre Bragg gratings," *Electron. Lett.* **32**(24), 2260–2261 (1996).

16 Stubbe R., Sahlgren B., Sandgren S., and Asseh A., "Novel technique for writing long superstructured fiber Bragg gratings," in *Photosensitivity and Quadratic Nonlinearity in Glass Waveguides: Fundamentals and Applications*, Vol. 22, 1995 OSA Technical Series (Optical Society of America, Washington DC, 1995), pp. PD1-(1–3) (1995).

17 Storøy H., "Fibre Bragg gratings and fibre optic structural strain sensing," Ph.D. Thesis, Norwegian University of Science and Technology, NTUT (1997).

18 Storøy H., Engan H. E., Sahlgren B., and Stubbe R., "Position weighting of fiber Bragg gratings for bandpass filtering," *Opt. Lett.* **22**(11), 784–786 (1997).

19 Kino G. S., *Acoustic waves: Devices, Imaging, and Analog Signal Processing.* Prentice Hall, New Jersey (1987).

20 Cole M. J., Loh W. H., Laming R. I., Zervas M. N., and Barcelos S., "Moving fibre/phase mask-scanning beam technique for enhanced flexibility in producing fibre gratings with a uniform phase mask," *Electron. Lett.* **31**(17), 92–94 (1995).

21 Cole M. J., Loh W. H., Laming R. I., Zervas M. N., and Barcelos S., "Moving fibre/phase mask-scanning beam technique for writing arbitrary profile fibre gratings with a uniform phase mask," in *Photosensitivity and Quadratic Nonlinearity in Glass Waveguides: Fundamentals and Applications*, Vol. 22, 1995 OSA Technical Series (Optical Society of America, Washington DC, 1995), pp. PD1-(1–3) (1995).

22 Ibsen M., Durkin Michael K., and Lamming R. I., "Chirped Moiré gratings operating on two-wavelength channels for use as dual-channel dispersion compensators," *IEEE Photon. Technol. Lett.* **10**(1), 84–86 (1998).

23 Campbell R. J. and Kashyap R., "Spectral profile and multiplexing of Bragg gratings in photosensitive fibre," *Opt. Lett.* **16**(12), 898–900 (1991).

24 Byron K. C., Sugden K., Bircheno T., and Bennion I., "Fabrication of chirped Bragg gratings in photosensitive fibre," *Electron. Lett.* **29**(18), 1659 (1993).

25 Kashyap R., Swanton A., and Armes D. J., "A simple technique for apodising chirped and unchirped fibre Bragg gratings," *Electron. Lett.* **32**(14), 1226–1228 (1996).

26 Kashyap R., Froehlich H.-G., Swanton A., and Armes D. J., "1.3 m long superstep chirped fibre Bragg grating with a continuous delay of 13.5 ns and bandwidth 10 nm for broadband dispersion compensation," *Electron. Lett.* **32**(19), 1807–1809 (1996).

27 Niay P., Bernage P., Douay M., Taunay T., Xie W. X., Martinelli G., Bayon J. F., Poignant H., and Delevaque E., "Bragg grating photoinscription within various types of fibers and glasses," in *Photosensitivity and Quadratic Nonlinearity in Glass Waveguides: Fundamentals and Applications*, Vol. 22, 1995 OSA Technical Series (Optical Society of America, Washington, DC, 1995), paper SUA1, pp. 66–69 (1995).

28 Douay M., Xie W. X., Taunay T., Bernage P., Niay P., Cordier P., Poumellec B., Dong L., Bayon J. F., Poignant H., and Delevaque E., "Densification involved in the UV-based photosensitivity of silica glasses and optical fibers," *IEEE J. Lightwave. Technol.* **15**(8), 1329–1342 (1997).

29 Grubsky V., Starburodov D. S. and Feinberg J., "Wide range and linearity near-UV induced index change in hydrogen-loaded fibers: Applications for Bragg grating fabrication," in *Bragg Gratings, Photosensitivity, and Poling in Glass Fibers and Waveguides: Applications and Fundamentals*, Vol. 17, OSA Technical Digest Series (Optical Society of America, Washington, DC, 1997), Paper BME3, pp. 156–158.

30 Malo B., Albert J., Hill K. O., Bilodeau F., and Johnson D. C., "Effective index drift from molecular hydrogen diffusion in hydrogen-loaded optical fibres and its effect on Bragg grating fabrication," *Electron. Lett* **30**(5), 442–444 (1994).

31 Bhakti F., Larrey J., Sansonetti P., and Poumellec B., "Impact of hydrogen in-fiber and out-fiber diffusion on central wavelength of UV-written long period gratings," in *Bragg Gratings, Photosensitivity, and Poling in Glass Fibers and Waveguides: Applications and Fundamentals*, Vol. 17, OSA Technical Digest Series (Optical Society of America, Washington, DC, 1997), paperBSuD4, pp. 55–57.

Chapter 6

Fiber Grating Band-pass Filters

Let the band pass. . . .

For many applications, the transmission characteristics of a fiber Bragg grating are really the wrong way around: it is a *band-stop* rather than a *band-pass* filter. For example, tuning a radio enables the *selection* of a channel, not the *rejection* of it from a broad frequency spectrum. However, a Bragg grating works quite in reverse, and therefore cannot be easily used for channel selection. Optical transmission systems also require a "channel-dropping" function, in which a channel is selected from a large spectrum of designated channels. These optical channels are on a coarse grid of 100 GHz (multiples and submultiples of), which is currently being debated. A system based on wavelength or frequency sliced channels is a logical one and will prevail in future telecommunications networks. The advantage of such a standardized system is not in doubt, only the allocation of the channels, which is a matter for discussion by international standards committees around the world. In view of the future worldwide integration of telecommunication services, it is only a matter of time before an industry standard emerges.

The immediate question that springs to mind is: Will fiber gratings play a role in emerging systems, given that their function is not the one naturally desired in a majority of application in filtering? The answer to

the question lies in their ability to invert the function to the desired one with a minimum of engineering and expense. The sales volume of gratings will crucially depend on how well and easily they fit this task. A problem needing a solution is ideal for creativity. To this end a number of options have appeared. None is ideal, but within the context of a wider technology, there are appropriate solutions for many applications, albeit at a cost.

What are the options? These may be categorized into two types. First are those that work in reflection, as is normally the case with Bragg gratings. These are principally the following:

1. The optical circulator with grating
2. The single grating in one arm of a coupler
3. (Possibly the most attractive) The in-coupler reflection band-pass filter
4. The dual grating Michelson interferometer
5. The dual grating Mach–Zehnder interferometer
6. The super-structure grating

Those that work in transmission include most notably:

7. The distributed feedback (DFB) grating
8. The Fabry–Perot interferometer
9. The composite moiré resonator
10. The chirped grating, or radiation loss with transmission window
11. The side-tap filter
12. The long-period copropagating radiation mode coupler
13. The polarization rocking coupler
14. The intermodal coupler
15. The in-coupler Bragg grating transmission filter

The above list may be subdivided into interferometric, which include devices 4–9, and noninterferometric. It is worth noting that although interferometric devices conjure up the image of sensitivity to external stimuli, it is not necessarily true of all in that category (devices 6, 7, and 9). By suitable design, devices 4, 5, and 8 have been rendered insensitive and demonstrated to be stable. All gratings are temperature and strain sensitive; however, the temperature sensitivity is low, <0.02 nm/°C, so that over a working temperature range of 100°C, the change in the op-

erating wavelength is only ~2 nm. As a fraction of the channel spacing (100 GHz or 0.8 nm), it is still too large and must be stabilized. Thus, schemes need to be developed to counter the effects of temperature. Passive packaging can isolate the grating from experiencing effects of strain. Both temperature and strain have been used along with grating-based band-pass filters to control novel functions such as optical add–drop multiplexers and demultiplexers.

We now consider some of these filters in detail, along with their attributes and shortcomings.

6.1 Distributed feedback, Fabry–Perot, superstructure, and moiré gratings

The general form of the band-pass filter described in this section is a grating or a combination of gratings physically written at the same location. The composite transmission spectrum of this band-pass filter can be a single or a series (one to many) of high transmission windows separated by bands that are rejected by reflection.

6.1.1 The distributed feedback grating

The distributed feedback fiber grating is probably the simplest band-pass filter and comprises a phase-step within the length of the grating. It is a Fabry–Perot filter with a gap of less than one Bragg wavelength. The position and the size of the phase step determine the position and the wavelength of transmission band. A schematic of this grating is shown in Fig. 6.1.

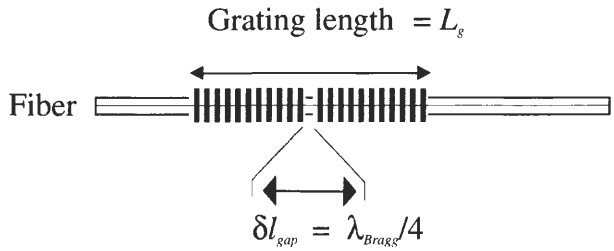

Figure 6.1: The fiber DFB Bragg grating. A transmission peak appears in the center of the band stop when the gap is precisely $\lambda/4$.

The DFB structure is used in semiconductor lasers to enable single frequency operation [1,2]. The single $\lambda/4$ phase-shifted DFB [1] has a pass band in the middle of the stop band. The pass band has a very narrow Lorentzian line shape. While this narrow pass band is useful for filtering, the need exists for broader-bandwidth, high-finesse transmission filters. Cascading several such structures leads to an improved, broader transmission bandwidth [3–5], and has been generally well known in electrical filter design. The developments in fiber Bragg grating technology have made it possible to fabricate direct in-fiber analogs. Low-loss, high-finesse filters, using both a single $\lambda/4$-shifted and cascaded phase-shifted DFB structures have been reported in the literature [6,7]. Rare-earth-doped fiber DFB lasers (see Chapter 8) have also been demonstrated [8].

Coupled-mode analysis developed in Chapter 4 leads directly to the fields in each grating. The matrix method provides a simple route to the transfer function of the DFB structure. Recalling Eq. (4.8.22), the transfer matrix of the DFB is

$$T_{DFB} = T^2 T^{ps} T^1, \tag{6.1.1}$$

where TP^s is the phase shift matrix shown in Eq. (4.8.19)

$$T^{ps} = \begin{bmatrix} e^{-i(\phi/2)} & 0 \\ 0 & e^{+i(\phi/2)} \end{bmatrix}. \tag{6.1.2}$$

Remembering that the transfer matrix elements of T^1 and T^2 are described by Eqs. (4.8.18)–(4.8.21) immediately leads to the solution for the DFB transfer function, T_{DFB}:

$$\begin{aligned} T^{DFB} &= \begin{bmatrix} T_{11}^2 T_{11}^1 T_{11}^{ps} + T_{12}^2 T_{21}^1 T_{22}^{ps} & T_{11}^2 T_{11}^1 T_{11}^{ps} + T_{12}^2 T_{22}^1 T_{22}^{ps} \\ T_{21}^2 T_{11}^1 T_{11}^{ps} + T_{22}^2 T_{21}^1 T_{22}^{ps} & T_{21}^2 T_{12}^1 T_{11}^{ps} + T_{22}^2 T_{22}^1 T_{22}^{ps} \end{bmatrix} \\ &= \begin{bmatrix} T_{11}^{DFB} & T_{12}^{DFB} \\ T_{21}^{DFB} & T_{22}^{DFB} \end{bmatrix}. \end{aligned} \tag{6.1.3}$$

The transmitted power according to Eq. (4.8.8) is

$$|\tau^{DFB}|^2 = \left| \frac{1}{T_{11}^{DFB}} \right|^2 = \frac{1}{T_{11}^{DFB}(T_{11}^{DFB})^*} = \left| \frac{1}{T_{11}^2 T_{11}^1 T_{11}^{ps} + T_{12}^2 T_{21}^1 T_{22}^{ps}} \right|^2, \tag{6.1.4}$$

where * indicates the complex conjugate, and $T_{22}^{ps} = (T_{11}^{ps})^*$.

From conservation of energy, we find that the reflectivity

$$|\rho^{DFB}|^2 = 1 - |\tau^{DFB}|^2. \tag{6.1.5}$$

Note that in general both grating sections need not be placed symmetrically around the phase step and that the gratings may have different bandwidths and refractive index modulation amplitudes. However, the simple band-pass filter has, in the center of a uniform grating, a $\pi/2$ phase step, which has the effect of introducing a single pass-band in the transmission spectrum. In this case, $T_{21}^1 = (T_{12}^2)^*$, and $T_{11}^1 = T_{11}^2$. Figure 6.2 shows the band-pass spectrum of two 3-mm-long gratings, each with a quarter-wavelength step in the center. The amplitudes of the refractive index modulation are 5×10^{-4} and 10^{-3}. Notice that although there is a very narrow transmission band in the center of the grating spectrum within a band stop of ~1 nm, there are strong side lobes on either side. The band pass is a highly selective filter within a relatively narrow band stop. A uniform grating of the same length but without the phase step has a bandwidth approximately half that of the full band stop of the DFB grating. The DFB grating may be viewed as being composed of two single gratings, each half the length of a uniform one.

The phase mask allows the replication of phase-shifted DFB structures into fibers in a simple and controlled manner [6]. This has been done successfully to produce a variety of band-pass DFB structures, and

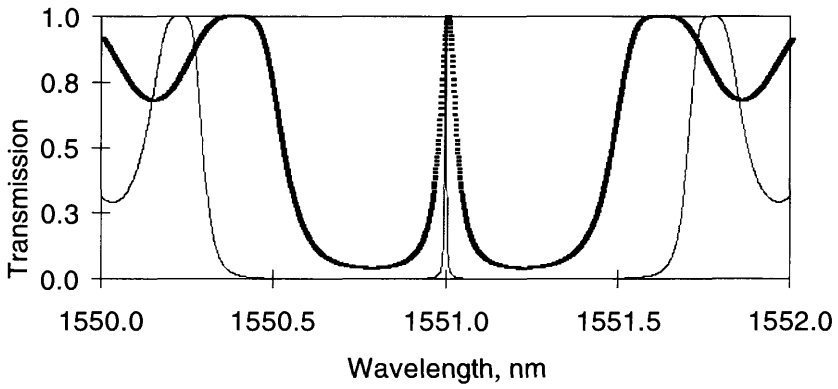

Figure 6.2: The calculated transmission spectrum of 3-mm-long DFB gratings, with a $\lambda/4$ phase-step and refractive index modulation 5×10^{-4} for the dashed line and 10^{-3} for the continuous line, respectively.

the transmission spectrum of one such grating is shown in Fig. 6.3. In this grating, a phase step of $\lambda/4$ was introduced in the middle of the phase mask and replicated. This type of grating is a simple Fabry–Perot interferometer that has a band stop inversely proportional to $\sim 0.25Lg$. A feature to note is the second peak on the side of the main band pass, which is due to the birefringence of the fiber estimated from the separation to be $\sim 1 \times 10^{-5}$. The combination of photoinduced and intrinsic birefringence becomes apparent with the extremely narrow band-pass structure of the DFB grating. The finesse of this DFB grating was ~67. The transmission peak is very sensitive to losses within the grating structure. Note that although the band pass has not been fully resolved, there is OH^- absorption loss in this grating because of hydrogenation, and consequently, the transmission peak is diminished.

Phase shifts within a grating can be produced in several ways. Canning and Sceats [7] showed that postprocessing the center of a uniform grating with UV radiation results in a permanent phase-shifted structure. This method relies on the fact that the UV radiation changes the refractive index locally to produce an additional phase shift [53]. The UV-induced refractive index change required in a 1-mm-long fiber for a $\lambda/4$ phase shift at a wavelength of 1530 nm is $\sim 3.8 \times 10^{-4}$, which is easily achieved. The DFB structure in a rare-earth-doped fiber is useful for ensuring single-frequency operation [9], in much the same way as semiconductor DFB lasers. An inexpensive high-quality fiber-compatible laser exhibiting extremely low noise is particularly attractive for telecommunications. Initial

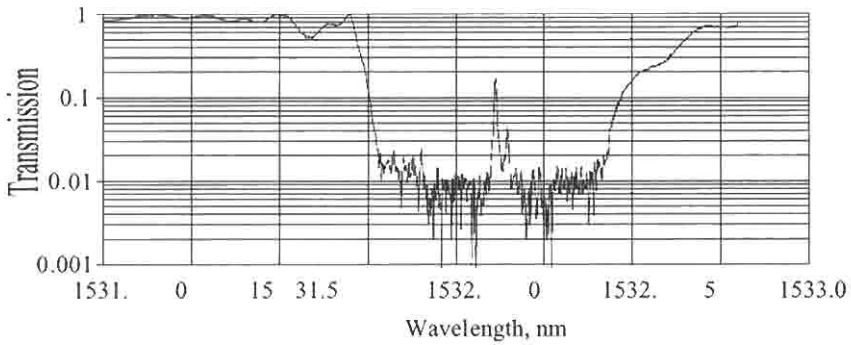

Figure 6.3: Transmission characteristics of an 8-mm-long DFB grating produced by replication of a phase mask with a $\lambda/4$ phase shift in the center [6].

laser diode pumped fiber DFB devices producing ~1 mW single-frequency radiation have already shown the promise of low noise of −160 dB/√Hz [9] (see Chapter 8).

Apodization of the grating leads not only to a smoothing of the side mode structure but also to a reduction in effective length of the grating. The reflectivity is reduced and the band-pass bandwidth increases. There are several apodization envelopes to choose from (see Chapter 5), and they all have a similar effect in unchirped DFB gratings: a reduced reflectivity due to the reduction in the effective length of the grating. Figure 6.4 shows the effect of two such apodization envelopes: the cosine and raised cosine (exponent = 2) for a 3-mm-long DFB with a refractive index modulation amplitude of 1×10^{-3} for both gratings.

Compared to Fig. 6.2, the side-mode structure has been smoothed out. This effect is especially useful for concatenated fiber DFB lasers operating at different wavelengths [10].

The shape of the band pass is not ideal for many applications; a flat top is desirable. In order to increase the bandwidth of the band pass, several concatenated phase steps may be used within a single grating. The principle has been known in filter design [11], and its use was proposed

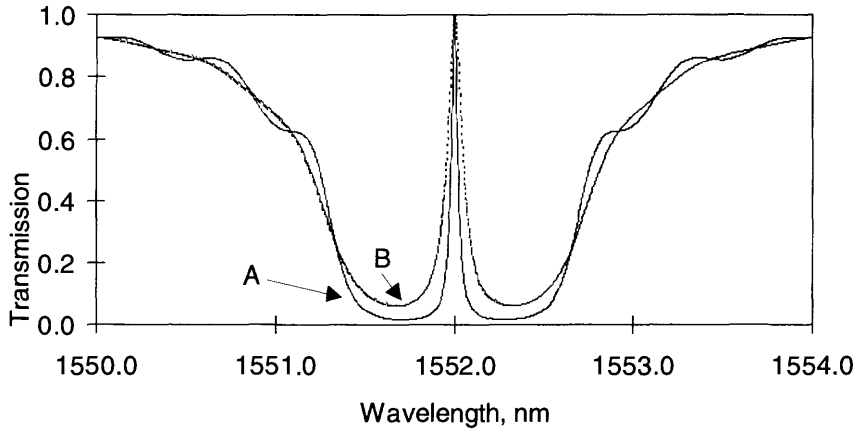

Figure 6.4: Transmission spectra for two 3-mm-long DFB gratings with cosine (A) and raised cosine (B) apodization. The stronger apodization (B) reduces the effective length of the grating and therefore the reflectivity. The FWHM bandwidths of the transmission peaks arc 0.1 nm (B) and 0.05 nm (A).

by Haus for semiconductor DFB structures [3,4]. Figure 6.5 shows the practical implementation of such a grating.

Agrawal and Radic [5] have shown that two phase steps place in the grating open a second band pass. The position and size of the phase step shifts the location of the band pass within the band stop of the grating spectrum. The transmission spectrum for a simple case of two symmetrically placed phase shifts of $\pi/2$ is shown in Fig. 6.6.

Two peaks have appeared in the transmission spectrum. The two band-pass peaks can be made to coalesce or move apart by altering the ratio of the lengths of the grating sections. By choosing several phase

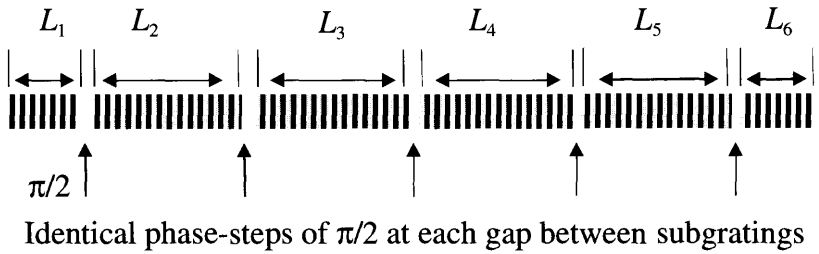

Figure 6.5: The schematic of a cascaded, quarter-wavelength shifted DFB filter, comprising gratings of identical length symmetrically placed around the center.

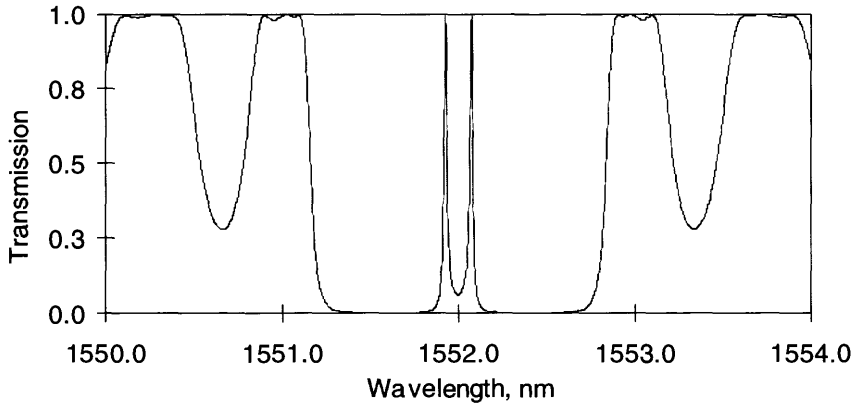

Figure 6.6: A 3-mm-long grating with two $\pi/2$ phase shifts 1 mm apart. The refractive index modulation amplitude is 1×10^{-3}.

shifts Zengerle and Leminger [4] demonstrated the ideal ratios of the lengths of the gratings for an optimized pass band. A quality factor s, defined as the ratio of the pass bandwidth at 10% and 90%, is 0.16 for a single phase-step DFB grating with a coupling constant $\kappa L \approx 2.9$. A length sequence of 1:2:2.17:2.17:2:1 appears to produce a ripple of only 0.3 dB within the pass band with a quality factor of ~0.87. This ratio of the grating lengths will produce the quality factor irrespective of the overall length of the grating. The design was for a semiconductor grating, and the target was for a 0.4-nm band-pass filter. In Fig. 6.5, six gratings are shown with intermediate phase shifts. The lengths $L_1 = L_6 : L_2 = L_5 : L_3 = L_4$ should therefore have the ratio of 1:2:2.17. Note the flat-top pass band.

Wei and Lit [12] have examined symmetrical configurations of 3 and 4 phase-shifted structures. Unity transmission occurs for a symmetrical three-grating-section filter with two $\pi/2$ phase shifts when the grating at either end is half the length of the grating(s) in between. Although this is not a unique condition for unity transmission at the Bragg wavelength (see, for example, Fig. 6.7) in a multisection grating, the three-section and four-section gratings (two phase shifts and three phase shifts) have been shown to have a near unity transmission at the Bragg wavelength if the ratio C of ~2 is maintained; i.e., for the four-section grating, $L_1 : L_2 : L_3 : L_4 \approx 1:2:2:1$, for a variety of coupling constants, κL up to ~2.5. It

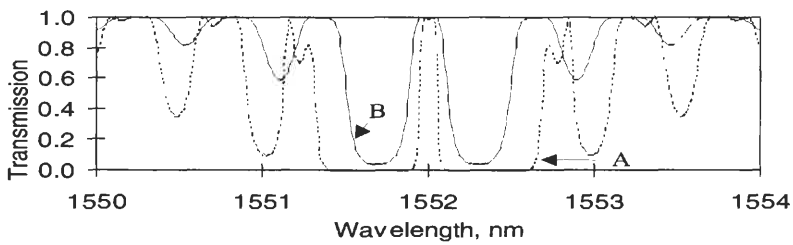

Figure 6.7: Transmission spectrum of two gratings with $4 \times \lambda/4$ cascaded phase step and cosine apodized envelope. Five equal-length gratings of 1.50 mm each have been used, giving a total length ~7.5 mm. The refractive index modulation amplitude is 5×10^{-4}(B) and 1×10^{-3}(A). The FWHM bandwidth of the central pass band is approximately 0.25 nm (B) and 0.1 nm (A); compare with the grating spectra in Fig. 6.4, which have the same individual grating lengths. The bandwidth of (A) above is the same as in Fig. 6.4B, but has a flat top and a squarer profile, with a quality factor of 0.65 (see text) for a κL of ~4.

appears that the ratio for the sections $C = 2$ is an asymptotic value for a flat-top band-pass filter. Increasing this ratio introduces a ripple in the band pass as a result of the individual band-pass peaks separating, while reducing it narrows the bandwidth of the pass band, also reducing the transmission. The ripple in the pass band may be kept between 1% and 5% for a ratio of $1.8 < C < 2.6$.

The bandwidth of the band pass is inversely dependent on the coupling constant. In order to maintain a reasonable bandwidth of the filter, coupling constants must remain low ($\kappa L \sim 1$), as should the grating section ($L_1 < 1$ mm). For example, in the three-section grating, section lengths of 0.5 and 1 mm with a $\kappa L_1 = 1.4$ will result in a bandwidth of ~0.25 nm.

These results change with larger number of sections. For example, Fig. 6.7A shows the transmission spectrum for a grating with a $\kappa L_1 \sim 1.4$, but with a FWHM bandwidth of ~0.1 nm. The bandwidth is exactly the same as the single-phase-step DFB grating shown in Fig. 6.4B, but the square top shows that the roll-off is steeper for the larger number of sections [12]. A major concern is the trade-off between the bandwidth and extinction. For many filter applications, an extinction of >30 dB is necessary. This requirement immediately points to a $\kappa L > 4.16$. Therefore, this filter may not be an ideal candidate, since both requirements may be difficult to achieve.

Fiber Bragg gratings with multiple phase-shifted sections have been realized for band-pass applications. Bhakti and Sansonetti [13] have modeled the response of gratings with up to eight phase-shifted sections. The design strategy was for an optimized band-pass filter with a ~0.8-nm bandwidth, as well as negligible in-band ripple. Increasing the number of sections was shown to make the pass band more rectangular, but reduced the stopped bandwidth. An asymptotic value for the band-stop bandwidth is approached with greater than 5 phase shifts and is twice the pass bandwidth. This is another severe limitation on the use of such filters. Phase masks with the appropriate quarter-wavelength shifts [6] were used to replicate a three-phase-shift grating. With careful UV illumination, the band pass was fully resolved and showed excellent agreement with theory [13]. The band-pass/stop widths were 0.88 nm/2.77 nm with a peak rejection of 13 dB. The optimized grating length were $L_1 = L_4 = 0.22$ mm and $L_2 = L_3 = 0.502$ mm, with a refractive index modulation amplitude of 1.5×10^{-3}.

While the principle of multiple phase shift within a single grating is useful, it has the additional effect of increasing the side-lobe structure despite apodization. The side lobes increase as a result of the formation of a super structure (see Chapter 3) and is discussed in the next section. Other methods need to be used to position the band pass and for a broader-bandwidth band pass and more controllable bandwidth of the band stop.

A simple technique to accurately create a band pass at a particular wavelength is to introduce a phase step within a chirped grating. A start and a stop Bragg wavelength characterize a chirped grating. In a linearly chirped grating, the position of the local Bragg wavelength is uniquely known. Placing a $\pi/2$ phase step at that point results in a band pass at the local Bragg wavelength.

Figure 6.8 shows the transmitted spectrum of two 10-mm-long gratings. Data A and B refer to the same spectrum, with B displayed on a 30 times expanded wavelength scale. A shows the effect of a single quarter-wavelength phase step in the center, while C shows the step at one-third the distance from the long-wavelength end of the grating. The effect of the stitch is localized in the reflected spectrum, and several more band-pass structures may be placed within this grating. For example, a band-pass every 2 nm is easily achieved. However, the effects of the super

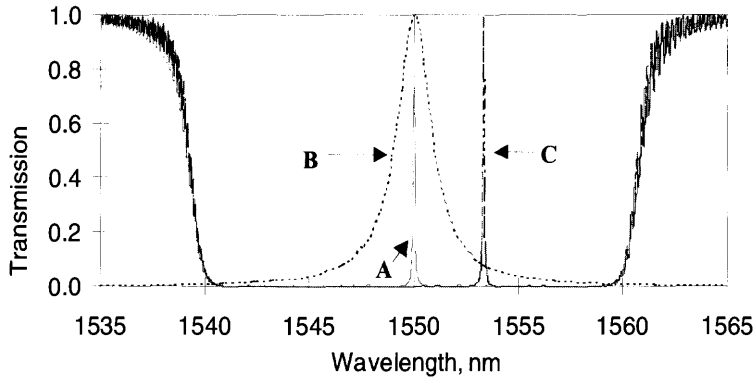

Figure 6.8: The transmission spectrum of a grating with a single $\pi/2$ phase step in the center of a chirped bandwidth of 20 nm (A). An ×30 expanded view of the band-pass spectrum is also shown (B). Also shown is the effect of placing the phase step at $2/3L_g$ (C); the band-pass peak shifts to the local Bragg wavelength. The grating is 10 mm long.

structure become apparent in that additional peaks appear and the band-pass spectrum acquires side lobes. A 10-mm-long grating transmission spectrum with 20 phase steps is shown in Fig. 6.9. Note that within the pass band of the grating there is a small associated dispersion since the grating is chirped. Since the gratings are used as a band-pass, rather than in reflection, dispersion is less of an issue, other than at the band edges. Apodization only helps slightly; it also reduces the bandwidth and the extinction at the edges of the grating, so that it is of limited value.

Blanking-off part of a chirped grating during fabrication instead of introducing phase steps is an effective way of creating a band-pass filter [14]. The net result is that part of the chirped grating is not replicated, thus opening a band gap. This principle is effective for a narrow-bandwidth band pass (1 nm) so long as $\kappa L < \pi$. With a stronger reflectivity grating, the bandwidth of the band stop increases to encroach on the band pass from both sides, reducing the pass-band width. An alternative technique uses UV postprocessing first reported for UV trimming of the refractive index of photosensitive waveguides [53], to erase part of the chirped grating written in a fiber [15]. In order to fabricate a single band pass within a broad stop band (>50 nm), several chirped gratings may be concatenated along side a chirped grating with the band gap. With care and choice of chirped gratings, single and multiple band-pass filters

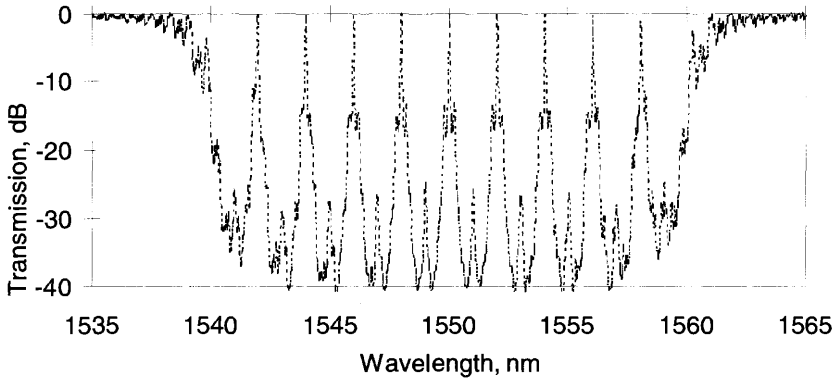

Figure 6.9: A $20 \times \pi/2$ phase-step grating band-pass filter. Each band pass has an extinction of >30 dB, but with some side-lobe structure at −15 dB. Ghosts appear between the main pass bands as a result of the super structure of phase steps at −30 dB transmission.

have been successfully demonstrated, with a pass/stop-bandwidth of 0.17 nm/11.3 nm and extinction of ~10 dB. A four-channel filter evenly spaced over a stop bandwidth of 50 nm has also been reported [15]. Insertion loss of these types of chirped filters is a problem, since radiation loss on the blue-wavelength side affects the maximum transmission of the pass band. As a consequence of large κL and radiation loss, a maximum transmission of ~75% was reported for these band-pass filters.

Broader pass-bandwidth filters may be fabricated by the use of concatenated chirped gratings [16]. The effects of "in-filling" due to the use of large κL values are diminished by increasing the band-pass width. The arrangement for such a filter allows better extinction in the stop band (>30 dB) while permitting the placement of the band-pass at the required wavelength. Additionally, chirped gratings show reasonably smooth stop band edges. Concatenating two such gratings with a nonoverlapping band stop results in a band pass between the two band-stop regions. While this scheme has been applied to chirped gratings, Mizrahi *et al.* [17] have shown that two concatenated highly reflective gratings with a pass band in between the Bragg wavelengths can be used as a band-pass filter. Radiation loss within the pass band are avoided by using a strongly guiding fiber, which further blue-shifts the radiation loss spectrum from the long-wavelength stop band. The bandwidth of the pass band was ~1.6 nm with an extinction in excess of 50 dB and a stop band of ~6 nm.

6.1.2 Superstructure band-pass filter

It has been shown that placing more than a single $\lambda/4$ phase step within the grating results in as many band-pass peaks appearing within the band stop [12]. This principle may be extended to produce the superstructure grating [18,22], but works in reflection. The reflection spectrum has several narrow-bandwidth reflection peaks. The principle has been used in semiconductor lasers to allow step tuning of lasers. However, a badly stitched phase mask will produce similar results. Since a phase mask is generally manufactured by stitching small grating fields together, errors arise if the fields are not positioned correctly. These random "phase errors" are like multiple phase shifts within the grating, resulting in multiple reflection peaks, each with bandwidth inversely proportional to the overall length of the grating, and spaced at wavelength intervals inversely pro-

portional to the length of the field size (see Chapter 3). Figure 6.10 shows the super structure on a 30-mm-long grating reproduced from a phase mask with stitching errors. Despite these errors, the grating reflection and phase response for the main peak are very close to being theoretically perfect [19]. The theory of superstructure gratings is discussed in Chapter 3.

For filter applications, it is necessary to achieve the appropriate characteristics. Here we consider the spectra of short superstructure gratings, which may be conveniently fabricated with an appropriate phase mask. Figure 6.11 shows the reflection and transmission characteristics of a superstructure grating, comprising 11 × 0.182 mm long gratings, each separated by 1.555 mm. The overall envelope of the transmission spectrum (see Fig. 6.11b) has been shown in Chapter 3 to be governed by the bandwidth of the subgrating.

Note in Fig. 6.11a that the bandwidth of the adjacent peaks becomes smaller. This is a function of the reflectivity at the edges of the grating. In order to use this filter as a band-pass filter, it is necessary to invert its reflection spectrum. This may be done by using a fiber coupler. However, the input signal is split into two at the coupler. One half is reflected from the grating and suffers another 3-dB loss penalty in traversing the

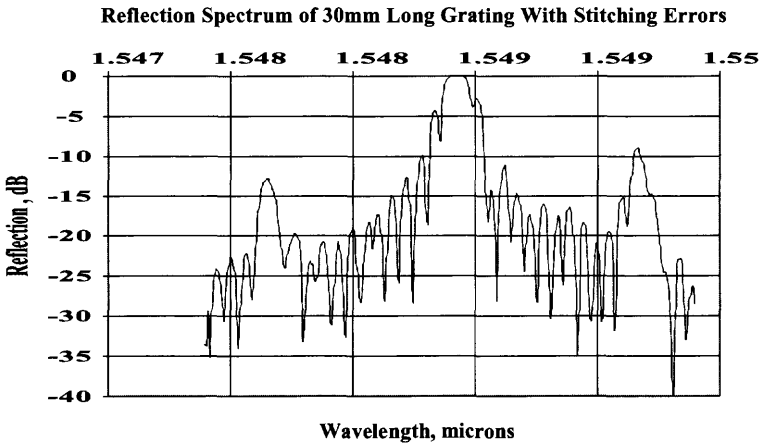

Figure 6.10: Reflection spectrum of superstructure grating. The disadvantage of the superstructure grating—the reflection coefficient cannot be made the same for each reflection [29]. This limitation can be overcome by using a different type of moiré grating [20], which has been discussed in Chapter 3.

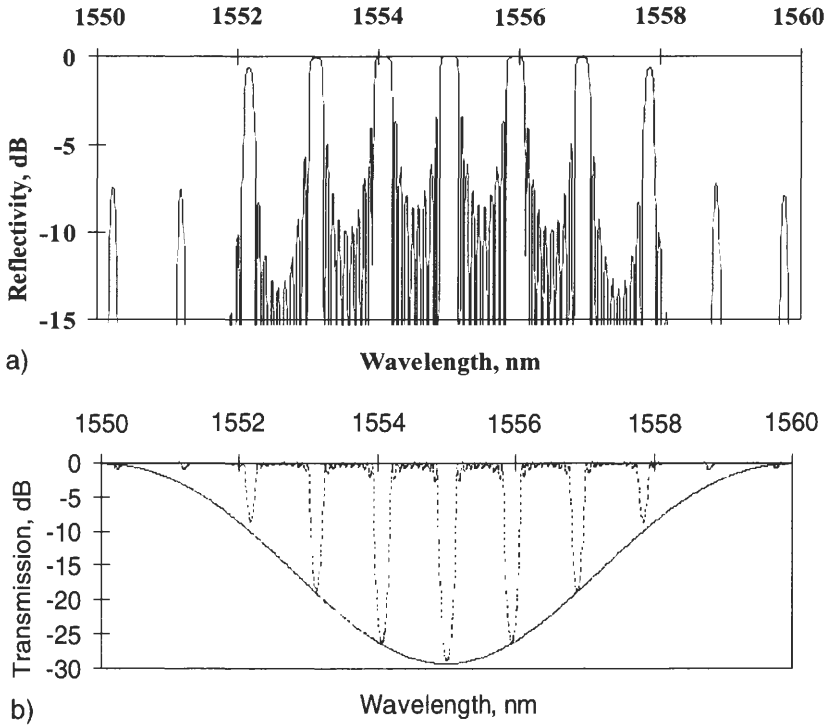

Figure 6.11: (a) The reflectivity spectrum of a superstructure grating with 9×222 micron grating sections separated by 1-mm gaps. Refractive index modulation amplitude is 10^{-3}. (b) The transmission spectrum of the grating shown in (a). Also shown is the transmission spectrum of a single section of the grating of 0.181 microns long. The envelope has been normalized to fit the superstructure spectra.

coupler once again. The reflected spectrum is therefore −6 dB relative to the input signal. A fiber circulator overcomes this loss penalty [21]. The insertion loss of a circulator is approximately 1 dB, so that an efficient multiple band-pass filter can be fabricated.

In an interesting demonstration, a chirped superstructure grating has been used for multiple-channel dispersion compensation, since the repeat band stops have a near-identical chirp [22]. The advantage of such a scheme is that it requires only a single temperature-stabilized grating to equalize several channels simultaneously, although the reflection coefficient varies for each reflection.

6.2 The Fabry–Perot and moiré band-pass filters

The fiber DFB grating is the simplest type of Fabry–Perot (FP) filter. Increasing the gap between the two grating sections enables multiple band-pass peaks to appear within the stop band. The bandwidth and the reflectivity of the gratings determine the free-spectral range and the finesse of the FP filter. The grating FP filter has been theoretically analyzed by Legoubin *et al.* [23]. Equations (6.1.4) and (6.1.5) describe the transfer characteristics of the filter and have been used in the simulation of the gratings in this section.

Figure 6.12 shows the structure of a Fabry–Perot filter. These filters work in the same way as bulk FP interferometers, except that the gratings are narrow-band and are distributed reflectors. A broader bandwidth achieved with chirped gratings creates several band-pass peaks within the stop band. Control of the grating length L and the separation δl allows easy alteration of the stop-band and the free-spectral range.

At zero detuning, the peak reflectivity of a FP filter with identical Bragg gratings is

$$R_{FP} = \frac{4R}{(1 + R)^2}, \tag{6.2.1}$$

where R is the peak reflectivity of each grating. Since the gratings are not point reflectors, the free-spectral range (FSR) is a function of the effective length of the grating, which in turn is dependent on the detuning. For a bulk FP interferometer, e.g., a fiber with mirrors, the FSR is [23]

$$FSR = \frac{1}{2dn_{eff}(\lambda)}. \tag{6.2.2}$$

The distance between the mirrors is d, and the effective index of the mode

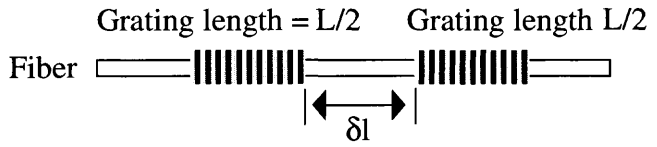

Figure 6.12: A schematic of a Fabry–Perot etalon filter. In the simple configuration, the gratings are identical, although in a more complicated band-pass filter, a dissimilar chirped grating may be used.

n_{eff} is a function of wavelength. For an equivalent fiber-grating-based FP interferometer, the thickness d becomes a function of wavelength, and only at the peak reflectance is the FSR largest. The effective thickness is the separation between the inner edges of the gratings plus twice the effective length of the gratings. Off resonance, the penetration into the grating is greater than on-resonance, leading to a bigger thickness. Therefore, at the edges of the FP bandwidth, the FSR becomes smaller.

The first in-fiber grating FP filter was reported by Huber [24]. A transmission bandwidth of 29 pm was reported. Further multi-band-pass in-fiber FP resonators have also been demonstrated [25]. In the latter report, a 100-mm-long FP interferometer was fabricated with two 95.5% reflecting gratings. A finesse of 67 was achieved with the free spectral range of 1 GHz and a pass bandwidth of 15 MHz. In order to measure the transmission spectrum of the FP, a piezoelectric stretcher was used to scan the fiber etalon in conjunction with a fixed frequency DFB laser source operating within the bandwidth of the grating band stop, at a wavelength of 1299 nm. A peak transmission of ~86% of the fringe maximum was also noted. Figure 6.13 shows the transmission characteristics of a FP filter made with two gratings, each 0.5 mm long with a 5 mm separation and a refractive index modulation of 2×10^{-4}. The weak ripple within the band-stop of the filter is due to the poor finesse of the FP but is ideal in WDM transmission to control solitons. The shortest gratings

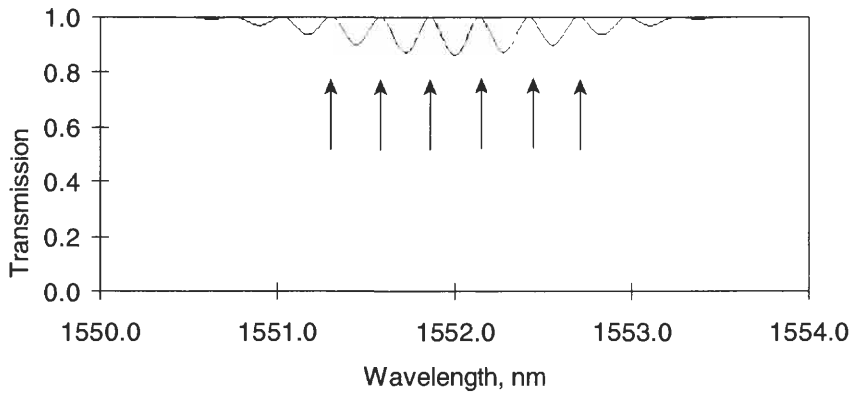

Figure 6.13: A FP filter with a 5-mm gap. Grating lengths are 0.5 mm with index modulation of 2×10^{-4}. The arrows show where WDM channels may be placed within the band-pass filter for soliton guiding.

in a FP filter reported to date are ~0.3 mm long, separated by a similar distance [26]. The resulting multiple band pass, which was a shallow ripple of ~50% transmission was used as a guiding filter in wavelength division multiplexed soliton transmission experiments to suppress Gordon–Haus jitter [27].

With stronger gratings, multiple band-pass filters with deeper band stops are easily possible. However, even slight loss in the grating (absorption due to OH^- ions) can degrade the transmission peaks substantially. It is therefore advantageous to use deuterated fiber for this type of a filter. Figure 6.14 demonstrates a 4-mm-long grating with a gap of 5 mm in the center. This filter shows ~30-dB extinction in the center of the band pass.

Note that all these filters have a similar narrow band-pass response that plagues the highly reflecting DFB grating filter. Thus, applications for such a grating are likely to be in areas in which either high extinction or high finesse, or low extinction and large bandwidth are required. Figure 6.15 shows the measured transmission of a 0.6-mm-long FP filter with a 2.5-mm gap. The pass bands have been measured with a resolution of 0.1 nm and are therefore not fully resolved. The structure should be deeper and much narrower. Nevertheless, the dips in transfer characteristics match the theoretical simulation extremely well with the parameters shown. Typically, the best results for band-pass peaks for this type of FP filter, using either chirped or unchirped gratings with an extinction of 30 dB, is ~70%.

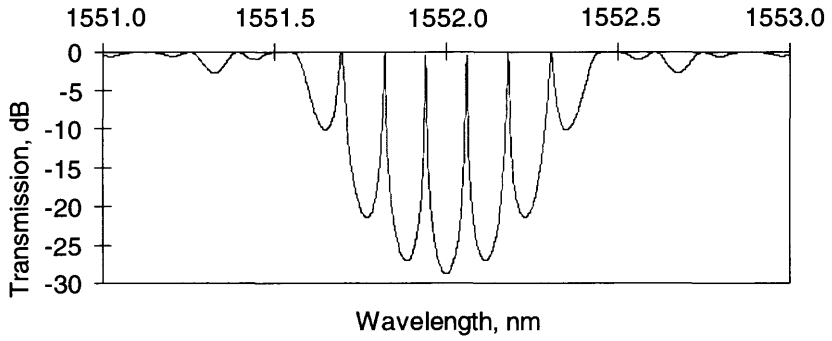

Figure 6.14: A 4-mm-long grating FP filter with a 5-mm gap and a Δn of 5×10^{-4}.

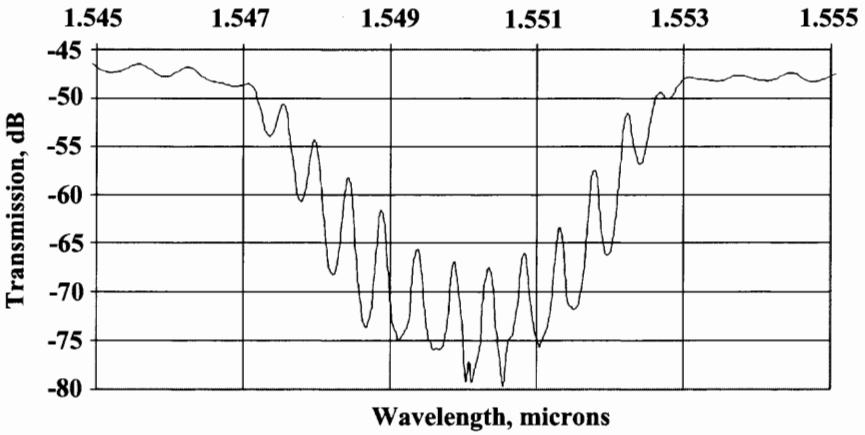

Figure 6.15: Measured transmission characteristics of a fiber FP filter. The length of each grating was 0.3 mm, a 2.5 mm gap and with a peak-to-peak refractive index modulation of 5×10^{-3}. A theoretical fit to the data shows excellent agreement, although the peak transmission has not been fully resolved in the measurement [29]. A maximum extinction of >30 dB was measured.

Wide-bandwidth (140-nm) fiber grating Fabry–Perot filters fabricated in boron–germanium codoped fibers have been demonstrated with a finesse of between 3 and 7 [28]. Two identically chirped, 4-mm-long gratings with a bandwidth of ~150 nm and reflectivity of >50% were written in the fiber, displaced from each other by 8 mm. The resulting FP interference had a bandwidth of 0.03 nm and a free-spectral range of 0.09 nm. A larger free-spectral range was obtained by overlapping the gratings with a linear displacement of 0.5 mm. These gratings had a bandwidth of 175 nm in the 1450–1650 nm wavelength window. A finesse of 1.6 with an FSR of 1.5 nm was demonstrated. These fiber-grating FP-like devices may find applications in fiber laser and WDM transmission systems.

A further possibility of opening up a gap within the stop band is to write two gratings of slightly different Bragg wavelengths at the same location in the fiber [30] to form a moiré fringe pattern. The physical reason why a band pass results may be understood by noticing that the phase responses of the gratings are not identical. Thus, at some wavelength, the phases can be out by π radians. If the wavelength difference is made larger, it is possible to create more than one band pass. The mechanics of producing such a band pass have been demonstrated by

slightly altering the angle of the incoming beams in between the writing of the two gratings [30]. Unless the angle can be measured accurately, it may be difficult to reproduce the results with precision. Two gratings can be superimposed in a fiber by writing one grating with a chirped phase mask [31] and then stretching the fiber before writing the second [32,33]. The basic principle of moiré grating formation is discussed in Chapter 5. However, for clarity, we consider the interference due to two UV intensity patterns to produce a grating with the refractive index profile

$$\Delta n(z) = \Delta n\left[2 + 2\cos\left(\frac{2\pi z}{\Lambda_e}\right)\cos\left(\frac{2\pi z}{\Lambda_g}\right)\right], \tag{6.2.3}$$

in which the slowly varying envelope with period Λ_e is a result of the difference between the two grating periods, and the chirped grating period is Λ_g. If the envelope has a single cosine cycle over the grating length (the grating periods have been chosen to be such; see Chapter 5), then the effect of the zero crossing of the envelope is equivalent to a phase step of $\pi/2$ at the Bragg wavelength (see Chapter 5, Section 5.2.7). This grating is simple to simulate using the matrix method; the apodization profile of the grating can be specified to have n cycles of a cosine function, where $n = 1$ is a single cycle of a cosine envelope (see Fig. 5.18). The computed transmission spectrum of this type of a band-pass filter is shown in Fig. 6.16. The experimentally achieved result is almost identical to that shown in Fig. 6.16 [33], apart from the short-wavelength radiation loss apparent just outside the band-stop spectrum in the measured result.

The problem with this type of phase-shifted grating has already been discussed: There remains a trade-off between bandwidth and extinction, although it is a convenient method of producing a multiple-band-pass filter by increasing the number of cycles of the modulation envelope.

6.3 The Michelson interferometer band-pass filter

The Michelson interferometer (MI) may be used as a fixed-wavelength band-pass filter. Since the coupler shown in Fig. 6.17 splits the input power equally into the two ports, the light that is reflected from a single 100% reflection grating (HR1) is again equally split between ports 1 and 2. Thus, only 25% of the light is available in the pass band at port 2.

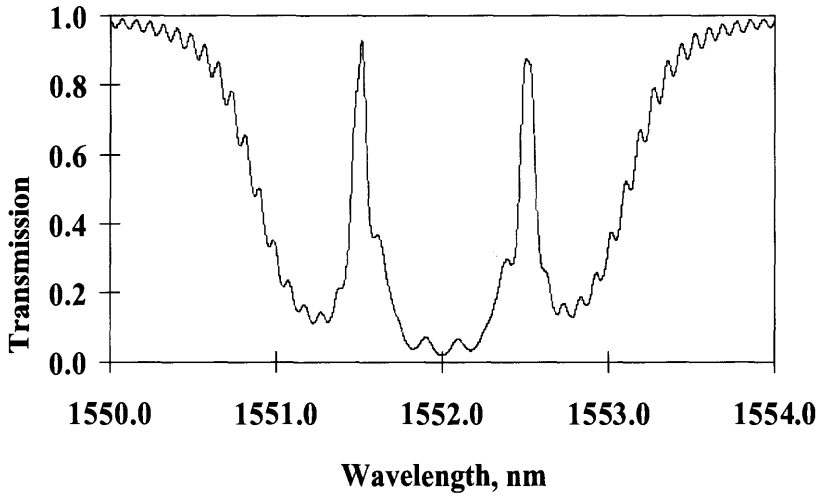

Figure 6.16: Transmission spectrum of a moiré grating with a single period cosine envelope of the modulation refractive index profile over the length of the grating. This grating is formed by colocating two chirped gratings with slightly different center wavelengths.

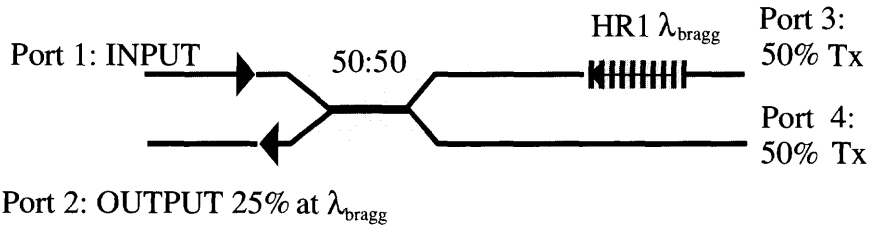

Figure 6.17: A fiber coupler with a single grating in one arm. The output in port 2 is 25% of the input power in port 1. The transmitted signal at the Bragg wavelength at port 3 is $(1 - R)$, where R is the grating reflectivity.

This arrangement works as an effective band-pass filter despite the loss. However, there are methods that be used to eliminate the insertion loss of this filter.

With two identical gratings, one in each arm of the MI, 100% of the reflected light can be routed to port 2. The principle of operation was originally proposed by Hill *et al.* [34], for a grating in a loop mirror

configuration. A similar device is shown in Fig. 6.18. The light reflected from HR2 arrives at the input port π out of phase with respect to light from HR1. Light from HR1 and HR2 arrives in phase at the output port 2, so that 100% of the light at the Bragg wavelength appears at this port. The through light is equally split at ports 3 and 4, incurring a 3-dB loss. However, the phase difference between the reflected wavelengths arriving at the coupler has to be correct for all the light to be routed to port 2.

The first demonstration of such a device in optical fibers was reported by Morey [35]. This all-fiber band-pass filter was made out of a standard fiber coupler with fiber gratings written into the two arms. Stretching the gratings showed limited tunability, but no data was available on stability of the filter. Since differential changes in the ambient temperature between the arms can detune the filter, it is essential that the two arms remain in close proximity and that the optical paths to and from the gratings be minimized.

The fiber Michelson interferometer has been used extensively for sensing applications with broadband mirrors deposited on the ends of the fiber [36]. The principle of operation of the grating-based filter is a simple modification of the equations that describe the broadband mirror device. We begin with the transfer matrix of the fiber coupler [37],

$$\begin{bmatrix} R \\ S \end{bmatrix} = \begin{bmatrix} \cos(\kappa L_c) & -i\sin(\kappa L_c) \\ -i\sin(\kappa L_c) & \cos(\kappa L_c) \end{bmatrix} \begin{bmatrix} A_i \\ B_i \end{bmatrix}, \tag{6.3.1a}$$

where R and S are the output field amplitudes at ports 3 and 4, A_i and B_i are the field amplitudes at ports 1 and 2 of the coupler, L_c is the coupling length of the coupler, and κ is the coupling constant, which

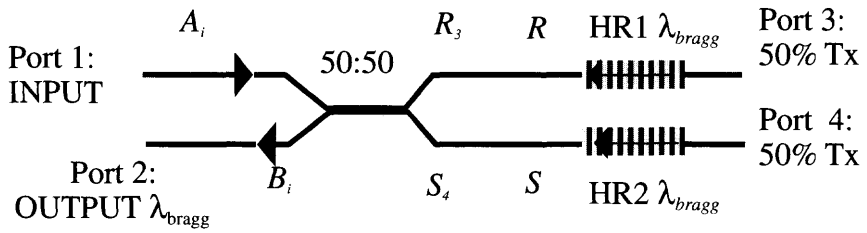

Figure 6.18: The Michelson interferometer band-pass filter. All the input light is equally split at the coupler into the output ports. The identical gratings in each arm reflect light at the Bragg wavelength, while allowing the rest of the radiation through.

depends on the overlap of the electric fields E_1 and E_2 of the coupled modes,

$$\kappa = -\frac{\omega\varepsilon_0}{4P_0}\int_{-\infty}^{+\infty}\int_{-\infty}^{+\infty}(n_{co}^2(x,y) - n_{cl}^2)E_1^* \cdot E_2\, dxdy, \qquad (6.3.1b)$$

where $n_{co}(x, y)$ is the transverse refractive index profile of the waveguides, n_{cl} is the cladding index and, P_0 is the total power.

For a small difference in the propagation constants, $\Delta\beta$ is small compared to the coupling coefficient, κ. Under these conditions, very nearly all the power can be transferred across from one fiber to the other [38]. With $\Delta\beta \approx 0$ and $(n_{co} - n_{cl})/n_{co} \ll 1$, the following expression for the coupling coefficient can be use [39]:

$$\kappa = \frac{\lambda}{2\pi n_c}\frac{u^2}{a^2v^2}\frac{K_0[w(h/a)]}{K_1^2(w)}. \qquad (6.3.1c)$$

a is the core radius, and the normalized waveguide parameters u, v, and w are defined in Chapter 4, h is the distance between the core centers, and the modified Bessel functions of order 0 and 1, K_0 and K_1, are due to the evanescent fields of the modes in the cladding.

Assuming that there is only a single field at the input port 1 of the coupler, $B_i = 0$. Introducing gratings in ports 3 and 4 with amplitude reflectivities and phases, $\rho_1 \exp[i\phi_1(\lambda)]$ and $\rho_2 \exp[i\phi_2(\lambda)]$ described by Eq. (4.3.11), the normalized field amplitudes at the input to the coupler in ports 3 and 4 are

$$\begin{aligned} R_3 &= \frac{A_3}{A_i} = \sigma_1\rho_1 \cos(\kappa L_c)\exp\left[2i\left(\frac{2\pi n_{eff}L_{f_1}}{\lambda} + \frac{\phi_1(\lambda)}{2}\right)\right] \\ S_4 &= \frac{B_4}{A_i} = -i\sigma_2\rho_2 \sin(\kappa L_c)\exp\left[2i\left(\frac{2\pi n_{eff}L_{f_2}}{\lambda} + \frac{\phi_2(\lambda)}{2}\right)\right], \end{aligned} \qquad (6.3.2)$$

in which the path lengths from the coupler to the gratings are L_{f1} and L_{f2}. The additional factors σ_1 and σ_2 include detrimental effects due to polarization and loss in arms 3 and 4. The output fields, R_1 and S_2, at ports 1 and 2 of the interferometer can be written down by applying Eq. (6.3.1a) again, with the input fields from Eq. (6.3.2). Therefore,

$$\begin{bmatrix} R_1 \\ S_2 \end{bmatrix} = \begin{bmatrix} \cos(\kappa L_c) & -i\sin(\kappa L_c) \\ -i\sin(\kappa L_c) & \cos(\kappa L_c) \end{bmatrix}\begin{bmatrix} R_3 \\ S_4 \end{bmatrix}. \qquad (6.3.3)$$

In Eq. (6.3.3) the normalized field amplitudes R_1 and S_1 fully describe the transmission transfer function of the Michelson interferometer band-

pass filter. Substituting Eq. (6.3.2) into Eq. (6.3.3), and remembering that $\mathrm{Re}(R, S) = 1/2(R, S + R^*, S^*)$, the transmitted power in each output port of the filter is the product of the complex field with their conjugate. By simple expansion and algebraic manipulation of the equations, the power transmittance at ports 1 and 2 can be shown to be

$$t_1 = \frac{1}{2}[2\sigma_1^2\rho_1^2\cos^4(\kappa L_c) + 2\sigma_2^2\rho_2^2\sin^4(\kappa L_c) - \sigma_1\sigma_2\rho_1\rho_2\sin^2(2\kappa L_c)\cos\delta] \quad (6.3.4)$$

$$t_2 = \frac{1}{4}[\sigma_1^2\rho_1^2 + \sigma_2^2\rho_2^2 + 2\sigma_1\sigma_2\rho_1\rho_2\cos\delta]\sin^2(2\kappa L_c), \quad (6.3.5)$$

where the phase difference δ between the reflections from the two gratings is

$$\delta = 2\left[\frac{2\pi n_{eff}}{\lambda}(L_{f_2} - L_{f_1}) + \frac{\phi_2(\lambda) - \phi_1(\lambda)}{2}\right]. \quad (6.3.6)$$

Equations (6.3.4) and (6.3.5) describe how the transmitted power at the output depends on the path-length difference, the reflectivities, and the Bragg wavelengths of the two gratings in the arms of the Michelson interferometer filter. For a 50:50 coupler, $\kappa L_c = \pi/4$; ignoring loss and polarization effects, Eqs. (6.3.5) simplify to

$$t_1 = \frac{1}{2}\left[\frac{1}{2}(\rho_1^2 + \rho_2^2) - \rho_1\rho_2\cos\delta\right] \quad (6.3.7)$$

$$t_2 = \frac{1}{2}\left[\frac{1}{2}(\rho_1^2 + \rho_2^2) + \rho_1\rho_2\cos\delta\right]. \quad (6.3.8)$$

Note that the power transfers is cyclic between the two ports, depending on the phase difference δ and which is of paramount importance for the proper operation of the filter. This cyclic behavior is well known for unbalanced broad band interferometers, but in this device it is restricted to the bandwidth of the gratings. The choice of the gratings determines the wavelength at which the interference will occur. With the phase difference $\delta = 2N\pi$ (where $N \geq 0$ is an integer), all the power is routed to port 1. This phase can to be adjusted mechanically [40], thermally [41], or permanently by optical "trimming" of the path using UV radiation [53].

Detuning of the interferometer is an important issue for the acceptable performance of the band-pass filter. As such, there are two parameters, which are variables in a filter of this type. Assuming that the

bandwidths of the two gratings are identical (nominally identical lengths and refractive index modulation amplitudes), the path difference may drift within the lifetime of the device, or the Bragg wavelengths may not be identical, or may change with time.

Figure 6.19 shows how the band-pass at port 2 varies with changes in the path length for two identical 99.8% reflectivity gratings. At zero phase difference, the transmission is a maximum. The rapid decrease in the band-pass peak with detuning of less than half a wavelength shows that phase stability is critical for the long-term operation of this device. As expected, the transmission drops to zero with a phase difference of $\pi/2$. In most practical cases, it is nearly impossible to match gratings in the two arms exactly, both in reflectivity (and therefore bandwidth) and the Bragg wavelength. The mismatches set a limit to the performance of a band-pass filter.

Figure 6.20 shows the reflectivity spectra of two raised cosine apodized MI gratings, which are offset in their Bragg wavelength by 1% of the FW bandwidth. For the gratings shown, this translates to 0.01 nm difference in the Bragg wavelengths and may well be at the limit of the technology for *routine* inscription and annealing of the gratings.

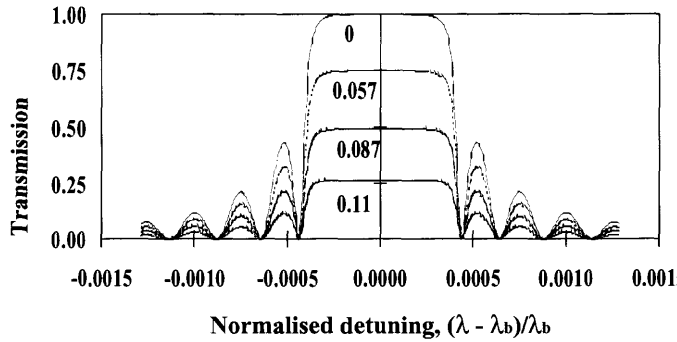

Figure 6.19: The band-pass characteristics of a Michelson interferometer filter showing how the band-pass peak varies with differential path-length difference between the two gratings as a function of normalized detuning. For the calculations, the grating parameters used are: refractive index modulation index amplitude of 1×10^3 and a length of 2 mm [42]. The numbers on the chart refer to the detunings as a fraction of the Bragg wavelength. The figure shows just how critically the path difference needs to be controlled for efficient operation.

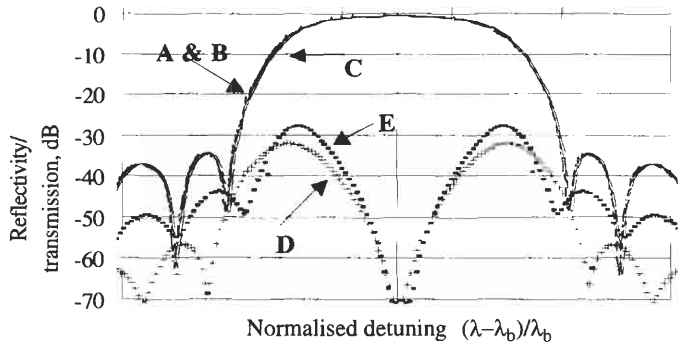

Figure 6.20: Reflection spectra of two 4-mm-long raised cosine apodized gratings mismatched by 0.01 nm (A, B), each with a reflectivity of ~85%. C is the transmission of the band-pass filter with a path-length difference of $0.006 \times \lambda_b$. D shows the light that appears in port 1 of the Michelson. To achieve better than −30 dB extinction (for D), the Bragg wavelengths must be matched to within 0.01 nm. E shows the rejected light in port 1 for cosine apodized gratings with the same Bragg wavelength mismatch. The in-band rejection is never better than −28 dB. With stronger gratings, the Bragg wavelengths have to be even better matched.

The pass band of the filter generally does not suffer from such a small wavelength detuning. Since the reflectivity ensures that only the reflected signal appears in the pass-band with typical insertion losses of between 1 and 0.3 dB [43], it is the remnant signal that appears in the through port (in the Michelson, it is port 1) that is difficult to suppress.

The detuned Bragg wavelength of the gratings translates into an additional imbalance in the path difference of approximately 1 mradian. While UV trimming can balance the paths very accurately, the small difference in the Bragg wavelengths of the two gratings remains. Despite this error, a rejection of greater than 30 dB has been reported [43] and is certainly not an easy achievement, requiring the matching of the Bragg wavelengths to ~0.01 nm. The theoretical spectra shown in Fig. 6.20 are in excellent qualitative agreement with the results of low-insertion-loss band-pass filters fabricated in optical fiber with matched gratings in the close proximity of a coupler [43]. Chirped gratings can be used in the Michelson to broaden the pass bandwidth [44].

With further mismatch in the Bragg wavelengths, the rejection in port 1 deteriorates. One can no longer have a high isolation, since there

is less overlap between the bandwidths of the gratings. The conditions approach the case of a single grating in the coupler arm, when there is no overlap of the grating spectrum. Thus, at least 25% of the input power appears at both ports 1 and 2. While the rejection becomes poor, the band-pass suffers because the bandwidth decreases as a direct result of the limited overlap. Figure 6.21 shows the reflection spectra of gratings in a Michelson that have been detuned by one-quarter of the unapodized FWFZ bandwidth (to the first zeroes). The refractive index modulation amplitude is 1×10^{-3} and the gratings are 4 mm long. Since the interferometer has been detuned as a result of the difference in the Bragg wavelengths, at zero phase difference the band-pass output is not at its maximum (small crosses). As the path difference is changed to $\pi/2$ radians (triangles), a dip begins to appear in the band pass, and with π phase difference (squares), "bat-ears" begin to appear, since at the edges of the band pass,

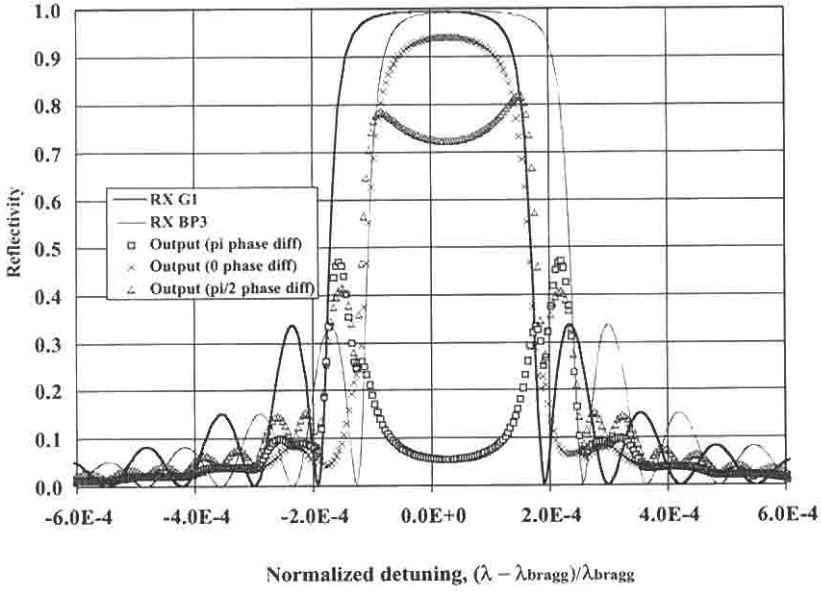

Figure 6.21: The band-pass characteristics show that with slight detuning (0.25 × FW bandwidth) between the two Bragg gratings, a slight reduction in the peak transmissivity occurs (crosses). However, there is an added benefit: reduction in the energy transmitted in the wings of the gratings, i.e., apodization occurs. Note that with larger path length difference, "bat-ears" appear on either side. These normally appear in the rejected port 1 (squares).

there is little overlap of the reflected spectra. Note that at some Bragg wavelength detuning, the interference of the reflected light at the coupler forms moiré fringes, and apodization of the band-pass spectrum begins to occur. In Fig. 6.21 (crosses), note the reduction of the side lobes as the dissimilar phases in the overlapped spectrum tend to cancel the formation of the side lobes.

The filter rejection becomes worse when the detuning is one-half of the FW bandwidth, as shown in Fig. 6.22. In this case, the zero path difference is well off the optimum for band-pass operation (triangles), while squares show the band pass response at π phase difference between the gratings. Although this spectrum is still not the optimized output, note the strong apodization in the wings. The nonoverlapped high-reflectivity (~100%) region (within the bandwidth of each grating) averages to approximately 25% of the input power, as in the case of the single-grating Michelson device.

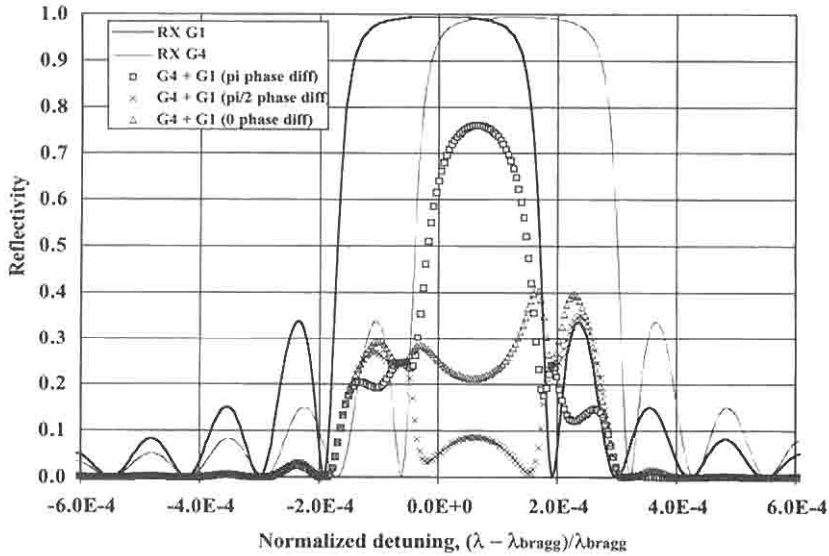

Figure 6.22: Two gratings detuned by approximately 0.5 × bandwidth of the grating. The band-pass characteristics are sensitive to the path-length difference between the Bragg reflection peaks due to differential phase response of the gratings. With detuning, the optimum band-pass shifts from the normal zero phase difference for matched Bragg wavelength case and develops additional structure, although apodization occurs, reducing the reflection in the wings.

6.3.1 The asymmetric Michelson multiple-band-pass filter

Figure 6.19 showed how output power in port 1 varies with path difference δl. The reflected power within the entire grating spectrum is exchanged between port 1 and 2 so long as the detuning

$$\delta l \ll \frac{\lambda^2}{2\Delta\lambda_g}, \tag{6.3.9}$$

where $\Delta\lambda_g$ is the FWFZ bandwidth of the grating. With larger path differences, $n_{\text{eff}}\Delta L_f = n_{\text{eff}}(L_{f1} - L_{f2})$, the phase variation δ as a function of wavelength, according to Eq. (6.3.4), becomes substantial across the bandwidth of the grating. Thus, the single uniform band pass of the filter begins to split into a sinusoidal wavelength with wavelength, restricted to the bandwidth of the grating [42]. Figure 6.23 shows the reflection spectrum of an apodized grating MI and the band-pass output of the filter with a path difference of 0.667 mm. Within the reflection spectrum of the grating, the band pass has three peaks. Each peak automatically has the maximum transmission possible for the band pass, i.e, determined by the reflectivities from the gratings.

With the detuning shown in Fig. 6.24, nine peaks appear within the same bandwidth of approximately ± 0.0005 detuning. Being a nonresonant device, the output is simply equivalent to the interference between

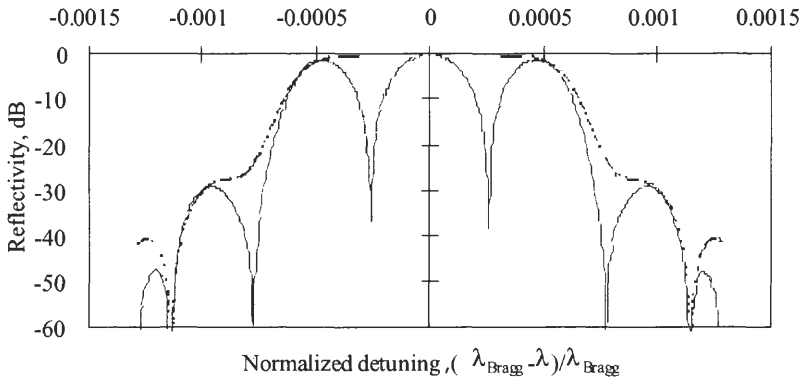

Figure 6.23: The reflectivity and band-pass spectrum of the asymmetric Michelson interferometer. The one-way path imbalance is 0.667 mm and the apodized gratings are 4 mm long with a Δn_{mod} of 1×10^{-3} [42].

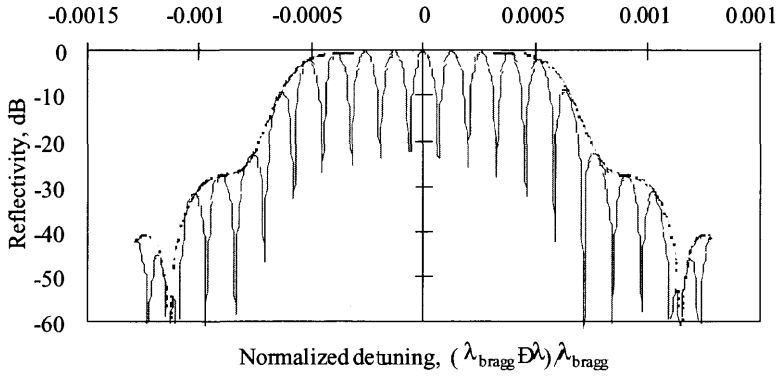

Figure 6.24: The apodized reflection (dashed line) and band pass (continuous line) of the asymmetric Michelson interferometer, with a path difference of 2.67 mm. The output is sinusoidal as in the case of a low-finesse FP interferometer.

two beam as a function of phase difference, hence the sinusoidal variation, also the case with the low-finesse FP interferometer. The wavelength difference $\delta\lambda$ between the peaks of the band pass is

$$\delta\lambda = \frac{\lambda^2}{2n_{eff}\Delta L_f + \Delta\phi(\lambda)}, \tag{6.3.10}$$

where $\Delta\phi(\lambda)$ is the differential phase of the two gratings, which becomes important when the gratings are dissimilar, for example, chirped. Using Eq. (6.3.10) one can calculate the exact number of pass bands within the bandwidth of the gratings. Note that with Bragg-wavelength detuned gratings, the resultant bandwidth for the pass bands is the difference between the individual bandwidths of the gratings. The measured response of such a filter is shown in Fig. 6.25. The extinction is 28 dB.

There are three possible combinations for arranging chirped gratings in the Michelson interferometer: both gratings with the same sign of the chirp, either both positive or both negative, or with opposite chirp. In Fig. 6.26, the first two arrangements are shown (A and B). The difference between A and B is that the dispersion of the gratings has been reversed, and that a pair of such filters may be used to compensate for most of the dispersion in each filter.

The transmission band pass of the identical-sign, linearly chirped grating Michelson interferometer with ΔL_f = 1.724 mm is shown in Fig. 6.27. The gratings are 5 mm long with a chirped bandwidth of 10 nm.

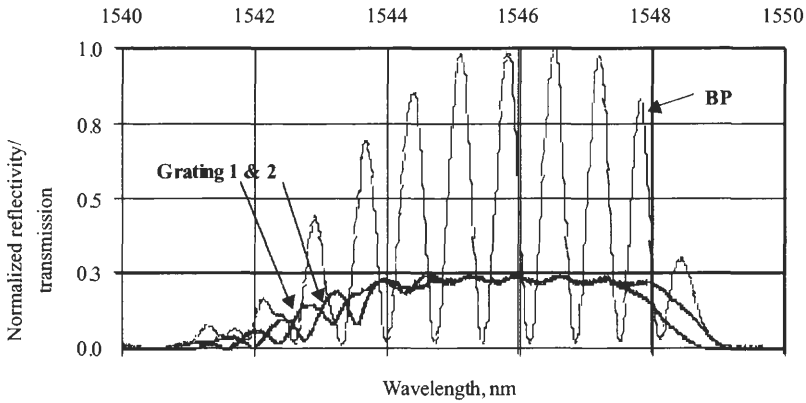

Figure 6.25: The reflection spectrum of each grating (1 and 2) measured *in situ* by bending the fiber in the other port to induce loss: hence the ~25% reflection. The normalized band-pass filter spectrum (BP) as a result of a path difference ΔL_f of ~1.33 mm [42].

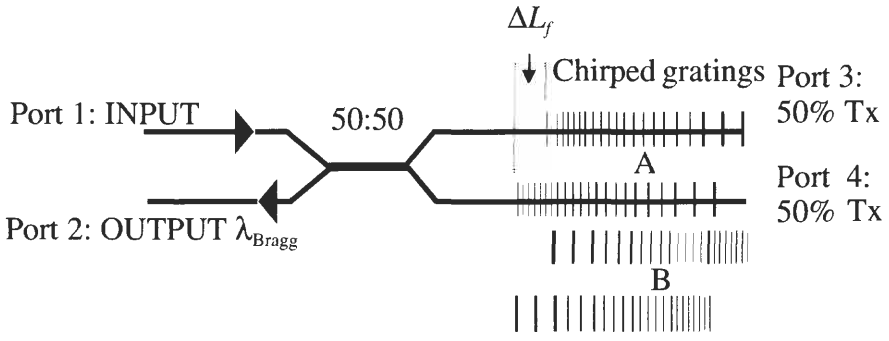

Figure 6.26: Chirped gratings in configurations A and B, each with a path imbalance of ΔL_f but with reversed sign of the chirp.

The unapodized gratings have a Δn_{mod} of 1×10^{-3}. The pass bandwidths of the channels are all identical and equal to the width of the channel spacing. The repeated pass bands can be adjusted by altering the path imbalance; in a demonstration, the paths were adjusted by stretching one arm of the interferometer to fit a grid of 1.1 or 2.2 nm using two 15-nm-bandwidth chirped gratings [45].

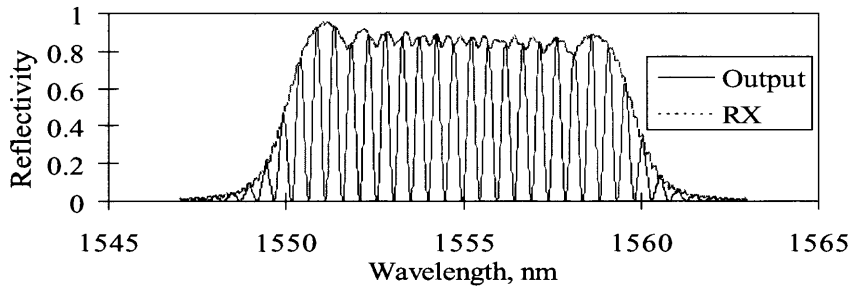

Figure 6.27: Band-pass and reflection spectra with two identically chirped gratings (L_g = 5 mm, chirp = 10 nm, and ΔL_f = 1.724 mm).

When the sign of the chirp of one of the gratings is reversed, the band-pass transmission characteristics change from regular repeated pass bands to a variable pass band. The path difference between the two gratings is reduced to zero at some wavelength. A gap opens at this point and the transmission is no longer uniform as in the previous cases. Ignoring dispersion, the phase difference between the light reflected from these two weakly reflecting, chirped gratings with a chirp of $\Delta\lambda_g$ nm relative to the wavelength λ_0 in the center of the grating, is

$$\delta(\lambda) = \frac{4\pi n_{eff} L_g}{\lambda}\left(\frac{\lambda_0 - \lambda}{\Delta\lambda_g}\right) - \frac{4\pi n_{eff} L_g}{\lambda}\left(\frac{\lambda - \lambda_0}{\Delta\lambda_g}\right) + \frac{4\pi n_{eff}\Delta L_f}{\lambda} \qquad (6.3.11)$$

$$= \frac{4\pi n_{eff} L_g}{\lambda}\left[2\left(\frac{\lambda_0 - \lambda}{\Delta\lambda_g}\right) + \frac{\Delta L_f}{L_g}\right],$$

where L_g is the length of the grating. It is apparent from Eq. (6.3.11) that the detuning $\delta = 0$ when

$$\lambda = \lambda_0 - \frac{\Delta\lambda_g \Delta\Lambda L_f}{2L_g}. \qquad (6.3.12)$$

If $\Delta L_f = 0$, $\delta = 0$ at the wavelength $\lambda = \lambda_0$. For a fixed chirp bandwidth, the detuning can be reduced to zero at any wavelength within the bandwidth of the grating by tuning ΔL_f. In Eq. (6.3.11) we have assumed that the lengths of the two gratings are identical. This need not be the case; it is enough that the bandwidth are identical, so that we have the extra parameter that can be adjusted. This also applies to the previous cases in which the sign of the chirp for both gratings was identical. The pass-

band period is now chirped, since the variation in the detuning is no longer constant close to the phase-matching wavelength.

Figures 6.28 and 6.29 demonstrate the effect of the counter-chirp of the gratings for the more general case of dissimilar length gratings. At the top of Fig. 6.28 is shown a schematic of the third combination for the chirped gratings (C) and the relative positions, orientations and lengths

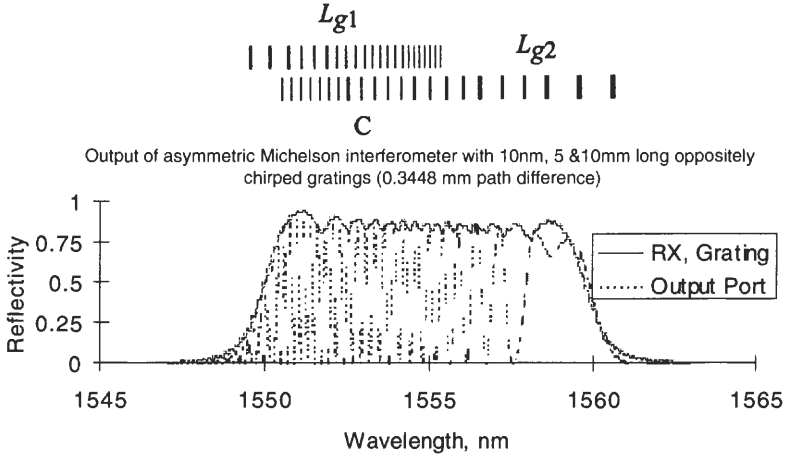

Figure 6.28: Above the chart is shown the arrangement of the gratings (C) used in this simulation of the asymmetrically placed grating Michelson interferometer BP with identical chirp bandwidth but dissimilar lengths (5 and 10 mm). Notice the chirp in the period of the pass bands. The reflectivity of one of the gratings is also shown.

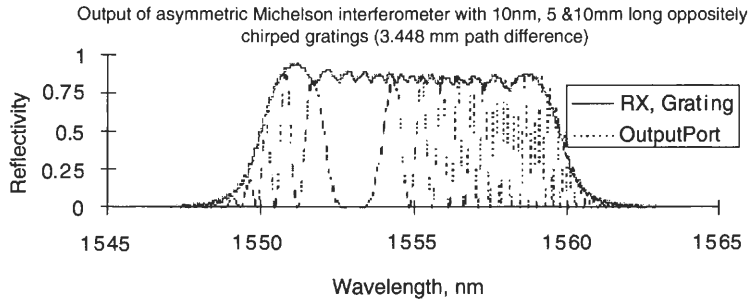

Figure 6.29: The band-pass response with a 3.448-mm path difference.

of the gratings. The first case is for 10- and 5-mm-long gratings, each with a chirped bandwidth of 10 nm and with a detuning of 0.344 mm (Fig. 6.28). The gap opens up close to one long-wavelength end of the grating, while with a larger ΔL_f of 3.44 mm in the second case, the gap shifts to the short wavelength end (Fig. 6.29). In either case, moving away from the phase-matching point [Eq. (6.3.12], the oscillations in the transmission spectrum become more rapid.

There are important issues relating to the asymmetric grating Michelson interferometer band-pass filter. First of all, any interferometer is sensitive to *differential* temperature and strain. The asymmetric interferometer is especially so; however, with fiber leads to the gratings kept in close proximity, the only region, which needs stabilization, is the *differential* path. For sensing applications, the broad bandwidth of the chirped grating is a distinct advantage. Stabilization of the paths may be done in a number of ways, for example by the application of a special polymer coating [46,47], or use of a substrate to compensate for the thermal expansion [48]. The filter has very high extinction, but the stability is polarization sensitive, and the transfer characteristics are sinusoidal with wavelength. The period and chirp are easily designed into the filter. Applications may be found in signal processing, sensors, multiplexing, and spectral slicing within a well-defined bandwidth. Ideally, it would be suited to fabrication in fused fibers, close to the coupler, or in planar form.

6.4 The Mach-Zehnder interferometer band-pass filter

The dual-grating Mach-Zehnder interferometer band-pass filter (GMZI-BPF) overcomes the severe limitation of the Michelson interferometer filter — the loss of 50% of the through transmitted light — by recombining the output at a coupler, as shown in Fig. 6.30. The scheme was proposed by Johnson *et al.* [49], and using etched gratings in a semiconductor waveguide Mach-Zehnder interferometer, Ragdale *et al.* [50] were able to show a device operation. A major drawback of a device fabricated in this way is the high intrinsic losses due to scatter, absorption, and input/output coupling, although large bandwidths are possible due to the use of short gratings resulting from the large modulation index of the grating (air and semiconductor). Additionally, once the device has been fabricated,

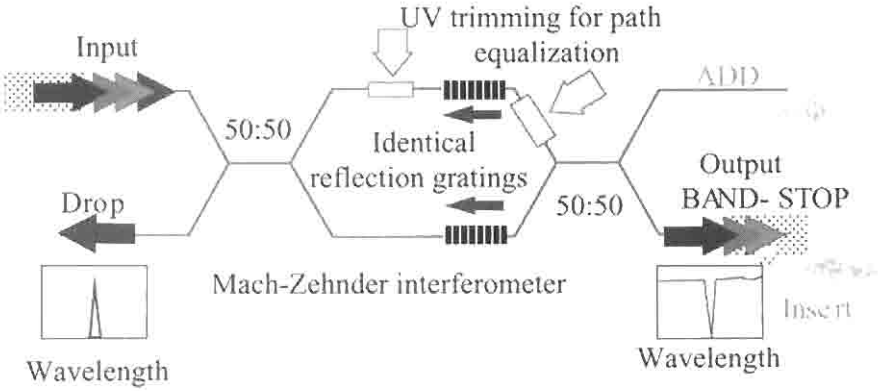

Figure 6.30: The Mach–Zehnder interferometer used as a band-pass filter. UV trimming of the paths has been shown to be a powerful tool for rebalancing the paths such that 100% of the light reflected from the gratings appears at the output port on the left [53,43]. By adjusting the phase difference at the coupler beyond the gratings, the output may be directed to either output port of the coupler.

phase adjustment between the guides to balance the interferometer is difficult without active control.

The first demonstration of a working band-pass device using the principle of the Mach–Zehnder interferometer (MZI) with two identical UV written gratings was in planar-Ge:silica waveguide form [53]. The device was an MZI with overclad ridge waveguides, which had been photosensitized using hot-hydrogen treatment [51]. "UV trimming" was used to balance the interferometer after the gratings were written, demonstrating this powerful technique also for the first time [53]. This is shown Fig. 6.30. "UV trimming" relies on photoinduced change in the refractive index to adjust the optical path-length difference. The 6-dB insertion loss for a single-grating band-pass filter was overcome and reducer to ~1.34 dB for the fiber pigtailed device, by UV trimming; much of it comprised coupling and intrinsic waveguide loss. The fiber gratings had a reflectivity of ~15 dB each and were well matched in wavelength. Approximately 10% of the light was reflected into the input port. Although the insertion loss of this MZI-BPF was not as low as later devices, the planar MZI has the advantage of being extremely stable to environmental effects. Since the demonstration, several groups used this scheme of UV trimming in fiber-based MZIs to demonstrate band-pass filters with better extinction and

insertion loss [43,52]. For proper operation, the output coupler needs to be balanced, requiring trimming on the RHSs of the gratings.

Indeed, it is simple to observe that the device can be used as an add multiplexer at the dropped wavelength if the same wavelength is locally injected at the port marked "Insert" (RHS, bottom). This wavelength will be routed through to the Add port performing the basic Add–Drop multiplexer function. Many of these MZIs may be cascaded to perform a multiple-wavelength band-pass function.

Cullen *et al.* [52] demonstrated a compact GMZI-BPF in fiber form. The device, based on two 50:50 splitting fused fiber couplers fabricated in boron–germania codoped fibers (Core–cladding index difference $\Delta n = 7 \times 10^{-3}$ and core diameter of 7 μm), with 1-meter tails. The two pieces of fiber were first tapered and fused to a constant diameter of 100 μm over a length of 20 mm. A 3-dB coupler was formed by further tapering one end of the fused region, until the desired splitting ratio of 50% was achieved. When the second coupler is made, if the path lengths in the two arms are identical, 100% of the light will appear in the crossed state, i.e., in port 4 when port 1 is excited. Allowing for fabrication loss and slight imbalance, between 95 and 99% of the light was available at port 4 after the second coupler was fabricated under the same conditions. The finished device had ~5 mm of space in the parallel fiber section between the couplers for the inscription of the gratings and for UV trimming. The advantage of such a structure is the relative stability of the MZI, since the couplers and the fused fiber regions are so close together. Any ambient temperature fluctuations affect both fibers equally. This was established by a measured change in the output power of the MZI of <0.05 dB over a temperature excursion of −20 to +60°C, with a wavelength window of 40 nm. It is necessary to mount the fibers on a mechanical support in order to proceed with grating inscription. A silica microscope slide is ideal for this application, since it enables the device to be supported, handled, aligned in the interferometer. For this device, gratings of 3-mm length were written in both arms under identical conditions using an intracavity CW frequency-doubled argon ion laser. The grating reflectivity can be monitored accurately by the size of the dip from the transmitted level at a few nanometers on the long-wavelength side of the Bragg wavelength (to avoid the radiation loss region on the blue side, as well as the side lobes on the red side of the grating spectrum). Once the two gratings are written using identical conditions, the device can be balanced by examining the reflection in port 1. Ideally, either a coupler or a circulator

may be used to monitor the reflection while optical trimming is undertaken in the region closest to port 1, to *minimize* the reflection at the Bragg wavelength [53]. Lastly, the output ports need to be balanced by trimming on the far side of the gratings. The power on the long-wavelength side of the Bragg wavelength can be steered to either port 3 or 4 as necessary. In their device Cullen *et al.* [52] reported an insertion loss of only 0.5 dB, and 0.35 dB for a standard fiber device. With 99% reflectors, strong radiation loss was noted on the blue side of the Bragg wavelength.

The long-term stability of the GMZI-BPF depends on the stability of the substrate and the uniformity of the stress and temperature gradients. Silica for the substrate is a good choice since it is better matched to the properties of the fiber. However, the Bragg wavelength in Ge:doped fiber shifts by ~16 pm/°C. Compensation of the drift can be countered by the use of packaging with an effective negative thermal expansion coefficient [54–56,47,48]. Athermalization using a β-eucrytite glass substrate has been shown to reduce the temperature sensitivity of fiber Bragg gratings to ~0.0022 nm/°C, and the drift in the wavelength was measured to be 0.02 nm after thermal cycling 60 times over a temperature excursion from −40°C to +85°C [56]. The glass is based on a stuffed derivative of the crystalline phase, β-quartz (LiO_2:Al_2O_3:$2SiO_2$). Normally, this phase has a large negative thermal expansion coefficient along the *c*-axis but forms a poor glass. Nucleated with TiO_2 and adjusting the glass composition to form β-eucrytite results in a stable glass melt. Heat treatment at above 1200°C forms the glass ceramic with the appropriate crystalline microstructure for a negative thermal expansion coefficient.

The principle of athermalization of delay through a fiber using a tube of oriented liquid-crystalline polymer [54] has also been used to athermalize gratings. A measured $d\lambda_{Bragg}/dT$ of 0.01 nm/°C for the uncompensated FBG was reduced to 0.13 nm/100°C after compensation, with no significant hysteresis during the temperature cycling from −40 to +80 °C [47]. Use of such materials as substrates for the GMZI-BP should result in robust devices.

6.4.1 Optical add–drop multiplexers based on the GMZI-BPF

Changing the phase in one of the arms of the MZI between the coupler and the gratings routes the reflected light to either the "drop" or the "input" port. Any method that can reliably alter the phase can be used

to switch the OADM. The parameters that can be altered are temperature [40,41] or strain to alter the phase difference between the arms of the MZI, or the Bragg wavelength of the gratings. To alter output state, the phase in one arm can be tuned reliably and requires a 10-mm length of fiber to be heated by~13°C. With strain, a fiber extension of $1/4\lambda_{\text{Bragg}}$ is required to switch the OADM.

Temperature tuning of the gratings requires a 65°C change to shift the fiber Bragg grating wavelength by ~0.8 nm. If the channels are spaced 1.6 nm apart, then a channel may be dropped by tuning the Bragg wavelength to match the channel wavelength and deselected by detuning. Tuning both gratings simultaneously by either strain or temperature while maintaining interferometric stability is not easy, so, this device requires careful engineering.

The GMZI-BPF can be used as an optical add–drop multiplexer (OADM). If the phase in one of the arms can be controlled actively, e.g., by a piezoelectric stretcher, then a wavelength may be either switched to the drop port or reflected back to the source. The insert function is operated in a similar manner by the use of a second piezoelectric stretcher on the RHS of one of the gratings in the MZI. The "drop" and "add" ports have fiber-coupler taps to monitor the state of the output and to control the piezoelectric stretchers to switch the GMZI-BPF using phase-locked loops [40]. A disadvantage of this scheme is that it always blocks the transmission of the channel, whether it is dropped or not, and it must be reinserted for forward transmission.

Mizuochi and Kitayama [57] combined a set of GMZI-BPFs to perform a two wavelength OADM function, which is shown in Fig. 6.31. The basic element of the device is a double GMZI-BPF with four identical gratings in the two MZIs, as well as an additional highly reflecting grating as an "isolator" between the two MZIs, shown in the top half of Fig. 6.31. The function of the additional grating is to prevent light at the grating Bragg wavelength from crossing from one MZI to the other, increasing isolation. This is particularly important because light inserted into the OADM can cross from one MZI to the other (from left to right and the reverse) to cause in-band coherent beat noise [58] (see Section 6.5). Light arriving from the left in the top half at port A1 is dropped at the Bragg wavelength λ_i and routed to the second GMZI-BPF in the lower half of the figure, containing gratings at another wavelength, λ_j. The dropped wavelength, λ_i therefore appears at C1. Similarly, light injected in C2 at the wavelength λ_i uses the "add" part of the top GMZI-BPF on the

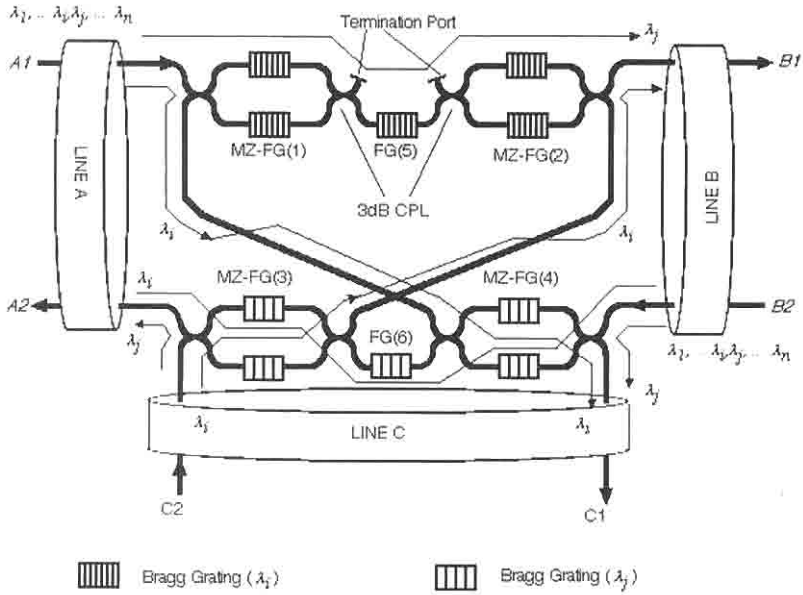

Figure 6.31: A two-wavelength cascaded GMZI-BPF with increased isolation between the add and drop ports (from: Mizuochi T. and Kitayama T., "Interferometric cross talk-free optical add/drop multiplexer using cascaded Mach-Zehnder fiber gratings," in *Technical Proc. of OFC '97*, pp. 176–177, 1997.) [57].

RHS and is routed to B2. All other wavelengths arriving at A1 simply go through the gratings and also appear at B1. Similarly, channels arriving at B2 are routed to A2, except for the channel at λ_j, which is dropped at C1 and reinserted from C2, to be routed to A2. The inclusion of the "isolating" grating reduces the leakage between A1 and B1 from -26 to -71 dB. The improvement is evident in the add–drop function, by a reduction in the power penalty of 1 dB due to the elimination of coherent beat noise. The use of higher reflectivity gratings in the MZIs should eliminate the need for the "isolator" grating, although short-wavelength radiation loss will remain a problem.

6.5 The optical circulator based OADM

The optical circulator has become extremely important for applications with fiber gratings. While the use of a fiber grating with a circulator is

an obvious method for converting the band stop to a band-pass filter, it is worthwhile to consider the benefits of such a configuration. The first reported use was as an ASE filter for an erbium amplifier [59]. The amplified signal is routed to the input of a circulator and reflected by a narrow-bandwidth grating in the second port. The grating filters the amplified spontaneous emission from the amplifier and routes the signal to the output port. The reduction in the out-of-band spontaneous emission can be considerable, but is determined by the quality of the reflectivity spectrum of the grating. Optical circulators have an insertion loss of only ~1 dB, turning this very simple device into a superb band-pass filter. Several gratings with different Bragg wavelengths may be cascaded to form a multiple band-pass filter. The addition of a second circulator leads to a simple method of performing an optical circulator based add–drop multiplexing (OC-ADM) function using gratings and is shown in Fig. 6.32. Channels injected at the "input" port are reflected by the gratings in between the two circulators and routed to the "drop" port. All other wavelengths continue to the "output" port. If the signals are injected at the "insert" port on the RHS of Fig. 6.32, the same gratings perform an insert function, routing the reflected channels to the "output" port, along with the rest of the channels from the "input" port. The low polarization sensi-

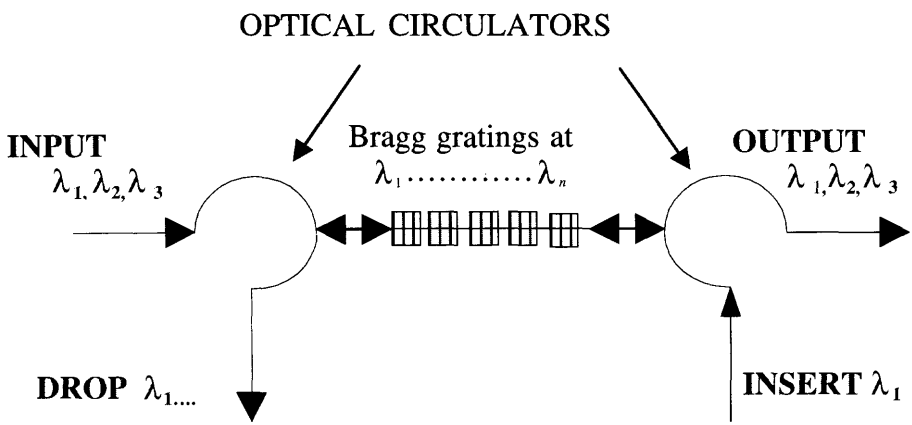

Figure 6.32: An OC-ADM using an all optical circulator. This device allows several channels to be dropped or added according to the number of fiber gratings between the circulators. The signal at the Bragg wavelengths are reflected and appear at the drop port, while the same gratings may be used to insert the same channels for wavelength reuse from the insert port.

tivity and extremely high return loss of the circulators are a distinct advantage for this type of function, despite their insertion loss of ~1 dB. Since the circulator-fiber grating band-pass filter is not interferometric, it is intrinsically stable in its operation, but remains an expensive solution for some application. However, for amplified long-haul fiber communication routes with large capacity (e.g., submarine systems), the cost of a few of circulators is unlikely to be an overriding factor.

The issues that need to be addressed with the OC-ADM are the channel-dependent insertion loss, intra- and cross-channel cross-talk, and the dispersion penalty due to the bandwidth of the gratings. Channel-dependent loss is primarily due to the "blue-wavelength" radiation loss exhibited by all fiber Bragg gratings. Thus, reflected light from the shorter-wavelength gratings may experience loss either in the drop *or* in the add function, unless the gratings are fabricated with care. Figure 6.32 shows a sequence of gratings reflecting at λ_1, $\lambda_2 \ldots \lambda_n$. The gratings are arranged so that the first grating reflects at the shortest wavelength and the last, λ_n, at the longest. A highly reflective grating transmission spectrum is shown in Fig. 6.33. The loss on the blue-wavelength side extends over a wide bandwidth. If each grating has similar transmission characteristics, spaced, say, 10 nm apart, the blue-wavelength radiation loss will increase with each additional grating. Light injected from the short wavelength side (e.g., from the "input" port) is reflected in sequence, so that the shortest wavelength is reflected first, and then the second shortest, and so on. Each wavelength λ_n has to traverse $n - 1$ gratings

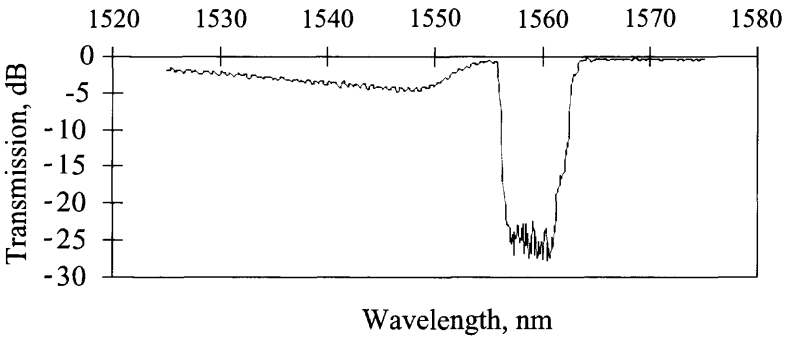

Figure 6.33: The measured transmission spectrum of a 7-nm full-bandwidth, highly reflecting chirped grating with the associated "blue"-wavelength loss extending over almost the entire gain bandwidth of an erbium amplifier.

reflecting at a wavelength *shorter* than λ_n. However, since the loss in traversing the grating is always on the short-wavelength side of the Bragg wavelength, each wavelength is reflected *without* incurring radiation loss.

The situation is different if the order of reflection is reversed, as is the case when the light is injected into the "insert" port. The longest wavelength is reflected first and so does not incur loss. The next wavelength (in this example, at ~1550 nm) to be reflected lies on the short-wavelength side of the reflection shown Fig. 6.32 and so suffers twice the radiation loss α of approximately 6–8 dB. Again, each wavelength λ_n has to traverse $n - 1$ gratings reflecting at *longer* wavelengths and suffers a loss of $(n - 1) \times \alpha$ dB. This loss causes severe skew in the wavelength response of the OADM. Although the radiation loss spectrum shown in Fig. 6.33 is very high and has a large bandwidth, the insertion loss argument applies to all such OADM devices. The insertion loss varies across the bandwidth but is always cumulative in one direction and can be more important for wavelengths that have not been dropped but lie on the short-wavelength side of the OADM. There are methods that can be used to reduce the radiation loss of the gratings, for example, by design of the fiber [60,61] to suppress radiation mode coupling, or by choosing the channel spacing such that none lie in the radiation loss region [17].

Intrachannel cross-talk occurs if the added channel is derived from the same source as the dropped channel and leaks through from the "insert" to the "drop" port. If a strong signal is added at the OADM, a small fraction leaks through to the drop port if the grating reflectivity is not very high. This small "breakthrough" can be of the same order of magnitude as the signal, which has been attenuated by the link loss and dropped at the OADM. If the added and dropped wavelengths are the same, signal beat noise occurs and degrades the bit error rate (BER). Alternatively, the breakthrough signal can cause simple cross-talk between adjacent channels that are dropped, in the same way it can be transmitted to the "add" port. The associated power penalty has been calculated to be

$$p_{coherent} = -10 \log(1 - 4\sqrt{r}) \tag{6.5.1}$$

for a ratio r of the leaked "add" and the dropped signal powers for coherent signals. This is much higher than for incoherent signals [62], for which

$$p_{incoherent} = -10 \log(1 - r). \tag{6.5.2}$$

Dispersion due to the gratings is an issue, which depends on the signal and grating bandwidths. Gratings show strong dispersion at the

edges of the reflection band (see Chapter 4). If the signal fills the grating or is severely limited by the grating bandwidth, apart from the simple pulse broadening (narrowed spectrum), additional dispersion from the band edges of the grating has the potential of causing severe pulse distortion. This area has only recently received attention [63].

Programmability of an OADM is often desirable, and there are several techniques available to integrate this feature. As has been seen with the GMZI-BPF, the most easily adjustable parameter is the path length difference from the coupler to the gratings, since tuning the Bragg wavelength of both gratings poses a difficult engineering problem. The OC-ADM is not an interferometric device, so that tuning of the gratings by stretching/compressing or heating is easily achieved. Quetel *et al.* [65] demonstrated this principle with a circulator and four gratings stretch tuned by piezoelectric (PZT) actuators, with a switching time of 40 μs and a voltage of only 50 V. Okayama *et al.* [64] proposed the use of a pair of identical gratings for each add/drop channel with two 4-port optical circulators for an OC-based tunable add–drop multiplexer (OC-TADM). Figure 6.34 shows the arrangement of the gratings for a four-channel OC-TADM. Channels arriving at the input port are reflected by the appropriate gratings, λ_1, λ_2, λ_4 in the top part of the circulator branch, *group* 1. Gratings 2 and 4 are tunable (by either temperature or strain); however, all channels are reflected and routed to the second set of gratings, λ_4, λ_2, λ_2, λ_1 in the bottom part of the circulator branch, *group* 2. In this section, gratings 3 and 1 are tunable. If each grating pair has identical Bragg wavelengths, *all* channels are routed to the drop port by reflections from *group* 2 gratings. However, since one of the gratings of the matched pair

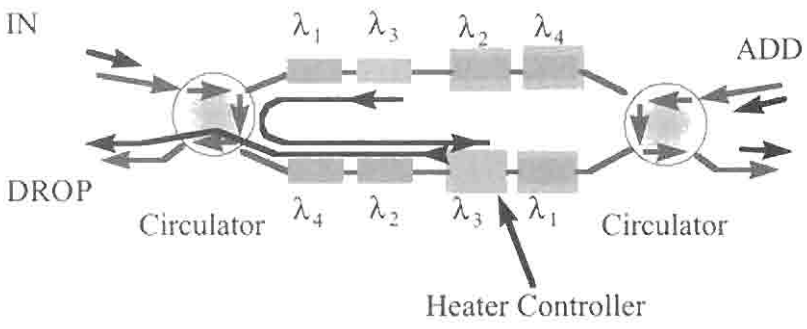

Figure 6.34: Dynamic wavelength selective add/drop mux–demux using tunable gratings (after Ref. [64]).

is tunable, it can be detuned, thus directing the channel at that wavelength to the through port.

Since the device is symmetric, the channel insert function is performed in a similar manner: When injected into the "add" port, the wavelengths are routed to the "through" port. Poor peak and high side-lobe reflectivity cause cross-talk. The use of unapodized (−14 dB side-lobes), 95% peak reflectivity gratings resulted with in poor cross-talk performance. With well-apodized, high-reflectivity gratings, low cross-talk performance is possible and the OC-TADM is appropriate for dense-WDM applications. In principle, piezoelectric stretchers can be used to make a fast OC-TADM, switchable in < 1 μs [65].

In a slightly simpler arrangement, Kim *et al.* [66] proposed the use of four identical gratings between two three-port circulators. The gratings are stretch tuned by piezoelectric stretchers, so that up to four channels can be dropped or inserted in any combination, when the Bragg wavelengths of the gratings are tuned to the channel wavelengths. Mechanical leverage designed into the grating mounts with the piezoelectric stretcher allows the Bragg wavelength of each grating to be tuned by 2.4 nm/120 V applied.

6.5.1 Reconfigurable OADM

These devices are based on optical switches and circulators and overcome some of the limitations of the OC-TADM and the GMZI-BPF. A schematic of the reconfigurable OADM (ROADM) is shown in Fig. 6.35. Two fiber

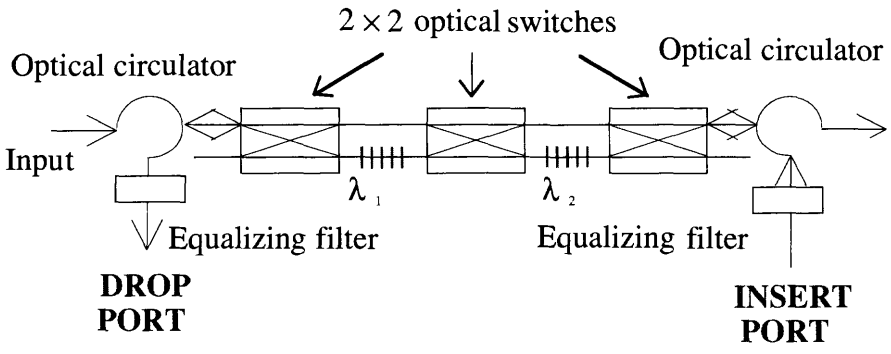

Figure 6.35: The reconfigurable optical add–drop multiplexer (ROADM) (after Ref. [67]).

circulators sandwich a set of optical cross-connect switches connected in series. Fiber gratings at the optical channel wavelengths are connected between one of the output ports of the cross-connect switches. This way, the incoming signals may be switched to the grating or bypass it. When switched to the grating, the channel at the grating wavelength λ_1 is dropped and routed to the drop port. All other channels proceed to the next switch, where the choice is repeated for the other channels. If, however, λ_1 bypasses the first grating, it goes on to the through port. The same applies to the other channels. At each two-by-two optical cross-point switch, a channel (or more, depending on the number of gratings between the switches) may be dropped. The ROADM is extremely flexible, allowing the node to be programmed relatively fast (<50 μs). The insertion loss of the optical switches is low (0.7 dB), and the device has been demonstrated as a two-channel ROADM [67], with a total insertion loss of 3 dB. The equalizing filters shown in Fig. 6.35 are intended to compensate for the loss of the switches and the gratings so that all channels suffer the same insertion loss.

A modification of the ROADM shown in Fig. 6.35 results in the simultaneous add–drop function, including automatic dispersion compensation of all channels, using dispersion compensating gratings (DCG) [68]. The channel dropping gratings are replaced by chirped dispersion compensating gratings. Uniform unchirped gratings can be used from either direction, whereas the dispersion of chirped gratings is reversed if it is turned around. Therefore, the chirped gratings cannot simply replace the unchirped gratings in the ROADM. Channels to be dropped are compensated for dispersion in the ROADM with DCGs. In order to dispersion compensate the "through" channels, the optical circuit has to be altered. The modified reconfigurable dispersion compensating ADM (RDC-ADM) is shown Fig. 6.36. The "through" channels are routed via the "through path" to the output circulator and reinjected into the cross-point switches. Each "through" channel is routed to the appropriate grating via the switches and dispersion compensated by reflection, to retrace the path to the circulator, and finally to the output. Channels are also inserted without reflection; they simply bypass the DCG allocated to their channel, so as to avoid the additional dispersion. The four-channel RDC-ADM was demonstrated with a 4×10 Gb/sec WDM system and used apodized 100-mm-long gratings for each channel designed to compensate for the dispersion of 8 km of standard fiber (1312 psec/nm). An important feature of the configuration was the arrangement of gratings and amplifiers to equalize the

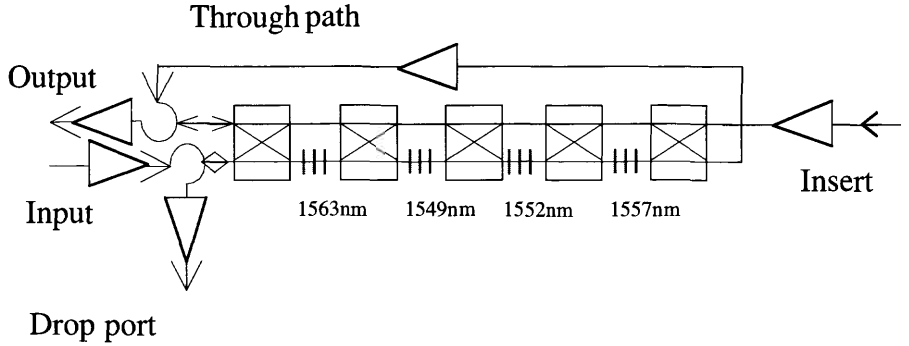

Figure 6.36: The RDC-ADM based on optical switches (after Ref.[68]).

insertion loss of the switches. The gratings are placed in the RDC-ADM such that the channel at the maximum gain of the amplifier is placed between the last pair of optical switches, and the lowest gain channel is reflected first [68].

6.6 The polarizing beam splitter band-pass filter

A filter based on an all-fiber polarization dividing coupler [69] changes the Michelson BPF into a noninterferometric device. The polarization splitting coupler allows only one of the orthogonally polarized eigenmodes to couple across to the other fiber. The coupler is fabricated to be an integral number of coupling lengths for one of the polarizations. Since the supermodes of the coupler have slightly different propagation constants, they have slightly different coupling lengths, $l_c(TE)$ and $l_c(TM)$, for the *TE* and *TM* polarized modes. By making the coupling region long, it can be arranged to be an odd number of coupling lengths for one polarization and an even number for the other. This ensures that only a single polarization couples across the coupler, while the other remains in the same fiber. Thus, the number of coupling lengths, N_c is

$$N_c \approx \frac{l_c}{\Delta l_c}, \tag{6.6.1}$$

where $\Delta l_c = |l_c(TE) - l_c(TM)|$, and $l_c \approx l_c(TE) \approx l_c(TM)$. As a result of

overcoupling, the device is wavelength sensitive, with a cyclic coupling response shown in Fig. 6.37. It has excellent polarization isolation over a narrow band of wavelengths but may be designed to operate at any desired wavelength by adjusting the parameters at the time of fabrication.

Figure 6.38 shows a schematic of the polarization splitting coupler in operation with Bragg gratings in ports 3 and 4. When operated at the correct wavelength, the polarization splitter will cross-couple only one of the two orthogonal polarization states in the input port 1, while the other propagates unaffected. If gratings are placed at the output ports of such a coupler, light at the Bragg wavelength is reflected and both polarizations are coupled back to the input port 1. If a quarter-wave plate is placed just before a grating and oriented such that at the output of the wave plate it is left-circularly polarized, on reflection from the grating it becomes right-circularly polarized. Traversing the wave plate once more the linearly polarized output of the wave plate is orthogonal to the incoming polarization. At the coupler, this state of polarization remains uncoupled and is routed to port 2 of the coupler. The same applies to the orthogonal polarization state, which also couples to port 2. Thus, as in the Michelson arrangement, the device operates as a polarization-*independent* band-pass filter [72]. Each

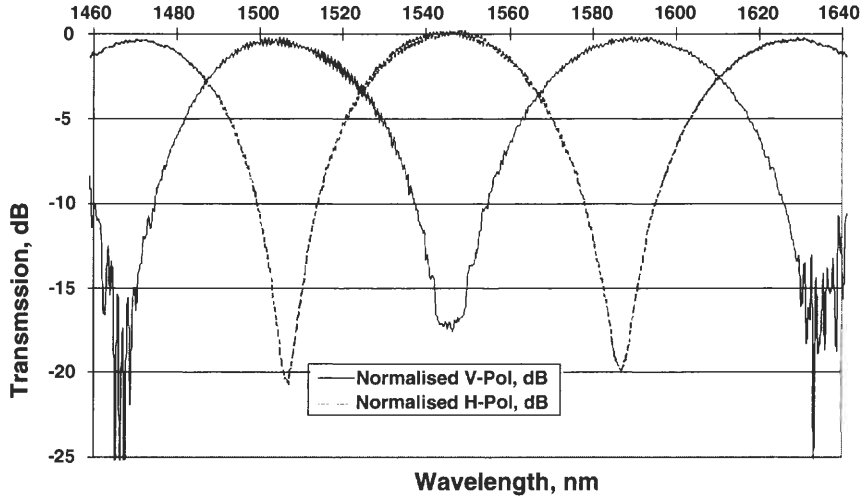

Figure 6.37: The transmission characteristics of the two orthogonal polarization states [72] at the output of the polarizing beam splitter. The extinction is well over 30 dB.

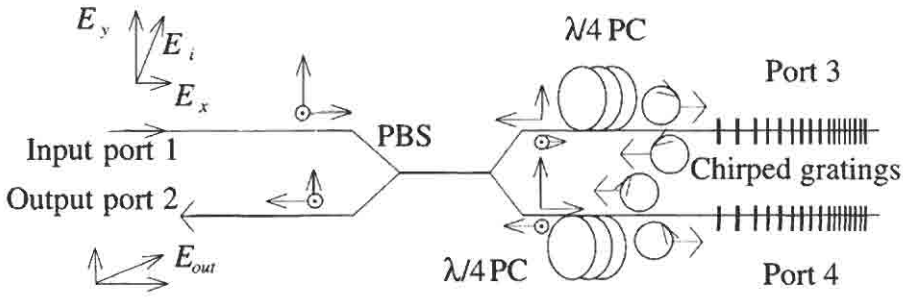

Figure 6.38: The polarization dividing band-pass filter in operation. The dashed arrows indicate the direction of propagation. The circles with arrows indicate the circularity of the polarization (after Ref [72]) PBS is a polarizing beam splitter. λ/4 PC is a quarter-wave polarization controller.

reflected polarization is routed to the output port of the coupler, reconstituting the original polarization, but is rotated by $\pi/2$.

The experimental arrangement using a cascade of four chirped gratings with two polarizing beam splitter band-pass filters (PBS-BPFs) is shown in Fig 6.39. The quarter-wave plates are simply a few turns of fiber in a polarization controller [70]. In this dispersion-compensating

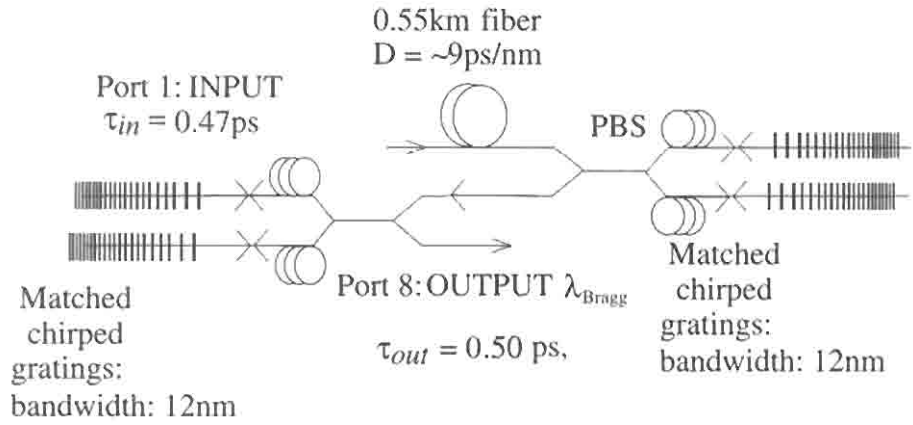

Figure 6.39: Dispersion compensation with four cascaded 8-mm-long, 12-nm bandwidth-chirped gratings and two PDBPF. The two polarization splitting band-pass filters shown here have been cascaded to enhance the dispersive effect of the chirped gratings [71,72].

PDBPF, 0.47-ps pulses at 1562 nm were stretched to 60 ps after propagation through 0.55 km of partially dispersion-shifted fiber (dispersion of 9 ps/nm). A pair of identical 8-mm-long chirped gratings with a bandwidth of 12 nm in the PDBPF routed the pulses to a second, identical DCG-PBS-BPF. The output port of the second PBS-BPF recovered pulses of 0.50 ps, a recompression ratio of 60/0.5 = 109 [72].

The PBS-BPF is a noninterferometric device but relies on the coincidence of the arrival of the pulses at the PDS after reflection. A delay between the arrival of the pulses translates into polarization mode dispersion (PMD). A change in the path of 1 mm is equivalent to ~10 ps PMD. For such short pulses, the paths were matched to <0.01 mm by stretching the fiber. Polarization variation in each arm causes an amplitude fluctuation. This device remains reasonably immune from physical disturbance, so long as the fibers after the PBS are not disturbed. Since all the components of this device are based on optical fiber, it has low insertion loss (~0.2 dB, typically, for the splitter).

The Michelson interferometer becomes the GMZI-ADM when a second coupler is included after the gratings. The same applies to the polarization dividing filter with a second PBS after the gratings. However, a major difference is the intrinsic stability of the latter device, since interferometer stability is no longer necessary. BER performance of transmission systems will degrade significantly as the PMD approaches half of the bit period. For a low BER at a transmission rate of 10 Gb/sec, a maximum path imbalance of a few millimeters would be required, which is easily achievable. The disadvantage of the filter is relatively small bandwidth of the PBS (see Fig. 6.36), so that channels can only be spaced close to the nulls of the PBS.

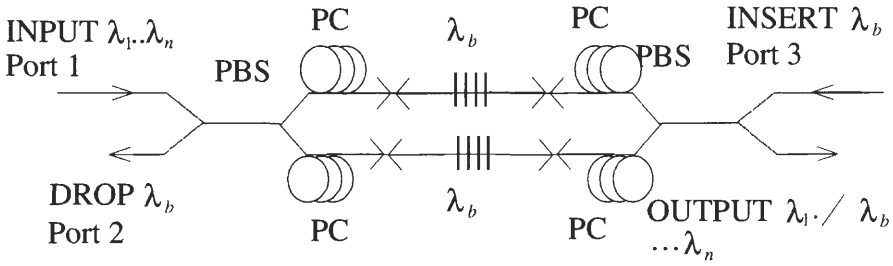

Figure 6.40: The polarizing beam splitter OADM. Multiple gratings between the PCs allow more than a single channel to be dropped and added simultaneously (after Ref. [73]).

A PBS-OADM has been demonstrated for a single channel using seven wavelengths spaced at 0.8-nm intervals. The center channel was dropped with a cross-talk penalty of 0.3 dB when the same wavelength was added at a transmission rate of 2.5 Gb/sec. Heating part of one arm of the PBS-OADM by 65°C induced a change of 0.3 dB at the output [73]. However, it remains to be seen how this device will function under full environmental testing. Figure 6.40 shows a schematic of the PBS-OADM [73].

6.7 In-coupler Bragg grating filters

Co- and contradirectional wavelength selective couplers have been known for a long time [74,75]. There are a number of ways that gratings in-couplers may be used to form band-pass filters. Figure 6.41 shows three different types of couplers, which include gratings to assist (grating-assisted coupler, GAC), to frustrate (grating-frustrated coupler, GFC) and to reflect (Bragg reflection coupler, BRC) light of a particular wavelength that meets the phase-matching requirements.

The period of the refractive index-perturbation for codirectional grating-assisted coupling [GAC, Fig. 6.41 (*i*)] between two dissimilar fibers is determined by the difference in the propagation constants of the two guides. This is generally small, and therefore the period is long. For weak overlap of the fields, the coupled-mode equations (see Chapter 4 on long-period gratings), describe the interaction between the modes. The coupling between the guides is sinusoidally periodic with length of the grating-assisted region. The coupling has a relatively broad bandwidth (tens of nanometers) and therefore poor wavelength selectivity, unless the device can be made very long.

A normally 100% coupler is strongly detuned by the dispersion of the grating and so fails to behave as a coupler near the Bragg wavelength, and is called a grating-frustrated coupler [GFC, Fig. 6.41 (*ii*)]. It works on the following principle: Two fibers with identical propagation constants will exchange power at all except the "grating-frustrated" wavelength. The in-fiber grating is a Bragg reflector at the frustrated-wavelength and is present in only one of the fibers. The far end of the input fiber becomes the "drop" port and is the one that does not contain the grating.

The Bragg reflecting coupler [BRC, Fig. 6.41 (*iii*) and (*iv*)] requires a perturbation with a short period, as is the case for Bragg reflection, being dependent on the sum of the magnitudes of propagation constants of

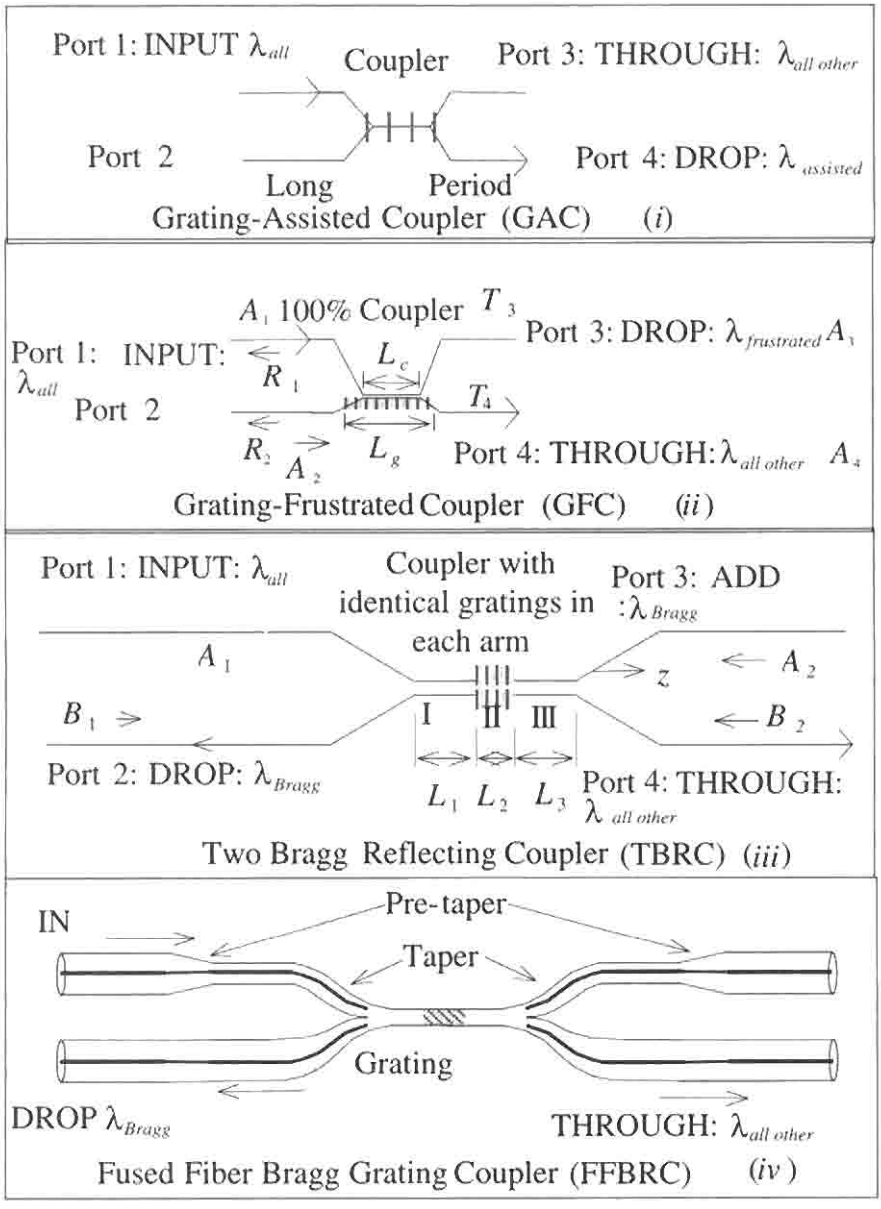

Figure 6.41: Some examples of band-pass filters with in-coupler gratings.

the two modes. This device can made with either two gratings in polished couplers [76,77] or a single one written into a fused coupler [78], since the perturbation has to be present in the entire cross-section of the coupling region. The dropped channel is reflected and routed to port 2 of the fiber coupler. In the following sections, the characteristics of the latter two devices are presented.

6.7.1 Bragg reflecting coupler OADM

The BRC-OADM [76–78] is probably the most promising of all the OADM devices that rely on interference. Essentially, this is a new twist to a range of generic devices based on the grating-assisted coupling action. Apart from being a simple device and having very low insertion loss, the BRC has the potential of fulfilling the requirements for a high extinction at the "dropped" as well as the "through" ports, and low back-reflection into the input port. Schematics of the BRC in the assembled and fused forms are shown in Fig. 6.41 (iii, iv). In its fused form, it comprises two fibers tapered down to form a long coupling region in which the fibers are kept parallel, followed by a short grating and another long coupling region before the fibers separate.

The principle of operation is probably the cleanest of all the different types of grating couplers and may be understood in the following phenomenological way: The light input into port 1 propagates adiabatically in the tapered region to excite the supermodes of the coupler. In this region, the two fibers merge into a single strand and become a glass rod without a core, surrounded by air. In a normal coupler without the grating, 100% of the light is transferred from one set of modes to the other to exit at port 4. If, however, a point reflector is placed at exactly half the coupling length, then the divided power between the modes travels backward toward ports 1 and 2, and the coupling process continues uninterrupted, apart from the π phase change induced by the reflection in all the supermodes. Thus, instead of propagation in the positive z-direction, the supermodes travel in the negative z-direction and interfere at the exit of the coupler and are routed by symmetry into port 2. In the BRC, the Bragg grating replaces the point reflector, which is wavelength selective, and routes light only near the bandgap into port 2. This simple picture is surprisingly accurate, despite the fact that coupling continues within the grating region, due to light penetration. It is immediately apparent that a strong grating would be preferable, although complications arise since the presence of the grating detunes the coupling action. The BRC can also be considered to be a close analog to the

Michelson/Mach–Zehnder interferometer with "zero-length" paths. This will become clear as one compares the theoretical performance of the BRC with that of the Michelson with *detuned* Bragg grating wavelengths. One essential difference between the two devices are the single grating as well as only one common path in the BRC, as opposed to two gratings and two paths in the Michelson interferometer. Many of the features of the BRC are easily understood by comparing it with the Michelson [79].

Theory of the BRC

The theory of the BRC has been worked out using coupled-mode analysis [76,80,77]. We closely follow the nomenclature of Ref. [77]. Referring to Fig. 6.41 (*iii*), the fibers and A and B have unperturbed propagation constants β_a and β_b, respectively, and the grating with a coupling constant of κ_{ac} exists in both fibers, evanescently coupled with a coupling constant κ. In region II, there are co- and counterpropagating modes, which are coupled together. The presence of the grating introduces a detuning of the propagation constants in each fiber, which are

$$\Delta\beta_a = \beta_a - \frac{\pi}{\Lambda_g} \tag{6.7.1}$$

$$\Delta\beta_b = \beta_b - \frac{\pi}{\Lambda_g} \tag{6.7.2}$$

$$\begin{aligned}\Delta\beta_{ab} &= \frac{1}{2}(\beta_a - \beta_b) \\ &= \frac{1}{2}(\Delta\beta_a - \Delta\beta_b).\end{aligned} \tag{6.7.3}$$

Coupling between counterpropagating modes of different fibers (A_1/B_2 and A_2/B_1) is only significant if the fibers are very strongly coupled, so that coupling occurs over a distance of a few wavelengths (when κ is of the order of $10^6 \mathrm{m}^{-1}$). Thus, these interactions can be ignored in a majority of cases. The mode fields propagate with the modified propagation constants and may be expressed as

$$A_1(z) = \tilde{A}_1(z)e^{i\Delta\beta_a z} \tag{6.7.4}$$

$$A_2(z) = \tilde{A}_2(z)e^{-i\Delta\beta_a z} \tag{6.7.5}$$

$$B_1(z) = \tilde{B}_1(z)e^{i\Delta\beta_b z} \tag{6.7.6}$$

$$B_2(z) = \tilde{B}_2(z)e^{-i\Delta\beta_b z}. \tag{6.7.7}$$

In region II, the coupled-mode equations take the matrix form

$$\begin{bmatrix} \tilde{A}_1' \\ \tilde{A}_2' \\ \tilde{B}_1' \\ \tilde{B}_2' \end{bmatrix} = \begin{bmatrix} -i\Delta\beta_a & -i\kappa_{ac} & -i\kappa & 0 \\ i\kappa_{ac}^* & i\Delta\beta_a & 0 & i\kappa \\ -i\kappa^* & 0 & -i\Delta\beta_b & -i\kappa_{ac} \\ 0 & i\kappa^* & i\kappa_{ac}^* & i\Delta\beta_b \end{bmatrix} \begin{bmatrix} \tilde{A}1 \\ \tilde{A}2 \\ \tilde{B}1 \\ \tilde{B}2 \end{bmatrix}, \tag{6.7.8}$$

where the prime indicates d/dz. Expressed as an eigenvalue equation, Eq. (6.7.8) results in the four eigenvalues (propagation constants) of the four supermodes of region II. These are arrived at by straightforward but tedious algebraic manipulation of Eq. (6.7.8) using standard techniques. The four eigenvalues are

$$\alpha_1 = \sqrt{|\kappa_{ac}|^2 - \left[\sqrt{|\kappa|^2 + \Delta\beta_{ab}^2} + \frac{\Delta\beta_a + \Delta\beta_b}{2}\right]^2} \tag{6.7.9}$$

$$\alpha_2 = \sqrt{|\kappa_{ac}|^2 - \left[\sqrt{|\kappa|^2 + \Delta\beta_{ab}^2} - \frac{\Delta\beta_a + \Delta\beta_b}{2}\right]^2} \tag{6.7.10}$$

$$\alpha_3 = -\sqrt{|\kappa_{ac}|^2 - \left[\sqrt{|\kappa|^2 + \Delta\beta_{ab}^2} + \frac{\Delta\beta_a + \Delta\beta_b}{2}\right]^2} \tag{6.7.11}$$

$$\alpha_4 = -\sqrt{|\kappa_{ac}|^2 - \left[\sqrt{|\kappa|^2 + \Delta\beta_{ab}^2} - \frac{\Delta\beta_a + \Delta\beta_b}{2}\right]^2}. \tag{6.7.12}$$

These are the most general solutions for the case when the fibers have different propagation constants. The eigenmodes associated with these eigenvalues have spatial fields that are expressed as the sum of individual modes of each fiber. The initial boundary values determine how each individual field grows (or decays). The first part of the analysis recognizes the fact that an input at either A_1 or B_1 results in coupling between the fibers through simple coupler action. This is described by the equation for the transfer function of the coupler [Eq. (6.3.1)], but with the appropriate coupling length, $L_c = L_1$, with input fields $A_1(0) = 1$ and $B_1(0) = 0$. At the boundary to the grating, the two fields $A_1(L_1)$ and $B_1(L_1)$ become the input to the grating. With the assumption that $A_2(L_1 + L_2) = 0$ and $B_2(L_1 + L_2) = 0$, the amplitudes of the four super-modes in region II are evaluated using Eq. (6.7.8). Finally, the backward propagating field amplitudes at the input to the coupler are propagated in reverse through the coupler to arrive at the amplitudes of the fields $A_2(0)$ and $B_2(0)$. Ideally,

with a point reflector (grating), the transmission through to the output ports would follow the equation for the coupler [Eq. (6.3.1a)], to route the entire out-off-band transmitted light to B_2. However, because of the finite length of the grating and the additional coupling that occurs in region II, region III may no longer be equal to region I for optimum performance, since $|\kappa|(L_1 + L_2 + L_3) = n\pi$.

As has been mentioned, a simple way of making such a device is to draw two identical fibers together to form a coupler and subsequently write a grating at the appropriate position, as shown in Fig. 6.41 (*iv*). With two fibers and two gratings, there is always a possibility of a small mismatch in the propagation constants after the fibers are polished and the device assembled. The refractive index mismatch maybe typically be $\sim 5 \times 10^{-5}$, resulting in ~95% coupling [38]. Gratings written into such fibers may therefore need to be written carefully in order to match the Bragg wavelengths. With a fused fiber coupler, the quality of the device can be very good with coupling approaching 100%, indicating the uniformity of the coupling region. Thus, assuming fibers with identical propagation constants, $\Delta\beta_{ab} = 0$, and the detuning $\Delta\beta_b = \Delta\beta$, simplifying Eqs. (6.7.9)–(6.7.12)

$$\alpha_1 = \sqrt{|\kappa_{ac}|^2 - (|\kappa| + \Delta\beta)^2} \tag{6.7.13}$$

$$\alpha_2 = \sqrt{|\kappa_{ac}|^2 - (|\kappa| - \Delta\beta)^2} \tag{6.7.14}$$

$$\alpha_3 = -\sqrt{|\kappa_{ac}|^2 - (|\kappa| + \Delta\beta)^2} \tag{6.7.15}$$

$$\alpha_4 = -\sqrt{|\kappa_{ac}|^2 - (|\kappa| - \Delta\beta)^2}. \tag{6.7.16}$$

Note that despite using phase-synchronous fibers, in Eqs. (6.7.13)–(6.7.16) the eigenvalues have been detuned from the exact phase-matching condition by κ.

To calculate the field at the input port 1 (return-loss) and the dropped port 2, the boundary conditions are applied. The dropped "transmission" in port 2 is

$$\tau_2 = \frac{B_2(0)}{A_1(0)} = \frac{1}{2}\frac{\kappa^*}{|\kappa|}\left[\frac{\kappa_{ac}^* \sinh(\alpha_1 L_2)}{i\alpha_1 \cosh(\alpha_1 L_2) + (\delta_1)\sinh(\alpha_1 L_2)} e^{-2i\phi} - \frac{\kappa_{ac} \sinh(\alpha_2 L_2)}{i\alpha_2 \cosh(\alpha_2 L_2) + (\delta_2)\sinh(\alpha_2 L_2)} e^{2i\phi}\right], \tag{6.7.17}$$

where the detuning, $\delta_1 = -|\kappa| - \Delta\beta$, $\delta_2 = |\kappa| - \Delta\beta$ and $\phi = (|\kappa| + \Delta\beta)L_1$.

Similarly, the back-reflected amplitude in port 1 is deduced as

$$\rho_1 = \frac{A_2(0)}{A_1(0)} = \frac{1}{2}\left[\frac{\kappa_{ac}^* \sinh(\alpha_1 L_2)}{i\alpha_1 \cosh(\alpha_1 L_2) + (\delta_1)\sinh(\alpha_1 L_2)} e^{-2i\phi} + \frac{\kappa_{ac} \sinh(\alpha_2 L_2)}{i\alpha_2 \cosh(\alpha_2 L_2) + (\delta_2)\sinh(\alpha_2 L_2)} e^{2i\phi}\right]. \tag{6.7.18}$$

We note that in Eq. (6.7.17) and (6.7.18), there are four terms of interest. The two terms in brackets can be immediately recognized to be identical to the reflectivity of two gratings at different Bragg wavelengths [see Eq. (4.3.11)], given by equating δ_1 and δ_2 to zero. Secondly, the phase term, 2ϕ, has two components; the first is due to the difference in the propagation constants of two modes propagating through a fiber of length, L_1, after being reflected by the grating. The second part, κL_1, is simply the accumulated phase change due to the coupling action of the coupler. The equivalent reflectivity and phase factors of two gratings as in Eq. (6.3.2) can replace the two terms within the square brackets of Eqs. (6.7.17) and (6.7.18):

$$\begin{aligned} \rho_1 e^{i\phi_1(\lambda)} &= \frac{\kappa_{ac}^* \sinh(\alpha_1 L_2)}{i\alpha_1 \cosh(\alpha_1 L_2) + (\delta_1)\sinh(\alpha_1 L_2)} \\ \rho_2 e^{i\phi_2(\lambda)} &= \frac{\kappa_{ac} \sinh(\alpha_2 L_2)}{i\alpha_2 \cosh(\alpha_2 L_2) + (\delta_2)\sinh(\alpha_2 L_2)}. \end{aligned} \tag{6.7.19}$$

We note that the magnitude of the reflectivity $\rho_1 = \rho_2$, since it is the same grating with identical parameters, only different detuning. The dropped transmission in Eqs. (6.7.17) and (6.7.18) may be further simplified to

$$\begin{aligned} \tau_2 &= \frac{1}{2}\rho_1[e^{i[\phi_1(\lambda)-2\phi]} - e^{i[\phi_2(\lambda)+2\phi]}] \\ \rho_1 &= \frac{1}{2}\rho_1[e^{i[\phi_1(\lambda)-2\phi]} + e^{i[\phi_2(\lambda)+2\phi]}], \end{aligned} \tag{6.7.20}$$

from which the power transmittance T_2 and back-reflectance R_1 are

$$T_2 = \frac{\rho_1^2}{2}[1 - \cos\delta] \tag{6.7.21}$$

$$R_1 = \frac{\rho_1^2}{2}[1 + \cos\delta], \tag{6.7.22}$$

where

$$\delta = \phi_1(\lambda) - \phi_2(\lambda) + 4|\kappa|L_1. \tag{6.7.23}$$

Interestingly, Eqs. (6.7.21) and (6.7.22) are exactly the same form as Eqs. (6.3.7) and (6.3.8), which describe the transfer characteristics of the *Michelson* interferometer with identical reflectivities but Bragg detuned gratings. In the BRC, the detuning is implicit in the phase factors ϕ_1 and ϕ_2 and calculated by equating δ_1 and δ_2 to zero, so that

$$\lambda^{1,2}_{Bragg} = 2n_{eff}\Lambda_g \frac{\pi}{\pi \pm \Lambda_g|\kappa|}, \tag{6.7.24}$$

where the sign in the denominator determines the perturbed Bragg wavelength of the slow, symmetric (negative sign) and fast (positive sign) antisymmetric supermodes. Note that for weak coupling, i.e., when $|\kappa| \to 0$, the splitting in the Bragg wavelength tends to zero. The detuning is *solely* dependent on the coupling constant of the coupler. For a given detuning, $2\Delta\lambda = \lambda^2_{Bragg} - \lambda^1_{Bragg}$, we can calculate the coupling constant by solving Eq. (6.7.24) as

$$|\kappa| \approx 2\pi n_{eff} \frac{\Delta\lambda}{(\lambda_{Bragg})^2}, \tag{6.7.25}$$

where λ_{Bragg} is the unperturbed Bragg wavelength.

Since the functional form of the properties of BRC band-pass filters are almost identical to that for the Michelson interferometer, the detuning that can be tolerated for low back reflection has been discussed in Section 6.3. For a back reflection of approximately -30 dB (requiring a detuning of $\sim$0.01 nm), we calculate the coupling constant $\kappa < 26\ \text{m}^{-1}$. This low value of the coupling constant is necessary to suppress the reflections on each side of zero detuning, as shown in Fig. 6.20. In a practical device, there is additional "apodization" due to the variation in the coupling constant in the tapered or curved region of the coupler, which will also tend to reduce the back-reflected light. For minimum back reflection, we note that T_1 in Eq. (6.7.20) is zero, so that the coupling length L_1 may be calculated as

$$L_1 = \frac{\pi + \phi_2(\lambda) - \phi_1(\lambda)}{4|\kappa|}. \tag{6.7.26}$$

Thus, for a low back reflection, the propagation constants of the fibers need to be matched carefully, as well as the Bragg wavelengths of the

gratings in each fiber. Fusing two fibers together creates a highly uniform taper with excellent physical symmetry. A fused coupler with a grating therefore has the potential of functioning as a device with the required characteristics.

A variant on the fused taper device is shown in Fig. 6.41 (*iv*), which relies on the propagation constants of the two fibers being *different* [78]. However, the overlap of the modes and the grating becomes very large, since the grating is in the entire waist region of the couple, and the fields are bounded by air. A tilted grating will therefore act as a mode converter when the Bragg matching condition is met,

$$\beta_1 + \beta_2 = \frac{2\pi}{\Lambda_g}, \tag{6.7.27}$$

where β_1 and β_2 are the propagation constants of the two odd and even modes.

This device has been demonstrated by Kewitsch *et al.* [78] with two identical fibers, one of which is pretapered as shown in Fig. 6.41 (*iv*) to change the propagation constant. A grating written in the waist at 1547 nm "dropped" 98% of the light in a bandwidth of 0.7 nm with a reported insertion loss of 0.1 dB. One problem with a fused taper device is the coupling to radiation modes of the fiber on the short-wavelength side of the Bragg wavelength, which can cause both cross-talk and loss.

6.7.2 Grating-frustrated coupler

The generic form of this device is shown in Fig. 6.41 (*ii*). The coupler consists of two fibers, which are assumed to be parallel, and a single Bragg grating is present in one waveguide alone. The grating-frustrated coupler can be modeled in several ways. These methods include supermodes of the structure [80,76] or using the coupled-mode theory developed by Syms [81]. Syms's model applies to a grating in both regions of the coupler and so has to be modified. In the following, the latter approach has been taken to model this device.

The analysis is in two stages as in the analysis of Bragg gratings: First, synchronous coupling is considered alone, i.e., at the Bragg-matched wavelength, and then the detuned case is analyzed.

For synchronous operation, both fibers have identical effective mode indexes at the Bragg wavelength: We ignore the perturbation introduced

by the grating. The evanescent fields of the two fibers overlap and an exchange of energy takes place.

The coupler can be analyzed by considering four modes with amplitudes $A_{1\ldots4}$. Mode 1 travels in the positive z-direction (from left to right) in the upper fiber, from $z = 0$ to $z = L$. Mode 2 also propagates along the positive z-direction in the lower fiber, from $z = 0$ to $z = L$. Mode 3 propagates in the negative z-direction in the upper fiber, from $z = L$ to $z = 0$. Last, mode 4 also propagates in the negative z-direction in the lower fiber, from $z = L$ to $z = 0$. The evolution of the mode amplitudes of the four waves is then described by a set of four first-order coupled differential equations.

There are three significant interactions that need to be considered:

1. Copropagating interactions between the modes of different waveguides (modes 1 and 2 as well as 3 and 4), as they do in a normal coupler without a grating. The overlap of the mode evanescent fields allows an exchange of energy to take place since the guides are phase matched. Because of symmetry considerations, a single coupling coefficient κ [Eq. (6.3.1c)] can be used.
2. Counterpropagating interaction between the modes of the same fiber. Modes 1 and 3, and 2 and 4, interact because of presence of the Bragg grating. The general form of the refractive index modulation of the grating, which allows this coupling, is given by Eq. (4.2.27). The phase mismatch is

$$\Delta\beta = \beta_1 + \beta_2 - \frac{2\pi N}{\Lambda_g}, \tag{6.7.28}$$

where the moduli of the mode propagation constants for the forward- and counterpropagating modes 1 and 2 are

$$\beta_1 = \beta_2 = \frac{2\pi n_{eff}}{\lambda}. \tag{6.7.29}$$

The phase-matched condition determines the optimum coupling between the forward- and backward-propagating modes when $\Delta\beta = 0$, at the Bragg wavelength. The presence of the grating promotes coupling between modes 2 and 4 since the grating is only in the lower waveguide, while modes 1 and 3 remain uncoupled. The coupling coefficient κ_{ac} for Bragg reflection is given by Eq. (4.3.6),

$$\kappa_{ac} = \frac{\pi\eta\overline{\Delta n}}{\lambda}. \tag{6.7.30}$$

3. We assume that there is no coupling between modes 1 and 4, 4 and 1, 2 and 3, and 3 and 2.

Taking the above considerations into account, the four coupled-mode equations which describe the coupling are

$$\begin{aligned}
\frac{dA_1}{dz} &= -i\{\kappa_c A_2\} \\
\frac{dA_2}{dz} &= -i\{\kappa_c A_1 + \kappa_{ac} A_4\} \\
\frac{dA_3}{dz} &= i\{\kappa_c A_4\} \\
\frac{dA_4}{dz} &= i\{\kappa_{ac} A_2 + \kappa_c A_3\}.
\end{aligned} \tag{6.7.31}$$

A similar procedure is followed as in the BRC coupler, and applying the boundary conditions results in the outputs of the device [82]. The grating-frustrated coupler works best when port 1 is excited (the fiber without the grating) with the grating extending along the entire coupling length and beyond, and with a coupler $\kappa L_c = \pi/2$. With this value of coupling, 100% of the power is transferred from one fiber to the other at a wavelength far removed from the Bragg condition, i.e., the device functions as a normal coupler. On-Bragg, the frustrated coupling depends on the strength of the grating coupling constant. The dependence of the transmission and reflection characteristics for port 1 excitation on the grating coupling strength is shown in Fig. 6.42.

Figure 6.43 shows the theoretical performance of a device similar to the one reported by Archambault *et al.* [83], with approximately 70% in the dropped port. Note that with increasing κL_c (over the coupling length), the on-Bragg wavelength transmission approaches unity, and the reflected power tends to zero. In practice, in-fiber gratings are limited to index modulations of $\sim 10^{-3}$, resulting in $\kappa L_c \approx 10$ for a coupling length of ~4 mm. Thus, the performance of this device is likely to remain limited, however elegant the principle, since the return loss remains high and dropped power will suffer a loss of ~1 dB, despite the insertion loss being intrinsically low (0.2 dB).

Figure 6.44 shows the transmission characteristics of a GFC with a $\kappa_{ac} L_c = 9$ ($\delta n = 2.75 \times 10^{-3}$, and $L_c = 1.57$ mm). The FWHM bandwidth is in excess of 4 nm, the pass-band transmission is >0.9, and the transmis-

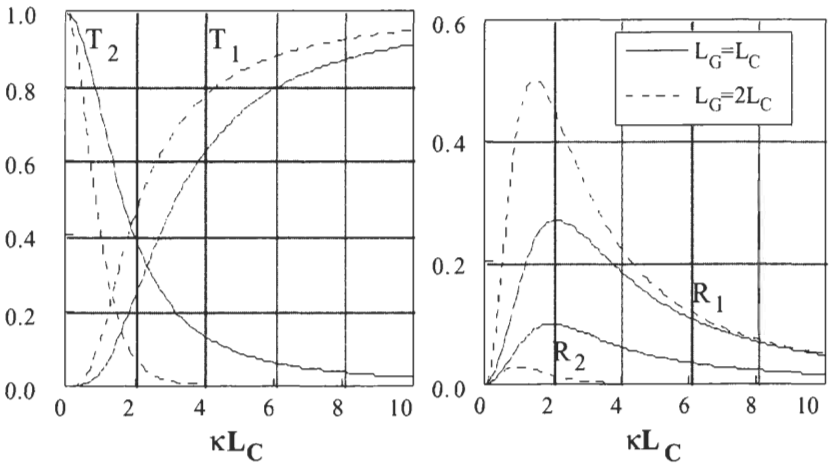

Figure 6.42: Transmission and reflection characteristics for the GFC as a function of the strength of the grating (courtesy Philip Russell from: Archambault J.-L., Russell P. St. J., Barcelos S., Hua P., and Reekie L., "Grating frustrated coupler: a novel channel-dropping filter in single-mode optical fiber,"*Opt. Lett.* **19**(3), 180–182, 1994. Ref. [83]).

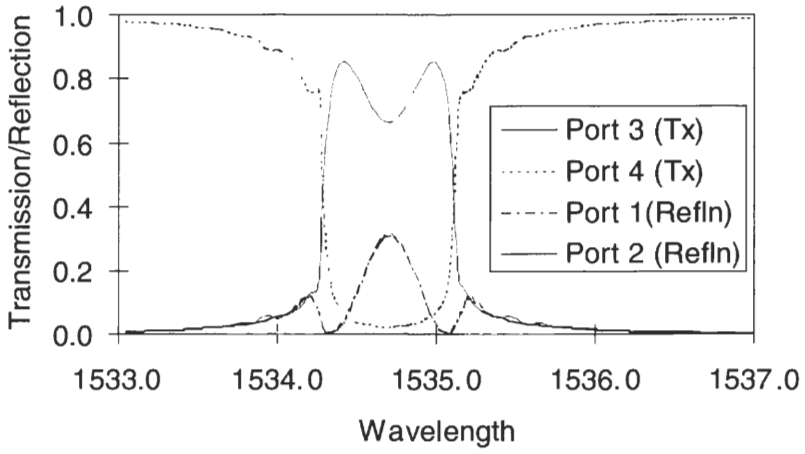

Figure 6.43: Transmission and reflection characteristics of a GFC. Simulation for L_c = 2.5 mm, L_g = 4.5 mm, $\delta n = 3 \times 10^{-4}$, n_{eff} = 1.45. λ_{Bragg} = 1534.7 nm (from: Wolting S., "Grating frustrated couplers," BT Research Laboratories Summer Studentship Report, 1995. Ref. [84]).

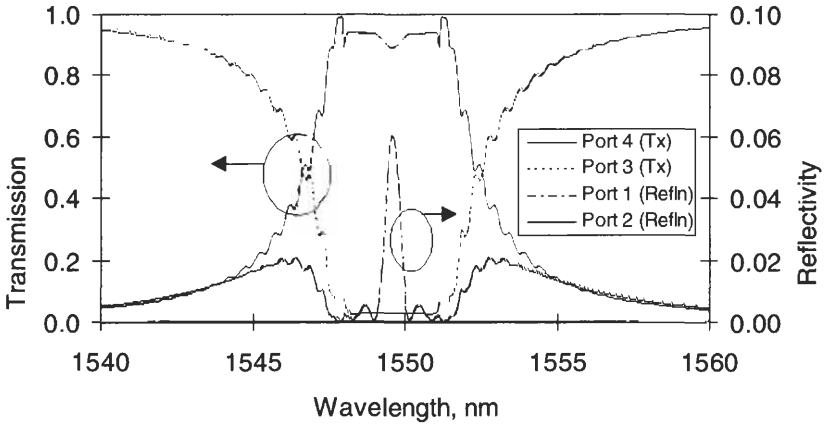

Figure 6.44: The transmission characteristics of the four ports of GFC with a $\kappa_{ac}L_c = 9$, $\delta n = 2.75 \times 10^{-3}$, and $L_c = L_g = 1.57$ mm (from Ref. [84]).

sion in the stop band is still of the order of ~0.05. As an OADM, this device is unlikely to have the performance necessary for telecommunications applications.

6.8 Side-tap and long-period grating band-pass filters

The theory of radiation mode coupling can be found in Chapter 4. Radiation mode coupling is generally used in applications requiring a lossy filter. For example, in flattening the gain spectrum of an erbium-doped fiber amplifier, a multiple side-tap grating (STG) filter [85] and the long-period grating (LPG) [86] have both been successfully used to eliminate the large variations within the gain bandwidth. The light "lost" from the fiber through radiation mode coupling can be substantial, if the grating is strong. Side-tap blocking filters can attenuate ~100% of the light within a narrow band, which can be tailored to span 100 nm or more. While STGs in general allow coupling to *all* order modes (odd and even, LP_{mn}), untilted LPGs couple guided-mode light to only $m = 0$ order modes (LP_{0n}). Choice of blaze angle and the v-value of the fiber easily tailor the loss spectrum and bandwidth of the STG. The bandwidth of the LPG is determined by the coherent interaction between the radiated cladding mode

and the guided mode over the long grating length (centimeters), with a bounded cladding. With an unbounded cladding, the loss spectrum of the LPG becomes extremely wide (>100 nm) [87], since the dispersion in ($n_{\text{eff}} - n_{\text{cladding}}$) is very weak. Figures 6.45*a* and *b* show light exiting from the side of a fiber by an STG and an LPG. The cladding mode has a better chance of interacting with the LPG. A ray exiting the core at an angle of 10° to the fiber axis will travel ~0.4 mm before being reflected back toward the grating in a 125-μm diameter fiber. Shallower angle rays may miss the STG altogether after the first reflection at the cladding–air interface. This is less likely in the LPG, which may be 2–10 times longer than a typical STG. Therefore, there may be continual exchange of energy between the radiated mode and the guided mode with the LPG, unless the cladding is made "infinite" by applying index-matching oil to the cladding. Instead of coupling to discrete radiation modes (approximately the same as the cladding modes), light is coupled to a continuum of the radiation field, so that a broadband loss spectrum is seen in transmission rather than a narrow bandwidth of the cladding mode [87].

Note that the angular distribution of the radiation for the LPG as a function of wavelength is reversed compared to the STG; i.e., the longest wavelengths exit at the largest angle (see Chapter 4).

The basic principle of the coupling relies on the phase-matching conditions, and the overlap integrals determine the strength and the wave-

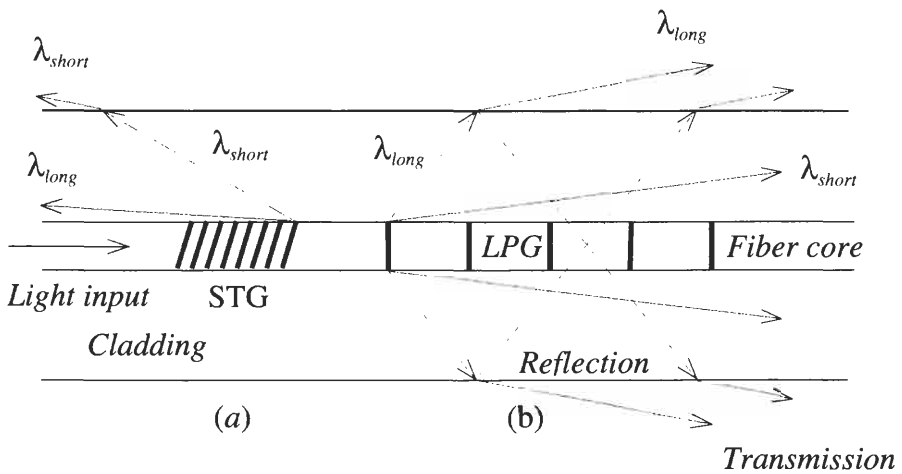

Figure 6.45: Light radiated from the STG and (b) from the LPG.

length dependence of the loss. There are two bounds to the loss spectrum, one on the short- and the other on the long-wavelength side: Light radiated out of the fiber core subtends a wavelength-dependent angle $\theta(\lambda)$ to the counterpropagation direction (STG) and copropagating (LPG), which depends on the inclination of the grating and period.

For the STG, this angle of the radiated light at wavelength λ in the infinite cladding is easily shown to be

$$\cos[\theta(\lambda)] = \frac{1}{n_{clad}}\left(\frac{\lambda}{\Lambda_g} N \cos\,\theta_g - n_{eff}(\lambda)\right), \tag{6.8.1}$$

where θ_g is the tilt of the grating with respect to the propagation direction, and N is the order of the grating. The angle at which the light exits from the side of the fiber varies as a function of wavelength and therefore can be used as a band-pass filter. The bandwidth of the radiated light can be shown to be approximately

$$\Delta\lambda \approx \frac{\Lambda_g \sin^2(\theta_g)}{2\,\cos(\theta_g)}. \tag{6.8.2}$$

However, the phase-matching condition alone does not determine the peak wavelength, in the general case when the grating is titled; the overlap integral together with the phase matching alters the spectrum and shifts the wavelength of maximum loss (see Chapter 4). Typical transmission loss and reflection spectra for a strong STG are shown in Fig. 6.46a, and

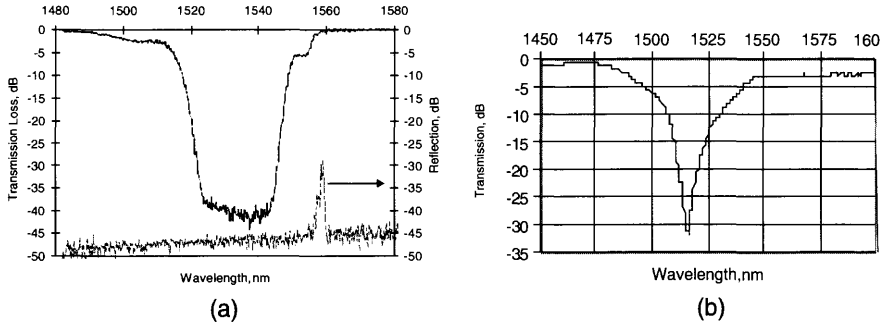

Figure 6.46: The transmission loss (and reflection) of (a) a 4-mm-long side-tap grating filter and (b) LPG filter with a 400-micron period, both written in a boron–germania codoped fiber.

the transmission loss spectrum of an LPG, in Fig. 6.46b. Both gratings were written in the same fiber.

The STG has been used as a spectrum analyzer by Wagener *et al.* [88]. A chirped grating blazed at 9° to the propagation direction was used to out-couple light from a fiber. The chirped grating had a decreasing period away from the launch end of the fiber. Since the angle $\theta(\lambda)$ subtended by the radiated light at a wavelength λ becomes smaller with reducing pitch [Eq. (6.8.1)], the focus of the light coupled out at different points is a function of the wavelength. The focal length is inversely proportional to the wavelength of the radiated light as [88]

$$f(\lambda) = \frac{\Lambda_g^2}{\cos(\theta_g)} \frac{L_g}{\delta\lambda_g} \frac{\sin[\theta(\lambda)]}{\lambda}, \tag{6.8.3}$$

where Λ_g is the nominal period of the chirped grating, n is the refractive index of silica, and L_g and $\delta\lambda_g$ are the length and the change in the period of the grating due to chirp (in nm), respectively. The radiated light was detected by a 256-element photodiode array, the center of which was arranged to be at the focus of the light at λ_c, the wavelength radiated by the center of the grating. A schematic of the device is shown in Fig. 6.47.

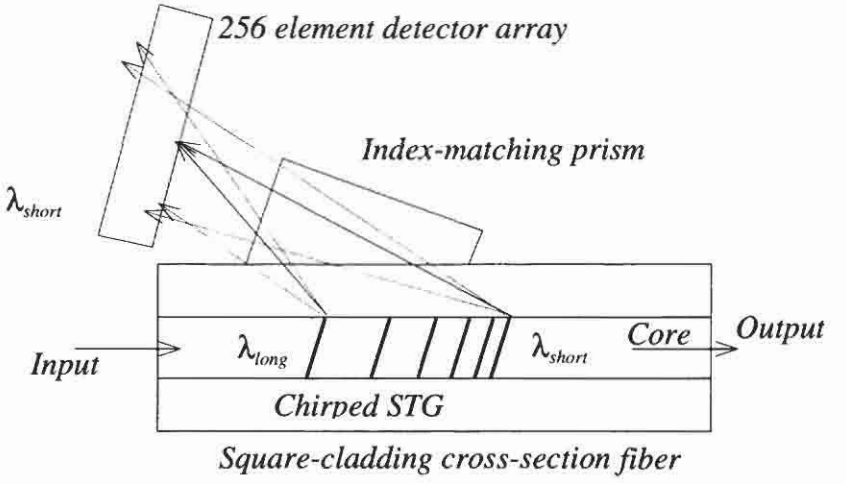

Figure 6.47: A schematic of the in-fiber chirped STG spectrum analyzer (after Ref. [88]).

A weak, 20-mm-long grating (Δ_g = 547 nm) with a chirp in the period of 1.92 nm (±0.96 nm) was used to tap ~5% of the light over a 35-nm bandwidth. An index-matched prism was placed in contact with a fiber of square cladding cross-section to promote good adhesion, to direct the light to the photodiode array.

The effective focal length was 160 mm. The resolution of the spectrometer was demonstrated to be 0.12 nm with a measured bandwidth of 14 nm, an insertion loss of <1 dB, a wavelength accuracy of ±0.03 nm, a power level accuracy of <0.25 dB, and a dynamic range of 35 dB. The spectrum of two resolved channels separated by 50, 100, and 200 GHz using this spectrometer is shown in Fig. 6.48 [88].

While this device is an excellent example of a band-pass filter, which is also tunable, the applications of the STG and the LPG in this area

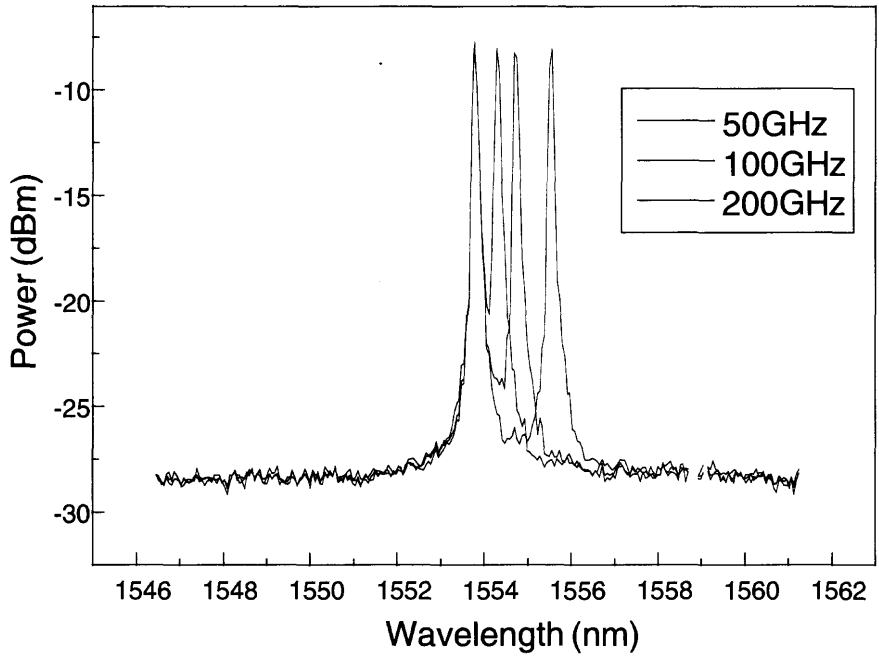

Figure 6.48: The spectrum of two channels as the detuning is increased from 50 to 100 to 200 GHz (courtesy T. Strasser, from Wagener J. L., Strasser T. A., Pedrazzani J. R., and DeMarco J., "Fiber grating optical spectrum analyzer tap," *In Tech. Digest of ECOC'97, Publn. No. 448*, Vol. 5, pp. 65–68. © IEE 1997 Ref. [88]).

have not really been exploited. It is envisaged that supervisory operations of fiber amplifiers is another possible application in which the filter that attenuates the spectrum can allow the monitoring of the performance and control of the amplifier characteristics.

6.9 Polarization rocking band-pass filter

Another type of band-pass filter is the polarization-converting filter. Much of the earlier work focused on the study of photoinduced polarization effects and fabrication of internally written filters [89–95]. The polarization sensitivity of fiber was recognized early in the development of photosensitive phenomena [96]. Birefringence can be photoinduced in Ge-doped fibers [97] because of preferential bleaching of defects [89]. Coupling between orthogonal polarizations was shown in elliptical core fibers due to dynamic changes in the birefringence [98]. A novel *counterpropagating* polarization coupling filter has also been reported, using internally written gratings [99]. It was shown that stress birefringence can be reduced in elliptical cored fibers illuminated with UV radiation [100]. Thus, in principle, the control of the birefringence by external means allows the fabrication of polarization coupling devices at any wavelength. In this section, we consider externally written filters, which can be fabricated for operation at any desired wavelength.

The theory of coupling between polarization can be found in Chapter 4. The band-pass filter functions by rotating the polarization of the input mode by $N\pi/2$. In order to discriminate between the two states, a polarizing component has to be used. A schematic of the filter is shown in Fig. 6.49.

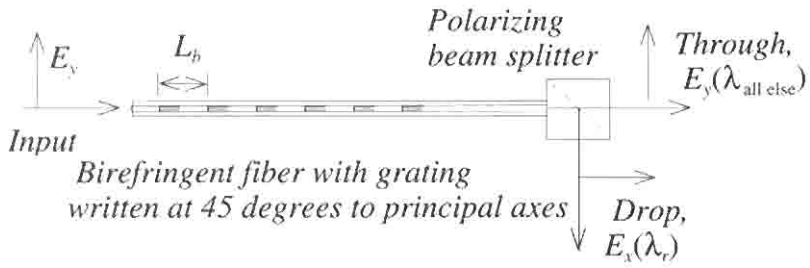

Figure 6.49: The polarization rocking "drop" filter.

Two types of polarization rocking filters can be fabricated. Birefringent polarization maintaining fiber can be used with a given predetermined beat length [101], or nonbirefringent fibers, which are deliberately made birefringent, may also be used [102]. In the first case, *Hill et al.* [101] showed that a filter with only 85 periods had a polarization conversion efficiency of 89% at a wavelength of 1292 nm in a FW bandwidth of ~8 nm. The filter length was reported to be 0.87 m, fabricated in an Andrew Corp. fiber with a birefringence $B = 1.27 \times 10^{-4}$. The transmission spectrum of this filter is shown in Fig. 6.50. The narrow bandwidth is a direct result of the high birefringence of the fiber. Apodized filters have also been demonstrated using the same principle, but with a grating coupling constant which is weighted as a function of length [103]. For the filter to function properly, care needs to be taken, since the input polarization has to remain stable.

In the second type of filter, a nonbirefringent fiber is wrapped on a cylinder to impart a known birefringence [104] (see Chapter 3). Given that the birefringence can be controlled, the beat length and therefore the rocking period is known. This methods allows the fabrication of very

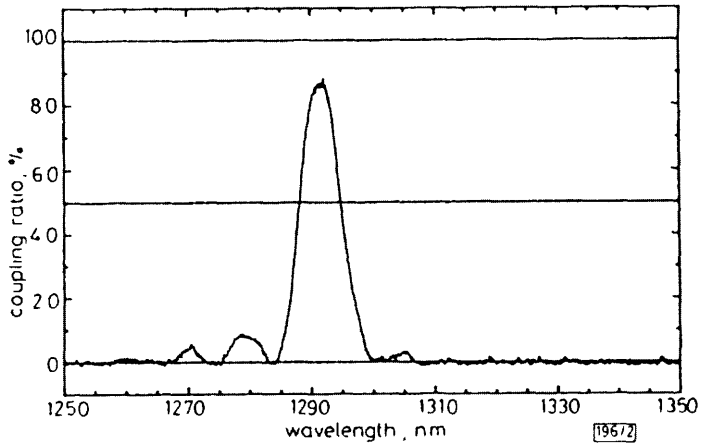

Figure 6.50: Transmission spectrum of an 85-step, polarization-rocking filter fabricated in a polarization maintaining fiber (from: Hill K. O., Bilodeau F., Malo B., and Johnson D. C., "Birefringent photosensitivity in monomode optical fibre: application to external writing of rocking filters," *Electron. Lett.* **27**(17), 1548, 1991. © IEE 1991. Ref. [101]).

long fiber filters, since the bend-induced birefringence is small (beat length ~0.75 m at 1550 nm) even with the tightest tolerable bend in standard telecommunications fibers [102]. The reported filter had a polarization coupling efficiency of ~100% at a peak wavelength of 1540 nm, with a FW bandwidth of 130 nm, in a filter that was only 17 beat lengths long (L_r = 10.89 m), with 27% of each beat length exposed to UV radiation (duty cycle of 27%).

The bandwidth of these filters between the first zeroes of the transmission spectrum follows from Eq. (4.4.12) as

$$\alpha L = \pm \pi, \tag{6.9.1}$$

so that the bandwidth, $2\Delta\lambda$, from Eq. (4.5.11)

$$2\Delta\lambda = \frac{2\pi\lambda L_b}{L_r}. \tag{6.9.2}$$

The fabrication of the rocking filter depends on the periodic exposure to UV radiation of *half* of the beat length of the fiber. This induces a refractive index modulation, which is only half of what it would be if the second half of the beat length was modulated by a *negative* index change, or if the rocking of the birefringence was truly $\pm\phi$ per beat length. This has the beneficial effect of halving the filter length L_r. This is particularly useful, because the rocking angle ϕ saturates at approximately 0.4°–0.5° per beat length with exposure to many pulses [105]. In order to overcome this problem, Psaila *et al.* [105] used a double pass scheme to double the rocking angle per beat length. In the first pass, the fiber was exposed at 45° to the birefringent axes, half of each beat length of 14 mm. The stationary fiber was exposed to a moving, pulsed UV beam through a 0.5-mm slit, with the UV polarization orthogonal to the fiber propagation axis. On the second scan, the fiber was rotated by 90° around the propagation axis, and the other half of the beat length was exposed in a similar manner. The result is the doubling of the rocking angle per beat length, leading to a rocking filter with ~98% conversion efficiency, only 33 beat lengths long, and with a FWFZ (full width to first zeroes) bandwidth of 20 nm.

It should be noted that the polarization coupler is a band-pass filter in transmission and that it converts either input polarization to its orthogonal state. As a consequence of this, a concatenation of two such filters results in a Mach–Zehnder type interferometer [106]. A schematic of this

filter is shown in Fig. 6.51. The transmitted output intensity can be shown to be [106]

$$I = \left(\frac{\kappa_{ac}^2}{\alpha^2}\sin^2\alpha L_r\right)\left[\cos^2\alpha L_r + \frac{\Delta\beta^2\sin^2\alpha L_r}{4\alpha^2}\right][1 + (1 + L_s)\cos(kB)], \qquad (6.9.3)$$

where $k = 2\pi/\lambda$, L_r is the length of the rocking filter, L_S is the distance between the two filters, $\kappa_{ac} = \Delta n/\lambda_r$, and B is the birefringence, $n_x - n_y$. The detuning parameter $\Delta\beta = \beta_x - \beta_y - 2\pi/\lambda$, with the usual definition of α (see Chapter 4). If the filter separation $L_s < L_{coh}L_b/\lambda$, where L_{coh} is the coherence length of the source, then strong interference is visible at the output.

Kannellopoulos *et al.* [106] fabricated the filter in Andrew Corp D-fiber with a polarization beat length of 4.35 mm (L_b) at a wavelength of 780 nm and $B = n_x - n_y = 1.8 \times 10^{-4}$. The core-to-cladding index difference was 3.3×10^{-2} with a higher mode cutoff of 710 nm. The rocking filters centered at 787 nm were 224.4 mm long (L_r) and separated by 320 mm (L_s). The period of the gratings was 4.4 mm, and they were written with 266-nm wavelength pulsed radiation, exposed to 2400 pulses at a peak intensity of 1.4 MW/cm^2. Each filter had a coupling efficiency of 7.5% so that the peak refractive index modulation $\delta\Delta n' = 9.7 \times 10^{-7}$. Figure 6.52 shows the transmission characteristics of the polarization coupling MZI. The output shows three peaks in transmission, each with a FW bandwidth of ~8 nm. The temperature sensitivity of the resonant wavelength of the filter is high (0.5 nm/°C) compared to that of Bragg gratings (0.006 nm/°C), and so the filter is suited to sensing temperature. When one of the filters is heated, the resonant wavelength shifts; alternatively, heating the section between the couplers influ-

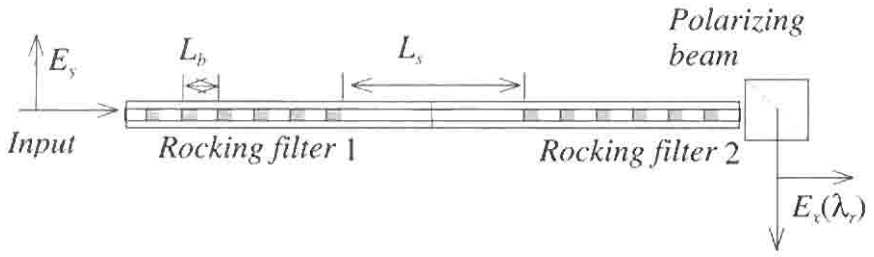

Figure 6.51: The polarization rocking Mach–Zehnder band-pass filter fabricated in birefringent fiber with two gratings written at 45° to principal axes (after Ref. [106]).

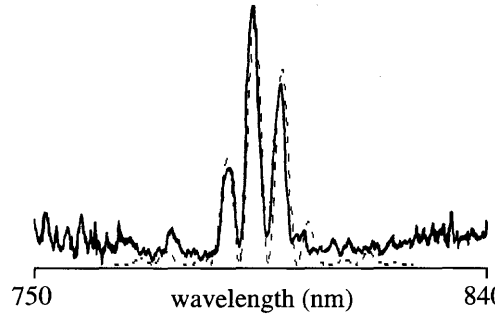

Figure 6.52: The transmission characteristics of the polarization coupling Mach–Zehnder interferometer (Courtesy S. Kannellopoulos, from: Kanellopoulos S. E., Handerek V. A. and Rogers A. J., "Compact Mach-Zehnder fibre interferometer incorporating photo-induced gratings in elliptical core fibers," *Opt. Lett.* **18**(12), 1013-1015, 1993. [106]).

ences the output state, from which a phase sensitivity of ~0.22 rad/°C was calculated over a temperature range of 150°C.

6.10 Mode converters

Mode converters work on a principle similar to that of the polarization converter. There are several types of mode-converting filters: those that couple one guided mode to another co- or counterpropagating guided mode, as well as those which couple a guided (or cladding) mode to a co- or counterpropagating cladding mode (or guided mode). Coupling of a guided mode to a co- or counterpropagating cladding mode has been partially covered in Section 6.8 on side-tap and long-period grating band-pass filters, and also in Chapter 4. Guided–guided co- and counterpropagating mode coupling devices will be discussed in this section. Other devices based on concatenated couplers for mode reconversion will also be discussed.

6.10.1 Guided-mode intermodal couplers

The theory of guided-mode coupling to both copropagating and counterpropagating guided/radiation modes can be found Chapter 4. Equations

(4.3.16), (4.4.11), and (4.4.12) govern the coupling of counter- and copropagating guided modes. Coupling of the modes of the same order is always possible, provided the phase-matching condition is met. The overlap integral, Eq. (4.4.5), for the coupling of dissimilar modes is zero, unless the transverse distribution of the refractive index modulation is not constant, breaking the symmetry. Thus, a slanted grating will increase the overlap integral between modes of different order, since the transverse refractive index modulation profile is no longer uniform. This was first reported by Park and Kim [107] using a novel internal mode-beat grating, by exciting a bimoded fiber at a wavelength of 514.5 nm from a CW argon laser. The beating of the modes automatically creates a blazed grating with the intensity of the laser radiation varying transversely across the core with the mode-beat period. This intensity grating induced a photoinduced grating, which created the mode converter. This principle has been extended by Ouellette [108] by recognizing that the phase-matching condition is met by more than one set of modes due to the nondegeneracy of the modes, but at longer wavelengths. Thus, a grating written at 488 nm by exciting a chosen pair of modes allowed the "reading" of the holographic grating at around 720 nm. Further experiments have demonstrated the sensitivity of the mode beat length to the applied strain [109], since the propagation constants of the fundamental and higher-order modes change differentially. These types of converters have applications in strain sensing and as nonlinear optical switches [110]. A phase-matching condition is also possible where the beat length $L_b \rightarrow \infty$ [111,112], allowing very long period gratings to be used.

A principle similar to the one reported by Park and Kim [107] has been used to fabricate mode converters at different wavelengths. The coupling between the LP_{11} and LP_{01} modes was made possible by slanting the grating using an external, point-by-point UV exposure technique [113], details of which may be found in Chapter 3.

A slit (12 μm) at an angle of 2–3° was used to expose the fiber at the first-order period of 590 μm ($N = 1$) mode beat length, $2\pi/[N(\beta_{LP01} - \beta_{LP11})]$, resulting in a mode converter at a wavelength of 820 nm in a Corning Telecommunications fiber with a higher-order mode cutoff of 1.1 μm [113]. The grating had typically 200–300 steps for 100% coupling, while overcoupled converters with 1000 periods were also reported. These convert the LP_{01} to the LP_{11} and then back again to the LP_{01}. Unlike polarization rocking filters, mode-converting gratings can be very strongly coupled, so that the side lobes of the *sinc* function in Eqs. (4.4.11) and

(4.4.12) become large with a large refractive index modulation, and multiple peaks can be seen in the transmission spectrum. A FWFZ of ~5 nm was observed. A higher-order mode stripper has to be used to observe the loss spectrum of this filter. For the band-pass function, the higher-order mode has to be selected. Alternatively, the higher mode can be excited preferentially in the overcoupled filter and stripped at the output so that the "dropped" wavelength is in the fundamental mode, with the through state in the LP_{11} mode.

Conversion from LP_{01} mode to the leaky counterpropagating LP_{11} mode has been observed in depressed-clad fibers in which tilted Bragg gratings were written [114]. In this case, the fiber supported the LP_{11} mode over short lengths, so that a "ghost" dip is observed in the transmission spectrum at a wavelength slightly shorter than the Bragg reflection wavelength. While the light is coupled into the LP_{11} mode, the reflection is not visible if the fiber on the input side of the gratings is mode stripped. Gratings with a tilt angle of 3° have been written in standard telecommunications fibers preexposed to raise the index to allow the LP_{11} mode to be supported [115] over the UV-exposed length. The overlap between the LP_{01} mode and the LP_{11} mode is almost the same as the LP_{01} mode for this tilt angle, so that efficient reflective mode coupling is possible. The side illumination induces a nonuniform refractive index change across the core, breaking the LP_{11} mode degeneracy and causing two reflections to occur. Depressed-cladding fibers have been examined by Haggans *et al.* [116] with a view to reducing the coupling to radiation and cladding modes.

Coupling to similar order modes does not require a transverse asymmetry in the grating (see Chapter 4). Therefore, the LP_{01} mode is coupled to the LP_{02} mode for both co- and contradirectional converters with a transversely uniform grating. The coupling constant κ_{ac} [117] is

$$\kappa_{ac} = \frac{\pi \Delta n}{\lambda} \left(\frac{w_{01} w_{02}}{v^2 (u_{01}^2 - u_{02}^2)} \right) \times \left(u_{01} \frac{J_0(u_{02})}{J_1(u_{02})} - u_{02} \frac{J_0(u_{01})}{J_1(u_{01})} \right), \tag{6.10.1}$$

where the subscripts refer to the mode, and u, w, and v are the normalized waveguide parameters defined in Chapter 4. The interaction of the $LP_{01} \rightarrow LP_{02}$ mode is particularly useful for narrow-band filters [118] and for broadband dispersion compensation [119]. In the latter application,

gratings between 27 and 35 mm long have been fabricated with periods ranging from 116 to 135 μm in few-moded fiber. Up to 85% coupling is obtained with a FWHM bandwidth of 25 nm. The step-chirped technique [120] can also be used to broaden the bandwidth for longer mode-converter gratings. A 65-mm-long grating with a 0.3-μm chirp over four sections has been demonstrated to have a peak coupling efficiency of 90% at 1556 nm and a FWHM bandwidth of 14 nm.

References

1. Haus H. A. and Shank C. V., "Anti-symmetric type of distributed feedback lasers," *J. Quantum Electron* **12**, 532–539 (1976).
2. Utaka K., Akiba S., and Matsushima Y., "1/4-shifted GaAsP/InP DFB lasers by simultaneous holographic exposure of negative and positive photoresists," *Electron. Lett.* **20**, 1008–1010 (1984).
3. Haus H. A. and Lai Y., "Theory of cascaded quarter wave shifted distributed feedback resonators," *IEEE J. Quantum Electron.* **28**(1), 205–213 (1992).
4. Zengerle R. and Leminger O., "Phase-shifted Bragg-grating filters with improved transmission characteristics," *J. Lightwave Technol.* **13**(2), 2354–2358 (1995).
5. Agrawal G. P. and Radic S., "Phase-shifted fiber Bragg gratings and their applications for wavelength demultiplexing," *IEEE Photon. Technol. Lett.* **6**, 995–997 (1994).
6. Kashyap R., McKee P. E., and Armes D., "UV written reflection grating structures in photosensitive optical fibres using phase-shifted phase-masks," *Electron. Lett.* **30**(23), 1977–1978 (1994).
7. Canning J. and Sceats M. G., "π-phase shifted periodic distributed structures in optical fibers by UV post-processing," *Electron. Lett.* **30**(16), 1244–1245 (1994).
8. Asseh H., Storoy H., Kringlebotn J. T., Margulis W., Sahlgren B., and Sandgren S., "10 cm long Yb^+ DFB fibre laser with permanent phase shifted grating," *Electron. Lett.* **31**, 969–970 (1995).
9. Loh W. H. and Laming R. I., "1.55 μm phase-shifted distribute feedback fibre laser," *Electron. Lett.* **31**(17), 1440–1442 (1995).
10. Hübner J., Varming P., and Kristensen M., "Five wavelength DFB fibre laser source for WDM systems," *Electron. Lett.* **33**(2), 139–140 (1997).
11. Zever I, *Handbook of Filter Synthesis.* Wiley, New York (1967).

12. Wei L. and Lit W. Y., "Phase-shifted Bragg grating filters with symmetrical structures," *IEEE J Lightwave Technol.* **15**(8), 1405–1410 (1997).

13. Bhakti F. and Sansonetti P., "Design and realization of multiple quarter-wave phase-shifts UV written bandpass filters in optical fibers," *IEEE J. Lightwave Technol.* **15**(8), 1433–1437 (1997).

14. Farries M. C., Sugden K., Reid D. C. J., Bennion I., Molony A., and Goodwin M. J., "Very broad reflection bandwidth (44 nm) chirped fibre gratings and narrow-bandpass filters produced by the use of an amplitude mask," *Electron. Lett.* **30**(11), 891–892 (1994).

15. Zhang I., Sugden K., Williams J. A. R., and Bennion I., "Post fabrication exposure of gap-type bandpass filters in broadly chirped fiber gratings," *Opt. Lett.* **20**(18), 1927–1929 (1995).

16. Sugden K., Zhang L., Williams J. A. R., Fallon L. A., Everall L. A., Chisholm K. E., and Bennion I., "Fabrication and characterization of bandpass filters based on concatenated chirped fiber gratings," *IEEE J. Lightwave Technol.* **15**(8), 1424–1432 (1997).

17. Mizrahi V., Erdogan T., DiGiovanni D. J., Lemaire P. J., MacDonald W. M., Kosinski S. G., Cabot S., and Sipe J. E., "Four channel fibre grating demultiplexer," *Electron. Lett.* **30**(10), 780–781 (1994).

18. Jayaraman V., Cohen D. A., and Coldren L. A., "Demonstration of broadband tunability of a semiconductor laser using sampled gratings," *Appl. Phys. Lett.* **60**(19), 2321–2323 (1992).

19. Leners R., Emplit P., Foursa D., Haelterman M., and Kashyap R., "6.1-GHz dark-soliton generation and propagation by a fiber Bragg grating pulse-shaping technique," *J Opt. Soc. Am. B (Optical Physics)* **14**(9), 2339–2347 (1997).

20. Ibsen M., Durkin Michael K., and Lamming R. I., "Chirped Moiré gratings operating on two-wavelength channels for use as dual-channel dispersion compensators," *IEEE Photon. Technol. Lett.* **10**(1), 84–86 (1998).

21. Huber D. R., "Erbium doped fiber amplifier with a 21 GHz optical filter based on an in-fiber Bragg grating," in *Tech. Digest of ECOC '92,* paper WeP2.2, 473 (1992).

22. Ouellette F., Krug P. A., Stephens T., Doshi G., and Eggleton B., "Broadband and WDM dispersion compensation using chirped sampled fibre Bragg gratings," *Electron. Lett.* **31**(11), 899–901 (1995).

23. Legoubin S., Douay M., Bernage P., and Niay P., "Free spectral range variations of grating-based Fabry–Perot photowritten in optical fibers," *J. Opt. Soc. Am. A* **12**(8), 1687–1694 (1995).

24. Huber D. R., "1.5 μm narrow bandwidth in-fiber gratings," in *Proc. of LEOS '91,* Paper OE3.1 (1991).

25. Morey W. W., Bailey T. J., Glenn W. H., and Meltz G., "Fiber Fabry–Perot interferometer using side exposed fiber Bragg gratings," in *Proc. of OFC '92,* p. 96 (1992).

26. Riant I., Borne S., and Sansonetti P., "Asymmetrical UV-written fibre Fabry–Perot for WDM soliton frequency guiding and equalisation," in *Photosensitivity and Quadratic Nonlinearity in Glass Waveguides: Fundamentals and Applications,* Vol. 22, 1995 OSA Technical Series (Optical Society of America, Washington DC, 1995), pp. SbB4-(18–21) (1995).

27. BT Internal Report, 1993.

28. Town G. E., Sugden K., Williams J. A. R., Bennion I., and Poole S. B., "Wideband Fabry–Perot like filters in optical fibers," *IEEE Photon. Technol. Lett.* **7**(1) (1995).

29. Kashyap R., unpublished.

30. Legoubin S., Fertein E., Douay M., Bermage P., Niay P., Bayon F., and Georges T., "Formation of Moiré gratings in core of germanosilicate fibre by transverse holographic double exposure," *Electron. Lett.* **27**(21) 1945 (1991).

31. Kashyap R., McKee P. F., Campbell R. J., and Williams D. L., "A novel method of writing photo-induced chirped Bragg gratings in optical fibres," *Electron. Lett.* **30**(12), 996–997 (1994).

32. Campbell R. J. and Kashyap R., "Spectral profile and multiplexing of Bragg gratings in photosensitive fibre," *Opts. Lett.* **16**(12), 898–900 (1991).

33. Everall L. A., Sugden K., Williams J. A. R., Bennion I., Liu X., Aitchison J. S., Thom S., and De La Rue R. M., "Fabrication of multi-pass band moiré resonators in fibers by the dual-phase-mask exposure method," *Opt. Lett.* **22**(19), 1473–1475 (1997).

34. Hill K. O., Johnson D. C., Bilodeau F., and Faucher S., "Narrow bandwidth optical waveguide transmission filters," "Electron. Lett. **23**(9), 465–466 (1987).

35. Morey W. W., "Tuneable narrow-line bandpass filter using fibre gratings," in *Proc. Conference on Optical Fiber Communications, OFC '91,* paper PD20-1.

36. Kashyap R. and Nayar B. K., "An all single-mode fibre Michelson interferometer sensor," *IEEE J. Lightwave Technol.* **LT-1**(3), 619–624 (1983).

37. Kogelnik H. and Schmidt R. V., "Switched directional couplers with alternating $\Delta\beta$," *IEEE J. Quantum Electron.* **QE-12**, 396–401 (1976).

38. Digonet M. J. F. and Shaw H. J., "Analysis of a tunable single mode optical fiber coupler," *IEEE J. Quantum Electron.* **QE-18**(4), 746–754 (1982).

39. Snyder A. W., "Coupled mode theory for optical fibers," *J. Opt. Soc. Am.* **62**, 1267–1277 (1972).

40. Nykolak G., de Barros M. R. X., Nielsen T. N., and Eskildsen L., "All-fiber active add-drop wavelength router," *IEEE Photon. Technol. Lett.* **9**(5), 605–606 (1997).

41. Hibino Y., Kitagawa T., Hill K. O., Bilodeau F., Malo B., Albert J., and Johnson D. C., "Wavelength division multiplexer with photoinduced Bragg gratings fabricated in a planar-lightwave-circuit-type asymmetric Mach–Zehnder interferometer," *IEEE Photon. Technol. Lett.* **8**(1), 84–86 (1996).

42. Kashyap R., "A new class of fibre grating based band-pass filters: The highly asymmetric interferometer," *Opt. Commun.* **153**, 14–18 (1998).

43. Bilodeau F., Malo B., Johnson D. C., Albert J., and Hill K. O., "High return loss narrowband all fiber bandpass Bragg transmission filter," *IEEE Photonics Technol. Lett.* **6**(1), 80 (1994).

44. Bilodeau F., Hill K. O., Theriault S., Malo B., Albert J., and Johnson D. C., "Broadband wavelength selective tap using an all fiber Mach-Zehnder interferometer and chirped photo induced Bragg gratings," in *Technical Digest of OFC '96,* paper WF5, p. 119 (1996).

45. Lewis S. A. F., Guy M. J., Taylor J. R., and Kashyap R., "An all fibre periodic spectral filter for the simultaneous generation of WDM channels from broad bandwidth pulsed sources," **34**(12), submitted 1998.

46. Kashyap R., Hornung S., Reeve M. H., and Cassidy S. A., "Temperature desensitisation of delay in optical fibres for sensor applications," *Electron. Lett.* **19**(24), 1039–1040 (1983).

47. Iwashima T., Inoue A., Shigematsu M., Nishimura M., and Hattori Y., "Temperature compensation technique for fibre Bragg gratings using liquid crystalline polymer tubes," *Electron. Lett.* **33**(5), 417–419 (1997).

48. Weidman D. L., Beall G. H., Chyung K. C., Francis G. L., Modavis R. A., and Morena R. M., in *Tech. Digest of ECOC '96,* Vol. 1, Paper MOB.3.5, p. 1.61–64 (1996).

49. Johnson D. C., Hill K. O., Bilodeau F., and Faucher S., "New design configuration for a narrow-band wavelength selective optical tap and combiner," *Electron. Lett.* **23**, 668 (1987).

50. Ragdale C. M., Reid T. J., Reid D. C. J., Carter A. C., and Williams P. J., "Integrated laser and add–drop optical multiplexer for narrowband wavelength division multiplexing," *Electron. Lett.* **28**(8), 712–714 (1992).

51. Maxwell G. D., Kashyap R., and Ainslie B. J., "UV written 1.5 μm reflection filters in single mode planar silica guides," *Electron. Lett.* **28**(22), 2016 (1992).

52. Cullen T. J., Rourke H. N., Chew C. P., Baker S. R., Bircheno T., Byron K., and Fielding A., "Compact all-fibre wavelength drop and insert filter," *Electron. Lett.* **30**(25), 2160–2162 (1994).

53. Kashyap R., Maxwell G. D., and Ainslie B. J., "Laser trimmed four-port bandpass filter fabricated in singlemode planar waveguides," *IEEE Photonics Tech. Lett.* **5**(2) 191 (1993).

54. Kashyap R., Hornung S., Reeve M. H., and Cassidy S. A., "Temperature desensitisation of delay in optical fibres for sensor applications," *Electron. Lett.* **19**(24), 1039–1040 (1983).

55. Kashyap R., Reeve M. H., Cassidy S. A., and Hornung S., "Temperature desensitisation of delay in fibres." UK Patent no. 8328204, 21 Oct. 1983, US Patent no. 4923278, 31 March 1987.

56. Morey W. W. and Glomb W. L., US Patent no. 5042898, 27 August 1991).

57. Mizuochi T. and Kitayama T., "Interferometric cross talk-free optical add/drop multiplexer using cascaded Mach-Zehnder fiber gratings," in *Technical Proc. of OFC '97,* pp. 176–177 (1997).

58. Chawki M. J., Berthou L., Delevaque E., Gay E., and Le Gac I., "Evaluation of an optical boosted add/drop multiplexer OBADM including circulators and fiber grating filters," in *Tech. Digest of ECOC '95,* paper Mo A.3.7 (1995).

59. Huber D. R., "Erbium doped amplifier with a 21 GHz optical filter based on an in-fiber Bragg grating," in *Proc. of ECOC '92,* pp. 473–476 (1992).

60. Delavaque E., Boj S., Bayon J.-F., Poignant H., Le Mellot J., Monerie M., Niay P., and Bernage P., "Optical fiber design for strong grating photo imprinting with radiation mode suppression," in *Proc. of Post-Deadline Papers of OFC '95,* Paper PD5 (1995).

61. Dong L., Reekie L., Cruz J. L., Caplen J. E., and Payne D. N., "Cladding mode suppression in fibre Bragg gratings using fibres with a depressed cladding," in *Tech. Digest of ECOC '96,* Vol. 1, Paper M0B.3.3, pp. 1.53–56 (1996).

62. Goldstein E. L., "Performance implications of crosstalk in transparent lightwave networks," *IEEE Photon. Technol. Lett.* **6**(5), 657 (1994).

63. Eggleton B. J., Lenz G., Litchinitser N., Patterson D. B., and Slusher R. E., "Implications of fiber grating dispersion for WDM communication systems," *IEEE Photon. Technol. Lett.* **9**, 1403–1405 (1997).

64. Okayama H., Ozeki Y., and Kunii T., "Dynamic wavelength selective add/drop node comprising tunable gratings," *Electron. Lett.* **33**(10), 881–882 (1997).

65. Quetel L., Rivollan L., Delevaque E., Gay E., and Le Gac I., "Programmable fibre grating based wavelength demultiplexer," in *Tech. Digest of OFC '96,* Paper WF6 (1996).

66. Kim S. Y., Lee S. B., Kwon S. W., Choi S. S., and Jeong J., "Channel-switching active add/drop multiplexer with tunable gratings," *Electron. Lett.* **34**(1), 104–105 (1998).

67. Okayama H., Ozeki Y., Kamijoh T., Xu C. Q., and Asabayashi I., "Dynamic wavelength selective add/drop node comprising fibre gratings and switches," *Electron. Lett.* **33**(5), 403–404 (1997).

68. Ellis A. D., Kashyap R., Crisp I., Malyon D. J., and Hueting, J. P., "Demonstration of an 80 Gb/s throughput, reconfigurable dispersion compensating WDM ADM using Deuterium sensitised 10 cm stop chirped fibre Bragg gratings," in *Proc. of ECOC '97,* Vol. 1, pp. 171–175 (1997).

69. Bircheno T. and Baker V., "A fibre polarisation splitter/combiner," *Electron. Lett.* **21**(6), 2521–2522 (1985).

70. Lefevre H. C., "Single-mode fibre fractional wave devices and polarisation controllers," *Electron. Lett.* **16**, 778–780 (1980).

71. Guy M. J., Chernikov S. V., Taylor J. R., and Kashyap R., "Low loss fibre Bragg grating transmission filter based on a fiber polarization splitter," *Electron. Lett.* **30**(18), 1512–1513 (1994).

72. Chernikov S. V., Taylor J. R., and Kashyap R., "All-fiber dispersive transmission filters based on fiber grating reflectors," *Opt. Lett.* **20**(14), 1586–1588 (1995).

73. Kim S. Y., Lee S. B., Chung J., Kim S. Y., Park I. J., Jeong J., and Choi S. S., "Highly stable optical add/drop multiplexer using polarization beam splitters and fiber Bragg gratings," *IEEE Photon. Technol. Lett.* **9**(8), 1119–1121 (1997).

74. Taylor H. F., "Frequency selective coupling in parallel dielectric waveguides," *Opt. Commun.* **8**, 423 (1973).

75. Elachi C. and Yeh P., "Frequency selective coupler for integrated optic systems," *Opt. Commun.* **7**, 201 (1973).

76. Baumann I., Seifert J., Nowak W., and Sauer M., Compact all-fiber add–drop multiplexer using fiber Bragg gratings," *IEEE Photon. Technol. Lett.* **8**(10), 1331–1333 (1997).

77. Orlov S. S., Yariv A., and Van Essen S., "Coupled mode analysis of fiber optic add–drop filters for dense wavelength division multiplexing," *Opt. Lett.* **22**(10), 688–690 (1997).

78. Kewitsch A. S., Rakuljic G. A., Willems P. A., and Yariv A., "An all-fiber, zero insertion loss add/drop filter for wavelength division multiplexing," in *Bragg Gratings, Photosensitivity, and Poling in Glass Fibers and Waveguides: Applications and Fundamentals,* Vol. 17, OSA Technical Digest Series (Optical Society of America, Washington DC, 1997), paper BTuA2, pp. 256–258.

79. Kashyap R., "A simplified approach to Bragg grating based Michelson and the in-coupler Bragg grating add-drop multiplexers," in *Tech. Digest of OFC '99,* paper TuN3, 1999.

80. Yariv A. and Yeh P., *Optical Waves in Crystals,* Chapter 6. Wiley, New York (1984).

81. Syms R. R. A., "Optical directional coupler with a grating overlay," *Appl. Opt.* **24**(5), 717–726 (1985).

82. Archambault J.-L., Ph.D. Thesis, University of Southampton (1994).

83. Archambault J.-L., Russell P. St. J., Barcelos S., Hua P., and Reekie L., "Grating frustrated coupler: a novel channel-dropping filter in single-mode optical fiber," *Opt. Lett.* **19**(3), 180–182 (1994).

84. Wolting S., "Grating frustrated couplers," BT Research Laboratories Summer Studentship Report (1995).

85. Kashyap R., Wyatt R., and McKee P. F., "Wavelength flattened saturated erbium amplifier using multiple side-tap Bragg gratings," *Electron. Lett.* **29**(11), 1025 (1993).

86. Vengsarkar A. M., Pedrazzani J. R., Judkins J. B., Lemaire P. J., Bergano N. S., and Davidson C. R., "Long-period fiber grating based gain equalisers," *Opt. Lett.* **21**, 336–338 (1996).

87. Stegull D. B. and Erdogan T., "Long-period fiber-grating devices based on leaky cladding mode coupling," in *Bragg Gratings, Photosensitivity, and Poling in Glass Fibers and Waveguides: Applications and Fundamentals,* Vol. 17, OSA Technical Digest Series (Optical Society of America, Washington DC, 1997), paper BTuA2, pp. 16–18.

88. Wagener J. L., Strasser T. A., Pedrazzani J. R., and DeMarco J., "Fiber grating optical spectrum analyser tap," in *Tech. Digest of ECOC '97, Publn. No. 448,* pp. 65–68.

89. Bardal S., Kamal A., and Russell P. St. J., "Photoinduced birefringence in optical fibres: a comparative study of low-birefringence and high-birefringence fibers," *Opt. Lett.* **17**(6), 411 (1992).

90. Russell P. St. J. and Hand D. P., "Rocking filter formation in photosensitive high birefringence optical fibres," *Electron. Lett.* **26**, 1846–1848 (1990).

91. Kanellopoulos S. E., Valente L. C. G., Handerek V. A., and Rogers A. J., "Comparison of photorefractive effects and photogenerated components in polarisation maintaining fibres," *SPIE* **1516**. "International Workshop on Photo-induced Self-Organisation effects in Optical Fibres," p. 200 (1991).

92. An S. and Sipe J. E., "Polarisation aspects of two-photon photosensitivity in birefringent optical fibers," *Opt. Lett.* **17**(7) (1992).

93. Handerek V. A., Kanellopoulos S. E., Jamshidi H., and Rogers A. J., "Simultaneous observation of photobleaching and photorefractive effects in germanium-doped optical fibers," *Photon. Technol. Lett.* **3**(3), 244–246 (1991).

94. Ouellette F., Gagnon D., and Porier M., "Permanent birefringence in Ge-doped fiber," *Appl. Phys. Lett.* **58**(17), 1813 (1991).

95. Poirier M., Thibault S., Lauzon J., and Ouellette F., "Dynamic and orientational behaviour of UV induced luminescence bleaching in Ge-doped silica optical fiber," *Opt. Lett.* **18**(11), 870 (1993).

96. Parent M., Bures J., Lacroix S., and Lapierre J., "Propriétés de polarisation des réflecterus de Bragg induits par photosensibilité dans les fibres optiques monomode," *Appl. Opt.* **24**(3), 354 (1985).

97. Ouellette F., Gagnon D., and Porier M., "Permanent birefringence in Ge-doped fiber," *Appl. Phys. Lett.* **58**(17), 1813 (1991).

98. Lauzon J., Gagnon D., LaRochelle S., Boulin F., and Ouellette F., "Dynamic polarization coupling in elliptical-core photosensitive fiber," *Opt. Lett.* **17**, 1664 (1992).

99. Kamal A., Kanellopoulos S. E., Archambault J.-L., Russell P. St. J., Handerek V. A., and Rogers A. J., "Holographically written reflective polarization filter in single-mode optical fibers," *Opt. Lett.* **17**(17), 1189–1191 (1991).

100. Wong D., Poole S. B., and Skeats M. G., "Stress-birefringence reduction in elliptical-core fibres under ultraviolet irradiation," *Opt. Lett.* **17**(24), 1773 (1992).

101. Hill K. O., Bilodeau F., Malo B., and Johnson D. C., "Birefringent photosensitivity in monomode optical fibre: application to external writing of rocking filters," *Electron. Lett.* **27**(17), 1548 (1991).

102. Johnson D. C., Bilodeau F., Malo B., Hill K. O., Wigley P. G. J., and Stegeman G. I., "Long length, long-period rocking filters fabricated from conventional monomode telecommunications optical fibres," *Opt. Lett.* **17**(22), 1635 (1992).

103. Malo B., Bilodeau F., Johnson D. C., and Hill K. O., "Title of ARTICLE," in *Optical Fiber Communication Conf.,* Vol. 5 of 1992 OSA Tech. Digest. Series (Optical Society of America, Washington D.C., 1992), paper PD23, p. 404, 1992.

104. Lefevre H. C., "Single-mode fibre fractional wave devices and polarisation controllers," *Electron. Lett.* **16**, 778–780 (1980).

105. Psaila D. C., de Sterke M., and Ouellette F., "Double pass technique for fabricating compact optical fibre rocking filters," *Electron. Lett.* **31**(13), 1093–1094 (1995).

106. Kannellopoulos S. E., Handerek V. A., and Rogers A. J., "Compact Mach–Zehnder fibre interferometer incorporating photo-induced gratings in elliptical core fibres," *Opt. Lett.* **18**(12), 1013–1015 (1995).

107. Park H. G. and Kim B. Y., "Intermodal coupler using permanently photoinduced grating in two mode optical fibre," *Electron. Lett.* **25**(12), 797 (1989).

108. Ouellette F., "Phase-matching of optical fibre photosensitive intermodal couplers in infra-red," *Electron. Lett.* **25**(23), 1590–1591 (1989).

109. Vengsarkar A. M., Greene J. A., and Murphy K. A., "Photoinduced refractive index changes in two-mode elliptical core fibers: sensing applications," *Opt. Lett.* **16**(19), 1541–1543 (1991).

110. Park H. G., Huang S. Y., and Kim B. Y., "All-optical intermodal switch using periodic coupling in a two-mode waveguide," *Opt. Lett.* **14**(16), 877–879 (1989).

111. Blake J. N., Huang S. Y., Kim B. Y., and Shaw. H. J., "Strain effects on lightly elliptical core two mode fibers," *Opt. Lett.* **12**, 732 (1987).

112. Ouellette F., "Theoretical aspects of intermodal couplers in photosensitive optical fibers," in *Tech. Digest of Integrated Photonics Research,* 1990, p. 96.

113. K. O., Malo B., Vineberg K. A., Bilodeau F., Johnson D. C., and Skinner I., "Efficient mode conversion in telecommunication fibre using externally written gratings," *Electron. Lett.* **26**(16), 1270 (1990).

114. Morey W. W., Meltz G., Love J. D., and Hewlett S. J., "Mode-coupling characteristics of photo-induced Bragg gratings in depressed cladding fiber," *Electron. Lett.* **30**, 730–731 (1994).

115. Johlen D., Klose P., Renner H., and Brinkmeyer E., "Strong LP_{11} mode splitting in UV side written tilted gratings," in *Bragg Gratings, Photosensitivity, and Poling in Glass Fibers and Waveguides: Applications and Fundamentals,* Vol. 17, OSA Technical Digest Series (Optical Society of America, Washington, DC, 1997), Paper BMG12, pp. 219–221.

116. Haggans C. W., Singh H., Varmer W. F., and Wang J.-S., "Analysis of narrow-depressed cladding fibers for minimization of cladding mode losses in fiber Bragg gratings," in *Bragg Gratings, Photosensitivity, and Poling in Glass Fibers and Waveguides: Applications and Fundamentals,* Vol. 17, OSA Technical Digest Series (Optical Society of America, Washington, DC, 1997), Paper BMG11, pp. 217–218.

117. Shi C.-X. and Okoshi T., "Analysis of a fiber $LP^{02} \leftrightarrow LP^{02}$ mode converter," *Opt. Lett.* **17**, 719 (1992).

118. Bilodeau F., Hill K. O., Malo B., Johnson D. C., and Skinner I. M., "Efficient, narrowband $LP_{01} \leftrightarrow LP_{02}$ mode converters fabricated in photosensitive fiber: Spectral response," *Electron. Lett.* **27**, 682–682 (1991).

119. Ky N. H., Limberger H. G., and Salathé R., "Efficient broadband intracore grating LP_{01}–LP_{01} mode converters for chromatic dispersion compensation," *Opt. Lett.* **23**(6), 445–447 (1998).

120. Kashyap R., McKee P. F., Campbell R. J., and Williams D. L., "A novel method of writing photo-induced chirped Bragg gratings in optical fibres," *Electron. Lett.* **30**(12), 996–997 (1994).

This page intentionally left blank

Chapter 7

Chirped Fiber Bragg Gratings

"Chirp" is the high-pitched varying sound emitted by certain birds and bats. Gratings that have a nonuniform period along their length are therefore known as chirped. Chirp in gratings may take many different forms. The period may vary symmetrically, either increasing or decreasing in period around a pitch in the middle of a grating. The chirp may be linear, i.e., the period varies linearly with length of the grating [1], may be quadratic [2], or may even have jumps in the period [3]. A grating could also have a period that varies *randomly* along its length [4], over and above a general trend; for example, uniform, linear chirp. Chirp maybe imparted in several ways: by exposure to UV beams of nonuniform intensity of the fringe pattern, varying the refractive index along the length of a uniform period grating [5], altering the coupling constant κ_{ac} of the grating as a function of position [6], incorporating a chirp in the inscribed grating [7], fabricating gratings in a tapered fiber [8], applying of nonuniform strain [9] etc., many of which have been covered in Chapter 3. All these gratings have special characteristics, which are like signatures and may be recognized as special features of the type of grating. Chirped gratings have many applications. In particular, the linearly chirped grating has found a special place in optics: as a dispersion-correcting and compensating device. This application has also triggered the fabrication of ultralong, broad-bandwidth gratings of high quality, for high-bit-rate transmission in excess of 40 Gb/sec over 100 km [10] or more [11] and in WDM transmission [12]. Some of the other applications include chirped

pulse amplification [13], chirp compensation of gain-switched semiconductor lasers [14], sensing [15], higher-order fiber dispersion compensation [16], ASE suppression [17], amplifier gain flattening [18], and band-blocking and band-pass filters [19].

7.1 General characteristics of chirped gratings

It has been recognized for a long time that gratings can be used for correcting chromatic dispersion [20–22]. Winful [23] proposed the application of a fiber grating filter for the correction of nonlinear chirp to compress a pulse in transmission in a long grating. It was also suggested that since these gratings display negative group-velocity dispersion, their application in dispersion compensation could be tailored by chirping of the grating [23]. These are known as dispersion compensating gratings (DCGs). Nonlinear transmission is also a subject of renewed interest in long gratings [24–28]. Kuo *et al.* [29] measured the negative-group-velocity dispersion of Bragg gratings in the visible wavelength region. While the dispersion in these gratings in transmission is large, a limiting factor is the narrow bandwidth over which they can be used to correct for linear dispersion [30,31]. The drawback of such an arrangement is that the gratings have to be used on the edge of the band and consequently introduce a loss penalty, since some of the light is reflected, although it has been shown that strong, long, highly reflective gratings can be used to compensate for dispersion in communication links in transmission with negligible loss [32], by proper design of the grating. For high-bit-rate systems, higher-order dispersion effects become important, dissipating the advantage of the grating used in transmission. The criteria used for the design of the grating to compress pulses in a near ideal manner are a compromise between the reduction of higher-order dispersion and pulse recompression. Bandwidths are limited with this configuration by the strength of the coupling constant and length of a realizable uniform period grating. Uniform period DCGs may find applications in closely spaced WDM systems.

If the coupling constant κ_{ac} is ramped linearly as a function of grating length, the grating exhibits strong dispersion. Used in reflection, an 81-mm-long grating had a coupling coefficient that was varied from zero to 12 cm^{-1} to achieve a dispersion of ~3.94 nsec/nm [6] but over a bandwidth of only ~0.2 nm. These gratings typically have >99% in-band reflectivity.

Despite the large dispersion, unchirped gratings have symmetrical delay characteristics, so that the dispersion changes sign when detuning from one side of the bandgap to the other [33]. With the several possibilities of using unchirped gratings for the management of dispersion, chirped gratings are even more attractive for this application, despite their use in reflection.

The application of reflective chirped gratings for dispersion compensation was originally suggested by Ouellette [34]. The group delay through a fiber is large in comparison with the dispersion of standard optical fibers at 1550 nm. A grating reflecting a band of wavelengths distributed over its length benefits from the large group delay in the fiber. We now assess the performance of chirped gratings as a dispersive filter specifically for the compensation of chromatic dispersion.

Figure 7.1 shows a schematic of a chirped grating, of length L_g and chirped bandwidth $\Delta\lambda_{\text{chirp}}$. Referring to Fig. 7.1, we note that the chirp in the period can be related to the chirped bandwidth, $\Delta\lambda_{\text{chirp}}$ of the fiber grating as

$$\begin{aligned}\Delta\lambda_{chirp} &= 2n_{eff}(\Lambda_{long} - \Lambda_{short}) \\ &= 2n_{eff}\Delta\Lambda_{chirp}\end{aligned} \tag{7.1.1}$$

The reflection from a chirped grating is a function of wavelength, and therefore, light entering into a positively chirped grating (increasing period from input end) suffers a delay τ on reflection that is approximately

$$\tau(\lambda) \approx \frac{(\lambda_0 - \lambda)}{\Delta\lambda_{chirp}} \frac{2L_g}{v_g}, \qquad \text{for } 2n_{eff}\Lambda_{short} < \lambda < 2n_{eff}\Lambda_{long}, \tag{7.1.2}$$

where λ_0 is the Bragg wavelength at the center of the chirped bandwidth of the grating, and v_g is the average group velocity of light in the fiber.

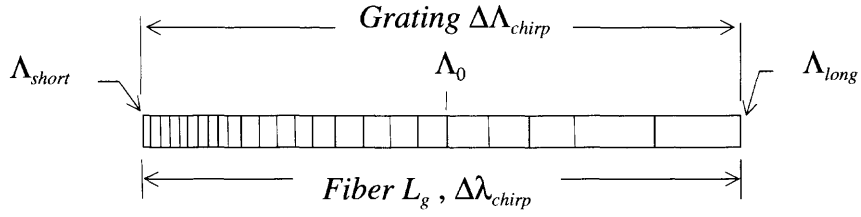

Figure 7.1: The chirped grating.

The effect of the chirped grating is that it disperses light by introducing a maximum delay of $2L_g/v_g$ between the shortest and longest reflected wavelengths. This dispersion is of importance since it can be used to compensate for chromatic dispersion induced broadening in optical fiber transmission systems. At 1550 nm, the group delay τ in reflection is ~10 nsec/m. Therefore, a meter-long grating with a bandwidth of 1 nm will have a dispersion of 10 nsec/nm.

An important feature of a dispersion-compensating device is the figure of merit. There are several parameters that affect the performance of chirped fiber Bragg gratings for dispersion compensation. These are the insertion loss (due to <100% reflectivity), dispersion, bandwidth, polarization mode-dispersion, and deviations from linearity of the group delay and group delay ripple. Ignoring the first and the last two parameters for the moment, we consider the performance of a chirped grating with linear delay characteristics, over a bandwidth of $\Delta\lambda_{\text{chirp}}$. Priest and Giallorenzi [35] have proposed a figure of merit for coherent communications, but taking into account only the dispersion and the bandwidth of the filter. This approach, while not entirely appropriate for chirped gratings owing to the larger parameter set, is never the less a guide in assessing the usefulness of the "ideal" chirped grating. It should be remembered that chirped gratings have a limited bandwidth over which the dispersion is useful, making them different from other truly broadband compensating devices, such as dispersion-compensating fiber [36].

We consider the propagation of an optical pulse in normalized units, in a frame of reference moving in the $+z$ direction at a group velocity v_g. The pulse amplitude $A(z, \tau)$, with a normalized amplitude $U(z, \tau)$, following Agrawal [37], is described as

$$A(z,\tau) = \sqrt{P_{in}}U(z,\tau)e^{-\alpha z/2}, \tag{7.1.3}$$

in which α is the attenuation coefficient of the fiber, P_{in} is the input power, and the frame of reference normalized to the initial pulse width T_0 is

$$\tau = \frac{1}{T_0}\left(t - \frac{v_g}{z}\right). \tag{7.1.4}$$

For a Gaussian pulse with a $1/e$- intensity half-width of T_0, the normalized amplitude is [38]

$$U(0,T) = e^{-T^2/2T_0^2}. \tag{7.1.5}$$

Transmission in a linearly dispersive system broadens the pulse, but does not change its shape, and is simply related to the input pulse width by [37]

$$\left(\frac{T_1}{T_0}\right)^2 = 1 + \frac{z}{L_D}, \tag{7.1.6}$$

which is the well-known formula for linear pulse broadening, remembering that the dispersion length is a function of the spectral width of the pulse and the linear group velocity dispersion (GVD) of the fiber, β_2, as

$$L_D = \frac{T_0^2}{\beta_2}. \tag{7.1.7}$$

Combining Eqs. (7.1.6) and (7.1.7) leads to

$$\left(\frac{T_1}{T_0}\right)^2 = 1 + \frac{z\beta_2}{T_0^2}. \tag{7.1.8}$$

Since the effect of dispersion in a linear system is additive, we may now modify the GVD parameter β_2 by including the dispersion of the grating for the bandwidth of the pulse so that the pulse broadening is

$$\left(\frac{T_1}{T_0}\right)^2 = 1 + \frac{\beta_2}{T_0^2} z + \frac{\beta_g}{T_0^2} L_g, \tag{7.1.9}$$

where β_g is the GVD of the grating of length L_g. We note that the dispersion D_f of the fiber is related to the GVD by [37]

$$\beta_2 = \frac{\lambda^2}{2\pi c} D_f. \tag{7.1.10}$$

A similar expression relates the fiber grating dispersion D_g to the grating GVD, but with the sign depending on the sign of the grating chirp. We now find that the pulse broadening for the Gaussian pulse is

$$\left(\frac{T_1}{T_0}\right)^2 = 1 + 2\pi c \frac{\Delta\lambda^2}{\lambda^2} (D_f z + D_g L_g), \qquad \text{for } \Delta\lambda \leq \Delta\lambda_{chirp}. \tag{7.1.11}$$

In Eq. (7.1.11) we have used the relationship between a transform-limited pulse width and its spectrum ($\delta\omega T_0 = 1$).

Note the stipulation on the bandwidth of the pulse, since dispersion compensation is only valid for the bandwidth of the grating. If the pulse bandwidth is larger, then the pulse recovery is

$$\left(\frac{T_1}{T_0}\right)^2 = 1 + \frac{2\pi c}{\lambda^2}(\Delta\lambda^2 D_f z + \Delta\lambda_{chirp}^2 D_g L_g), \qquad \text{for } \Delta\lambda > \Delta\lambda_{chirp}. \tag{7.1.12}$$

For perfect recompression, $D_f z = -D_g L_g$, and the pulse remains unaltered at the output of the fiber, so long as the bandwidth of the pulse is smaller than the bandwidth of the grating. We can now define a figure of merit (FOM) for the bandwidth of the grating, since the maximum compression ratio that can be achieved is

$$\left(\frac{T_1}{T_0}\right)^2 = 1 + \frac{2\pi c}{\lambda^2}(\Delta\lambda_{chirp}^2 D_g L_g) = 1 + M^2. \tag{7.1.13}$$

We can redefine Eq. (7.1.13) by recognizing that the dispersion D_g of the grating is almost exactly 10 nsec/m/$\Delta\lambda_{\text{chirp}}$, so that

$$M^2 = \frac{2\pi c}{\lambda^2}(\Delta\lambda_{chirp} L_g \times 10^{-8}). \tag{7.1.14}$$

We note that the FOM is proportional to the square root of the length and the chirped bandwidth of the grating. Here, we remind ourselves that we have used the 1/*e* bandwidth of the grating. The conversion from the Gaussian 1/*e* width to its FWHM width, which is more commonly used, may be done by using the following relationship:

$$\frac{T_{FWHM}^2}{T_0^2} = 4 \ln 2. \tag{7.1.15}$$

It is clear from Eq. (7.1.13) that the pulse broadening, which can be compensated for, is

$$\Delta T^2 = T_1^2 - T_0^2 = M^2. \tag{7.1.16}$$

As an example, a 1-meter-long grating with a bandwidth of 10 nm will have $M = 280$. This means that an input pulse can undergo a pulse broadening of ~280 times its initial pulse width and be recompressed. The dependence of the FOM on the grating bandwidth for maximum

recompression is shown in Fig. 7.2. In the simple analysis just given, it is necessary to recognize that the chirped grating response is far from ideal. The actual reflection and detailed delay characteristics can have a profound influence on the performance, especially when the grating is to be used for compensation of large dispersion in ultrahigh-bit-rate systems. However, the FOM is a good indicator of the best possible performance of a grating and may be used to compare the performance achieved with gratings. Ultimately, the most important parameters that characterize a transmission link's performance are the bit-error rate (BER), loss penalty, and error floor. The influence of deviations from ideal transfer characteristics on the BER and loss penalty is considered in Section 7.5.

7.2 Chirped and step-chirped gratings

We have seen the theory of fiber Bragg gratings in Chapter 4. Although it is possible to mathematically express the coupled modes in a way that exactly mimics the grating function, the methods of computation are numerical, since no suitable analytical solutions are available. The transfer matrix method (TMM) is ideally suited to chirped gratings, since the grating may be broken up into smaller sections of uniform period and/or refractive index profile. While there are other methods for extracting the

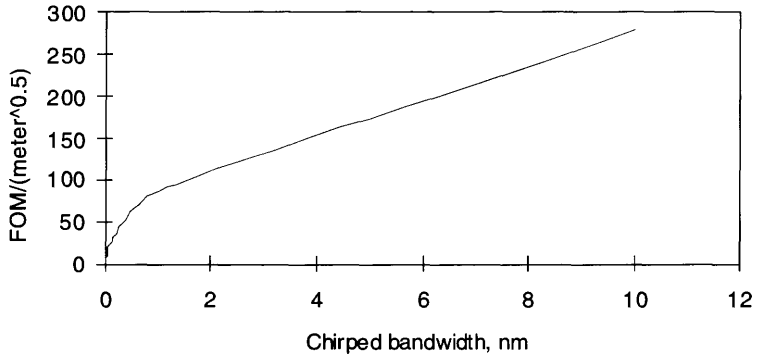

Figure 7.2: The maximum pulse re-compression FOM per $\sqrt{}$(meter) of grating length. For optimum compression, the bandwidth of the pulse is the same as the chirped grating bandwidth. As the bandwidth gets smaller, the pulse width becomes larger, so that the figure of merit drops.

reflection, transmission, and group-delay response (see Chapter 4), in the following we use the TMM approach to evaluate the transfer characteristics of arbitrarily chirped gratings. There are naturally limitations to the application of the TMM. Since coupled mode analysis depends on the slow variation of the parameters of the grating as a function of the wavelength of light, e.g., chirp, refractive index modulation, and coupling constant κ_{ac}, it is not possible to compute entirely "arbitrary" gratings (see Chapter 4, Grating Simulation). Apart from this limitation, there are other questions that need addressing: for example, in the synthesis of chirped fiber Bragg gratings, what constitutes a continuous chirp in view of the fact that most gratings exhibit quasi-continuous chirp, and the influence of apodization on the dispersion and reflection characteristics. First it is necessary to view the grating as a physical entity, in which coupling parameters are a weak function of space. Thus, it may be seen that a chirped grating, shown in Fig. 7.3, is merely a uniform period grating that has been slightly perturbed.

How many sections do there need to be in grating (c) for it to be indistinguishable from a grating that is continuously chirped (b)? In other words, how small can the chirp parameter, $d\phi(z)/dz$ [Eqs. (4.3.9) and (4.3.10)] be for a given length of grating? In order to answers this question, we consider the bandwidth characteristics of the uniform period Bragg grating. We note that the bandwidth of an unchirped grating section δl is

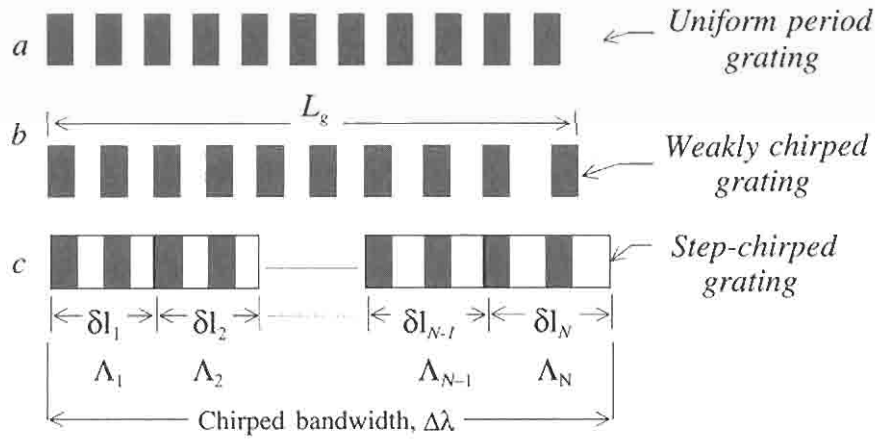

Figure 7.3: A uniform grating (a), a weakly chirped grating (b), and a step chirped grating (c).

$$\delta\lambda = \frac{\lambda^2}{2\pi n_{eff}\,\delta l}\sqrt{(\kappa_{ac}\delta l)^2 + \pi^2}, \tag{7.2.1}$$

from Eq. (4.6.14), and we have assumed that each section is identical in length δl. For most of the gratings of interest here, we assume that $(\kappa\delta l)^2 \ll \pi^2$. The phase matching condition for the section requires that

$$\lambda_{Bragg} = 2\Lambda_g n_{eff}, \tag{7.2.2}$$

where Λ_g is the period of the grating section. The period is nearly constant for gratings with a small percentage chirp. Remembering that $\delta l = L_g/N$, we get

$$\frac{N}{L_g} = \frac{2n_{eff}\,\delta\lambda}{\pi\lambda_{Bragg}^2}. \tag{7.2.3}$$

When $N = 1$, the bandwidth of the grating is simply the bandwidth $\Delta\lambda'$ of the unchirped grating of length L_g. For the chirped grating with a bandwidth $>\Delta\lambda'$, made of sections, the bandwidth of each section can only be greater than the bandwidth of the unchirped grating (being shorter in length), but can equal the bandwidth of the chirped grating only if it is the appropriate length. Applying the relationship [Eq. (7.2.3)] for bandwidths greater than the unchirped bandwidth, $\Delta\lambda'$, we simply allow the bandwidth of each section to be identical to the bandwidth $\Delta\lambda_{chirp}$ of the chirped grating, i.e.,

$$\delta\lambda = \Delta\lambda_{chirp}, \tag{7.2.4}$$

so that for a fiber Bragg grating at a wavelength of 1550 nm, $N/L_g \cong 0.4\Delta\lambda_{chirp}$ steps/(mm-nm). Finally, we arrive at the relationship between the number of steps per unit length and the chirped bandwidth,

$$\frac{N}{L} = \frac{2n_{eff}\,\Delta\lambda_{chirp}}{\pi\lambda_{Bragg}^2}. \tag{7.2.5}$$

Here λ_{Bragg} is the central Bragg wavelength of the chirped grating. The simple relationships of Eqs. (7.2.4) and (7.2.5) are minimum requirements for the step chirped grating and should approximate to a continuously chirped grating. It may be seen immediately that there is an intuitive feel about the conclusion — that the bandwidth of each step of the grating should be at least as large as the chirp of the whole grating. Increasing the number of steps, i.e., $\delta l \to 0$, approaches the continuously chirped

grating. A more detailed analysis [39] bears out the simple conclusion; a more accurate (to 1%) fit increases the bandwidth of each step by only 40% [39]. Curiously, the comparison between gratings of the same chirp but different number of steps gets better if the total chirp is reduced by $\Delta\lambda_{chirp}/N$. The convergence to the asymptotic transfer characteristics is faster for all SCGs with the chirp bandwidth adjustment, although this is especially true for those with a few sections. For a large number of sections, this really does not matter. For all the following simulations, the bandwidth adjustment has been included.

Figures 7.4 and 7.5 show the calculated reflectivity and delay, respectively, of an SCG (L_g = 100 mm, $\Delta\lambda_{chirp}$ = 0.75 nm) grating with 200 sections (2 steps/mm) and an SCG with only 0.42 steps/mm [total steps = 42, according to Eq. (7.2.5)]. It is immediately apparent that the agreement between the two spectra is good. The reflectivity spectrum has a ripple that is characteristic of unapodized gratings, as does the group delay. The strong ripple in the group delay plays an important role in the recompression of a dispersed pulse. While there is an average delay slope, the ripple frequency becomes smaller toward the end from which the reflection is measured. This is true for even continuously chirped gratings, and the influence of apodization is examined in Section 7.3.

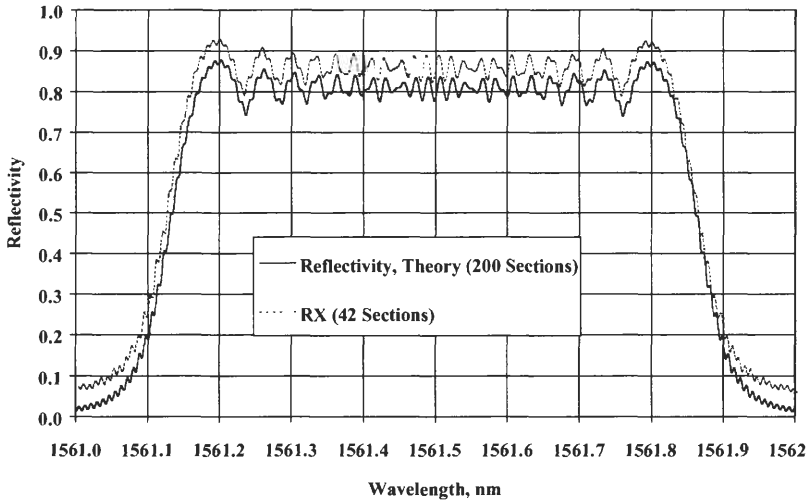

Figure 7.4: Reflectivity of a 100-mm-long SCG with 200 sections as well as 42 sections. The reflectivity curves have been offset to allow easy examination.

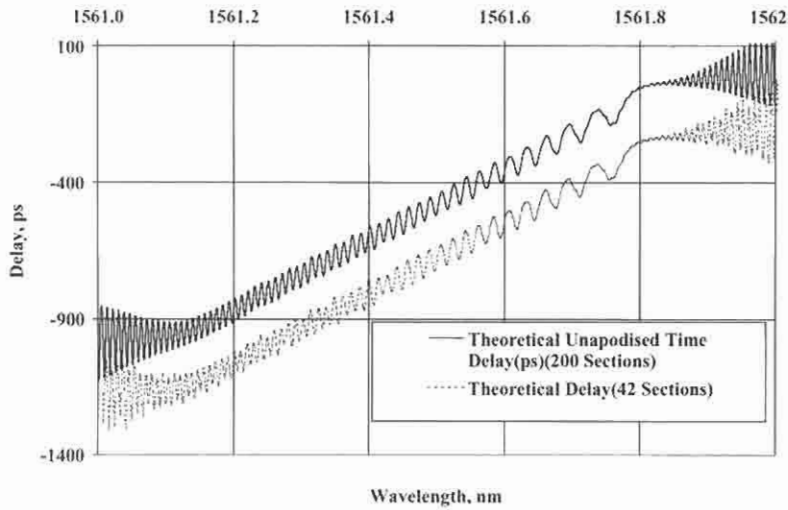

Figure 7.5: Comparison of the delay characteristics of the SCGs shown in Fig. 7.4. For the 200-section grating, $N/L_g = 2$ steps/mm, while for the 42-section grating, $N/L_g = 0.42$ steps/mm.

We now examine a 4-mm-long SCG with a chirp of 1 nm. The minimum number of sections of this grating according to Equation (7.2.5) is 2. Simulations of the reflectivity and delay are shown in Figs. 7.6 and 7.7, respectively, for two and three sections. Along with these gratings the characteristics of a 50-section grating is also shown. The grating characteristics are surprisingly similar despite the few sections, especially noting the positions of the zeroes and the central part of the reflection spectrum. The agreement is equally valid for apodized fiber Bragg gratings [39]. For convenience, it may be simple to double the minimum number of calculated sections for good linearly chirped gratings.

The design of quasi-linearly chirped gratings has been represented graphically in Fig. 7.8. This design diagram shows that a grating must be divided into a minimum number of sections per millimeter for a given chirp, irrespective of the length of the grating. The criterion used for the design is that the total group delay of a continuously chirped grating with the same coupling constant and length as the step-chirped grating should differ by less than 1% of its maximum value. For example, the maximum deviation in the delay ripple in a 100-mm-long unapodized grating should be less than 10/psec across 90% of the available bandwidth. This result

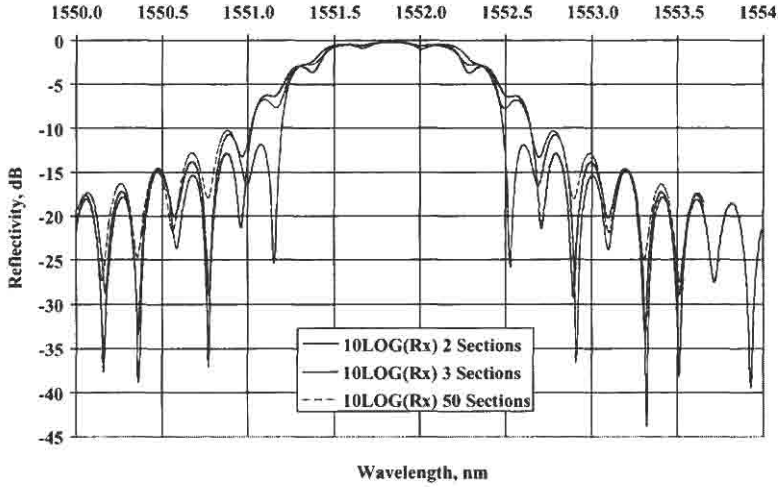

Figure 7.6: The reflectivity of 4-mm-long, 1-nm chirp SC gratings with 50 (dashed line: N/L_g = 12.5 steps/mm), 2 (gray line: N/L_g = 0.5 steps/mm), or 3 sections (continuous line: N/L_g = 0.75 steps/mm).

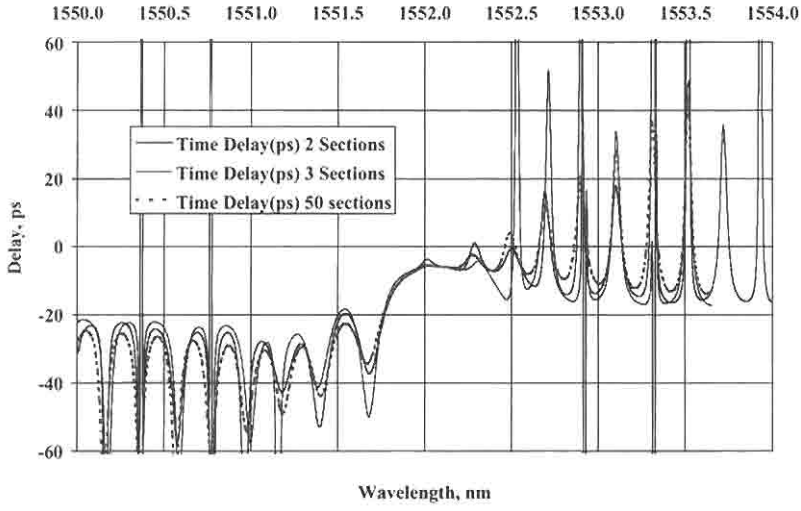

Figure 7.7: Theoretical delay of 4-mm-long, 1-nm chirp SC gratings with 50 (dashed line), 2 (grey line), and 3 (continuous line) sections. Notice that even with so few sections as determined by the simple relationship of Equation (7.2.5), the characteristics are very similar.

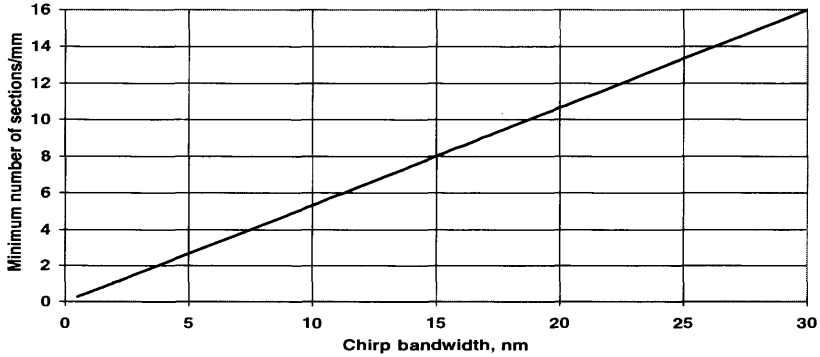

Figure 7.8: Design diagram for step-chirped gratings (Reprinted from Kashyap R., "Design of step chirped gratings," *Optics Commun.*, Copyright (1997), 461–469, with permission from Elsevier Science. Ref [39]).

is numerically evaluated and serves as a useful guide for a variety of chirped gratings [39].

We now consider the effect of having far fewer sections than the required minimum in a chirped grating. When this happens, the bandwidth of each section is no longer sufficient to overlap with the bandwidth of succeeding sections, so that the reflection spectra break up into several discrete peaks, each representing the effect of the single sections. However, the residual reflections due to the edges of the gratings (start/stop, see Section 7.4) do interfere with the others, causing the peaks to be altered from the smooth curves of uniform period gratings. The transmission spectrum of a 5-nm bandwidth, 8-mm-long grating is shown in Fig. 7.9 for two values of refractive index modulation: A, Δn = 4e-4 and B, Δn = 1e-3, as well as a continuously chirped grating (C, Δn = 1e-3). Note that while the increase in the reflectivity smoothes out the structure, the spectrum deviates from the continuously chirped grating spectrum. In particular, the side-lobe structure, which is absent in curve C, is obviously present in curve B.

For the design of broadband reflectors, it is important to incorporate the correct number of sections; otherwise, the dispersion characteristics will suffer dramatically, as will the out-of-band reflectivity. The out-of-band reflection in continuously chirped gratings is generally apodized, since the distributed reflections from all the "different" sections may be thought to add in a way that averages out any coherent buildup. Within

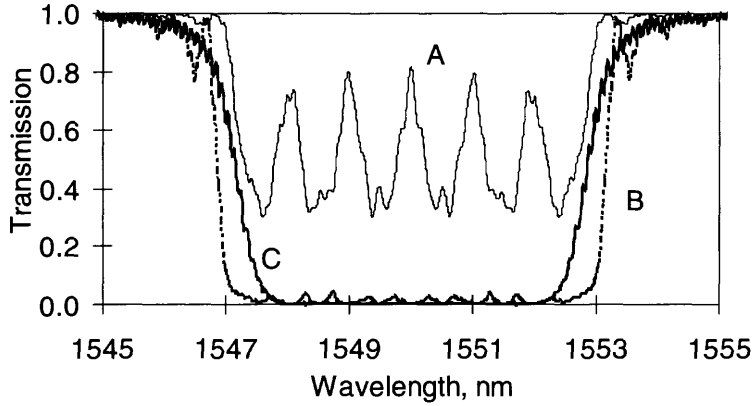

Figure 7.9: The effect of too few sections in a grating of length 8 mm with a bandwidth of 5 nm. For 6 sections and a small refractive index (A, 0.75 sections/mm, $\Delta n = 4 \times 10^{-4}$) the spectrum breaks up into individual peaks. The minimum number of sections for a continuously chirped grating is 3 sections/mm. For stronger refractive index modulation (B, $\Delta n = 1 \times 10^{-3}$), the grating "appears" continuously chirped. However, neither the delay (not shown) nor the reflectivity spectrum matches those of the continuously chirped gratings, C.

the band, it is an entirely different story. The edges of a grating have a large impact on the reflection ripple as well as the delay ripple, as seen in Figs. 7.4 and 7.5. Consequently even small broadband reflections can change the ripple in the delay spectrum.

7.2.1 Effect of apodization

In Chapter 5 we saw the effect of apodization on gratings; the immediate effect was the dramatic reduction in the side-lobe levels in the reflection spectrum. Chirped gratings tend to have lower side-mode structure in their reflection spectra to begin with, and the advantage of apodization is in the reduction of internal interference effects that cause the group delay to acquire a ripple. We consider here the properties of chirped gratings, which have reflectivities of the order of 10 dB, suited to the compensation of linear dispersion in fibers, and study the influence of apodization. While the details of both the reflection and group delay spectra change with the strength of the coupling constant of the grating, general observations remain essentially unchanged. The chirped grating

is a continuously distributed reflector. Ideally, light entering into a chirped grating from one end should be dispersed in exactly the opposite way when entering from the other end. Early measurements on chirped gratings did show this feature [40]. However, the gratings were short, had a large bandwidth, and consequently had a small dispersion. Dispersion is not generally reversible with unapodized chirped gratings. To understand this phenomenon, we remind ourselves that light entering from the short-wavelength end of a highly reflective chirped grating is reflected such that only a small fraction of the short-wavelength light penetrates through to the other end of the grating, while the long-wavelength light does. On entering from the long-wavelength end of the grating, exactly the opposite occurs. The detailed delay ripple is a result of the interference between the broadband reflection due to the edge of the grating and the distributed nature of the reflection of the grating [41].

As a crude comparison, when light enters from the long-wavelength end of the grating, the interference is predominantly due to the large long-wavelength reflection from the front of the grating and the small broadband reflection due to the front edge. Short-wavelength light penetrates the dispersive grating and is predominantly reflected from the rear end; it, too, interferes with the low broadband reflection from the front end. In neither case does the rear end of the grating play a strong role. Since the dispersion increases with greater penetration into the grating, the delay ripple frequency increases with decreasing wavelength (see Fig. 7.5). With the launch direction reversed, exactly the opposite occurs: The delay ripples increase in frequency with increasing wavelength. Therefore, light dispersed by reflection from the short-wavelength end of the chirped grating *cannot be undone* by reflection from the long-wavelength end! The simulated result of this asymmetry is shown in Fig. 7.10. The sign of the frequency chirp in the delay ripple is insensitive to the launch direction i.e., the frequency of the chirp is always from a low to a high frequency (Fig. 7.10, B and C) when viewed from either end.

The role played by the rear end of the grating is apparent when the coupling constant κ_{ac} is apodized asymmetrically. In this example we consider a grating with a profile of the refractive index modulation as shown in Fig. 7.11a. The grating profile is half-cosine apodized so that the light launched from the long-wavelength end sees a gradually increasing coupling constant. The amplitude of the light reflected from the front end of the grating is now lower than in an unapodized grating, and long-wavelength light penetrates more deeply so that the amplitude at the

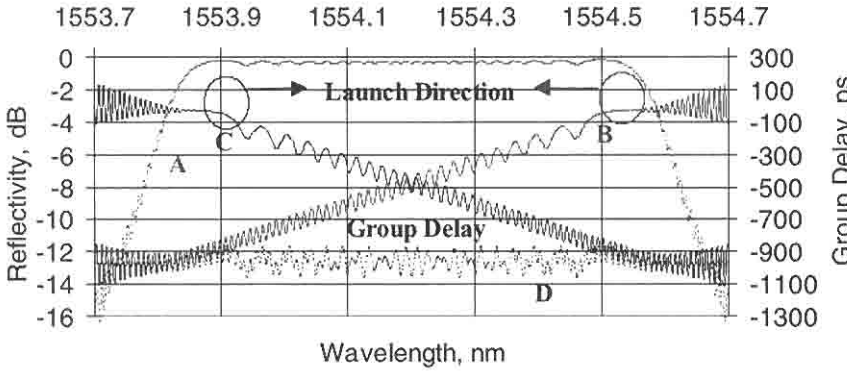

Figure 7.10: Reflection and delay spectrum of an unapodized 100-mm-long grating with a chirped bandwidth of 0.75 nm. The reflection spectrum remains unchanged when measured from either end (A). The group delays (B and C) have been computed for light launched in the direction shown, from the short-wavelength end (B) and the long-wavelength end (C). The net dispersion, which is the sum of the two, is shown as curve D. This residual dispersion prevents full recompression of a pulse dispersed by the grating.

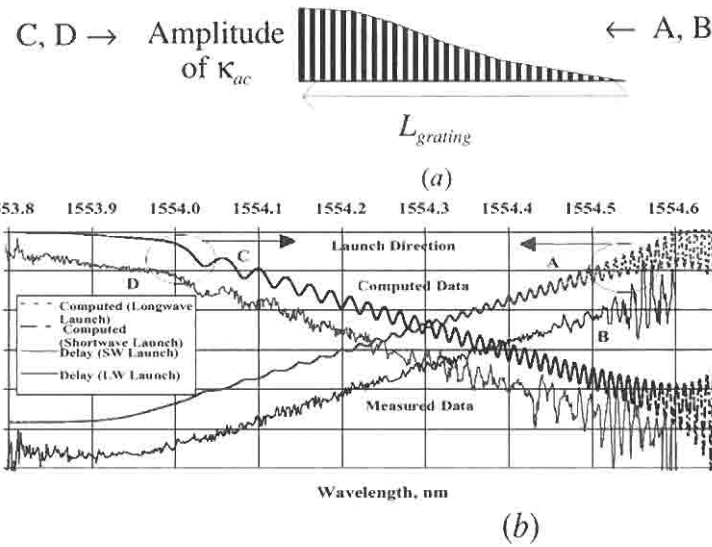

Figure 7.11: Apodization profile of the half-cosine long wavelength-edge apodized chirped grating is shown on above the figure in (a). Measured and computed group delay (b), when measured in both directions.

rear end is higher than in the unapodized grating. The broadband reflection from the input of the grating has now been reduced significantly due to apodization. Hence, the ripple should disappear on the long-wavelength end. However, we notice that the ripple is of the order of that of the unapodized grating, but now *of higher frequency* at the input end, Fig. 7.11b, A. This is indicative of interference from the reflection off the rear end of the grating. Note, too, that the ripple has the *lowest frequency* and disappears at the shortest wavelengths, quite the reverse of the unapodized grating, with reduced interference from the launch end (due to apodization). The corresponding measured result for this type of a grating is shown in Fig. 7.11b, B [42].

On the other hand, when light is launched into the short-wavelength end, the reflected delay ripple is almost *identical* to that of an unapodized grating (Fig. 7.11b, C and D). The apodized long-wavelength end does not play a role in generating the delay ripple.

This result is of particular importance for long chirped gratings. When one half of a grating remains unapodized while the other half is cosine apodized, the results are even more dramatic, as shown in Fig. 7.12. Shown in curve A is the group delay of an unapodized grating, while B and C refer to the grating profiles shown above the figure in (B) and (C) with light launched in the directions shown for each grating. The group delay ripple measured from the long wavelength end, B, has all but disappeared for the long-wavelength apodized grating, and the residual ripple at the long-wavelength edge is again due to the interference from the short-wavelength end. For light launched into the long-wavelength end in the short-wavelength apodized grating (C), the group delay ripple C is as for the unapodized grating, A.

The implication of the apodization is as follows: Long chirped gratings for dispersion compensation require apodization only on the long wavelength end of the grating. The type of apodization (see Chapter 5) will determine the bandwidth reduction in the reflectivity spectrum. The unapodized short wavelength end, provides extra bandwidth, with a small penalty on the long wavelength end due to the residual ripple.

An important factor, that influences the performance of chirped gratings in dispersion compensation is the deviation of the delay from linearity and group delay ripple. Symmetrically apodized gratings offer the prospect of excellent dispersion compensation [43]. The group delay differences from linear delay and reflectivity for commonly found cosine and raised cosine profile apodized gratings are shown in Fig. 7.13. The gratings have

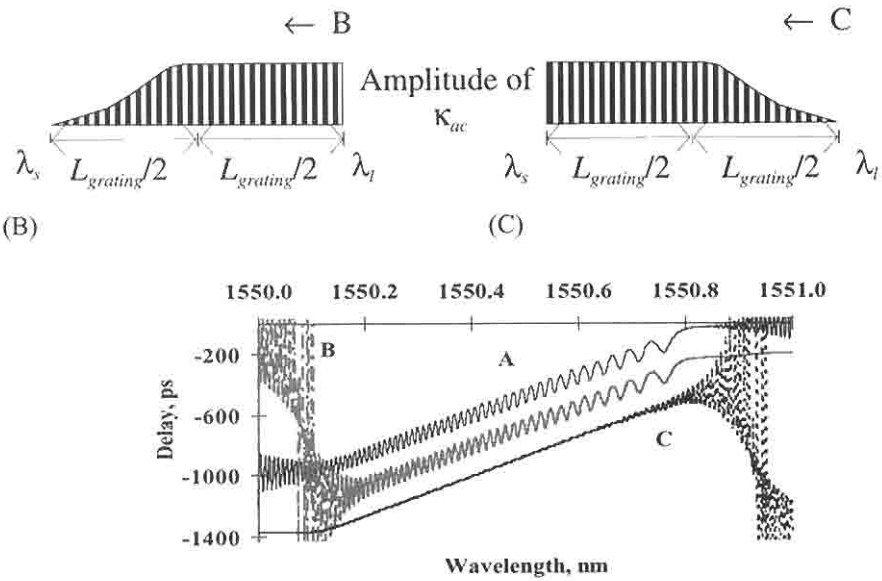

Figure 7.12: Apodization profiles (half-cosine over half the grating) and respective launch directions shown in (B) and (C). Group delay compared for long wavelength launch into a grating, A: unapodized, B: short-wavelength apodized, and C: long-wavelength apodized (after Ref. [42]).

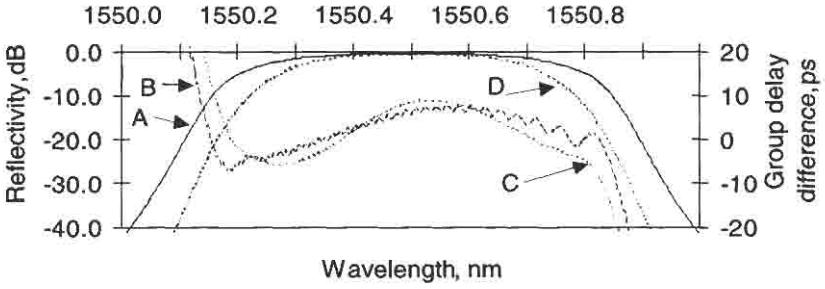

Figure 7.13: Reflectivity (A) and group delay difference (B) of cosine apodized grating as well as reflectivity (D) and group delay difference (C) for raised cosine apodized grating.

a peak reflectivity of ~90% and are 100 mm long with a bandwidth of 0.75 nm (D_g = ~1310 psec/nm), designed for compensation of the dispersion of 80 km of standard telecommunications fiber (D_f = 17 psec/nm/km). The group delays have two features in common: The dispersion curves deviate from linearity slowly across the bandwidth of the grating, and they are flat within ±5 psec. With higher-reflectivity gratings, the curvature worsens. Note, however, that the stronger, raised cosine apodization eliminates the delay ripple almost entirely, but reduces the available bandwidth. Roman and Winnick [44] have shown that using Gel'fand–Levitan–Marchenko inverse scattering analysis, it is possible to design a grating with a near perfect amplitude and quadratic phase response to recompress transform limited pulses.

With asymmetric apodization as shown in Figs. 7.11 and 7.12, apodizing only one end of the grating has a beneficial effect of better bandwidth utilization than symmetrically apodized gratings, since less of the grating length is used in the apodization process. There is a slight increase in the peak-to-peak group delay ripple on the long-wavelength side, as seen in Fig. 7.12, but it is still <5 psec over a wider bandwidth. With a stronger coupling constant and a different apodization function (e.g., tanh), we note that less of the light reaches the rear end of the grating, so that the ripple reduces still further. However, the curvature also increases. Figure 7.14 shows the reflection and group delay difference spectra of a symmetric

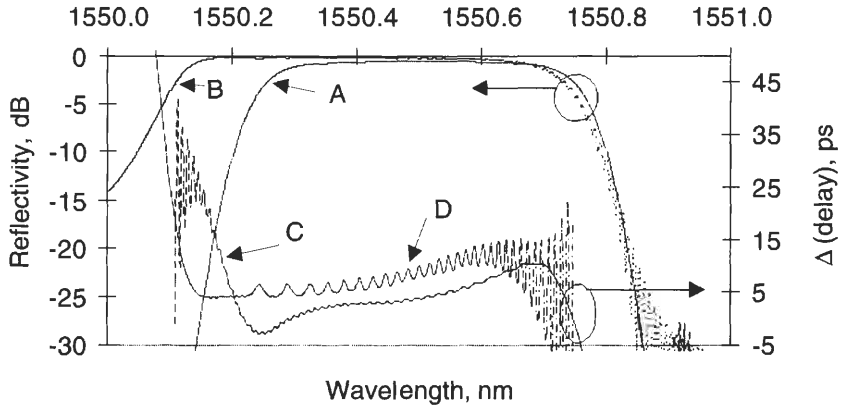

Figure 7.14: Comparison between the delay and reflection spectra of asymmetrically (B, D), and symmetrically (A, B) apodized gratings.

and an asymmetric tanh apodized grating. The bandwidth of the asymmetric apodized grating, B, is now wider than that of the symmetric apodised grating, A, and so is the group delay difference, D. The peak reflectivity of B is 98%, whereas that of A is 90%. There is also a small ripple acquired in both the reflection and group-delay spectra (C and D). With lower reflectivity, the ripple in the asymmetrically apodized grating *increases,* rather than decreasing as is the case with the symmetrically apodized grating [41].

7.2.2 Effect of nonuniform refractive index modulation on grating period

During fabrication, it is necessary to ensure that the grating receives the correct UV dose along its length. If the dose varies, so does the effective refractive index modulation and therefore κ_{ac}. A constant increase in the UV dose with length merely chirps the grating. However, *random* variations are generally common with pulsed lasers, since the UV radiation has hot spots across the beam, with the result that the grating is no longer uniformly exposed. While this may not be a problem for many filtering applications, it does degrade the performance of the group delay in chirped gratings, limiting performance. Ouellette [4] reported the effect of a noisy refractive index profile and dither in the period of the grating on the reflection and dispersion characteristics. It was found that, apart from a general increase in the out-of-band reflection, the group delay was also degraded. A period variation of 0.03 nm (~5%) over a length scale of 1 mm degraded the delay spectrum substantially. This is a serious issue for the fabrication of high-quality gratings. Even with perfect phase masks, such factors as the random variations in the effective index of the mode, UV dose, or vibration during fabrication will cause deterioration in the quality of the grating.

We consider the likely effect of a maximum variation of ~10% of the refractive index modulation amplitude, Δn (7.5×10^{-5}), but over different scale lengths of 50, 100, and 200 microns. These are expected to be typical regions over which the refractive index modulation varies. In order to model this behavior, we have assumed that each section of the scale length varies in the index modulation entirely at random with a *maximum* value of 1×10^{-5}. This is realistic despite the averaging effect of multiple pulse exposure, since the peak UV intensities can fluctuate over several orders. The results of the simulations of the deviation from linearity of the delay

and the transmission spectra are shown in Figs. 7.15 and 7.16. The uniformly exposed curve A is degraded rapidly on the 50 micron length scale with a high frequency ripple (C), to a slowly varying, more uniform, but larger-amplitude ripple across the spectrum with increasing length scale (C to D). The last curve D is consistent with observations of delay ripple variation [45].

It is very difficult to distinguish small differences from the reflection spectra of high reflectivity gratings [4]. We therefore choose to observe the grating transmission spectra, which can clearly resolve these differences. Figure 7.16 shows the transmission spectra, shifted vertically in order to highlight the small changes in the curves, using the same data as in Fig. 7.15. The noise on the spectra is apparent, although the energy in the reflected light is only slightly affected. The significant effect of the noisy profile is on the delay ripple. The variation $\delta\lambda_{Bragg}$ in the Bragg wavelength as a function of the change in the refractive index $\Delta\delta n$ and the grating period $\delta\Lambda_g$ is

$$\delta\lambda_{Bragg} = 2\Lambda_g \eta \delta\Delta n + 2n_{eff}\,\delta\Lambda_g, \tag{7.2.6}$$

where η is a core overlap factor of ~0.9. The shift in the Bragg wavelength

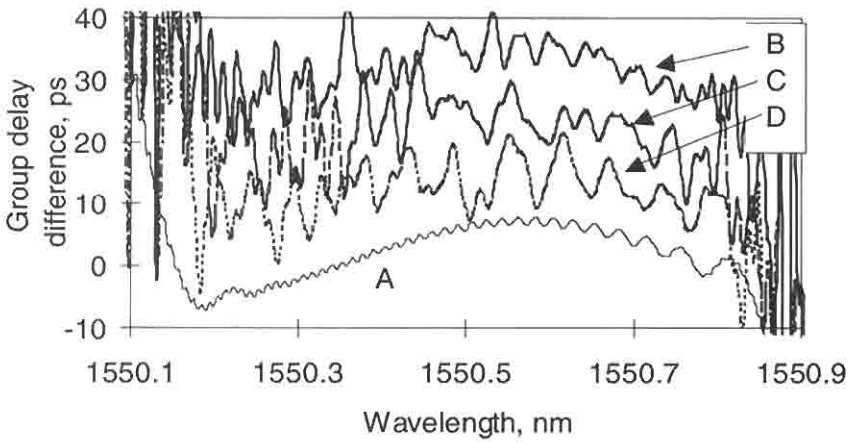

Figure 7.15: Group delay difference from a slope of 1310 psec/nm for cosine apodized 100-mm-long grating (90% reflector) with no variation (A) in the refractive index modulation, $\delta\Delta n$; random variation of up to 1×10^{-5} over a length scale of 50-micron sections (B); 100-micron sections (C); and 200-micron sections (D).

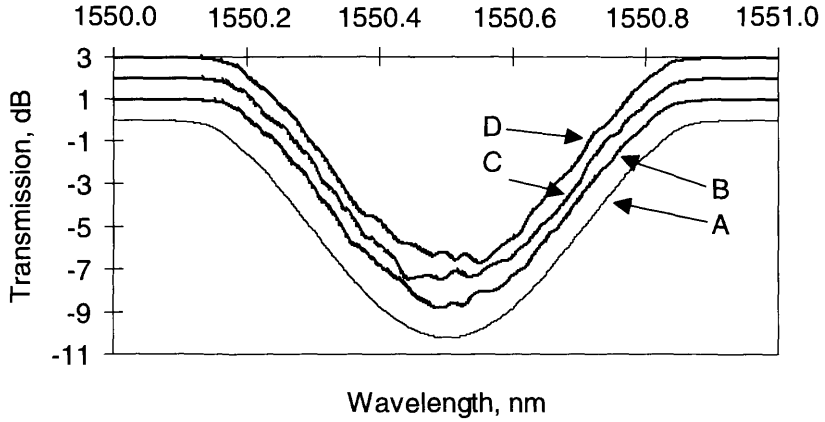

Figure 7.16: The transmission spectra of four cosine apodized gratings (L_g = 100 mm, $\Delta n = 7.5 \times 10^{-5}$, $\Delta\lambda_{chirp}$ = 0.75 nm) as a function of random variation in the refractive index modulation. A has $\delta\Delta n = 0$; B, C and D have a maximum random variation $\delta\Delta n = 1e \times 10^{-5}$ over length scales of 50, 100, and 200 microns, respectively, as in Fig. 7.15.

amounts to ~10 pm at a wavelength of 1550 nm for an index change of 1×10^{-5}. The same change in the wavelength occurs for a random variation in the Bragg wavelength period $\delta\Lambda_g$ of ~3.42pm.

7.3 Super-step-chirped gratings

Chapter 3 introduces the fabrication of ultralong gratings. One of the methods of generating ultralong gratings is by stitching together a set of short chirped gratings, to form the super-step-chirped grating (SSCG) [46]. The structure is schematically shown in Fig. 5.18, Chapter 5. Here we consider the influence of an imperfect stitch between two sections of the SSCG. Figure 7.17 shows three step-chirped gratings with gaps in between. The first SCG (LHS) begins at λ_1 and finishes at λ_2, in N sections, each with an integral number of periods. The number of periods is adjusted so that each section is nominally the same length within the length of a period. The second SCG begins with a period $\lambda_2 + \delta\lambda$ and ends at a period $\lambda_2 + (N - 1)\ \delta\lambda$. The two gratings are written sequentially, ideally with zero gap in between. In a perfect grating, the periods would simply follow

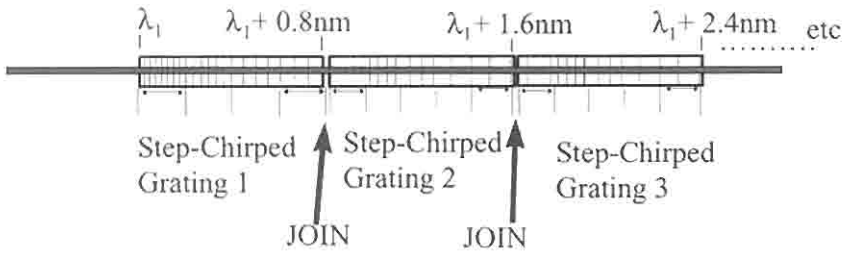

Figure 7.17: A schematic of the super-step-chirped grating (SSCG). Each grating is of nominally an identical integer number of periods [47].

each other, without a perturbation. In reality, unless care is taken, there is a small error $\delta l/\Lambda_2$ at the join. This error will ultimately have an effect on the performance of the grating.

We now compare this with a uniform period grating with a phase step. A phase step of a quarter wavelength, as we have seen in Chapter 6, introduces a bandgap in the reflection spectrum. The effect is similar in gratings, which have a small chirp, since the Bragg wavelengths of two adjacent sections are only slightly different, and the reflection spectrum is strongly overlapped. This is indeed the case with SCGs and is shown in Fig. 7.18. The reflection spectrum centered at the wavelength of the join shows the quarter wavelength dependence of the bandgap. However, the dependence changes with increasing gap, but the join is also invisible at

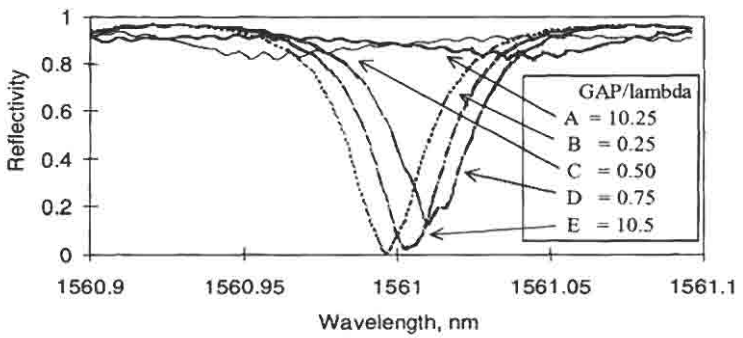

Figure 7.18: The reflection spectrum of the join region of 2 × 100 mm long SCGs as a function of the gap at the join in fractions of the Bragg wavelength. The gratings are 100 mm long with a chirped bandwidth of 0.75 nm each.

a gap of 10.25 λ_{Bragg}. The group delay is more sensitive but is only affected when light crosses the gap. This means that light launched from the long-wavelength end experiences a change in the group delay ripple on the short-wavelength side of the gap, and vice versa when traveling from the short-wavelength end. This has implications for SSCGs made with more than two SCGs. The grating nearest the launch end remains essentially unaffected, while the group delay ripple of subsequent gratings deteriorates.

Figure 7.19 shows the effect of the join on the group delay. At the join, there is a localized discontinuity, which becomes narrower as the gap gets larger, and almost disappears. Simulations have shown that large gaps (5 mm) tend to smooth out the effect of the join, but the delay through the gap does introduce a step change in the group delay on either side of the join.

We see a relative increase in the noise from the long-wavelength end (launch end). In comparison, a 500-mm-long SSCG grating with random stitching errors at every 100 mm is shown in Fig. 7.20 [46]. Here, the stitching produces small spikes at the join, and also a general increase in the noise at the short-wavelength end. These are believed to be due to

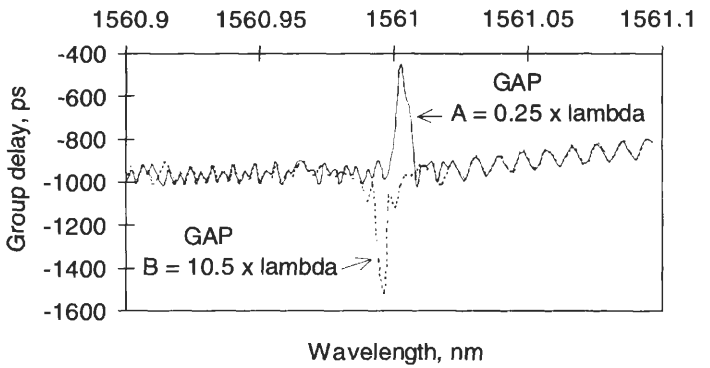

Figure 7.19: The group delay at the join of the gratings shown in Fig. 7.18 for two values of the gap: 0.25 (A) and 10.5 (B) times the Bragg wavelength. The delay spike is localized to the join and is not apparent from the long-wavelength end of the grating. In this simulation, the light enters the long-wavelength end of the grating. The effect is reversed if the light is launched from the short-wavelength end.

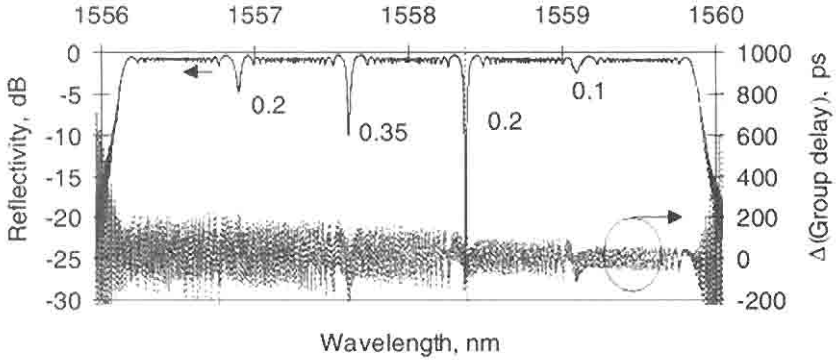

Figure 7.20: The reflectivity and group delay difference of a 500-mm-long SSCG with random stitching errors, shown as a fraction of the Bragg wavelength.

the cumulative effects of each join. However, as has been reported, these gratings may still be useful for dispersion compensation at 10 Gb/sec [48].

In Fig. 7.21 is shown the measured reflectivity and relative group delay characteristics of a 400-mm-long SSCG made in four sections with random stitching errors. We note that the characteristics of the relative group delay are better than the simulation suggests. This is probably due to small random variations in the chirp of each grating section.

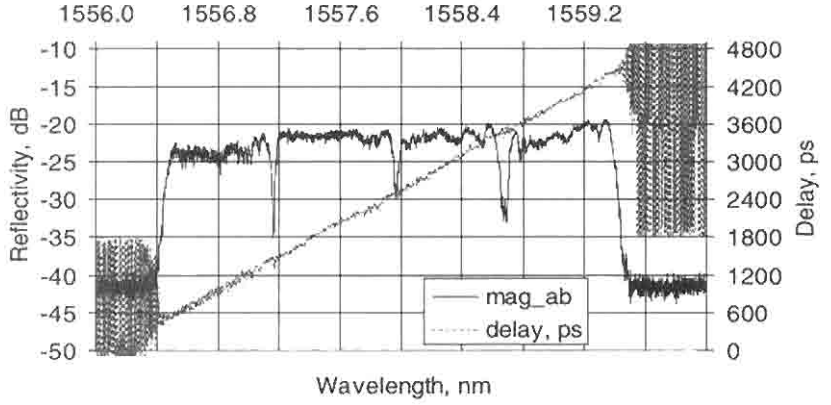

Figure 7.21: The measured characteristics of a 400-mm-long SSCG with a chirped bandwidth of ~3 nm and random stitching errors. Compare with Fig. 7.20.

The computed reflectivity and group delay of a 1.3-meter-long SSCG [48] with a bandwidth of ~10 nm and no stitching errors are shown in Fig. 7.22a. The overall reflectivity is similar to shorter gratings, but as the bandwidth is increased, the shorter wavelength end group delay suffers less from the broadband reflection of the long-wavelength edge of the grating. Note that in this simulation, the resolution of the computation (1 pm) has lost the information on the group delay ripple. Figure 7.22b shows a high-resolution simulation (0.1 pm) of the reflectivity and group delay, to highlight the GDR of the first part of a 1-meter-long unapodized grating. A detail of the group delay ripple of $\sim\pm 60$ ps is shown in Fig. 7.22c.

Long gratings with only a small amount of apodization on the long-wavelength end (normally the input end for dispersion compensation) will remove a substantial part of the group delay ripple and should be useful for transmission rates in excess of 10 Gb/sec.

7.4 Polarization mode dispersion in chirped gratings

An issue that becomes important at high transmission bit rates (>10 Gb/sec) is the effect of polarization mode dispersion (PMD). As the transmission rate increases, the bit period reduces. If any component in the transmission path is birefringent, the different pulse arrival times of the two polarizations can degrade the BER. In long transmission systems, these two polarization mix stochastically, so that pulse broadening is not easy to compensate [49]. In a short grating component, however, PMD is not generally large in transmission, since the pulse arrival times are simply due to the difference in the propagation constants of the two polarization states times the length of the grating. In a chirped dispersion compensating reflection grating (DCG), the effect of birefringence is more severe, causing a large additional dispersion. PMD, or more correctly, birefringence induced PMD, in unapodized gratings is more of a nuisance than in unapodized gratings.

In order to assess the impact on the PMD of birefringence in a fiber, whether intrinsic or due to the process of fabrication of a grating, we examine how the Bragg wavelength of a grating is affected by a change

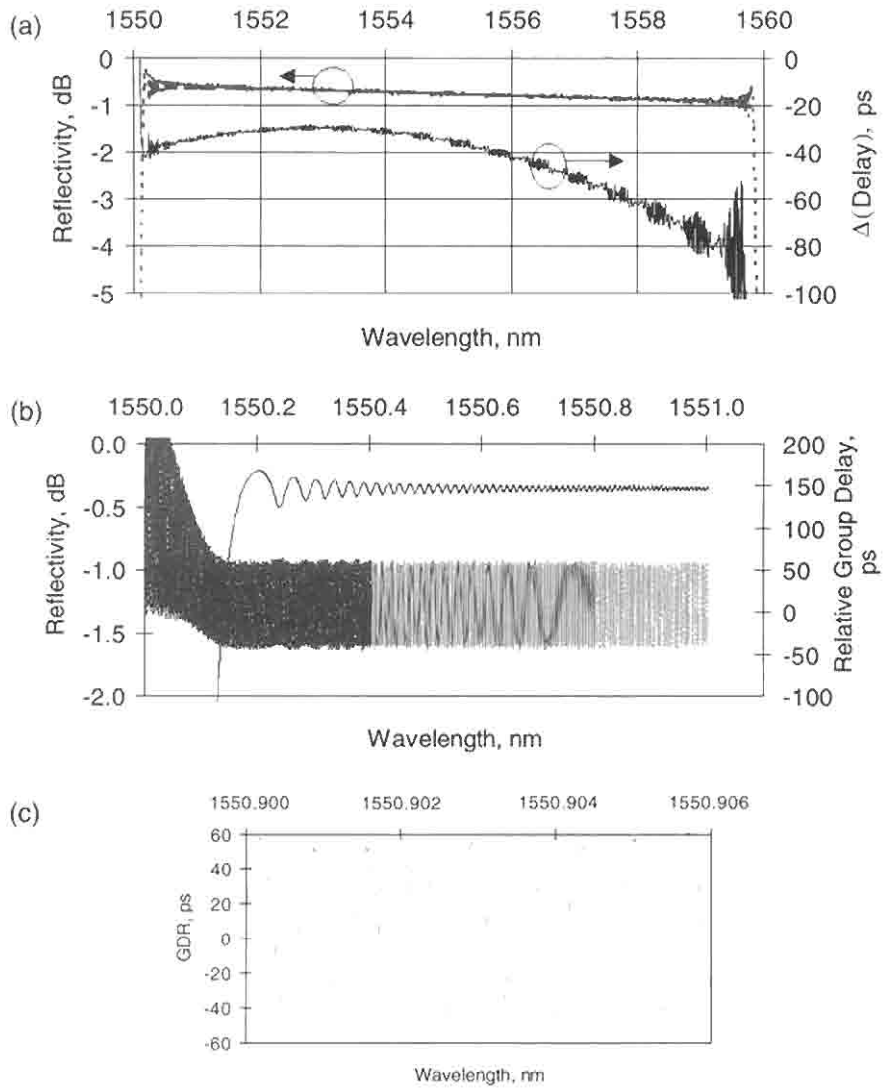

Figure 7.22: (a) The simulated reflectivity and group delay difference form a linear slope of 1310 psec/nm, for a 1.3-m-long SSCG with no stitching errors. (b) High resolution (0.1-pm) simulation of a 1-meter-long grating showing the reflectivity and the group delay ripple. (c) Detail of the relative group delay ripple of (b).

in the effective index of a mode. We assume that the central Bragg wavelength of a chirped grating is

$$\lambda_{Bragg} = 2n_{eff}\Lambda_g, \tag{7.4.1}$$

so that the change in the reflection wavelength as a function of the change in the mode index becomes,

$$\delta\lambda_{Bragg} = \lambda_{Bragg}\frac{\delta n_{eff}}{n_{eff}}. \tag{7.4.2}$$

Equating the change in the mode index to the birefringence in the fiber leads to

$$\delta\lambda_{Bragg} = \lambda_{Bragg}\frac{B}{n_{eff}}. \tag{7.4.3}$$

For a DCG with a dispersion of D_g psec/nm, a change in the Bragg wavelength as a result of the change in the *polarization* induces a delay, $\tau_{PMD} = \delta\lambda_{Bragg}D_g$, from which we get the result

$$\tau_{PMD} = \lambda_{Bragg}B'D_g, \tag{7.4.4}$$

where B' is the normalized birefringence, $\sim B/n_{eff}$. Equation (7.4.4) shows that the PMD is dependent on the dispersion and birefringence but *not* on the length of the grating. A chirped reflection grating with a perfectly linear dispersion of 1310 psec/nm and a birefringence of 10^{-5} at a wavelength of 1550 nm will have a PMD of 28 psec! This result is of the order that has been reported in apodized DCGs [50]. It is clear that even a small birefringence causes a severe PMD penalty. Figure 7.23 shows how the PMD changes with grating dispersion as a function of birefringence. For high dispersion values, it may be impossible to achieve the low birefringence needed for a low PMD value. For example, a dispersion of 5 nsec/nm and a PMD of 1 psec require a birefringence of $\sim 6 \times 10^{-8}$, a value that may not be achievable even with gratings in standard fibers.

The problem is compounded if the DCG is unapodized. From Eq. (7.4.3) we note that the change in the Bragg reflection wavelength is $\sim$0.02 nm for a birefringence of 1×10^{-5} at a wavelength of 1550 nm. Since there is a high-frequency ripple of period $\sim$0.01 nm on the short-wavelength side of the DCG shown in Fig. 7.10, on an overall average dispersion slope of 1310 psec/nm, large jumps in PMD may occur, even with very weak birefringence. These jumps could be of the order of the amplitude of the ripple (100 psec).

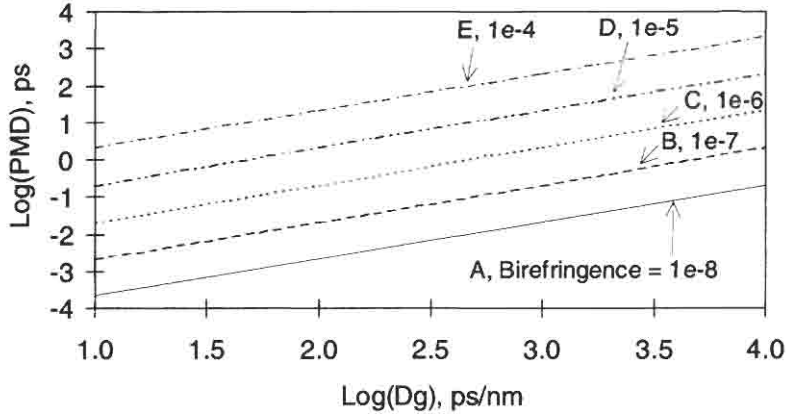

Figure 7.23: PMD vs dispersion in a DCG for five values of birefringence, A ($B = 1 \times 10^{-8}$), B ($B = 1 \times 10^{-7}$), C ($B = 1 \times 10^{-6}$), D ($B = 1 \times 10^{-5}$), and E ($B = 1 \times 10^{-4}$).

7.5 Systems measurements with DCGs

Ultimately, the effectiveness of the DCG is determined by the bit error rate (BER). This measurement is an indicator of the how many errors are received within a certain time window. Generally, a system is expected to achieve a minimum BER of 1 bit in 10^{-9} at the transmission rate, without and with the DCG. Some undersea systems require even lower BERs (e.g., 10^{-15}). However, in order to compare the transmission performance, the power has to be increased at the receiver to compensate for insertion loss and any nonlinear dispersion in the DCG. This is usually expressed as a penalty in decibels at the BER.

There are several parameters that influence the BER. As has been seen, the DCG has an operating bandwidth that needs to accommodate the signal down to −20 dB, to reduce the dispersive effects of spectral filtering. Ideally, a filter matched to the signal bandwidth with perfect dispersion compensation is required with zero insertion loss. Other considerations, such as the effect of different types of apodization on the group delay ripple (GDR) as well as the ripple in the reflected signal of a DCG, PMD, insertion loss, and so on, cause an additional penalty.

There have been many demonstrations of dispersion compensation using DCGs: from compensation of the chirp from a semiconductor laser

using a half-Gaussian refractive index modulation induced chirped grating [2], to the measurement of dispersion in a grating [5], to the first report of DC in a transmission through a fiber [51,52]. In the last demonstration, 400-fsec pulses at a bit rate of 100 Gb/sec was transmitted through 245 m of standard telecommunications fiber and were recompressed with an 8-mm-long 12-nm bandwidth DCG to 450 fsec after dispersing to 30 psec, a compression ratio of ~65. Since these demonstrations many more measurements of DC have been reported using a variety of gratings: notably, dispersion-tunable chirped gratings at 10- and 20-Gb/sec transmission rates with a 5-cm-long grating and 80 km of fiber using strain tuning [53], as well as 220 km at 10 Gb/sec and 100-mm-long temperature-tuned chirped gratings [54]. A novel offset core fiber grating has also been reported for strain tuned dispersion compensation of 270 km of standard fiber at 10 Gb/sec [55,56]. Fixed wavelength, 100-mm-long, chirped gratings have also been used at 10 Gb/sec transmission with up to 500 km of standard fiber [57,11]. Longer gratings, up to 400 mm [58], have been used at 40 Gb/sec over 109 km of fiber, and in excess of 1-m-long gratings with a bandwidth of ~10 nm at 10 Gb/sec over 100 km of standard fiber in a WDM transmission system with up to 11 wavelengths simultaneously [48]. Other WDM experiments at 10 Gb/sec have shown DC at four wavelengths over 100 km using a single superstructure chirped grating (see Chapters 3 and 6) [59].

The long transmission lengths at high bit rates are possible with multiple chirped gratings, either lumped [60,61] or cascaded [12]. In the latter scheme, 8×20 Gb/sec transmission over 315 km used four 1-meter-long continuously chirped gratings at 3×80 km $+ 1 \times 75$ km hops, and 8×10 Gb/sec over 480 km was demonstrated using six 1-meter-long continuously chirped, 6.5-nm bandwidth gratings [62,63] at 80-km hops. The demonstrated results showed near ideal operation at 10 Gb/sec, despite the 4 to 10 psec polarization mode dispersion of each grating, although at 20 Gb/sec there was some polarization dependence. A pseudo random bit sequence of $2^{31} - 1$ was used for the 10 Gb/sec bit stream (and multiplexed for the 20 Gb/sec) for each wavelength spaced at nominally 0.8 nm.

The schemes used for lumped gratings are shown in Fig. 7.24. Either, band-pass filters can be used with identical pairs of gratings as in Fig. 7.24a, or circulators with four or more ports may be used.

Cascading of chirped gratings reduces the available bandwidth and hence system tolerance in multihop routes. This effect is due to filtering

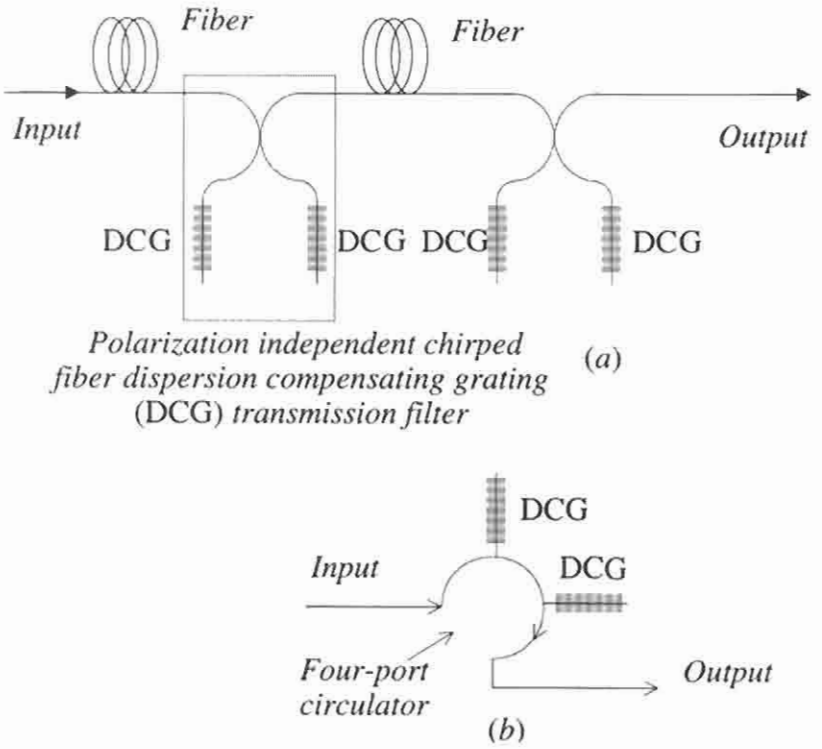

Figure 7.24: The lumped DCG in two configurations: (a) as a band-pass filter (after Ref. [64]) and (b) multiport circulator [65].

at the edges of the grating and is seen clearly in Fig. 7.25. The reflectivity of a cascade of 10 identical hyperbolic-tanh profile gratings shows that the −10 dB (from the peak) signal bandwidth is reduced from 0.8 to 0.6 nm. For this simulation, the reflectivity was ~90% at the peak for the single 100-mm-long grating with a chirped bandwidth (FW) of 0.75 nm. After the tenth reflection the incurred insertion loss was ~5 dB at the peak.

These figures indicate the ideal case for identical gratings. If, however, there is a variation in the bandwidth and the reflectivity, the penalty is worse. For system design, the signal bandwidth determines the bandwidth of the grating. The roll-off of the reflectivity (and therefore the type of apodization) will determine the bandwidth of each grating. Allowance

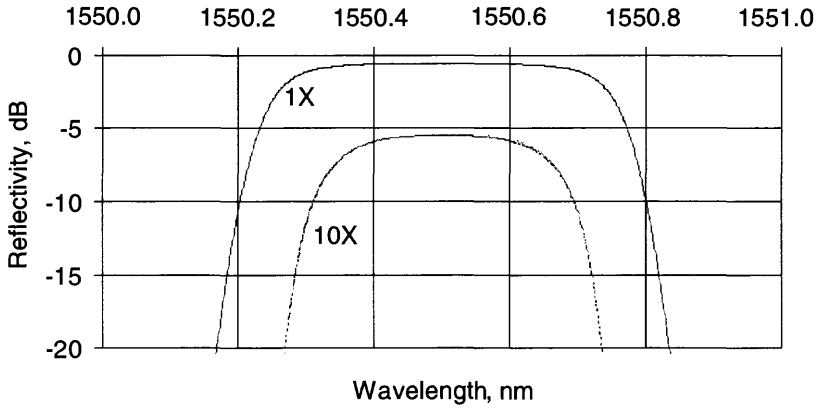

Figure 7.25: The reflectivity of a single and 10 cascaded, 100-mm-long hyperbolic tanh apodized gratings (chirped bandwidth of 0.75 nm and peak–peak refractive index modulation of 7.5×10^{-5}).

also has to be made for drift of the grating wavelengths and the signal source.

For the GDR, cascading of the gratings may have a beneficial effect if the ripple cancels; alternatively, it may increase where it is in phase. This is especially important for unapodized or imperfectly apodized gratings. Some of the large-amplitude high-frequency GDR generated in a cascade of identically apodized gratings is reduced with random variations in the grating profiles. Figure 7.26 shows the relative GDR of a cascade of three identical gratings of type B (in Fig. 7.15) and a for a cascade of all three gratings, B, C, and D.

7.5.1 Systems simulations and chirped grating performance

The theoretical aspects of DCG in systems applications have been considered by the several workers [30,66–70]. Of the many indicators of the performance of a grating, the receiver eye penalty is probably the most significant. As a number alone, it is not very useful, since the properties of the DCG are not constant across the bandwidth. One clearly needs to know the effect of the insertion loss, the change in the reflected power as a function of detuning, and the influence of the nonlinear dispersion.

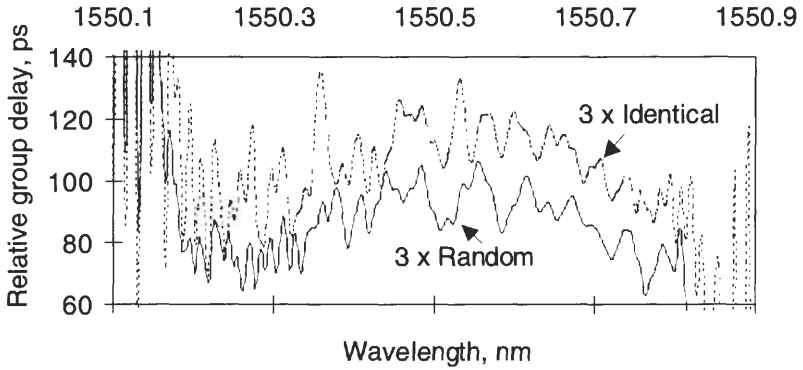

Figure 7.26: Relative GDR for a sequence of three identical chirped gratings of type B in Fig. 7.15, and a mix of types B, C, and D.

Bungarzeanu [71] reported the computer-aided simulation of chirped gratings with a view to understanding the performance of DCGs by comparing the receiver eye closure penalty as a function of detuning across the bandwidth of different apodization profile gratings. This method of analysis is a direct approach to understanding the effect of the group delay ripple, nonlinear dispersion across the bandwidth of the grating, designed for a particular route length. By altering the bit rate, it is possible to map out the point at which the grating will be limited (a) by bandwidth limitation of the grating and (b) by the cumulative effects of the nonlinearity and GDR. The principle of the model is as follows: A 128-bit-long pseudorandom sequence is coded as a non-return-to-zero (NRZ) complex envelope, which is chirp-free. In principle, RZ and chirp may be added. The fiber has a linear dispersion and is a flat-top band-pass filter. The receiver, with a 3-dB bandwidth of 0.75 × bit rate is a fourth-order Bessel-type band-pass filter and is designed to meet the ITU-T guidelines [72]. The time domain output is analyzed and compared with that of an undispersed system to quantify the eye-closure penalty. Figure 7.27 shows the system used for the simulation. It is easy to see how the system can be extended for a more involved simulation.

Figure 7.28a shows the result of the simulations for a transmission over 100 km of standard fiber at a bit rate of 10 Gb/sec, for a 150-mm-long DCG with a dispersion of 1.7 nsec/nm and a FW bandwidth of 107 GHz (0.86 nm). Shown are the results for an unapodized and cosine-and

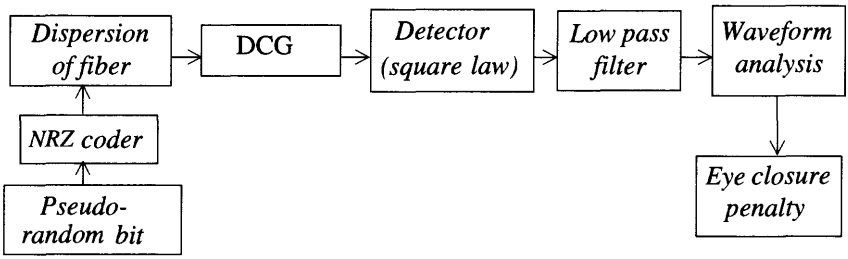

Figure 7.27: The block diagram of the simulation for the calculation of the eye penalty (after ref. [71]).

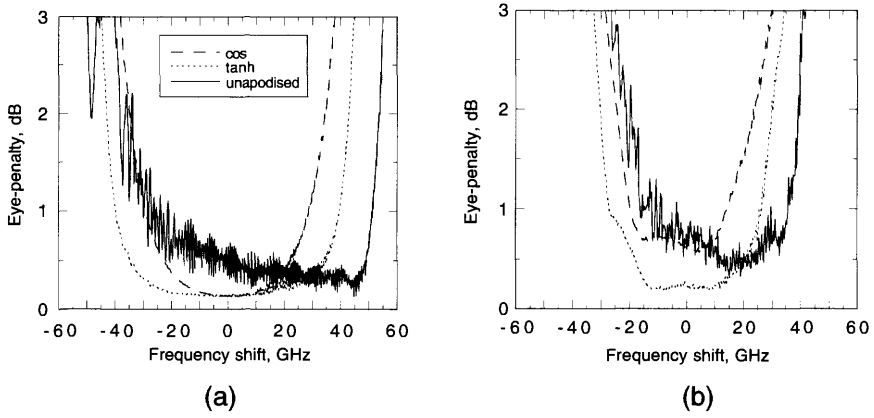

Figure 7.28: The eye-penalty for unapodized and cosine-and tanh-apodized, 150-mm-long gratings for a 10^7-1 NRZ pseudo-random bit sequence, at a bit rate of 10 Gb/sec (a) and 40 Gb/sec (b) (courtesy C. Bungarzeanu [71]).

hyperbolic-tan-apodized profiles as a function of detuning. While the eye penalty is very low (<0.5 dB) close to the short-wavelength end of the unapodized grating, it steadily increases toward the long-wavelength end. Note that the bandwidth is similar to that of the tanh-, but larger than that of the cosine-apodized grating. Also shown in Fig. 7.28b are the simulations for 40 Gb/sec transmission. Here, too, we see that the penalty is only slightly higher than for the tanh-apodized grating (note that the bandwidth for a NRZ is half that of an RZ bit sequence), and the bandwidths are almost identical. Owing to the restricted bandwidth, the detuning is significantly narrower for the cosine-apodized grating.

We note that at the longer-wavelength end of the unapodized grating, the eye penalty fluctuates because of the GDR frequency becoming closer to the transmission frequency, since the eye closes as a result of the additional dispersion. This becomes less important for 40 Gb/sec, since more of the grating bandwidth is being used for dispersion compensation, and the fluctuations on the long-wavelength side also become smaller. This result has been further investigated by Garthe *et al.* [73] for long gratings. The conclusions are similar, in that the eye penalty has a maximum value depending on the position in the bandwidth, because the GDR frequency induces satellite pulses that may coincide with adjacent time slots.

Figure 7.29 shows the reflection and relative group delay of a 200-mm-long SSCG made with two 100-mm-long chirped gratings. Low-repetition-rate ultrahigh-speed measurements performed on this grating with a dispersion of 1310 psec/nm and bandwidth of 1.5 nm at the output of 77 km of standard telecommunications fiber [74] shows that a 3.8 psec input pulse sits on a wide low-level pedestal at the output. The pedestal, which is limited to approximately two bit periods, has the detrimental effect of causing the eye to close slightly when the entire bandwidth of the grating is used. However, systems transmission experiments performed on the same grating at 40 Gb/sec over 77 km of standard fiber indicate that the received eye remains open, as shown in Fig. 7.30, which without the DCG is completely closed.

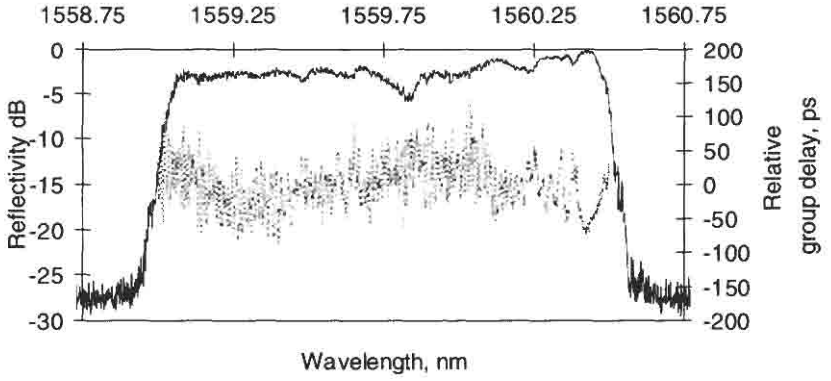

Figure 7.29: The reflectivity and relative group delay of a 200-mm SSCG (dispersion of 1310 psec/nm) [74].

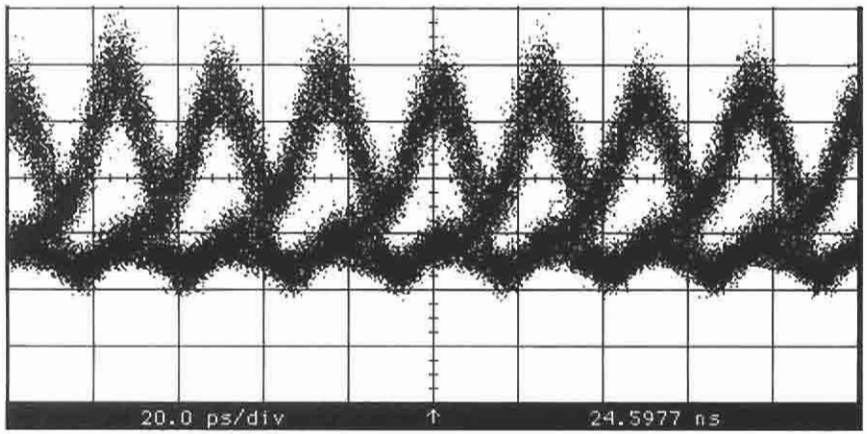

Figure 7.30: The received signal eye diagram at a transmission bit rate of 40 Gb/sec (1550 nm) after 80 km of optical standard fiber and a 200-mm-long unapodized SSCG dispersion compensating grating (courtesy D. Nesset, BT Laboratories).

7.6 Other applications of chirped gratings

As we have seen, pulses propagating in a fiber are broadened by dispersion. There is a broadening if the pulse is not transform limited and it is chirped. Thus, the individual parts of the spectrum arrive at different times and can skew the pulse. If the chirp is a time-varying function, then jitter is also introduced. On the other hand, in a dispersion-free system, neither the chirp introduced by any component nor the source bandwidth causes the pulse to be broadened. If a chirped grating compensates for the dispersion of a fiber, then the dispersion and jitter induced in chirped pulses is automatically compensated [75]. Further, pulses can be compressed or dispersed depending on the sign of the chirp, by launching the pulse in a fiber with either anomalous or normal dispersion. If a pulse is chirped, then it is possible to compensate for the chirp using a chirped fiber grating and to compress the pulse [14,76–80]. The grating may also be used for nonlinear pulse compression [81] of pulses that have been spectrally broadened and linearly chirped through self-phase modulation (SPM) and propagation in normally dispersive optical fiber [82].

For high-power use, chirped gratings are especially suitable for reducing nonlinear effects in the fiber by stretching pulses, reducing the peak power before amplification [13,83].

Adjustment of the chirp of the grating also allows the effects of higher-order dispersion to be canceled [10].

References

1. Byron K. C., Sugden K., Bircheno T., and Bennion I., "Fabrication of chirped Bragg gratings in photosensitive fibre," *Electron. Lett.* **29**(18), 1659 (1993).
2. Eggleton B., Krug P. A., and Poladin L., "Dispersion compensation by using Bragg grating filters with self induced chirp," in *Tech. Digest of Opt. Fib. Comm. Conf., OFC '94,* p. 227.
3. Farries M. C., Sugden K., Reid D. C. J., Bennion I., Molony A., and Goodwin M. J., "Very broad reflection bandwidth (44 nm) chirped fibre gratings and narrow-bandpass filters produced by the use of an amplitude mask," *Electron. Lett.* **30**(11), 891–892 (1994).
4. Ouellette F., "The effect of profile noise on the spectral response of fiber gratings," in *Bragg Gratings, Photosensitivity, and Poling in Glass Fibers and Waveguides: Applications and Fundamentals,* Vol. 17, OSA Technical Digest Series (Optical Society of America, Washington, DC, 1997), paper BMG13, pp. 222–224.
5. Hill K. O., Bilodeau F., Malo B., Kitagawa T., Theriault, Johnson D. C., and Albert J., "Aperiodic in fibre gratings for optical fiber dispersion compensation," in *Technical Digest of Post-Deadline Papers,* PD2-1, *Opt. Fib. Comm. Conf., OFC '94.*
6. Stephens T., Krug P. A., Brodzeli Z., Doshi G., Ouellette F., and Poladin L., "257 km transmission at 10 Gb/s in non dispersion shifted fibre using an unchirped fibre Bragg grating dispersion compensator," *Electron. Lett.* **32**(17), 1559–1561 (1996).
7. Kashyap R., McKee P. F., Campbell R. J., and Williams D. L., "A novel method of writing photo-induced chirped Bragg gratings in optical fibres," *Electron. Lett.* (12), 996–997 (1994).
8. Okude S., Sakai T., Wada A., and Yamauchi R., "Novel chirped fiber grating utilizing a thermally diffused taper-core fiber," in *Proc. of OFC '96,* paper TuO7, pp. 68–69.

9. Putnam M. A., Williams G. M., and Friebele E. J., " 'Fabrication of tapered, strain-gradient chirped fibre Bragg gratings," *Electron. Lett.* **31**(4), 309–310 (1995).

10. Laming R. I., Ibsen M., Durkin M., Cole M. J., Zervas M. N., Ennser K. E., and Gusmeroli V., "Dispersion compensation gratings," in *Bragg Gratings, Photosensivity, and Poling in Glass Fibers and Waveguides: Applications and Fundamentals,* Vol. 17, OSA Technical Digest Series (Optical Society of America, Washington, DC, 1997), Paper BTuA7, pp. 271–273.

11. Loh W. H., Laming R. I., Robinson N., Cavaciuti A., Vaninetti, Anderson C. J., Zervas M. N., and Cole M. J., "Dispersion compensation over distances in excess of 500 km for 10 Gb/s systems using chirped fibre gratings," *IEEE Photon. Technol. Lett.* **8**, 944 (1996).

12. Garrett L. D., Gnauck A. H., Forgherieri, and Scarano D., "8 × 20 Gb/s–315 km–480 km WDM transmission over conventional fiber using multiple broadband fiber gratings," in *Tech. Digest of Conf. On Opt. Fiber Commun., OFC '98,* Post-Deadline paper, PD18/1–4.

13. Boskovic A., Guy M. J., Chernikov S. V., Taylor J. R., and Kashyap R., "All-fiber diode pumped, femtosecond chirped pulse amplification system," *Electron. Lett.* **31**(11), 877–879 (1995).

14. Gunning P., Kashyap R., Siddiqui A. S., and Smith K., "Picosecond pulse generation of <5 ps from gain-switched DFB semiconductor laser diode using linearly step-chirped fibre grating," *Electron. Lett.* **31**(13), 1066–1067 (1995).

15. Kersey A. D. and Davis M. A., "Interferometric fiber sensor with a chirped grating distributed sensor element," *Proc. OFS '94,* pp. 319–322, Glasgow, UK (1994).

16. Williams J. A. R., Bennion I., and Doran N. J. "The design of in-fiber Bragg grating systems for cubic and quadratic dispersion compensation," *Opt. Commun.,* **116**(1–3), 62–66 (1995).

17. Farries M. C., Ragdale G. M., and Reid D. C. J., "Broadband chirped fiber Bragg grating filters for pump rejection and recycling in erbium doped fibre amplifiers," *Electron. Lett.,* 28, 487–489 (1992).

18. Kashyap R., Wyatt R., and McKee P. F., "Wavelength flattened saturated erbium amplifier using multiple side-tap Bragg gratings," *Electron. Lett.* **29**(11), 1025 (1993).

19. Zhang I., Sugden K., Williams J. A. R., and Bennion I., "Postfabrication exposure of gap-type bandpass filters in broadly chirped fiber gratings," *Opt. Lett.* **20**(18), 1927–1929 (1995).

20. Treacy E. B., "Optical pulse compression with diffraction gratings," *Quantum Electron.* **QE-5**, 454 (1969).

21. Nakatsuka H., Grischkowsky D., and Balant A. C., "Nonlinear picosecond pulse propagation through optical fibers with positive group velocity dispersion," *Phys. Rev. Lett.* **47**, 910 (1981).

22. Shank C. V., Fork R. L., Yen R., Stolen R. H., and Tomlinson W. J., *Appl. Phys. Lett.* **40**, 761 (1982).

23. Winful H. G., "Pulse compression in optical fiber filters," *Appl. Phys. Lett.* **46**(6), 527 (1985).

24. See, for example, Sterke C. M. de, and Sipe J. E., "Gap solitons," in *Progress in Optics XXXIII* (E. Wolf, Ed.), Chapter III. Elsevier, Amsterdam (1994).

25. Eggleton B. J., Slusher R. E., Strasser T. A. and Sterke M. de, "High intensity pulse propagation in fiber Bragg gratings," in *Bragg Gratings, Photosensitivity, and Poling in Glass Fibers and Waveguides: Applications and Fundamentals,* Vol. 17, OSA Technical Digest Series (Optical Society of America, Washington, DC, 1997), Paper BMB1, pp. 114–116.

26. Chen L. R., Benjamin S. D., Smith P. W. E., and Sipe J. E., "Ultrashort pulse propagation through fiber gratings: Theory and experiment," *ibid.,* paper BMB2, pp. 117–119.

27. Taverner D., Broderick N. G. R., Richardson D. J., and Ibsen M., "Nonlinear switching and multiple gap soliton formation in a fibre Bragg grating," *ibid.,* paper BMB3, pp. 120–123.

28. Broderick N. G. R., Taverner D., Richardson D. J., Ibsen M., and Laming R. I., "The optical pushbroom in action" *ibid.,* paper BMB4, pp. 123–125.

29. Kuo C. P., Österberg U., Seaton C. T., Stegeman G. I., and Hill K. O., "Optical fibers with negative group-velocity dispersion in the visible," *Opt. Lett.* **13**(11), 1032–1034 (1988).

30. Ouellette F., "Limits of chirped pulse compression with an unchirped Bragg grating filter," *Appl. Opt.* **29**(32), 4826 (1990).

31. Eggleton B. J., Stephens T., Krug P. A., Doshi G., Brodzeli Z., and Ouellette F., "Dispersion compensation over 100 km at 10 Gb/sec using a Bragg grating in transmission," in *Tech. Digest. of OFC '96,* post-deadline paper PD5 (1–5).

32. Litchinistser N. M., Eggleton B. J., and Patterson D. B., "Fiber Bragg gratings for dispersion compensation in transmission: theoretical model and design criteria for nearly ideal pulse recompression," *J. Lightwave Technol.* **15**(8), 1301–1313 (1997).

33. Hinton K., "Ramped, unchirped fiber gratings for dispersion compensation," *J. Lightwave Technol.* **15**(8), 1141–1418 (1997).

34. Ouellette F., "Dispersion cancellation using linearly chirped Bragg grating filters in optical waveguides," *Opt. Lett.* **12**(10), 847 (1987).

35. Priest R. G. and Giallorenzi T. G., "Dispersion compensation in coherent fiber-optic communications," *Opt. Lett.* **12**, 622–625 (1987).

36. Boness R., Nowak W., Vobian J., Unger S., and Kirchoff J., "Tailoring of dispersion compensation fibers with high compensation ratios up to 30," *Pure Appl. Opt.*, **5**, 333 (1995).

37. Agrawal G. P., *Nonlinear Fiber Optics,* 2nd ed. Academic Press, New York (1995).

38. Marcuse D., *Appl. Opt.* **19**, 1563 (1980).

39. Kashyap R., "Design of step chirped gratings," *Optics Commun.* **136**(5,6), 461–469 (1997).

40. Boskovic A., Taylor J. R., and Kashyap R., "Forty times dispersive broadening femtosecond pulses and complete recompression in a chirped fibre grating," *Opts. Commun.* **119**, 51–55 (1995).

41. Bonino S., Norgia M., and Riccardi E., "Spectral behaviour analysis of chirped fibre Bragg gratings for optical dispersion compensation," in *Proc. of ECOC '97, IEE Conf. Pub. No. 448,* Vol.3, pp. 194–197.

42. Kashyap R. and Lacerda-Rocha M. de, "On the group delay of chirped fibre Bragg gratings," *Opt. Commun.* **153**, 19–22 (1998).

43. Hill K. O., Thériault S., Malo B., Bilodeau F., Kitagawa T., Johnson D. C., Albert J., Takiguchi T., Kataoka T., and Hagimoto K., "Chirped in-fibre grating dispersion compensators: Linearisation of dispersion characteristic and demonstration of dispersion compensation in 100 km, 10 Gbit/s optical fibre link," *Electron. Lett.* **30**(21), 1755–1756 (1994).

44. Roman J. E. and Winnick K. A., "Waveguide grating filters for dispersion compensation and pulse compression," *IEEE J Quantum Electron* **29**(3), 975 (1993).

45. Ark wright J., Stephens T., Stepanov D. Yu, Krug P., Smith B., Doshi G., Joffe G., and Ouellette F., "Fibre gratings for dispersion compensation," in *Proc. of ECOC '97, IEE Conf. Pub. No. 448* (1997).

46. Kashyap R., Froehlich H-G., Swanton A., and Armes D. J., "Super-step-chirped fibre Bragg gratings," *Electron. Lett.* **32**(15), 1394–1396 (1996).

47. Kashyap R., Froehlich H-G., Swanton A., and Armes D. J., "1.3 m long super-step-chirped fibre Bragg grating with a continuous delay of 13.5 ns and bandwidth 10 nm for broadband dispersion compensation," *Electron. Lett.* **32**(19), 1807–1809 (1996).

48. Kashyap R., Ellis A., Malyon D., Froehlich H-G., Swanton A., and Armes D. J., "Eight wavelength × 10Gb/s simultaneous dispersion compensation over 100 km singlemode fibre using a single 10 nm bandwidth, 1.3 metre long, super-step-chirped fibre Bragg grating a continuous delay of 13.5 ns,"

in *Proc. of Post Deadline Papers of the 22nd ECOC '97,* Oslo, Norway, Sept. 15–19 (1996).

49. Curti F., Diano B., Marchis G. C., and Matera F., "Statistical treatment of the principal states of polarization in single-mode fibers," *J. Lightwave Technol.,* **8**(8), 1162–1166 (1990).

50. Bonino S., Norgia M., Riccardi E., and Schiano M., "Measurement of polarisation properties of chirped fibre gratings," in *Technical Digest of OFMC '97,* pp. 10–13.

51. Kashyap R., Chernikov S. V., McKee P. F., and Taylor J. R., "30 *ps* chromatic dispersion compensation of 400 *fs* pulses at 100 *Gbit/s* using an all fibre photoinduced chirped reflection grating," *Electron. Lett.* **30**(13), 1078 (1994).

52. Kashyap R., Chernikov S. V., McKee P. F., Williams D. L., and Taylor J. R., "Demonstration of dispersion compensation in all-fibre photoinduced chirped gratings," *Pure Appl. Opt.* **4**, 425–429 (1995).

53. Garthe D., Lee W. S., Epworth R. E., Bircheno T., and Chew C. P., "Practical dispersion equaliser based on fibre gratings with a bitrate length product of 1.6 Tb/s-km," post-deadline paper, in *Technical Digest of ECOC '94,* pp. 11–14.

54. Laming R. I., Robinson N., Scrivener P. L., Zervas M. N., Barcelos S., Reekie L., and Trucknott J. A., "Dispersion tunable grating in a 10-Gb/s 100–220 km step-index fiber link," *IEEE Photon. Technol. Lett.* **8**(3), 428–430 (1996).

55. Krug P. A., Stephens T., Yoffe G., Ouellette F., Hill P., and Doshi G., "270 km transmission at 10 Gb/s in nondispersion shifted fiber using an adjustably chirped 120 mm long fiber Bragg grating dispersion compensator," in *Tech. Digest of Conf. on Opt. Fiber Commun., OFC '95,* post-deadline paper PDP27.

56. Krug P. A., Stephens T., Yoffe G., Ouellette F., Hill P., and Doshi G., "Dispersion compensation over 270 km at 10 Gb/s using an offset-core fibre Bragg grating," *Electron. Lett.* **19**, 877–879 (1994).

57. Loh W. H., Laming R. I., Gu X., Zervas M. N., Cole M. J., Widdowson T., and Ellis A. D., "10 cm chirped fibre Bragg grating for dispersion compensation at 10 Gb/s over 400 km of non-dispersion shifted fibre," *Electron. Lett.* **31**(25), 2203–2204 (1995).

58. Dong L., Cole M. J., Ellis A. D., Durkin M., Ibsen, Gusmeroli V., and Laming R. I., "40 Gb/s 1.55 μm transmission over 109 km of non-dispersion shifted fibre with long continuously chirped gratings," in *Tech. Digest of Conf. on Opt. Fiber Commun., OFC '97,* post-deadline paper PD6.

59. Ouellette F., Krug P. A., Stephens T., Doshi G., and Eggleton B., "Broadband and WDM dispersion compensation using chirped sampled fibre Bragg gratings," *Electron. Lett.* **3**(11), 899–901 (1995).

60. Chernikov S. V., Kashyap R., and Taylor J. R., "Dispersion compensation of a 100-Gb/s optical fibre transmission by using a chirped fibre grating transmission filter," *Tech. Digest of Conf. on Opt. Fiber Commun., OFC '95,* paper WB5, pp. 99–100.

61. Taverner D., Richardson D. J., Barcelos S., Zervas M. N., Reekie L., and Laming R. I., "Dispersion compensation of 16 ps pulses over 100 km of step-index fibre using cascaded chirped fibre gratings," *Electron. Lett.* **31**(12), 1004–1006 (1995).

62. Cole M. J., Geiger H., Laming R. I., Zervas M. N., Loh W. H., and Gusmeroli V., "Broadband dispersion compensation chirped fibre Bragg gratings in a 10 Gb/s NRZ 110 km standard step index monomode fibre link," *Electron. Lett.* **33**(1), 70–71 (1997).

63. Dong L., Cole M. J., Ellis A. D., Durkin M., Ibsen M., Gusmeroli V., and Laming R. I., "40 Gb/s 1.55 μm RZ transmission over 109 km of non-dispersion shifted fiber with long continuously chirped fibre gratings," *Electron Lett,* **33**, 1563–1565 (1997).

64. Chernikov S. V., Taylor J. R., and Kashyap R., "All-fiber dispersive transmission filters based on fiber grating reflectors," *Opt. Lett.* **20**(14), 1586–1588 (1995).

65. Huber D. R., "Erbium doped amplifier with a 21 GHz optical filter based on an in-fiber Bragg grating," in *Proc. of ECOC '92,* pp. 473–476 (1992).

66. Ouellette F., Cliche M., and Gagnon S., "All-fiber devices for chromatic dispersion compensation based on chirped distributed resonant coupling," *J. Lightwave Technol.* **12**(10), 1728–1737 (1994).

67. Mason P. L., Penty R. V., and White I. H., "Multiple stage dispersion compensation in long haul optical fibre systems using chirped fibre Bragg gratings," *Electron. Lett.* **30**(15), 1244–1245 (1994).

68. Pastor D., Capmany J., Ortega D., Tatay V., and Marti J., "Design of apodized linearly chirped fiber gratings for dispersion compensation," *J. Lightwave Technol.* **14**(11), 2581–2588 (1996).

69. Litchinitser N., and Patterson D., "Analysis of fiber Bragg gratings for dispersion compensation in reflective and transmissive geometries," *J. Lightwave Technol.* **15**(8), 1323–1328 (1997).

70. Ennser K., Zervas M. N., and Laming R. I., "Optimization of linearly chirped grating dispersion compensated system," *Opt. Fiber Technol.* **3**, 120–122 (1997).

71. Bungarzeanu C., "Computer aided design of linearly chirped fibre gratings used as broadband dispersion compensators," in *Proc. of ITA–Information,*

Telecommunications, Automata Journal, Vol. 15, No. 1–3, 1997, ISSN 0351-7748.

72. *International Telecommunications Union-T, Recommendation G. 957.*
73. Garthe D., Milner G., and Cai Y., "System performance of broadband dispersion compensating gratings," *Electron. Lett.* **34**(6), 582–583 (1998).
74. Guy M. J., Taylor J. R., and Kashyap R., "Demonstration of the possibility of >100 Gbit/s transmission over 77 km of standard fibre using a super-step-chirped fibre grating dispersion compensator," *Opt. Commun.* **150**, 77–80 (1998).
75. Kawase L., Carvalho M. C. R., Margulis, and Kashyap R., "Transmission of chirped optical pulses in fibre grating dispersion compensated system," *Electron. Lett.* **33**(2), 152–154 (1997).
76. Eggleton B. J., Krug P. A., Poladin L., Ahmed K. A., and Liu J-F, "Experimental demonstration of compression of dispersed optical pulses by reflection from a self-chirped optical fiber Bragg gratings," *Opt. Lett.* **19**, 877–879 (1994).
77. Rottwitt K., Guy M. J., Boskovic A., Noske D. U., Taylor J. R., and Kashyap R., "Interaction of uniform phase picosecond pulses with chirped and unchirped photosensitive fibre Bragg gratings," *Electron. Lett.* **30**(12), 995–996 (1994).
78. Pataca D. M., Rocha M. L., Kashyap R., and Smith K., "Bright and dark pulse generation in an optically mode-locked fibre laser at 1.3 μm," *Electron. Lett.* **31**(1), 35–36 (1995).
79. Guy M. J., Chernikov S. V., Taylor J. R., Moodie D. G., and Kashyap R., "Generation of transform limited optical pulses at 10 GHz using an electro-absorption modulator and a chirped fibre Bragg grating," *Electron. Lett.* **31**(8), 671–672 (1995).
80. Morton P. A., Mizrahi V., Kosinski S. G., Mollenauer L. F., Tanbun-Ek T., Logan R. A., Coblentz D. L., Sargent A. M., and Wecht K. W., "Hybrid soliton pulse source with fibre external cavity and Bragg reflector," *Electron. Lett.* **28**(6), 561 (1992).
81. Williams J. A. R., Bennion I., and Zhang L., "The compression of optical pulses using self-phase modulation and linearly chirped Bragg gratings in fibers," *IEEE Photon. Technol. Lett.* **7**(5), 491–493 (1995).
82. Tomlinson W. J., Stolen R. H., and Shank C. V., "Compression of pulses chirped by self-phase modulation in fibers," *J. Opt. Soc. Am. B* **1**, 139–149 (1984).
83. Galvanauskas A., Fermann M. E., Harter D., Sugden K., and Bennion I., "All-fiber femtosecond pulse amplification circuit using chirped Bragg gratings," *Appl. Phys. Lett.* **66**, 1053–1055 (1995).

This page intentionally left blank

Chapter 8

Fiber Grating Lasers and Amplifiers

The arrival of the in-fiber Bragg grating could not have been at a better time for rare-earth-doped fiber. Research and development in the field of doped fibers was at such a stage that fiber amplifiers were already commercially available; thus, fiber Bragg gratings were a natural progression for combining the attributes of the fibers and amplifiers, as well as semiconductor devices. Their success in this area are due to the near-perfect reflection characteristics of the grating and the ultralow insertion loss, as well as the ease with which they can be tailored for a particular application. One of the most attractive features of the in-fiber Bragg grating is its transparency to wavelengths outside of the band stop. Apart from becoming integral components of narrow-band lasers, the side-tap filter and the long-period grating have also been particularly useful for equalizing the gain of optical fiber amplifiers. This chapter introduces some of the applications of fiber gratings in narrow-band, low-chirp lasers and mode-locked, short-pulse sources, as well as in tailoring the gain and stability of amplifiers.

8.1 Fiber grating semiconductor lasers: The FGSL

Semiconductor laser diode technology has been refined to produce low-threshold, high-power and narrow-linewidth devices (distributed feedback

lasers for a large number of applications [1]. The linewidth may be further narrowed by the use of a long external cavity. This technique has attracted much attention over the years [2]. Early work showed that while there was a benefit in line-narrowing from the linewidth enhancement factor of long external cavities, the instabilities were thought to be too difficult to overcome. In particular, reflections from intracavity elements such as the residual front facet reflections greatly affected the performance of the laser, except in the case of strong coherent feedback [3]. Much of the earlier work was limited to weak feedback due to in- and out-coupling losses to the external cavity. Wyatt and Devlin demonstrated line-narrowed (10 kHz) tunability over 55 nm in an InGaAsP 1.5-μm laser, using a bulk diffraction grating as the external cavity frequency selective mirror [4]. A semiconductor laser integrated with an etched Bragg reflector in a waveguide demonstrated the possibility of a compact configuration [5]. The fiber Bragg grating thus became the next obvious choice for an external reflector owing to its narrow bandwidth, with the possible advantage of defining the lasing wavelength and the potentially low coupling loss. Destroying the front facet reflectivity of a semiconductor laser and replacing it with a narrow-band fiber Bragg grating as an external cavity reflector is probably the worst possible configuration for making a high-quality laser. First of all, the semiconductor chip with cleaved facet mirrors forms an ultralow-loss cavity, since the mirrors are an integral part of the laser gain medium. Secondly, the laser semiconductor chip alone forms the shortest gain cavity, reducing the roundtrip time to a minimum and thereby allowing direct high-speed modulation. Thirdly, the high reflectivity of the output facet of the laser (~33%) is broadband; any external reflections returning to the laser, other than at the lasing wavelength, are attenuated equally, reducing the possibility of destabilizing laser operation. On the other hand, the fiber Bragg grating external-cavity semiconductor laser has several major limitations. The output facet reflectivity of the laser chip has to be reduced to low levels. The addition of a fiber in the cavity requires good coupling and low residual subcavity reflections in order to reduce intracavity losses and poses negligible return loss to wavelengths other than within the bandwidth of the Bragg grating. The cavity length increases correspondingly by the incorporation of a reflective Bragg element at some point within the fiber, increasing the cavity roundtrip time. What has the FGSL (or FGL) to offer to make it worth pursuing?

First, the fiber Bragg grating has a temperature coefficient [6] of wavelength change ~6–8 times lower than that of a semiconductor laser,

potentially increasing the wavelength stability of the laser in a hybrid configuration. Second, fiber Bragg gratings can be routinely fabricated at precise wavelengths and are therefore suited to mass production; wavelength control makes them useful for wavelength division multiplexing (WDM) applications that require extremely tight tolerances [7]. Third, the longer laser formed by the incorporation of the external cavity reduces the linewidth in direct relation to the length [8]. Fourth, semiconductor lasers suffer from chirp as a result of cavity length change during direct modulation. The longer FGSL dilutes the carrier induced cavity length change in the semiconductor during modulation, by confining it to the much smaller fraction of the laser length.

It is usual to quantify the operational sensitivity of a semiconductor laser by the linewidth enhancement factor α as [9,10]

$$\alpha = -\frac{4\pi}{\lambda}\frac{dn/dN}{dg/dN}, \tag{8.1.1}$$

where λ is the lasing wavelength, dn is the change in the refractive index of the laser, and dg/dN is the differential gain. In a semiconductor laser, the change in the gain and the refractive index is over the entire length of the laser L_s. With an extended cavity in which only part of the cavity is active, the influence of both these quantities is limited, with the result that the effect of the refractive index change (on the cavity length) is diluted.

The change in the laser wavelength $\delta\lambda$ as a function of injected carriers is given by

$$\delta\lambda = \lambda\frac{\partial l_{carrier}}{L_{laser}}, \tag{8.1.2}$$

where $\partial l_{carrier}$ is the change in the optical length of the semiconductor with injected current, and λ is the lasing wavelength. The inverse dependence of the shift in the wavelength on the laser cavity length demonstrates the advantage of the longer cavity [11].

Further, the wide gain bandwidth of the semiconductor chip in conjunction with a fiber Bragg grating used to define the operating wavelength can increase the yield, potentially allowing the use of *all* chips on a wafer. This becomes especially important with the tight specification for WDM system wavelengths. Semiconductor production technology of DFB lasers requires that each laser be measured for wavelength prior to packaging and consequently has implications for the replacement of faulty

lasers in WDM systems, where stocks may need to be maintained for each laser. The concept of retaining a fiber grating as part of the transmitter card, while replacing only the active gain medium when faulty, may have a cost advantage by reducing stocks. Finally, for telecommunications and sensor applications, lasers need to be pigtailed after fabrication. If the fiber grating is allowed to define the lasing wavelength, the two functions of operating wavelength and pigtailing may further reduce fabrication/packaging costs. These advantages are considered worthwhile to overcome the difficulties involved in optimizing laser chip-to-fiber coupling.

The first semiconductor laser to use an external cavity of an etched in-fiber Bragg grating was reported by Brinkmeyer *et al.* [12]. This laser used a standard uncoated Fabry–Perot fiber pigtailed laser chip operating at 1.3 microns, which was fusion spliced to an etched fiber grating, forming 2-meter-long cavity. With the twin coupled cavities (laser chip and laser chip with fiber grating), single-frequency operation of the laser was demonstrated with a linewidth of ~50 kHz. The narrow bandwidth of the grating (26 GHz) was much less than the FP mode spacing (140 GHz), although the long cavity longitudinal mode spacing was only 50 MHz. The reflectivity of the front facet of the FP laser $\rho_{FP} \approx 32\%$, while the reflectivity ρ_{fbg} of the grating is very low, ~0.01%; however, the combined coupled cavities results in a constructive interference with a contrast ratio of

$$|\rho_{FP} + \rho_{fbg}|^2/|\rho_{FP} - \rho_{fbg}|^2 \approx 1.07, \tag{8.1.3}$$

so that when the cavity length is tuned for constructive interference, the modes of the long fiber cavity have a differential gain that is higher than the FP laser modes. This demonstration showed that the selectivity and additional reflectivity of the external cavity grating have a beneficial effect even in such a simple configuration. Etched gratings in fibers as external cavity mirrors have also been used with 1500-nm diodes [13].

Morey *et al.* [14] showed the use of a photoinduced fiber Bragg grating with a semiconductor laser to operate at the grating wavelength of 820 nm. A schematic of the FGSL device is shown in Fig. 8.1. An antireflection-coated (~0.5% reflectivity) FP GaInAsP/InP buried-heterostructure 1.5-μm laser chip is coupled with a lensed fiber with a narrowband reflection grating spliced to it to form the external resonator [15]. The lensed fiber is aligned to maximize the output coupling and welded in place. This laser demonstrates a low chirp, which is restricted by the limited bandwidth

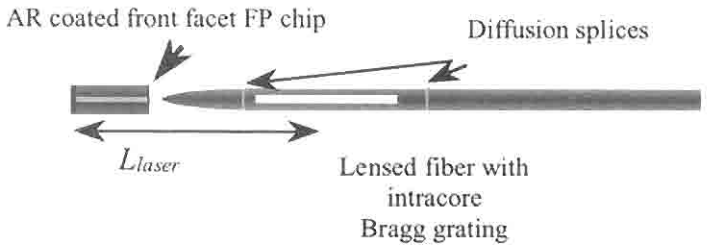

Figure 8.1: The external fiber grating semiconductor laser with an AR-coated FP chip coupled to a lensed fiber [3]. The measured chirp was instrument limited to be <0.5 MHz when modulated with NRZ pulses at 1.2 Gb/sec [15].

of the grating and the reduced change in the cavity length according to Eq. (8.1.2).

The linewidth of the laser for the 60-mm-long cavity was measured to be <50 kHz. The bias current varied between the threshold of 30 mA and 150 mA, changed the operating wavelength by <0.1 nm. The package temperature was controlled to ±5°C. A potentially low-cost FGSL operating at 1.3 μm with ~1 mW output power with an operating wavelength change of only 2 nm, over a temperature range of 100°C, has also been reported [16] for Access networks at 622 Mb/sec transmission rates.

The intracavity interference effects cause the modes of the laser to hop. This has been observed in experiments with FGSLs [11]. It was shown that as the lensed end of the external cavity fiber is moved away from the AR coated facet of the laser, the laser output drops until it stops lasing in a cyclic manner. These experiments showed the importance of the phase of the reflected light entering the cavity. If the free spectral range of the subcavity of the semiconductor is much larger than that of the external grating reflector, then the laser wavelength mode will pull within the grating bandwidth. The differential gain between the different external fiber grating cavity modes determines which wavelength lases at any one time. Changing the length of the cavity is similar to changing the bias current, and therefore requires some mechanism to compensate this effect.

In an effort to counter the detrimental effects of the variation of the phase as a function of bias current or modulation in the FGSL, a variation in the design using a chirped external grating reflector may be used, as is shown in Fig. 8.2 [17,18].

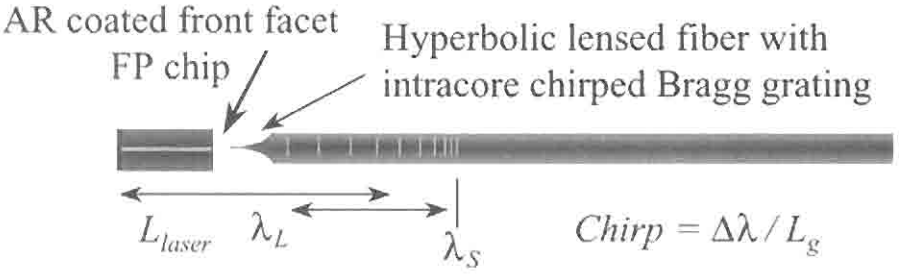

Figure 8.2: The chirped external fiber grating cavity laser [17]. The special AR-coated hyperbolic lens on the end of the fiber provides high-efficiency coupling of >98% [19], which in turn allows stable single-mode operation over a large output power (15 mW).

The principle of operation of chirped grating is to compensate for the current induced change in the optical cavity length of the semiconductor. As the length of the semiconductor cavity changes by δl_s to maintain an integral number of periods within the laser cavity, the wavelength shifts, altering the cavity length. In principle, the wavelength should shift smoothly as the bias current is altered.

In this case, the grating had a deliberate chirp of 0.28 nm with decreasing wavelengths away from the gain medium, a reflectivity of 33%, and a grating length of 10 mm. The fiber lens had a hyperbolic shape to maximize coupling to the grating. The coupling efficiency of this type of lens can be as high as 98% [19]. With an HR coating on the rear and an AR coating on the output facet, the threshold of the device was measured to be 7 mA, operating single-frequency at fiber output powers of >15 mW. A side-mode suppression ratio (SMSR) of 56 dB was also demonstrated at a bias current of 250 mA(~25 mW output power). The linewidth was measured to be between 100 and 540 kHz (close to a mode hop), depending on the bias current.

An important application of the fiber Bragg grating is for stabilization of erbium amplifier pump lasers operating at 980 nm [20,21]. Since the pump absorption band is narrow, it is useful to maintain the pump wavelength accurately. It was found empirically that placing a 4% reflector reflection grating approximately 50–100 mm away from the AR-coated facet of a high-power pump-laser chip caused it to lock to the grating. Temperature variations of 50°C pulled the wavelength by ~0.2 nm, showing that the requirement for a thermoelectric cooler may not be necessary.

Such a long cavity (as with the one described earlier [12]) works under the regime of "coherence collapse" [22], where the coherence length of the diode modes is much shorter than the laser cavity length.

An alternative method of controlling the wavelength of the laser is to use the fiber grating at the rear facet of the chip [23]. The output coupler is a standard fiber pigtail. This device was fabricated in a package with all the in and out coupling with aspherical collimating lenses, as well as an isolator in the output path. The advantage of this scheme is the use of a highly reflective grating (>95%), potentially increasing the output power. The grating had a bandwidth of <0.4 nm, which was burnt-in at 350°C for 6 min. The fabrication technique is claimed to have a reproducibility of ±0.05 nm, allowing devices to be fabricated to ITU-T standards for dense WDM. With temperature control of the package, both the grating and the laser chip are maintained at the same temperature. Consequently, the stability of the wavelength was reported to be better than ±0.005 nm, with an output power stability within ±0.02 dB. This laser, as is common with well-designed FEGSLs had a measured linewidth of <30 kHz and a side-mode suppression ratio of >50 dB.

A combination of a reflective amplifier and a large spot laser has resulted in a robust laser, which may be operated over a wide temperature range without temperature control [24]. This type of laser has good wavelength stability as a function of temperature and therefore is ideally suited to applications in Access to a local area network, with the potential of being a low-cost source. Figure 8.3 shows a schematic of this laser. The gain medium is a semiconductor chip, which has a passive tapered waveguide to allow the mode to expand so that it has a mode-field close to that of a standard telecommunications fiber. Further, the waveguide is arranged to terminate at an angle to the output facet. The large mode field size

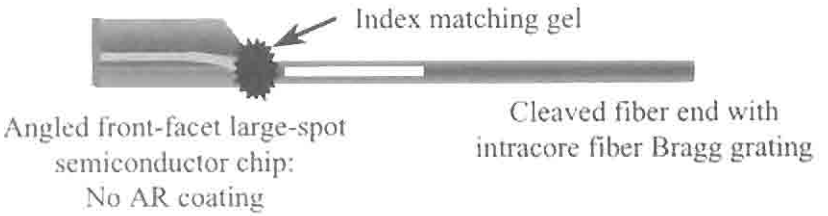

Figure 8.3: The large spot-angled facet, cleaved standard fiber FGSL [24].

allows good coupling to a cleaved standard fiber [24,25], which can be covered in index matching gel to reduce end reflections to a very low level. The angled facet ensures low back reflection, virtually eliminating the formation of a subcavity. No ripple due to intracavity reflections can be seen in the amplified spontaneous emission (ASE) spectrum. The positive effect of such a design is the lack of mode competition between subcavity modes as the current is ramped. A large-bandwidth (0.3-nm) fiber Bragg grating reflector allows the lasing mode to tune slightly in wavelength as the laser is modulated, with the virtual absence of mode hops.

The alignment is simplified with the help of a mini silicon-optical bench. A key on the bench allows easy positioning and soldering of the laser chip. A silicon micro-machined vee-groove aligned to the laser completes the passive alignment of the assembly. A glass sliver is then used to bond the fiber in place with epoxy. The gap between the laser and the fiber-end is then filled with gel. The package may then be completed by injection molding [25] or by hermetic sealing. A photograph of the packaged laser is shown in Figure 8.4.

8.2 Static and dynamic properties of FGLs

The light–current characteristics are shown in Fig. 8.5. The kink-free curve shows mode-hop-free operation as a function of bias current. The extremely low hysteresis in the wavelength of the laser as the current is altered, shows the potential of such a device. Typical of most FGLs is the weak temperature dependence of the lasing wavelength when the grating

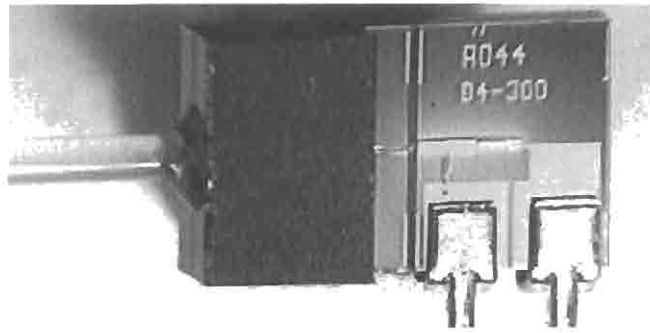

Figure 8.4: Photograph of packaged laser large spot laser FGL (photograph courtesy C. Ford, BT Laboratories).

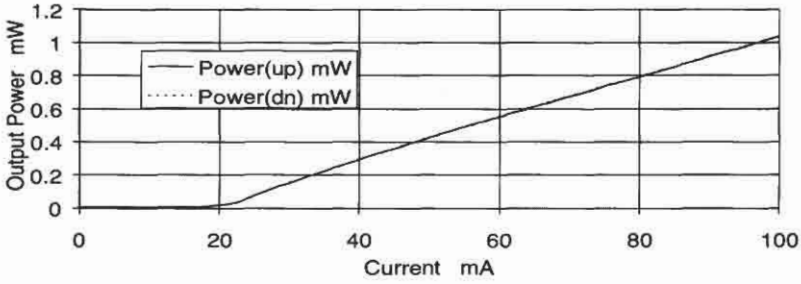

Figure 8.5: *L–I* characteristics (up and down) of large-spot angled facet laser at 20°C with index-matched gel between laser facet and cleaved fiber end. (Courtesy M. C. Brierley, BT Laboratories.)

is heated along with the laser. Mode hopping may be observed as the temperature is increased, as shown in Fig. 8.6. The cavity length determines the magnitude of the wavelength hop, and for this laser, it is ~0.16 nm. Note that the overall change in the lasing wavelength is approximately 0.4 nm for a 25°C change in temperature. With an unheated grating, the drift in the wavelength is made almost insignificant. The increased stability of a short-cavity semiconductor laser in an external long passive cavity has also been demonstrated [11].

With an AR-coated front facet reflectivity of 5×10^{-5} and a grating reflectivity of 28%, it has been shown that this type of laser may be

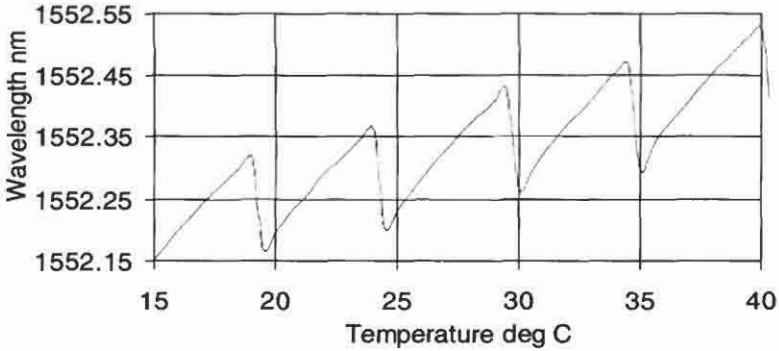

Figure 8.6: Wavelength vs temperature characteristics of the large mode-field FGL with index-gel. The grating is heated along with the laser chip. (Courtesy M. C. Brierley, BT Laboratories.)

ramped from threshold to 100 mA without a mode hop, and with a wavelength change of only 0.1 nm [24].

The static and dynamic chirp measurements of 500-μm-long AR-coated (reflectivity $\sim 1 \times 10^{-5}$) angled facet GaAsPInP buried-heterostructure amplifier chips [24] show that the static chirp of the dominant FGL mode is ~ -0.06 GHz/mA, while the dynamic chirp is reduced to 0.016 GHz/mA. The fiber Bragg grating had a reflectivity of 30% with a FWHM bandwidth of 0.3 nm. This data is shown in Figs. 8.7a and 8.7b. This laser has also been

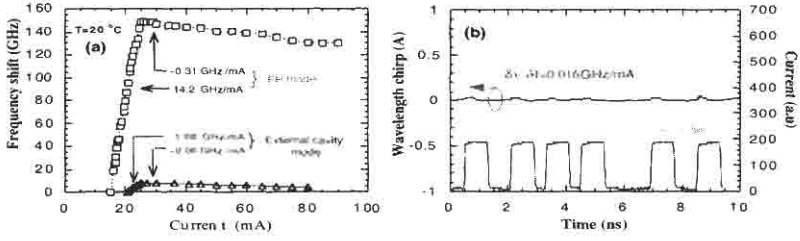

Figure 8.7: (a) Static chirp of external cavity and FP modes of the FGL; (b) shows the dynamic chirp under active modulation (from: Timofeev F. N., Bayvel P., Mikhailov V., Lavrova O. A., Wyatt R., Kashyap R., Robertson M. and Midwinter J. E., "2.5 Gbit/s directly modulated fibre grating laser for WDM networks", *Electron. Lett.*, **33**(16), 1406–1407, July, 1997. © IEE 1997, Ref. [30]).

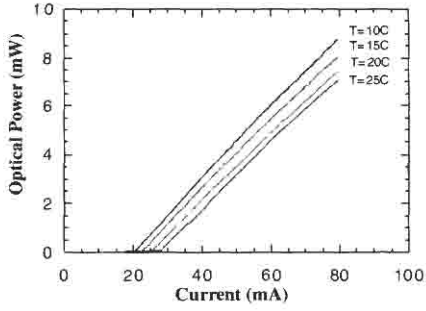

Figure 8.8: The kink-free light output characteristics of an angled-facet FGL with a 7-mm external cavity, as a function of temperature. Measured side-mode suppression ratio is -45 dB and RIN is -145 dB/Hz (from: Timofeev F. N., Bayvel P., Mikhailov V., Lavrova O. A., Wyatt R., Kashyap R., Robertson M. and Midwinter J. E., "2.5 Gbit/s directly modulated fibre grating laser for WDM network", *Electron. Lett.*, **33**(16), 1406–1407, July 1997. © IEE 1997, Ref. [30]).

shown to have extremely good thermal behavior, with the elimination of mode hops. The *L–I* characteristic at different temperatures shows kink-free operation over a wide temperature range, and the laser is therefore suitable for WDM applications. Figure 8.8 demonstrates the excellent coupling (high output power) and the smooth light output curves [30].

As a wavelength selector for a laser, the fiber Bragg grating offers a unique solution. The broad-gain bandwidth of semiconductor lasers combined with the quality of single-mode fiber connectors resulted in a "wavelength-uncommitted" laser [26]. A schematic of this device is shown in Fig. 8.9. The basic device consists of an AR-coated laser chip with a short fiber pigtail terminated in a fiber connector. Fiber Bragg gratings at various wavelengths, also packaged in fiber-FC-PC connectors, are then used to define the operating wavelength of the laser. A set of gratings allows a large

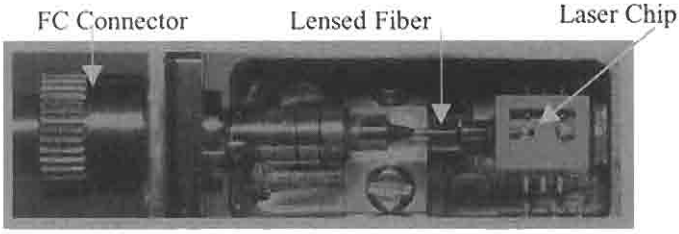

Figure 8.9: Wavelength-uncommitted laser [26].

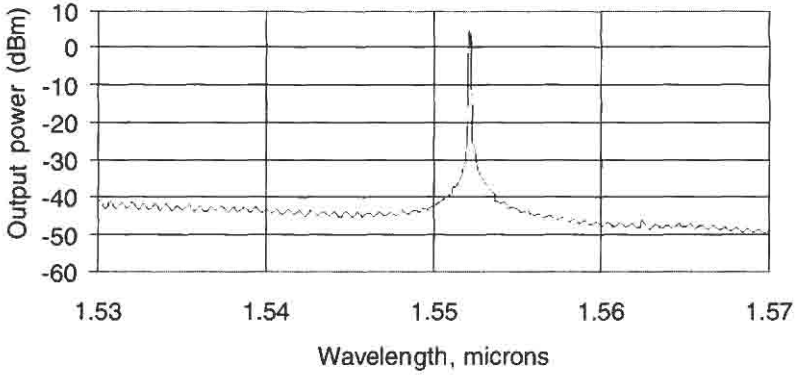

Figure 8.10: SMSR of ~50 dB for a fiber grating semiconductor laser with an output power of ~2 mW.

part of the gain band to be used. A semiconductor laser was shown to lase from 1480 to 1573 nm. The SMSR was measured to be ~50 dB for such a laser, at a power output of 1 mW in the fiber. Figure 8.10 shows the emission spectrum. This laser was shown to operate single-frequency at all wavelengths. However, the temperature has to be controlled carefully to prevent mode hopping and allow stable operation. A combination of the uncommitted laser concept and the large-spot laser should result in a cheap solution for wavelength selection.

Apart from applications that require the use of a modulation technique external to the laser, direct modulation of FGLs is desirable for low-cost devices. A large number of factors, such as electrical capacitance and inductance, cavity roundtrip, bandwidth of the external grating, and the interplay between the sub- and supercavity reflections, influence the dynamic behavior of FGLs. It has been shown that an external cavity laser with strong feedback can operate with high stability [3].

Provided the laser is operated within mode hops, the modulated performance has been shown to be excellent at transmission rates in excess of 2.5 Gb/sec [27–30]. Further, application of a FGL for millimetric-wave generation has been investigated [31]. In the latter demonstration, the modulation frequency injection locks two otherwise unstable lasing modes within the grating reflection spectrum to produce a high spectral purity RF beat signal at ~35 GHz.

With a short external cavity multi-quantum-well (MQW) FGL, modulation at >10 Gb/sec is possible for optical fiber transmission [32]. This design relies on the high-differential gain and low intrinsic chirp of a strained MQW, AR-coated front facet FP laser and the high-speed chip design using semi-insulating blocking layers. The linewidth of this laser was measured to be 40 kHz (~13 GHz roundtrip resonance; 8-mm external cavity), with −3 dB modulation bandwidth of ~15 GHz. The frequency response of the laser for different bias currents is shown in Fig. 8.11. The external cavity resonance is clearly visible as the current is increased to 100 mA. Measurements have shown that the chirp of this laser remains <10 MHz/mA compared with ~250 MHz/mA for a standard DFB laser. With a 2-mm-long external-cavity FGL, the frequency response is extended beyond 20 GHz [32].

8.2.1 Modeling of external cavity lasers

Figure 8.12 shows a schematic of a semiconductor laser coupled to an external cavity. Also shown are the parameters that need to be taken into account

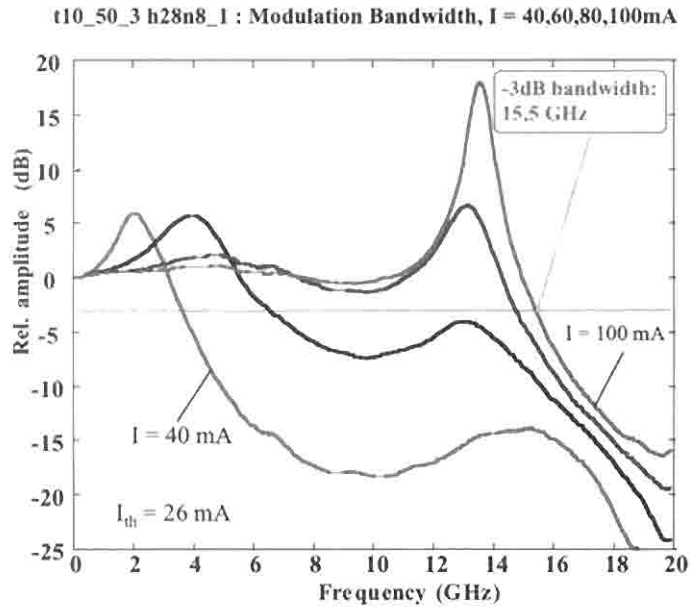

Figure 8.11: The frequency response of a FGL comprising a high-speed strained MQW and 8-mm-long external cavity (from: Paoletti P., Meliga M., Oliveti G., Puleo M., Rossi G., and Senepa L., "10 Gbit/s ultra low chirp 1.55 μm directly modulated hygrid fiber grating semiconductor laser source," in *Tech. Digest of ECOC'97*, pp. 107–110, 1997. © IEE 1997, Ref. [32]).

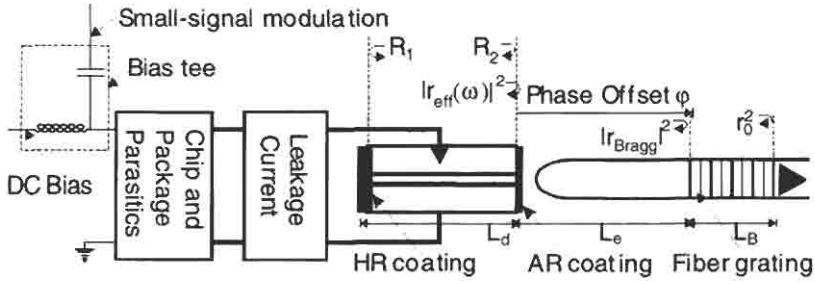

Figure 8.12: Schematic diagram modeling of the FGL. (AR: antireflective coating; HR: high reflective coating) (from: Premaratne M., Lowery A. J., Ahmed Z., and Novak D., "Modelling noise and modulation performance of fiber Bragg grating external cavity lasers," *IEEE J. Selected Topics in Quantum Electron.* **3**(2), 290–303, 1997. © IEEE 1997, Ref. [33]).

for modeling the laser: the reflectivities of the front and rear facets, the reflectivity and length of the grating, and the phase offset between the laser and the grating (passive fiber cavity), as well as the electrical contribution due to leakage, parasitics in the packaging, bias, and modulation signals.

Premaratne *et al.* [33] have presented a comprehensive rate-equation model for strong feedback taking account the many internal reflection of the composite cavity, based on the work of Park *et al.* [34], as well as the delayed fields from the reflections. Multiple reflections are accounted for by assuming that the field components are stationary [35]. Their analysis is therefore restricted to periodic and nonperiodic steady-state solutions. Transient response of FGLs has been investigated by Berger [36], while mode locking of the FGL to produce soliton like pulses has been modeled by Morton *et al.* [37,38].

The rate equations used to model the FGL are of the form [39,40]

$$\frac{d\boldsymbol{E}(t)}{dt} = \left(i\omega + \frac{1}{2}(G(N) - \alpha_{scatt}) + \frac{\ln(\rho)}{\tau_L}\right)\boldsymbol{E}(t), \tag{8.2.1}$$

where $G(N)$ is the spatially averaged gain at the average carrier density, N, resonant cavity, ω is the operating angular frequency with external feedback, α_{scatt} is the scattering loss, ω_r is the reference angular frequency of the field envelope, $\overline{E}(t)$,

$$\overline{E}(t) = \sqrt{I(t)}e^{i[\omega_r t + \varphi(t)]}, \tag{8.2.2}$$

$I(t)$ is the instantaneous intensity at time, t, and $\varphi(t)$ the instantaneous phase.

In Fig. 8.13 is shown the modeled steady-state *L–I* characteristics of a typical FGL with strong feedback and relatively large front-facet reflectivity of 0.04, and grating length of 8 mm. The choice of the initial phase condition at the interface determines the occurrence of the mode hop at around 30 mA, at either side of which the laser operates in a single longitudinal mode. The instability in this region is a result of the multimode nature of the long external cavity, predominantly due to the residual front-facet reflection.

Mode hopping can be eliminated by careful choice of operating temperature, as shown in Fig. 8.6, or by the reduction of the front-facet reflectivity. Interference effects due to delayed fields of the external cavity have been shown to be critical for predicting the stable performance of the FGL [33]. This effect of resonance-peak spectral splitting (RPSS) is shown in Fig. 8.14.

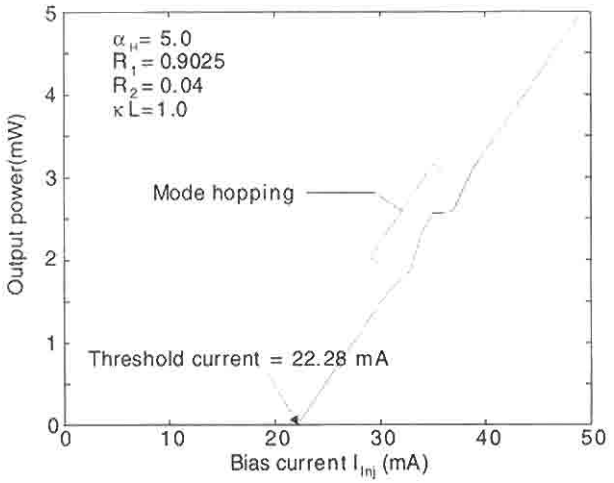

Figure 8.13: The *L–I* characteristics for an FGL laser with 4 GHz external cavity with a relatively large front-facet reflectivity (from: Premaratne M., Lowery A. J., Ahmed Z., and Novak D., "Modelling noise and modulation performance of fiber Bragg grating external cavity lasers," *IEEE J. Selected Topics in Quantum Electron.* **3**(2), 290–303, 1997. © IEEE 1997, Ref. [33]).

As the modulation frequency (close to the roundtrip frequency) is varied as a function of bias current, the output of the laser undergoes a series of peaks and dips. At a bias current of 37 mA, a steady single resonance peak is established, leading to stable operation. This situation is similar to the instabilities in the lasing characteristics of FGLs observed by Timofeev *et al.* [11] under modulation. Modeling shows the importance of the intracavity interference [33] in the vicinity of the mode-hopping regime. The alpha parameter strongly influences the RPSS, with low values of α and front-facet reflectivity favoring stable operation. The relative intensity noise (RIN) spectra also show the appearance of RPSS as α is increased [33].

8.2.2 General comments on FGLs

It appears that reduced-length laser diode chips and short external cavities favor single-mode, mode-hop-free operation [11]. Further, low facet-reflectivity, high-speed MQW designs, and strong feedback from the fiber grating promote good-quality modulation characteristics [3,24,32]. Vari-

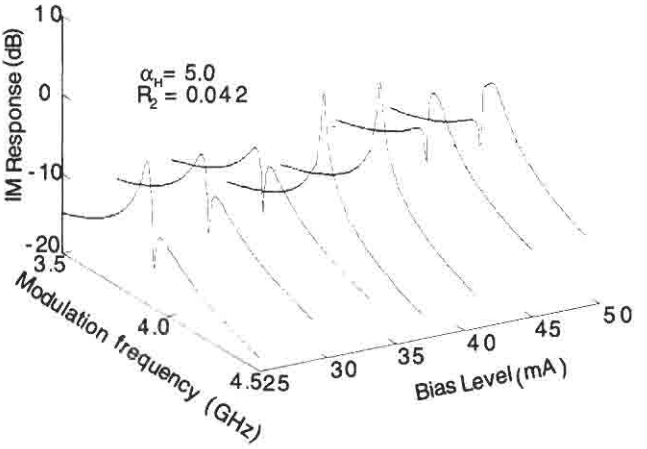

Figure 8.14: Change of RPSS vs bias current. Note the splitting position variation with bias current (4-GHz external cavity). The splitting may be reduced by a reduction in the front facet reflectivity (from: Premaratne M., Lowery A. J., Ahmed Z., and Novak D., "Modelling noise and modulation performance of fiber Bragg grating external cavity lasers," *IEEE J. Selected Topics in Quantum Electron.* **3**(2), 290–303, 1997. © IEEE 1997, Ref. [33]).

ous designs for the FGL show the alternatives available in reducing front-facet reflectivity by the use of a reflective amplifier [24], increasing coupling by the use of hyperbolic lenses formed on the ends of the fiber [19], chirped gratings to promote smooth *L–I* characteristics and allow stable mode-locking as well as the generation of soliton pulses [17,18], high-speed MQW designs for wide-bandwidth operation [32], plug-in gratings to allow selection of lasing wavelengths [26], and the use of coherence collapse for the injection locking of pump lasers [21]. The benefits of FGLs remain in the ability to define the lasing wavelength [26] and the low chirp [15,28,32] in improving the utilization of laser chips from manufactured wafers.

8.3 The fiber Bragg grating rare-earth-doped fiber laser

The concept of fiber lasers dates back to 1960. Snitzer [41] demonstrated a rod waveguide of smallish dimensions (0.5-mm diameter) doped with

ions of neodymium and dielectric end mirrors, which produced pulsed radiation when pumped with a flash lamp. Although it may be argued that the device was not a true *fiber* laser, the difference is merely in the detail, since it was a waveguide. With the advent of low-loss single-mode fibers [42] and the subsequent rare-earth-doped single-mode fibers [43], the early lasers still depended on external mirrors to choose the appropriate emission line. Although fibers enabled efficient end-pumping of these lasers, there were cases, as with Nd-doped fiber, in which the suppression of lasing of an adjacent competing line became difficult owing to the discrimination required of the resonator mirrors [44]. The problems were further compounded by the use of bulk reflectors or by the deposition of mirrors directly on the end faces of fibers [45]. In- and out-coupling had to be achieved through some form of mechanical alignment of mirrors, with high power densities at the mirror/fiber interface that usually needed a layer of index-matching oil for good optical contact. The first demonstration of the use of a narrowband in-line fiber reflector for a fiber laser used a 70% reflectivity grating etched into the core of a side-polished fiber [46]. While this scheme had the advantage of producing a narrow-bandwidth reflector (~0.8 nm FWHM), it had the disadvantage of being a device that needed considerable mechanical processing. The principle of tunability had already been demonstrated using a bulk diffraction grating as a frequency-selective reflector [47].

Thus, the photosensitive fiber Bragg grating, which was narrowband, low loss, and of adjustable bandwidth, was wholly suited to application in fiber lasers. The availability of compact high-power pump lasers at 1480 and 980 nm has made the fiber laser simple to fabricate. The high gain available in rare-earth-doped fibers allowed a nominal 0.5% reflection grating and a 100% bulk mirror with 30 m of erbium-doped fiber laser to produce 300 mW of power at 1537.5 nm when pumped with 600 mW of 980-nm pump [48] in the first photoinduced grating-based fiber laser. The ability to write Bragg gratings directly into rare-earth-doped fibers compatible with photosensitive fibers has resulted in a variety of successful demonstrations using either single or multiple gratings to form the resonator [49]. In the following section, generic examples of some of these lasers along with their properties will be examined.

Figure 8.15 shows a simple configuration of a single-cavity design of a fiber laser. The rare-earth-doped fiber has Bragg gratings as wavelength-selective mirrors. The laser is end-pumped via a WDM coupler normally through an optical isolator.

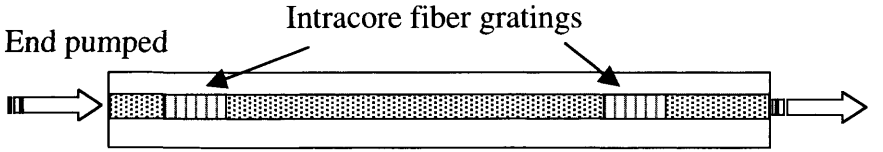

Figure 8.15: A schematic of the fiber Bragg grating rare-earth-doped fiber laser. The simple configuration encloses a piece of rare-earth-doped fiber between two Bragg matched gratings and is end-pumped.

The simple configuration allows a single-frequency laser [50,51] or twin laser configuration to be pumped in series with a single pump [52,53], or enables multiwavelength operation for sensor applications [54]. The transparency of the gratings to all other wavelengths allows closely spaced wavelengths to be emitted from one laser source, or the cascading of the laser with an amplifier section in a master oscillator power amplifier (MOPA) configuration [55]. A review of these lasers covers some of the general aspects [56]. Some of these lasers are considered in the following sections.

Spatial hole-burnt gratings may be used to stabilize semiconductor lasers. In the case, a piece of unpumped erbium fiber is used with a Bragg grating as the external cavity with an AR-coated semiconductor chip. The standing wave formed in the erbium doped fiber forms a population grating and line-narrows the laser. The 3-m-long cavity with a 1535-nm grating reflector was measured to have a linewidth of ~1 kHz [57].

High-power, double-clad Yb: doped fiber lasers with integral gratings in the cladding have achieved output powers in excess of 6.8 W in a single longitudinal mode [58]. At 1090 nm, 9-W fiber lasers are available that can be used as pumps for amplifiers and Raman oscillators (Section 8.7) [59].

8.4 Erbium-doped fiber lasers

The erbium ion in germanosilicate fiber has a three-level laser transition ($^4I_{13/2} \rightarrow {}^4I_{15/2}$), which may be modeled using the simplified three-level energy diagram of Digonnet [60]. A simple model for single-mode operation of an erbium fiber laser incorporating fiber gratings shows that the transient energy density per lasing mode is [61]

$$\frac{dE_n(z)}{dt} = \alpha I_n(z) - \gamma I_n(z), \tag{8.4.1}$$

where α and γ are the gain and loss for the lasing mode n. With negligible propagation losses, the loss is given as

$$\gamma = -\ln[R_o(\lambda)R_{HR}(\lambda)], \tag{8.4.2}$$

where $R_O(\lambda)$ and $R_{HR}(\lambda)$ are the reflectivity of the output coupling and high reflector gratings, respectively, at wavelength, λ.

The gain in terms of the steady-state ion population densities may be defined as

$$\alpha = (\sigma_e N_2 - \sigma_a N_1), \tag{8.4.3}$$

where the emission and absorption cross-sections are σ_e and σ_a, respectively.

The gain for two-moded lasers may be simplified in terms of the saturation intensity in the strong pump regime to

$$\alpha \approx \alpha_0 \left[1 - \frac{I_1(z)}{I_{sat}} - \frac{I_2(z)}{I_{sat}}\right], \tag{8.4.4}$$

where the saturation intensity is a function of the emission and absorption cross-sections, and α_0 is the small-signal unsaturated gain. The lasing photon intensities I_1 and I_2 are periodic within the cavity as a result of the formation of standing waves.

Using Eq. (8.4.4) in Eq. (8.4.1), the intensity of each steady-state mode is

$$I_{1,2} = \frac{I_{sat}}{3}\left(1 - \frac{\gamma_{1,2}}{\alpha_0}\right) - \frac{2}{3} I_{1,2}. \tag{8.4.5}$$

The slope efficiency at single-mode operation is then

$$\eta = \frac{\lambda_p}{3\lambda_1}\left[\frac{\sigma_p}{\sigma_a + \sigma_e}\right]\left[1 - \frac{\gamma_1}{\alpha_0}\right]\frac{A_1}{A_p}, \tag{8.4.6}$$

where σ_p is the ground-state absorption cross-section, A_1 is the lasing mode area, and A_p is the pump mode area. Substituting Eq. (8.4.5) into Eq. (8.4.1) and solving for the loss for the second mode results in the condition for stable single-mode operation,

$$\gamma_2 > \frac{\alpha_0}{3} + \frac{2\gamma_1}{3}. \tag{8.4.7}$$

Equation (8.4.7) states that the loss of the second mode must be greater than a third of the single pass gain plus the cavity roundtrip loss for the first mode. The reflectivity of the grating may be computed by the methods presented in Chapter 4 and used to determine the reflectivity for a given length of doped fiber with an unsaturated gain of α_0 per meter.

With the gratings written in highly doped erbium-doped fiber, the additional gain within the gratings must also be taken into account, since the effective reflectivity is increased [62]. The best region for single-mode operation is when the free-spectral range is twice the expected shift in the lasing frequency induced by perturbations and cavity length changes. This is greatly assisted by making the cavity as short as possible.

8.4.1 Single-frequency erbium-doped fiber lasers

Erbium-doped-fiber grating lasers (EDFGLs) offer a simple and elegant solution for wavelength selection, providing a very narrow linewidth as well as a high degree of wavelength stability. They are also compatible with optical fiber systems and can be easily integrated with other fiber components, such as WDM couplers and fiber isolators.

Tests performed on an externally modulated single-frequency EDFGL have confirmed its robust suitability for error-free high-speed application in transmission systems [50]. The laser is fabricated with 600 ppm GeO_2:Al_2O_3 doped silica fiber with a refractive index difference of 0.023 (core diameter of 2.6 μm) and cutoff at 880 nm. The tight confinement ensures high efficiency, and aluminum reduces the concentration-quenching effects that reduce the lifetime of the upper laser level, also leading to instabilities [63]. The gain of this fiber was reported to be ~10 dB/m, with an overall length of the laser of 4.4 cm, including gratings (98% O/P coupler and ~100% broadband high reflector), using the linear cavity design shown in Fig. 8.15. Pumped at 1480 nm, the laser is operated close to threshold to ensure single-mode operation and amplified in a MOPA configuration through an optical isolator. The packaged laser is sensitive to vibration that drives relaxation oscillation at a frequency of ~150 kHz. These oscillations can be actively controlled by using a feedback scheme to control the diode-pump laser and reduced to insignificant levels [50,64,65]. The error-free performance of several EDFGLs in transmission experiments at 2.5 and 5 Gb/sec been have reported [66,50,67], using external

Mach–Zehnder modulators. Upto 60 mW of single-frequency power has been achieved using a MOPA configuration [68].

Other configurations for single-frequency operation use long gratings with a bandwidth less than the cavity mode-spacing [69,70], and operation at 1 micron using Nd:doped fiber has been shown with intracore gratings [71].

Composite cavity lasers

There are several methods for achieving single- and multifrequency operation of EDFGLs. As outlined already, short lasers with narrowband reflectors are simple candidates; however, a composite cavity topology can enforce stable single-frequency operation by longitudinal mode control, adapted from semiconductor lasers [72–75]. The principle relies on a small additional feedback element in the form of a short Fabry–Perot, which modulates the gain spectrum of the main fiber laser cavity. Figure 8.16 shows the linear cavity configuration. The basic laser cavity gratings have reflectivities of 0.9 and 0.8 with a weaker reflection of 0.1 as the external reflector. The gain of the composite cavity is modulated, increasing the discrimination between the modes. Since the lasing mode is influenced by the composite cavity, a single mode tunes with temperature changes but does not exhibit mode hops [53]. The 10-mm-long high erbium dopant concentration fiber (120 dB/m absorption at 1530 nm) is spliced to fiber gratings, forming a composite cavity ~7 cm long; 980-nm pumping with a Ti:sapphire laser showed a threshold of 50 mW. The linewidth of this laser is ~40 kHz using conventional heterodyne techniques. The gain

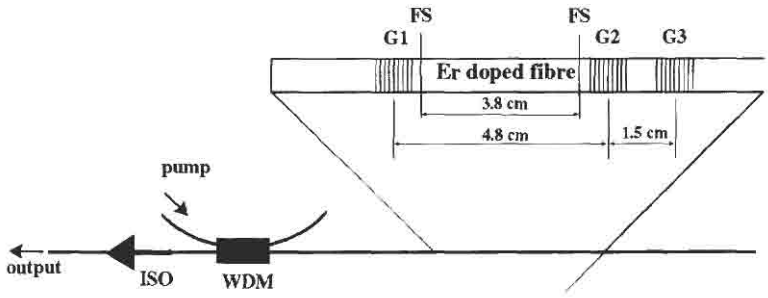

Figure 8.16: A schematic of the composite cavity single-frequency EDFGL [53].

bandwidth of such a laser with and without the extra etalon is shown in Fig. 8.17. With the external etalon, the gain is modulated at a frequency separation determined by the spatial separation and reflectivities of the gratings. The simulation in Fig. 8.17 shows the composite reflection spectrum of the two gratings without the additional feedback (dashed curve) and with feedback (solid curve). In this laser, the period of the frequency separation is 28 GHz without feedback and ~7 GHz with the etalon approximately half the mode spacing of the composite laser. The use of a very short gain region with respect to the cavity length (a factor of 3–4) eliminates the relaxation oscillation observed in other cavity designs [50] using erbium fiber.

Composite fiber gratings with ring or loop mirror cavities [76] are other possible configurations, and for single frequency operation with intra-cavity frequency selector [77]. An example of this cavity is shown in Fig. 8.18 in a loop mirror arrangement. In this cavity, the loop mirror is a broadband mirror, while the external fiber Bragg grating is a band-selecting element. The isolators inside the loop-mirror ensure unidirectional operation, while the incorporation of an ultranarrow band-pass

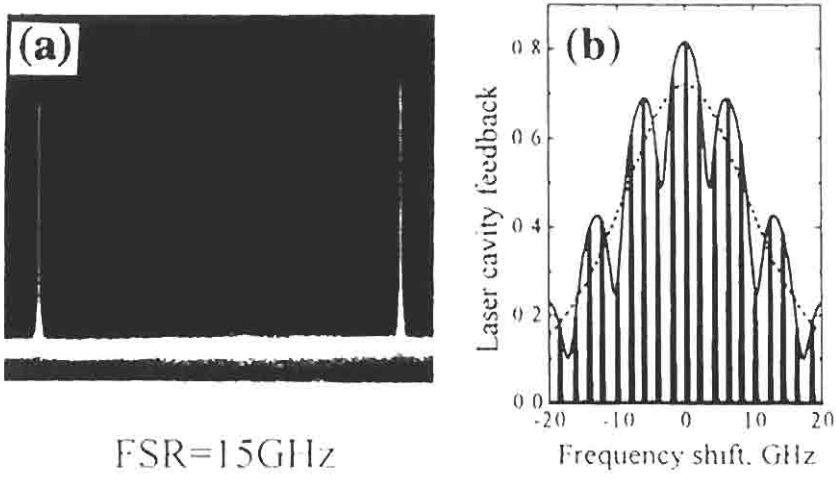

Figure 8.17: The reflectivity and mode selection spectra of the coupled-cavity EDFGL. Laser with feedback (solid line), and laser without feedback (dashed line) (from: Chernikov S. V., Taylor J. R., and Kashyap R., "Coupled-cavity erbium fiber lasers incorporating fiber grating reflectors", *Opt Lett* **18**(23), 2023 (1993). (after Ref. [53])).

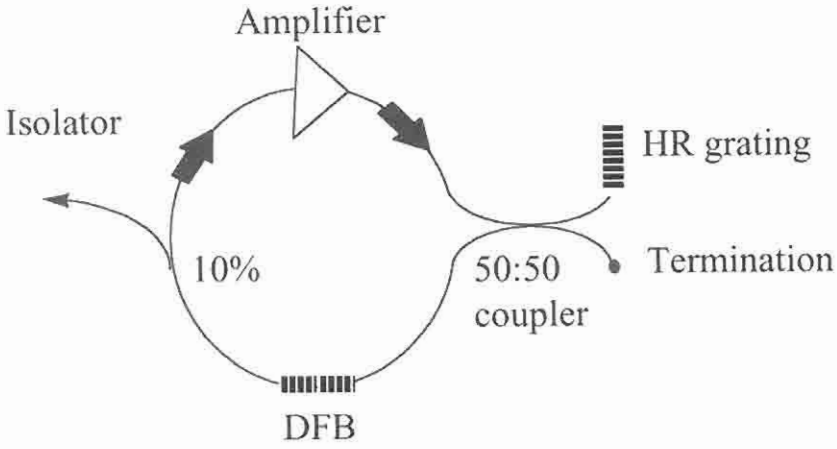

Figure 8.18: The loop mirror cavity for single-mode operation, incorporating a DFB band-pass filter and an erbium-doped fiber amplifier (after Ref. [77]).

DFB fiber Bragg grating (see Chapter 6), also inside the loop, enforces single-frequency operation. The laser may be tuned by applying compressive or extensive strain on the intracavity DFB grating or, in the absence of the DFB grating, the external grating. Single-frequency operation of such a laser with a 0.075-nm band-pass DFB grating shows a linewidth of ~2 kHz, with side-mode suppression of 50 dB. However, the long cavity with a mode spacing of 11.4 MHz mode hops and requires the use of stabilizing elements [77].

Replacing the DFB band-pass intra-cavity filter by an acousto-optic tunable filter (AOTF) may extend the principle of this type of a laser. Ramping the AOTF sweeps the output frequency of the laser with <0.1-nm linewidth [78].

To improve the strength of the grating, a specially deposited photosensitive ring cladding can be fabricated with a rare-earth-doped core. This scheme allows the core to have a high dopant concentration, while preserving the fiber's photosensitivity and allowing short, high-strength grating to be inscribed for laser fabrication [79,80].

8.5 The distributed feedback fiber laser

The principle of the distributed-feedback (DFB) structure, generally applied to semiconductor lasers [81], is easily translated to doped fiber

lasers. Figure 8.19 shows a schematic of the laser, which is identical to a Fabry–Perot laser, except that the two gratings are separated by only a quarter-wavelength (see Chapter 6). The phase shift generates a gap in the reflection spectrum, allowing narrow single-frequency operation.

With the possibility of writing gratings directly into erbium-doped fibers (see Chapter 2), DFB lasers may be fabricated with ease, especially since long gratings (~100 mm) require modest refractive index modulations to produce a high reflectivity. The first reported DFB laser operated at 1 micron and was fabricated in ytterbium-doped fiber [82]. It has been successfully demonstrated in erbium-doped fibers for 1500-nm operation [83,84] and extended by cascading five DFB lasers separated in wavelengths by ~1 nm each, pumped by a single 1489-nm diode laser [85].

Simple modeling of a DFB laser may be achieved by including a gain (complex term) in κ_{dc} in [Eqs. (4.3.5) and (4.3.6)], so that $\Delta\beta$ is modified by $i\gamma$, where γ is the gain per meter. Numerical simulation of the transfer function in Chapter 4 [Eq. (4.8.22)] of the DFB is shown in Fig. 8.20 as a function of increasing gain. As the gain increases, the side modes of the DFB structure begin to lase.

There are two possibilities for inducing a phase shift in the grating: one which is localized, or by distributing the phase shift along the length, as discussed in Chapter 6. The model takes account of the variation in the gain as a result of pump depletion. It has been shown for a 5-cm-long DFB laser that positioning the discrete π phase-shift away from the center of the laser, at $\sim 0.6L_{DFB}$, increases the output power by as much as 60%. For a phase shift distributed over 1 cm of the same laser, the optimum value acquires a slightly larger value of 1.3π radians [86].

The position of the phase shift changes as a direct result of spatial hole burning, since the intensity is highest at the center of the laser for a symmetrically positioned phase shift. The distributed phase-shift laser is as efficient as the discrete off-center phase-shifted laser.

Figure 8.19: The EDFGL distributed feedback laser (EDFGL-DFB). The phase shift of $\pi/2$ forms a band pass in transmission.

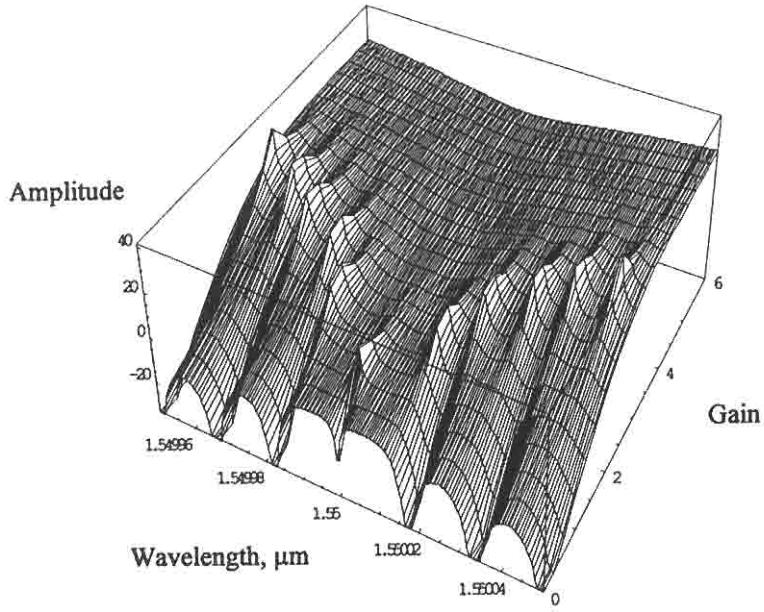

Figure 8.20: The transmission spectrum of a 100-mm-long DFB laser as a function of the gain.

8.5.1 Multifrequency sources

Dual-frequency and multifrequency sources can be built by combining techniques presented in the preceding sections. A novel and particularly simple arrangement is the four-grating coupled cavity arrangement based on the single-frequency laser shown in Fig. 8.16. By adding an extra grating matched to the external grating in Fig. 8.16, a dual-frequency laser is formed. In order to ensure the coupling between the cavities, the grating bandwidths are chosen to overlap slightly. This configuration produces a robust laser that performs as a *single* entity, and a schematic is shown in Fig. 8.21. The emission spectra consist of two single-frequency lasing modes at defined by the grating pairs, and tune without mode hops. However, the difference frequency tunes with temperature, strain, or pump power (thermally induced). The coupled cavity reported by Chernikov *et al.* [52] operated at a difference frequency of 59.1 GHz centered around 1545 nm, with a long-term average linewidth of ~16 kHz and a stability of the dual frequency of ~3 MHz.

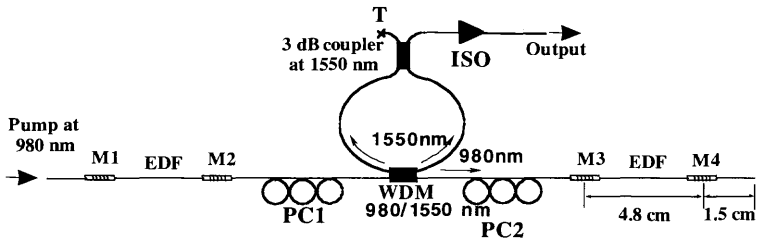

Figure 8.21: The coupled-cavity dual-frequency source (from: Chernikov S. V., Kashyap R., McKee P. E., and Taylor J. R., "Dual frequency all fiber grating laser source," *Electron. Lett.* **29**(12), 1089, 1993. © IEEE 1993, Ref. [52]).

Multifrequency operation in ring lasers has been reported with the use of a grating with a multiple wavelength reflection spectrum. Up to 8 wavelengths have been shown to lase simultaneously. While single-frequency operation (~10 kHz linewidth) has been demonstrated, in such long lasers, mode hopping is common, and special attention must be paid to stabilize the operation [87].

8.5.2 Tunable single-frequency sources

The gain bandwidth of doped fibers is several tens of nanometers. Tunability is possible with fiber Bragg gratings by strain or temperature tuning (see Chapter 3). Ball and Morey [88] stretch-tuned a pair of Bragg gratings of a 100-mm-long erbium fiber laser and showed 9 GHz mode-hop-free operation. Since the gratings and the fiber length tune together, the laser remains stable. Compression tuning can extend the tuning range, and a tuning range of 32 nm has been reported for a short EDFGL (3 cm) in a MOPA configuration. Continuous single-frequency tuning was observed with the laser producing 3 mW of output. A feedback loop is necessary to stabilize the operation of the laser to reduce relaxation oscillations [89]. Compression tuning of a Yb/Er laser using a mirror and Bragg grating configuration has shown sub milliwatt thresholds and both strain and compression tuning ranges of up to 25 nm [90].

8.6 Bragg grating based pulsed sources

We have seen that the FGL can be used as a pulsed source for optical fiber transmission, either directly modulated or mode-locked [15,17,

18,24,27,32]. We have also seen that the EDFGL is an excellent candidate as a source [50]. There are several alternative methods of generating short pulses in conjunction with gratings, for example, semiconductor laser pulse compression in a chirped grating [91,92], using the dual-frequency source and adiabatic soliton pulse compression [93] and linear actively mode-locked fiber laser [94].

Pulse compression of gain-switched DFB and FP lasers [95] is possible using a dispersive delay line, since the emitted pulse is chirped in time and frequency. If the dispersion of the delay line is opposite to that of the pulse, it may be compressed. Chirped gratings (see Chapter 7) are ideal candidates, since they are compact and the dispersion can be tailored for a particular application. The experimental setup is shown in Fig. 8.22. A pulse train at 500 MHz from a gain-switched DFB laser is reflected from a chirped grating and the recovered pulse is compressed. Figure 8.23 shows autocorrelation

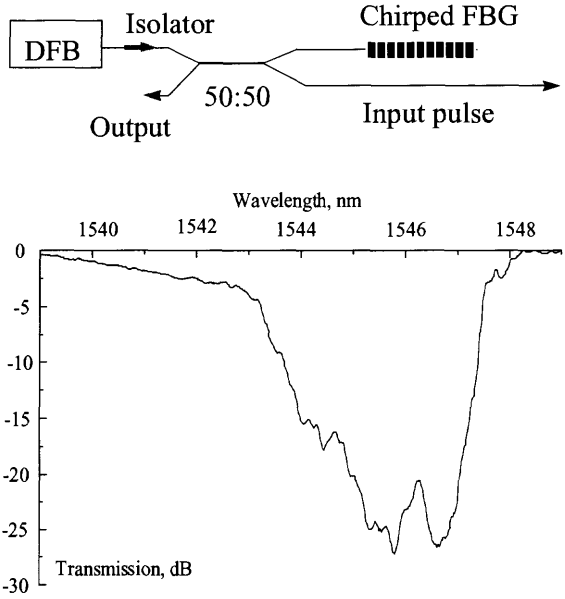

Figure 8.22: Experimental setup for pulse compression and transmission spectrum of the chirped fiber grating (from Gunning P., Kashyap R., Siddiqui A. S., and Smith K., "Picosecond pulse generation of <5ps from gain-switched DFB semiconductor laser diode using a linearly ste-chirped grating," *Electron. Lett.* **31**(13), 1066–1067, 1995. © IEEE 1995, Ref. [91]).

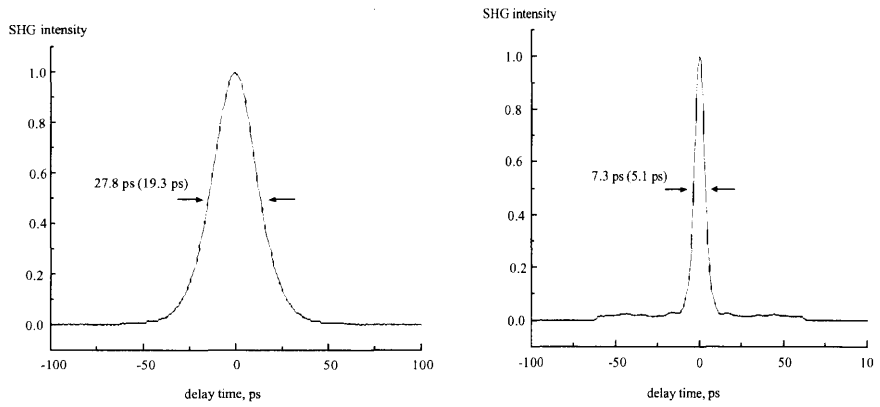

Figure 8.23: Input pulse from the gain-switched DFB (a) and reflected pulse form the chirped fiber Bragg grating (from Gunning P., Kashyap R., Siddiqui A. S., and Smith K., "Picosecond pulse generation of <5ps from gain-switched DFB semiconductor laser diode using a linearly ste-chirped grating," *Electron. Lett.* **31**(13), 1066–1067, 1995. © IEEE 1995, Ref. [91]).

traces of the input and reflected pulse from the grating. The gain-switched pulse has chirped a bandwidth of ~1.5 nm, and the 6-mm-long grating slightly filters the spectrum while recompressing the pulse. A small residual pedestal is due to the uncompensated part of the spectrum. The technique is simple and requires a minimum of control.

The second scheme for compressing a sine wave into pulses is based on a combination of adiabatic perturbation and average soliton regimes of propagation. During an adiabatic perturbation, there is a balance between the dispersive and nonlinear contribution by a change in the soliton duration [96]. In the average soliton regime, there is balance between the periodically varying dispersion and nonlinearity [97]. The use of this scheme allows the slow transformation of a modulated input signal into a soliton. An amplified optical sine wave is launched into a long length of fiber. It periodically undergoes self-phase modulation in a zero-dispersion section of a fiber, increasing the spectral content and linear dispersion in a high-dispersion part of the transmission line. By selecting the appropriate combination of dispersion and nonlinearity, the average dispersion of the link is reduced approximately exponentially. The reducing average dispersion continually compresses the optical sine wave into soliton pulses.

A similar scheme for generating solitons was reported using dispersion decreasing fiber [98], based on the earlier predictions [99]. The source used for pulse generation is the dual-frequency EDFGL source shown in Fig. 8.21 [100]. The narrow line-widths of this source produce an optical beat signal. To eliminate stimulated Brillioun scattering, different germania concentration fibers are used in the 20-section comblike dispersion profiled fiber (CDPF), with a total length of ~7.5 km. A beat signal at an amplified power of 190 mW and frequency of 59.1 GHz are converted into pedestal-free sech^2-shaped pulses with a FWHM of 2.2 psec, at a wavelength of 1545 nm [93]. Several other configurations based on the beat-frequency generation may be found in Ref. [101].

Mode-locking of fiber lasers has been investigated in a variety of "figure-eight" configurations [102] using fiber gratings to generate multi-wavelength pulses. Actively mode-locked dark-pulse generation from a praseodymium-doped fiber laser with a chirped grating has also been reported [103].

8.7 Fiber grating resonant Raman amplifiers

Raman scattering is a process in which a small fraction of the incident light is scattered by the vibrational modes within a material to generate a Stokes photon, downshifted in frequency. Stimulated Raman scattering (SRS) is a process by which the Stokes photon interacts with the pump photon to generate another Stokes photon and is described by the imaginary part of the nonlinear susceptibility, $\chi^{(3)}(-\omega_s;\omega_p,-\omega_p,\omega_s)$. The Stokes field grows exponentially with the length of the medium. Since its discovery [104], SRS has been a topic of considerable research [105]. SRS can be a very efficient process, strongly depleting the pump power. With the advent of optical fibers, the observation of SRS has become very easy because of the high power densities in the core, low optical loss, and long interaction lengths. The Raman gain, which depends on the scattering cross-section, has been measured in silica optical fibers [106]; the bandwidth, because of the amorphous nature of the glass, is extremely large, extending over some 40 THz with a peak at 13 THz from the pump wavelength. Below the threshold for SRS, a signal photon, downshifted from the pump frequency, experiences gain if it lies within the gain bandwidth. This is the principle of Raman amplification [107].

If a fiber is placed between mirrors and pumped, the Stokes field sees a roundtrip gain of

$$G = e^{2g_R I_0 L_{eff}}, \tag{8.7.1}$$

where g_R is the Raman gain coefficient, I_0 is the intensity of the pump, L_{eff} is the effective length of the fiber $\sim 1/\alpha_{pump}$ (the fiber loss at the pump wavelength), and the factor of 2 is for the double pass. The pump intensity at which the Stokes field overcomes the cavity losses for a given set of mirror reflectivities is called the threshold for oscillation. For 10 m of fiber, a CW threshold can be reduced to ~1 W [108,109]. As the pump power is increased, the Stokes field S_1 increases until the threshold for the second-order Stokes S_2 is reached, at which point energy is transferred to S_2. At this point, a signal at the third Stokes frequency will experience gain, and so on. This is also the principle of the resonant Raman amplifier. This type of a multi-Stokes oscillator has been demonstrated by Stolen *et al.* [110,111], who generated five Stokes orders of independently tunable radiation.

Perhaps one of the most elegant components that is the direct result of the high transparency of Bragg gratings outside the band stop is the Raman fiber grating laser, the RFGL. This laser has opened many opportunities in communications, by allowing amplification in *any* part of the communication spectrum by appropriate choice of pump lasers and fiber Bragg gratings.

The general cavity configuration for a resonant Raman laser [112] is shown in Fig. 8.24.

This laser has been shown to produce 1.5 W at 1485 nm when pumped by a diode-pumped Yb^{+3} double-clad laser. The Yb^{+3} pump at 1117 nm

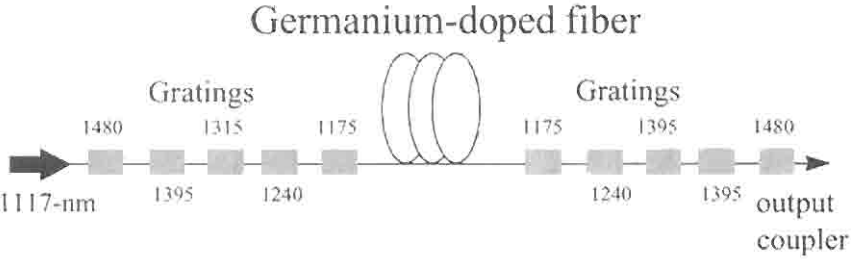

Figure 8.24: Cascaded fiber grating resonant Raman 1480-nm pump laser for pumping erbium amplifiers [113].

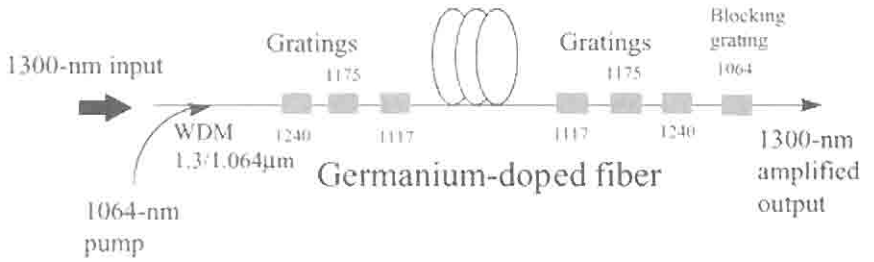

Figure 8.25: Schematic of a 1300-nm cascaded fiber grating resonant Raman amplifier [115].

produces in excess of 6 W CW. The five stages Stokes of conversion is remarkable, showing ultralow loss of <0.2 dB per grating.

For 1300-nm amplifiers, two configurations can be used. The linear cavity shown in Fig. 8.25 uses WDM couplers and a set of gratings to allow gain in the 1300 nm window when pumped by a 1.064 nm source. The gain is available at the fourth Stokes wavelength. These amplifiers have gains as high as 40 dB with saturated output powers of 24 dBm. With higher germania concentration (higher Raman gain) the pump power can be lowered to 300 mW while providing a gain of 25 dB [114].

The theoretical noise figure for Raman amplifiers is 3 dB [116], while the achieved figures are around 4.4 dB at 40 dB gain in a ring configuration [117,118].

The advantage of using bidirectional pumping as in a ring cavity is reduced cross-talk and polarization sensitivity.

These amplifiers are increasing in importance as the requirement for the optical bandwidth increases. In regions of the communications window in which amplification is difficult, e.g., 1350–1500 nm, *cascaded* fiber grating resonant amplifiers are likely to provide unique solutions.

8.8 Gain-flattening and clamping in fiber amplifiers

Rare-earth-doped optical fiber amplifiers are important components in transmission systems. The transmission bit-rate × distance product is almost limitless in laboratory-based demonstrations [119]. This is primarily due to the "zero-transmission loss" through periodic amplification as

well as the management of dispersion. The fiber amplifier has enabled undersea transmission over thousands of kilometers. With the increasing demand for bandwidth, wavelength division multiplexing (WDM) of optical channels is seen to be a viable solution for increasing transmission capacity at a given transmission rate, in point-to-point routes [120].

The important issues in amplified transmission systems for WDM applications are the available gain, the gain uniformity across the bandwidth of an amplifier, the robustness to transient switching of WDM channels in single and cascaded amplifier chains, and the overall noise figure. The gain spectrum and upper-state lifetimes of an erbium-doped fiber amplifier vary as a function of the core dopants. High-germanium erbium-doped fibers have a highly nonuniform gain with a bandwidth of ~35 nm from 1530 to 1565 nm, peaking at approximately 1535 nm. The use of aluminum reduces the nonuniformity, making the gain spectrum flatter, while ytterbium as a codopant with erbium allows an efficient transfer of energy from the available high-power diode pumps at 980 nm (a wavelength at which erbium suffers from excited-state absorption, reducing efficiency) to the required transition in the 1550-nm wavelength region for amplification. The latter shifts the gain peak to >1540 nm, while narrowing the gain bandwidth. Along with the nonuniformity in the gain, the doped fiber amplifier is homogeneously broadened. While allowing amplification across the wide gain bandwidth, the gain available at any wavelength is dependent on the simultaneous presence or absence of other wavelength channels; thus, gain may be depleted from a saturating signal from an existing channel as another channel is switched on. As the gain in a single amplifier fluctuates, the problem is exacerbated with a chain of cascaded amplifiers, leading to severe cross-talk. Nonuniform gain across the bandwidth of the amplifier produces a wavelength-dependent low-frequency cross-talk penalty. Apart from the signal degradation, severe damage to components is a possibility because spiking with intermittent interruption and resumption of transmission. The inversion and thus the gain is also pump-power dependent, leading to gain changes as the pump source ages. For analog transmission systems the problem is worse, because the local gain slope leads to harmonic distortion, degrading the received signal. Schemes have been developed to stabilize the gain of fiber amplifiers as well as flatten the gain variation over a wide bandwidth. Fiber gratings offer simple solutions to solve both these problems. In the following sections, we look at a specific example of gain

flattening and gain stabilization and a combination of the two, using fiber gratings.

8.8.1 Amplifier gain equalization with fiber gratings

In Chapter 4 the properties of side-tap gratings (STG) and long-period gratings (LPG) were described. Both types of gratings may be used as narrowband, wavelength-specific, loss-inducing components. In particular, the STG, which is a tilted Bragg grating, couples a narrowband at the short-wavelength side of the Bragg reflection wavelength to a continuum of the radiation field in the case of the unbounded cladding. This requires matching the cladding with an appropriate oil/polymer to destroy the well-defined boundary. For an appropriate blaze angle, which also minimizes Bragg reflection into the guided mode, the radiated light has an angular and spectral bandwidth. At this blaze angle, the period of the grating determines the wavelength of peak loss. Adjustment of the grating period at the same tilt angle enables the loss to be placed at any position within the gain spectrum of the amplifier. It should be noted that coupling to the radiation field for the first-order grating interaction is restricted to a *local* loss spectrum, close to the Bragg reflection wavelength, and hence a combination of several such spectra allows the fabrication of complex spectral loss features. By appropriate choice of filters, the filter loss may be matched to the inverse of the gain variation in the erbium amplifier to flatten the gain spectrum. Both single [121] and multiple [122] STGs have been used to tailor the gain spectrum of erbium amplifiers. In the first instance, a single, 4-dB peak-loss, 10-nm bandwidth (full-width) grating was placed at the 1533-nm peak of the erbium amplifier, eliminating the gain variation. By appropriate choice of the grating period (with the use of a phase mask) the peak loss is moved anywhere within the gain bandwidth. The inversion and therefore the gain shape is dependent on the pump power. The filter is thus appropriate for a given inversion (gain).

Figure 8.26 shows eight such loss spectra with approximately identical shapes, but with different peak-loss wavelengths and insertion loss. Each filter is ~8 mm long with an external blaze angle of ~8°, chosen to minimize back reflection, written in a boron–germanium codoped fiber with a core diameter of ~12 microns (see Chapter 3).

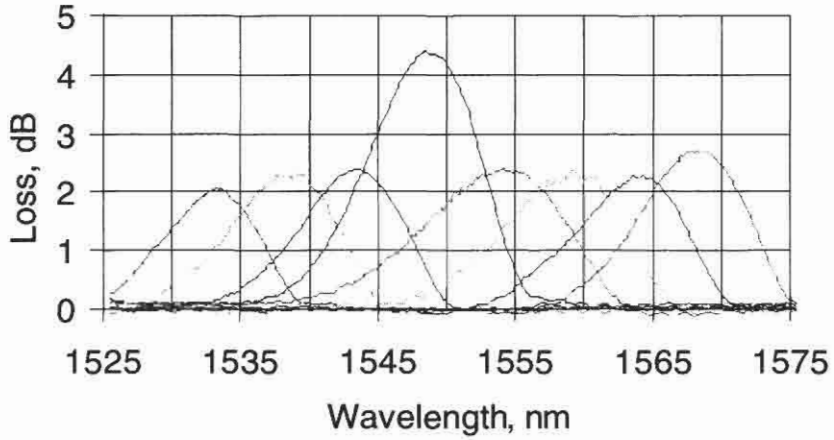

Figure 8.26: Radiation loss spectrum of eight STG filters written at an external blaze angle of 8° in a fiber with a core diameter of ~12 microns [122].

The use of multiple STG filters allows tailoring complex gain spectra with a greater degree of accuracy. The peak deviation over 3 dB from a fixed gain of 13.7 dB across the bandwidth of the amplifier is conveniently reduced to ±0.3 dB by the use of in-line STGs [122] and is shown in Fig. 8.27. The required loss spectrum is deconvolved into a number of contributions from individual gratings, prior to fabrication of the filter.

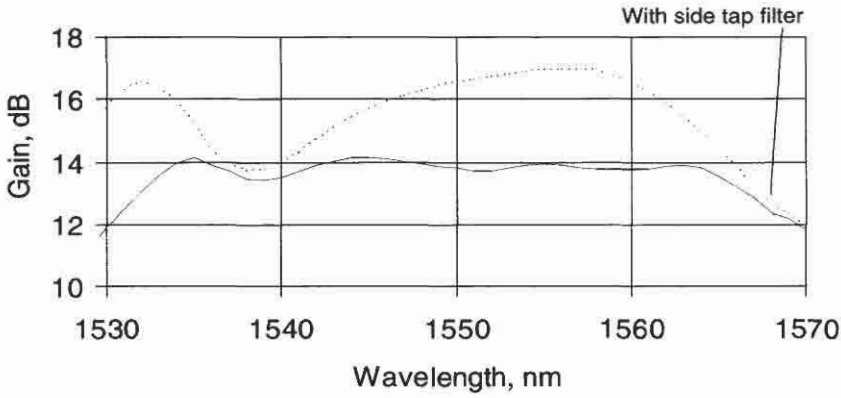

Figure 8.27: The ASE spectrum of a saturated erbium amplifier without and with a composite STG gain equalizing filter [122].

With this information, the filter is fabricated with the amplifier at its operating inversion level, allowing live gain tailoring. In this instance up to nine individual STGs were written to match the variation in the gain. Each grating can be ~1 mm long, making the entire gain equalization filter to be less than 10 mm. Such a filter may be written using a single phase mask appropriately designed to give the desired loss at each wavelength, by scaling the length of each grating or with an appropriate amplitude shading [123]. A distinct advantage of the STG is that the uncompensated temperature sensitivity of the loss spectrum is similar to that for Bragg grating, making the filter intrinsically stable. With temperature compensation as with Bragg gratings, the variation in the loss spectrum may be eliminated altogether over the required operating temperature range.

The tilt angle for the STG is chosen to minimize back-reflection into the guided mode (see Chapter 4). The transmission and reflection spectra of two STGs with peak-loss wavelengths separated by ~10 nm are shown in Fig. 8.28. The combined transmission loss of the two gratings it ~12 dB. The first grating is written at a blaze angle close to that required for a minimum reflection, while the second is written at a larger angle to increase the bandwidth of the composite filter. Each grating has a loss of approximately 6 dB. The first STG, which peaks at the shorter wavelength, has a reflectivity of −35 dB, while the unoptimized longer wavelength loss STG shows an increased reflection of ~21 dB. Typically, the gain variation in the amplifier spectrum requires each STG to have a

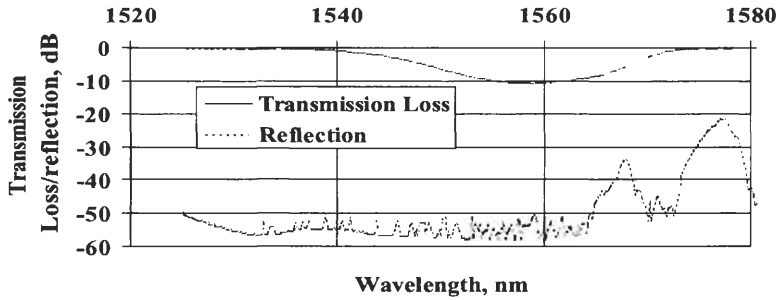

Figure 8.28: The transmission and reflection spectra of two STGs written in the same fiber. The 6-dB peak-loss STG 1 at the shorter wavelength has a reflection of −35 dB. The second unoptimized STG at a larger tilt angle has a higher reflection of −21 dB.

peak loss of less than 3 dB, resulting in a maximum back-reflection of <-40 dB.

Thus, a concatenation of STGs may be used effectively to flatten the gain of an optical amplifier, with low back-reflection. The design of the fiber to alter the bandwidth of the filters has been discussed in Chapter 4. This approach allows finer structures in the gain spectra to be matched more closely [124].

The application of LPGs for tailoring the gain of optical amplifiers has also attracted interest. The main feature of the LPG is the coupling of the guided mode to a forward-propagating *cladding* mode, one of which is selected from a large number, to induce the desired loss at the appropriate wavelength within the gain spectrum. It should be remembered that several mode interactions, widely separated in wavelength, occur in tandem for a given grating period. As such, LPGs have been used to equalize the gain of erbium amplifiers [125,126] and as ASE-suppressing filters. The technique used for forming the gain-equalizing filter is identical to that for the STG and has been already described [122]. There are major differences between the STG and the LPG. The latter exhibits more than a single loss peak separated by ~30–60 nm, depending on the type of fiber used for the filter. Written in standard telecommunications fiber, the temperature sensitivity of the LPG is roughly 4–5 times that of the STG. However, it has a low back-reflection into the guided mode of ~ -80 dB.

Unless the LPG is fabricated in special temperature-stabilized fiber, the amplifier gain equalization remains temperature sensitive, leading to gain tilt. Finally, the wavelength of the peak loss is a function of the refractive index of the material surrounding the cladding. With an appropriate low-index polymer coating, the cladding mode resonance is made insensitive to the surrounding material. The LPG has been used extensively in gain equalization of amplifiers and remains an important component.

Another method of equalizing the gain of an erbium amplifier is by the use of two or more apodized reflection gratings in series with an optical isolator. The resultant spectrum is shown in Fig. 8.29. Gain equalization to approximately ± 0.5 dB may be achieved with this simple arrangement.

Since gain flatness of the optical amplifier with filters is dependent on the level of inversion, it becomes particularly attractive to combine the filter with all-optical gain control, which is considered in the next section.

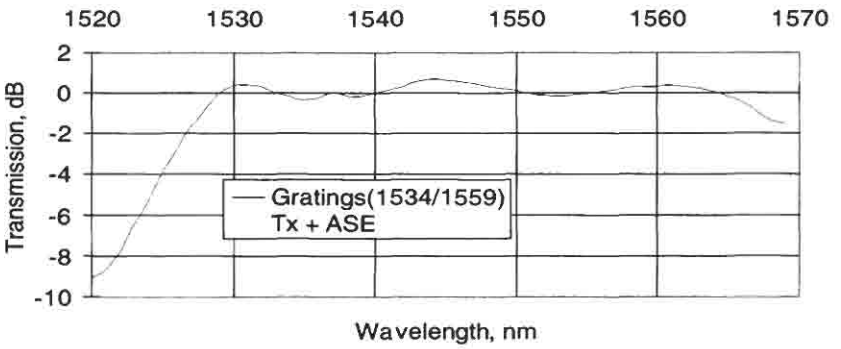

Figure 8.29: The simulated gain spectrum of an erbium amplifier equalized by two reflection gratings of lengths 0.2 and 0.061 mm centered at 1534 and 1559 nm. (The refractive index modulations for the two gratings are 3.5×10^{-3} and 1.06×10^{-3}).

8.8.2 Optical gain control by gain clamping

There are a variety of ways of stabilizing the gain of erbium-doped fiber amplifiers. In particular, sampling the state of the amplifier and deriving some sort of feedback, for example, signal levels [127], ASE [128], or a dedicated probe [129], to adjust the amplifier's pump power, or sacrificial injected signals have also been proposed [130,131]. These in turn limit in the frequency response by introducing electrical delays in the feedback loop. A simpler and more elegant all-optical approach to gain stabilization of an erbium doped fiber amplifier was first reported by Zirngibl [132], using lasing action in a ring cavity configuration. In a homogeneously broadened system, the inversion and therefore the gain remains constant irrespective of input signal level or the number of input channels. The amplifier remains robust against transients and to the switching of channels, so long as the amplifier continues to lase at some wavelength within the amplification window. The gain is maintained at the expense of the flux in the lasing mode. This "gain-clamped" amplifier is especially useful for cascading and in dynamically changing optical networks. The amplifier design is greatly simplified by the use of a linear cavity made with narrowband, highly reflecting Bragg gratings [133]. Delevaque *et al.* demonstrated a gain-clamped erbium amplifier lasing at 1480 nm with the aid of narrowband grating reflectors, pumped at 980 nm.

The properties of all-optical gain-controlled amplifiers, pumped at 1480 nm, and lasing at longer wavelengths, have been studied by Massicott *et al.* [134]. The cavity configuration used for gain control, pumped at 1480 nm, is shown in Figure 8.30.

The amplifier cavity contains a length of erbium-doped fiber with two narrowband Bragg-matched fiber grating reflectors. Along with these gratings, a STG filter with a specified intracavity, loss is included close to the output end to control the intracavity loss and reduce the effect of stray reflections. Above a certain threshold pump power at which the cavity gain equals the intracavity loss, lasing occurs at a wavelength λ_1, clamping the gain across the gain bandwidth due to the homogeneous nature of the transition. With an increase in the pump power, energy is stored in the lasing flux, while maintaining the inversion, and therefore the gain. Signal wavelengths experience a fixed gain up to a certain critical input level, at the expense of the lasing flux. Once the input signal is large enough to extract all the energy from the lasing mode, the amplifier ceases to lase. Thereafter, the amplifier inversion (and gain) is uncontrolled and is dependent on the pump power and signal levels as for a normal erbium-doped fiber amplifier.

Figure 8.31 demonstrates the automatic optical gain controlled amplifier in operation. The amplifier consists of a 25-m length of erbium-doped fiber with a core diameter of 5.3 μm and refractive index difference of 0.013. The peak saturable absorption of the fiber is 6.1 dB/m with a background loss of 8 dB/km measured at a wavelength of 1.1 μm. The laser cavity is defined by two Bragg grating reflectors at 1520 nm, written in hydrogen-loaded GeO_2-SiO_2 fiber. The reflectivity of each grating is 94% with a 3-dB bandwidth of less than 0.4 nm. The splices dominate

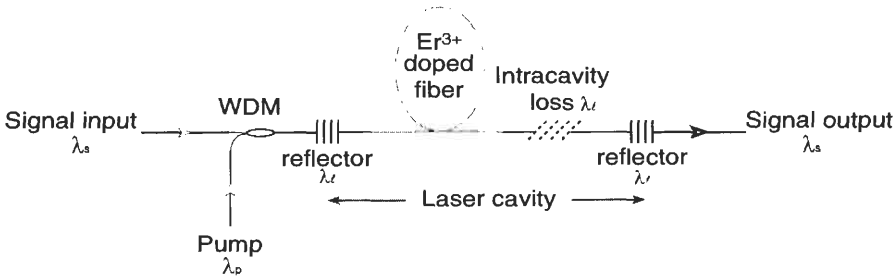

Figure 8.30: Amplifier with linear optical AGC.

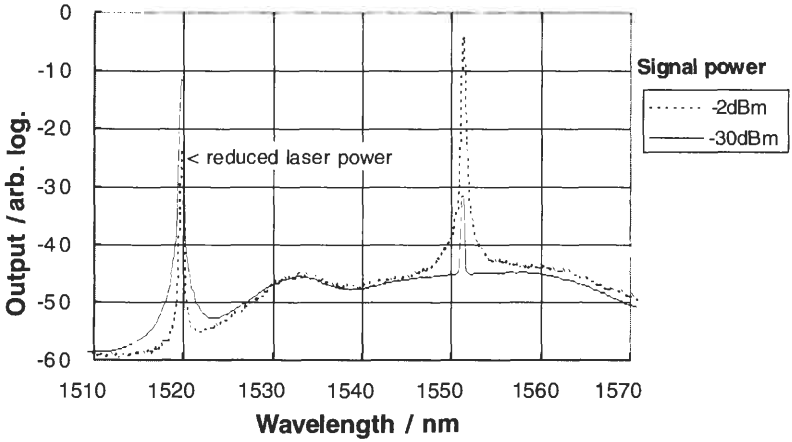

Figure 8.31: Output spectra of all-optical AGC amplifier, lasing at 1520 nm [134].

the cavity loss at 2.5 dB, single pass. The pump power in the fiber from a 1480-nm diode laser was approximately 80 mW.

Figure 8.31 shows the compensatory effect of the control laser in the broadband output spectra. As the input signal is increased to −2 dBm from the small signal level (−30 dBm), there is more than 10 dB of reduction in the residual laser output power. The inversion (and therefore the gain) in both cases remains the same. The excess noise in the high signal case is an artifact due to the side modes of the signal DFB source.

The evolution of the amplifier gain at 1550 nm, as a function of input signal level for four different pump powers is shown in Fig 8.32. A gain of nearly 16 dB is maintained up to an input signal power level of about −5 dBm, at the maximum pump power level of 80 mW.

The pump power no longer determines the amplifier's gain in the gain-controlled regime, only its maximum controlled output power. This is a desirable feature for a well-managed amplifier.

The dynamic performance of amplifiers with and without gain control is compared in Figs. 8.33 and 8.34. To test the transient response of the amplifiers an input signal of −10 dBm is modulated at 54 Hz and the outputs monitored on an oscilloscope, as shown in Fig. 8.33.

Without the signal present, the population inversion builds up in the uncontrolled amplifier. When the signal is injected, the output overshoots,

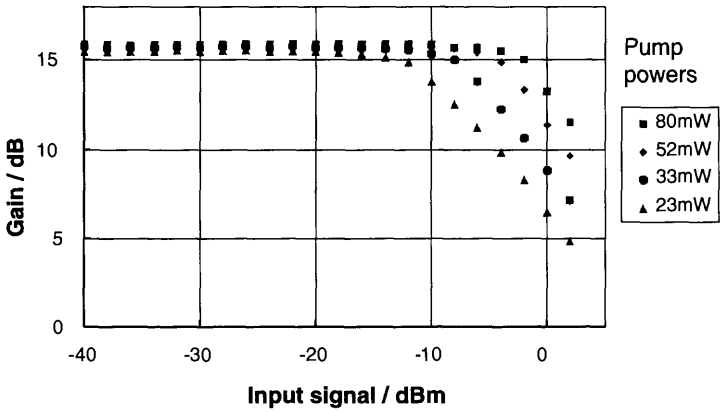

Figure 8.32: Gain characteristic of AGC amplifier. Lasing wavelength: 1520 nm; signal wavelength: 1550 nm; signal power: −30 dBm (from: Massicott J. F., Willson S. D., Wyatt R., Armitage J. R., Kashyap R., and Williams D., "1480nm pumped erbium doped fibre amplifier with all optical automatic gain control," *Electron. Lett.* **30**(12), 962–963, 1994. © IEE 1994, Ref. [134]).

producing a spike before a new equilibrium is reached. In the optical gain-controlled amplifier, the spike is eliminated.

Additionally, the induced cross-talk is also eliminated, as shown in Fig. 8.34. A small counterdirectionally propagating probe at 1560 nm is strongly affected in the uncontrolled amplifier but remains unaffected with AGC. In the absence of AGC, the CW probe output power more than doubles when the saturating signal is blocked, whereas in the controlled case, a change of less than 0.5% in output is seen.

To eliminate the residual laser power at 1520 nm, an additional STG [122] with a rejection of 30 dB is used. BER measurements performed at 2.5 Gb/sec show no penalty as a result of operating the amplifier in the optical gain-controlled regime.

A combination of both gain control and gain equalization forms a highly desirable amplifier. A GEQ filter composed of a concatenated set of STG filters, (as discussed in Section 8.8.1) added to the AGC amplifier output shows excellent GEQ-AGC. The flattened spectral shape is maintained for as long as the amplifier is operated within the gain-controlled range.

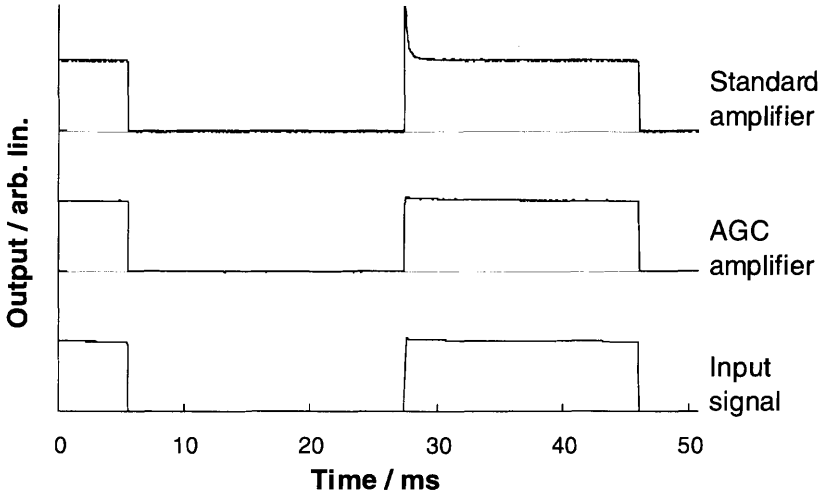

Figure 8.33: 1550-nm input signal modulated at 54 Hz (bottom trace), signal amplified using gain control (middle trace), and signal amplified without gain control (top trace) (from: Massicott J. F., Wilson S. D., Wyatt R., Armitage J. R., Kashyap R., and Williams D., "1480nm pumped erbium doped fibre amplifier with all optical automatic gain control," *Electron. Lett.* **30**(12), 962–963, 1994. © IEE 1994, Ref. [134]).

8.8.3 Analysis of gain-controlled amplifiers

For an amplifying fiber in which the Er^{3+} ion population inversion profile is approximated to be constant across the fiber core, the wavelength-dependent gain coefficient is given by

$$g_{(\lambda)} = \Gamma_{(\lambda)} N[(\sigma_{e(\lambda)} + \sigma_{a(\lambda)})n_2 - \sigma_{a(\lambda)}], \tag{8.8.1}$$

where $\sigma_{e(\lambda)}$ and $\sigma_{a(\lambda)}$ are the emission and absorption cross-sections, respectively, N is the axial Er^{3+} ion density, n_2 is the fraction of ions in the excited state, and $\Gamma_{(\lambda)}$ is the confinement factor representing the overlap between the propagating mode and the radial ion density distribution. In an amplifier in which gain control is in operation, the population inversion, and hence n_2, is set by the lasing condition, and amplifier gain calculations can be made without reference to the magnitudes of pump and signal power levels. The total linear loss at the laser cavity wavelength is

$$\text{Cavity loss} = e^{2g(las)L}. \tag{8.8.2}$$

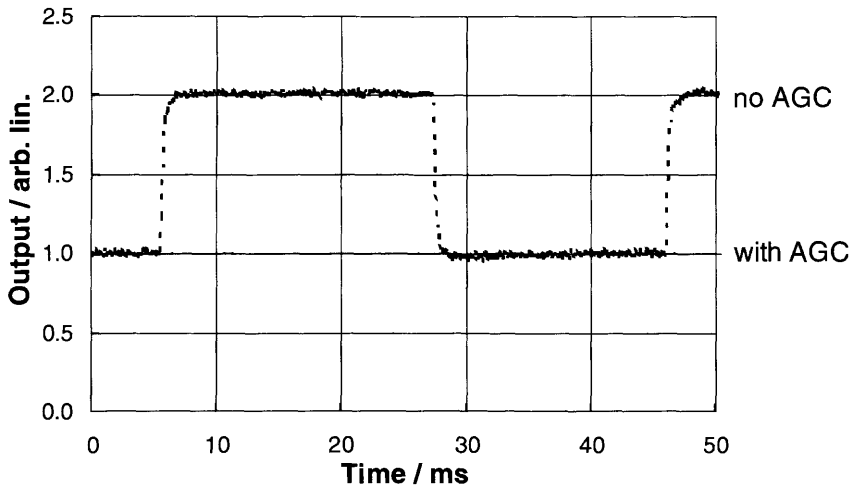

Figure 8.34: Cross-talk experienced by a contradirectionally propagating small signal 1560-nm probe to a modulated 1550-nm signal. Probe amplified using gain control (solid) and without gain control (dashed) [134].

Determination of the minimum required pump power to maintain gain control in the presence of signals of known magnitude is more involved. Approximate amplifier analyses (e.g., [135]) can be employed, but values so obtained substantially underestimate the actual power requirements. Principally, this is because no account is taken of pair induced quenching effects that degrade power conversion efficiencies even in low Er^{3+} ion concentration fibers [136].

8.8.4 Cavity stability

The gain stability of the amplifier is determined by the stability of the control laser wavelength and the laser cavity loss. The laser wavelength is fixed by the narrow-linewidth grating reflectors that have a temperature sensitivity of ~0.01 nm/°C. To avoid changes in cavity loss if drifting should occur, the use of one narrow- and one broader-band reflector is preferable. Reflections at the laser wavelength from other parts of the transmission system will alter the effective cavity loss, as will polarization dependence combined with birefringence in the fiber. The use of high-reflection gratings with an associated intracavity side-tap attenuator, as

opposed to reflectors of lower reflectivity, offers greater resilience to stray light from other parts of the transmission system.

8.8.5 Noise figure

The signal-spontaneous beat-noise figure for an amplifier is often given as

$$F_{(\nu)} = \frac{P^{sp}_{(\nu)}}{h\nu\delta\nu(G_{(\nu)} - 1)}, \tag{8.8.3}$$

where $P^{sp}_{(\nu)}$ is the spontaneous emission power at frequency ν, measured in a bandwidth $\delta\nu$. Over a length of fiber in which the population inversion is constant, the noise figure for that inversion can be calculated using

$$F_{(\lambda)} = 2\Big/\left(1 - \frac{\sigma_{a(\lambda)}}{\sigma_{e(\lambda)}}\frac{n_1}{n_2}\right). \tag{8.8.4}$$

It can be seen that for a given wavelength, the best noise figure is obtained for the highest possible inversion i.e., maximum n_2/n_1.

In a full-length amplifier, whether or not it is gain controlled, the local population inversion varies along the fiber length. The overall noise figure of the amplifier is predominantly determined at the signal input end [137], as spontaneous emission generated at the input experiences the full amplifier gain before being detected within the bandwidth of the signal receiver.

In an AGC amplifier, the evolution of the population inversion is, in part, determined by the laser power. For good overall noise performance, it is beneficial to minimize the laser power at the input in order to ensure that, as far as possible, the input inversion is determined by the shorter-wavelength pump source. This involves implementing as asymmetric a cavity configuration as possible. This is achieved by locating the bulk of the cavity loss at the signal output end of the amplifier and by choosing the wavelength of the control laser to be in a high-gain region of the spectrum requiring a correspondingly high cavity loss.

Figure 8.35 shows the measured gain and noise figures of an AGC amplifier with a linear control laser cavity at 1530 nm [138]. The pump and signal powers are referenced to the input and output of the doped fiber and the measured noise figures are compared with data obtained using a full numerical amplifier model [139]. In one case the cavity loss

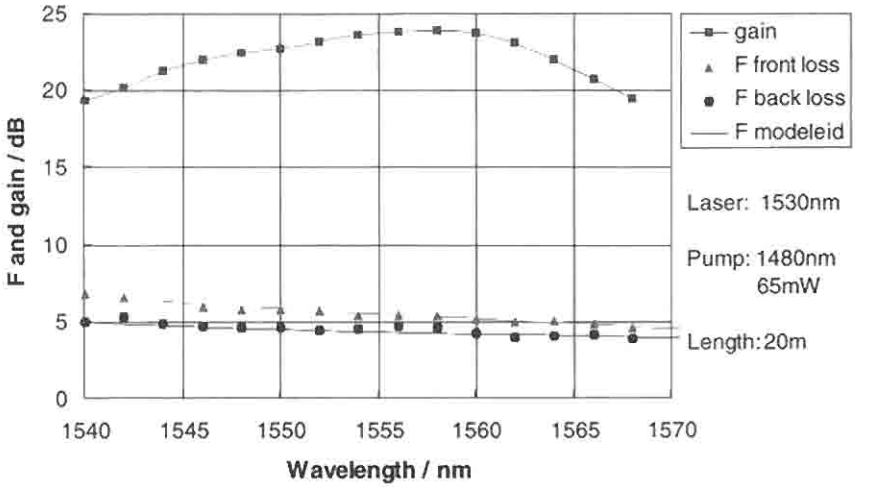

Figure 8.35: Gain and noise figure for an AGC amplifier in two cavity implementations (courtesy J. Massicott, BT Laboratories).

grating is placed at the front end of the cavity, and in the other, at the back. The gain spectra for the two cases were identical to within experimental error, but the expected noise figure improvement is achieved when the cavity loss is located at the signal output end of the laser cavity.

References

1 Betti S., De Marchais G., and Iannone E., *Coherent Optical Communications System*, Wiley, New York (1995).

2 Olsson A. and Tang C. L., "Coherent optical interference effects in external cavity semiconductor lasers," *IEEE J. Quantum Electron.* **QE-17**, 1320–1323 (1981).

3 Tkach R. W. and Chraplyvy A. R., "Regimes of feedback effects in 1.5 μm distributed feedback laser," *J. Lightwave Technol.* **LT-4**, 1655–1661 (1986).

4 Wyatt R. and Devlin W. J., "10kHz linewidth 1.5 μm, InGaAsP external cavity laser with 55nm tuning range," *Electron. Lett.* **19**, 110–112 (1983).

5 Olsson N. A., Henry C. H., Kazarinov R. F., Lee H. J., and Orlowsky K. J., "Performance characteristics of a 1.5 μm single frequency semiconductor

laser with an external waveguide Bragg reflector," *IEEE J. Quantum Electron.* **QE-43**, 143–147 (1988).

6 Meltz G. and Morey W. W., "Bragg grating formation and germanosilicate fiber photosensitivity," *SPIE* **1516**, International Workshop on Photo-induced Self-Organisation effects in Optical Fibres," p. 185 (1991).

7 ITU-T specification of wavelength for WDM.

8 Adams M. J., Steventon A. J., Devlin W., and Henning I., *Semiconductor Lasers for Long Wavelength Optical Fibre Communication Systems,* Peter Peregrinus (1987).

9 Osinski M. and Buus J., "Linewidth broadening factor in semiconductor lasers — an overview," *IEEE J. Quantum. Electron.* **QE-23**(1), 9–21 (1987).

10 Olsson N. A., Henry C. H., Kazarinov R. F., Lee H. J., and Johnson B. H., "Relation between chirp and linewidth reduction in external Bragg reflector semiconductor laser," *Appl. Phys. Lett.* **47**, 183–185 (1985).

11 Timofeev F. N., Bayvel P., Reekie L., Tucknott J., Midwinter J. F., and Payne D. N., "Spectral characteristics of a reduced cavity single mode semiconductor fiber grating cavity for applications in dense systems," in *Proc. of 21st European Conf. Optic. Commun., ECOC'95*, Brussels, Belgium, paper TuP. 26, pp. 477–480 (1995).

12 Brinkmeyer E., Brennecke W., Zürn M., and Ulrich R., "Fiber Bragg reflector for mode selection and line-narrowing of injection lasers," *Electron. Lett.* **22**(3), 134–135 (1986).

13 Park C. A., Rowe C. J., Buus J., Reid D. C. J., Carter A., and Bennion I., "Single-mode behaviour of a multimode 1.55 μm laser with a fiber grating external cavity," *Electron. Lett.* **22**, 1132–1134 (1986).

14 Morey W. W., Meltz G., and Glenn W. H., "Fiber optic Bragg grating sensors," SPIE **1169,** *Fiber optics Sensors VII*, pp. 98–107 (1989).

15 Bird D. M., Armitage J. R., Kashyap R., Fatah R. M. A., and Cameron K. H., "Narrow line semiconductor laser using fiber grating," *Electron. Lett.* **27**, 1115 (1991).

16 Williams D. L., Ainslie B. J., Kashyap R., Sherlock G., Smith R. P., and Collins J. V., "Temperature stable 1.3 μm laser with Bragg fiber grating external cavity for access networks," in *Proc of ECOC'93*, pp. 209–212 (1993).

17 Morton P. A., Mizrahi V., Lemaire P. J., Tanbun-Ek, Logan R. A., Presby H. M., Erdogan T., Woodward S. L., Phillips M. R., Sargent A. M., and Wecht K. W., "High power narrow-linewidth stable single-mode hybrid," in *Proc. Conference on Optical Fiber Communications, OFC'94 Technical Digest*, Paper WG4, p. 102 (1994).

18 Morton P. A., Mizrahi V., Tanbun-Ek, Logan R. A., Lemaire P. J., and Presby, H. M., "Stable single mode hybrid laser with high power and narrow linewidth," *Appl. Phys. Lett.* **64**, 2634–2636 (1994).

19 Edwards C. A., Presby H. M., and Stulz L. W., "Effective reflectivity of hyperbolic micro lenses," *Appl. Opt* **32**, 2099 (1993).

20 Giles C. R., Erdogan T., and Mizrahi V., "Simultaneous wavelength stabilisation of 980nm pump lasers," *IEEE Photon. Technol. Lett.* **6**, 907–909 (1994).

21 Ventrudo B. F., Rogers G. A., Lick G. S., Hargreaves D., and Demayo T. N., "Wavelength and intensity stabilisation of 980nm diode lasers coupled to fiber Bragg gratings," *Electron. Lett.* **30**(25), 2147–2149 (1994).

22 Petermann K., in *Laser Diode Modulation and Noise,"* Chapter 7. Kluwer Academic Publishers, Dordrecht (1991).

23 Pan J. J., Jing X. L., and Shi Y., "Fiber grating stabilized source for dense WDM systems," in *Proc. of Optical Fiber Conf., OFC'97*, paper WL48, p. 213.

24 Campbell R. J., Armitage J. R., Sherlock G., Williams D. L., Smith R. P., Robertson M. J., and Wyatt R., "Wavelength stable uncooled fiber grating semiconductor laser for use in an all optical WDM access network," *Electron. Lett.* **32**, 119–120 (1996).

25 Collins J. V., Lealman I. F., Fiddyment P. J., Jones C. A., Waller R. G., Rivers L. J., Cooper K., Perrin S. D., Neild M. W., and Harlow M. J., "Passive alignment of a tapered laser with more than 50% coupling efficiency," *Electron Lett.* **31**(9), 730–731 (1995).

26 Kashyap R., Payne R., Whitley T., and Sherlock G., "Wavelength uncommitted lasers," *Electron. Lett.* **30**(13), 1065 (1994).

27 Timofeev F. N., Bayvel P., Midwinter J. E., Wyatt R., Kashyap R., and Robertson M., "2.5Gbit/s dense WDM, transmission in standard fibre using directly modulated fibre grating lasers," *Electron Lett.* **33**(19), 1632–1633 (1997).

28 Timofeev F. N., Bayvel P., Mikhailov V., Gambini P., Wyatt R., Kashyap R., Robertson M., Campbell R. J., and Midwinter J. E., "Low chirp, 2.5 Gbit/s directly modulated fibre grating laser for WDM networks," in *Technical Digest of Conf. on Opt. Fib. Commun., OFC'97*, p. 296 (1997).

29 Timofeev F. N., Bayvel P., Midwinter J. E., Wyatt R., Kashyap R., and Robertson M., "2.6 Gbit/s dense WDM transmission in standard fibre using directly modulated fibre grating lasers," *Electron Lett.* **33**(19), 1632–1633 (1997).

30 Timofeev F. N., Bayvel P., Mikhailov V., Lavrova O. A., Wyatt R., Kashyap R., Robertson M., and Midwinter J. E., "2.5 Gbit/s directly modulated fibre grating laser for WDM network," *Electron. Lett.* **33**(16), 1406–1407 (1997).

31 Timofeev F. N., Bennett S., Griffin R., Bayvel P., Seeds A., Wyatt R., Kashyap R., and Robertson M., "High spectral purity millimetre-wave modulated opti-

cal signal generation using fibre grating lasers," *Electron. Lett.* **34**(7), 668–669 (1998).

32 Paoletti P., Meliga M., Oliveti G., Puleo M., Rossi G., and Senepa L., "10 Gbit/s ultra low chirp 1.55 μm directly modulated hygrid fiber grating semiconductor laser source," in *Tech. Digest of ECOC'97*, pp. 107–110 (1997).

33 Premaratne M., Lowery A. J., Ahmed Z., and Novak D., "Modelling noise and modulation performance of fiber Bragg grating external cavity lasers," *IEEE J. Selected Topics in Quantum Electron.* **3**(2), 290–303 (1997).

34 Park J. D., Seo D. S., and McInerney J. G., "Self-pulsation in strongly coupled asymmetric external cavity semiconductor lasers, *IEEE J. Quantum Electron.* **26**, 1353–1362 (1990).

35 Rong-Qing H. and Shang-Ping T., "Improved rate equations for external cavity semiconductor lasers," *IEEE J. Quantum. Electron.* **25**, 11580–1584 (1989).

36 Berger O., "Dynamische Modellierung von Fasergitterlasern für optoelektronische Mikrowellenerzeugung," Diplomarbeit, Universität Duisberg (1998).

37 Morton P. A., Mizrahi V., Kosinski S. G., Mollenauer L. F., Tanbun-Ek T., Logan R. A., Coblentz D. L., Sargent A. M., and Wecht K. W., "Hybrid soliton pulse source with fibre external cavity and Bragg reflector," *Electron. Lett.* **28**(6), 561 (1992).

38 Morton P. A., Mizrahi V., Andrekson P. A., Tanbun-Ek T., Logan R. A., Lemaire P., Coblentz D. L., Sargent A. M., Wecht K. W., and Sciortino P. F., Jr. "Mode locked hybrid soliton pulse source with extremely wide operating frequency range," *IEEE Photonics Tech. Lett.* **5**(1), 28 (1993).

39 Ahmed Z. and Tucker R. S., "Small-signal IM response of grating-terminated external cavity semiconductor lasers," *IEEE J. Selected Topics in Quantum Electron.* **1**, 505–515 (1995).

40 Tomita A. and Suzuki A., "Optical feedback effect on bistable laser diodes," *Opt. Quantum Electron.* **15**, S75–S82 (1987).

41 Snitzer E. and Koester C. J., "Amplification in a fiber laser," *Appl. Opt.* **3**, 1182–1186 (1964).

42 Ainslie B. J., Beales K. J., Cooper D. M., Day C. R., and Rush J. D., "Monomode fibre with ultra-low loss and minimum dispersion at 1.55 μm," *Electron. Lett.* **18**, 842–844, 1982.

43 See, for example, *Optical Fiber Lasers and Amplifiers* (France P. W., Ed.). Blackie and Sons, London (1991).

44 Øbro M., Pedersen J. E., and Brierley M. C., "Gain enhancement in Nd^{3+} doped ZBLAN fibre amplifier using mode coupling filter," *Electron. Lett.* **28**(1), 99–100 (1992).

45 Miller I. D. and Hunt M. H., "Optical fibre locating apparatus ," UK Patent no. 89301940, 27 February 1989.

46 Jauncey I. M., Reekie L., Mears R. J., Payne D. N., Rowe C. J., Reid D. C. J., Bennion L., and Edge C., "Narrow-linewidth fiber laser with integral fiber grating," *Electron. Lett.* **22**(19), 987–988 (1986).

47 Wyatt R., "High power broadly tunable erbium-doped silica fiber laser," *Electron. Lett.* **25**(22), 1498–1499 (1989).

48 Kashyap R., Armitage J. R., Wyatt R., Davey S. T., and Williams D. L., "All-fiber narrowband reflection gratings at 1500 nm, *Electron. Lett.* **26**(11), 730 (1990).

49 Ball G. A., Morey W. W., and Waters J. P., "Nd^{3+} fiber laser utilising intra-core Bragg reflectors," *Electron Lett* **26**(21), 1829 (1990).

50 Mizrahi V., DiGiovanni D., Atkins R. M., Park Y., and Delavaux J-MP "Stable single-mode erbium fiber grating laser for digital communication," *IEEE J. Lightwave Technol.* **11**(12), 2021 (1993).

51 Zyskind J. L., Mizrahi V., DiGiovanni D. J., and Sulhoff J. W., "Short single-frequency Erbium-doped fiber laser," *Electron. Lett.* **28**, 1385 (1992).

52 Chernikov S. V., Kashyap R., McKee P. F., and Taylor J. R., "Dual frequency all fiber grating laser source," *Electron Lett.* **29**(12), 1089 (1993).

53 Chernikov S. V., Taylor J. R., and Kashyap R., "Coupled-cavity erbium fiber lasers incorporating fiber grating reflectors," *Opt. Lett.* **18**(23), 2023, 1993, and Chernikov S. V., Taylor J. R., and Kashyap R., "Integrated all optical fiber source of multigigahertz soliton pulse train," *Electron. Lett.* **29**(20), 1788 (1993).

54 Ball G. A., Morey W. W., and Cheo P. K., "Single- and multipoint fiber-laser sensors," *IEEE Photonics Tech. Lett.* **5**(2), 267 (1993).

55 Ball G. A. and Morey W. W., "Narrow-linewidth fiber laser with integrated master oscillator-power amplifier," *Proc. Conference on Optical Fiber Communications, OFC'92*, p. 97 (1992).

56 Archambault J. L. and Grubb S. G., "Fiber gratings in lasers and amplifiers," *J. Lightwave Technol.* **15**(8), 1378–1390 (1987).

57 Loh W. H., Laming R. I., and Zervas M. N., "Single frequency erbium fiber external cavity semiconductor laser," *Appl. Phys. Lett.* **66**(25), 3422–3424 (1995).

58 Grubb S. G., "High power fiber amplifiers and lasers" in *Proc. of OFC'95*, Tutorial Session (1996).

59 SDL FL-10, SDL Inc., 80 Rose Orchard Way, San Jose, CA. USA.

60 Digonnet M. J. F., "Closed-form expressions for the gain in three- and four-level laser fibers," *IEEE J. Quantum Electron.* **26**, 1788–1796 (1990).

61 Ball G. A. and Glenn W. H., "Design of a single-mode linear-cavity erbium fiber laser utilising Bragg reflectors," *J. Lightwave Technol.* **10**(10), 1338 (1992).

62 Ball G. A., Glenn W. H., Morey W. W., and Cheo P. K., "Modelling of short, single-frequency, fiber lasers in high-gain fiber," *IEEE Photonics Tech. Lett.* **5**(6), 649 (1993).

63 Le Boudec P., Francois P. L., Delevaque E., Bayon J.-F., Sanchez E., and Stephan G. M., "Influence of ion pairs on the dynamical behaviour of Er^{3+} doped fiber lasers," *Opt. & Quantum. Electron.* **25**, 501 (1993).

64 Ball G. A., Hul-Allen G., Holton C. E., and Morey W. W., "Low noise single frequency linear fibre laser," *Electron. Lett.* **29**, 1623–1625 (1993).

65 Kane T. J., "Intensity noise in diode-pumped single-frequency Nd:YAG lasers and its control by electronic feedback," *IEEE Photon. Technol. Lett.* **2**(4), 244–245 (1990).

66 Zyskind J. L., Sulhoff J. W., Magill P. D., Reichmann K. C., Mizrahi V., and DiGiovanni D. J., "Transmission at 2.5 Gbit/s over 654 km using an erbium-doped fiber grating laser source," *Electron. Lett.* **29**(12), 1105 (1993).

67 Delavaux J.-M. P., Park Y. Y., Mizrahi V., and DiGiovanni D. J., "Long term bit error rate transmission using an erbium fiber grating laser transmitter at 5 and 2.5 Gb/s," in *Tech. Proc. of ECOC'93*, paper TuC3.3, pp. 69–71 (1993).

68 Ball G. A., Hul-Allen G., Holton C. E., and Morey W. W., "60 mW 1.5 μm single-frequency low noise fibre laser MOPA," *IEEE Photon. Technol. Lett.* **6**(2), 192–194 (1994).

69 Kringlebotn J. T., Archambault J. L., Reekie L., Townsend J. E., and Payne D. N., "Highly-efficient, low-noise grating-feedback Er^{+3}:Yb^{3+} codoped fibre laser," *Electron. Lett.* **30**(12), 972–973 (1994).

70 Kringlebotn J. T., Morkel P. R., Reekie L., Archambault J. L., and Payne D. N., "Efficient diode-pumped single frequency erbium:ytterbium fibre laser," *IEEE Photonics Technol. Lett.* **5**(10), 1162 (1993).

71 Allain J. Y., Bayon J.-F., and Monerie M., "Ytterbium-doped silica fiber laser with intracore Bragg gratings at 1.02 μm," *Electron. Lett.* **29**, 309 (1993).

72 Coldren L. A., Millar B. I., Iga K., and Rentschler J. A., "Monolithic two-section GaInsAsP/InP active optical resonator devices formed by reactive ion etching," *Appl. Phys. Lett.* **38**, 315 (1981).

73 Tsang W. T., Olsson N. A., and Logan R. A., "High speed direct single-frequency modulation with large tuning rate and frequency excursion in cleaved coupled cavity semiconductor laser," *Appl. Phys. Lett.* **42**, 650 (1983).

74 Lang R. J., Yariv A., and Salzman J., "Laterally coupled cavities semiconductor lasers," *IEEE J. Quantum Electron.* **QE-23**, 395 (1987).

75 Dianov E. M. and Okhotnikov O. G., *Sov. Lightwave Commun.* **2**, 823 (1992).

76 Pan J. J. and Shi Y., "Tunable Er^{+3}-doped fibre ring laser using fibre grating incorporated by optical circulator or fibre coupler," *Electron. Lett.* **31**(14), 1164–1165 (1995).

77 Guy M. J., Taylor J. R., and Kashyap R., "Single-frequency erbium fibre ring laser with intracavity phase-shifted fibre Bragg grating narrowband filter," *Electron. Lett.* **31**(22), 1924–1925 (1995).

78 Yun S. H., Richardson D. J., Culverhouse D. O., and Kim B. Y., "Wavelength-swept fiber laser with frequency-shifted feedback," in *Tech. Digest of OFC'97*, pp. 30–31 (1997).

79 Dong L., Loh W. H., Caplen J. E., Hsu K., Minelli J. D., and Reekie L., "Photosensitive Er/Yb optical fibers for efficient single-frequency fiber lasers," in *Tech. Digest of OFC'97*, pp. 29–30 (1997).

80 Dong L., Loh W. H., Caplen J. E., Hsu K., Minelli J. D., and Reekie L., "Efficient single-frequency fiber lasers with novel photosensitive Er/Yb optical fibers," *Opt. Lett.* **22**(10), 694–696 (1997).

81 Utaka K., Akiba S., and Matsushima Y., "$\lambda/4$-shifted GaAsP/InP DFB lasers by simultaneous holographic exposure of negative and positive photoresists," *Electron. Lett.* **20**, 1008–1010 (1984).

82 Asseh H., Storoy H., Kringlebotn J. T., Margulis W., Sahlgren B., and Sandgren S., "10 cm long Yb^{+} DFB fibre laser with permanent phase shifted grating," *Electron. Lett.* **31**, 969–970 (1995).

83 Sejka M., Varming P., Haübner J., and Kristensen M., "Distributed feedback Er^{+3} doped fibre laser," *Electron. Lett.* **31**(17), 1445–1446 (1995).

84 Loh W. H. and Laming R. I., "1.55 μm phase-shifted distribute feedback fibre laser," *Electron. Lett.* **31**(17), 1440–1442 (1995).

85 Hübner J., Varming P., and Kristensen M. "Five wavelength DFB fibre laser source for WDM systems," *Electron. Lett.* **33**(2), 139–140 (1997).

86 Lauridsen V. C., Sondergaard T., Varming P., and Povlsen J. H., "Design of distributed feedback fiber lasers," *In Proc. of ECOC'97*, Vol. 3, pp. 39–42 (1997).

87 Graydon O., Loh W. H., Laming R. I., and Dong L., "Triple-frequency operation of an Er-doped twin-core fiber loop laser," *IEEE Photon. Technol. Lett.* **8**(1), 63–65 (1996).

88 Ball G. A. and Morey W. W., "Continuously tuneable single-mode erbium fiber laser," *Opt. Lett.* **17**(6), 420 (1992).

89 Ball G. A. and Morey W. W., "Compression-tuned single-frequency Bragg grating fiber laser," *Opt. Lett.* **19**(23), 1979–1981 (1994).

90 Hsu K., Loh W. H., Dong L., and Miller C. M., "Efficient and tunable Er/Yb fiber grating lasers," *J, Lightwave Technol.* **15**(8), 1438–1441 (1997).

91 Gunning P., Kashyap R., Siddiqui A. S., and Smith K., "Picosecond pulse generation of <5 ps from gain-switched DFB semiconductor laser diode using a linearly ste-chirped grating," *Electron. Lett.* **31**(13), 1066–1067 (1995).

92 Eggleton B. J., Krug P. A., Poladin L., Ahmed K. A., and Liu J.-F., "Experimental demonstration of compression of dispersed optical pulses by reflection from a self-chirped optical fiber Bragg grating," *Opt. Lett.* **19**, 877–879 (1994).

93 Chernikov S. V., Taylor J. R., and Kashyap R., "Comblike dispersion-profiled fiber soliton pulse train generation," *Opt. Lett.* **19**(8), 539–541 (1994).

94 Davey R. P., Fleming R. P. E, Smith K., Kashyap R., and Armitage J. R., "Mode-locked erbium fibre laser with wavelength selection by means of a fibre Bragg grating reflector," *Electron. Lett.* **27**(22), 2087–2088 (1991).

95 Ahmed K. A., Eggleton B. J., Liu H. F., Krug P. A., and Ouellette F., "Simultaneous mode-selection and pulse compression of gain switched pulses from a Fabry–Perot laser using a 40 mm chirped optical fiber grating," *IEEE Photon. Technol. Lett.* **7**, 158–160 (1995).

96 Karpman V. I. and Solov'ev V. V., "A perturbational approach to the two-soliton systems," *Physica D*(3), 487–502 (1981).

97 Mollenauer L. F., Evangelides S. G., and Haus H. A., "Long distance solution propagation using lumped amplifiers and dispersion shifted fiber," *IEEE J. Lightwave Technol.* **9**, 194 (1991).

98 Chernikov S. V., Dianov E. M., Richardson D. J., Laming R. I., and Payne D. N., "114 Gb/s soliton train generation through Raman self scattering of a dual frequency beat signal in dispersion decreasing optical fiber," *Appl. Phys. Lett.* **63**, 293–295 (1993).

99 Mamyshev P. V., Chernikov S. V., and Dianov E. M., "Generation of fundamental soliton trains for high-bit rate optical fibre communication lines," *IEEE J. Quantum. Electron.* **27**, 2347–2355 (1991).

100 Kashyap R., Chernikov S. V., and Taylor J. R., "Fibre laser and beat frequency sources based on fibre gratings for microwave and ultrafast processing," *Int. J. Optoelectron.* **11**(2), 87–92 (1997).

101 Chernikov S. V., Kashyap R., Guy M. J., Moodie D. G., and Taylor J. R., "Ultrahigh-bit-rate optical sources and application," *Phil. Trans. R. Soc. Lond. A* **354**, 719–731 (1996).

102 Noske D. U., Guy M. J., Rottwitt K., Kashyap R., and Taylor J. R., "Dual-wavelength operation of a passively mode-looked 'figure-of-eight' ytterbium-erbium fibre soliton laser," *Opts. Comm.* **108**, 297–301 (1994).

103 Pataca D. M., Rocha M. L., Kashyap R., and Smith K., "Bright and dark pulse generation in an optically mode-locked fibre laser at 1.3 mm," *Electron. Lett.* **31**(1), 35–36 (1995).

104 Woodbury E. J. and Ng W. K., "Ruby laser operation in the near IR", *Proc. IRE 50,* 2347, 1962.

105 See, for example, Shen Y. R., *The Principles of Nonlinear Optics*. Wiley, New York (1984).

106 Stolen R. H., "Nonlinearity in fiber transmission," *Proc. IEEE* **68**(10), 1232–1236 (1980).

107 Akoi Y., "Properties of fiber Raman amplifiers and their applicability to digital optical communication systems," *Lightwave Technol.* **6**, 1225 (1988).

108 Hill K. O., Kawasaki B. S., and Johnson D. C., "CW Brillouin laser," *Appl. Phys. Lett.* **28**, 608 (1976).

109 Jain R. K., Chinlon Lin, Stolen R. H., Pleibel W., and Kaiser P., "A high-efficiency tunable cw Raman oscillator," *Appl. Phys. Lett.* **30**(3), 162–164 (1977).

110 Stolen R. H., Chinlon Lin, and Jain R. K., "A time-dispersion-tuned fiber Raman oscillator," *Appl. Phys. Lett.* **30**(7), 340–342 (1977).

111 Stolen R. H. and Lin C., "Fiber Raman lasers," in *CRC Handbook of Laser Science and Technology, Supplement I: Laser*, CRC Press (1991).

112 Grubb S. G., "High power diode-pumped fiber lasers and amplifiers," in *Proc. of OFC'95*, paper TuJ1, pp. 41–42 (1995).

113 Grubb S. G., "High power 1.48 μm cascaded Raman laser in germanosilicate fiber," in *OFC'95, the Conference on Optical Communication*, Vol. 8, 1995 Technical Digest Series, Postconference Edition, pp. 41–42 (1995).

114 Dianov E. M., Abramov A. A., Bubnov M. M., Shipulin A. V., Prokhorov A. M., Semjonov S. L., and Schebunjaev, "Demonstration of 1.3 μm Raman fiber amplifier gain os 25 dB at a pumping power of 300 mW," *Opt. Fib. Technol.* **1**, 236–238 (1995).

115 Grubb S. G., Erdogan T., Mizrahi V., Strasser T., Cheung W. Y., Reed W. A., Lemaire P. J., Miller A. E., Kosinski S. G., Nykolak G., and Becker P. C., "1.3 μm cascaded Raman amplifier in germanosilicate fibers," in *Proc. of OAA'94*, paper PD3 (1994).

116 Desurvire E., Chapter 2, pp. 108, in *Erbium Doped Fiber Amplifiers*. Wiley, New York (1994).

117 Stentz A. J., Nielsen T., Grubb S. G., Strasser T. A., and Pedrazzani J. R., "Raman ring amplifier at 1.3 μm with analog-grade noise performance and output power of 23 dBm," in *Proc. of OFC'96*, paper PD16, pp. 391–394 (1996).

118 Hansen P. B., Stentz A. J., Eskilden L., Grubb S. G., Strasser T. A., and Pedrazzani J. R., "High sensitivity 1.3 μm optically pre-amplified receiver using Raman amplification," *Electron. Lett.* **32**(23), 2164–2165 (1996).

119 Nakazawa M., Yamada E., Kubota H., and Suzuki K., "10 Gb/s soliton data transmission over 1 million kilometers," *Elec. Lett.* **27**, 1270–1272 (1991).

120 Hill G. R., Fernandes L., and Cadeddu R., "Building the road to optical networks," *Br. Telecom. Engg.*, **16**, 2–12 (1997).

121 Kashyap R., Wyatt R., and Campbell R. J., "Wideband gain flattened erbium fibre amplifier using a photosensitive fibre blazed grating," *Electron. Lett.* **29**(2), 154–155 (1993).

122 Kashyap R., Wyatt R., and McKee P. F., "Wavelength flattened saturated erbium amplifier using multiple side-tap Bragg gratings," *Electron. Lett.* **29**(11), 1025–1026 (1993).

123 Kashyap R., unpublished (1993).

124 Holmes M. J., Kashyap R., Wyatt R., and Smith R. P., "Development of radiation mode filters for WDM," in *Proc. of IEE Symposium on WDM Technology*, IEE, 16–17 (June 1998).

125 Dianov E. M., Karpov V. I., Kurkov A. S., Medvedkov O. I., Prokhorov A. M., Protopopov V. N., and Vasil'ev S. A., "Gain spectrum flattening of erbium doped fiber amplifier using long period grating," in *Photosensitivity and Quadratic Nonlinearity in Glass Waveguides: Fundamentals and Applications*, Vol. 22, 1995 OSA Technical Series (Optical Society of America, Washington, DC, 1995), pp. SbB3-(14–17) (1995).

126 Vengsarkar A. M., Pedrazzani J. R., Judkins J. B., Lemaire P. J., Bergano N. S., and Davidson C. R., "Long-period fiber grating based gain equalisers," *Opt. Lett.* **21**, 336–338 (1996).

127 Ellis A. D., Percival R. M., Lord A., and Stallard W. A., "Automatic gain control in cascaded erbium-doped fibre amplifier systems," *Electron. Lett.* **3**, 193 (1991).

128 Bayart D., Clesca B., Hamon I., and Beylat J. L., "1.55 μm fluoride-based EDFA with gain-flatness control for multiwavelength applications," *Electron. Lett.* **17**, 1407 (1994).

129 Motoshima K., Leba L. M., Chen D. N., Downs M. M., Li T., and Desurvire E., "Dynamic compensation of transient gain saturation in erbium-doped fibre amplifiers by pump feedback control," *IEEE Photon. Technol. Lett.* **12**, 1423 (1993).

130 Desurvire E., Zirngible M., Presby H. M., and DiGiovanni D., "Dynamic gain compensation in saturated erbium-doped fibre amplifiers," *IEEE Photon Technol. Lett.* **5**, 453 (1991).

131 Motoshima K., Shimizu K., Takano K., Mizuochi T., and Kitayama T., "EDFA with dynamic gain compensation for multiwavelength transmission systems," *OFC'94 Technical Digest*, 191 (1994).

132 Zirngibl M., "Gain control in erbium-doped fibre amplifiers by an all-optical feedback loop," *Electron. Lett.* **27**(7), 560–561 (1991).

133 Delevaque E., Georges T., Bayon J. F., Monerie M., Niay P., and Berage, P., "Gain control in erbium-doped fibre amplifiers by lasing at 1480 nm with photoinduced Bragg gratings written on the fibre ends," *Electron. Lett.* **29**(12), 1112–1113 (1993).

134 Massicott J. F., Willson S. D., Wyatt R., Armitage J. R., Kashyap R., and Williams D., "1480 nm pumped erbium doped fibre amplifier with all optical automatic gain control," *Electron. Lett.* **30**(12), 962–963 (1994).

135 Saleh A. A. M., Jopson R. M., Evankow J. D., and Aspell J., "Modeling of gain in erbium-doped fibre amplifiers," *IEEE Photon. Technol. Lett.* **2**(10), 714 (1990).

136 Georges T., Delevaque E., Monerie M., Lamouler P., and Bayon J. F., "Pair induced quenching in erbium doped silicate fibers," *IEEE Optical Amplifiers and Their Applications, Technical Digest*, Vol. 17, p. 71 (1992).

137 Olshansky R., "Noise figure for erbium-doped optical amplifiers," *Electron. Lett.* **24**(22), 1363–1365 (1988).

138 Massicott J. F., Lebre C., Wyatt R., Kashyap R., Williams D., and Yu A., "Low noise, all-optical gain controlled Er3+ doped fibre amplifier using asymmetric control laser cavity design," *Electron. Lett.* **32**(9), 816–817 (1996).

139 Yu A. and O'Mahony M. J., "Properties of gain controlled erbium doped fibre amplifiers by lasing," *Electron Lett.* **31**(16), 1348 (1995).

Chapter 9

Measurement and Characterization of Gratings

The transfer characteristics of a grating are of primary importance for a number of applications. For example, in high-bit-rate applications, it is necessary to know if the grating will impart additional dispersion and, if so, how much. Gratings can be used in a vast number of demanding applications, such as sensing in harsh environments, or in undersea optical fiber transmission that requires components to survive the 25-year design lifespan of the system. For long-term use, it is essential to know whether or not the grating will maintain its designed characteristics over the lifetime. It is also important to know, as it is for optical fibers, the integrity of its mechanical strength for the same reasons. Thus, reliability is a big issue. The transmission characteristics of certain gratings may be affected by the out-gassing and annealing processes more than others; the resonance wavelengths of *all* gratings drift because of the out-diffusion of molecular hydrogen in high-pressure sensitized fibers. Stress relaxation can complicate matters, by altering the induced refractive index modulation. Sensitivity of the Bragg wavelength with temperature and strain has to be taken into account for such applications as in band-pass filters. Gratings have to be annealed to stabilize their properties for long-term use. The bandwidth, reflection profile, and phase response of gratings require special measurement techniques for proper characterization. In this chapter we shall consider some of the parameters that are of impor-

tance and techniques that have been developed for characterization. These include reflectivity and transmission spectrum, bandwidth, average refractive index change and refractive index modulation coefficient, grating uniformity and quality of apodization, insertion loss, radiation loss, and group delay of chirped gratings, drift due to out-diffusion of hydrogen, temperature effects during measurements, PMD, and stress changes. Methods that have been reported for the measurement of thermal decay of gratings will be covered in the final section. The aim of this chapter is to provide an overview of the properties of optical fibers used for grating fabrication, including thermal annealing and characterization of fiber gratings and mechanical strength.

9.1 Measurement of reflection and transmission spectra of Bragg gratings

The nice thing about gratings is that their growth can be monitored during the inscription process. Since the fabrication is noninvasive, apart from stripping part of the coating, the input and output ends of the fiber are often accessible. Usually the source at the wavelength of interest is an edge-emitting diode, which provides sufficient output power for a variety of measurements. Alternatively, white light may be coupled into the fiber, although the dynamic range is limited. The amplified spontaneous emission from a fiber amplifier is a very good broadband source, and the choice is available to cover the 900–1700 nm wavelength band. It is normal to have either a circulator or a 50:50 fiber splitter between the source and the grating to be measured. The most sensitive method for detecting gratings is in reflection, and for this reason it is best to measure gratings in reflection for diagnostic purposes and display the signal on an optical spectrum analyzer. The basic apparatus for measuring Bragg grating reflection and transmission is shown in Fig. 9.1. The inset shows an alternative arrangement using the coupler.

Reflections just above the noise floor of the spectrum analyzer are easily displayed. When a grating is written into the fiber, a reflection peak appears which may be checked for the wavelength. At the same time, the transmission spectrum shows no change until the grating reflectivity is a few percent. A useful guide is the 3.5% reflection from the cleaved far end of the fiber to calibrate the actual reflection from the

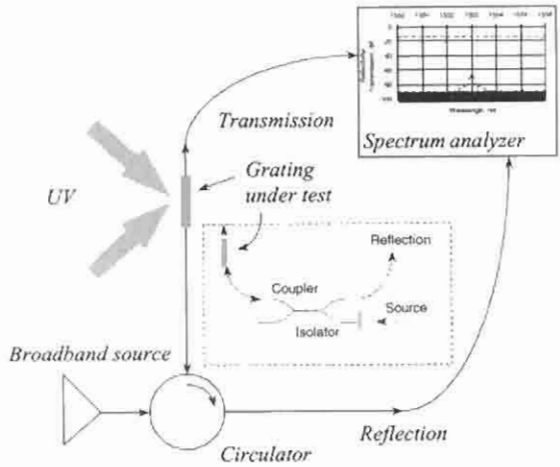

Figure 9.1: Apparatus to measure the transmission and reflection spectrum of Bragg gratings.

grating (see Fig. 9.2). For a uniform grating with a reflectivity R, we can calculate the coupling coefficient, $\kappa_{ac}L$, as

$$\kappa_{ac} L = \tanh^{-1}(\sqrt{R}). \tag{9.1.1}$$

With this information and the measured bandwidth, $2\Delta\lambda$, between the first zeroes (FWFZ), the grating length L is uniquely defined as per Eq. (4.6.14),

$$2\Delta\lambda = \frac{\lambda^2}{\pi n_{eff} L} \sqrt{(\kappa_{ac}L)^2 + \pi^2}. \tag{9.1.2}$$

From the length, we may calculate the refractive index modulation $\nu\overline{\Delta n}$ as in Eqs. (4.6.3) and (4.3.6), with a fringe visibility ν,

$$\kappa_{ac} = \frac{\pi\eta\nu\overline{\Delta n}}{\lambda}. \tag{9.1.3}$$

Eqs. (9.1.1) and (9.1.2) are plotted in Fig. 9.3 for three different values of grating length, 1, 2, and 8 mm, as a function of the coupling constant κ_{ac}. The data has been plotted for a Bragg wavelength of 1550 nm. The wavelength shift $\delta\lambda$ as the grating grows can be calculated from Eq. (4.6.4),

$$\delta\lambda = 2\lambda\eta \frac{\Delta n}{n}, \tag{9.1.4}$$

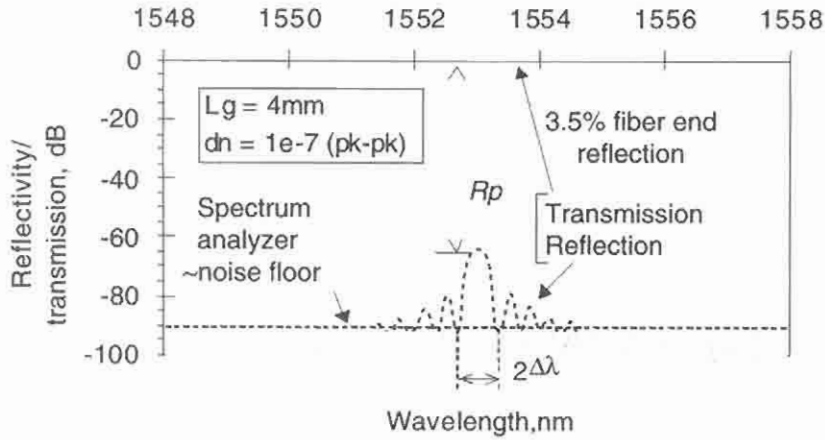

Figure 9.2: The reflection spectrum of a 4-mm-long grating with a refractive index modulation amplitude of only 10^{-7}. At this stage it is undetected in transmission. Also shown is the ~3.5% reflection from the cleaved end of the fiber, assuming that there are no losses in the reflected light. The very weak Bragg reflected signal is easily detected. The noise floor for a spectrum analyzer resolution of 0.1 mm is shown only as an example.

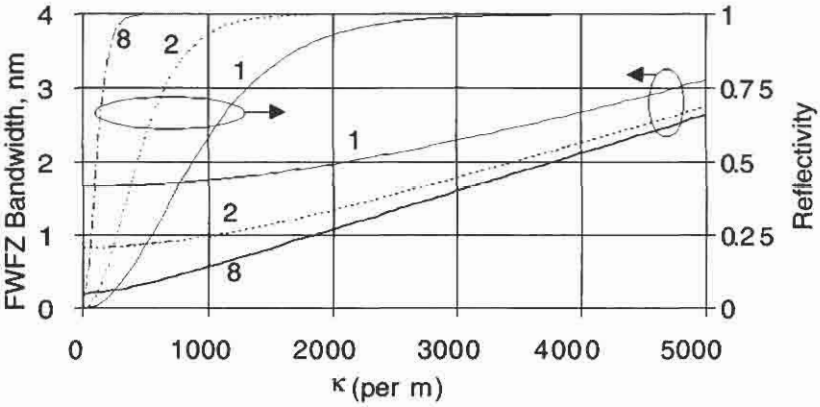

Figure 9.3: The reflectivity and bandwidth of three Bragg gratings as a function of the coupling constant κ_{ac} at a wavelength of 1550 nm. The numbers refer to the lengths in millimeters. Note that for large values of the coupling constant, the grating bandwidth grows linearly. As a guide, the maximum refractive index modulation amplitude, Δn, for $\nu = 1$, and overlap, $\eta = 0.8$, is $\sim 3 \times 10^{-3}$ (at $\kappa_{ac} = 5000\ \mathrm{m}^{-1}$).

where we remind ourselves that Δn is the ac index change and λ is the Bragg wavelength at the start of the growth of the grating.

As the grating grows, it shifts to longer wavelengths and this is shown in the transmission spectra in Fig. 9.4. Along with the shift is shown the effect of a nonuniform UV beam profile. This has been assumed to have a Gaussian profile, as with many laser beams, and causes a chirp in the grating [1], since the Bragg wavelength is proportional to the effective mode index. There are two effects of the nonuniform UV beam profile: The grating acquires additional structure on the short-wavelength side (Fig. 9.4) as it grows, and the peak reflectivity drops for the same refractive index modulation amplitude, as is seen for the uniform profile grating in Fig. 9.5.

Comparing the uniform and the Gaussian intensity profile grating, the effect on the bandwidth is only slight. The long-wavelength edge of the Gaussian profile grating is apodized.

We now compare the Gaussian intensity profile with the Gaussian apodized grating, i.e., one in which the refractive index modulation changes with the length of the grating, but not the mode effective index (see Chapter 5), and find that the short-wavelength structure disappears and the peak reflectivity increases with apodization. The reason for this is that the Bragg wavelength of the apodized grating is constant and the

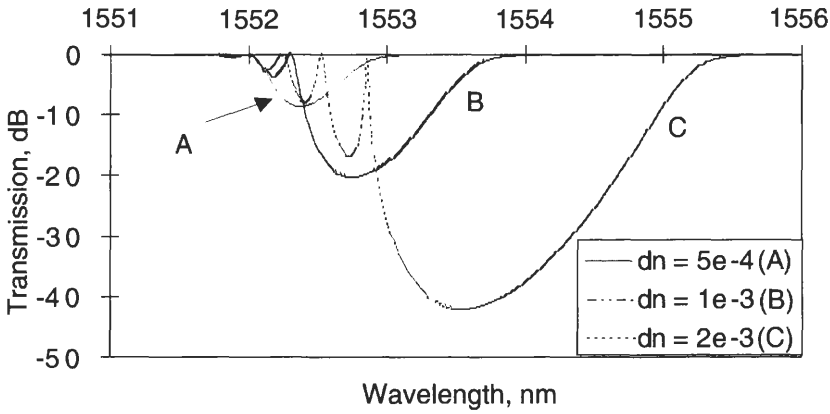

Figure 9.4: The shift in the Bragg wavelength and the appearance of the Fabry–Perot structure on the short-wavelength side of a Gaussian intensity profile grating as the UV-induced refractive index modulation amplitude increases.

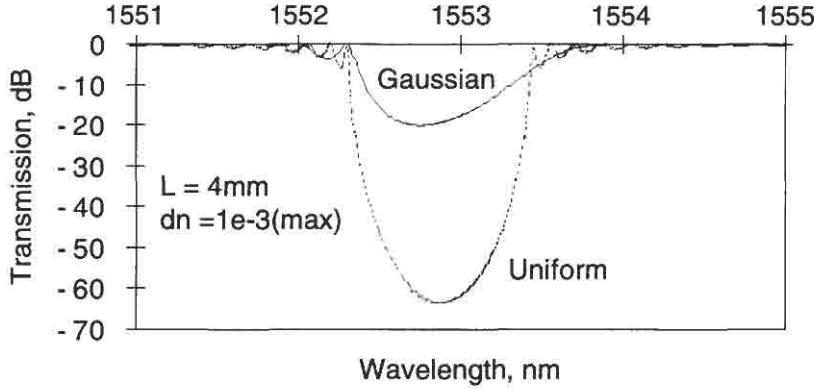

Figure 9.5: A uniform amplitude profile grating compared with a Gaussian amplitude profile grating.

reflection is not spread over a larger bandwidth, and so the effective length is longer. (See Fig. 9.6.)

The maximum reflectivity can be calculated by measuring the transmission dip T_d in dBs. The translation from the measured dip to the reflectivity is

$$R = 1 - 10^{-T_d/10}, \tag{9.1.5}$$

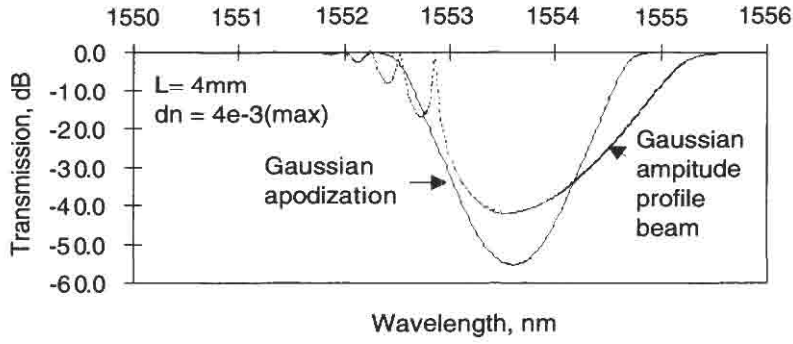

Figure 9.6: Comparison of chirp induced in a strong grating due to the amplitude profile of the writing beam and a Gaussian profile apodized grating with the same parameters. The FWFZ bandwidth is approximately the same, but the slope on the long wavelength side is different, as well as the structure on the short wavelength side.

or from the peak of the reflected signal R_p below the transmitted signal it is (as shown in Fig. 9.2)

$$R = 10^{-R_p/10}. \tag{9.1.6}$$

The data is shown in Fig. 9.7. For example, in Fig. 9.2, the reflected signal is shown to be ~70 dB below the transmission level. This translates to a reflectivity of 10^{-5}%.

Alternatively, a 10-dB transmission dip is equivalent to a reflectivity of 90%, 20 dB is 99%, and so on. It is assumed that there is no additional loss in the reflected signal as compared with the transmitted signal. If the loss is known, the transmitted level or the reflection peak must be adjusted accordingly.

Special care needs to be taken when measuring transmission dips in excess of ~30 dB because of the limited resolution of the spectrum analyzer. The slit width of the spectrum analyzer is not a delta function, and there is substantial leakage from the spectral region outside of the slit bandwidth. Integrated, it amounts to more signal being transmitted and affects the spectrum mostly at the dip in the grating transmission. There are several solutions to this problem. Obviously, a better spectrum analyzer is one, or a tunable laser source may be used in conjunction with a conventional spectrum analyzer, ensuring that the scanning of the laser and the spectrum analyzers are synchronized [2] with an appropriate slit width. The combined side-mode suppression and the slit width reduces

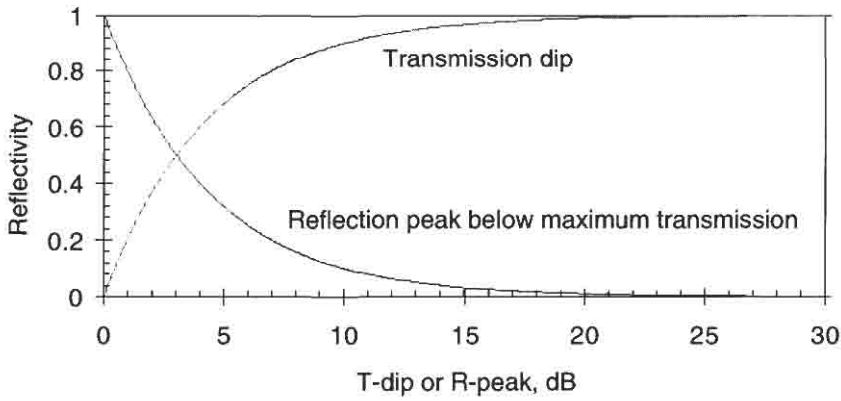

Figure 9.7: Reflectivity as a function of the dip in the transmission spectrum of a grating or as the reflection peak below transmitted signal.

the captured noise. Such a measurement is shown in Fig. 9.8, in which the spectrum of a strong 4-mm-long grating spectrum with a transmission dip of >60 dB has been resolved. In addition to the very steep long-wavelength edge, it has structure on the short wavelength that is due to cladding mode coupling and Gaussian chirp.

Clearly, chirp is not a feature that is desirable for simple transmission filters. We now consider the spectra of uniform period gratings and the effect of apodization. Figure 9.9 shows the reflection spectrum of unapod-

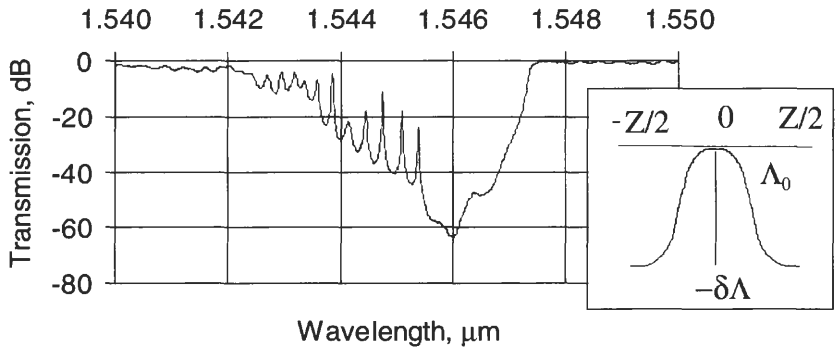

Figure 9.8: The measured grating is ~4 nm long with an estimated index modulation of 4×10^{-3}. The beam intensity profile had a Gaussian shape. The inset shows the change in the Bragg wavelength across the length of the grating.

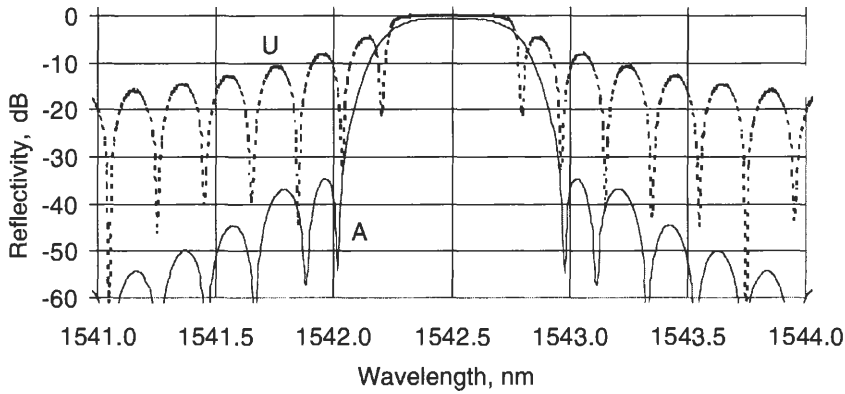

Figure 9.9: Reflection spectra of 4-mm-long unapodized and $\cos^2$ apodized gratings with a refractive index modulation amplitude of 4×10^{-4}.

ized and apodized ($\cos^2$ profile) gratings. The unapodized grating is nominally a 100% reflection grating, and the apodized one has identical length and refractive index modulation. The effect of apodization is to reduce the effective length to approximately $L/2$. As a result, the FWFZ bandwidth approximately matches the second zeroes of the unapodized grating. Note that the reflectivity is also reduced (~halved). To generate an apodized grating with the same bandwidth, the length has to be approximately doubled, and the coupling constant has to be adjusted, so that an 8-mm-long raised cosine apodized grating will have the same approximate bandwidth and reflectivity.

In order to resolve the reduced side lobes for the apodized grating, the spectrum analyzer linewidth should be selected to remove artifacts and a false noise floor.

9.2 Perfect Bragg gratings

It is possible to make very high-quality uniform-period Bragg gratings. This is because optical fiber has very uniform properties. The theoretically calculated reflection, along with the measured spectrum, of a 30-mm-long grating is shown in Fig. 9.10. The grating was fabricated by scanning a phase mask with a UV beam [3].

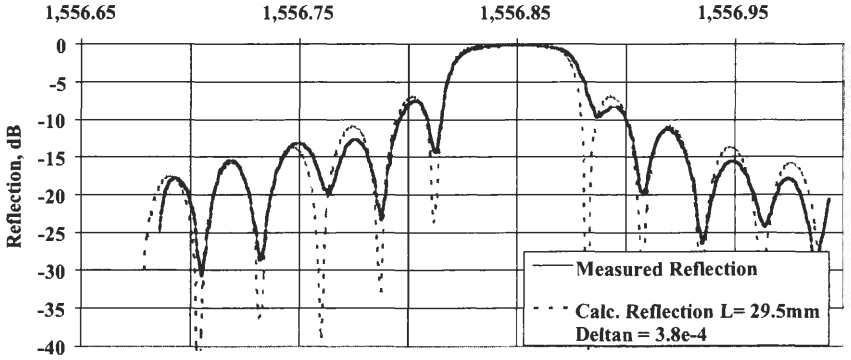

Figure 9.10: Measured and computed reflection spectrum of a 29.5-mm-long fiber Bragg grating, produced by the scanned phase-mask technique [4]. The uniformity of the grating is indicated by the close agreement between the zeroes of the theoretical and measured response.

The agreement between measurement and theory is very good, with the zeroes matching across almost the entire spectrum shown. Notice the slight deviations, especially at the first side-lobe zero (RHS), and the third side-lobe zero (LHS). These features are indicative of slight chirp and nonuniformity in the writing process. Nevertheless, this grating has ~28,000 grating periods and shows a near-ideal response. One way to measure such a narrow bandwidth is to use a high-quality tunable laser source and a spectrum analyzer for reasons of resolution. It is difficult to measure such gratings accurately in transmission with a broadband source, since the bandwidth is almost the same as that of commercially available optical spectrum analyzers (0.07 nm FWHZ). Although this grating has a transmission dip of ~14 dB, the spectrum remains unresolved in transmission with a spectrum analyzer.

Gratings with such performance are particularly useful where the phase response is required along with the reflection characteristics in filtering applications, such as in pulse shaping and dark soliton generation [4].

9.3 Phase and temporal response of Bragg gratings

Figure 9.11 shows the computed reflection and accumulated phase-spectrum of a uniform-period unapodized Bragg grating. The measurement of phase of a grating can only be made by the measurement of the grating's complex amplitude reflectivity. A technique has been proposed for the reconstruction of the phase of the grating using arguments based on causality and minimum phase performed on the measured reflection spectrum of a grating, with reasonable success [5]. This may be done by using interferometric techniques to characterize weak gratings (<20% reflectivity) [6–9]. These measurements have at best limited spatial resolution, or are difficult to implement, being interferometric. Other more direct methods include the use of a network analyzer for the measurement of dispersion [10,11]. The use of the network analyzer relies on the dispersion being constant over the frequency region of interest, and strictly it is better suited to measuring apodized chirped gratings. This technique has been applied to gratings to measure their dispersion [12,13]. Another method for testing of a grating or phase mask uses a probe transverse to the grating [14].

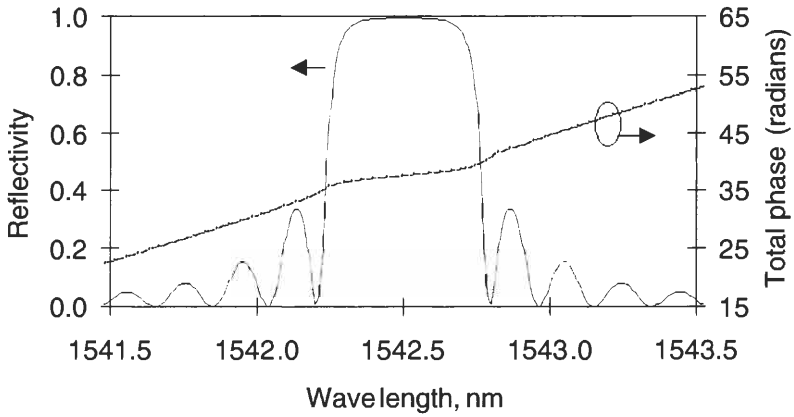

Figure 9.11: The reflectivity and phase of a 4-mm-long unapodized grating with a refractive index modulation amplitude of 4×10^{-4}.

Typically, the accumulated phase for a 4-mm-long grating is a few tens of radians, as shown in Fig. 9.11.

The group delays of the two gratings used for Fig. 9.9 are shown in Fig. 9.12. The strong dispersion at the edges of the band stop limits the useful bandwidth of a band-pass filter, especially in high-speed applications [15,16]. In Ref. [16] asymptotic expressions may be found for the

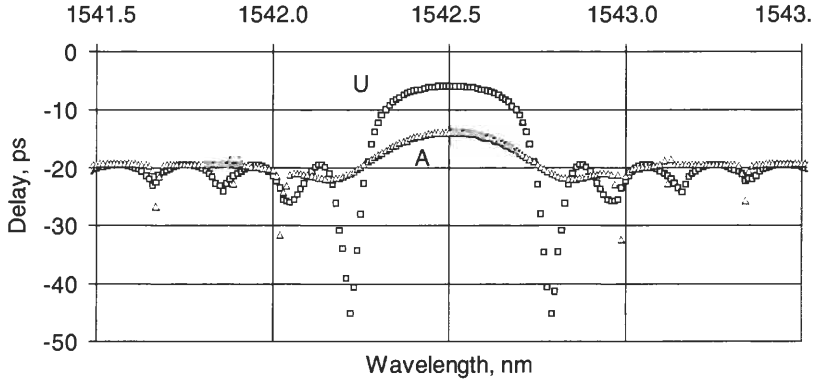

Figure 9.12: Dispersion of 4-mm-long unapodized (U) and apodized (A) gratings.

dispersion on the long-wavelength side of the band stop of apodized gratings, useful for dense DWM systems. Note that the dispersion at the band edge of the grating reaches several tens of picoseconds for the unapodized grating and is much reduced in the apodized grating. Despite the apodization, there is a curvature in the center of the band stop, which may be useful to compensate for the chirp of a source [15].

The group delay shown in Fig. 9.12 is for gratings with uniform characteristics. Often there is a chirp involved, which has a significant effect on the dispersion. We note that the group delay characteristics of the uniform gratings remain symmetric about the center of the bandgap. With chirp in a grating, the group delay changes sign on one side of the band stop, and this is shown in the calculated response in Fig. 9.13. The unapodized grating acquires less pronounced zeroes and the group delay, a point of inflection.

To characterize the group delay of gratings, a measurement setup based on the vector-voltmeter [17] is shown in Fig. 9.14. In this method, light from a tunable single-frequency source is modulated at a frequency f and is launched into a grating under test. The reflected (or transmitted) signal is compared via a circulator with the modulated input signal in a vector voltmeter. As the wavelength of the source is tuned, the delay in the reflected light from the grating changes. The vector-voltmeter compares the phase of the modulated light and translates it into a phase difference. Thus, the phase at the modulated frequency f is measured.

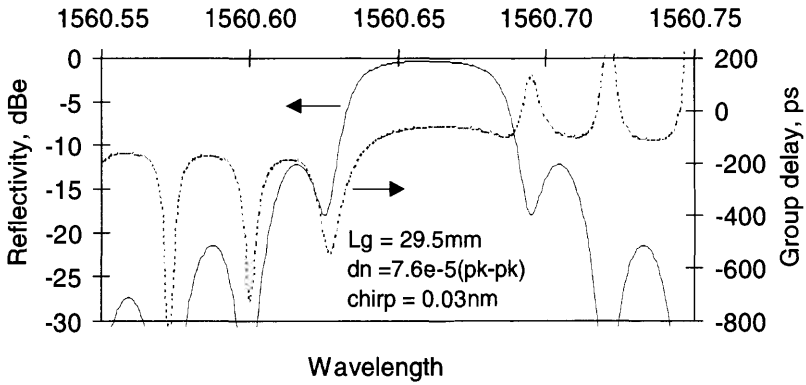

Figure 9.13: Simulated response of a 29.5-mm-long grating with a 0.03-nm chirp and refractive index modulation of 7.6×10^{-5} (peak-to-peak).

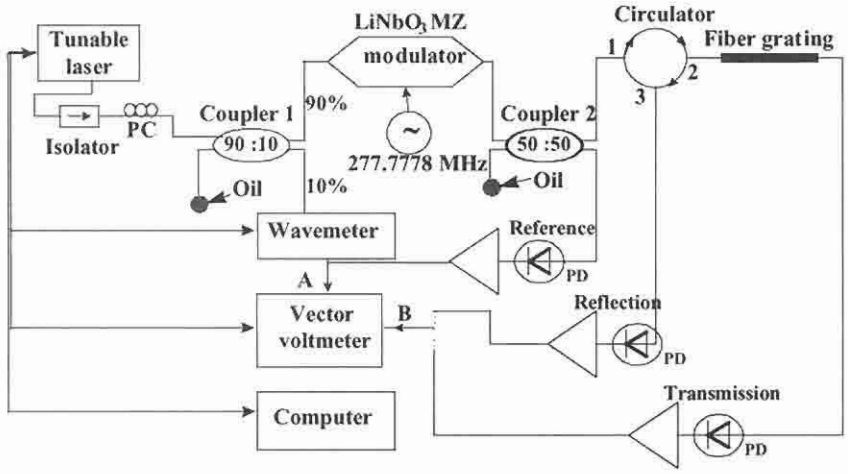

Figure 9.14: A schematic of the apparatus for the measurement of group delay, reflectivity, and transmission of gratings (after Ref. [17]).

With a judicious choice of the modulation frequency, e.g., 277.77778 MHz, one degree of phase change is equivalent to a delay τ of 10 psec, as [18]

$$\tau = \frac{1}{360f} \text{ sec deg}^{-1}. \tag{9.3.1}$$

Under computer control, this data may be acquired quickly with a minimum of processing. The resolution of the measurement may be increased by increasing the modulation frequency, but it is nominally ~1 psec or better. With such a resolution, care needs to be taken, since temperature variations during the course of the measurements can cause errors. Changes in the path lengths of the fiber used in the setup and also in the polarization affect the measurement. It is for these reasons that the paths are kept to a minimum and a reference frequency is generated optically after the modulator. Any amplitude and phase changes are then common to both the reference and the signal, minimizing errors.

The reflection and group delay of a 30-mm-long grating of the type shown in the simulation of Fig. 9.13 are shown in Fig. 9.15. We note that the similarity is striking between the two grating spectra, in both reflectivity and group delay. It is therefore possible to characterize the measured spectra using simple simulation, since fiber-grating spectra can be so good. Note that the reflectivity spectra is in dB (electrical) = 2 ×

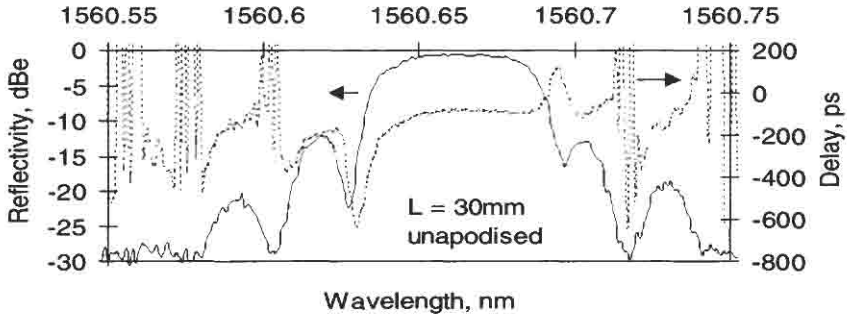

Figure 9.15: The spectra of a 30-mm-long grating measured using the vector voltmeter.

dB (optical). The grating reflectivity can be measured in transmission, to normalize the peak of the reflectivity spectra. The results for an identical but apodized grating are equally good.

We now move on to the spectrum of a longer grating, of the type used in dispersion compensation. There are a few points that need to be remembered. In Chapter 7 the delay response of long gratings is considered in detail, and it is found that long gratings need to be characterized with high wavelength resolution if the GDR (group delay ripple) spectrum is to be resolved. In making measurements, a wavelength resolution of 1 pm is generally sufficient. The measured reflectivity and group delay of a raised cosine apodized, 100-mm-long grating is shown in Fig. 9.16. The

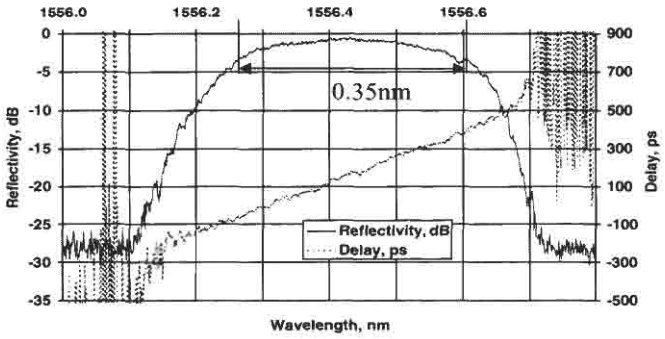

Figure 9.16: The reflectivity and delay of a 100-mm-long chirped grating with a chirped bandwidth of 0.75 nm [19], measured with a resolution of 1 pm.

data has been measured with 1 pm resolution, and the GDR is adequately resolved. We can measure the 3-dB optical (6-dBe) reflectivity bandwidth by comparing the transmitted signal level with R_p, remembering that the measurements are in dBe.

This grating is designed to compensate the dispersion for ~80 km of standard optical fiber, as has been presented in Chapter 7. With unapodized gratings the low resolution masks the detail and a comparison is shown in Fig. 9.17. Here two measurements of the same grating made with 10 pm and 1 pm are compared. The GDR is apparent with the higher resolution. With longer gratings this factor becomes even more critical.

As we have seen in Chapter 7, for 1-meter-long unapodized gratings, the GDR frequency has a period of ~1.5 pm. To resolve the GDR, other means have to be adopted, such as the use of a multisection DFB laser [17], which can be electrically tuned. This is a very time-consuming task, since other factors such as the ambient temperature need to be controlled very accurately. The drift of the wavelength with temperature of a chirped grating is an issue. The grating should be temperature controlled in order to get an accurate measurement. With a change in the local Bragg wavelength of several pm/°C, a stable environment is essential for the measurement.

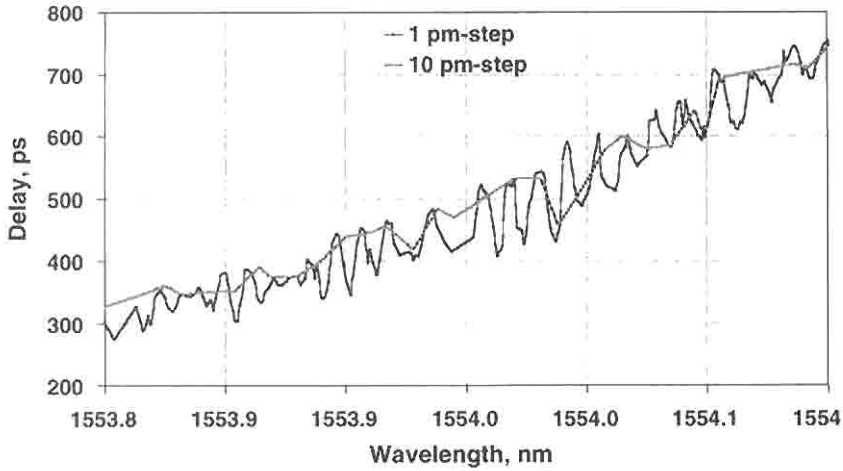

Figure 9.17: Resolution dependence of the group delay of an unapodized chirped grating (after Ref. [17]).

Finally, we consider the drift of the Bragg wavelength with the out-diffusion of hydrogen for a fiber after the grating has been written. With a typical period of measurement of tens of minutes to an hour, the out-diffusion of hydrogen (or deuterium) must be taken into consideration, as has been shown in Chapter 2 [20,21]. In Fig. 9.18 we see the drift in the Bragg wavelength of a chirped grating monitored over a period of 45 days from the inscription of the grating, immediately after removal from the cold storage. The fiber is deuterium soaked at 200 bar at the start. By the end of 45 days, the total drift in the wavelength is approximately -1.65 nm, and it continues to shift very slowly.

With technological improvements, it will be necessary to measure even longer gratings, perhaps longer than 10 meters. The measurement of one of these gratings (reflection spectrum of a 2-meter-long WDM channelized grating is shown in Fig. 9.19) can take several hours at picometer resolution. Here it becomes important that the grating be collectively maintained at the same temperature for the duration of the measurement.

A fast technique has been reported by Ouellette *et al.* [22], which relies on the intrinsic birefringence B of the fiber. By alternately measuring the orthogonal polarization reflected, $S2$, and launched, $S1$, signals from the spectrum analyzer, the group delay is shown to be

$$\tau = \frac{n\lambda}{4\pi Bc} \cos^{-1}\left(S1 - \frac{S2}{S1} + S2\right). \tag{9.3.2}$$

This method requires the calibration of the fiber birefringence. This technique may prove to be valuable, since it is simple, although there is no information available on the resolution.

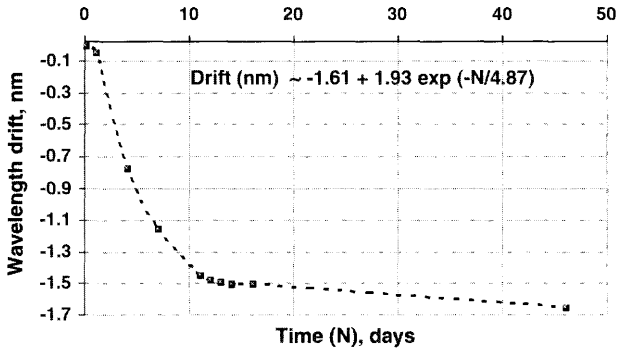

Figure 9.18: The drift in the Bragg wavelength of a chirped grating with time due to deuterium out-diffusion [17].

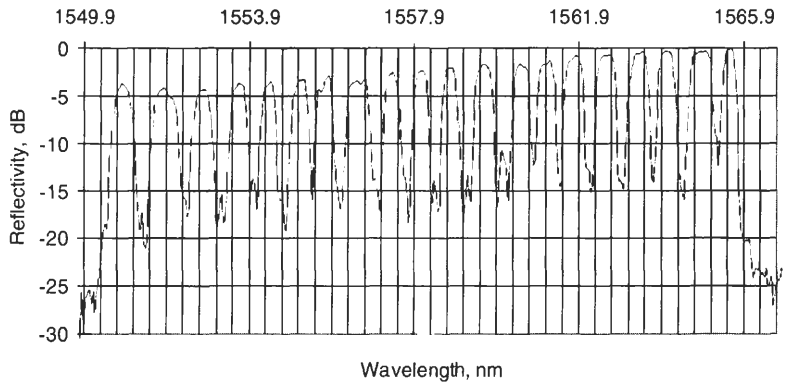

Figure 9.19: The reflection spectrum of a 2-meter-long grating fabricated at BT Laboratories. Both radiation and loss due to deuteration reduce the reflected signal from the shorter wavelength gratings. The combined loss of deuteration and radiation is 2 dB/m [26].

We remind ourselves that for the dispersive properties of gratings with a reflectivity of between 10 and 15 dB, the time delay τ may be calculated as

$$\tau = \frac{2n_{eff}L_g}{c}, \tag{9.3.3}$$

where L_g is the length of the grating and c is the speed of light. For a signal pulse with a transform-limited bandwidth, $\Delta\lambda$ equal to the bandwidth of the grating chirp, the dispersion can be simply described as

$$D = \frac{2n_{\text{eff}}L_g}{c\Delta\lambda} = \frac{2L}{\nu_g\Delta L}, \tag{9.3.4}$$

where L is the physical length of the grating, and ν_g is the group velocity of the pulse. The effects of dispersion can be considerable even in a short grating since the group delay in a fiber is 5 nsec m^{-1}, and in reflection it is doubled.

We have seen in Chapter 7 how PMD can affect the GD of gratings. The measurement of PMD, or rather birefringence, can be made simply by launching light along the two orthogonal birefringent axes of the fiber grating and observing the wavelength shift. Meltz and Morey [23] reported a birefringence-induced Bragg wavelength shift of ~0.1 nm, equivalent to an induced birefringence at 1550 nm of $\sim 2.3 \times 10^{-5}$. This value is high

and the Bragg wavelengths are therefore easily separated in a spectrum analyzer. By rotating the polarization of the UV writing beam so that it is along the fiber axis, the UV-induced birefringence can be reduced from ~5% of the UV-induced refractive index change to around 0.5% [24]. This area has received more attention recently, with the application of setup similar to that shown in Fig. 9.14 to measure the group delay difference of two polarization states. Also applied is the Jones matrix approach to map out all the polarization states in the fiber. The comparison between the two methods is good. Measured polarization-induced delay is reported to be ~28 and 7 psec for two chirped gratings written in different fiber [25].

Clearly this is an area that will receive attention as the deployment of fiber gratings for dispersion compensation becomes widespread.

9.3.1 Measurement of the grating profile

The use of simulation is an excellent method for characterizing the measured spectrum of a grating. By knowledge of the physical length, the reflectivity and the shape of a grating, it is possible to identify a couple of parameters to choose in order to allow the simulation. This has been demonstrated for the spectra shown in Figs. 9.13 and 9.15. More complex structure can be analyzed theoretically, as has been amply demonstrated by Ouellette *et al.* [27] for stitching errors produced by phase masks. For example, random errors in the stitching cause the bandwidth of a uniform-period grating to broaden and acquire noise. The errors can be calculated from the simulation. Alternative techniques exist for assessing the refractive index profile of a grating. These include optical low-coherence reflectometry (OLCR), originally used to detect small flaws in optical waveguides [28,29], applied to fiber gratings by Lamblet *et al.* [30], and the method of side scatter from a grating, demonstrated by Krug *et al.* [31]. An interesting and very simple technique is the application of "heat scan" to probe the chirp in a grating [32,33]. The grating is probed with a fine hot wire while the reflection characteristics are being monitored. A detuning of the Bragg wavelength as a function of probe position measures the chirp. These are in addition to other methods already mentioned as being appropriate for assessing phase masks [9,14]. It is important to know the sources of "noise" on a grating, or correct for a flaw [34–36], since the out-of-band spectra may deteriorate. It should be mentioned that optical time-domain reflectometry (OTDR, or back-scatter) has also

been used to locate gratings. In the next section we will consider the OLCR method and side-scatter as two techniques to assess Bragg gratings.

Optical low-coherence reflectometry

The scheme is based on a fast scanning Michelson interferometer, with the grating as the mirror in one arm, and a scanning broadband mirror (BBM) in the reference arm. Reflected light from the grating and the mirror interferes at a photodiode. The source has a large bandwidth so that the coherence length is short, and therefore interference is only visible over a short region of the grating when the path lengths are within the coherence length. The path difference between the arms is adjusted by moving the reference mirror so that different points within the grating are sampled. A schematic of the apparatus is shown in Fig. 9.20 [37]. The moving reference mirror is mounted on a motorized stage with a long scan length to allow easy adjustment of the paths. The phase modulator is provided to derive a lock-in signal. With reference to a 100% reflection, a cleaved end with approximately 4% end reflection registers a signal at −14 dB. The measurement has range with a noise floor at −140 dB with a bandwidth of 1 Hz.

The source should have low spectral ripple to avoid artifacts. The coherence length, and therefore the resolution of the measurement in the fiber is

$$l_c = \frac{4 \ln 2}{\pi} \frac{\lambda^2}{\Delta\lambda_{FWHM}}, \tag{9.3.5}$$

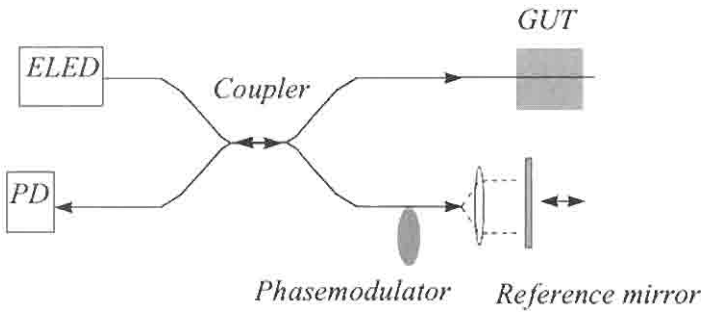

Figure 9.20: A schematic of the OLCR apparatus (after Ref. [37]).

where $\Delta\lambda_{FWHM}$ is the source linewidth and λ is the center wavelength, and the resolution $R = l_c/2n$ where n_g is the group index. For $\Delta\lambda_{FWHM}$ = 55 nm at λ = 1300 nm, we get l_c = 18.3 μm and hence R = 9.1 μm.

The grating spectra are recorded by scanning the reference mirror. In a modified version of the setup, a rotating corner cube is used for increasing the speed of data acquisition. A typical OLCR spectrum is shown in Fig. 9.21. Here the front end reflection is followed by a decay in the signal with penetration depth; this is followed by another increase in the signal as the light exits the far end of the grating at a distance z = 1.222 mm, equivalent to a physical length of z/n_{eff} = 0.84 mm.

The exponential decrease in the signal is proportional to the strength of the grating, while the initial fast rise at the entrance and soon after the first exponential decay is due to the abrupt starting and ending of the grating — a top-hat function. The further oscillations observed are due to the Fabry–Perot modes as the light rattles around within the grating. The measured spectra are the Fourier transform of the product of the amplitude reflectivity of the grating and the spectral distribution of

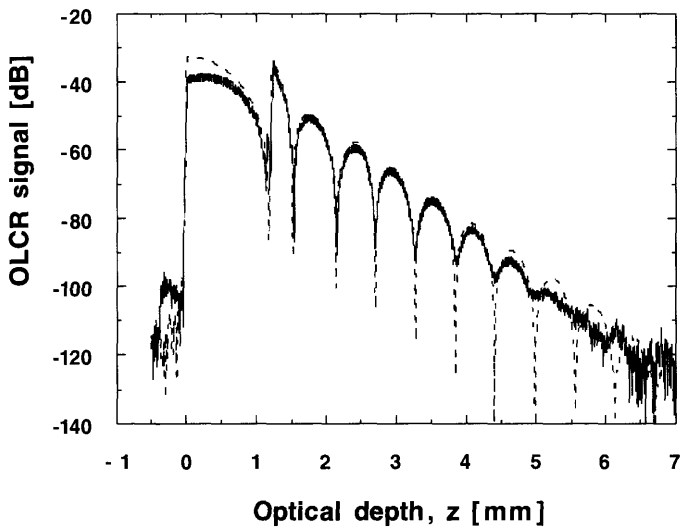

Figure 9.21: The OLCR spectrum of a 0.84-mm-long grating (courtesy Hans Limberger from: Lambelet P, Fonjallaz P Y, Limberger H G, Salathé R P, Zimmer C and Gilgen H H, "Bragg Grating Characterization by Optical Low-Coherence Reflectometry", *IEEE Phot. Technol. Lett.*, 5, 565–567, 1993. © 1993 IEEE.[30]).

the source. The free parameter is the refractive index modulation of the sinusoidal period, since the Bragg wavelength is known, and the length of the grating is found from the length of the scan between the start of the spectrum and the reflection at the end of the grating. The zeroes of the OLCR spectrum are a very sensitive function of the refractive index modulation amplitude, and therefore provide an accurate value. The inverse Fourier transform of the OLCR data and deconvolution of the source spectrum give the grating spectrum. This is shown with the measured grating reflection spectrum in Fig. 9.22. The agreement is altogether excellent.

This technique has been applied by Malo *et al.* [38] to measure the profile of an apodized grating. It is claimed that the relative precision with which the refractive index modulation may be measured is around 1% [30].

Side-scatter measurements

Bragg gratings scatter radiation out of the fiber both within and outside of the bandgap. This is due to a number of reasons, not least radiation

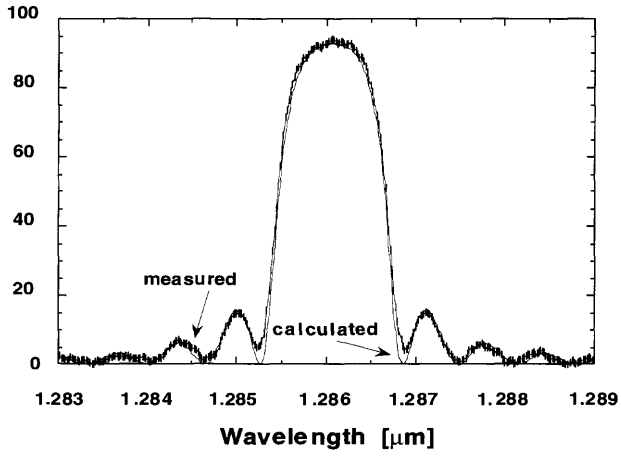

Figure 9.22: Measured and calculated reflection spectra (from the data obtained by OLCR measurement; see Fig. 9.21) as a function of wavelength for an in-fiber grating with a period of 0.443 μm, a length of 0.84 mm, and a modulation depth of $\Delta n = 1.16 \times 10^{-3}$ (courtesy Hans Limberger from: Lambelet P, Fonjallaz P Y, Limberger H G, Salathé R P, Zimmer C and Gilgen H H, "Bragg Grating Characterization by Optical Low-Coherence Reflectometry", *IEEE Phot. Technol. Lett.*, 5, 565–567, 1993. © 1993 IEEE. [30]).

mode coupling of light into the cladding, which can be detected easily [39]. The writing process causes an asymmetry, which assists a directional coupling to the cladding modes (see Chapter 4). Apart from the coherent scattering mechanism, there is also in coherent scatter due to damage in the core as in a Type II grating [40]. This type of grating scatters light because of large surface irregularities at the core–cladding boundary. A third type of scattering mechanism is incoherent and is due to the inhomogeneity in refractive index modulation through the length of the grating. The latter has been investigated by Janos *et al.* [41]. There appears to be a pronounced scatter out of the fiber perpendicular to the direction of the writing beam. The observed anisotropy is consistent with the production of "scattering elements" within a few microns of the core. The scattering loss ranges from 0.2 dB/cm in highly doped Yb/Er phosphosilicate fiber with gratings inscribed with a pulsed laser 193-nm source, to 5×10^{-5} dB/cm for a boron-codoped fiber with a CW 244-nm source.

A technique that measures the sideways diffraction from a fiber Bragg grating is used to characterize the grating refractive index profile. A schematic of this method is shown in Fig. 9.23. In this arrangement, light from a He–Ne laser is focused form the side of the fiber, incident at an angle θ_i to the normal. The schematic of the side-scatter measurement is

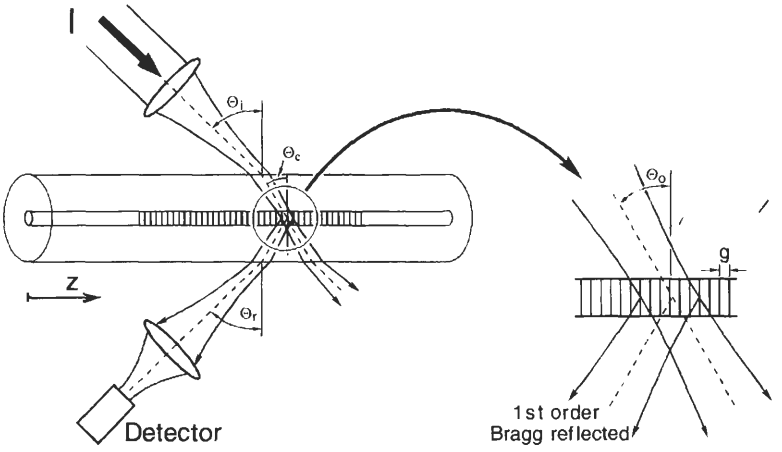

Figure 9.23: The side-diffraction scheme for characterizing Bragg gratings (from: Krug P, Stolte R and Ulrich R, "Measurement of index modulation along an optical fiber Bragg grating", *Opt. Lett.*, **20**(17), 1767–1769, 1 September 1995. [31]).

shown in Fig. 9.23. As has been seen in Chapter 3 on fabrication of gratings with a phase mask, the incident light must have a wavelength less than the period of the grating in the fiber in order to have a first-order diffraction. Referring to Fig. 9.23, which defines the angles, and from phase matching conditions, we find [31]

$$\sin\theta_r = \sin\theta_i = n_{clad}\sin\theta_{clad} = n_{core}\sin\theta_{core} = n_{eff}\frac{\lambda_{probe}}{\lambda_{Bragg}}, \tag{9.3.6}$$

where n_{eff} is the effective index of the fiber at the probe wavelength, so that the probe wavelength must be greater than the Bragg wavelength of the grating by a factor of the effective index of the fiber. The input light is reflected at the incident angle, θ_i. In the weak scattering limit, the cross-section σ_i (as fraction of the incident peak-power density) is given by the following expression, assuming that the grating has a pure sinusoidal period [31], and the focused spot size w_i in the core is much greater than the core radius a:

$$\sigma_i \approx 1.66k^2a^3w_i\Delta n^2\frac{\sin^2\gamma_{core}}{\cos^2\theta_{core}}. \tag{9.3.7}$$

Here Δn is the local refractive index modulation amplitude, k is the wave vector at the incident wavelength λ_{probe}, and γ_{core} is the angle between the reflected and incident beams and ignores reflection losses. Owing to the geometry of the scattering region, γ_{core} is polarization sensitive and s-polarized light; the reflected power is maximum at $\gamma_{core} = \pi/2$.

Typical parameters used for the experiment are a beam waist of 5 μm, using a 10-mm focal length focused ~37 μm in front of the surface of the fiber to give a spot size of approximately 10 μm at the core (after focusing from the core–cladding surface) with an incident angle of 45.3°. The equivalent internal angle $\theta_{core} = 29.4°$. The input power needs to be high for a good signal-to-noise ratio, and was reported in the experiments to be 5 mW. The resolution in this arrangement is limited to the spot size of 10 μm.

The fiber grating is scanned in front of the fixed laser beam, so that the data may be recorded as a function of position along the grating. Good correlation between the measurement and the simulated transmission spectrum of the grating has been reported [31,35]. The side-diffraction profile of a Gaussian apodized grating is shown in Fig. 9.24. From this profile, it is simple to simulate the grating transfer function to establish a correlation.

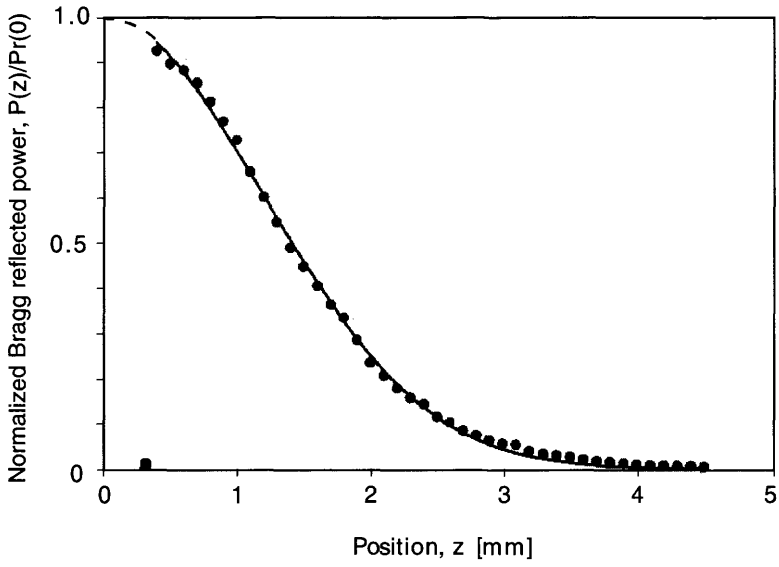

Figure 9.24: The profile of the light diffracted from a Bragg grating using the side-diffraction scheme (from: Krug P, Stolte R and Ulrich R, "Measurement of index modulation along an optical fiber Bragg grating", *Opt. Lett.*, **20**(17), 1767–1769, 1 September 1995. [31]).

The assumption of Eq. (9.3.7) restricts the application of this technique to gratings with *slowly* varying chirp by a variation of the grating period and to average refractive index ($\delta\lambda/\Lambda < 1^{-3}$), with no saturation in Δn. The chirp is limited by the numerical aperture of the focused beam.

Figure 9.25 shows the refractive index modulation profiles of four gratings commonly encountered in Bragg grating technology.

9.3.2 Measurement of internal stress

The refractive index changes induced by UV irradiation appear to affect the internal stress in the core [42]. There are conflicting observations, both of which are supported by experimental evidence [43]. In this section we consider the measurement of internal stress by optical means [44,45]. The technique is simple and requires the measurement of the state of the polarization of a focused spot of light (typically 3 μm diameter) transversely incident on the fiber, as it is scanned through the core region,

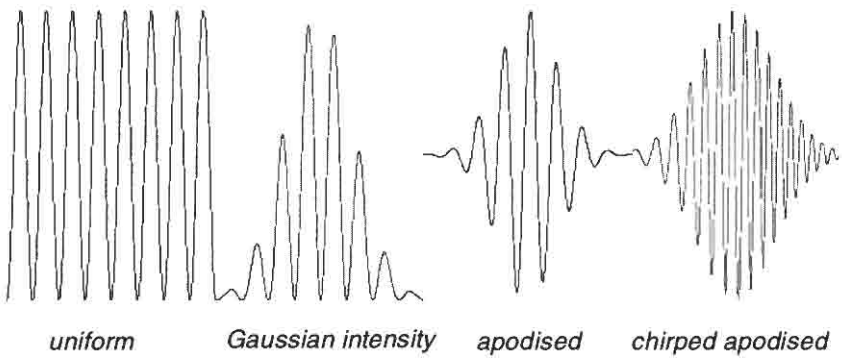

Figure 9.25: Four commonly encountered grating refractive index modulation profiles.

implemented by Fonjallaz *et al.* [46]. It therefore is a polarimetric measurement, which requires the polarization of the incident beam to be at 45° to the orthogonal birefringent axes of the fiber. The fiber is immersed in index-matching fluid to minimize beam deviations. The transmitted light is analyzed as a function of the translation distance of the incident beam. The retardation δ at the output provides the information on the stress distribution $\sigma_z(z)$ from an Abel integral equation [44],

$$\sigma_z(r) = -\frac{1}{\pi C}\int_r^R \frac{\delta'(y)}{\sqrt{y^2 - r^2}}\,dy, \tag{9.3.8}$$

where the prime indicates differentiation with respect to the transverse coordinate y, R is the radius of the fiber, and C is the stress-optic coefficient of silica. A change in the axial stress changes the refractive index by the stress-optic coefficient. The three components of the refractive index change, n_r, n_θ, and n_z, are related to the axial, circumferential, $\sigma_\theta(r)$, and radial, $\sigma_\rho(r)$ components of the stress-optic coefficients as [47]

$$\begin{aligned} n_r &= n_0 - B_2\sigma_r - B_1(\sigma_\theta + \sigma_z) \\ n_\theta &= n_0 - B_2\sigma_\theta - B_1(\sigma_r + \sigma_z) \\ n_z &= n_0 - B_2\sigma_z - B_1(\sigma_\theta + \sigma_z). \end{aligned} \tag{9.3.9}$$

In Eq. (9.3.9) the refractive index components are for light waves that have their electric field components in each of the three directions. The

refractive index of the fiber is n_0 without stress, and the stress-optic coefficients B_1 and B_2 are both positive, with $B_1 = 4.12 \times 10^{-5}$ mm^2 kg^{-1} and $B_2 = 0.64 \times 10^{-5}$ mm^2 kg^{-1} [48]. The radial component of the stress may be calculated from the axial component as [49]

$$\sigma_r(r) = \frac{1}{r^2}\int_r^R \sigma_z(s)sds. \tag{9.3.10}$$

The sign of the axial stress is found by measurements on silica fibers with and without strain, and through symmetry properties, $\sigma_r(r) = \sigma_\theta(r) = \sigma_z(r)/2$. The axial stress $\sigma_\theta(r)$ indicates positive axial tension for a positive sign and compressive strain with a negative sign.

By measuring the stress profile, the changes in the refractive index can be calculated as a function of the UV irradiation. Experiments performed by Fonjallaz *et al.* [46,50] have found that the axial stress increased with UV inscription of gratings, contrary to the stress-relief model [42]. The fibers are found to be either under slight axial compression or under tensile stress before UV irradiation (between -5 and $+1.6$ kg mm^{-2}). The stress changes before and after UV irradiation of a fiber with a Ge concentration of 12% are shown in Fig. 9.26. The maximum stress on the axis of the fiber is found to be 14.2 kg mm^{-2}. An increase in the tension

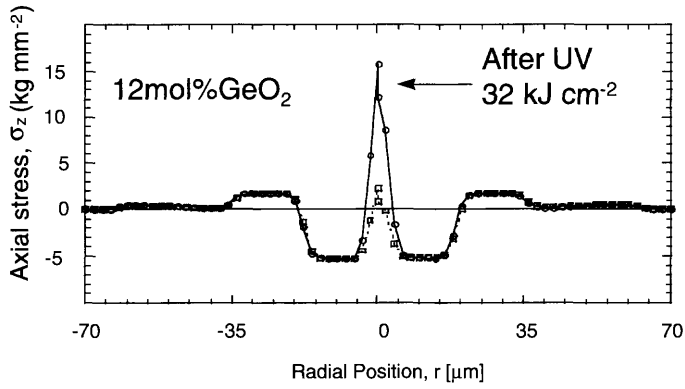

Figure 9.26: The measured radial stress profile of a fiber before and after the inscription of the grating (courtesy Hans Limberger [46]). (from: Fonjallaz P Y, Limberger H G, Salathé, Cochet F and Leuenberger B, "Tension increase corellated to refractive index change in fibers containing UV written Bragg gratings", *Opt. Lett.*, *20*(11), 1346–1348, 1 June 1995.)

is equivalent to a reduction in the refractive index; the implication is that the stress changes counter the overall change in the UV-induced refractive index, since this is *positive* (the Bragg wavelength moves to longer wavelengths with increase in refractive index of the core).

The net result of tension increase is that approximately 30% of the UV-induced refractive index change is *negative* and other factors, presumably compaction and changes in the UV absorption spectrum, increase the overall refractive index [51].

9.4 Strength, annealing, and lifetime of gratings

Reliability of fiber Bragg gratings is essential for long-term usage in telecommunications. There are two aspects that need to be taken into account: the mechanical strength and longevity of the grating. Mechanical strength of optical fiber is degraded through intense UV exposure, while the strength of the refractive index modulation of the grating begins to decay from the time of fabrication. The decay is slow but of concern unless treated. Careful handling and packaging of the UV-exposed grating may preserve the mechanical strength component.

The issue of mechanical strength is common with the deployment of optical fibers; they need to be tested to assure 25-year survivability. The process of grating inscription generally requires the removal of the protective primary coating of the fiber prior to exposure. While a special polymer may be used for through coating inscription [52], this is not generally the case. The mechanical removal damages the surface unless chemical means are used [53]. UV exposure can further reduce the strength [54]. Some form of protective coating must be applied to conserve the strength, if the fiber is to be handled mechanically [55].

9.4.1 Mechanical strength

The issue of mechanical reliability of in-fiber Bragg gratings has been extensively studied [56–58]. The degradation in the strength of a fiber is due to the growth of cracks on the surface at tiny flaws. Stress concentration at these flaws propagates and causes the fiber to fail. The failure strength can be dramatically lowered over that of pristine fiber. A convenient method of comparing the strength of different fibers is by the mea-

surement of dynamic fatigue. From the dynamic fatigue tests it is possible to predict the lifetime to failure by determining the distribution of flaws. The strength of optical fiber exposed to pulsed KrF radiation is dramatically reduced from a mean breaking strength of ~4.8 GPa for pristine fiber to 1.2 GPa. Recoating the fiber immediately after exposure restores the breaking strength. With CW 244-nm radiation, the strength is almost unchanged [59], but the long-term survivability is compromised, while hydrogen loading has little influence on the breaking strength. For a failure probability of 1×10^{-3}, the operational stress must be less than ~1 GPa for a 20-year lifetime [59], using a test length of 100 mm and a grating of ~8 mm.

9.4.2 Bragg grating lifetime and thermal annealing

The thermal stability of Bragg gratings is of prime importance if fabricated components are to function properly over their required life. For example, the a reduction in the reflectivity of a fiber Bragg grating used in an add–drop multiplexer from 40 to 30 dB could cause a degradation in crosstalk between channels. It is therefore essential to be able not only to predict the decay of the grating strength, but also to find ways to stabilize it.

Experimental observations of the decay in the reflectivity of gratings have resulted in a model that predicts the lifetime of gratings. It is generally agreed that observations on all fibers other than hydrogen-loaded follow a power-law dependence, originally proposed by Erdogan *et al.* [60,61]. The essential differences are the exact values of the coefficients that are used in the model.

The model proposes that the coupling constant of a grating $\kappa_{ac}L$ decays according to the following power law:

$$\eta = \frac{\kappa_{ac}L}{\kappa_{ac}L|_{t=0}} = \frac{1}{1 + At^{\alpha}}. \tag{9.4.1}$$

Here the denominator on the LHS is the initial value of the coupling constant at the time of writing of the grating. The constants A and α are temperature dependent and are found by plotting the normalized coupling constant η as a function of time. For convenience, the time parameter t may be normalized by unit time, e.g., 1 min to make Eq. (9.4.1) dimensionless. By measuring the decay of several gratings at different tempera-

tures as a function of time, and fitting the data with Eq. (9.4.1), the values of A and η can be evaluated for a particular fiber.

According to the model, the exponent $\alpha = T/T_0$ and $A = A_0 e^{\alpha T}$, so that T_0 is the fitted parameter when α is evaluated. Based on a theoretical approach, the model assumes that there is a distribution of trapped states after UV exposure (distribution of induced defects, DID). The thermal depopulation of these states into the conduction band has a release rate that is dependent on temperature and the energy E as

$$\nu(E) = \nu_0 e^{-E/k_B T}, \tag{9.4.2}$$

where k_B is the Boltzmann constant. States below the demarcation energy E_d may be easily depopulated at a given temperature T. The time taken to decay is related to the demarcation energy as

$$t \approx \frac{1}{\nu(E_d)}. \tag{9.4.3}$$

In Fig. 9.27 is shown the decay of the normalized coupling constant of gratings elevated to three different temperatures, Equation (9.4.1) can be expressed in terms of the release rate as

$$\eta = \frac{1}{1 + [\nu(E)t]^{\alpha}}. \tag{9.4.4}$$

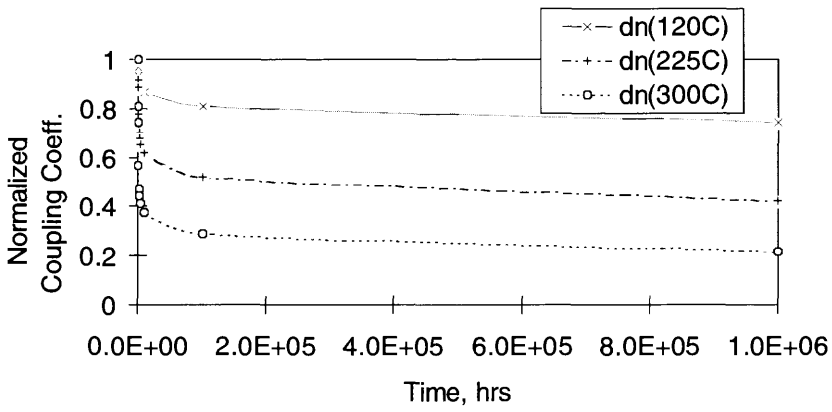

Figure 9.27: The thermal decay of boron–germanium codoped fibers, computed from the fitted data [62].

Using Eqs. (9.4.2)–(9.4.4), a Fermi–Dirac function describes the decay in the normalized coefficient,

$$\eta = \frac{1}{1 + e^{(E_d - E_0)/k_B T_0}}, \tag{9.4.5}$$

where E_0 is the peak of the distribution. We note that $A = v(E)^{\alpha}$ and is dependent on the release rate at energy E and on α. The distribution of the defects (DID) is calculated from Eqs. (9.4.2) and (9.4.5) and is

$$g(E) = \frac{N(0)}{k_B T} \frac{e^{(E-E_0)/k_B T_0}}{[1 + e^{(E-E_0)/k_B T_0}]^2}. \tag{9.4.6}$$

In Figure 9.27 is plotted the decay of the normalized coupling constant as a function of time for three different values of temperature [62]. The trend in the decay of the strength of gratings is typical. However, the magnitudes vary greatly. The computed A values from the fitted data to curves such as in Fig. 9.27 give the result shown in Fig. 9.28 in which a linear relationship may be seen when A is plotted on a logarithmic scale. This also ensures the validity of the data.

Alpha is similarly plotted in Fig. 9.29. Again, the linearity of the data should be such that it should pass through zero.

It turns out that the dependence of the decay of hydrogen-loaded boron-germanium fibers is much faster than that of unloaded fibers [62,63]. It has been speculated by the use of a more complex model that the DID in hydrogen-loaded fibers is not a single Gaussian distribution but a flat top [64,65]. It has also been suggested that the distribution

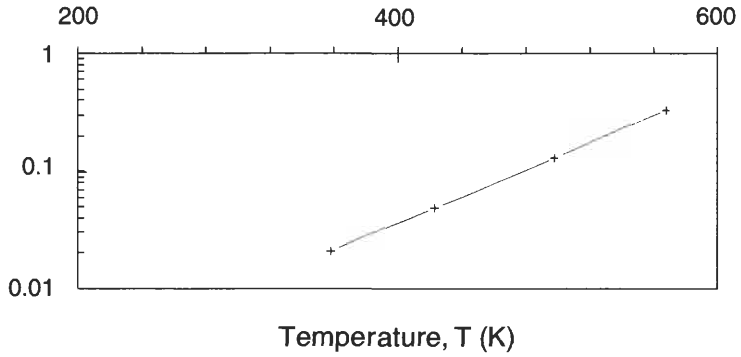

Figure 9.28: Relationship between A and the annealing temperature [62].

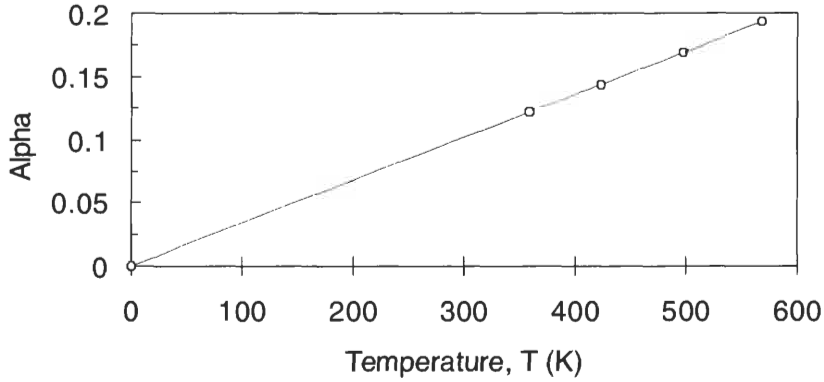

Figure 9.29: The fitted α to data on boron–germanium codoped fiber [62].

may be expressed as a stretched exponential [66]. However, there is no consensus as to a valid model. Riant *et al.* have pointed out the existence of at least two DIDs, and these are shown in Fig. 9.30. The contribution of each DID changes with temperature. It seems sensible that there may be several such DIDs, which play a role in determining the exact nature of the thermal decay of gratings.

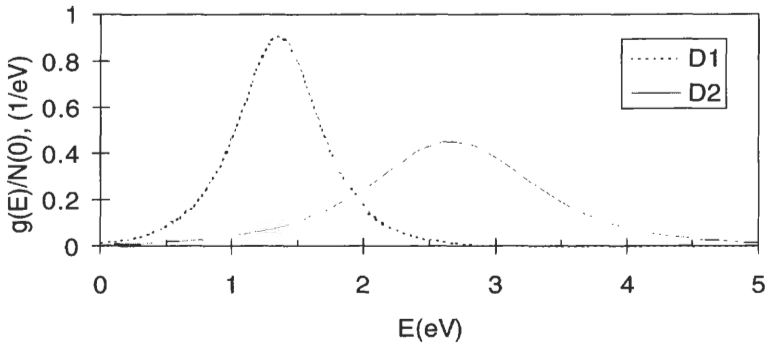

Figure 9.30: The distribution of the energy states of two DIDs in hydrogen-loaded fibers [67]. One defect is centered at 1.35 eV and has a narrow distribution, whereas the second, at 2.67 eV, has a much broader distribution.

9.4.3 Accelerated aging of gratings

Annealing a grating at an elevated temperature for a short time removes the fast decay, so that at lower temperatures, the decay rate slows down. This is the principle of accelerated aging [60,68]. The relationship between the annealing temperature T_2 and the lifetime of a grating operated at temperature T_1 is given by the simple relationship

$$t_2 = e^{aT_0[(T_1/T_2)-1]} t^{T_1/T_2}, \tag{9.4.7}$$

where the annealing time is t_2 and the time over which the grating is to be used is t_1. The parameter a has been defined in section 9.4.2.

The data for boron–germanium codoped fiber [62] with $a = 1.31 \times 10^{-2}\ \mathrm{K}^{-1}$ and $T_0 = 2941$ K is shown in Fig. 9.31, for an expected grating lifetime of 25 years at 300 K. The relationship between the time of annealing and the anneal temperature shows that annealing at 480 K for 1 min is equivalent to 25 years at 300 K. In order to ensure that the grating meets the specification for the application, this initial "burning-in" phase must be taken into account, since there is a reduction in the refractive index modulation.

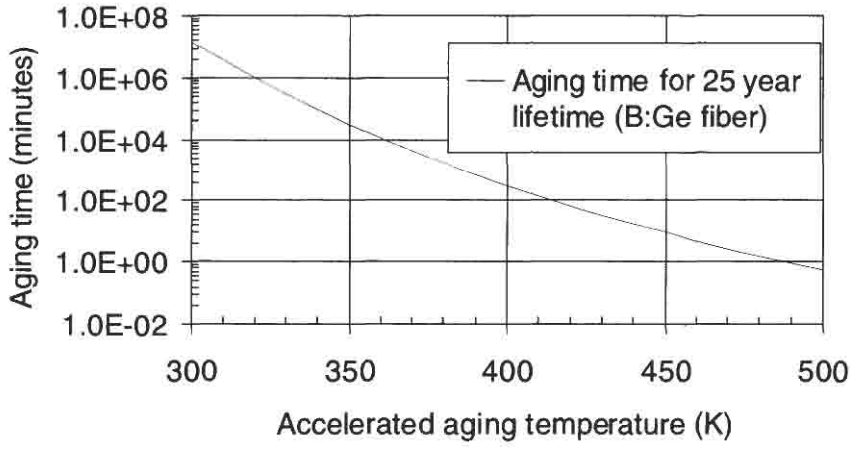

Figure 9.31: Accelerated aging characteristics of boron-germanium co-doped fiber [62], for a predicted lifetime of 25 years.
Accelerated aging characteristics of boron-germanium co-doped fiber [62], for a predicted lifetime of 25 years.

References

1. Mizrahi V. and Sipe J. E., "Optical properties of photosensitive fiber phase gratings," *J. Lightwave Technol.* **11**(10), 1513–1517 (1993).
2. Kashyap R., McKee P. F., Armes D. J., Shabeer M., and Cotter D. C., "Measurement of ultra-steep edge, high rejection fibre Bragg grating filters," *Electron. Lett.* **31**(15), 1282–1283 (1995).
3. Martin J., Lauzon J., Thibault S., and Ouellette F., "Novel writing technique of long highly reflective in fiber gratings and investigation of the linearly chirped component," post-deadline paper PD29-1, 138, *Proc. Conference on Optical Fiber Communications, OFC '94,* (1994).
4. Kashyap R., M. de Lathouwer, Emplit Ph, Haelterman M., Campbell R. J., and Armes D. J., "Dark soliton generation using a fibre Bragg grating," Photosensitivity and Quadratic Nonlinearity in Glass Waveguides: Fundamentals and Applications, OSA Annual Meeting, Oregon, 9–11 September, 1995.
5. Carballar A. and Muriel M. A., "Phase reconstruction from the reflectivity in fiber Bragg gratings," *J. Lightwave Technol.* **15**(8), 1314–1322 (1997).
6. Campbell R. J. and Kashyap R., "Spatial refractive index distribution of self-organized Bragg gratings in germanosilicate fiber," in *Tech. Digest of the Optical Soc. Am. Annual Meeting, OSA '93,* p. 148 (1993).
7. Ohn M. M., Huang S. Y., Sandgren S., and Mesures R., "Measurement of fiber grating properties using an interferometric and Fourier transform based technique," in *Conf. on Optical Fib. Commun., OFC '97,* pp. 154–155 (1997).
8. Barcelos S., Zervas M. N., and Laming R., "Characterization of chirped fiber Bragg gratings for dispersion compensation," *Opt. Fiber Technol.,* 213–215 (1996).
9. Sandel D. and Noé R., "Chirped fiber Bragg gratings for optical dispersion compensation: how to improve their fabrication accuracy," in *Tech. Digest of ECOC '96,* Vol. 2, pp. 233–236 (1996).
10. Hill K. O., Bilodeau F., Malo B., Kitagawa T., Theriault, Johnson D. C., and Albert J., "Aperiodic in fibre gratings for optical fiber dispersion compensation," in *Technical Digest of Post Deadline papers,* PD2-1, *Proc. Conference on Optical Fiber Communications, OFC '94,* (1999).
11. Devaux F., Sorel Y., and Kerdlies J. F., "Simple measurement of fiber dispersion and chirp parameter of intensity modulated light emitter," *J. Lightwave Technol.* **11**(12), 1937–1940 (1993).
12. Lauzon J., Thibault S., Martin J., and Ouellette O., "Implementation and characterization of fiber Bragg gratings linearly chirped by a temperature gradient," *Opt. Lett.* **19**(23), 2027–2029 (1994).

13. Roman J. E., Frankel M. Y., and Esman R. D., "High resolution technique for characterizing chirped fiber gratings," in *Tech. Digest of Conf. on Opt. Fib. Commun., OFC '98,* pp. 6–7 (1998).

14. Brinkmeyer E., Stolze G., and Johlen D., "Optical space domain reflectometry (OSDR) for determination of strength and chirp distribution of fiber gratings," in *Bragg Gratings, Photosensitivity, and Poling in Glass Fibers and Waveguides: Applications and Fundamentals,* Vol. 17, OSA Technical Digest Series (Optical Society of America, Washington, DC, 1997), paper BSuC2, pp. 33–35.

15. Nykolak G., Lenz G., Eggleton B. J., and Strasser T. A., "Impact of grating dispersion on WDM system performance," in *Tech. Digest of Conference on Optical Fiber Communications, OFC '98,* paper TuA3, pp. 4–5 (1998).

16. Sipe J. E., Eggleton B. J., and Strasser T. A., "Evolution of transmission dispersion characteristics of nonuniform gratings for DWDM systems," *ibid.,* paper TuA2, 3–4 (1998).

17. Lacerda-Rocha M. and Kashyap R., "Repeatability in the characterization of chirped Bragg gratings," in *Proc. Optical Fibers Measurements Conference, OFMC '98,* (1998).

18. Kashyap R. and Reeve M. H., "Single ended fibre strain and length measurement in the frequency domain," *Electron. Lett.* **16**(18), 689–690 (1980).

19. Kashyap R., Swanton A., and Armes D. J., "A simple technique for apodising chirped and unchirped fibre Bragg gratings," *Electron. Lett.* **32**(14), 1226–1228 (1996).

20. Malo B., Albert J., Kill K. O., Bilodeau F., and Johnson D. C., "Effective index drift from molecular hydrogen loaded optical fibres and its effect on Bragg *grating fabrication," Electron. Lett.* **30**(5), 442–444 (1994).

21. Bhakti F., Larrey J., Sansonetti P., and Poumellec B., "Impact of in-fiber and out-fiber diffusion on central wavelength of UV-written long period gratings," in *Bragg Gratings, Photosensitivity and Poling in Glass Fibers and Waveguides: Fundamentals and Applications,* Vol. 17, 1997 OSA Technical Series (Optical Society of America, Washington, DC, 1997), paper BSuD2, pp. 55–57 (1997).

22. Ouellette F. and Stephanov D. Y., "A new technique for measuring the group delay of chirped fiber Bragg gratings," in *Tech. Digest of Conf. on Opt. Fiber Commun., OFC '97,* pp. 153–154 (1997).

23. Meltz G. and Morey W. W., "Bragg grating formation and germanosilicate fiber photosensitivity," in *SPIE* **1516**, pp. 185–199 (1991).

24. Erdogan T. and Mizrahi V., "Characterization of UV induced birefringence in photosensitive Ge-doped silica optical fibers," *J. Opt. Soc. Am. B* **11**(10), 2100–2105 (1994).

25. Bonino S., Norgia M., Riccardi E., and Schiano M., "Measurement of polarisation properties of chirped fibre gratings," in *Technical Digest of OFMC '97,* pp. 10–13 (1997).

26. Ellis A. D., Kashyap R., Crisp I., Malyon D. J., and Heuting J. P., "Demonstration of an 80 Gb/s throughput reconfigurable dispersion compensating WDM Adm using deuterium sensitised 10 cm step chirped fibre Bragg gratings," in *Proc. of ECOC '97,* (1997).

27. Ouellette F., Krug P. A., and Pasman R., "Characterisation of long phase masks for writing fibre Bragg gratings," *Optical Fiber Technol.* **2**, 281–284 (1996).

28. Takada K., Yokohama I., Chida K., and Noda J., "New measurement system for fault location in optical waveguide devices based on an interferometric technique," *Appl. Opt.* **26**, 1603–1606 (1987).

29. Danielson B. L. and Wittenberg C. D., "Guidedwave reflectometry with micrometer resolution," *Appl. Opt.* **26**, 2836–2842 (1987).

30. Lambelet P., Fonjallaz P. Y., Limberger H. G., Salathé R. P., Zimmer C., and Gilgen H. H., "Bragg grating characterization by optical low-coherence reflectometry," *IEEE Phot. Technol. Lett.* **5**, 565–567 (1993).

31. Krug P., Stolte R., and Ulrich R., "Measurement of index modulation along an optical fiber Bragg grating," *Opt. Lett.* **20**(17), 1767–1769 (1995).

32. Margulis W., Carvalho I. C. S., and Govea P. M. P., "Heat scan: a simple technique to study gratings in fibers," *Opt. Lett.* **18**(12), 1016–1018 (1998).

33. Sandgren S., Sahlgren B., Asseh A., Margulis W., Laurell F., Stubbe R., and Lidgard A., "Characterization of Bragg gratings in fibers with the heat-scan technique," *Electron. Lett.* **31**, 665–666 (1995).

34. Loh W. H., Cole M. J., Zervas M. N., and Laming R. I., "Compensation of imperfect mask with moving fibre-scanning beam technique for production of fibre gratings," *Electron. Lett.* **31**(17), 1483–1485 (1995).

35. Ouellette F., Krug P. A., and Pasman R., "Characterisation of long phase masks for writing fibre Bragg gratings," in *Photosensitivity and Quadratic Nonlinearity in Glass Waveguides: Fundamentals and Applications,* Vol. 22, 1995 OSA Technical Series (Optical Society of America, Washington, DC, 1995), pp. 116–119.

36. Ouellette F., "The effect of profile noise on the spectral response of fiber gratings," in *Bragg Gratings, Photosensitivity, and Poling in Glass Fibers and Waveguides: Applications and Fundamentals,* Vol. 17, OSA Technical Digest Series (Optical Society of America, Washington, DC, 1997), paper BMG13, pp. 222–224.

37. Limberger H. G., Fonjallaz P. Y., Lambelet P., Salathé R. P., Zimmer C., and Gilgen H. H., "Fiber grating characterization by OLCR measurements," *European Conference on Optical Fibre Communications,* paper MoP2.1 (1993).

38. Malo B., Thériault S., Johnson D. C., Bilodeau F., Albert J., and Hill K. O., "Apodised in-fibre Bragg grating reflectors photoimprinted using a phase mask," *Electron. Lett.* **31**(3), 223—225 (1995).

39. Fonjallaz P. Y., Limberger H. G., and Salathé R. P., "Bragg grating with directional, efficient and wavelength selective fiber out coupling," in *Tech. Digest of Opt. Fiber Commun., OFC '95,* paper WN3, pp. 160–161 (1995).

40. Archambault J-L., Reekie L., and Russell P. St. J., "100% reflectivity Bragg reflectors produced in optical fibres by single excimer pulses," *Electron. Lett.* **29**(5), 453 (1993).

41. Janos M., Canning J., and Sceats M. G., "Incoherent scattering losses in optical fiber Bragg gratings," *Opt. Lett.* **21**(22), 1827–1829 (1996).

42. Sceats M. G. and Krug P., "Photoviscous annealing — dynamics and stability of photorefractivity in optical fibers," in *SPIE* **2044**, 113–120 (1993).

43. See, for example, Douay M., Xie W. X., Taunay T., Bernage P., Niay P., Cordier P., Poumellec B., Dong L., Bayon J. F., Poignant H., and Delevaque E., "Densification involved in the UV based photosensitivity of silica glasses and optical fibers," *J. Lightwave Technol.* **15**(8), 1329–1342 (1997).

44. Chu P. L. and Whitbread T., "Measurement of stress in optical fiber and preform," *Appl. Opt.* **21**, 4241–4245 (1982).

45. Bachmann P. K., Hermann W., Wher H., and Weichert D. U., "Stress in optical waveguides. 1: Preforms," *Appl. Opt.* **25**(7), 1093–1098 (1986).

46. Fonjallaz P. Y., Limberger H. G., Salathé R. P., Cochet F., and Leuenberger B., "Tension increase correlated to refractive index change in fibers containing UV written Bragg gratings," *Opt. Lett.* **20**(11), 1346–1348 (1995).

47. Scherer G. W., "Stress-induced index profile distribution in optical waveguides," *Appl. Opt.* **19**, 2000 (1980).

48. Primark W. and Post D., "Photoelastic constants of vitreous silica and its elastic coefficient of refractive index," *J. Appl. Phys.* **30**, 779 (1959).

49. Hermann, Hutjens W. and Wiechert D. U., "Stress in optical waveguides. 3: Stress induced index changes," *Appl. Opt.* **28**, 1980–1983 (1989).

50. Limberger H. G., Fonjallaz P. Y., Salathé R. P., and Cochet F., "UV induce stress changes in optical fibers," in *Photosensitivity and Quadratic Nonlinearity in Glass Waveguides: Fundamentals and Applications,* Vol. 22, 1995 OSA Technical Series (Optical Society of America, Washington, DC, 1995), paper SAD4, pp. 56–60.

51. Limberger H. G., Fonjallaz P. Y., Salathé R. P., and Cochet F., "Compaction- and photoelastic-induced index changes in fiber Bragg gratings," *Appl. Phys. Lett.* **68**, 3069–3071 (1996).

52. See, for example, Starodubov D. S., Grubsky V., Feinberg J., Dianov D., Semjonov S. L., Guryanov A. N., and Vechkanov N. N., "Fiber Bragg gratings with reflectivity >97% fabricated through polymer jacket using near-UV radiation," in *Bragg Gratings, Photosensitivity, and Poling in Glass Fibers and Waveguides: Applications and Fundamentals,* Vol. 17, OSA Technical Digest Series (Optical Society of America, Washington, DC, 1997), post-deadline paper PD1.

53. Limberger H. G., Valeras D., Salathé R. P., and Kotrotsios, "Mechanical degradation of optical fibers induced by UV light," *Proc. SPIE* **2841**, 84–93 (1996).

54. Feced R., Roe-Edwards M. P., Kanellopoulos S. E., Taylor N. H., and Handerek V. A., "Mechanical strength degradation of UV exposed optical fibres," *Electron. Lett.* **33**(2), 157–159, 16 January 1997.

55. Putnam M. A., Askins C. G., Smith G., and Fribele E. J., "Method for recoating fiber Bragg gratings with polyimide," in *Industrial and Commercial Applications of Smart Structures Technology,* Slater J. A., Vol. 2044 pp. 359–362. SPIE, Bellingham, WA (1997).

56. Kapron F. P. and Yuce H. H., "Theory and measurement for predicting stressed fiber lifetime," *Opt. Eng.* **30**(6), 700–708 (1991).

57. Mitsunaga Y., Katsuyama Y., Kobayashi H., and Ishida Y., "Failure prediction for long-length optical fibers based on proof testing," *J. Appl. Phys.* **53**(7), 700 (1982).

58. See, for example, *Proc. of the First European COST Workshop 246 on Bragg grating Reliability,* IOA-EPFL (1995).

59. Limberger H. G., Valeras D., and Salathé R. P., "Reliability aspects of fiber Bragg gratings," in *Proc. of Optical. Fibre Meas. Conf., OFMC '97,* 18–123 (1997).

60. Erdogan T. and Mizrahi V., "Decay of UV induced fiber Bragg gratings," *Proc. Optical Fiber Conference, OFC '94,* p. 50 (1994).

61. Erdogan T., Mizrahi V., Lemaire P. J., and Monroe D., "Decay of ultraviolet-induced fiber Bragg gratings," *J. Appl. Phys* **76**(1), 73–80 (1994).

62. Baker S. R., Rourke H. N., Baker V., and Godchild D., "Thermal decay of fiber Bragg gratings written in boron and germanium codoped silica fiber," *J. Lightwave Technol.* **15**(8), 1470–1477 (1997).

63. Patrick H., Gilbert S. L., Lidgard A. and Gallagher M. D., "Annealing of Bragg gratings in hydrogen loaded optical fibers," *J. Appl. Phys.* **78**(5), 2940–2945 (1995).

64. Guo J. Z. Y., Kannan S. and Lemaire P. J., "Thermal stability of optical add/drop gratings for WDM systems," in *Tech. Digest of OFC '97,* paper ThJ6, pp. 285 (1997).

65. Kannan S., Gou J. Z. Y., and Lemaire P. J., "Thermal reliability of strong Bragg gratings written in hydrogen sensitized fibers," in *Tech. Digest of OFC '97* paper TuO4, pp. 84–85 (1996).

66. Egan R. J., Inglis H. G., Hill P., Krug P. A., and Ouellette F., "Effects of hydrogen loading and grating strength on the thermal stability of fiber Bragg grating," in *Tech. Digest of OFC '96,* paper TuO3, pp. 83–84 (1996).

67. Robert G. and Riant I., "Demonstration of two distributions of defect centers in hydrogen loaded high germanium content fibers," in *Tech. Digest of OFC '97,* paper WL18, pp. 180–181 (1997).

68. Williams D. L. and Smith R. P., "Accelerated lifetime tests on UV written intracore gratings in boron germanium co-doped silica fibre," *Electron. Lett.* **31**(24), 2120–2121 (1995).

Index

Optics and Photonics
(Formerly Quantum Electronics)

N.S. Kapany and J. J. Burke, *Optical Waveguides*
Dietrich Marcuse, *Theory of Dielectric Optical Waveguides*
Benjamin Chu, *Laser Light Scattering*
Bruno Crosignani, Paolo DiPorto and Mario Bertolotti, *Statistical Properties of Scattered Light*
John D. Anderson, Jr., *Gasdynamic Lasers: An Introduction*
W. W. Duly, *CO_2 Lasers: Effects and Applications*
Henry Kressel and J. K. Butler, *Semiconductor Lasers and Heterojunction LEDs*
H. C. Casey and M. B. Panish, *Heterostructure Lasers: Part A. Fundamental Principles; Part B. Materials and Operating Characteristics*
Robert K. Erf, Editor, *Speckle Metrology*
Marc D. Levenson, *Introduction to Nonlinear Laser Spectroscopy*
David S. Kilger, editor, *Ultrasensitive Laser Spectroscopy*
Robert A. Fisher, editor, *Optical Phase conjugation*
John F. Reintjes, *Nonlinear Optical Parametric Processesi n Liquids and Gases*
S. H. Lin, Y. Fujimura, H. J. Neusser and E. W. Schlag, *Multiphoton Spectroscopy of Molecules*
Hyatt M. Gibbs, *Optical Bistability: Controlling Light with Light*
D. S. Chemla and J. Zyss, editors, *Nonlinear Optical Properties of Organic Molecules and Crystals, Volume 1, Volume 2*
Marc D. Levenson and Saturo Kano, *Introduction to Nonlinear Laser Spectroscopy, Revised Edition*
Govind P. Agrawal, *Nonlinear Fiber Optics*
F. J. Duarte and Lloyd W. Hillman, editors, *Dye Laser Principles: With Applications*
Dietrich Marcuse, *Theory of Dielectric Optical Waveguides, 2nd Edition*
Govind P. Agrawal and Robert W. Boyd, editors, *Contemporary Nonlinear Optics*
Peter S. Zory, Jr. editor, *Quantum Well Lasers*
Gary A. Evans and Jacob M. Hammer, editors, *Surface Emitting Semiconductor Lasers and Arrays*
John E. Midwinter, editor, *Photonics in Switching, Volume I, Background and Components*
John E. Midwinter, editor, *Photonics in Switching, Volume II, Systems*
Joseph Zyss, editor, *Molecular Nonlinear Optics: Material, Physics, and Devices*
Mario Dagenais, Robert F. Leheny and John Crow, *Integrated Optoelectronics*
Govind P. Agrawal, *Nonlinear Fiber Optics, Second Edition*
Jean-Claude Diels and Wolfgang Rudolph, *Ultrashort Laser Pulse Phenomena: Fundamentals, Techniques, and Applications on a Femtosecond Time Scale*
Eli Kapon, editor, *Semiconductor Lasers I: Fundamentals*
Eli Kapon, editor, *Semiconductor Lasers II: Materials and Structures*
P. C. Becker, N. A. Olsson, and J. R. Simpson, *Erbium-Doped Fiber Amplifiers: Fundamentals and Technology*
Raman Kashyap, *Fiber Bragg Gratings*